Cerium Complexes for
para-Quinone and Carbon Dioxide
Activation

DISSERTATION

der Mathematisch-Naturwissenschaftlichen Fakultät

der Eberhard Karls Universität Tübingen

zur Erlangung des Grades eines

Doktors der Naturwissenschaften

(Dr. rer. nat.)

vorgelegt von

M. Sc. Uwe Bayer

aus Hermannstadt/Rumänien

Tübingen

2020

Gedruckt mit Genehmigung der Mathematisch-Naturwissenschaftlichen Fakultät der Eberhard Karls Universität Tübingen.

Cerium Complexes for

para-Quinone and Carbon Dioxide

Activation

Uwe Bayer

Preface

The following PhD thesis consists of a survey on the reactivity of rare-earth-metal complexes toward carbonylic compounds and carbon dioxide, a summary of the main results, and original scientific papers. The work has been carried out at the Institut für Anorganische Chemie of the Eberhard Karls Universität Tübingen, Germany, over the period from May 2017 to September 2020 under the supervision of Prof. Dr. Reiner Anwander. Funding has been gratefully received from the Deutsche Forschungsgemeinschaft (DFG).

Parts of this thesis have been presented at international and national conferences as poster contributions.

Acknowledgements

First of all, I would like to thank my supervisor Prof. Dr. Reiner Anwander. Thank you for accepting me in your high standard synthesis laboratory, providing me with this very interesting research topic, and for your helpful advices in any scientific problem. Thank you for giving me the opportunity to attend international and national conferences to present my work and exchange with other researchers.

Special thanks go to Dr. Cäcilia Maichle-Mössmer for all help regarding crystal structure determinations and your helpful discussions. Further thanks to Dr. Daniel Werner for his kind introduction into the world of cerium redox chemistry.

My thanks also go to Dr. Klaus Eichele and Kristina Strohmaier for maintaining the high standard equipment, as well as their help in all aspects regarding NMR spectroscopy. Additionally, I'd like to thank Dr. Wolfgang Leis, Dominik Brzecki, and Dr. Andreas Berkefeld for conducting the DOSY NMR and EPR experiments and Wolfgang Bock for performing elemental analyses.

I further thank Tobias Wolf and especially Elke Niquet for their maintaining the laboratory equipment and their friendly and always helpful nature. Many thanks to Sabine Ehrlich for all her administrative work and helping me to understand any kind of form and to Nadja Wettering for her IT support. Additionally, I want to thank the staff of the metal, electronics and glass workshops for manufacturing and repairing lab equipment.

I also would like to thank my current and former coworkers of the Anwander group. Especially Dr. Verena Birkelbach, Dr. Lorenz Bock, Alexandros Mortis, and Dr. Renita Thim-Spöring for all the nice moments with you in and outside of the lab, for all the discussions, chemistry related or not, and for your friendship. Further thanks go to Damir Barisic, Tassilo Berger, Martin Bonath, Denis Burghardt, Dennis Buschmann, Dr. Dominic Diether, Dr. Jochen Friedrich, Dr. Christoph Hollfelder, Markus Katzenmayer, Felix Kracht, Lars Hirneise, Jakob Lebon, Dr. Yucang Liang, Dr. Leilei Luo, Eric Moinet, Theresa Rieser, Dr. Dorothea Schädle, Dr. David Schneider, Andrea Sonström, Georgios Spiridopoulos, Dr. Christoph Stuhl, Simon Trzmiel, Dr. Benjamin Wolf, for the very supportive and friendly atmosphere in the lab.

Verena, thank you for being the great person you are! Finding my love and spending so much time at work and in private life with you is such a great gift. Thank you for your love and support every day!

Zu guter Letzt möchte ich mich ganz herzlich bei meiner Familie bedanken. Meinen Eltern (Margareta und Hans-Dieter) sowie meinem Bruder Udo, gilt mein Dank für ihre uneingeschränkte Unterstützung jeglicher Art vor und während meines Studiums und während der Doktorarbeit.

Contents

Abbreviations

Ar	Aryl	Dipp	2,6-Di*iso*propylphenyl
Bn	Benzyl	do	Donor
bq	*p*-Benzoquinone	DOSY	Diffusion-ordered spectroscopy
*n*Bu	*n*-Butyl	DRIFT	Diffuse Reflectance Infrared Fourier Transform
*t*Bu	*tert*-Butyl	EA	Elemental Analysis
cbz	Carbazolyl	*e.g.*	*exempli gratia*
COSY	Correlated Spectroscopy	EPR	Electron Paramagnetic Resonance
Cp	Cyclopentadienyl	Et	Ethyl
Cp*	C_5Me_5	*et al.*	*et alii* or *et aliae*
Cp'	$C_5H_4SiMe_3$	HMBC	Heteronuclear Multiple Bond Correlation
Cp''	$C_5Me_4SiMe_3$	HMPA	Hexamethylphosphoramide
CV	Cyclic Voltammetry	HSQC	Heteronuclear Single Quantum Coherence
DEPT	Distortionless Enhancement by Polarization Transfer	INEPT	Insensitive Nuclei Enhanced by Polarization Transfer
DME	Dimethoxyethane	IR	Infrared
Ln	Rare-earth metals (Sc, Y, La – Lu)	Py	Pyridine

Me	Methyl	r.t.	Ambient temperature
Me$_2$pz	Dimethylpyrazolyl	SBA	Santa Barbara Amorphous
MMA	Methyl methacrylate	sq	Semiquinone
Nacnac	1,3-Diketiminato	TBAB	Tetra-*n*-butyl ammonium bromide
NHC	N-heterocyclic carbene	TGA	Thermogravimetric analysis
NMR	Nuclear Magnetic Resonance	TMEDA	Tetramethylethylenediamine
OEP	Octaethylporphyrin	THF	Tetrahydrofuran
OTf	Triflato	Tp^{Me,Me}	Tris(3,5-dimethyl-pyrazolyl) borato
Ph	Phenyl	UV-Vis	Ultraviolet–Visible
*i*Pr	*iso*-Propyl	VT	Variable temperature
pyr	Pyrrolyl		

Summary

Due to its readily accessible tetravalent oxidation state, the element cerium occupies a special position within the rare-earth metal series (Sc, Y, La-Lu). Even though organometallic cerium redox chemistry has gained a lot of interest in the past years, it offers still enigmas in its chemistry, which need to be solved.

At first, the literature-known synthesis for ceric amide complex [Ce{N(SiHMe$_2$)$_2$}$_4$], a versatile precursor for the synthesis of homoleptic Ce^{IV} compounds, was investigated. Separation of the Li cation in ate-complex [Ce{N(SiHMe$_2$)$_2$}$_4$Li(thf)] by introducing donor molecules (d) other than THF, and subsequent oxidation of the resulting complexes [Ce{N(SiHMe$_2$)$_2$}$_4$][Li(do)$_x$] with 1,4-benzoquinone, leads to a cleaner product in higher yields than the previously known syntheses.

Further, the investigation of tetravalent hydroquinolato-bridged cerium compounds of the composition [(CeL$_3$)$_2$(μ-O$_2$C$_6$R$_4$)] were of interest. Therefore, homoleptic trivalent cerium precursors were oxidized with 1,4-benzoquinone derivatives. After successful oxidation, the isolated compounds were electrochemically examined in their stabilization of the tetravalent oxidation state. Using Ce^{III} siloxides as precursors together with tetramethyl-1,4-benzoquinone, the isolation and characterization of cerous semiquinolato complexes [(CeL$_2$(thf)$_2$)$_2$(μ-O$_2$C$_6$Me$_4$)$_2$] (L = OSi(OtBu)$_3$ or OSiiPr$_3$) was feasible.

Lastly, the reactivity of both homoleptic Ce^{III} and Ce^{IV} dimethyl pyrazolates [Ce$_4$(Me$_2$pz)$_{12}$] and [Ce(Me$_2$pz)$_4$]$_2$ as well as silica grafted rare-earth-metal pyrazolates toward CO$_2$ was examined, showing the reversible insertion of carbon dioxide into the Ce$-$N(Me$_2$pz) bond. Molecular CO$_2$-inserted products [Ce$_4$(Me$_2$pz·CO$_2$)$_{12}$] and [Ce(Me$_2$pz·CO$_2$)$_4$] were synthesized and investigated in reversibility of the CO$_2$ insertion in solution and the solid state. For the hybrid materials, a reversible CO$_2$ uptake of up to 20 wt% has been observed in the solid state. Both complexes as well as the hybrid materials showed catalytic activity in cycloaddition reactions of carbon dioxide and epoxides. Especially ceric [Ce(Me$_2$pz)$_4$]$_2$ exhibited good turnover numbers for less sterically demanding epoxides, even under mild conditions. Further, also for sterically demanding as well as internal epoxides, it showed good turnover numbers at elevated temperatures and CO$_2$ pressures as well. While silica grafted-hybrid materials did not increase the catalytic activity, the reusability was tremendously affected.

Zusammenfassung

Aufgrund der einfach zugänglichen vierwertigen Oxidationsstufe nimmt das Element Cer eine Sonderstellung unter den Seltenerdmetallen (Sc, Y, La-Lu) ein. Obwohl der Cer-basierten metallorganischen Redoxchemie in den letzten Jahren viel Interesse gewidmet wurde, wirft sie weiterhin grundlegende Fragestellungen auf.

Zunächst wurde die literaturbekannte Synthese des Cer-Amid-Komplexes $[Ce\{N(SiHMe_2)_2\}_4]$, welcher eine vielseitige Vorstufe für homoleptische Ce^{IV}-Komplexe darstellt, untersucht. Die Separation des Li-Kations im At-Komplex $[Ce\{N(SiHMe_2)_2\}_4Li(thf)]$ durch Einführung anderer Donormoleküle (do) sowie die anschließende Oxidation der entstandenen $[Ce\{N(SiHMe_2)_2\}_4][Li(do)_x]$ mit 1,4-Benzochinon führte zu einem saubereren Produkt in höheren Ausbeuten als bei publizierten Synthesen.

Weiterhin war die Untersuchung von vierwertigen, Hydrochinolat-verbrückten Cer-Verbindungen mit der Zusammensetzung $[(CeL_3)_2(\mu\text{-}O_2C_6R_4)]$ von Interesse. Hierbei wurden homoleptische, dreiwertige Cer-Silylamid- und -Siloxid-Vorstufen mit 1,4-Benzochinonderivaten oxidiert. Nach erfolgreicher Oxidation wurden die isolierten Verbindungen elektrochemisch auf ihre Stabilisierung der vierwertigen Oxidationsstufe hin untersucht. Bei Verwendung von Ce^{III}-Siloxiden als Vorstufen zusammen mit Tetramethyl-1,4-Benzochinon konnten die dreiwertigen Cer-Semichinolate $[(CeL_2(thf)_2)_2(\mu\text{-}O_2C_6Me_4)_2]$ (L = $OSi(OtBu)_3$ oder $OSiiPr_3$) isoliert und charakterisiert werden.

Sowohl die homoleptischen Ce^{III}- und Ce^{IV}-Dimethylpyrazolate $[Ce_4(Me_2pz)_{12}]$ und $[Ce(Me_2pz)_4]_2$ als auch auf Silica immobilisierte Seltenerdmetall-Pyrazolate insertieren unerwartet effektiv Kohlenstoffdioxid in die $Ce-N(Me_2pz)$-Bindung unter Ausbildung von $[Ce_4(Me_2pz\cdot CO_2)_{12}]$ und $[Ce(Me_2pz\cdot CO_2)_4]$. Die Reversibilität der CO_2-Insertion konnte in Lösung und Festkörper nachgewiesen werden. Die Hybridmaterialien zeigten eine reversible CO_2 Aufnahme von bis zu 20 Gew%. Die Komplexe wie auch die Hybridmaterialien erwiesen sich außerdem in der Cycloaddition von Kohlenstoffdioxid und Epoxiden als katalytisch aktiv. Besonders das vierwertige $[Ce(Me_2pz)_4]_2$ wies ausgezeichnete Umsatzzahlen für sterisch weniger anspruchsvolle Substrate (Epoxide), unter milden Bedingungen auf. Weiterhin ergaben sich auch für sterisch anspruchsvollere sowie interne Epoxide gute Umsatzzahlen bei erhöhter Temperatur und höheren CO_2-Drücken. Während die Hybridmaterialien keine Steigerung der katalytischen Aktivität aufwiesen, konnte jedoch ihre Wiederverwertbarkeit gezeigt werden.

Publications

Publications incorporated into this thesis

Paper I A Facile Route toward Ceric Silylamide [Ce{N(SiHMe$_2$)$_2$}$_4$]

U. Bayer, L. Bock, C. Maichle-Mössmer, R. Anwander

Eur. J. Inorg. Chem. **2020**, 101 – 106

https://doi.org/10.1002/ejic.201901023

Paper II Effective and Reversible Carbon Dioxide Insertion into Cerium Pyrazolates

U. Bayer, D. Werner, C. Maichle-Mössmer, R. Anwander

Angew. Chem. Int. Ed. **2020**, *59*, 5830 – 5836

Angew. Chem. **2020**, *132*, 5879 – 5885

https://doi.org/10.1002/anie.201916483

https://doi.org/10.1002/ange.201916483

Paper III Cerium Pyrazolates Grafted onto Mesoporous Silica SBA-15: Reversible CO$_2$ Uptake and Catalytic Cycloaddition of Epoxides and Carbon Dioxide

U. Bayer, Y. Liang, R. Anwander

Inorg. Chem. **2020**, *59,* 14605 – 14614

https://doi.org/10.1021/acs.inorgchem.0c02502

Paper IV The cerium–quinone redox couples put under scrutiny

U. Bayer, D. Werner, A. Berkefeld, C. Maichle-Mössmer, R. Anwander

Chem. Sci. **2021**, DOI: 10.1039/D0SC04489J

https://doi.org/10.1039/D0SC04489J

Publications with minor contributions

Paper V Unique and contrasting structures of homoleptic lanthanum(III) and cerium(III) 3,5-dimethylpyrazolates

D. Werner, U. Bayer, N. E. Rad, P. C. Junk, G. B. Deacon, R. Anwander

Dalton Trans. **2018**, *47*, 5952 – 5955

https://doi.org/10.1039/C8DT00338F

Paper VI   Emergence of a New [NNN] Pincer Ligand via Si–H-Bond Activation and *β*-Hydride Abstraction at Tetravalent Cerium

D. Werner, U. Bayer, D. Schädle, R. Anwander

Chem. Eur.J. **2020** *26*, 12194 – 12205

https://doi.org/10.1002/chem.202000625

Poster presentations

Poster I   Effect of Donor Ligand on the Oxidizability of ate-complex $[Ce[N(SiHMe_2)_2]_4Li(thf)]$

U. Bayer, L. Bock, R. Anwander

XXVIII. Tage der Seltenen Erden, Tübingen, Germany, *October 4-6*, **2017**.

Poster II   Cerium Benzoquinone Redox Chemistry

U. Bayer, D. Werner, C. Maichle-Mössmer, R. Anwander

43rd International Conference on Coordination Chemistry ICCC, Sendai, Japan, *July 30-August 4*, **2018**.

Poster III   Reactivity of Cerium towards Benzoquinone Derivatives

U. Bayer, D. Werner, C. Maichle-Mössmer, R. Anwander

19. Vortragstagung f. Anorganische Chemie der Fachgruppen Wöhler-Vereinigung u. Festkörperchemie u. Materialforschung, Regensburg, Germany, *September 24-27,* **2018**.

Personal Contribution

Paper I:

All reactions and analyses described were planned and conducted by Lorenz Bock and myself. Analyses include one-dimensional (^{1}H, ^{7}Li$\{^1$H$\}$) NMR spectroscopic methods, and DRIFT spectroscopy. Manuscript writing was also done by Lorenz Bock and me.

Elemental analyses were performed by Wolfgang Bock. The structural analyses by single crystal X-ray diffraction were performed by Dr. Cäcilia Maichle-Mössmer and myself.

Paper II:

All reactions and analyses described were planned and conducted by myself (except [Ce(Me$_2$pz)$_4$(thf)] and [Ce$_3$(Me$_2$pz)$_9$(Me$_2$pz·CO$_2$)$_3$(thf)]). Analyses include one-dimensional (^{1}H, ^{13}C$\{^1$H$\}$) NMR spectroscopic methods, DRIFT and *in situ* IR spectroscopy. Manuscript writing was also done by me. The synthesis and characterization of [Ce(Me$_2$pz)$_4$(thf)] and [Ce$_3$(Me$_2$pz)$_9$(Me$_2$pz·CO$_2$)$_3$(thf)] was done by Dr. Daniel Werner.

Elemental analyses were performed by Wolfgang Bock, TGA measurements by Arin-Daniel Fuhrmann, and DOSY NMR spectra by Dr. Wolfgang Leis. The structural analyses by single crystal X-ray diffraction were performed by Dr. Cäcilia Maichle-Mössmer, Dr. Daniel Werner and myself.

Paper III:

All reactions and analyses described were planned and conducted by myself (except of parent material SBA-15$_{500}$). Analyses include one-dimensional (^{1}H) NMR spectroscopy, DRIFT spectroscopy, and N$_2$-physisorption. Manuscript writing was also done by me. Synthesis and characterization of parent material SBA-15$_{500}$ was done by Dr. Yucang Liang and determination of the surface Si−OH groups was conducted by Alexandros Mortis.

Elemental analyses were performed by Wolfgang Bock, ^{1}H MAS and ^{13}C CP/MAS NMR spectroscopic measurements were done by Stefanie Wagner. The structural analyses by single crystal X-ray diffraction were performed by Dr. Cäcilia Maichle-Mössmer and myself.

Paper IV:

All reactions and analyses described were planned and conducted by myself (except [Ce$_3$(bpad)(pasq)(Me$_2$pz)$_6$(thf)], [Ce(Me$_2$pz)$_2$(μ-O$_2$C$_{14}$H$_8$)(thf)$_2$]$_2$ and [{Ce(tBu$_2$pz)$_3$(thf)}$_2$(μ-O$_2$C$_6$Me$_4$)]). Analyses include one-dimensional (^{1}H, ^{13}C{^{1}H}, ^{29}Si DEPT45 and ^{29}Si INEPTND), two-dimensional (^{1}H-^{13}C HSQC, ^{1}H-^{13}C HMBC, ^{1}H-^{1}H COSY, ^{1}H-^{29}Si HSQC) NMR spectroscopic methods, DRIFT spectroscopy, UV-Vis spectroscopy, CV experiments, and Evans' Method (magnetic moment). Manuscript writing was also done by me. The crystal structures of [(Ce{N(SiMe$_3$)$_2$}$_3$)$_2$(μ-O$_2$C$_6$Me$_4$)] and [(Ce{N(SiMe$_3$)$_2$}$_3$)$_2$(μ-O$_2$C$_6$$tBu_2H_2$)] were obtained by Dr. Daniel Werner. The synthesis and characterization of [Ce$_3$(bpad)(pasq)(Me$_2$pz)$_6$(thf)], [Ce(Me$_2$pz)$_2$(μ-O$_2$C$_{14}$H$_8$)(thf)$_2$]$_2$ and [{Ce(tBu$_2$pz)$_3$(thf)}$_2$(μ-O$_2$C$_6$Me$_4$)] were done by Dr. Daniel Werner.

Some reactions and analyses were conducted during my master thesis.

Elemental analyses were performed by Wolfgang Bock, ^{1}H-^{29}Si HSQC NMR was done by Alexandros Mortis and EPR measurements by Dominik Brzecki and Dr. Andreas Berkefeld. The structural analyses by single crystal X-ray diffraction were performed by Dr. Cäcilia Maichle-Mössmer, Dr. Daniel Werner and myself.

Paper V:

The synthesis of [Ce$_4$(Me$_2$pz)$_{12}$]·¾-hexane starting from CeCl$_3$(thf)$_{1.04}$ was reproduced by myself and variable temperature ^{1}H NMR studies have been conducted by Kristina Strohmaier. NMR scale protonolysis reactions of [Ce{N(SiMe$_3$)$_2$}$_3$] with various equivalents of Me$_2$pzH as well as the ^{1}H NMR spectroscopic analyses of [Ce$_4$(Me$_2$pz)$_{12}$]·¾-hexane and [Ce(Me$_2$pz)$_3$]$_n$ in THF-d_8 were done by myself.

Paper VI:

The syntheses of [Ce{N(SiHMe$_2$)$_2$}$_4$] and [Ce(Me$_2$pz)$_4$]$_2$·½toluene starting from CeCl$_3$(thf)$_{1.04}$ were reproduced by myself. NMR-scale reactions of [Ce{N(SiHMe$_2$)$_2$}$_4$] with [Ce(Me$_2$pz)$_4$]$_2$·½toluene and [Ce(Me$_2$pz)$_4$]$_2$·½toluene with H$_2$ were conducted and ^{1}H NMR spectroscopic analyses of the reactions were done by myself.

Objective of this Thesis

The main emphasis of this thesis is to investigate the reactivity of trivalent and tetravalent cerium complexes toward different carbonylic compounds.

Chapter A gives an overview of the activation of carbonylic groups mediated by rare-earth-metal complexes. Focus will be on the insertion products of ketones, redox-enhanced carbonyl activation, the activation of carbon dioxide as well as in homogenous catalytic conversion of CO_2.

Chapter B contains a summary of the main results of this thesis and is divided in three parts:

- Optimization of the Synthesis of Ceric [Ce{N(SiHMe$_2$)$_2$}$_4$]
- Cerium Pyrazolates in Carbon Dioxide Activation
- Cerium Benzoquinone Redox Chemistry

In **Chapter C** unpublished results, which are not part of a publication or manuscript, are presented. This contains further cerium pyrazolates and cerium pyrrolates.

Chapter E is a compilation of publications.

A

Rare-Earth Metal Mediated Carbonyl-Group Activation

1 Introduction

Due to their high oxophilicity and their distinct LEWIS acidity, rare-earth metal (Sc, Y, La-Lu) compounds efficiently activate carbonylic C=O double bonds. Therefore, it is not surprising that numerous syntheses of organic compounds involving a carbonylic substrate are conducted using rare-earth-metal complexes either in stoichiometric or catalytic amounts. A prominent example for versatile use in organic synthesis are rare-earth-metal triflates, which have been employed as LEWIS acidic catalysts for many years.[1] Also known for a long time is the "GRIGNARD-like" reduction of ketones with divalent lanthanides Sm and Yb[2–6] or the C−C coupling reactions promoted by CeCl3/LiR or Ce-amalgam to promote.[7–10] Similarly, ceric ammonium nitrate (CAN) is known to mediate C−C coupling reactions, incorporating carbonylic compounds and also for its application in oxidation reactions of alcohols to produce C=O double bonds.[11,12] Rare-earth-metal complexes, in particular alkoxides, also catalyze the MEERWEIN-PONNDORF-VERLEY reduction. Hereby, aldehydes and ketones are reduced to the corresponding alcohol in the presence of sacrificed alcohol L (L = solvent, iPrOH in general).[13–18] It is noteworthy to mention that the reversed reaction, the OPPENAUER oxidation, can also be mediated by rare-earth-metal complexes. Furthermore, rare-earth-metal methylidenes and alkylidenes can react in TEBBE analogous C−O metathesis reactions with ketones giving lanthanide-oxo species and terminal olefins.[19–28] Rare-earth-metal complexes are not only known for their catalytic or stoichiometric transformations of ketones and aldehydes, but also for initiating polymerization reactions involving carbonylic monomers. These polymerization reactions include ring-opening polymerizations of lactones[29–41], polymerization of methacrylates[31,36,42–45] or co-polymerization of lactones and olefins.[46–50]

Moreover, rare-earth metals are capable of activating carbon dioxide. Being one of the main greenhouse gases, the conversion of CO_2 is an essential target of modern chemistry.[51–55] For instance, lanthanide complexes have revealed promising performance as catalysts in co-polymerization of carbon dioxide and epoxide.[56–62] Likewise, numerous rare-earth-metal based pre-catalysts are known to promote the related cycloaddition of CO_2 and epoxides.[62–69] The hydrosilylation of carbon dioxide is another reaction successfully mediated by Ln(III) (pre-)catalyst,[70,71] while the reductive C-C coupling to form carbonylic/amino acids was accomplished by SmI_2,[72,73] methanol carboxylation[74–77], as well as the electrochemical reduction to carbonaceous materials (cf. chapter 4.5 for a more extensive overview of rare-earth-metal complexes in homogenous catalysis of CO_2).[78] Nevertheless, not only the conversion of carbon dioxide, but also storage and separation from gas mixtures can be

delivered using rare-earth-metal based materials or complexes. Consequently, various lanthanide-based MOFs, mainly using carboxylato linkers, have been synthesized and probed in their ability for CO_2-uptake.[79–82]

This overview will focus on the structurally elucidated rare-earth-metal complexes resulted from a ketone or carbonylic compound insertion or activation and carbon dioxide insertion products. As rare-earth metals are well established in the synthesis of organic compounds, the knowledge of metal-organic intermediates or exemplary complexes is crucial for understanding and improving such transformations. Therefore, the compounds will be sorted by their structural motives and, if discussed in the publications, details on their reactivity and applicability in (catalytic) reactions are presented. The first part covers adducts and insertion products of ketones and aldehydes. Part 2 will focus on the redox enhanced activation of ketones and the characterized metal-organic products. The last part emphasizes CO_2-insertion products and of CO_2 and the use of such rare-earth-metal complexes for catalytic CO_2 conversion. As this thesis refers to various oxidation states of the rare-earth-metal centers, distinct colors display their oxidation state (Ln^{II}: orange, Ln^{III}: blue, Ln^{IV}: red) and also, the inserted organic molecules are drawn in green for an easier understanding.

2 Carbonyl Insertion Products

2.1 Insertion into Ln-Alkyl and -Hydrido Bonds

A first detailed study on the organometallic chemistry of lanthanides and carbonylic moieties was carried out by TEUBEN and coworkers in 1992, investigating the reactivity of rare-earth-metal alkyls and hydrides $[Cp*_2LnR]_n$ (Ln = La, Ce; R = $CH(SiMe_3)_2$, n = 1; R = H, n = 2) toward different ketones.[83] While the bulky di-*tert*-butyl ketone did not react with the alkyl precursors, insertion was observed into the La−H-bond of $[Cp*_2LaH]_2$ adduct giving complex $[Cp*_2La(OCHtBu_2)(OCtBu_2)]$ (**1**) with an additional ketone donor. Reacting the alkyls with two equivalents of acetone led to the formation of lanthanide aldolates $[Cp*La(OC(Me)_2CH_2COMe)]$ (**2^{Ln}** Ln = La, Ce). Most likely, the aldolate is formed *via β*-H elimination of the ketone, coordination of a second ketone and subsequent nucleophilic attack to form the aldolate ligand (Scheme A1). Complexes **2^{Ln}** have also been synthesized using precursors $[Cp*_2Ln\{CH(SiMe_3)_2\}]$ (Ln = La, Ce) and aldol 4-hydroxy-4-methyl-2-pentanone. Using 3-pentanone, instead of acetone, the reaction stops at the mixed enolato-ketone complexes $[Cp*_2Ln(OC(Et)CHMe)(OCEt_2)]$ (**3^{Ln}** Ln = La, Ce). Reacting the alkyls with 5-hydroxy-5-ethyl-heptanone to generate the aldolate products did also yield **3**. Thus, these enolato-ketone complexes seem to be the thermodynamically favored products.
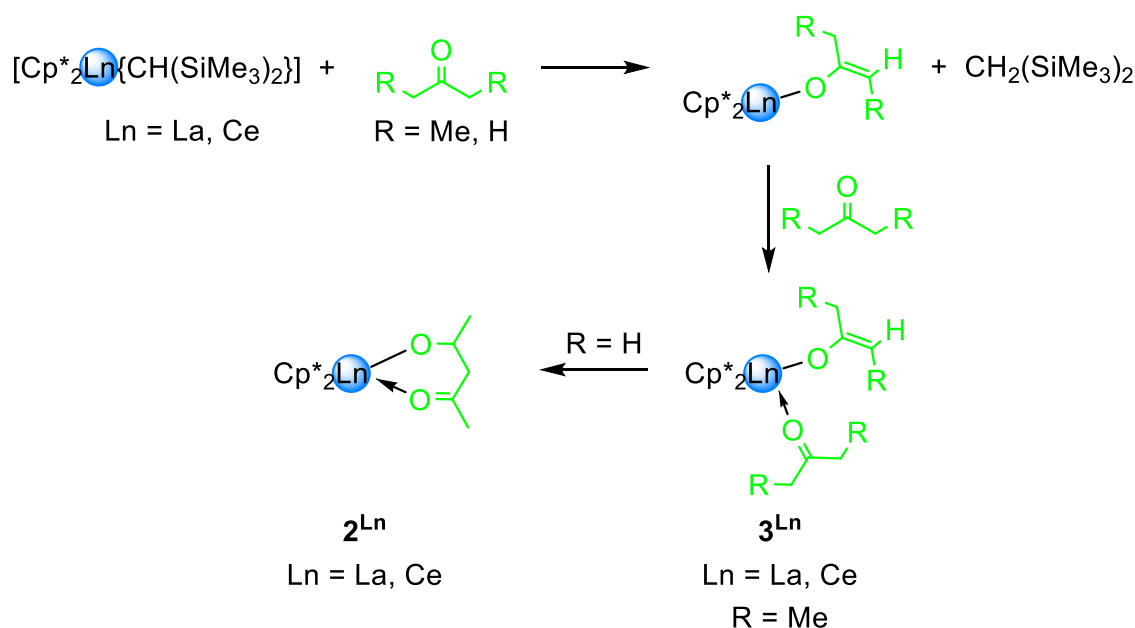
Scheme A1. Formation of aldolates **2^{Ln}** and mixed enolato ketone complexes **3^{Ln}**.

These results show that the activation of ketones is doubtlessly initiated by the coordination of a ketone to the metal center. According to this, various donor adducts of carbonyls have been described since the early 90s. These donor adducts comprise: $[\{(SiMe_3)_2N\}_3Ln(OCPh_2)]$ (**4^{Ln}** Ln = Y, La, Ce, Pr, Eu, Tb, Yb)[84,85], $[Cp_3Pr(n\text{-butylacetate})]$ (**5**)[86], $[Cp_3Ln(OC(NMe_2)_2)]$ (**6^{Ln}** Ln = Ce, Nd)[87], $[Cp_3Ln(OCPh_2)]$ (**7^{Ln}** Ln = Y, Ce, Pr, Dy)[85,88,89], $[Cp*_2YCl(do)]$ (do = OCPh_2 **8**, MMA (methyl methacrylate) **9**, ε-caprolactone **10**, hmpa (hexamethylphosphoric triamide) **11**, ε-caprolactam **12**, 1-methyl-2-pyrrolidinone **13**, *N,N'*-dimethyl propylene urea **14**)[90], $[Cp*_2YCl(\varepsilon\text{-caprolactam})_2]$ (**15**)[90], $[Cp*_2Ln(do)_2][BPh_4]$ (**16^{Ln}** do = OCMe_2, Ln = Y, Sm; or **17^{Ln}** do = OCPh_2, Ln = Y, Sm)[91], $[\{(SiMe_3)_2N\}_2Ln(OC_{13}H_8)]$ (**18^{Ln}** Ln = Ce, Pr)[85], $[Cp_3Ln(OC_{13}H_8)]$ (**19^{Ln}** Ln = Ce, Pr)[85] and $[(ArO)_2Sc\{OC(Me)_2CH_2PPh_2\}(OCPh_2)]$ (**20** Ar = $C_6H_3tBu_2$-2,6)[92]. Carbonyl group coordination (and hence activation) is generally evidenced by significantly elongated C=O bonds, lower-energy C=O stretch vibrations and low field shifted ^{13}C NMR signals.

As seen for **1**, rare-earth-metal hydrides can insert a ketone to yield an alkoxide complex (Scheme A2). This reactivity was also observed by YASUDA *et al.* upon reacting $[Cp*_2SmH]_2$ with MMA, which exhibited catalytic activity in MMA polymerization.[93] They succeeded in the isolation of $[Cp*_2Sm\{(MMA)_2H\}]$ (**21**) as an intermediate in the polymerization reactions. The congeneric hydrido complex $[(C_5H_4tBu)_2SmH]_2$ was found to insert two molecules of acetone to give dimeric $[(C_5H_4tBu)_2Sm(\mu\text{-OCHMe}_2)]_2$ (**22**).[94] Reacting Sc-borohydride complex $[(Nacnac)Sc(NHAr)(HBEt_3)]$ (Nacnac = $ArNC(CH_3)CHC(CH_3)NAr$, Ar = Dipp = $C_6H_3iPr_2$-2,6) with benzophenone afforded insertion into the Sc−H-bond to produce $[(Nacnac)Sc(NHAr)(OCHPh_2)]$ (**23**) and separation of BEt_3.[95] Similarly, the mixed iodido hydrido complex LnI_2H gave $[LnI_2\{OC_{14}H_8(NHDipp)\}(dme)_2]$ (**24^{Ln}** Ln = Nd, Dy) as insertion products of N-(2,6-di*iso*propylphenyl)-9,10-phenanthrenequinonimine.[96]

L = monoanionic ligand
R = hydrido, alkyl or aryl
R' = alkyl or aryl
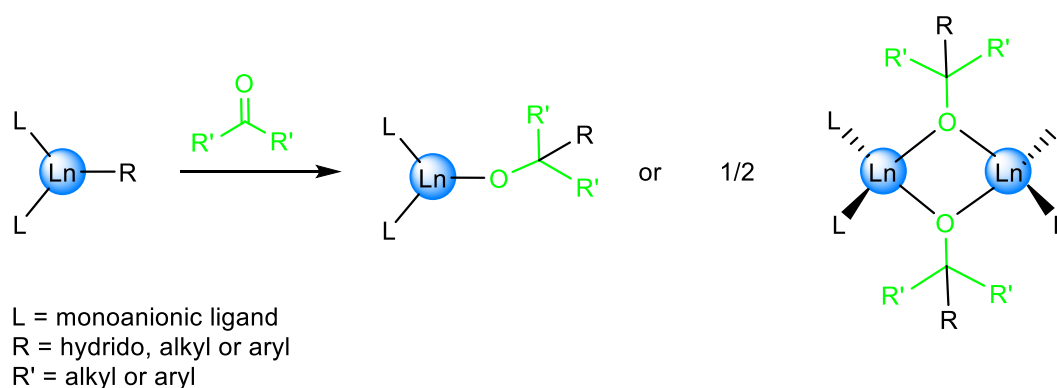
Scheme A2. Reactivity of ketones toward rare-earth-metal alkyls, aryls or hydrides.

The insertion of a ketone into a Ln−C-bond was first described by STAROSTINA *et al.*[97] Reacting [YbPh$_2$] with fluorenone gave [PhYb(OC(Ph)C$_{12}$H$_8$)] (**25**). Similar observations were made by ARNOLD *et al.* in 1993.[98] Upon treatment of octaethylporphyrin (OEP) stabilized scandium alkyls [(OEP)ScR] (R = Me, CH$_2$SiMe$_3$, CH$_2$*t*Bu) with acetone, the complexes [(OEP)Sc(O*t*Bu)] (**26**), [(OEP)Sc(OC(Me)$_2$CH$_2$SiMe$_3$)] (**27**), and [(OEP)Sc(OC(Me)$_2$CH$_2$*t*Bu)] (**28**) were obtained. In 2006, homoleptic [YMe$_3$]$_n$ was shown to insert three molecules of fluorenone to yield [Y(OC(Me)C$_{12}$H$_8$)$_2$(μ-OC(Me)C$_{12}$H$_8$)]$_2$ (**29**) by our group.[99] Shortly afterwards OKUDA and coworkers reported on a series of alkoxides resulting from ketone insertion into Y−C-bonds of yttrium mono- and bis alkyls [Y(CH$_2$SiMe$_3$)(thf)$_5$][BPh$_4$]$_2$ and [Y(CH$_2$SiMe$_3$)$_2$(thf)$_x$(12-crown-4)$_y$][BPh$_4$] (with x = 4, y = 0 or x = 1, y = 1).[100] Being highly reactive toward aliphatic ketones, like acetone, 3-pentanone or acetophenone, yielding a mixture of non-isolable species, only insertion products of the reactions with benzophenone and fluorenone could be isolated. This is ascribed to a *β*-H deprotonation of aliphatic ketones. Isolated products were [Y{OC(Ph)$_2$CH$_2$SiMe$_3$}(thf)$_5$][BPh$_4$]$_2$ (**30**) [Y{OC(CH$_2$SiMe$_3$)C$_{12}$H$_8$}(thf)$_5$][BPh$_4$]$_2$ (**31**), [Y{OC(Ph)$_2$CH$_2$SiMe$_3$}$_2$(thf)$_x$(12-crown-4)$_y$][MPh$_4$] (**32**^{M} with x = 4, y = 0, M = B, Al or **33**^{M} with x = 1, y = 1, M = B, Al) and [Y{OC(CH$_2$SiMe$_3$)C$_{12}$H$_8$}$_2$(thf)$_x$(12-crown-4)$_y$][MPh$_4$] (**34**^{M} with x = 4, y = 0, M = B, Al or **35**^{M} with x = 1, y = 1, M = B, Al). Analogous reactivity was observed in the synthesis of [Y(OC(Me)Ph$_2$)$_2$(thf)$_4$][BPh$_4$] (**36**), [Y(OC(Me)Ph$_2$)(thf)$_5$][BPh$_4$] (**37**)[101], [{2-(2-CH$_3$OC$_6$H$_3$NC(H)(CH$_2$SiMe$_3$))C$_4$H$_3$N}Lu(OC(CH$_2$SiMe$_3$)Ph$_2$)]$_2$ (**38**, Figure A1)[102], [(DippForm)Sm(OC(Ph)$_2$CCPh)(thf)] (DippForm = *N,N'*-bis(2,6-di*iso*propylphenyl) formamidinate **39**, Figure A1)[103], [Cp*Lu{OC(*t*Bu)C(SiMe$_3$)C(Ph)C(Ph)C(SiMe$_3$)(LiCl(thf))}]$_2$ (**40**, Figure A1)[104] or [{(SiMe$_3$)$_2$N}$_2$YI{OC(Ph)$_2$CH$_2$PPh$_3$}] (**41**)[105]. Upon treatment of **41** with Ph$_3$PO, 1,1-diphenyl ethylene was produced in good yields.

38   **39**   **40**
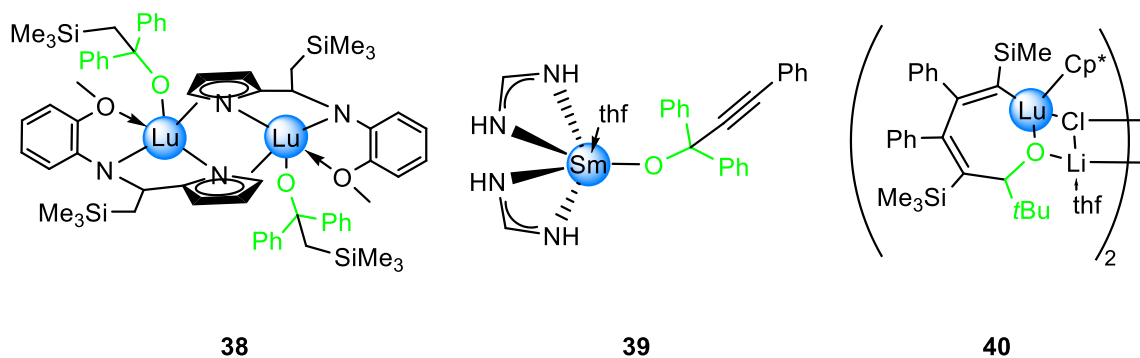
Figure A1. Benzophenone-inserted complexes **38** and **39** and pivaldehyde inserted complex **40**.

In 2010 [YCp$_3$] was shown to insert benzophenone into the Y−Cp bond under thermal conditions.[89] At 85 °C [Cp$_2$Y(OC(Ph)$_2$C$_5$H$_5$)(thf)] (**42**) was formed and addition of *n*-BuLi and subsequent elimination of LiCp yielded dimeric [CpY(μ-OCPh$_2$C$_5$H$_4$)]$_2$ (**43**) bearing the dianionic ligand OC(Ph)$_2$C$_5$H$_4$. At higher temperatures (110 °C) C−O-bond activation occurred, concomitant with the formation of olefin Ph$_2$C=C$_5$H$_4$, and hydroxy species [Cp$_2$Y(μ-OH(thf))(μ-OC(Ph)$_2$C$_5$H$_4$)YCp] (**44**, Figure A2). Similar ketone insertion reactions with olefin formation were also observed by HONG *et al.* in the reaction of trimetallic methylidene [(NCN)$_3$Lu$_3$(μ-Me)$_3$(μ_3-Me)(μ_3-CH$_2$)] (NCN = PhC(NDipp)$_2$) with two equivalents of acetophenone giving α-methylstyrene and [(NCN)$_3$Lu$_3$(μ-Me)$_3$(μ_3-OC(Ph)Me$_2$)(μ_3-O)] (**45**, Figure A2).[23] In the same year HOU and coworkers found that congeneric Cp' stabilized Tm methylidene inserts benzophenone with subsequent C−H-bond activation to produce [Cp'$_3$Tm$_3$(μ-Me)$_3$(μ_3-OC(C$_6$H$_4$)$_2$Me)] (**46**) under release of methane.[24] Three years later CUI and coworkers described the reaction of alkylidene complex [(BODDI)Lu$_2$(CH$_2$SiMe$_3$)$_2$(μ-CHSiMe$_3$)] (BODDI = DippNC(Me)CHCOCHC(Me)NDipp) with five equivalents of benzophenone producing alkene Ph$_2$CCHSiMe$_3$ and benzophenone inserted complex **47** (Figure A2).[25]
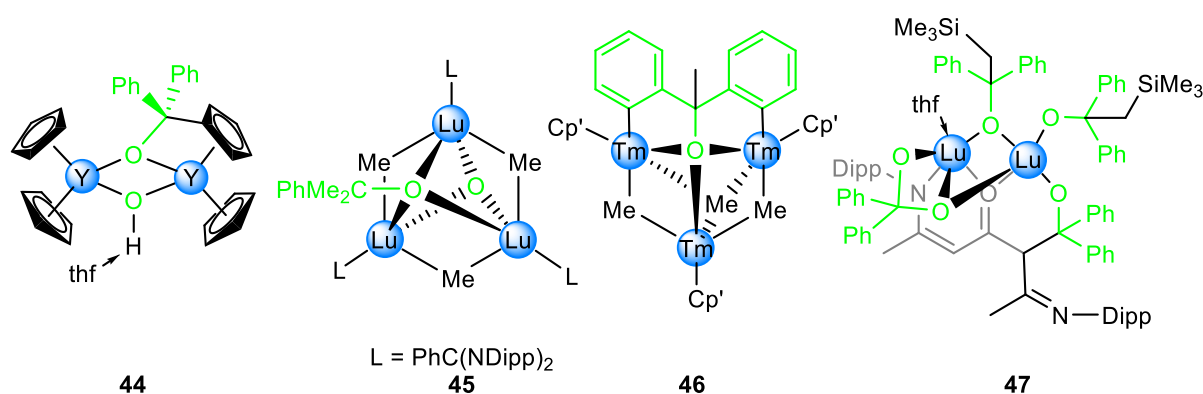
Figure A2. Ketone insertion products **44** – **47** with a precedential C−O metathesis reaction.

Noteworthy, in the latter complex benzophenone inserted not only into a Ln−C bond, but also into a formed Ln−O-bond and *via* nucleophilic attack of the ligand producing a C−C coupling product. Similar observations were made by SCHOLZ *et al.* in 2001 by treating [{(thf)Li(*t*Bu-DAD)}$_2$Sm(μ-Cl)$_2$Li(thf)$_2$] (*t*Bu-DAD = (*t*Bu)NCH=CHN(*t*Bu)) and [{(thf)$_2$Li(*t*Bu-DAD)}{(thf)Li(*t*Bu-DAD)}SmI] with two equivalents of benzophenone yielding [SmX{OC(Ph)$_2$CH{CH=N*t*Bu}N*t*Bu}$_2$Li$_2$(thf)] (**48^X** X = Cl, I, Figure A3).[106] In 2017, SCHELTER and coworkers reacted trivalent lanthanide compound [(PNP)Ln{N(SiMe$_3$)$_2$}$_2$] (PNP = bis[2-(di*iso*propylphosphino)-4-methylphenyl]-amido; Ln = La, Ce) with two equivalents of

benzophenone to give [(PNP)Ln{N(SiMe$_3$)$_2$}{N(SiMe$_3$)(SiMe$_2$CH$_2$CPh$_2$O)}(OCPh$_2$)] (**49^{Ln}** Ln = La, Ce, Figure A3).[107] This reaction proceeded *via* insertion of the ketone into the C−H-bond of one SiMe$_3$ group and the formation of a dianionic ligand as well as release of HN(SiMe$_3$)$_2$.
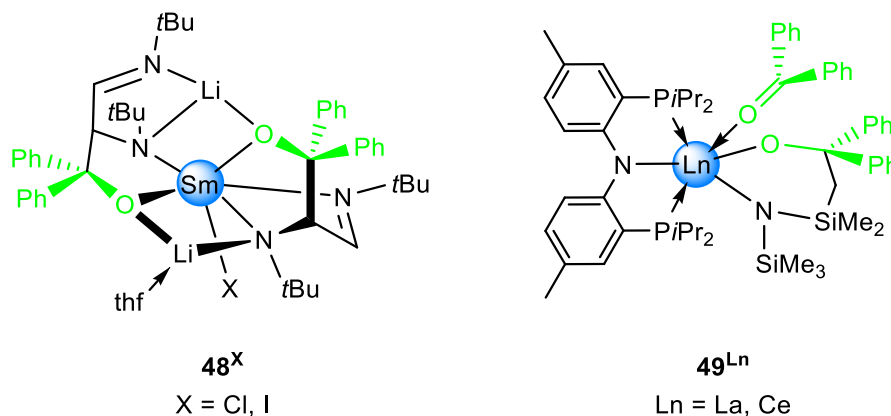

Figure A3. Complexes **48** and **49** resulting from a C−C coupling of the ligand and benzophenone.

2.2 Insertion into Ln−Heteroatom Bonds

In 2006 the group of ZHOU described the insertion of PhEtCCO into Ln−O bond of [Cp$_2$Ln(μ-OH)(thf)]$_2$ (Ln = Y, Er, Yb) and the respective formation of carboxylates [Cp$_2$Ln(O$_2$CCHPhEt)] (**50^{Ln}** Ln = Y, Er, Yb).[108] Similar reactivity toward congeneric sulfide complexes [Cp$_2$Ln(μ-SR)]$_2$ was found yielding α-thiolate-substituted enolate [Cp$_2$Ln(μ-OC(SR)CPh$_2$)] (**51^{Ln}** R = Bn, Ln = Y, Er, Yb or **52** R = Ph, Ln = Yb, Figure A4).[109] In 2016, ROESKY and coworkers reported an dimeric benzoate-bridged [Cp*$_2$Sm(μ-O$_2$CPh)]$_2$ (**53**, Figure A4) accessible *via* treatment of samarocene oxide [Cp*$_2$Sm-O-SmCp*$_2$] with benzoic acid anhydride.[110] CHEN *et al.* found that reacting the scandium imide complex [(NN-Nacnac)Sc=NDipp] (NN-Nacnac = MeC(NDipp)CHC(Me)(NCH$_2$CH$_2$N(Me)CH$_2$CH$_2$NMe$_2$)) with two equivalents of MMA yields [(NN-Nacnac)Sc{OC(OMe)CMe(CH$_2$NAr)CH$_2$CMeC(OMe)O}] (**54**, Figure A4) as a result of a 2+4 cycloaddition involving the Sc=NR imido moiety and MMA with subsequent Michael addition of another MMA molecule.[111,112]
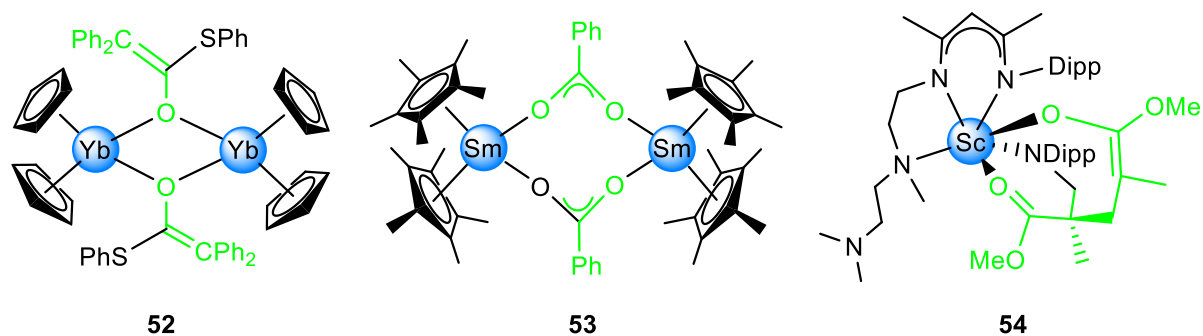
Figure A4. Complexes **52**, **53**, and **54** resulting from the reaction of a carbonyl moiety with a Ln−heteroatom bond.

In 2017 a detailed study of the reversible benzophenone insertion into ceric Ce−N(Me$_2$pz) (Me$_2$pz = 3,5 dimethyl pyrazolyl) bond, giving a OCPh$_2$Me$_2$pz (pdpm) ligand, was described by our group.[113] A temperature dependent benzophenone insertion of up to three equivalents of benzophenone into [Ce(Me$_2$pz)$_4$]$_2$ was found (Scheme A3). However, only [Ce(Me$_2$pz)$_2$(pdpm)$_2$] (**55**) could be structurally characterized. In comparison, using trivalent [Ln(Me$_2$Pz)$_3$(thf)]$_2$ yielded [Ln$_2$(Me$_2$pz)$_3$(μ-pdpm)$_3$] (**56^{Ln}** Ln = La, Ce) for the larger rare-earth metals and [Lu(Me$_2$pz)(μ-Me$_2$pz)(μ-pdpm)]$_2$ (**57**) for the small-sized Lu congener with the metal center with the smaller ionic radius.
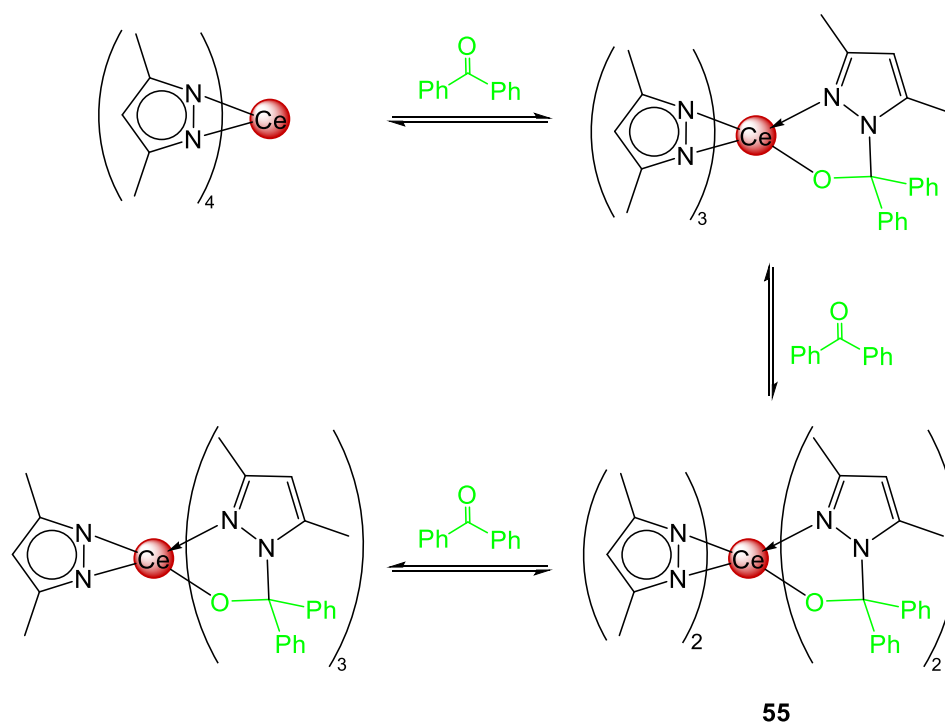
Scheme A3. Equilibria of the benzophenone insertion into the Ce−N(Me$_2$pz) bond.

Finally, complexes bearing phosphorous substituted ligands with or without Ln−P interaction were probed for carbonyl activation. In 2018, the group of CHEN showed that [(ArO)$_2$Sc{OC(Me)$_2$CH$_2$PPh$_2$}] (Ar = C$_6$H$_3$tBu$_2$-2,6) form frustrated LEWIS pairs (FLPs) upon reaction with ketones, α,β-unsaturated carbonylic compounds or α-diketones.[92] These FLPs include [(ArO)$_2$Sc{OC(Me)$_2$CH$_2$PPh$_2$C(HPh)O}] (**58**, Figure A5) *via* addition of benzaldehyde, [(ArO)$_2$Sc{OC(Me)$_2$CH$_2$PPh$_2$C(Ph)CC(Ph)O}] (**59**, Figure A5) *via* addition of 1,3-diphenyl-2-propyn-1-one, [(ArO)$_2$Sc{OC(Me)$_2$CH$_2$PPh$_2$C(HR)CHC(Ph)O}] (R = C(O)Ph **60**, CCHPh **61**, Figure A5) *via* addition of *trans*-1,2-dibenzoylethylene or 1,5-diphenylpenta-2,4-dien-1-one respectively, and [(ArO)$_2$Sc{OC(Me)$_2$CH$_2$PPh$_2$OC(Ph)C(Ph)O}] (**62**, Figure A5) upon addition of benzil. The same group also described the insertion into scandium phosphinoalkylidene [(Nacnac)Sc{C(SiMe$_3$)PPh$_2$}(thf)] of cyclohexanone and 2-cyclohexen-1-one giving [(Nacnac)Sc{C(SiMe$_3$)PPh$_2$C((CH$_2$)$_5$)O}] (**63**) and [(Nacnac)Sc{C(SiMe$_3$)PPh$_2$C((CH)$_2$(CH$_2$)$_3$)O}] (**64**, Figure A5), respectively.[114]
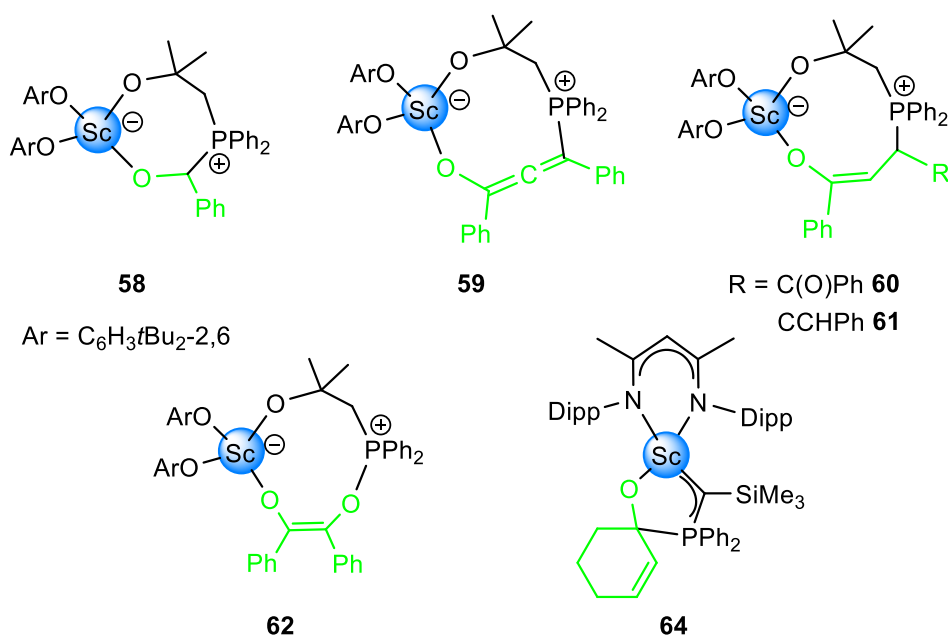
Figure A5. Frustrated LEWIS pairs **58**, **59**, **60**, **61**, and **62**, and complex **64**, formed *via* insertion of a carbonylic moiety into Ln−P bond.

3 Redox-Enhanced Carbonyl Activation

3.1 Activation of Ketones

Divalent lanthanides (Sm^{II}, Eu^{II}, Yb^{II}) or Ce^{III} are prone to redox chemistry with carbonylic substrates. Starting in the early 90s, WAKATSUKI and HOU reported on various works on the oxidation of divalent rare-earth-metal complexes with ketones like benzophenone or fluorenone.[115–117] There the ketones undergo a one-electron reduction forming a ketyl radical being reminiscent of the sodium/benzophenone system. For example the reaction of $[(ArO)_2Sm(thf)_3]$ (Ar = $C_6H_2tBu_2$-2,6-Me-4) with one equivalent of fluorenone led to the isolation of $[(ArO)_2Sm(OC^•C_{12}H_8)(thf)_2]$ (**65**).[116] This product reversibly dimerizes upon treatment with the less donating solvent mixture *n*-hexane/diethyl ether giving a coupling product of two fluorenyl ligands as bimetallic samarium pinacolate $[\{(ArO)_2Sm(OEt_2)_2\}(\mu$-pinacolato)]_2 (**66** pinacolato = 1,2-bis(biphenyl-2,2'-diyl)ethane-1,2-diolate, Scheme A4). Such dimerization is counteracted in case of surface-grafted Sm(II) compound due to its isolation.[118]

Ar = $C_6H_2tBu_2$-2,6-Me-4   **65**   **66**
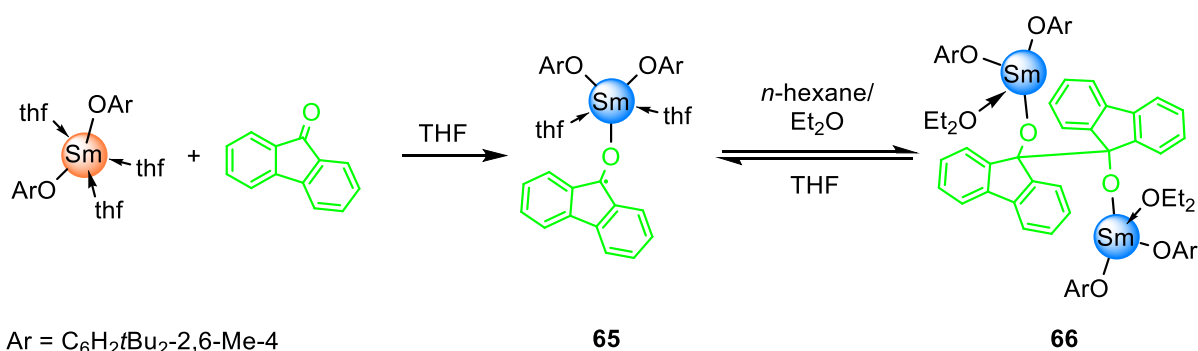
Scheme A4. Stepwise formation of samarium pinacolate **66** *via* redox activation of fluorenone.

The first tris(ketyl) samarium complex $[Sm(OC^•C_{12}H_8)_3(hmpa)_3]$ (**67**) was obtained by treating samarium metal with three equivalents of fluorenone in HMPA.[117] Complex **67** also dimerized giving complex **68** featuring two bridging pinacolato ligands (Scheme A5).
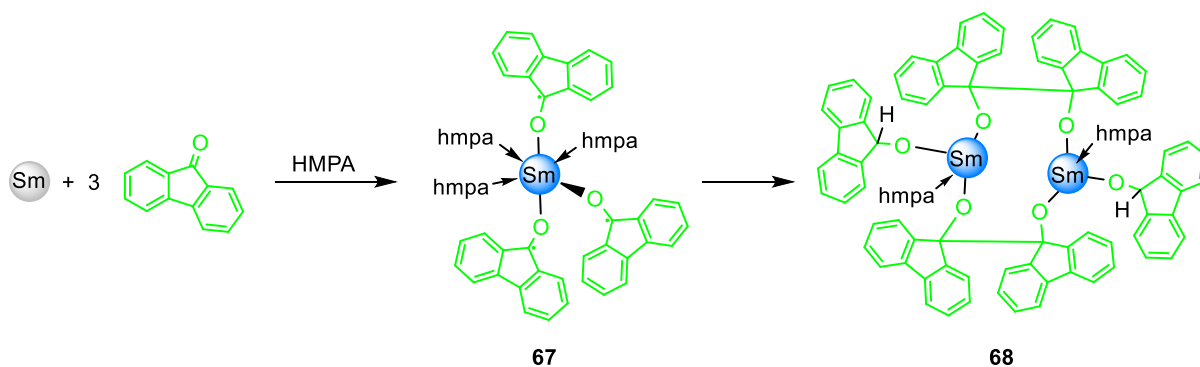
Scheme A5. Synthesis of tris(ketyl) complex **67** and dimerization to complex **68**.

In 1998, the same group published a series of Ln^{III} mono ketyl complexes for Yb and Sm, analogous to complex **65**, with various monoanionic co-ligands, like Cp* or N(SiMe$_3$)$_2$ and with THF and HMPA as donor molecules, as a result of a one-electron oxidation with fluorenone.[119] All of these complexes showed the same dimerization behavior as compound **65** and upon treatment with HCl the pinacol derivative 1,2-bis(biphenyl-2,2'-diyl)ethane-1,2-diol was isolated, while oxidation with air gave fluorenone. Furthermore, the oxidation of divalent Ln-aryloxides with benzophenone was attempted. Although successfully oxidized, isolation of a Ln(III)-ketyl complex was not feasible and only the product of the reaction with solvent protons to [(OAr)Yb(OCHPh$_2$)$_2$(hmpa)$_2$] (**69**) could be characterized.

Using fluorenone as a one-electron oxidant for divalent lanthanides, multiple complexes bearing a ketyl radical as ligand have been isolated in recent years: [{(C$_5$Me$_4$)SiMe$_2$NPh}Yb(OC$^{\bullet}$C$_{12}$H$_8$)(thf)$_2$] (**70**)[120], [Tp^{Me,Me}$_2$Sm(OC$^{\bullet}$C$_{12}$H$_8$)] (**71** Tp^{Me} = tris(3,5-dimethyl-pyrazol-1-yl)borate)[121,122], [(DippForm)$_2$Yb(OC$^{\bullet}$C$_{12}$H$_8$)(thf)] (**72**)[123]. In contrast to the aforementioned complexes, a dimerization of complexes **71** and **72** could be prevented by utilization of bulky co-ligands.

Utilizing benzophenone instead of fluorenone leads to an oxidation of divalent lanthanides and the formation of ketyl radicals (OC$^{\bullet}$Ph$_2$) as well. Complexes of the general composition [LLn(OC$^{\bullet}$Ph$_2$)] were first isolated by CLEGG *et al.* in 1997 as revealed by [{(SiMe$_2$OMe)(SiMe$_3$)$_2$C}$_2$Sm(OC$^{\bullet}$Ph$_2$)] (**73**), resulting from the reaction of [Sm{C(SiMe$_3$)$_2$(SiMe$_2$OMe)}$_2$] with benzophenone.[124] Other examples of isostructural complexes are [Tp^{Me,Me}$_2$Sm(OC$^{\bullet}$Ph$_2$)] (**74**)[121,122] and [{py(Ph$_3$P=NCH$_2$)$_2$-2,6}Yb(OC$^{\bullet}$Ph$_2$)I$_2$] (**75**)[125]. The group of DEACON showed the tendency of these complexes to dimerize. Isolation of [{Yb(NCS)$_2$(thf)$_3$}$_2$(μ-OC(Ph)$_2$C(Ph)$_2$O)] (**76**) and [(DippForm)$_2$(thf)Ln{μ-OC(Ph)=(C$_6$H$_5$)C(Ph)$_2$O}Ln(DippForm)$_2$] (**77^{Ln}** Ln = Sm or Yb) was observed upon treatment

of the divalent precursors with benzophenone.[103,126] This indicates formation of a Ln[III]-ketyl complex followed by dimerization. In contrast to fluorenone complexes, benzophenone radicals show two possible dimerization products: a pinacolato-like dimer as seen for the fluorenone complexes and a head-to-tail coupled species as in "GOMBERGS Dimer" of the trityl radical (Scheme A6).[127,128] Using benzaldehyde instead of benzophenone, MARQUES and coworkers obtained dimeric $[(Tp^{Me,Me}_2Sm)_2(\mu\text{-OCH(Ph)-CH(Ph)O})]$ (**78**) as a result of a one-electron oxidation of divalent $[SmTp^{Me,Me}_2]$.[121]

L = monoanionic ligand
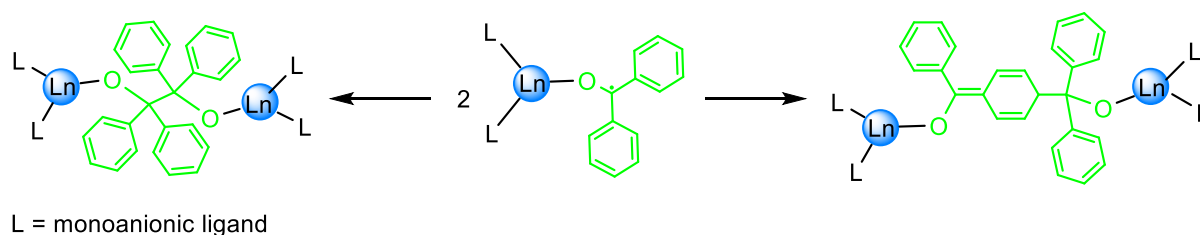
Scheme A6. Different dimerization patterns of $[L_2Ln(OC^\bullet Ph)]$.

Although one-electron reduction of benzophenone by divalent lanthanide complexes seems favored, a rare example of two-electron reduction and formation of the benzophenone-dianion was reported by the group of HOU in 2001.[129] Treatment of $[\{(C_5Me_4)SiMe_2PAr)\}Sm(thf)_3]$ (Ar = C_6H_2-tBu$_3$-2,4,6) with half an equivalent of benzophenone, afforded dimeric complex $[\{((C_5Me_4)SiMe_2PAr)Sm(thf)\}_2(\mu\text{-OCPh}_2)]$ (**79**) (Scheme A7).
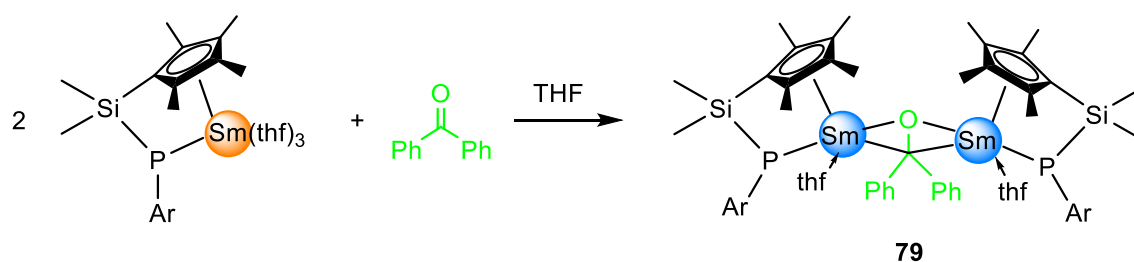
Scheme A7. Two-electron reduction of benzophenone and formation of complex **79**.

In 2017, WERNER *et al.* examined the reaction of divalent complex $[(DippForm)_2Yb(thf)]$ with tetraphenyl-cyclopentadienone (tetracyclone O=C_5Ph_4) yielding radicalic species $[(DippForm)_2Yb(OC_5Ph_4)]$ (**80**). [123] Reacting **80** with KH resulted in a ligand redistribution forming diketyl complex $[(DippForm)Yb(OC_5Ph_4)_2]$ (**81**). Oxidation of activated samarium metal with tetracyclone gave a two electron reduction of the ketone yielding the divalent complex $[Sm_2(\mu\text{-OC}_5Ph_4)(\mu_3\text{-OC}_5Ph_4)(thf)_3]_2$ (**82**).

3.2 Activation of Quinones

Utilizing 1,4-*p*-benzoquinone, SEN *et al.* oxidized two equivalents of cerous [Ce(OCtBu$_3$)$_3$] under formation of hydroquinolato-bridged Ce^{IV} complex [{Ce(OCtBu$_3$)$_3$}$_2$(μ-O$_2$C$_6$H$_4$)] (**83**, Scheme A8).[130] Changing 1,4-*p*-benzoquinone to 2,6-di-*tert*-butyl-1,4-*p*-benzoquinone resulted in the isolation of ceric semiquinolato complex [(tBu$_3$CO)$_3$Ce(O$_2$C$_6$H$_2$$tBu_2$-2,6)] (**84**) (Scheme A8). Despite missing structural elucidation due to rapid decomposition of **84**, the molecular connectivity was supported by NMR and EPR spectroscopy. Similar hydroquinolato-bridged ceric complexes have also been reported by the group of SCHELTER and our group, comprising [{(Li$_3$(Et$_2$O)$_{3.5}$)((BINOLate)$_3$Ce)}$_2$(μ-O$_2$C$_6$H$_4$)] (**85**),[131] [(Ce{N(SiMe$_3$)$_2$}$_3$)$_2$(μ-O$_2$C$_6$H$_4$)] (**86**),[132] and [(CeCp^R$_3$)$_2$(μ-O$_2$C$_6$H$_4$)] (**87** Cp^R = C$_5$H$_4$Me and **88** C$_5$H$_4$(SiMe$_3$))[133].

Scheme A8. Oxidation of [Ce(OCtBu$_3$)$_3$] with 1,4-*p*-benzoquinone and 2,6-di-*tert*-butyl-1,4-*p*-benzoquinone.

The oxidation of cerous dimethyl pyrazolate [Ce(Me$_2$pz)$_3$]$_n$ with 1,4-*p*-benzoquinone was also attempted by our group.[134] Although an immediate color change from yellow to dark purple indicated oxidation, only trivalent species [Ce$_3$(Me$_2$pz)$_5$(phcd)$_2$(thf)$_2$] (**89** phcd = 1,4-bis(3,5-dimethylpyrazol-1-yl)cyclohex-2,5-diene-1,4-diolato, Figure A6) could be isolated. Attempted oxidation of *in situ* generated ate-complex "[Ce(Me$_2$pz)$_4$Li(thf)$_x$]" with 1,4-*p*-benzoquinone resulted in bridging hydroquinolate moiety and subsequent reduction of the formed Ce^{IV} species as found in the isolable product [Li$_4$Ce$_4$(Me$_2$pz)$_{10}$(thf)$_4$(pzHq)$_2$] (**90** pzHq = 2-(3,5-dimethylpyrazol-1-yl)1,4-hydroquinolato, Figure A6).[135]

Figure A6. Complexes **89** and **90** formed *via* reaction of cerous dimethyl pyrazolates with 1,4-*p*-benzoquinone.
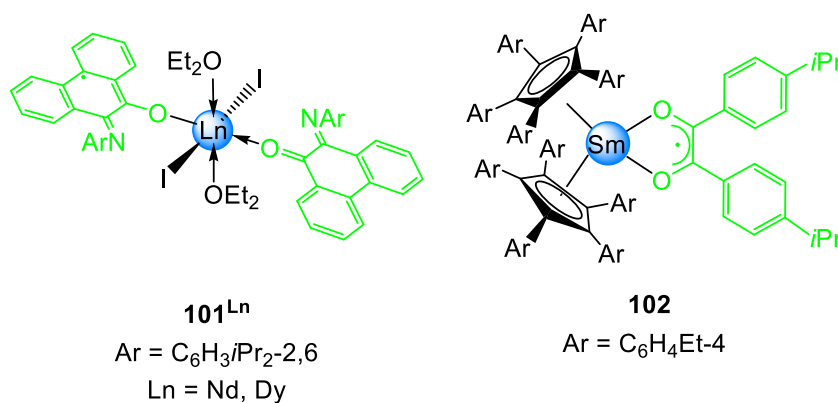
In 2007, studies on the oxidation of Sm^{II} compounds using different benzoquinone derivatives have been conducted by Domingos *et al.*[121,122] As observed for the cerium reactions, the addition of half an equivalent of 1,4-*p*-benzoquinone or anthraquinone to [SmTp$^{Me,Me}_2$] led to the formation of [(Tp$^{Me,Me}_2$Sm)$_2$(μ-O$_2$C$_6$H$_4$)] (**91**, Scheme A9) and [(Tp$^{Me,Me}_2$Sm)$_2$(μ-O$_2$C$_{14}$H$_8$)]. Use of equimolar amounts of benzoquinone resulted in a color change to dark blue, indicating the formation of a semiquinone radical, which, however, could not be isolated. By replacing Sm for Eu, for the purpose of stabilizing the formed semiquinone, it was possible to isolate and characterize semiquinolato complex [Tp$^{Me,Me}_2$Eu(O$_2$C$_6$H$_4$)] (**92**, Scheme A9). In this case, adjusting stoichiometry did not lead to a hydroquinolato-bridged species as seen for the Sm congener. Stable Sm(III) semiquinolate complex could yet be synthesized by employing the sterically bulkier benzoquinone derivatives 2,6-di-*tert*-butyl-1,4-*p*-benzoquinone giving [Tp$^{Me,Me}_2$Sm(O$_2$C$_6$H$_2$tBu$_2$-2,6)] (**93**) and 3,5-di-*tert*-butyl-1,2-*o*-benzoquinone giving [Tp$^{Me,Me}_2$Sm (O$_2$C$_6$H$_2$tBu-3,5)] (**94**), respectively.

Scheme A9. Difference in reactivity of [SmTp$^{Me,Me}_2$] and [EuTp$^{Me,Me}_2$] toward 1,4-*p*-benzoquinone.

Comparable reactivity was also observed by DEACON and coworkers when reacting divalent [(DippForm)$_2$Yb(thf)$_2$] with 3,5-di-*tert*-butyl-1,2-*o*-benzoquinone, 9,10-phenanthrenequinone and 1,2-acenaphthenequinone to generate trivalent semiquinolates [(DippForm)$_2$Yb(O$_2$C$_6$H$_2$tBu-3,5)] (**95**), [(DippForm)$_2$Yb(O$_2$C$_{14}$H$_8$)] (**96**), and [(DippForm)$_2$Yb(O$_2$C$_{12}$H$_6$)] (**97**).[123] Aiming at homoleptic semiquinolates KUZYAEV *et al.* reacted rare-earth metals (Sm, Eu, Dy, Tm, Yb) with three equivalents of 3,5-di-*tert*-butyl-1,2-*o*-benzoquinone.[136] Although the results from elemental analyses and FTIR spectroscopy seemed promising, the only structurally elucidated compound was [Tm$_3$(SQ)$_4$(Cat)$_2$(QH)(dme)$_2$] (**98** SQ = semiquinone, Cat = catecholate, Q = quinone). Using excess of the respective metals led to the formation of catecholate-complexes [Ln$_4$(Cat)$_6$(thf)$_x$] (**99**$^{\mathbf{Ln}}$ Ln = Sm, Eu, Tm, Yb).

The "semiquinonolate-like" complexes [Ln(O(NDipp)C$_{14}$H$_8$)$_3$] (**100**$^{\mathbf{Ln}}$ Ln = Sc, Yb) and [LnI$_2$(O-(NDipp)C$_{14}$H$_8$)(O=(NDipp)C$_{14}$H$_8$)] (**101**$^{\mathbf{Ln}}$ Ln = Nd, Dy, Figure A7) were obtained *via* one-electron reduction of N-(2,6-di-*iso*propylphenyl)-phenanthren-*o*-iminoquinone with either the rare-earth metal or the bis iodide complex, respectively. Similarly [{C$_5$(C$_6$H$_4$Et-4)}$_2$Sm((OC)$_2$(C$_6$H$_4$iPr-4)$_2$)] (**102**, Figure A7) could be accessed by reacting sandwich complex [Sm{C$_5$(C$_6$H$_4$Et-4)}$_2$] with cuminil.[137,138]

101$^{\mathbf{Ln}}$
Ar = C$_6$H$_3$iPr$_2$-2,6
Ln = Nd, Dy

102
Ar = C$_6$H$_4$Et-4

Figure A7. Complexes **101**$^{\mathbf{Ln}}$ and **102** resulted from the oxidation with a "quinone-like" oxidant.

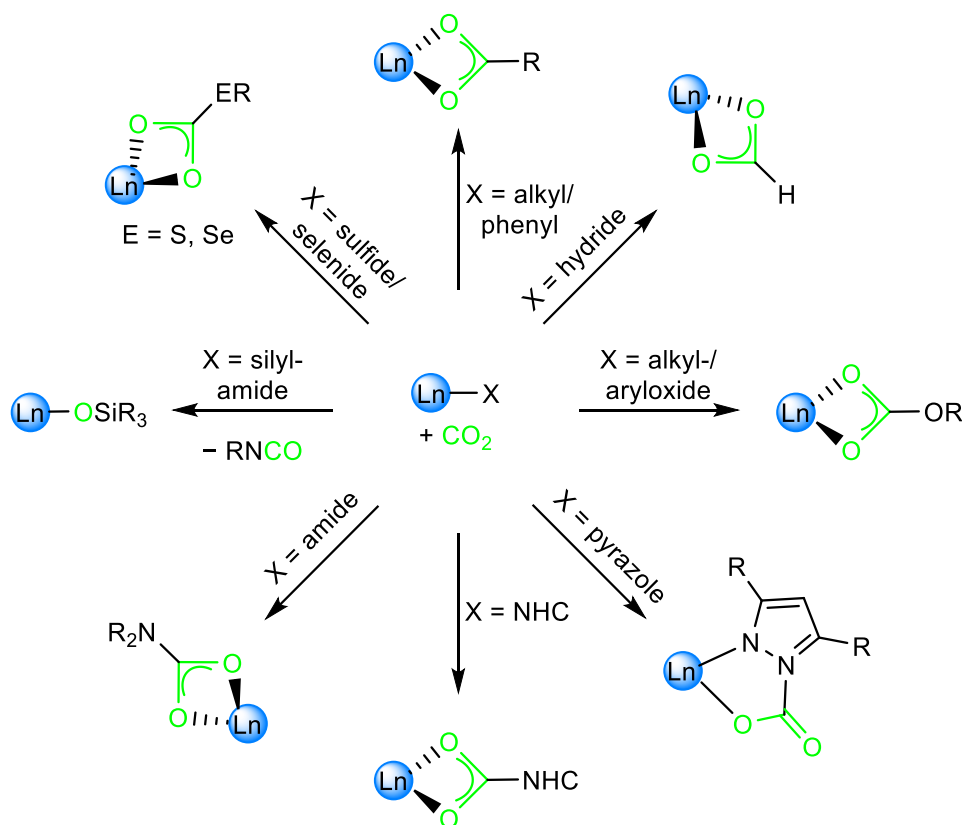# 4 Carbon Dioxide Activation

4.1 Insertion into Ln σ-Bonds

First attempts to isolate CO_2 insertion products of rare-earth-metal complexes were made by BOCHKAREV *et al.* in 1983 by reacting homoleptic silylamides [Pr{N(SiMe_3)_2}_3] and [Nd{N(SiMe_3)_2}_3] with carbon dioxide.[139] However, structural elucidation of the products was not possible, later investigations by their group gave more details of that reaction.[140] Analysis of the side products revealed the formation of Me_3SiNCO, (Me_3Si)_2O and Me_3SiNCNSiMe_3. They concluded that the reactions proceeds *via* CO_2 insertion and formation of carbamate complexes [Ln{O_2CN(SiMe_3)_2}_3] which then decompose giving siloxides "Ln(OSiMe_3)" and isocyanate Me_3SiNCO. This isocyanate then reacts either with the formed siloxide yielding a rare-earth-metal cyanate "Ln-OCN" and the found siloxane (Me_3Si)_2O or with a Ln silylamide giving a siloxide "Ln(OSiMe_3)" and carbodiimide Me_3SiNCNSiMe_3 (Scheme A10). Finally, another molecule of carbon dioxide can insert into the Ln−O(siloxide) bond giving carbonate complex "Ln(O_2COSiMe_3)" explaining the strong adsorption bands in the range from 1300 to 1700 cm^{-1} in the IR spectrum. Recent studies from SCHELTER *et al.* confirmed the formation of a siloxide complex upon insertion of carbon dioxide into a Ln−N(silylamide) bond.[141]

Scheme A10. Proposed cascade reaction of the CO_2 insertion into Ln−N(silylamide).

In the end of the 80s and in the early 90s, the first examples of rare-earth-metal complexes resulting from CO_2 insertion came up. In 1989 ST. CLAIR and SANTARSIERO isolated [Cp*_2Sc(O_2CC_6H_4Me-4)] (**103**) formed through addition of CO_2 to phenyl complex [Cp*_2Sc(C_6H_4Me-4)] at low temperatures.[142] One year later the group of TILLEY described the reaction of [Cp_2Sc(SiR_3)(thf)] with carbon dioxide giving the silanecarboxylate complex [Cp_2Sc(μ-O_2CSiR_3)]_2 (SiR_3 = Si(SiMe_3), Si(*t*BuPh_2)) (**104** and **105**).[143] In the following years
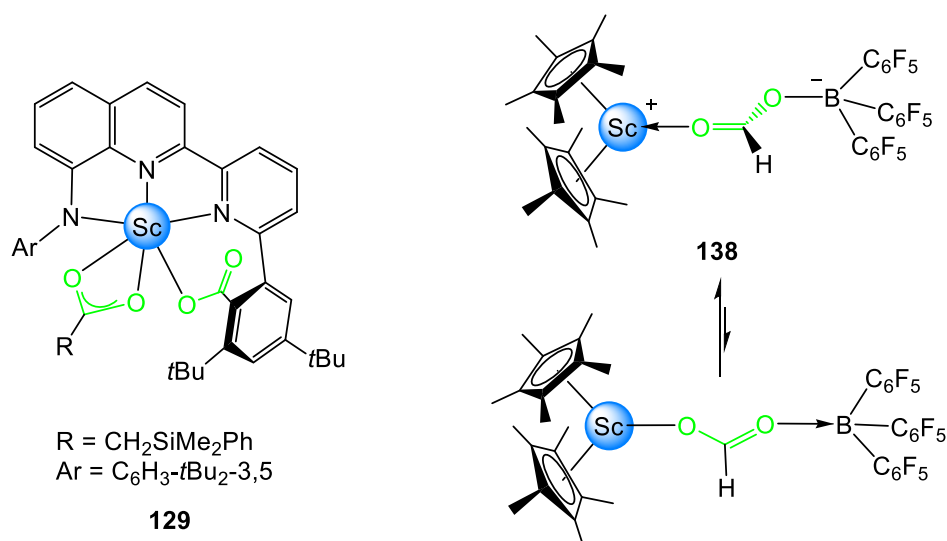
various examples of carboxylate complexes derived from the reaction of CO_2 and cyclopentadienyl-supported rare-earth-metal alkyls were reported (Scheme A11), *e.g.* [Cp$_2$Y{O$_2$C(CH$_2$)$_3$NMe$_2$}] (**106**),[144] [Cp*$_2$Sm(μ-O$_2$CCH$_2$CH=CH$_2$)]$_2$ (**107**),[145] [Cp*$_2$Ln(O$_2$CC$_5$Me$_5$)] (**108**[Ln] Ln = La, Ce, Pr, Nd, Sm)[146,147], [PCp*Y(O$_2$CCH$_2$SiMe$_3$)$_2$] (**109** PCp* = 1,2,3-trimethyl-*1H*-cyclopentadienyl[*l*] phenanthrene),[148] [Cp*$_2$La(O$_2$CC$_5$Me$_5$)(Ph$_3$PO)] (**110**)[149], [Cp*$_2$Y(μ-O$_2$CEt)]$_2$ (**111**)[150] or [(C$_5$H$_3$*t*Bu$_2$)$_2$Sm(O$_2$CC≡CPh)]$_2$ (**112**).[151]

Scheme A11. Different insertion patterns of carbon dioxide into rare-earth-metal σ-Bonds. For the sake of clarity, only monomeric structures without co-ligands are shown.

Other products formed *via* CO_2 insertion into lanthanide-alkyl bonds with bulky dianionic co-ligands like [(OEP)Sc(O$_2$CMe)] (OEP = octaethylporphyrin; **113**)[98] or [(tol-B$_2$Pz$_4$Py)Sc(O$_2$CMe)] (**114**).[152] Utilizing aluminate complexes [Sm{(μ-OC$_6$H$_4$Ph$_2$-2,6)$_2$AlMe$_3$}]$_2$, also known as alkyls in disguise, GAMBAROTTA *et al.* were able to insert CO_2 into a [Sm−μ-Me−Al] unit giving the heterobimetallic carboxylate [Sm{(μ-OC$_6$H$_3$Ph$_2$-2,6)$_2$AlMe$_2$}{(μ-O$_2$CMe)-(OC$_6$H$_3$Ph$_2$-2,6)AlMe$_2$}(dme)] (**115**).[153] Reacting dialkyls with CO_2 resulted in the insertion of two equivalents of carbon dioxide and the formation of bis(carboxylate) compounds as shown by CUI *et al.* for [Cp"Ln(μ-O$_2$CCH$_2$SiMe$_3$)$_2$]$_2$ (**116**[Ln] Ln = Sc, Y, Lu)[57], OKUDA *et al.* for [Y(thf)$_3$(μ-O$_2$CCH$_2$SiMe$_3$)$_2$]$_2$[BPh$_4$]$_2$ (**117**) and [Y(12-crown-

4)(μ-O$_2$CCH$_2$SiMe$_3$)$_2$]$_2$[B(C$_6$H$_4$F-4)$_4$]$_2$ **(118)** [100], and Zhang *et al.* for [(DippNC(Ph)NDipp)Ln(μ-O$_2$CCH$_2$C$_6$H$_4$-NMe$_2$-2)$_2$]$_2$ **(119^{Ln}** Ln = Sc, Y, Lu)[154] and [(DippNC(NBn$_2$)NDipp)Ln(μ-O$_2$CCH$_2$C$_6$H$_4$-NMe$_2$-2)$_2$]$_2$ **(120^{Ln}** Ln = Y, La, Dy, Lu)[155]. Similar results were obtained by the group of PIERS when treating [(DippNC(*t*Bu)CHC(*t*Bu)NDipp)ScR$_2$] with stoichiometric amounts and with excess carbon dioxide to obtain mixtures of CO$_2$ inserted products [(DippNC(*t*Bu)CHC(*t*Bu)NDipp)Sc(μ_n-O$_2$CR)R]$_n$ **(121** R = Me, *n* = 2 or **122** R = CH$_2$SiMe$_3$, *n* = 1), [(DippNC(*t*Bu)CHC(*t*Bu)NDipp)Sc(O$_2$CR)$_2$] (R = Me **123**; R = CH$_2$SiMe$_3$ **124**) and [{O$_2$CH(C(*t*Bu)NDipp)$_2$}Sc(μ-O$_2$CR)$_2$]$_2$ (R = Me **125**; R = CH$_2$SiMe$_3$ **126**).[70] The cationic complex [(DippNC(*t*Bu)CO$_2$CHC(*t*Bu)NDipp)Sc(μ-O$_2$CMe)]$_2$[H$_3$CB(C$_6$F$_5$)$_3$]$_2$ **(127)**, generated by addition of B(C$_6$F$_5$)$_3$ and subsequent treatment with CO$_2$, displayed reversible CO$_2$ insertion as observed by NMR spectroscopic measurements. Just recently the insertion of CO$_2$ into a Ln−C(nacnac)-bond was observed by CHEN and coworkers. Treatment of [LYb(μ-I)(thf)]$_2$ (L = [MeC(NDipp)CHC(Me)NCH$_2$CH$_2$NMe$_2$]) with CO$_2$ gave [{MeC(NDipp)CH(CO$_2$)C(Me)NCH$_2$CH$_2$NMe$_2$}Yb(μ-I)]$_2$ **(128)**.[156] In 2014, the insertion of two equivalents of CO$_2$ into a mixed Sc alkyl-aryl complex [(AbP)Sc(CH$_2$SiMe$_2$Ph)] (AbP = N-(3,5-di-*tert*-butylphenyl)-2-(6-(3,5-di-*tert*-butylphenyl)pyridine-2-yl)quinolone-8-amido) forming the bis-carboxylato complex [(AbPCO$_2$)Sc(O$_2$CCH$_2$SiMe$_2$Ph)] **(129**, Figure A8) was described.[157,158] Upon activation of HSiEt$_3$ with B(C$_6$F$_5$)$_3$, **129** has been probed as a catalyst in hydrosilylation reactions of CO$_2$.

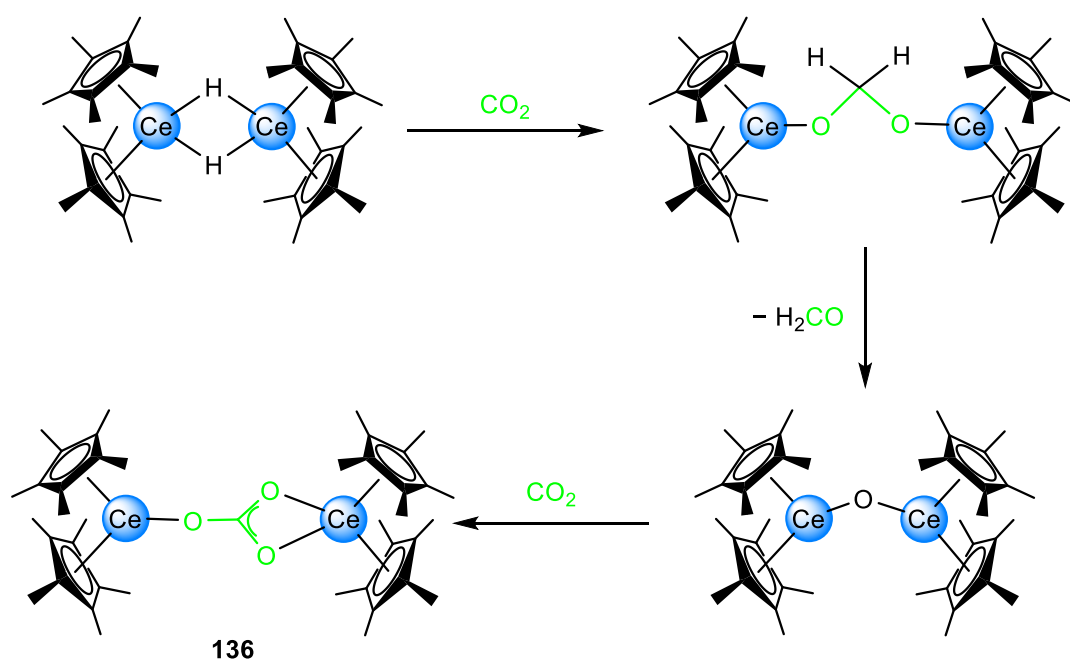**Figure A8.** Scandium complexes as active (pre)catalysts in hydrosilylation reactions of CO$_2$.

In 2015 CHEN and coworkers isolated [(LSc)$_2$(μ-O$_2$CCH$_2$CO$_2$)(μ-PDipp)] (**130** L = [MeC(NDipp)CHC(NDipp)Me]) as a double insertion product of two equivalents of CO$_2$ into the Sc−CH$_2$−Sc bonds the methylidene precursor [(LSc)$_2$(μ-CH$_2$)(μ-PDipp)] (Figure A9).[159] A similar carbon dioxide double insertion was found by XU *et al.* when examining the reaction of a lutetacyclopentadiene complex with excess CO$_2$, giving [Lu{O$_2$CC(SiMe$_3$)C(Ph)C(Ph)C(SiMe$_3$)CO$_2$(Li(thf))}$_3$] (**131**, Figure A8).[104]

Figure A9. Complexes **130** and **131** resulting from a double CO$_2$ insertion into Ln−C-bonds.

Analogous to the rare-earth-metal alkyl complexes, the activation of carbon dioxide with hydrido complexes led to the formation of lanthanide formates as it was shown by the group of HOU in 2004.[160] Reacting tetrametallic complex [{Cp''Y(μ-H)}$_4$(Me$_3$SiCCHCHCSiMe$_3$)] with CO$_2$, complex [(Cp''Y)$_4$(μ-O$_2$CH$_2$)$_2$(Me$_3$SiCCHCHCSiMe$_3$)] (**132**) was successfully isolated. With longer reaction times the release of formaldehyde occurred and the mixed-formato-carbonato complex [(Cp''Y)$_4$(μ-O$_2$CH$_2$)(μ-CO$_3$)(Me$_3$SiCCHCHCSiMe$_3$)] (**133**) and the bis-carbonato complex [(Cp''Y)$_4$(μ-CO$_3$)$_2$(Me$_3$SiCCHCHCSiMe$_3$)] (**134**) were formed (Scheme A12). In 2008, Cui *et al.* reported the insertion of CO$_2$ into a Ln−H- as wells into the Ln−OAr-bond of a mixed hydrido-aryloxy complex.[59] As a result isolation of the mixed foramto-carboxylato complexes [Cp''Ln(μ-O$_2$CH)(μ-O$_2$COAr)]$_2$ (**135^{Ln}** Ln = Y, Dy, Lu, Ar = C$_6$H$_2$tBu-2,6-Me-4) was achieved. The starting compounds were further successfully probed as catalysts in the copolymerization of CO$_2$ and cyclohexene oxide.

**Scheme A12.** Stepwise formation of complex [(Cp"Y)$_4$(μ-CO$_3$)$_2$(Me$_3$SiCCHCHCSiMe$_3$)] (**134**).

Other insertion products resulting from a carbon dioxide activation of a lanthanide hydrido complex are [{Cp*$_2$Ce(thf)}$_2$(μ-O$_2$CO)] (**136**),[161] which was most likely formed through CO$_2$ activation, followed by formaldehyde elimination and another CO$_2$ insertion step into the Ce−O−Ce bond (Scheme A13) as well as the hydrido congener of the aforementioned scandium complex **114** by Piers and coworkers [(tol-B$_2$Pz$_4$Py)Sc(O$_2$CH)] (**137**).[152] In 2013 Berkefeld *et al.* published the formato complex [Cp*$_2$Sc{μ-O$_2$CHB(C$_6$F$_5$)$_3$}] (**138**) resulting from the CO$_2$ insertion into the B−H bond of the contact ion pair [Cp*$_2$Sc][HB(C$_6$F$_5$)$_3$}] (Figure A8).[71] Although, this insertion does not proceed at a rare-earth-metal center this complex is noteworthy to be mentioned, especially because it was shown to be active in the catalytic hydrosilylation of carbon dioxide.

Scheme A13. Stepwise formation of complex [{Cp*$_2$Ce(thf)}$_2$(μ-O$_2$CO)] (**136**).

As seen for complexes **135^{Ln}**, rare-earth-metal aryloxides tend to form carbonates upon treatment with CO$_2$. This was also shown by the groups of BOYLE and KEMP with the isolation of complexes [Ln(μ-O$_2$COAr)(OAr)$_2$]$_2$ (**139^{Ln}** with; Ln = Y, Ce, Sm, Dy, Er, Yb, Lu and Ar = C$_6$H$_3$$tBu_2$-2,6) by inserting one molecule of CO$_2$ into homoleptic aryloxides [Ln(OAr)$_3$].[162]

Like alkoxides, other chalcogenido complexes (sulfides and selenides) also engage in CO$_2$ insertion processes. This was shown by EVANS and coworkers in 2006 when reacting [Cp*$_2$Sm(μ-EPh)]$_2$ with CO$_2$ and forming [Cp*$_2$Sm(μ-O$_2$CEPh)]$_2$ (with E = S **140** or Se **141**).[163] In contrast to the alkoxide congeners, the selenido complex **141** showed reversible CO$_2$ insertion and the formation of [Cp*$_2$Sm(μ-SePh)(thf)] (Scheme A14) in THF.
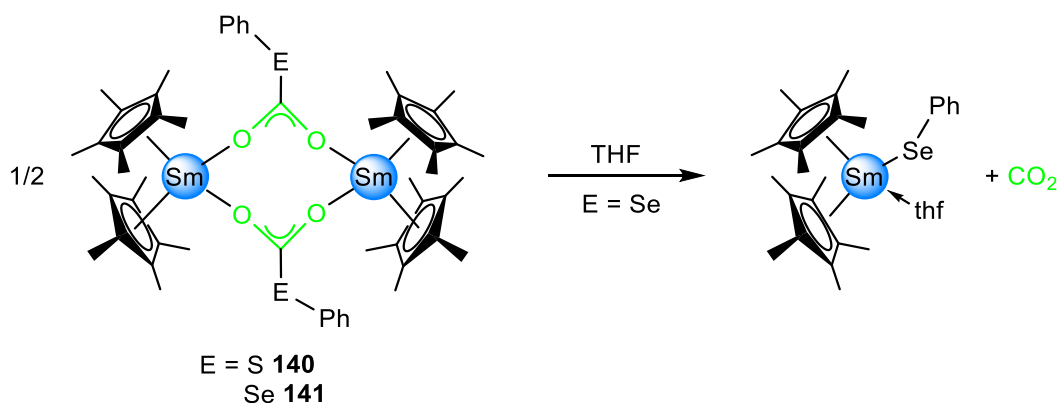
Scheme A14. Reversibility of CO$_2$ insertion into the Ln$-$Se-bond shown with complex **141**.

Carbon dioxide insertion into Ln−N amido bonds and the formation of carbamato ligands was also observed. In 2001, the group of EVANS described the formation of [Cp*$_2$Y(μ-O$_2$CNC$_6$H$_{10}$O)]$_2$ (142) as a result of the CO$_2$ insertion into the ε-caprolactam-ligated complex [Cp*$_2$Y(NC$_6$H$_{10}$O)].[164] Later, the di-*iso*-propylcarbamato complex [Ce$_4$(O$_2$CN*i*Pr$_2$)$_{12}$] (143) was synthesized by reacting CeCl$_3$(dme) with HN*i*Pr$_2$ and CO$_2$.[165] Only recently, our group found that both cerous and ceric pyrazolates [Ce$_4$(Me$_2$pz)$_{12}$] and [Ce(Me$_2$pz)$_4$] reversibly insert one equivalent of CO$_2$ in each Ce−N(Me$_2$pz) bond giving carbamato-type complexes [Ce$_4$(Me$_2$pz·CO$_2$)$_{12}$] (144, Figure A10) and [Ce(Me$_2$pz·CO$_2$)$_4$] (145, Figure A10).[166] By adjusting the stoichiometry of this insertion reaction it was possible to isolate [Ce$_3$(Me$_2$pz)$_9$(Me$_2$pz·CO$_2$)$_3$(thf)] (146) as a possible intermediate of the CO$_2$ insertion. This system was also probed as catalyst in the cyclic addition reaction of CO$_2$ and epoxides. However, with TONs up to 300, it showed only moderate catalytic activity.

144   **145**
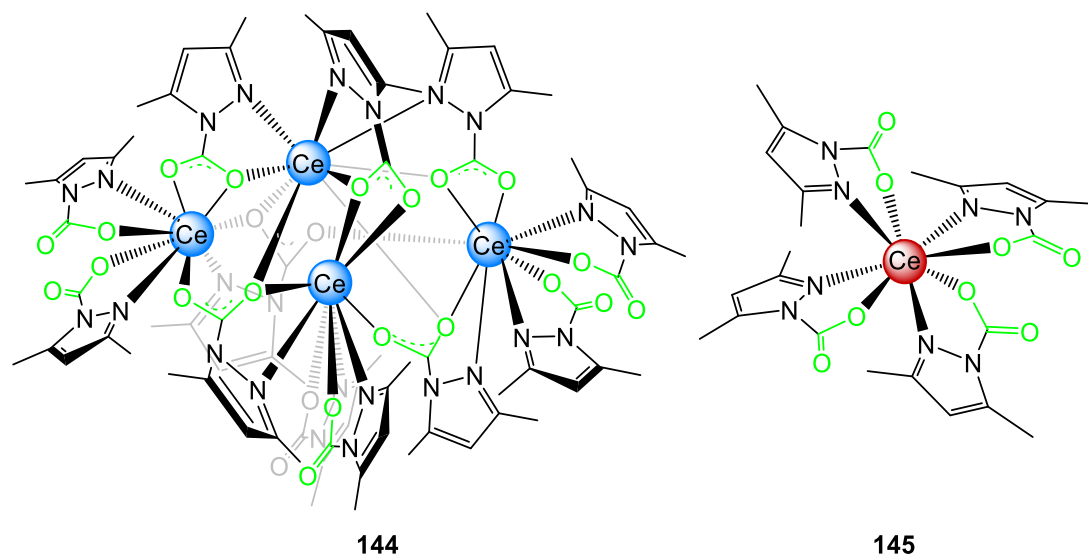
Figure A10. CO$_2$ insertion products **144** and **145** of homoleptic cerium pyrazolates.

4.2 Insertion into Ln−X Multiple Bonds

The first carbon dioxide insertion into a Ln−N imido bond was described by the group of ZHOU in 2013 for trimetallic complex [(NCN)$_3$Lu$_3$(μ-Me)$_3$(μ_3-Me)(μ_3-NPh)] yielding [(NCN)$_3$Lu$_3$(μ-O$_2$CMe)$_3$(μ_3-O$_2$CMe)(μ_3-O$_2$CNPh)] (147, Figure A11).[167] Carbon dioxide insertion into a Ln−N imido double bond was initially observed by CHEN and coworkers when treating scandium imido complex [(NN-Nacnac)Sc=NDipp] with CO$_2$ affording a double insertion of CO$_2$ and forming complex [NN-NacnacSc(O$_2$CN(Dipp)CO$_2$] (148, Figure A11).[111,112] Just

recently such reactivity was also found for the cerium imido complex [(TriNOx)Ce=NAr^F{Cs(dme)$_2$}] (TriNOx = [((2-tBuNO)C$_6$H$_4$CH$_2$)$_3$N]$^{3-}$, Ar^F = C$_6$H$_3$(CF$_3$)$_2$-3,5) producing [(TriNOx)Ce(O$_2$CNAr^F)][Cs(py)$_2$] (**149**, Figure A11) when treated with CO$_2$ in pyridine.[168] In contrast to the scandium complex **148**, complex **149** inserts only one equivalent of CO$_2$ due to the presence of the cesium counterion which was found to play an important role in the carbon dioxide activation. For comparison, the separated ion pair complex [(TriNOx)Ce=NAr^F][Cs(2.2.2-cryptand)] did show activation of CO$_2$, however no isolable products could be obtained.

L = PhC(NDipp)$_2$
147   **148**   **149**
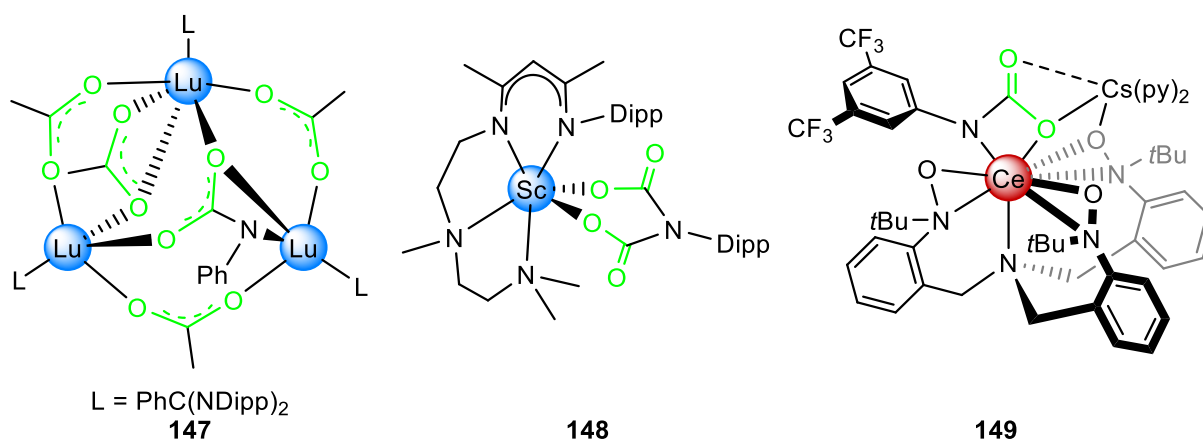
Figure A11. Complexes resulted from the insertion into a Ln−N(imido) bond.

4.3 Insertion into Ln−NHC Bonds

In recent years, especially ARNOLD and coworkers investigated the CO$_2$ insertion into Ln−C(NHC) bonds (Figure A12). Initially the structural characterization of a product of the carbon dioxide insertion in mixed amido NHC complexes [Ln{N(SiMe$_3$)$_2$}$_2$(CMe$_2$CH$_2$(1-C{NCH$_2$CH$_2$NDipp})]] (Ln = Y, Ce) or [Ce{N(SiMe$_3$)$_2$}(C(Me)$_2$CH$_2$(1-C{NCH$_2$CH$_2$NDipp})$_2$] was not feasible.[169] However, isolation of [Sc(μ-OCMe$_2$CH$_2$(1-O$_2$CC{NCHCHNiPr}))$_3$]$_n$ (**150**), provided full prove of carbon dioxide insertion into the Ln−NHC-bond.[170] Moreover, cerous CO$_2$-inserted NHC complexes [(Ce(L^R·CO$_2$)$_3$)] (with L^R = C$_6$H$_2$O-2-tBu-3,5(1-C{N(CH)$_2$N(R)} and R = iPr **151**, tBu **152** or Mes **153**, Figure A12) were described.[171] While complexes **151** and **152** did not show any reversibility in CO$_2$ insertion, this insertion process was found to be partially reversible for complex **153**. The latter complex was also active in cycloaddition reaction of CO$_2$ and epoxides. Shortly after, SIMLER et al. described the syntheses of divalent compounds [Ln(IPr)$_3$(thf)$_3$]I$_2$ (**154^{Ln}** Ln = Eu, Yb, IPr = 1,3-bis(2,6-

di*iso*propylphenyl)imidazol-2-ylidene) and $[Ln(IMes)_2(thf)_4]I_2$ (**155**[**Ln**] and Ln = Eu, Yb, IMes = 1,3-bis(2,4,6-trimethylphenyl)imidazol-2-ylidene) according to transmetallation of the corresponding NHC silver iodide with the respective rare-earth metal. Subsequent treatment with carbon dioxide afforded insertion into the Ln−C(NHC) bond (Figure A12).[172]
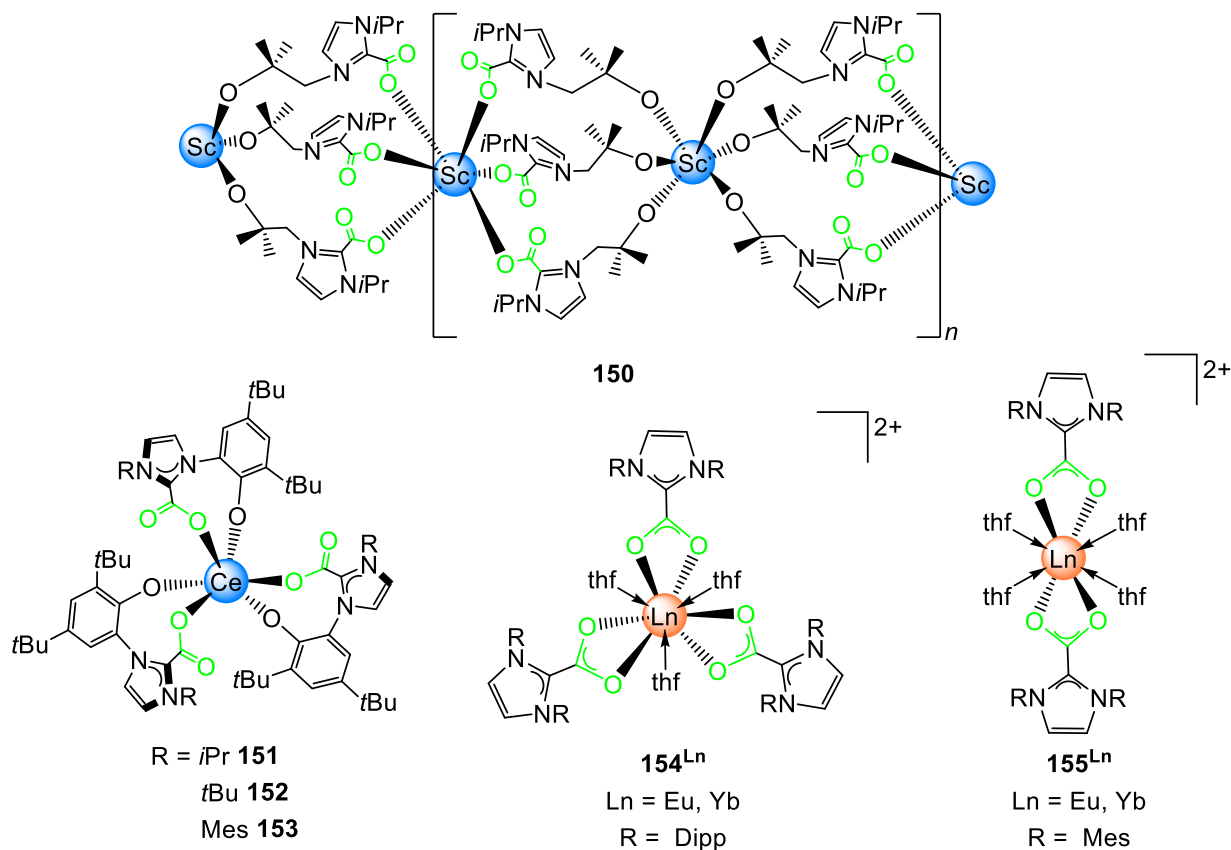

Figure A12. CO_2-inserted Ln-NHC complexes.

4.4 Redox-enhanced CO_2 Activation

Carbon dioxide activation at complexes of divalent lanthanides (Sm, Yb) can proceed *via* reductive coupling and formation of a bridging oxalato ligand. These reactions were investigated by the groups of EVANS as well as MAZZANTI affording oxolate complexes with the general composition $[\{L_2Ln\}(\mu-O_2CCO_2)]$ (Ln = Sm: **156** L = Cp*,[146,173] **157** L = $C_5Me_4(SiMe_2(CH_2CH=CH_2))$,[174] **158** L = $\{DippN\}_2CNCy_2$,[175] Ln = Yb, **159** L = $OSi(OtBu)_3$[176–178]). Similar complexes have been isolated by EVANS and coworkers through replacement of $(N_2)^{2-}$ in $[\{(C_5Me_4H)_2Lu(thf)\}_2(\mu-N_2)]$ upon treatment with CO_2 giving $[\{(C_5Me_4H)_2Lu\}_2(\mu-O_2CCO_2)]$ (**160**),[179] or by reoxidizing low-valent scandium in the mixture $[Sc\{N(SiMe_3)_2\}_3]/KC_8/18$-crown-6 with CO_2 to yield oxalato complex $[(\{N(SiMe_3)_2\}_3Sc)_2(\mu-$

$O_2CCO_2)][K_2(18\text{-crown-}6)_3]$ **(161)**.[180,181] It was also possible to isolate complex $[\{N(SiMe_3)_2\}_3Sc(\mu\text{-}OCO)K(18\text{-crown-}6)]_n$ **(162)** from this reaction mixture, a Sc^{III} ate-complex with bridging CO_2^{2-} moieties. A comparable structural motif was also found earlier by the group of EVANS in the reaction of the yttrium congener with CO_2 producing $\{[(\mu\text{-}OCO)\{N(SiMe_3)_2\}_3Y(\mu\text{-}OCO)][K(18\text{-crown-}6)]\}_n$ **(163)**.[182] Oxalato-bridged complexes have also been generated by utilizing *in situ* formed CO_2. Thermal treatment of a mixture of a carbon or amino acid with a trivalent rare-earth-metal nitrate resulted in reduction of the rare-earth-metal center. Subsequent reductive coupling of the CO_2 and reoxidation of the metal (Scheme A15) gave complexes $[Ln_2(3,5\text{-PDC})_2(H_2O)_4(\mu\text{-}C_2O_4)]\cdot2H_2O$ (**164^{Ln}** Ln = Sm, Eu, Tb, Dy, Ho, Er, PDC = pyridinedicarboxylate)[183–185] and $[\{La(H_2O)_3(MoO_4)\}_2(\mu\text{-}C_2O_4)]_n$[186] **(165)**.
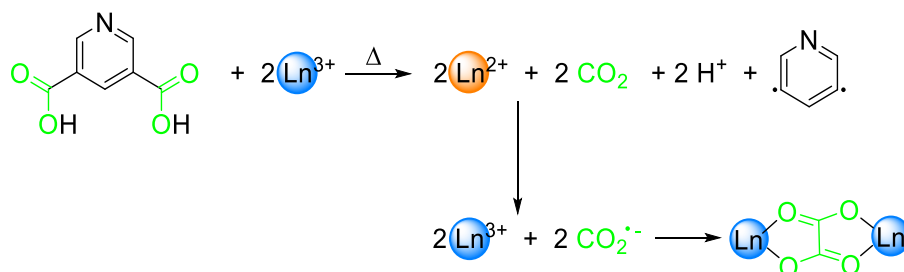
Scheme A15. Proposed mechanism for the formation of the bridging oxalato ligand in the reaction of pyridinedicarboxylic acid and rare-earth-metal nitrides under thermal conditions.

The use of divalent lanthanides can also lead to the formation of bridging carbonato moieties under oxidation of the metal center and release of carbon monoxide. Examples for such reactions are $[\{(por)Sm\}_2(\mu\text{-}CO_3)]$ (por = trans-N,N′-dimethyl-meso-octaethylporphyrinogen, **166**)[187], $[\{(C_5tBu_2H_3)Sm\}_2(\mu\text{-}CO_3)]$ (**167**,[188] $[\{(C_5tBu_3H_2)Sm\}_2(\mu\text{-}CO_3)]$ (**168**)[188] or $[\{(OTf)_2Sm\}_4(\mu_3\text{-}CO_3)_2]$ **(169)**[189] whereas the latter complex needed traces of O_2 or N_2O for an initial oxidation step. Just recently, the MAZZANTI group investigated the reaction of $[Ln\{Si(OtBu)_3\}_4K_2]$ or $[Ln_2\{Si(OtBu)_3\}_4]$ (Ln = Sm, Yb) with CO_2, and focused on the selectivity of oxalate and carbonate formation.[176–178] They found a solvent dependency which, in case of the dimeric complexes $[Ln_2\{Si(OtBu)_3\}_4]$, highly favors the formation of the carbonate complexes whereas the insertion of CO_2 into ate complexes $[Ln\{Si(OtBu)_3\}_4K_2]$ gives an almost equal distribution of oxalate and carbonate complexes. Another route for the synthesis of carbonato complexes was described by WILLIAMS and LEUNG by treating ceric oxo precursors, with CO_2 to generate $[(L_{OEt})_2Ce(O_2CO)]$ **(170)** supported by the KLÄUI tripodal ligand ($L_{OEt} = [Co(\eta^5\text{-}C_5H_5)\{P(O)(OEt)_2\}_3]^-$).[190–192]

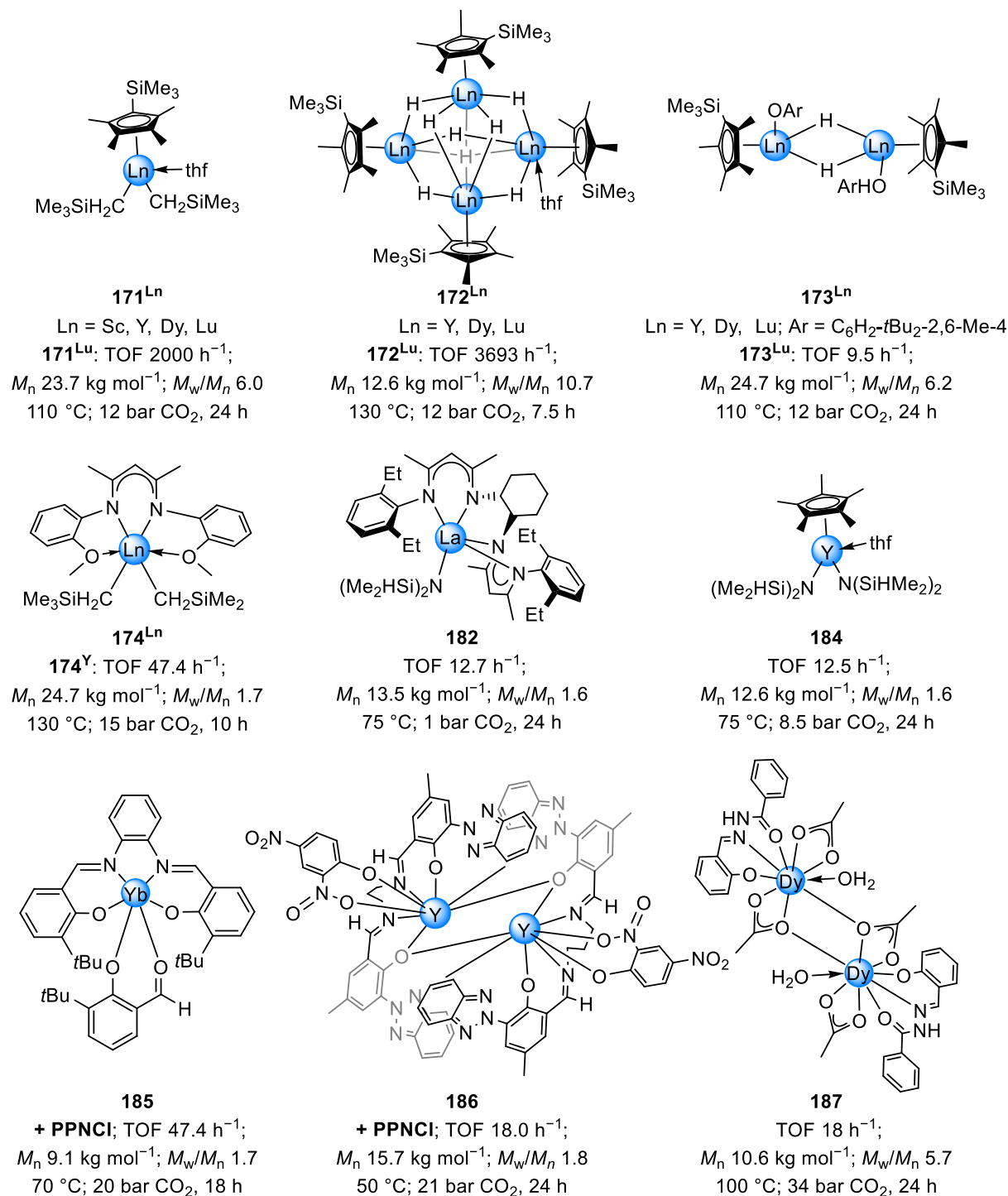## 4.5 Rare-Earth-Metal Complexes for Homogenous Catalytic Conversion of CO_2

For a successful application in a catalytic reaction, the reversibility of carbon dioxide insertion is advantageous. Therefore, it is not surprising that only a small number of rare-earth-metal based catalysts have been probed in CO_2-concerned catalysis. Due to their highly oxophilic nature rare-earth metals as a rule favors irreversible strong Ln−O-bonds, compared to the large number of transition-metal complexes used in homogenous catalytic CO_2 conversion.[193,194] However, some reactions are known to be catalyzed by rare-earth-metal complexes, which will be highlighted in the following.
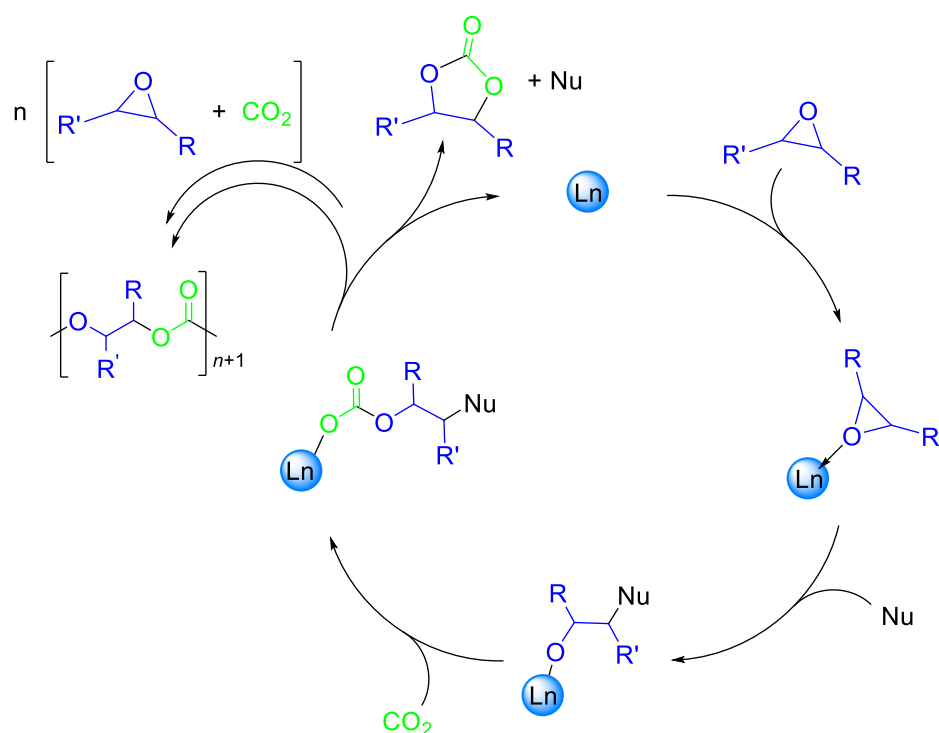
Scheme A16. Simplified, possible reaction mechanism for the copolymerization and cycloaddition of carbon dioxide and epoxides using Ln and nucleophile Nu as catalyst system. Adopted from Ref. [195]

The most investigated reaction is the copolymerization of carbon dioxide and epoxides to yield biodegradable polycarbonates (Scheme A16). Though, the catalyst systems involved routinely ternary mixtures (Ln complex/salt, aluminum/zinc alkyl, and glycerin)[196–202] or a heterobimetallic Ln-Co/Zn complex.[203–209] However, lanthanide-only complexes are also known to initiate copolymerization reactions of carbon dioxide and epoxides. In 2005, CUI *et al.* successfully applied alkyl and hydride complexes [Cp''Ln(CH$_2$SiMe$_3$)$_2$(thf)] (**171^{Ln}** Ln = Sc, Y, Dy, Lu) and [{Cp''Ln(μ-H)$_2$}$_4$(thf)] (**172^{Ln}** Ln = Y, Dy, Lu) as well as the CO_2 inserted complexes **116^{Ln}** as catalysts for these reactions (Figure A13).[57] They found good TOFs up to

$3693\ h^{-1}$ and M_n values up to $39.8\ kg\ mol^{-1}$, but only poor polydispersity indices from 2.46 to 10.68. Similarly, other Ln-alkyl and -hydride complexes have been described to catalyze these reactions, like $[Cp''Ln(OAr)(\mu\text{-}H)]_2$ (**173**[Ln] Ln = Y, Dy, Lu; Ar = C_6H_2-tBu$_2$-2,6-Me-4)[59] and $[(nacnac)Ln(CH_2SiMe_3)(thf)_x]$ (Ar = C_6H_4-OMe-2: **174**[Ln] = Sc, Y, Lu, x = 0; Ar =
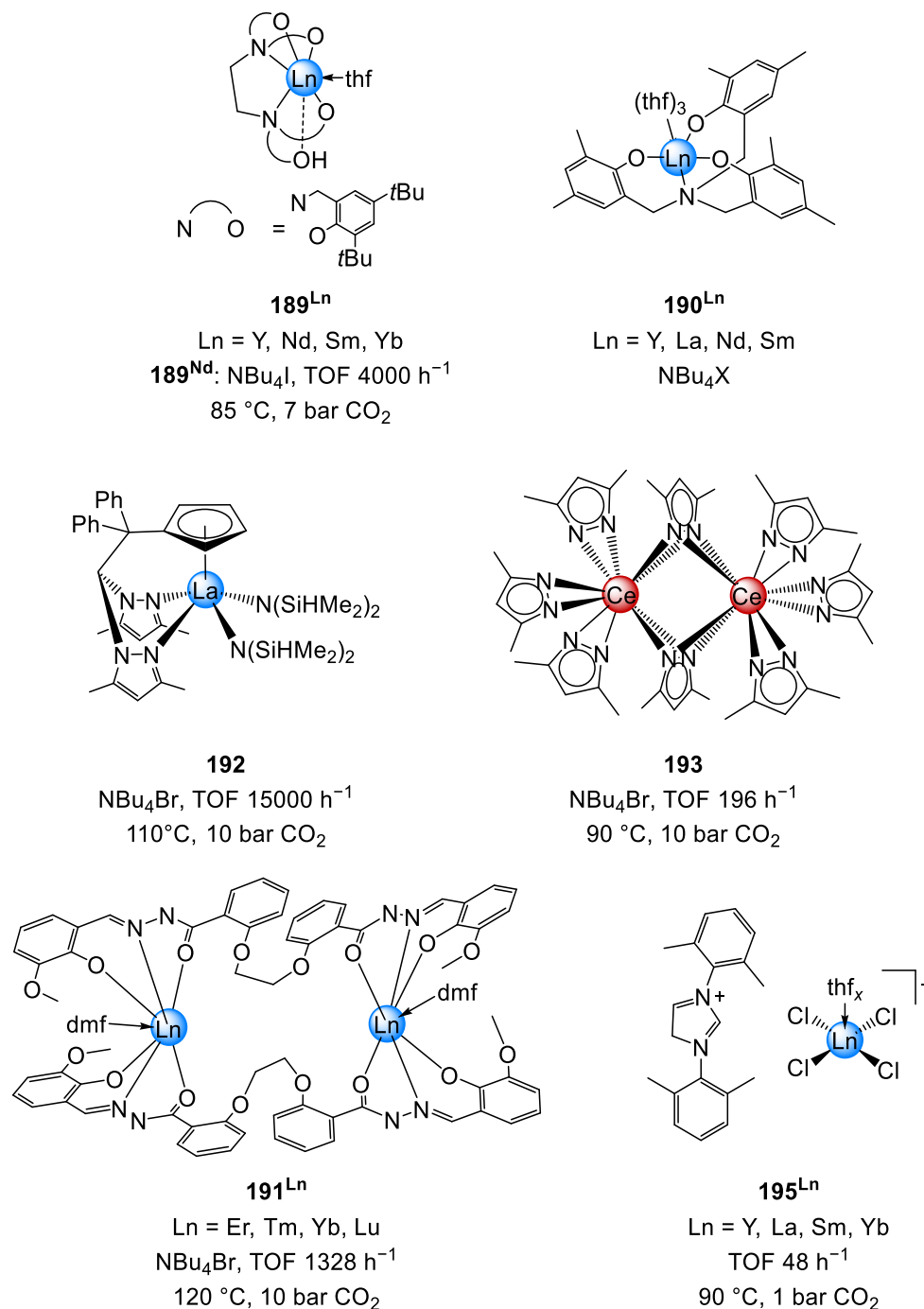

171[Ln]
Ln = Sc, Y, Dy, Lu
171[Lu]: TOF 2000 h^{-1};
M_n 23.7 kg mol^{-1}; M_w/M_n 6.0
110 °C; 12 bar CO$_2$, 24 h

172[Ln]
Ln = Y, Dy, Lu
172[Lu]: TOF 3693 h^{-1};
M_n 12.6 kg mol^{-1}; M_w/M_n 10.7
130 °C; 12 bar CO$_2$, 7.5 h

173[Ln]
Ln = Y, Dy, Lu; Ar = C$_6$H$_2$-tBu$_2$-2,6-Me-4
173[Lu]: TOF 9.5 h^{-1};
M_n 24.7 kg mol^{-1}; M_w/M_n 6.2
110 °C; 12 bar CO$_2$, 24 h

174[Ln]
174[Y]: TOF 47.4 h^{-1};
M_n 24.7 kg mol^{-1}; M_w/M_n 1.7
130 °C; 15 bar CO$_2$, 10 h

182
TOF 12.7 h^{-1};
M_n 13.5 kg mol^{-1}; M_w/M_n 1.6
75 °C; 1 bar CO$_2$, 24 h

184
TOF 12.5 h^{-1};
M_n 12.6 kg mol^{-1}; M_w/M_n 1.6
75 °C; 8.5 bar CO$_2$, 24 h

185
+ PPNCl; TOF 47.4 h^{-1};
M_n 9.1 kg mol^{-1}; M_w/M_n 1.7
70 °C; 20 bar CO$_2$, 18 h

186
+ PPNCl; TOF 18.0 h^{-1};
M_n 15.7 kg mol^{-1}; M_w/M_n 1.8
50 °C; 21 bar CO$_2$, 24 h

187
TOF 18 h^{-1};
M_n 10.6 kg mol^{-1}; M_w/M_n 5.7
100 °C; 34 bar CO$_2$, 24 h

Figure A13. Rare-earth-metal based catalysts for the copolymerization of CO$_2$ and epoxides. TOF, M_n and M_w/M_n are given. If different catalytic systems were investigated, only the conditions giving the highest TOF are stated. If not stated otherwise, no co-catalyst was used (PPN = bis(triphenylphosphine)iminium).

C_6H_2-Me$_3$-2,4,6: **176^{Ln}** Ln = Y, Lu, x = 1; Ar = C_6H_5: **176** Ln = Lu, x = 1)[60] (Figure A13). While complexes **173^{Dy}**, **173^{Lu}**, **175^{Ln}** and **176** also accomplished high polydispersity indices (> 2.0), complexes **173^{Y}** and **174^{Ln}** displayed significantly lower M_w/M_n values of 1.4 to 1.8. Other than alkyls and hydrides, Ln silylamides have also been shown to initiate the copolymerization of CO_2 and epoxides. These complexes include [(nacnac)Ln{N(SiXMe$_2$)$_2$}] (Ar= C_6H_2-Me$_3$-2,4,6; X = Me: **177** Ln = La; X = H: **177^{Ln}** Ln = Y, La), [{C_2H_4(nacnac)$_2$}Ln{N(SiXMe$_2$)}] (X = Me: **179^{Ln}** Ln = Y, La; X = H: **178^{Ln}** Ln = Y, La), [{$C_2(C_4H_8)$(nacnac)$_2$}Ln{N(SiXMe$_2$)}] (X = Me: **181** Ln = La; X = H: **182** Ln = La)[56] (Figure A13), [(Nacnac)Y{N(SiHMe$_2$)$_2$}$_2$] (**183** Ar = C_6H_5) and [Cp*Y{N(SiHMe$_2$)$_2$}$_2$(thf)] (**184**)[58] (Figure A13). Furthermore, donor-functionalized alkoxides are also described to act as catalysts in the presence of a co-catalyst. For example [(salen)Yb(OC$_6$H$_3$-tBu-2-CHO-6)] (**185**)[61], [(BiIBTP)Y(OC$_6$H$_2$-(NO$_2$)$_2$-2,4)] (**186** BiIBTP = bis(benzotriazole iminophenolate))[210], and Schiff-base dysprosium complex [(hb)Dy(μ-OAc)(OAc)(H$_2$O)]$_2$ (**187** hb = (2-hydroxyphenyl)methylene benzohydrazide, Figure A12)[211]. Even though, several rare-earth-metal complexes have been shown to initiate copolymerization reactions of carbon dioxide and epoxides, they are all outperformed by their heterobimetallic congeners. Just recently, the groups NOZAKI and MASHIMA published a study on the mixed lanthanide-cobalt complexes [(L)LnCo$_3$(OAc)$_3$(H$_2$O)$_4$(MeOH)] (**188^{Ln}** Ln = La, Ce, Pr, Nd, Sm, Eu, Gd; L = tris(N$_2$O$_2$) hexaoxime ligand) which revealed TONs up to 13000 and M_n values up to 114 kg mol^{-1} for **188Nd** with polydispersity indices of 1.04 to 1.06 for all **188^{Ln}** (130 °C, 20 bar CO_2, 8 h).[209]

Closely related and also occurring as a side reaction in polymerization reactions is the cycloaddition of CO_2 and epoxides. Therefore, various rare-earth-metal complexes are known to perform as a catalyst in these reactions. As seen before, heterobimetallic Ln-Zn-based catalysts are known to promote this transformation.[206,207,212] Furthermore, commercially available compounds like oxy-chlorides or triflates were shown to catalyze such cyclization reactions.[63,68] However, we want to emphasize the potential of rare-earth-metal based catalyst by highlighting recent work on organometallic compounds. In 2014, YAO and coworkers reported the first organometallic complexes to be successfully applied in cycloadditions of carbon dioxide and epoxides.[64] They used the ethylenediamine-bridged tetra(phenol) (LH$_4$) ligated complexes [(LH)Ln(thf)] (**189^{Ln}** Ln = Y, Nd, Sm, Yb) together with tetra-n-butyl ammonium salts and achieved TOFs up to 4000 h^{-1} for the conversion of propylene oxide to propylene carbonate (Figure A14). Employing **189Nd**/nBu$_4$NI, found as the most efficient catalyst system, even the desired conversion of various terminal and internal epoxides was successful. The same group later described amine-bridged tri(phenolato) stabilized complexes

[{(OC$_6$H$_4$Me$_2$-2,4-CH$_2$-6)$_3$N}Ln(thf)$_3$] (**190^{Ln}** Ln = Y, La, Nd, Sm; Figure A14) to catalyze not only the formation of cyclic carbonates but also the reaction of epoxide, aniline, and CO$_2$ to yield oxazolidinones.[62] Again, the Nd-based complex **190Nd** turned out to be the most efficient. Another example of rare-earth-metal complexes with a polydentate ligand was published by the group of Liu using the salicylyl hydrazine (sh) complexes [(sh)Ln(dmf)]$_2$ (**191^{Ln}** Ln = Er, Tm,

189^{Ln}
Ln = Y, Nd, Sm, Yb
189Nd: NBu$_4$I, TOF 4000 h^{-1}
85 °C, 7 bar CO$_2$

190^{Ln}
Ln = Y, La, Nd, Sm
NBu$_4$X

192
NBu$_4$Br, TOF 15000 h^{-1}
110°C, 10 bar CO$_2$

193
NBu$_4$Br, TOF 196 h^{-1}
90 °C, 10 bar CO$_2$

191^{Ln}
Ln = Er, Tm, Yb, Lu
NBu$_4$Br, TOF 1328 h^{-1}
120 °C, 10 bar CO$_2$

195^{Ln}
Ln = Y, La, Sm, Yb
TOF 48 h^{-1}
90 °C, 1 bar CO$_2$

Figure A14. Rare-earth-metal based catalysts for the cycloaddition of CO$_2$ and epoxides. Co-catalyst, TOF (if mentioned in the publication) and reaction conditions are given below the catalysts. If different catalytic systems were investigated, only numbers for the conditions giving the highest TOF are stated.

Yb, Lu) which revealed TOFs up to 1328 h^{-1} for the conversion of styrene oxide. In 2017, Martínez *et al.* employed lanthanum heteroscorpionate complex to efficiently catalyze the cycloaddition of carbon dioxide and epoxides.[66] Accordingly [{C$_5$H$_4$C(Ph)$_2$C(Me$_2$pz)$_2$}La{N(SiHMe$_2$)$_2$}] (**192**, Figure A14) was not only shown to be very active (TOF up to 15000 h^{-1}, highest TOF reported for rare-earth-metal catalysts) but also to be very useful for the formation of terminal, internal, and bio-based cyclic carbonates. Likewise, our group showed the homoleptic cerium dimethyl pyrazolates [Ce(Me$_2$pz)$_4$]$_2$ (**193**, Figure A14) and [Ce$_4$(Me$_2$pz)$_{12}$] (**194**) catalyze, albeit, with only poor turnover frequencies (max. 196 h^{-1}).[166] Hence, dimethyl pyrazolato seems to be a very versatile ligand for the insertion and transformation of carbon dioxide. YAO and coworkers also studied the 1,3-bis(2,6-di*iso*propylphenyl) imidazolium (IPr) complexes [IPr][LnCl$_4$(thf)$_x$] (**195^{Ln}** Ln = Y, La, Sm, Yb, Figure A14) revealing single component behavior for the catalytic formation of cyclic carbonates.[67]

Another reaction catalyzed by rare-earth-metal complexes is the tandem hydrosilylation of carbon dioxide yielding methane and siloxane in the presence of B(C$_6$F$_5$)$_3$. This reaction was first described by the group of PIERS in 2013 using scandium formato borate [Cp*$_2$Sc{μ-O$_2$CHB(C$_6$F$_5$)$_3$}] (**138**, Figure A8).[71] Other catalysts are [(AbPCO$_2$)Sc(O$_2$CCH$_2$SiMe$_2$Ph)] (**129**, Figure A8) and the amidopyridinate (N,N,N) stabilized alkyls [(N,N,N)Ln(CH$_2$SiMe$_3$)$_2$] (**196^{Ln}**, Ln = Sc, Y).[157,158,213] Crucial for this reaction is the presence of B(C$_6$F$_5$)$_3$ which is considered to activate the silane, while the activation of carbon dioxide is occurring at the rare-earth-metal center. A simplified, possible mechanism is given in scheme A17.
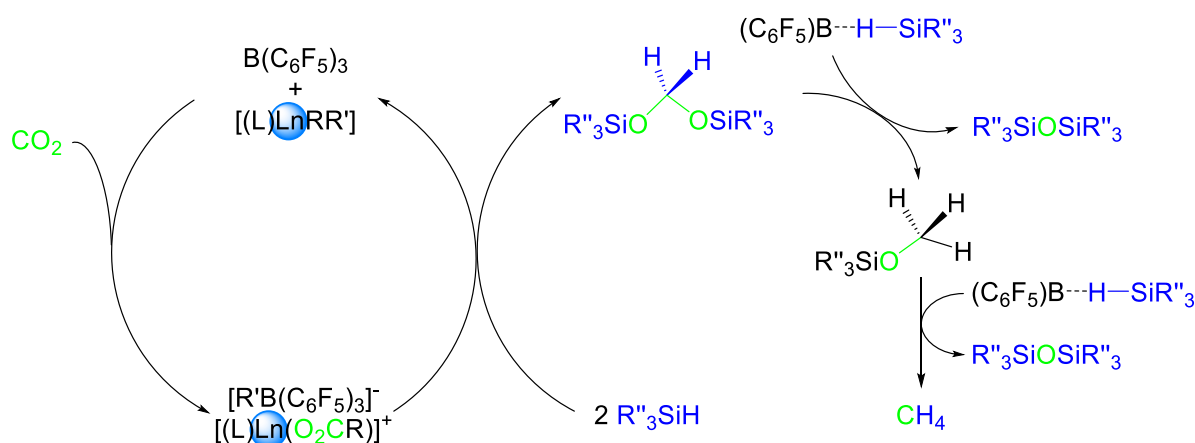
Scheme A17. Simplified, possible reaction mechanism for the hydrosilylation of carbon dioxide and the formation of methane using complex [(L)LnRR'] and B(C$_6$F$_5$)$_3$ as catalytic system. Adopted from Ref. [213]

Furthermore, lanthanides, in particular Sc(OTf)$_3$, are also implemented in the catalytic cascade hydrogenation of carbon dioxide giving MeOH.[214,215] In this reaction, CO_2 reacts with hydrogen catalyzed by a ruthenium based catalyst to yield formic acid followed by an esterification with an alcohol, catalyzed by Sc(OTf)$_3$ (Scheme A18). In a last step, this ester reacts with hydrogen, using another ruthenium- or iridium-based catalyst, under release of an alcohol and water.
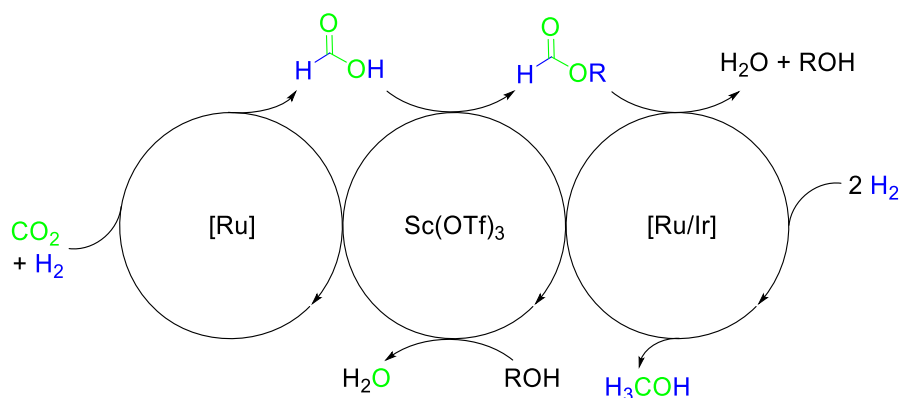
Scheme A18. Simplified catalytic cycle for the cascade hydrogenation of carbon dioxide and the formation of methanol using Sc(OTf)$_3$ and other ruthenium- or iridium-based catalysts for the different steps. Adopted from Ref. [215]

B

Summary of the Main Results

1   Optimization of the Synthesis of Ceric [Ce{N(SiHMe₂)₂}₄]

Organometallic Ce^{IV} complexes are mainly generated *via* three different synthesis routes: salt metathesis, protonolysis reactions using ceric precursors and oxidations using cerous precursors.[216] Due to the high pK$_a$ value of silylamine $HN(SiHMe_2)_2$ (pK$_a$(THF) = 22.8),[217] tetravalent $[Ce\{N(SiHMe_2)_2\}_4]$ (**A**) emerged as a broadly applicable precursor for the synthesis of homoleptic Ce^{IV} species.[123,132,218–221] As the published syntheses suffered from various drawbacks, *e.g.* low overall yields and complicated synthesis pathways, one goal of this work was to modify the synthesis in order to generate **A** in good yields in a preferably easier way.

With addition of donor solvent (do) to ate complex $[Ce\{N(SiHMe_2)_2\}_4Li(thf)]$ (**B**) it was possible to isolate solvent-separated ion-pair complexes of the general composition $[Ce\{N(SiHMe_2)_2\}_4][Li(do)_x]$ (**C^{do}** with do, x = py, 4; dme, 3; tmeda, 2; 12-crown-4, 1 and thf, 4) (Scheme B1, Figure B1). The formation of the separated ion-pair type complex **C^{thf}** could be shown *via* ^7Li NMR spectroscopy upon addition of stoichiometric amounts of THF to a solution of **B** in C_6D_6.
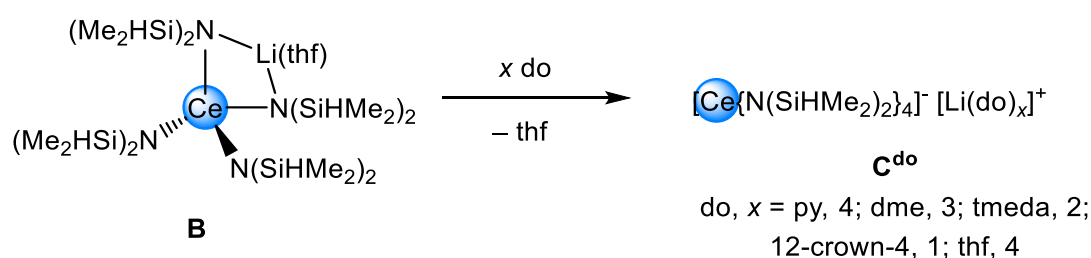
Scheme B1. Formation of the solvent-separated ion-pair type complexes $[Ce\{N(SiHMe_2)_2\}_4][Li(py)_4]$ (**C^{py}**), $[Ce\{N(SiHMe_2)_2\}_4][Li(dme)_3]$ (**C^{dme}**), $[Ce\{N(SiHMe_2)_2\}_4][Li(tmeda)_2]$ (**C^{tmeda}**), $[Ce\{N(SiHMe_2)_2\}_4][Li(12-crown-4)(thf)]$, (**C$^{12-crown-4}$**), and $[Ce\{N(SiHMe_2)_2\}_4][Li(thf)_4]$ (**C^{thf}**).
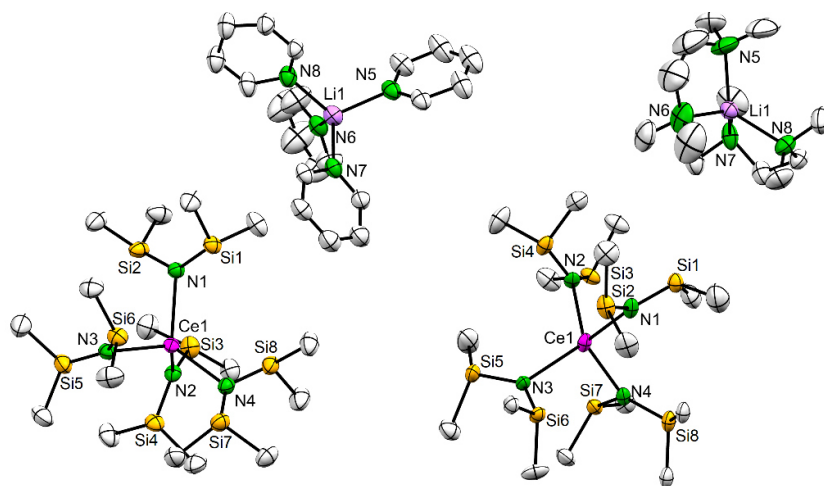
Figure B1. Crystal structures of **C^{py}** (left), and **C^{tmeda}** (right, **Paper I**).
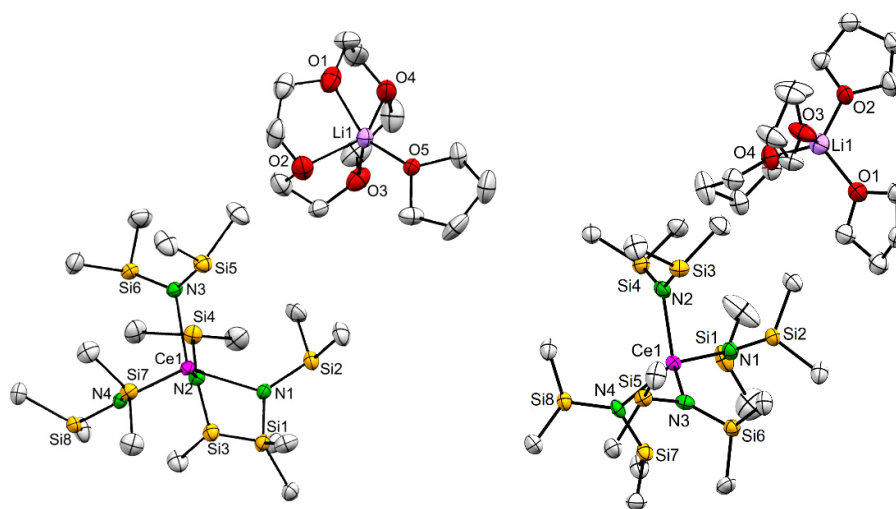
Figure B1 continued. Crystal structures of $\mathbf{C^{12\text{-}crown\text{-}4}}$ (left), and $\mathbf{C^{thf}}$ (right, **Paper I**).

The separation of the lithium cation was also validated by the DRIFT spectra of the complexes. These display only one broad absorption band for the Si−H vibrations as a result of the more symmetric surrounding of the cerium centers.

Oxidation of complexes $\mathbf{C^{do}}$ with one equivalent of 1,4-*p*-benzoquinone gave **A** plus a lithium semiquinolate "{Li(do)}sq" as an insoluble by-product (Scheme B2). Benzoquinone was chosen as an oxidant due to the easily separable by-product which is formed during the reaction, however, the definite composition of the lithium semiquinolate could not be elucidated. After filtration and removal of the solvent the crude yield and purity of **A** was determined. While $\mathbf{C^{dme}}$ and $\mathbf{C^{12\text{-}crown\text{-}4}}$ gave highest yields (75 and 73%) but minor impurities, the oxidation of $\mathbf{C^{py}}$ gave decently lower yields (59%) but almost no impurities.
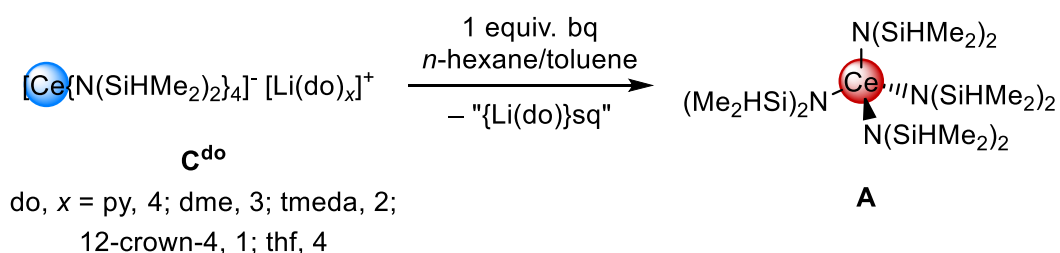
Scheme B2. Oxidation of the ate complexes $\mathbf{C^{do}}$ with benzoquinone to afford $[Ce\{N(SiHMe_2)_2\}_4]$ (**A**).

The benefits of donor-induced ion-pair separation for the oxidation of ate complexes $\mathbf{C^{do}}$ are attributed to the shielding of the lithium cation which prevents it from interacting with the anionic Ce fragment. These effects of preorganization of an ate complex in order to oxidize it have also been reported by the group of SCHELTER.[222–224]

2   Cerium Pyrazolates for Carbon Dioxide Activation

Organometallic rare-earth metal-based CO_2 activation leads to mostly irreversible insertion processes under the formation of carboxylates, formates, carbonates, carbamates or siloxides.[165,173,174,176–178,187,188] However, cerium was shown to efficiently engage in reversible CO_2 insertion.[169,171] As it was recently observed, homoleptic tetravalent $[Ce(Me_2pz)_4]_2$ (**D**) was able to reversibly insert benzophenone. An objective of this work was to examine the reactivity of **D** and $[Ce_4(Me_2pz)_{12}]$ (**E**) toward carbon dioxide.

Stirring a solution of either ceric **D** or cerous **E** in toluene or THF under 1 bar of CO_2 pressure gave the CO_2 inserted products $[Ce(Me_2pz·CO_2)_4]$ (**F**, Figure B2, Scheme B3) and $[Ce_4(Me_2pz·CO_2)_{12}]$ (**G,** Figure B3, Scheme B3).

$$[Ce(Me_2pz)_4]_2 \quad \xrightarrow[\substack{\text{a) THF, }-40\,°C \\ \text{b) toluene, r.t.}}]{\text{exc. } CO_2} \quad 2\,[Ce(Me_2pz·CO_2)_4]$$

$$\textbf{D} \qquad\qquad\qquad\qquad\qquad\qquad \textbf{F}$$

$$[Ce_4(Me_2pz)_{12}] \quad \xrightarrow[\text{toluene, r.t.}]{\text{exc. } CO_2} \quad [Ce_4(Me_2pz·CO_2)_{12}]$$

$$\textbf{E} \qquad\qquad\qquad\qquad\qquad \textbf{G}$$
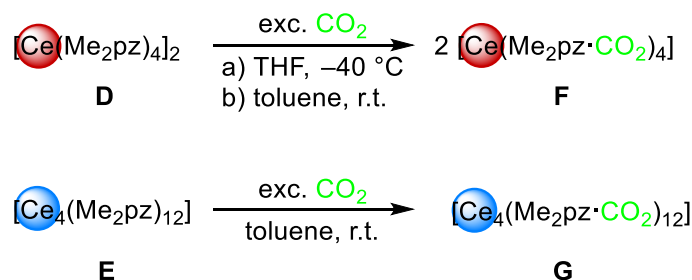
Scheme B3. Insertion of CO_2 into the Ce–N(Me_2pz) bond of $[Ce(Me_2pz)_4]_2$ at a) −40 °C in thf or b) ambient temperature in toluene and $[Ce_4(Me_2pz)_{12}]$ in toluene (**Paper II**).
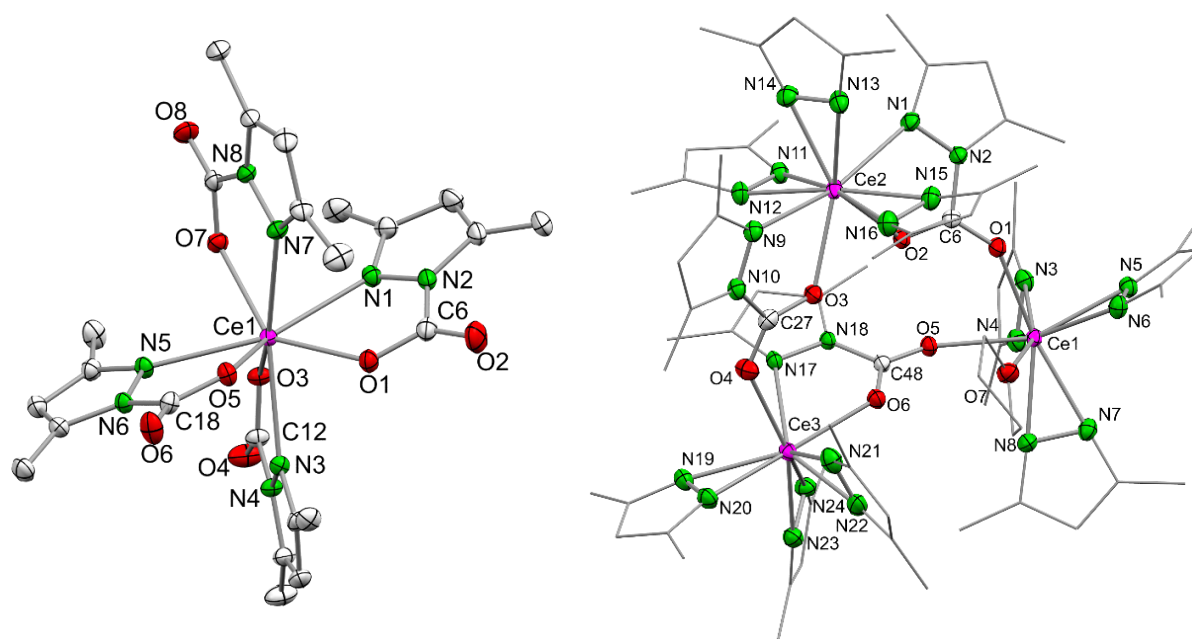
Figure B2. Crystal structures of $[Ce(Me_2pz·CO_2)_4]$ (**F**) and $[Ce_3(Me_2pz)_9(Me_2pz·CO_2)_3(thf)]$ (**H**).
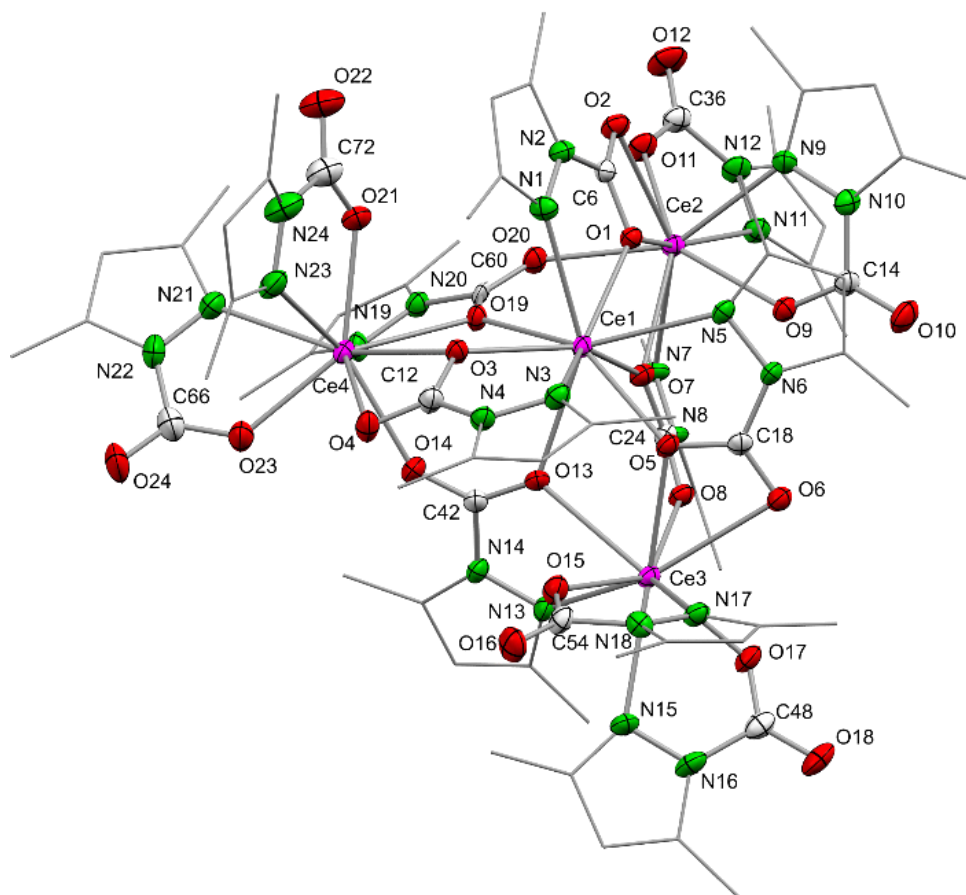
Figure B3. Crystal structure of $[Ce_4(Me_2pz \cdot CO_2)_{12}]$ (**G**).

VT NMR experiments in toluene-d_8 have shown that this insertion is partially reversible forming the putative species $[Ce(Me_2pz \cdot CO_2)_2(Me_2pz)_2]$. In THF-$d_8$ complete de-insertion of CO_2 was observed upon heating to 60 °C. After recooling the samples, a reinsertion of carbon dioxide was found (Scheme B4). The reversibility in THF was also revealed by *in situ* IR spectroscopic measurements as the absorption band corresponding to the inserted CO_2 decreased while the level of free carbon dioxide raised. The CO_2 insertion was also found to be reversible in the solid state, which was examined by TGA measurements.

Treatment of $[Ce(Me_2pz)_4(thf)]$ (**D**^{thf}) in *n*-hexane with an equimolar amount of CO_2 gave heteroleptic trimetallic complex $[Ce_3(Me_2pz)_9(Me_2pz \cdot CO_2)_3(thf)]$ (**H**) (Figure B2) as a possible intermediate formed during the reaction of **D** with carbon dioxide in THF. VT NMR studies revealed, besides high fluxional behavior of the asymmetric ligand environment, deinsertion of CO_2 at elevated temperatures.
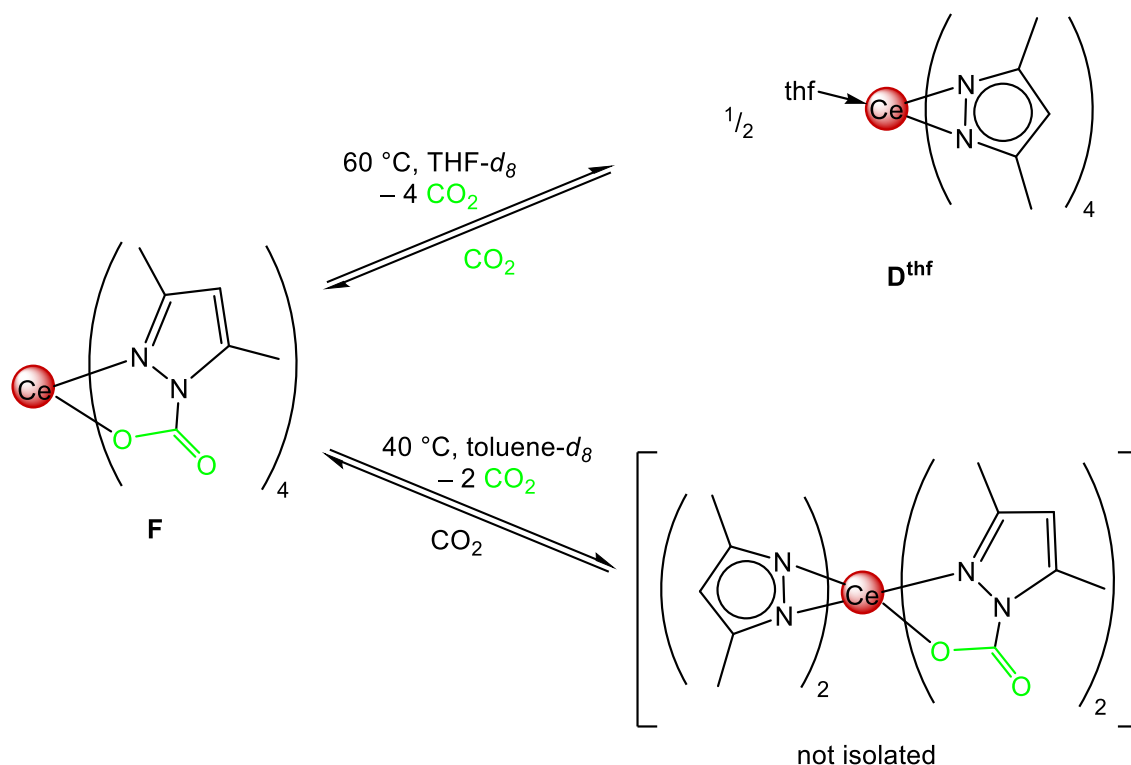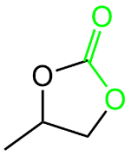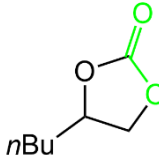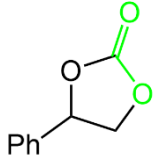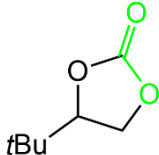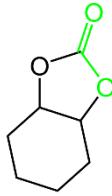
Scheme B4. Reversibility of the carbon dioxide insertion into the Ce–N(Me$_2$pz) bond.

As other rare-earth-metal complexes are known to catalyze the cycloaddtion of CO_2 and epoxides,[64,66,67] **D** and **E** were examined in their ability to act as catalyst in such reactions. Various epoxides were reacted using 0.5 mol% of **D** or 0.25 mol% of **E** as catalyst and 1 mol% of tetra-*n*-butylammonium bromide (TBAB) as cocatalyst under constant pressure of CO_2 (Scheme B5). For epoxides with less sterically demanding substituents, the reactions proceed very fast. However, with increasing bulkiness of the substituents the turnover numbers of the catalysis dropped rapidly (Table B1). Nevertheless, it is noticeable that ceric **D** outperforms cerous **E** in its catalytic activity.
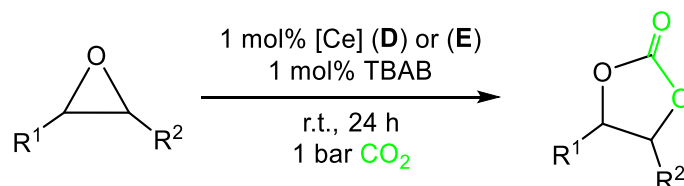
Scheme B5. Catalytic formation of cyclic carbonates from epoxides using **D** or **E** as catalyst and TBAB as cocatalyst.

Table B1. TON of the catalytic cycloaddition of epoxides and CO_2 after 24 h at ambient temperature. [a] at 90 °C and 10 bar CO_2 pressure after 1 h. [b] at 90 °C and 10 bar CO_2 pressure after 24 h.

		*n*Bu	Ph	*t*Bu	
D	93	61	20	12	2
E	98	25	13	3	-
D	196[a]	98[a]	24[a]	168[b]	154[b]

Increasing temperature and carbon dioxide pressure resulted in a significant increase of the TONs making the cycloaddition of sterically demanding or internal epoxides feasible (Table B1).

Ceric complex **D** has shown to be prone to reduction during catalysis as it reacts with TBAB under formation of $[Ce(Me_2pz·CO_2)_4][NnBu_4]$ (**I**) (Figure B4). This species was found in trace amounts in the reaction mixtures and inactive in the catalytic cycloaddition of epoxides and carbon dioxide. Although having examined the formation of this side product by treatment of **D** with stoichiometric amounts of TBAB in the absence of epoxides, the oxidation product of this redox reaction could not be identified.
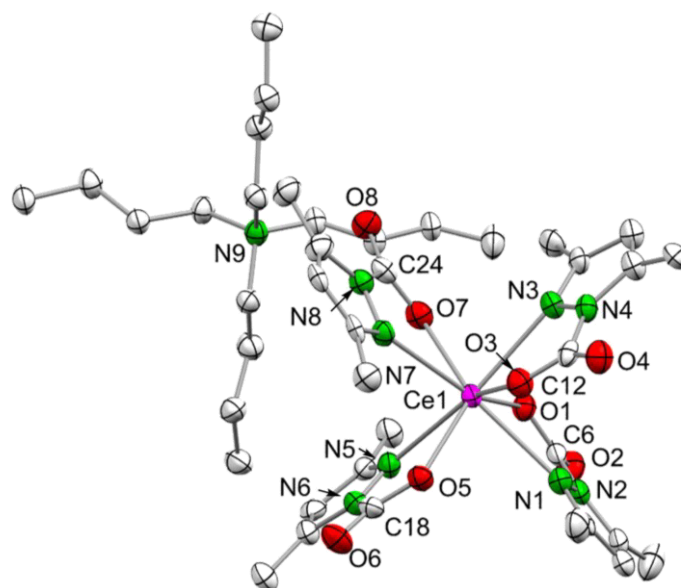
Figure B4. Crystal structure of $[Ce(Me_2pz·CO_2)_4][NnBu_4]$ (**I**).

To enhance the reactivity towards CO_2 and generate an easily separable catalyst, tetravalent and trivalent cerium pyrazolates **D**, **D^{thf}**, **E** and $[Ce(Me_2pz)_3(thf)]_2$ (**J^{Ce}**) as well as the lanthanum complex $[La(Me_2pz)_3(thf)]_2$ (**J^{La}**) have been grafted onto mesoporous silica SBA-15$_{500}$. Therefore, SBA-15$_{500}$ was treated with excess of the organo-metal precursors in *n*-hexane to generate the hybrid materials $[Ce(Me_2pz)_4]_2$@SBA-15$_{500}$ (**HD**), $[Ce(Me_2pz)_4(thf)]$@SBA-15$_{500}$ (**HD^{thf}**), $[Ce_4(Me_2pz)_{12}]$@SBA-15$_{500}$ (**HE**), $[Ce(Me_2pz)_3(thf)]_2$@SBA-15$_{500}$ (**HJ^{Ce}**), and $[La(Me_2pz)_3(thf)]_2$@SBA-15$_{500}$ (**HJ^{La}**). Notably, the supernatants of the grafting reactions did not contain any "free" Me$_2$pzH, which would be produced during the protonolysis reaction, indicating the formation of donor-stabilized surface complexes of the composition $[Ln(Me_2pz)_x(Me_2pzH)]_n$. Similar donor-adducts can be found in the supernatant of the grafting of tetravalent **HD** and **HD^{thf}** in the formation of $[Ce(Me_2pz)_4(Me_2pzH)]$. Analyses of the hybrid materials revealed complete consumption of the surface Si−OH groups and high metal contents of about 10 wt% for the Ce^{IV}-based materials **HD** and **HD^{thf}** and about 20 wt% for the Ln^{III}-based **HE**, **HJ^{Ce}**, and **HJ^{La}**. N$_2$-physisorption measurements show a drastic decrease of the pore diameters and volumes, which is even more distinct for the hybrid materials featuring trivalent metal centers. Therefore, the formation of dimetallic or higher aggregated Ce^{III}-surface species can be assumed, whereas monometallic grafting seems to be favored for the Ce^{IV} pyrazolates (Scheme B6).
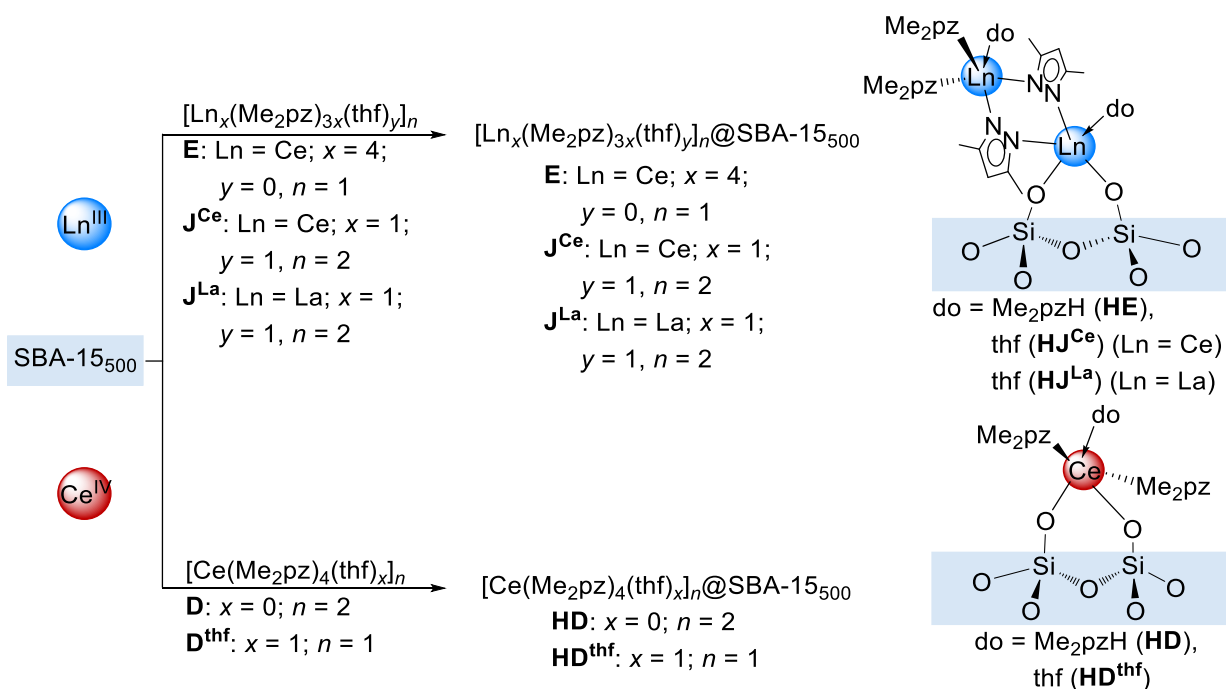
Scheme B6. Direct grafting approach of the Ln pyrazolates **D**, **E**, and **J** yielding hybrid materials **HD**, **HE** and **HJ**. A possible bipodal surface species is shown on the right (**Paper III**).

A model complex for the surface species was synthesized by reacting [Ce{OSi(OtBu)$_3$}$_3$Cl] with one equivalent of K(Me$_2$pz) yielding [KCe{OSi(OtBu)$_3$}$_4$(Me$_2$pz)] (**K**) (Figure B5) along with other products. One of the other products has been identified as [K{OSi(OtBu)$_3$}(Me$_2$pzH)] which co-crystalizes from concentrated n-pentane / Et$_2$O mixtures. The ^{1}H NMR spectrum of the crude product showed two main species containing both tris-*tert*butoxy-siloxy and dimethyl pyrazolyl groups, suggesting **K** and [K{OSi(OtBu)$_3$}(Me$_2$pzH)] as the main products. Unfortunately, complex **K** could not be purified, which made other analytics unfeasible. Treatment of the crude product with CO$_2$ in toluene-d_8 gave a color change from orange to colorless and the ^{1}H NMR spectrum of the reaction mixture gave signals indicative of a successful CO$_2$ insertion. The latter causes an asymmetric Me$_2$pz·CO$_2$ moiety and hence a split resonance of the methyl groups.
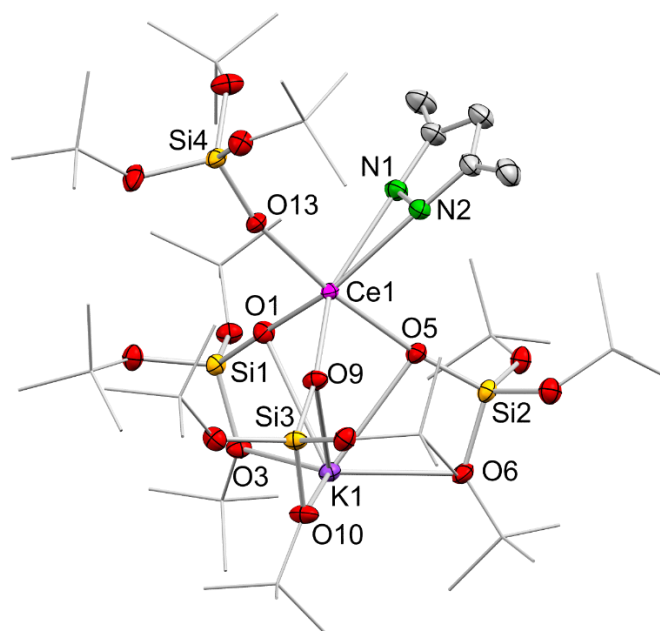
Figure B6. Crystal structure of KCe{OSi(OBu)$_3$}$_4$(Me$_2$pz) (**K**).

Treatment of hybrid materials **HD** to **HJ** with CO$_2$ led to a lightening in color and an increase of in weight of the materials indicating a successful insertion of CO$_2$. This was also supported by DRIFT spectroscopy, displaying strong C−O vibrations at 1600 to 1750 cm^{-1} and ^{13}C CP/MAS spectroscopy of the diamagnetic hybrid materials, revealing resonances at approximately 150 ppm for inserted CO$_2$ (Figure B6). Strikingly, the hybrid materials based on trivalent lanthanides showed a CO$_2$ uptake of about 20 wt%, whereas the tetravalent hybrid materials gave only 10 wt% of inserted CO$_2$ in accordance with the lower metal contents and therefore grafted complexes. To investigate into the reversibility of the CO$_2$ insertion, TGA measurements have been conducted for CO$_2$@[La(Me$_2$pz)$_3$(thf)]$_2$@SBA-15$_{500}$ showing a de-

insertion of CO_2 in three steps at ~50, 100 and 150 °C, respectively. Regrettably, no TGA measurements could be obtained for the cerium-based hybrid materials due to their instability.
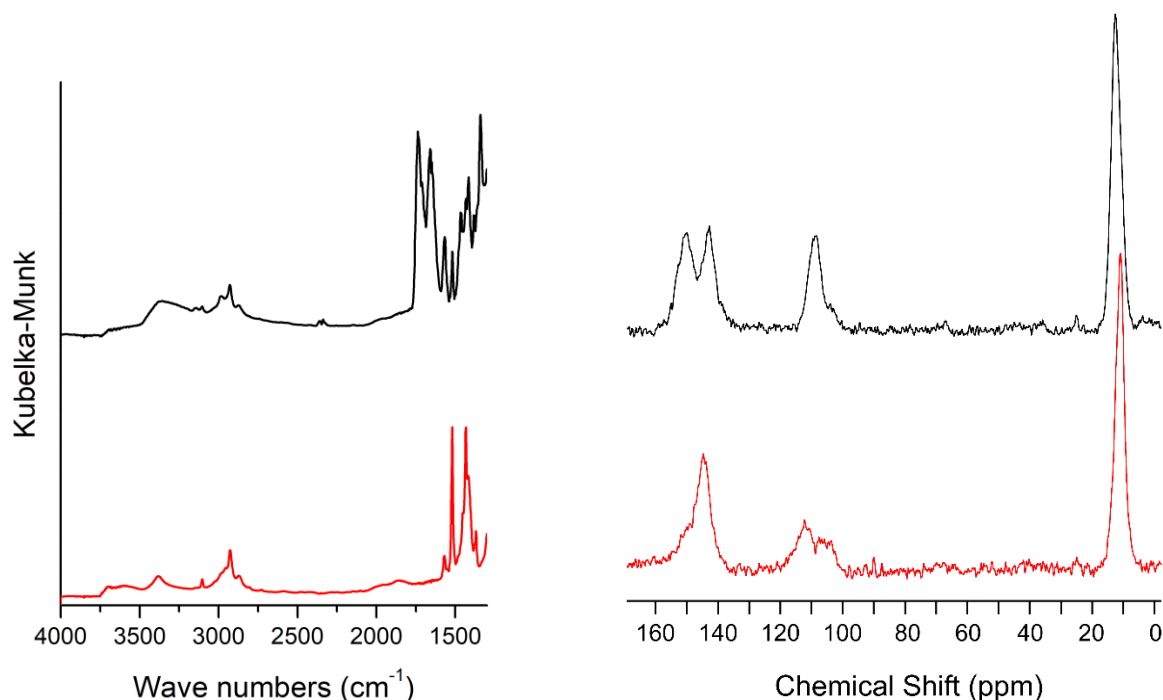
Figure B7. Left: stacked DRIFT spectra of **HD** before (red) and after (black) treatment with CO_2 and right: ^{13}C CP/MAS NMR spectra of **HD** before (red) and after (black) treatment with CO_2.

In a final step, the hybrid materials were screened regarding their applicability for the use as catalyst in cycloaddition of epoxides and CO_2 together with TBAB as a co-catalyst. To identify the most active catalyst 0.1 mol% of **HD** to **HJ** and TBAB have been probed for the conversion of propylene oxide under 10 bar CO_2 pressure at 90 °C for 24 h. In contrast to the homogenous catalysts **D** and **E**, no significant influence of the oxidation state was found as all hybrid materials gave conversions between 66 and 77%. By using 0.5 mol% of tetravalent hybrid material **HD** and TBAB, excellent turnovers could be obtained for sterically less demanding epoxides (>99% for propylene oxide, 94% for 1,2-epoxyhexane, 91% for styrene oxide) after 24 h at 90 °C and 10 bar CO_2 pressure. However, significantly lower turnovers were detected when using sterically demanding epoxides like 3,3-dimethyl-1,2-epoxybutane (66%). The reusability of the catalyst was investigated with 0.5 mol% **HD^{thf}** and TBAB at ambient temperature and 1 bar CO_2 pressure for the conversion of propylene oxide. After 24 h, the conversion was determined by ^1H NMR spectroscopy and the hybrid material was washed with Et_2O before addition of fresh propylene oxide and TBAB. Within four runs, the conversion only dropped from 70% to 45% demonstrating a good recyclability of the grafted rare-earth-metal pyrazolates.

3 Cerium Benzoquinone Redox Chemistry

The role of 1,4-*p*-benzoquinone in Ce^{III} → Ce^{IV} oxidation chemistry is unique among the commonly used oxidants. Oxidation of trivalent cerium ate complexes of the general composition [CeL$_4$M(do)$_x$] or [CeL$_4$][M(do)$_x$] (with L = monoanionic ligand and M = alkali metal cation) leads to the formation of homoleptic ceric complexes CeL$_4$ and an alkali-metal hydro-/semiquinolate as by-product.[132,225,226] However, the reaction of 1,4-*p*-benzoquinone with homoleptic cerous complexes of the composition CeL$_3$ typically results in the formation of hydroquinolato bridged Ce^{IV} complexes [(CeL$_3$)$_2$(μ-O$_2$C$_6$H$_4$)].[130–133] Part of this thesis was to investigate the influence of different 1,4-benzoquinone derivatives in the formation of such hydroquinolato bridged Ce^{IV} compounds.

First, the reaction of different trivalent cerium precursors [Ce{N(SiMe$_3$)$_2$}$_3$] (**L**), [Ce{OSi(O*t*Bu)$_3$}$_3$]$_2$ (**M**), and [Ce{OSi*i*Pr$_3$}$_3$]$_2$ (**N**) toward various 1,4-*p*-benzoquinone derivatives was elucidated (Scheme B7, Figures B8 and B9, **Paper III**). Therefore, a broad range of stronger oxidative (with electron-withdrawing substituents) to weaker oxidative benzoquinones (with electron-donating substituents) was investigated.
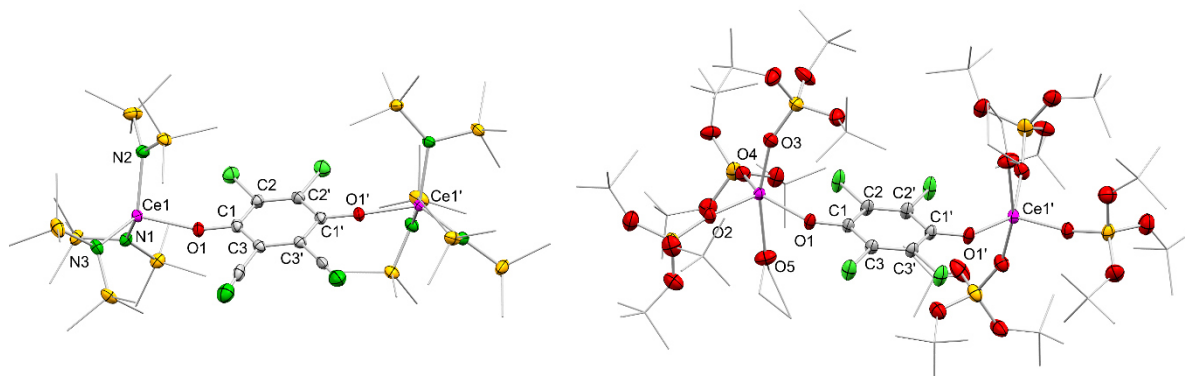
Figure B8. Crystal structures of [(Ce{N(SiMe$_3$)$_2$}$_3$)$_2$(μ-O$_2$C$_6$CN$_2$Cl$_2$)] (**O**^{ddhq}, left) and [(Ce{O(Si(O*t*Bu)$_3$}$_3$)$_2$(μ-O$_2$C$_6$Cl$_4$)] (**P**^{Cl4hq}, right).
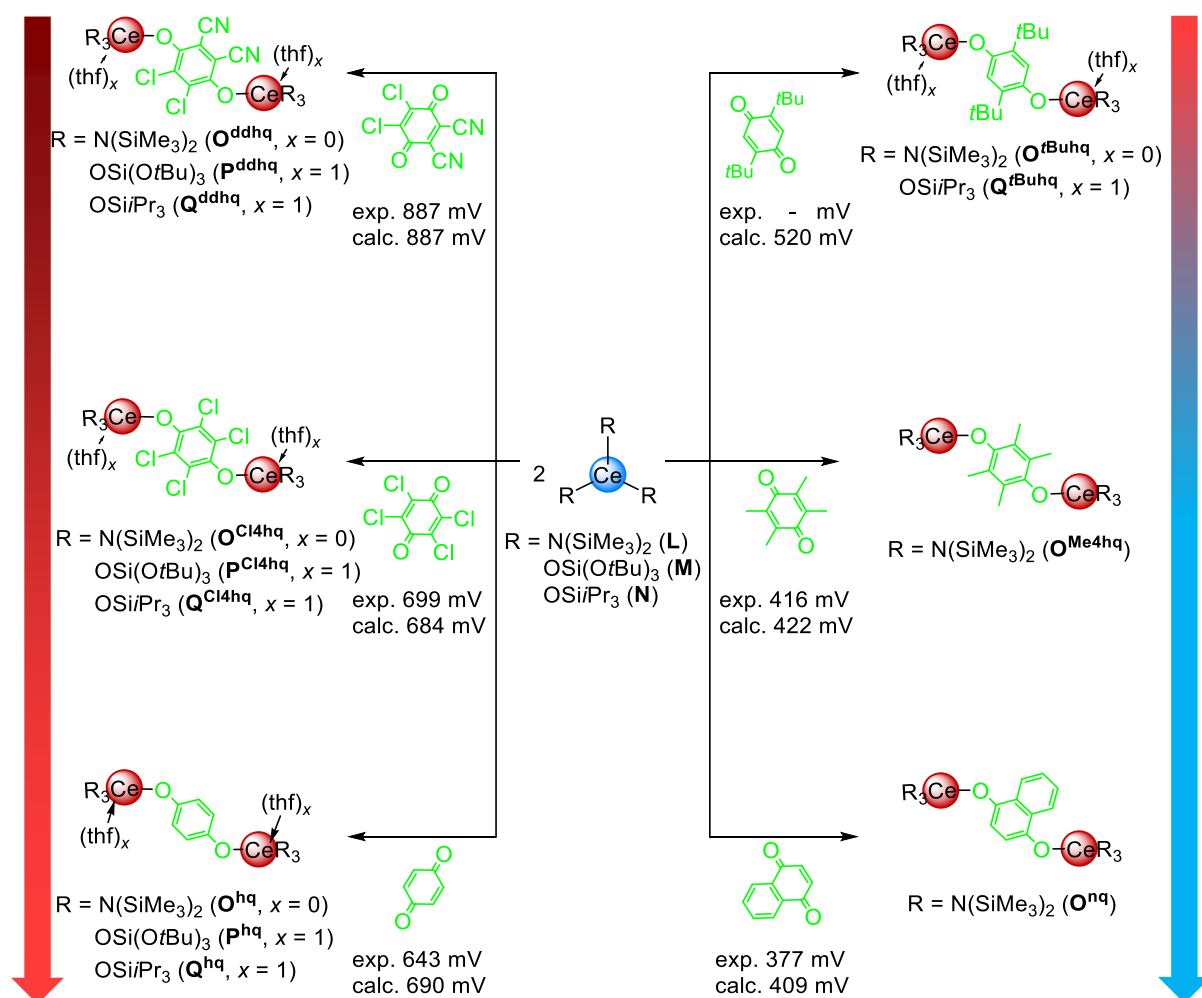
Scheme B7. Reactivity of cerous precursors [Ce{N(SiMe₃)₂}₃] (**L**), [Ce{OSi(O*t*Bu)₃}₃]₂ (**M**), and [Ce{OSi*i*Pr₃}₃]₂ (**N**) toward different benzoquinone derivatives to yield hydroquinolato bridged complexes [(CeL₃)₂(μ-O₂C₆R₄)] (**O**^{ddhq} to **O**$^{naphtho-hq}$). The oxidation strength of the 1,4-*p*-benzoquinone derivatives are indicated by the arrows next to the products (red: strong; blue: weak) and the experimental and calculated values are given below the benzoquinones.[227]

The isolation of tetravalent hydroquinolato bridged complexes succeeded for the silylamides and both siloxides using the stronger oxidative benzoquinones with electron-withdrawing substituents giving complexes **O**^{ddhq} to **Q**^{hq}. While it was possible to obtain Ce^{IV} complexes using cerous silylamide **L** with 2,5-di-*tert*-butyl-1,4-benzoquinone, tetramethyl-1,4-*p*-benzoquinone and 1,4-naphthoquinone, the isolation of a tetravalent compound with the siloxide complexes succeeded only for [(Ce{OSi*i*Pr₃}₃(thf))₂(μ-O₂C₆H₂*t*Bu₂-2,5)] (**Q**^{tBuhq}). The isolated complexes showed the same structural motif, two cerium centers bridged by hydroquinolato linkers (Ce−O bond lengths 2.084(6)−2.233(2) Å) and three co-ligands (**O**: Ce−N bond lengths 2.211(2)−2.265(5) Å; **P**, **Q**: Ce−O bond lengths 2.066(2)−2.153(2) Å). Siloxy complexes **P** and **Q** are additionally stabilized by one THF donor molecule.
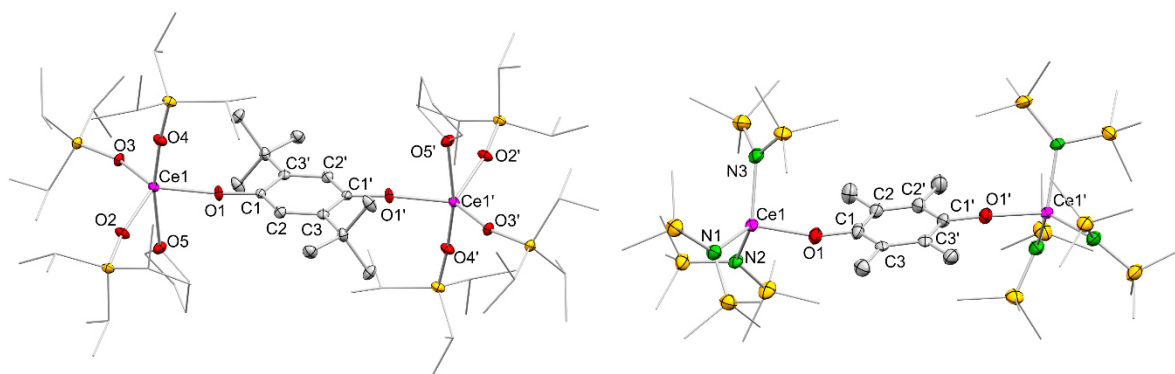
Figure B9. Crystal structures of [(Ce{OSi*i*Pr$_3$}$_3$(thf))$_2$(μ-O$_2$C$_6$H$_2$*t*Bu$_2$-2,5)] (**Q^{tBuhq}**, left) and [(Ce{N(SiMe$_3$)$_2$}$_3$)$_2$(μ-O$_2$C$_6$Me$_4$)] (**O^{Me4hq}**, right).

The stabilization of the tetravalent oxidation state in complexes **O^{ddhq}** to **Q^{hq}** was also examined *via* CV experiments. Complexes **O^{tBuhq}** to **O^{nq}** were not stable in solution, especially when using polar solvents. Therefore, no CV measurements could be conducted for those complexes. These experiments underlined that Ce^{IV} is best stabilized using trisalkyl siloxy OSi*i*Pr$_3$, then trisalkoxy siloxy OSi(O*t*Bu)$_3$ and the least stabilization was found for silylamido N(SiMe$_3$)$_2$ as the co-ligand. For the influence of the bridging hydroquinolato moieties the stabilization of the tetravalent oxidation state was found to be in reversed order of the oxidation potentials of the corresponding 1,4-*p*-benzoquinone derivatives (μ-O$_2$C$_6$H$_4$ > μ-O$_2$C$_6$Cl$_4$ > μ-O$_2$C$_6$CN$_2$Cl$_2$) (Figure B7). This was attributed to the electron deficient nature of the bridging hydroquinolato linker and the resulting lower donation of electron density toward the cerium center.
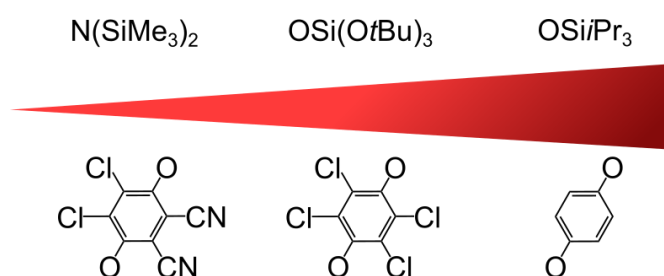
Figure B7. Trends for the stabilization of the tetravalent oxidation state in ceric complexes **O^{ddhq}** to **Q^{hq}** determined by CV measurements.

The electrochemical reduction was also mimicked by chemical reduction of **O^{hq}**, using CoCp$_2$ as reducing agent, giving cerous ate-complex [(Ce{N(SiMe$_3$)$_2$}$_3$)$_2$(μ-O$_2$C$_6$H$_4$)][CoCp$_2$]$_2$ (**R**) (Scheme B8). Whereas both cerium centers have been reduced and no change in the oxidation state of the hydroquinolato linker has been observed. As a result, the crystal structure shows the same motif as **O^{hq}** with bond lengths elongated by approximately 0.2 Å due to the change of oxidation state and two cobaltocenium cations (Figure B10).
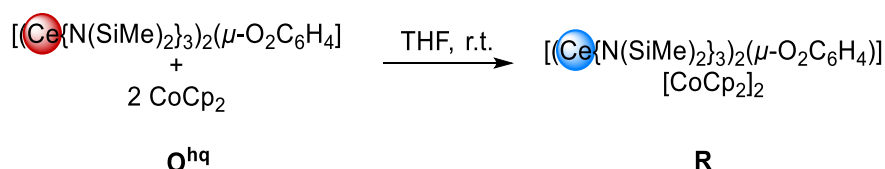
Scheme B8. Reduction of **O**^{hq} with two equivalents of cobaltocene.
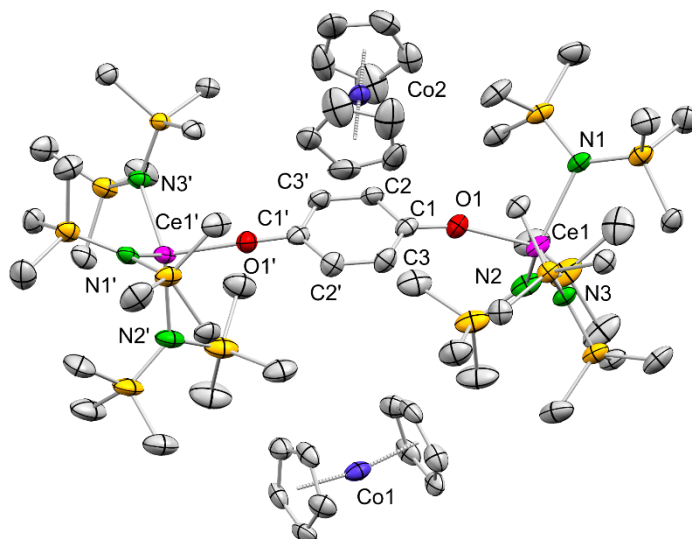
Figure B10. Crystal structure of $[(Ce\{N(SiMe_3)_2\}_3)_2(\mu\text{-}O_2C_6H_4)][CoCp_2]_2$ (**R**).

The reaction of cerous siloxides **M** and **N** with tetramethyl-1,4-*p*-benzoquinone did not lead to the hydroquinolato bridged Ce^{IV} complexes, but it gave the semiquinolate complexes $[(Ce\{OSi(OtBu)_3\}_2(thf)_2)_2(\mu\text{-}O_2C_6Me_4)_2]$ (**S^{OtBu}**) and $[(Ce\{OSiiPr_3\}_2(thf)_2)_2(\mu\text{-}O_2C_6Me_4)_2]$ (**S^{iPr}**) together with homoleptic $[Ce\{OSi(OtBu)_3\}_4]$ and $[Ce\{OSiiPr_3\}_4]$ as by-products (Scheme B8). The crystal structures of **S^{OtBu}** and **S^{iPr}** revealed dimeric cerium complexes bridged by two stacked semiquinolato linkers (Ce−O bond lengths 2.370(3)−2.446(7) Å) and two siloxy ((Ce−O bond lengths 2.219(9)−2.249(3) Å)) as well as two THF ligands for each cerium center (Figure B12). In contrast to the bridging hydroquinolato moieties, the semiquinolato ligands show two shortened (1.360(7) to 1.401(6) Å) and four elongated C−C bond lengths (1.436(7) to 1.463(8) Å) in accordance to the non-aromatic nature of the semiquinolato six-membered ring. EPR measurements showed only signals for Ce^{III}, indicating a radical-radical π-bonding as it was recently found for other Ln^{III}-semiquinolates.[228]
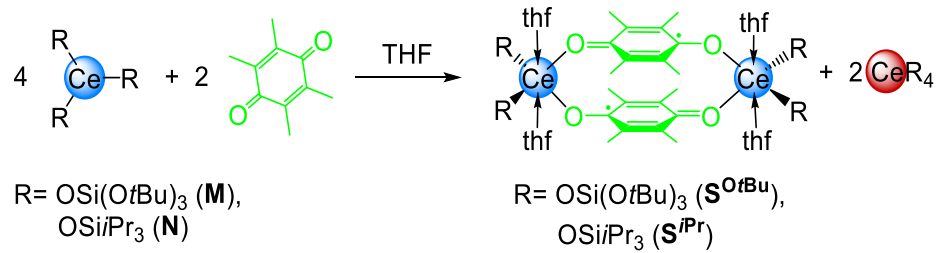
Scheme B9. Synthesis of semiquinolates S^{OtBu} and S^{iPr}.
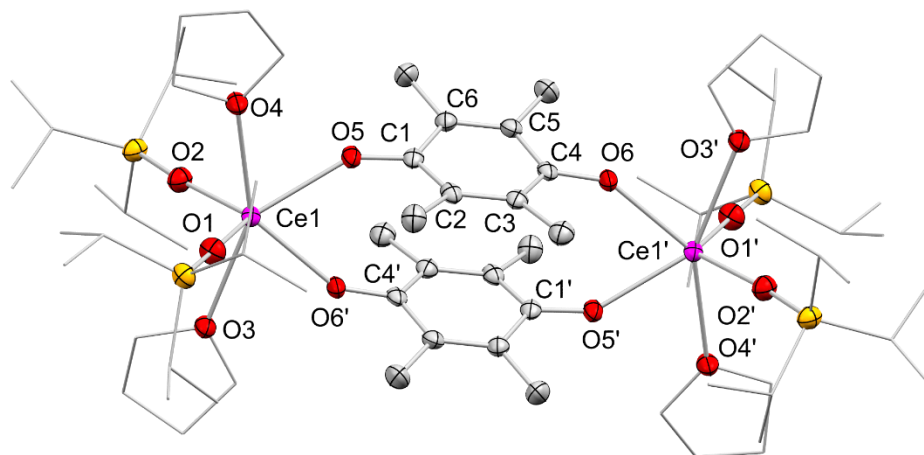
Figure B11. Crystal structure of $[(Ce\{OSi\mathit{i}Pr_3\}_2(thf)_2)_2(\mu\text{-}O_2C_6Me_4)_2]$ (S^{iPr}).

C

Unpublished Results

1 Effect of Substituents of Cerium Pyrazolates in Carbon Dioxide Activation

Introduction

As shown before, both trivalent and tetravalent cerium dimethylpyrazolates can reversibly insert CO_2. Therefore, it was of interest to elucidate the reactivity of other cerous and ceric pyrazolates toward carbon dioxide.

Results and Discussion

Homoleptic cerous precursor $[Ce\{N(SiMe_3)_2\}_3]$ was treated with three equivalents di-phenyl-pyrazole (HPh$_2$pz) to afford $[Ce(Ph_2pz)_3]_x$, according to a literature known protocol for the synthesis of homoleptic trivalent cerium pyrazolates.[134] Upon recrystallization from THF. $[Ce(Ph_2pz)_3(thf)_3]$ (**T**, Scheme C1) was obtained as yellow crystals in good yield (72%). The crystals were suitable for X-ray diffraction but of bad quality. Therefore, only a connectivity of **T** could be obtained (Figure C1).
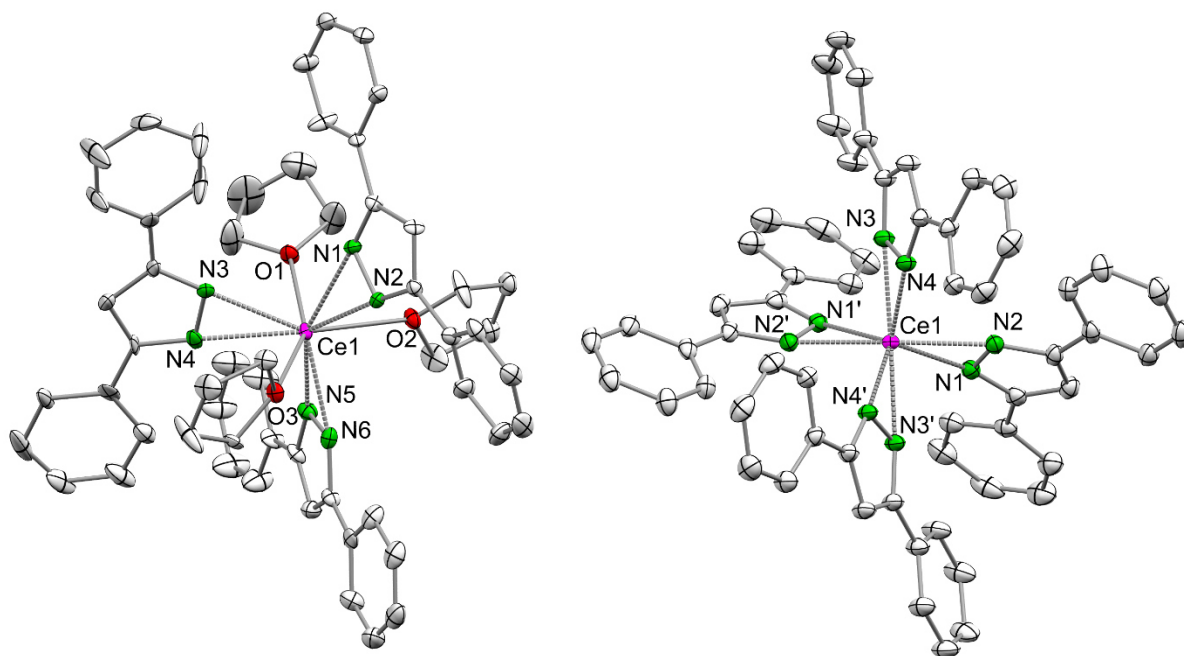
Figure C1. Connectivity of $[Ce(Ph_2pz)_3(thf)_3]$ (**T**, left) and crystal structure of $[Ce(Ph_2pz)_4]$ (**V**, right). Complex **T** was investigated by the group of DEACON at the same time.[229]

Tetravalent cerium precursors $[Ce\{N(SiHMe_2)_2\}_4]$ was reacted with four equivalents of di-*tert*-butyl-pyrazole (H*t*Bu$_2$pz),[134] HPh$_2$pz or 3-*tert*-butyl-5-methyl-pyrazole (H*t*BuMepz),

respectively, to generate homoleptic ceric complexes $[Ce(R_2pz)_4]_n$ ($R_2pz = tBu_2pz$ **T**, Ph_2pz **V** *t*BuMepz **W**, Scheme C1).
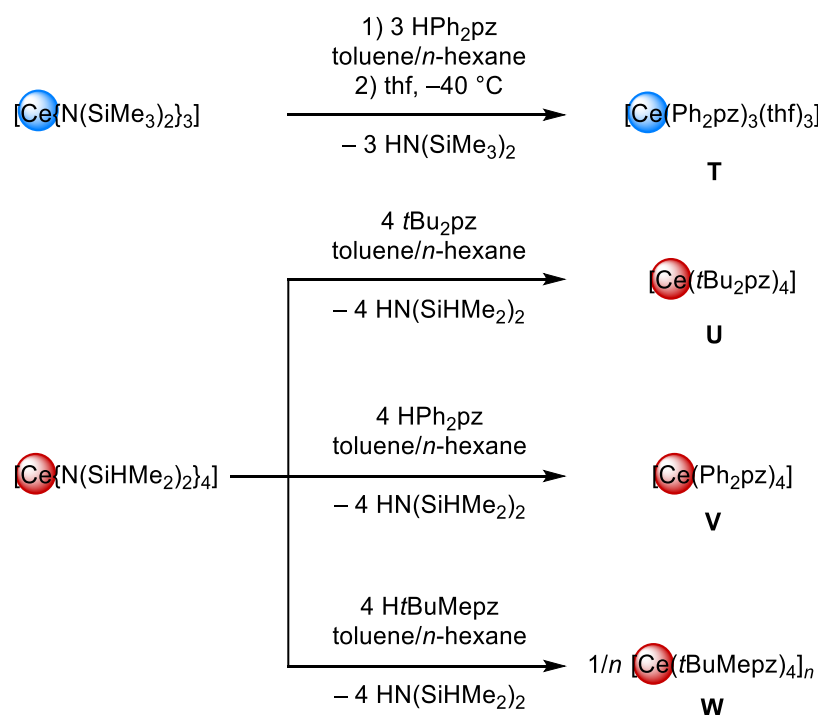
Scheme C1. Synthesis of cerous **T** and ceric **U** to **W**.

Crystals of complex **V** suitable for X-ray diffraction have been obtained from a concentrated solution in toluene. The crystal structure revealed an 8-coordinated cerium center surrounded by four η^2 coordinated diphenylpyrazolato moieties (Figure C1). The Ce1–N bond lengths (2.3380(16) to 2.3790(16) Å) are comparable to other "terminal" Ce^{IV}–N(pz) bonds (**S**: 2.322(4) to 2.365(4) Å; **D**: 2.319(3) to 2.384(2)).[134] Compound **W** was obtained as a dark red sticky solid. The general composition of $[Ce(tBuMepz)_4]_n$ was confirmed *via* ^{1}H NMR spectroscopy showing singlets at 1.24 ppm for the *t*Bu groups, at 2.22 ppm for the methyl groups, and at 6.15 ppm for the C-H of the five-membered pyrazole ring. However, elemental analysis displayed some extent of impurification, indicated by an increased carbon value most likely from remaining solvent.

The insertion of CO_2 into the Ce-N(pyrazol) bond was examined *via in situ* IR measurements showing no insertion of CO_2 for **U**, slow insertion for **V**, and fast insertion for **W** (Figure C5-C7), indicated by an increasing intensity of characteristic C−O vibrations at around 1600 to 1800 cm^{-1}. However, insertion processes are slower and less efficient than observed for the

dimethyl pyrazolates **D** and **E** (**Paper II**). Crystallization and structural elucidation of CO_2 inserted products was not successfull.

Experimental Section

General Procedures. All manipulations were performed under an inert atmosphere (Ar) using a glovebox (*MBraun* 200B; <0.1 ppm O_2, <0.1 ppm H_2O), or according to standard Schlenk techniques in oven-dried glassware. The solvents were purified with Grubbs type columns (MBraun SPS, solvent purification system) and stored in a glovebox. [Ce{N(SiMe$_3$)$_2$}$_3$], [Ce{N(SiHMe$_2$)$_2$}$_4$], and [Ce(tBu$_2$pz)$_4$] (**U**) were synthesized according to published procedures.[132,134,230] C_6D_6, toluene-d_8, and THF-d_8 were purchased from *Euriso-top* and pre-dried over NaK alloy and filtered off prior use, THF-d_8 was re-condensed. NMR spectra were recorded at 26 °C with a Bruker AVII+400 (^{1}H: 400.13 MHz) using J. Young valve NMR spectroscopy tubes. ^{1}H shifts are referenced to a solvent resonance and reported in parts per million (ppm) relative to tetramethylsilane. Analyses of NMR spectra were performed with ACD/NMR Processor Academic Edition (product version: 12.01). Infrared spectra were recorded on a *ThermoFisher Scientific* NICOLET 6700 FTIR ($\tilde{v}$= 4000 – 400 cm^{-1}) spectrometer using a DRIFTS chamber with dry KBr/sample mixtures and KBr windows. Elemental analysis (C, H, N) was performed on an *Elementar vario MICRO cube*. *In situ* IR spectra were recorded on a METTLER TOLEDO ReactIR 15.

[Ce(Ph$_2$pz)$_3$(thf)$_3$] (T). [Ce{N(SiMe$_3$)$_2$}$_3$] (0.50 g, 0.81 mmol) in *n*-hexane (3 mL) was added to a suspension of HPh$_2$pz (0.53 g, 2.4 mmol) in toluene (7 mL). After 1 h all volatiles were removed under reduced pressure. Crystallization from concentrated THF solutions gave **T** as pale yellow crystals. Yield: 0.59 g (0.58 mmol, 72%). ^{1}H NMR (THF-d_8, 400.13 MHz, 26 °C) δ = 12.94 (s, 3 H, C−H pz), 12.37 (d, 12 H, C−H Ph), 8.31 (dd, 12 H, C−H Ph), 7.96 (t, 6 H, C−H Ph), 3.59 (m, 12 H, α-CH(thf)), 1.78 (m, 12 H, β-CH(thf)) ppm. IR (DRIFT): $\tilde{v}$ = 3062 (m), 3037 (m), 2975 (m), 2883 (m), 1604 (m), 1467 (s), 1422 (w), 1399 (w), 1063 (m), 1027 (s), 970 (s), 915 (m), 868 (m), 762 (s), 703 (m), 696 (s), 684 (m), 417 (m) cm^{-1}; elemental analysis (%) calcd. for C$_{57}$H$_{57}$CeN$_6$O$_3$ (1014.24): C 67.50, H 5.66, N 8.29; found: C 67.25, H 5.67, N 7.88.

[Ce(Ph$_2$pz)$_4$]·tol (V). [Ce{N(SiHMe$_2$)$_2$}$_4$] (0.40 g, 0.60 mmol) in *n*-hexane (2 mL) was added to a suspension of HtBuMepz (0.33 g, 2.4 mmol) in toluene (2 mL). After 1 h all volatiles were removed under reduced pressure. Crystallization from concentrated toluene solutions gave **V** as dark purple crystals. Yield: 0.52 g (0.47 mmol, 79%). ^{1}H NMR (C_6D_6, 400.13 MHz, 26 °C): = 7.78 (m, 16 H, C−H Ph), 7.11 (s, 4 H, C−H pz), 6.91 (m, 24 H, C−H Ph) ppm; IR (DRIFT): $\tilde{v}$ = 3064 (w), 3036 (w), 2916 (w), 1944 (w), 1883 (w), 1807 (w), 1755 (w), 1682 (w), 1602 (w), 1562 (w), 1489 (w), 1467 (s), 1421 (m), 1401 (m), 1335 (w), 1282 (w), 1254 (w), 1151 (w), 1103 (w), 1072 (w), 1018 (m), 999 (m), 965 (m), 914 (w), 837 (w), 809 (w), 760 (s), 731 (s), 700 (s), 692 (m), 678 (m), 666 (w), 537 (w), 481 (w), 465 (w), 429 (m), 422 (m), 405 (w) cm^{-1}; elemental analysis (%) calcd. for C$_{67}$H$_{52}$CeN$_8$ (1109.33): C 72.54, H 4.73, N 10.10; found: C 72.40, H 4.52, N 10.68.

[Ce(*t*BuMepz)₄]ₙ (W). [Ce{N(SiHMe₂)₂}₄] (0.40 g, 0.60 mmol) in toluene (2 mL) was added to a suspension of HPh₂pz (0.53 g, 2.4 mmol) in toluene (2 mL). After 2 h all volatiles were removed under reduced pressure giving **W** as a dark red sticky solid. Due to impurities in the crude product, no yield was determined. ^{1}H NMR (C₆D₆, 400,13 MHz, 26 °C): = 6.15 (s, 4 H, C−H pz) , 2.22 (s, 12 H, Me), 1.24 (s, 36 H, *t*Bu) ppm; IR (DRIFT): $\tilde{v}$= 3105 (w), 2961 (vs), 2924 (s), 2901 (s), 2862 (m), 1558 (w), 1508 (s), 1474 (m), 1458 (m), 1425 (s), 1387 (m), 1362 (m), 1291 (w), 1237 (s), 1210 (w), 1124 (w), 1084 (w), 1032 (w), 1020 (w), 994 (m), 962 (w), 819 (w), 797 (m), 718 (w), 700 (w), 686 (w), 567 (w), 507 (m) cm^{-1}; elemental analysis (%) calcd. for C₃₂H₅₂CeN₈ (688.94): C 55.79, H 7.61, N 16.26; found: C 57.17, H 7.49, N 16.29.
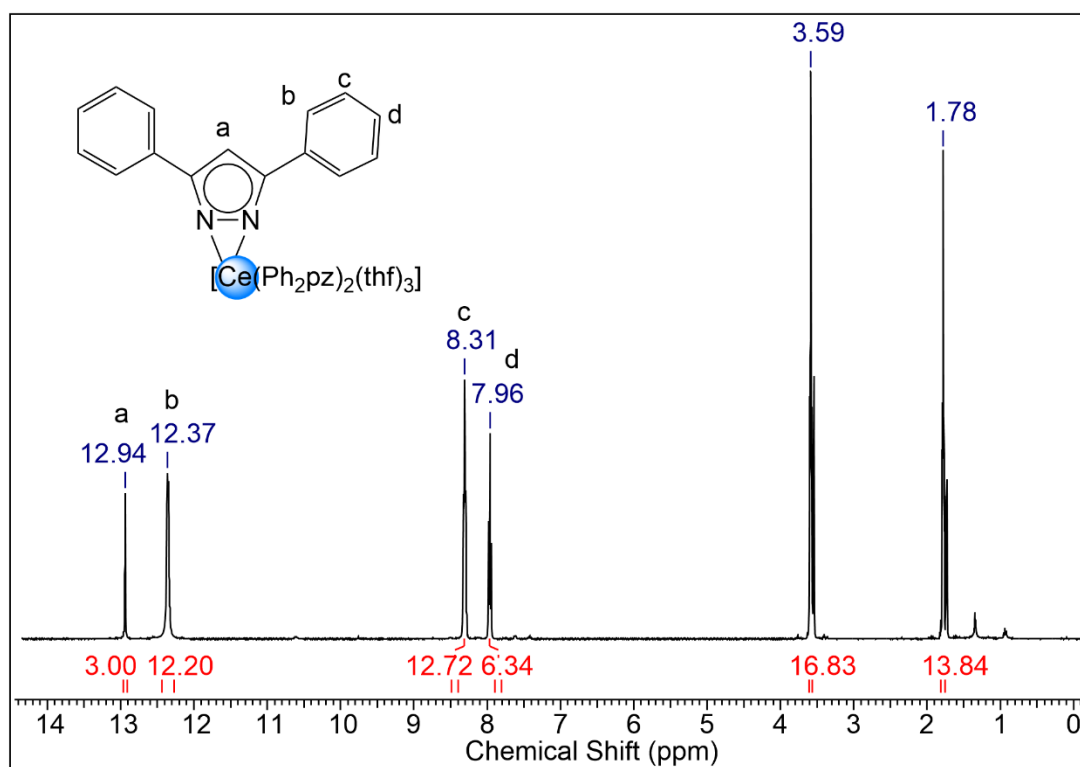
Figure C2. ^{1}H NMR spectrum (THF-d_8, 400.13 MHz, 26 °C) of **T**.
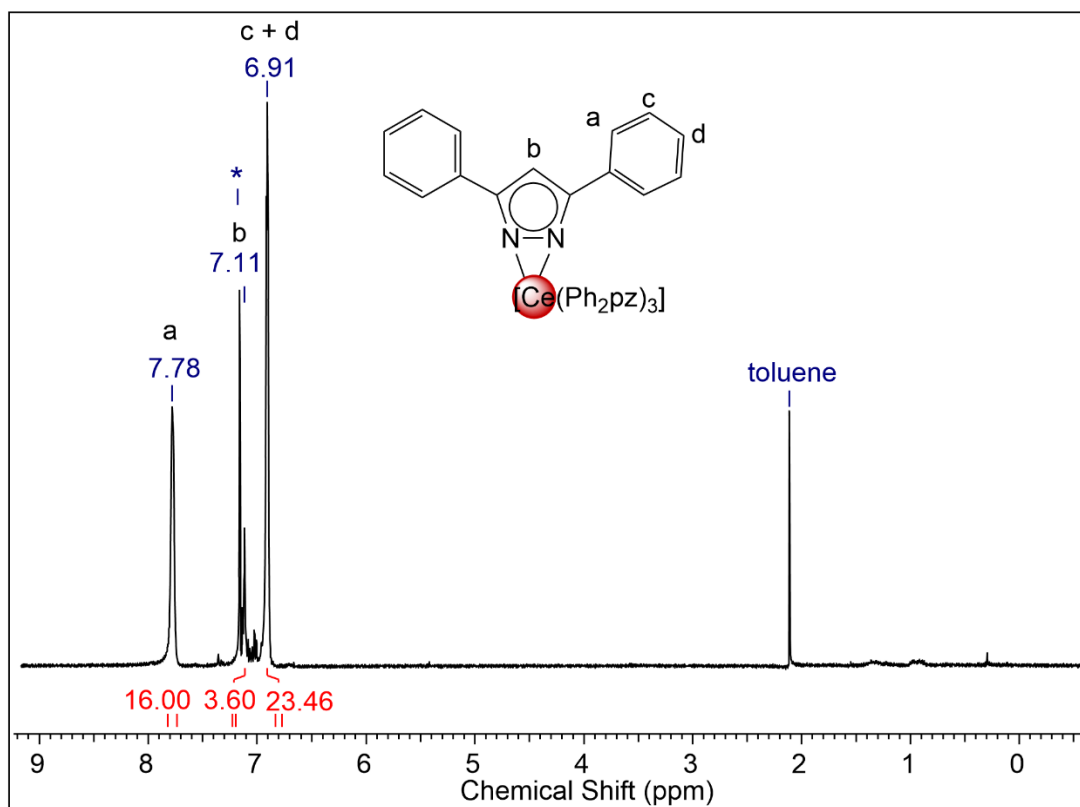
Figure C3. ^{1}H NMR spectrum (C$_6$D$_6$, 400.13 MHz, 26 °C) of **V**.
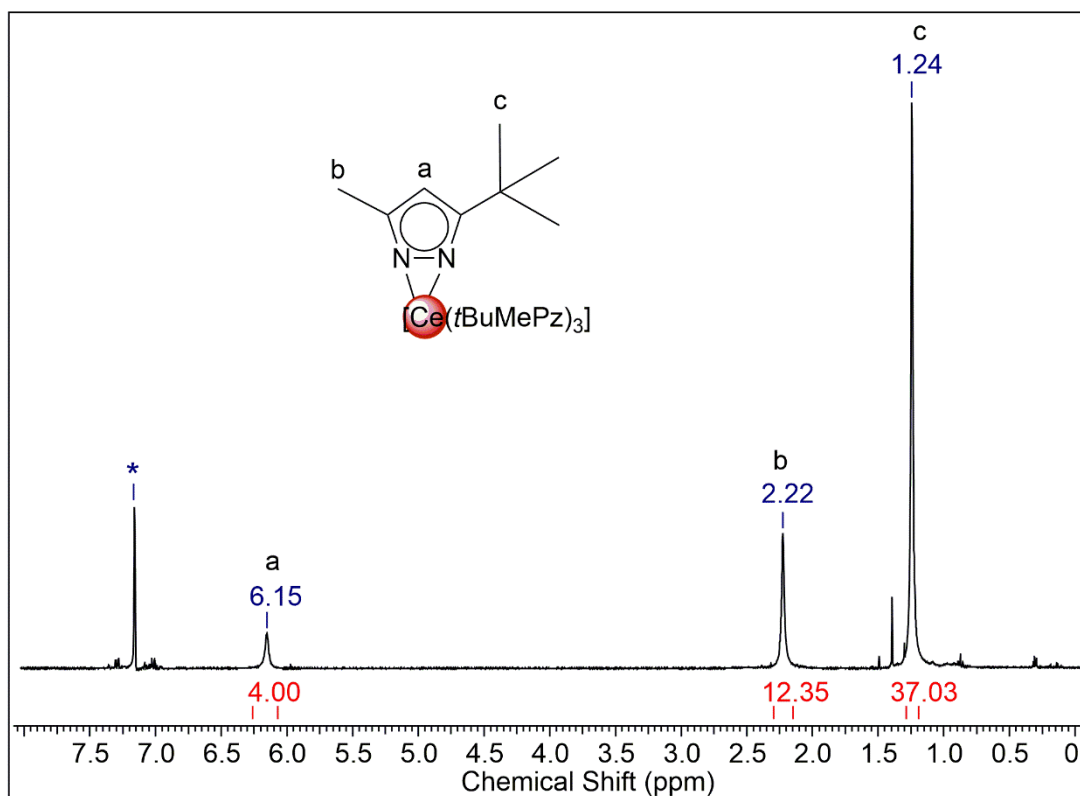
Figure C4. ^{1}H NMR spectrum (C$_6$D$_6$, 400.13 MHz, 26 °C) of **W**.
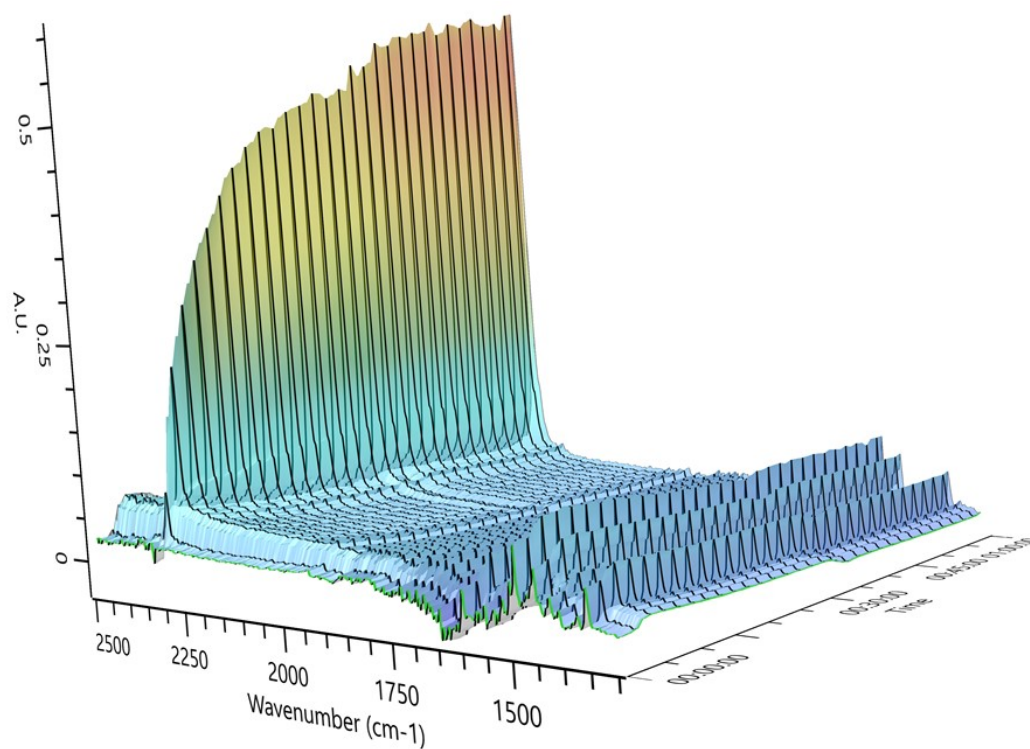
Figure C5. *in situ* IR measurement of the reaction of **U** with CO$_2$ at −20 °C.
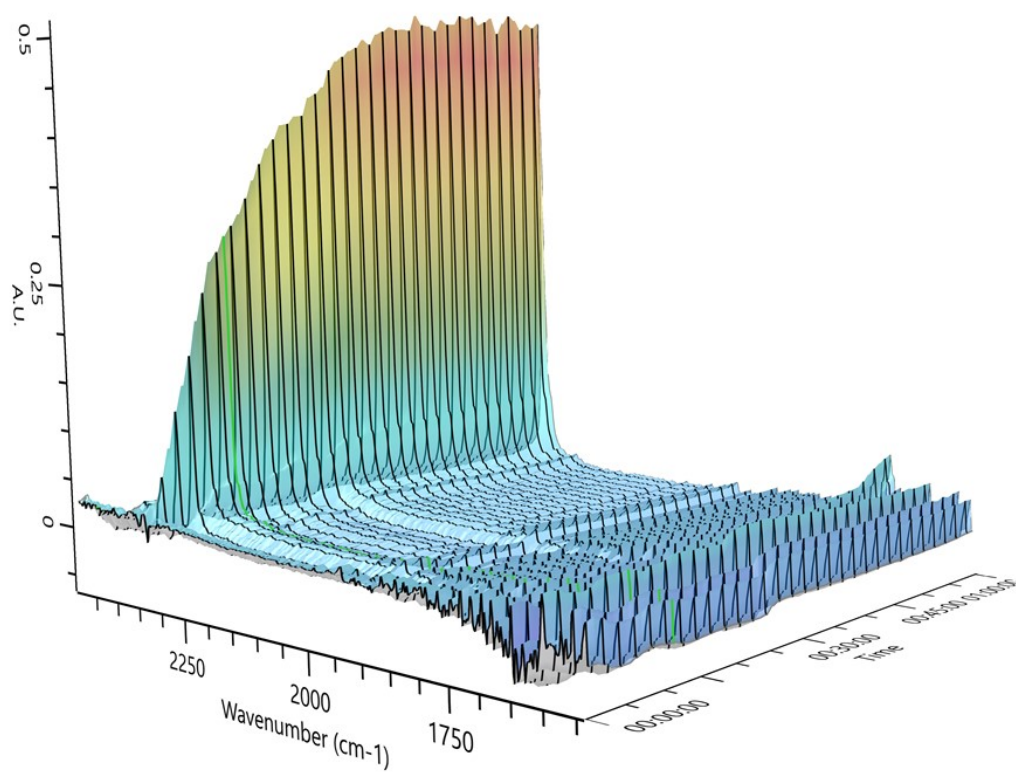
Figure C6. *in situ* IR measurement of the reaction of **V** with CO$_2$ at −20 °C.
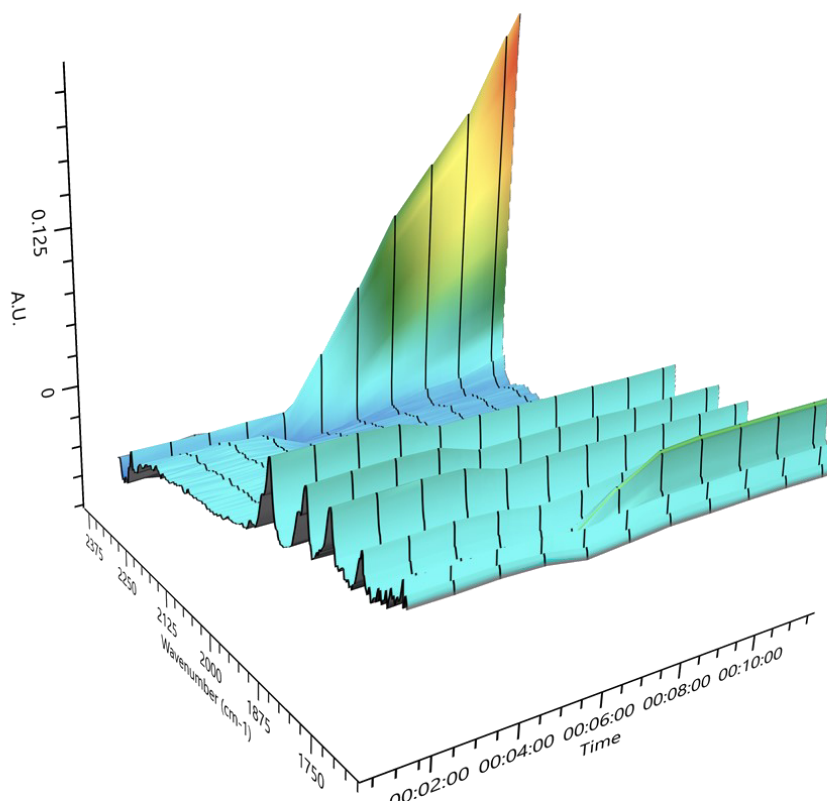
Figure C7. *in situ* IR measurement of the reaction of **W** with CO$_2$ at −20 °C.

2 Cerium Pyrrolates for Carbon Dioxide Activation

Introduction

While the chemistry of homoleptic cerium pyrazolates has been thoroughly investigated,[134,229,231] examples of homoleptic cerium pyrrolates are still unexplored. Even though pyrrolyl-based pincer-type ligands are well established, complexes bearing pyrrole as a ligand are very scarce in literature.[232–234] The only structurally characterized complexes of this kind are [Cp$_2$Lu(pyr)(thf)] and [Cp*$_2$Y(pyr)(thf)] from SCHUMANN *et al.* and [Cp$_2$Y(OC(Me)$_2$CH$_2${HC(*i*PrNCH$_2$CH$_2$N)})(pyr)] from ARNOLD *et al.*[235,236] As cerium pyrazolates have shown to be very efficient in reversible CO$_2$ insertion reactions as well as in catalytic cycloaddition of CO$_2$ and epoxides,[166] the synthesis of homoleptic ceric and cerous pyrrolates and their reactivity toward carbon dioxide was envisaged.

Results and Discussion

Syntheses of trivalent cerium pyrrolates have been attempted *via* different routes (salt metathesis route: CeCl$_3$* + 3 or 4 Li(pyr); protonolysis routes: [Ce{N(SiMe$_3$)$_2$}$_3$] + 3 Hpyr or [Ce{N(SiHMe$_2$)$_2$}$_4$Li(thf)] + 4 Hpyr). Disadvantageously, Li pyrrolate and the resulting Ce^{III} complexes are only soluble in donor solvents, like THF. Therefore, work-up procedures and isolation of any salt metathesis product was not feasible due to similar solubility properties of the metathesis salt (LiCl). The reaction of [Ce{N(SiMe$_3$)$_2$}$_3$] resulted mainly in the isolation of starting material. Upon addition of four equivalents of pyrrole to ate complex [Ce{N(SiHMe$_2$)$_2$}$_4$Li(thf)], immediate precipitation was observed. Crystallization from a concentrated THF solution gave [Ce(pyr)$_3$(μ-pyr)(thf)]$_2$[Li(thf)$_4$]$_2$ (**X**, Scheme C2) as colorless crystals. The ^{1}H NMR spectrum of **X** shows two broadened singlets for the pyrrolato protons at 4.23 and 7.39 ppm.
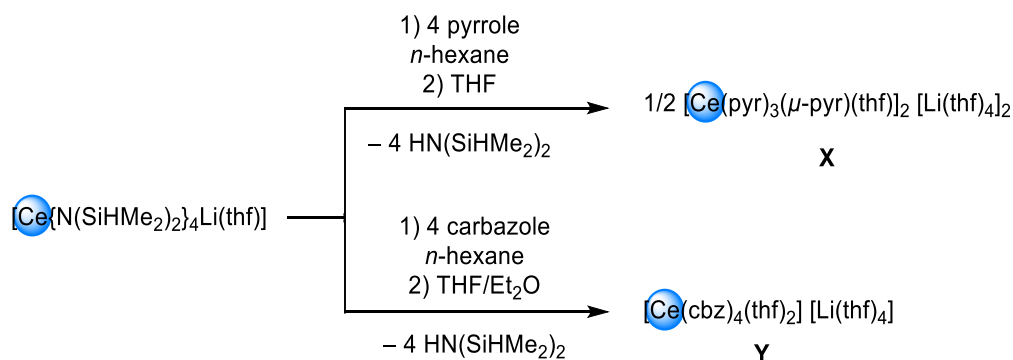

Scheme C2. Syntheses of ate-complexes **X** and **Y**.

The crystal structure of **X** revealed a separated ion pair featuring a dicerium dianionic entity (Figure C8). Each cerium center is 8-coordinated surrounded by three terminal pyrrolato moieties (Ce1–N 2.475(2) to 2.515(2) Å), two bridging pyrrolato ligands bridging the cerium centers in η^1 (Ce1–N4 2.622(2) Å) and η^5 fashion (Ce1–Ct 2.575(16) Å) and one THF donor molecule. The Ce–N bond lengths are slightly elongated compared to other Ce^{III} ate-complexes ([Ce{N(SiHMe$_2$)$_2$}$_4$][Li(do)$_x$] (**C^{do}** with do, x = py, 4; tmeda, 2; 12-crown-4, 1 and thf, 4; Ce–N 2.377(6) to 2.438(6) Å; [Ce{N(SiMe$_3$)$_2$}$_4$][Na(thf)$_4$(Et$_2$O)] Ce–N 2.434(6) to 2.448(6) Å), due to its higher CN (CN 8 vs 4).[237,238]
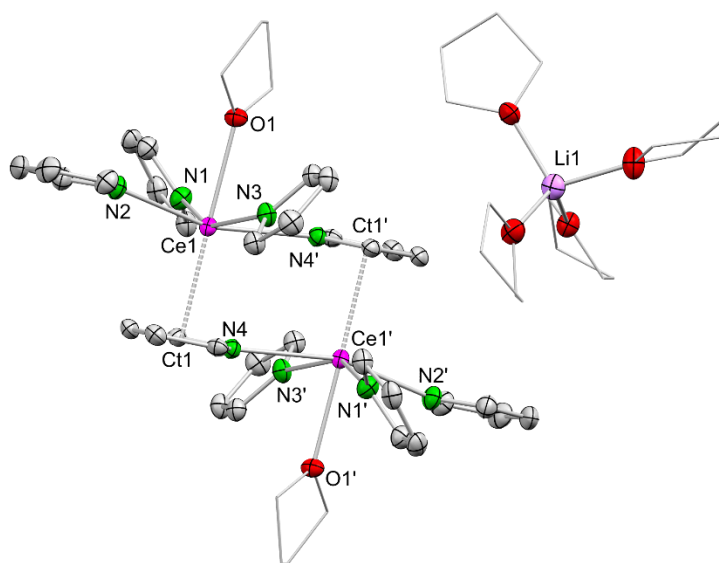
Figure C8. Crystal Structure of [Ce(pyr)$_3$(μ-pyr)(thf)]$_2$[Li(thf)$_4$]$_2$ (**X**). One [Li(thf)$_4$]$^+$ is omitted for clarity.

Reacting [Ce{N(SiHMe$_2$)$_2$}$_4$Li(thf)] with four equivalents of carbazole in *n*-hexane gave a colorless precipitate. Recrystallization from a 1:1 mixture of THF and Et$_2$O gave off-white crystals of [Ce(cbz)$_4$(thf)$_2$][Li(thf)$_4$] (**Y**, Scheme C2). The ^{1}H NMR spectrum of **Y** shows various broadened singlets. Due to the paramagnetic Ce^{III} center, assignment of the signals was not possible. The crystal structure of **Y** shows a 6-coordinated cerium center surrounded by four carbazolyl ligands, two THF donor molecules and a [Li(thf)$_4$]$^+$ counter ion (Figure C9). As seen before, the Ce1–N bond lengths (2.480(4) to 2.531(4) Å) are slightly elongated compared to other separated ion-pair type ate-complexes.
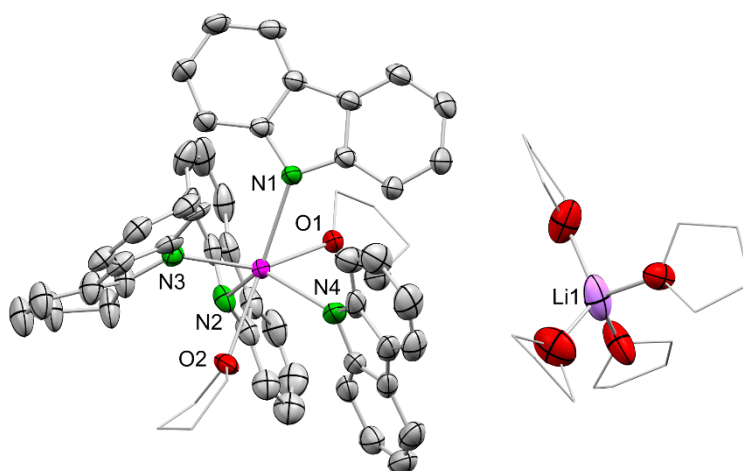
Figure C9. Crystal structure of [Ce(cbz)$_4$(thf)$_2$][Li(thf)$_4$] (**Y**).

Oxidation of **X** and **Y** was attempted using 1,4-*p*-benzoquinone as an oxidant to afford homoleptic [Ce(pyr)$_4$] and [Ce(cbz)$_4$]. Upon addition of 1,4-*p*-benzoquinone an immediate color change from yellow to dark green and dark purple, respectively and precipitation of a voluminous dark powder occurred, indicative for successful oxidation and therefore separation of a lithium hydroquinolate. After removal of the precipitate by filtration and solvent under reduced pressure, a dark green or dark purple powder was obtained, respectively. Upon dissolving of the powders in THF-*d$_8$* for NMR analysis both solutions immediately lost their colors, which indicates the reduction of the species. This reduction process was also supported by the NMR spectra which showed paramagnetic signals in both cases. Isolation of both products did not succeed.

The reactivity of **X** and **Y** toward CO$_2$ was examined. In both cases a color change was observed upon addition of CO$_2$ and the signals in the ^{1}H NMR spectra were shifted compared to the starting material (Figure C15 and C16). After removing the solvent under reduced pressure DRIFTS measurements were conducted showing strong absorption bands in the region for C−O vibrations (Figure C10). Both, the NMR and IR spectroscopic measurements, give hints to a successful CO$_2$ insertion. The reversibility of this insertion has to be investigated.
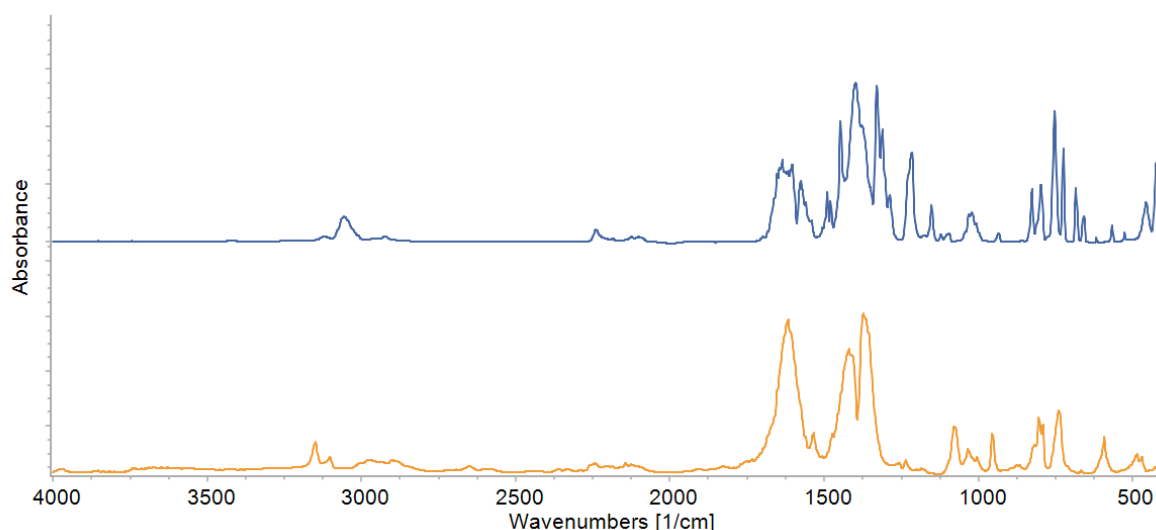
Figure C10. Stacked DRIFT spectra of the reactions of **X** (orange trace) and **Y** (blue trace) with CO_2.

Experimental Section

General Procedures. All manipulations were performed under an inert atmosphere (Ar) using a glovebox (*MBraun* 200B; <0.1 ppm O_2, <0.1 ppm H_2O), or according to standard Schlenk techniques in oven-dried glassware. The solvents were purified with Grubbs type columns (MBraun SPS, solvent purification system) and stored in a glovebox. [Ce{N(SiHMe$_2$)$_2$}$_4$Li(thf)] was synthesized according to published procedures.[132] Benzene-d_6 (C_6D_6), toluene-d_8, and THF-d_8 were purchased from *Euriso-top* and pre-dried over NaK alloy and filtered off prior use, THF-d_8 was re-condensed. NMR spectra were recorded at 26 °C with a Bruker AVII+400 (^1H: 400.13 MHz) or a Bruker AVIIIHD-300 (^1H: 300.13 MHz, ^7Li 116.64 MHz) using J. Young valve NMR spectroscopy tubes. ^1H NMR shifts are referenced to internal solvent residual signals and are reported in parts per million (ppm) relative to tetramethylsilane. ^7Li spectra are reported relative to LiCl. Analyses of NMR spectra were performed with ACD/NMR Processor Academic Edition (product version: 12.01). Infrared spectra were recorded on a *ThermoFisher Scientific* NICOLET 6700 FTIR ($\tilde{v}$= 4000 – 400 cm^{-1}) spectrometer using a DRIFTS chamber with dry KBr/sample mixtures and KBr windows.

[Ce(pyr)$_3$(μ-pyr)(thf)]$_2$[Li(thf)$_4$]$_2$ (X). Pyrrole (141 mg, 2.11 mmol) in *n*-hexane (3 mL) was added to a stirred solution of [Ce{N(SiHMe$_2$)$_2$}$_4$Li(thf)] (394 mg, 0.526 mmol) in *n*-hexane (5 mL). Immediately, a colorless precipitate was formed. After one hour all volatiles were removed under reduced pressure. The resulting solid was recrystallized from THF giving **X** as colorless crystals. Yield: 189 mg (0.122 mmol, 46%). ^1H NMR (THF-d_8; 400.11 MHz, 26 °C) δ = 7.39 (bs), 4.23 (bs) ppm; ^7Li-NMR (THF-d_8, 116,64 MHz, 25 °C) δ = 2.0 ppm. DRIFTS: $\tilde{v}$ = 3085 (w), 1441 (w), 1365 (w), 1213 (vw), 1200 (vw), 1140 (w), 1078 (m), 1048 (w), 1021 (s), 894 (w), 858 (w), 789 (vs), 751 (m), 670 (w), 660 (m), 416 (w) cm^{-1}.

[Ce(cbz)$_4$(thf)$_2$][Li(thf)$_4$] (Y). [Ce{N(SiHMe$_2$)$_2$}$_4$Li(thf)] (406 mg, 0.557 mmol) in *n*-hexane (5 mL) was added to a stirred suspension of carbazole (363 mg, 2.23 mmol) in *n*-hexane (5 mL). After one hour, a yellow precipitate was formed, and volatiles were removed under reduced pressure. The resulting solid

was recrystallized from THF/Et$_2$O (1:1) giving **Y** as off-white crystals. Yield: 486 mg (0.415 mmol, 74%).
^{1}H NMR (THF-d_8; 400.11 MHz, 26 °C) δ = 8.64 (d), 7.90 (bs), 7.70 (d), 7.32 (d), 7.02 (bs), 6.70 (bs) 6.28
(s), 6.04 (s), 5.30 (s), 4.22 (d), 3.62 (s, α-CH(thf)), 1.77 (s, β-CH(thf)), 0.33 (bs), −10.16 (bs) ppm; ^{7}Li-
NMR (THF-d_8, 116,64 MHz, 25 °C) δ: −0.3 ppm. DRIFTS: $\tilde{v}$ = 3418 (vw), 3054 (w), 2979 (w), 2878 (w),
1635 (m), 1576 (m), 1541 (m), 1489 (m), 1479 (m), 1447 (s), 1395 (vs), 1329 (vs), 1312 (s), 1287 (m),
1216 (m), 1151 (w), 1121 (vw), 1043 (w), 934 (vw), 889 (vw), 826 (m), 797 (m), 753 (s), 725 (m), 684
(m), 658 (w), 617 (vw), 567 (vw), 526 (vw), 458 (w), 425 (m) cm^{-1}.
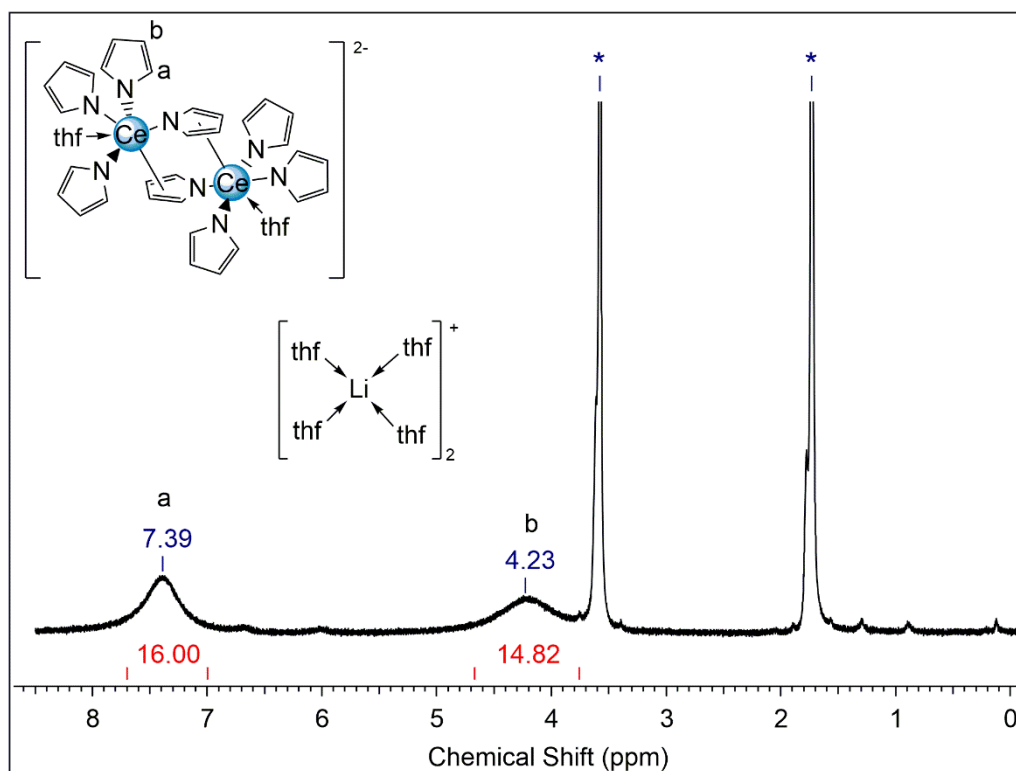
Figure C11. ^{1}H NMR spectrum (THF-d_8, 400.13 MHz, 26 °C) of **X**.
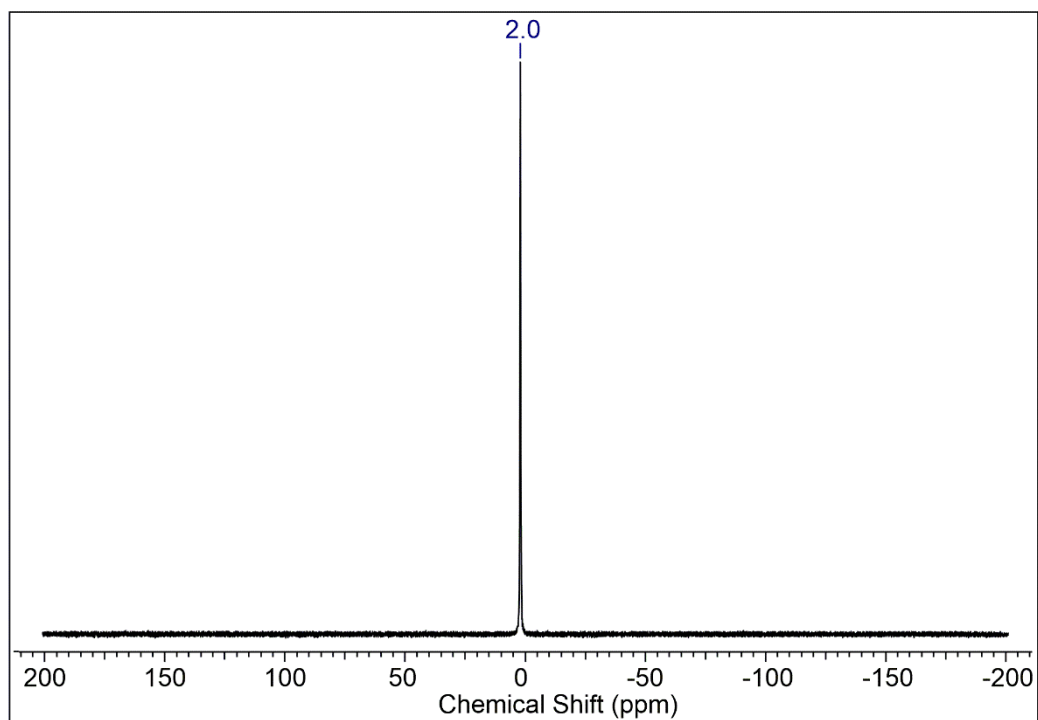
Figure C12. ^{7}Li NMR spectrum (THF-d_8, 116.64 MHz, 26 °C) of **X**.
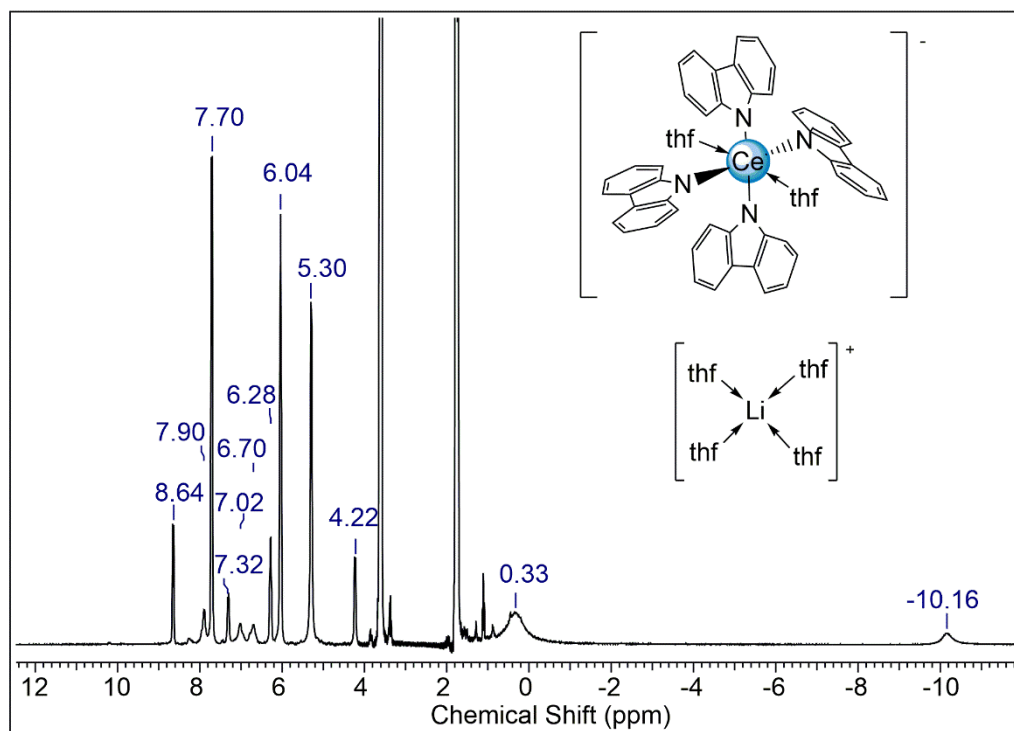
Figure C13. ^{1}H NMR spectrum (THF-d_8, 400.13 MHz, 26 °C) of **Y**.
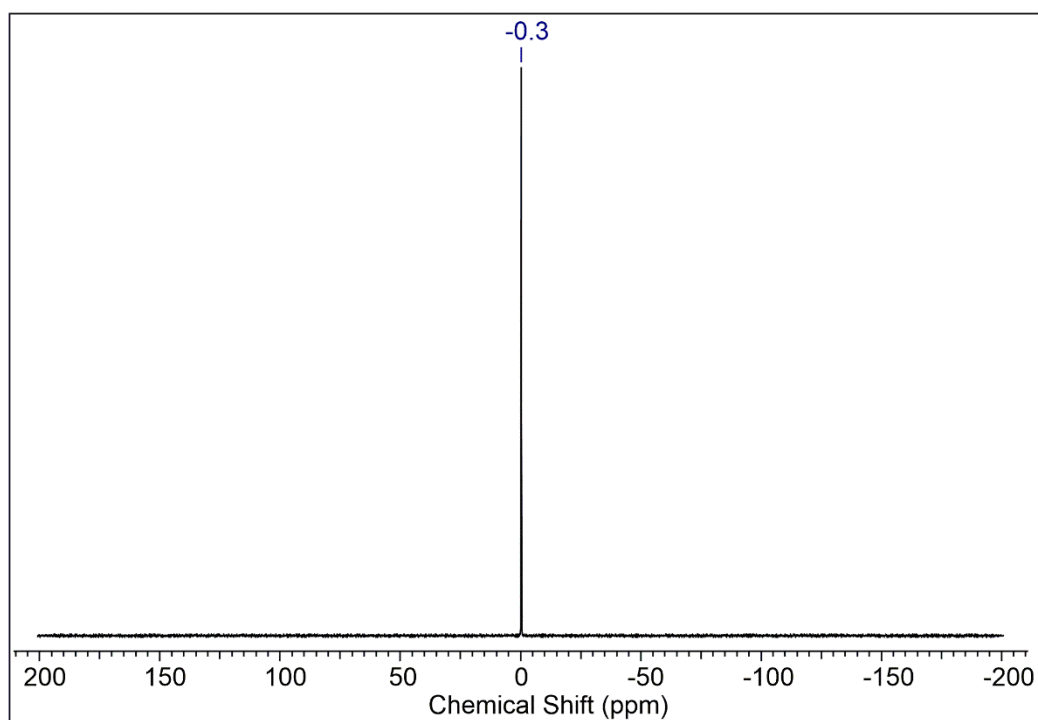
Figure C14. ^{7}Li NMR spectrum (THF-d_8, 116.64 MHz, 26 °C) of **Y**.
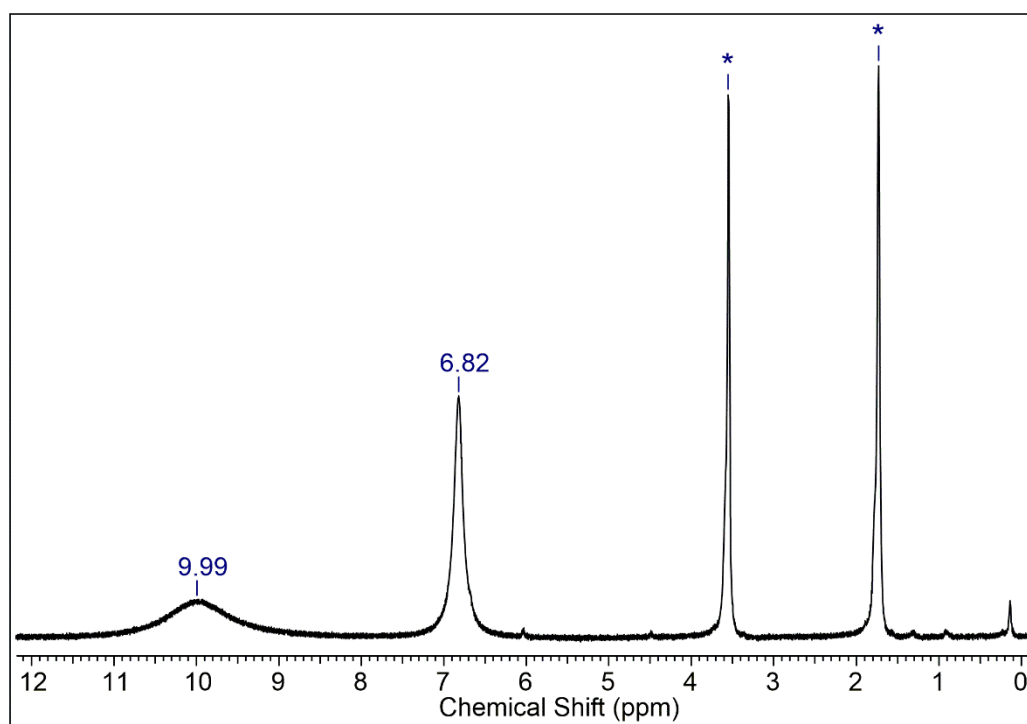
Figure C15. ^{1}H NMR spectrum (THF-d_8, 400.13 MHz, 26 °C) of **X** + CO_2.
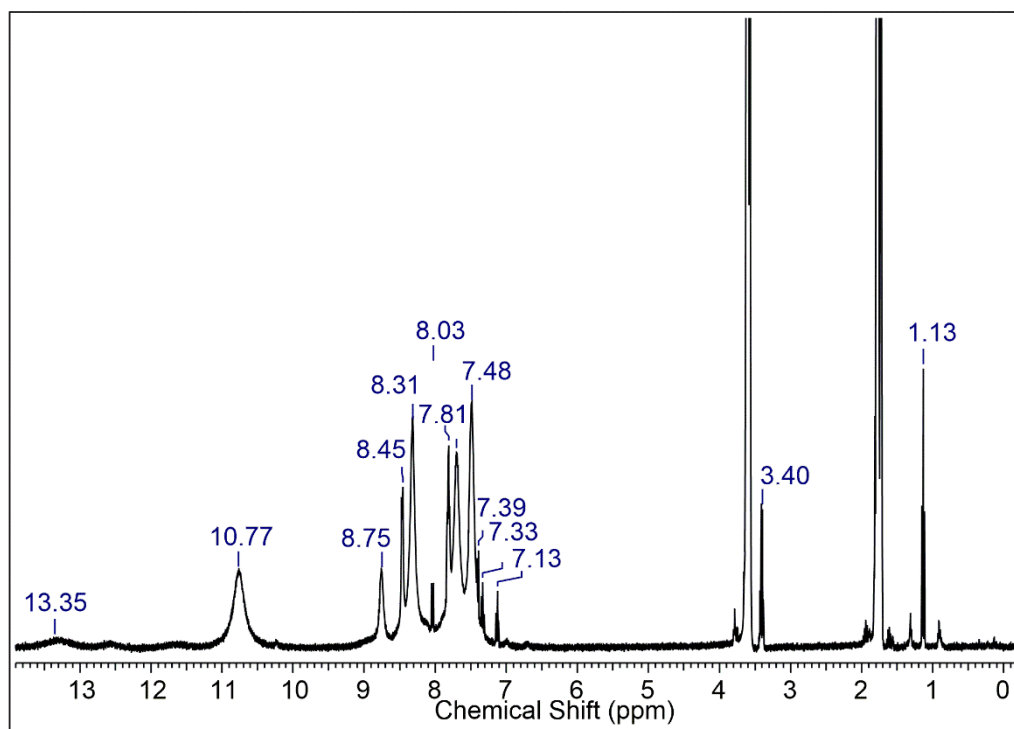
Figure C16. ^{1}H NMR spectrum (THF-d_8, 400.13 MHz, 26 °C) of **Y** + CO_2.

Table C1. Crystallographic data for compounds **T**, **V**, **X** and **Y**.

	T	V	X	Y
formula	$C_{57}H_{57}CeN_6O_3$	$C_{74}H_{60}CeN_8$	$C_{72}H_{112}Ce_2Li_2N_8O_{10}$	$C_{72}H_{80}CeLiN_4O_6$
M [g·mol⁻¹]	1014.24	1201.42	1543.81	1244.46
λ [Å]	0.71073	0.71073	0.71073	0.71073
color	yellow	purple	colorless	colorless
crystal dimensions [mm]	0.153 x 0.130 x 0.090	0.500 x 0.095 x 0.092	0.172 x 0.150 x 0.113	0.259 x 0.153 x 0.080
crystal system	triclinic	orthorhombic	triclinic	triclinic
space group	$P\bar{1}$	Pbcn	$P\bar{1}$	$P\bar{1}$
a [Å]	13.9226(11)	23.7563(12)	11.6442(14)	12.3890(10)
b [Å]	18.5657(16)	12.7848(7)	13.6044(16)	13.5313(11)
c [Å]	25.223(2)	19.3528(10)	14.1370(17)	18.6323(15)
α [°]	76.9370(10)	90	61.905(3)	88.927(2)
β [°]	85.8600(10)	90	71.159(3)	88.581(2)
γ [°]	87.5439(10)	90	86.648(3)	81.026(2)
V [Å³]	6047.2(9)	5877.8(5)	1857.9(4)	3084.0(4)
Z	4	4	1	2
F(000)	6960	2472	802	1298
T [K]	100(2)	173(2)	100(2)	100(2)
ρ_{calcd} [g·cm⁻³]	4.375	1.358	1.380	1.340
μ[mm⁻¹]	16.062	0.827	1.269	0.795
Data / restraints / parameters	24141 / 0 / 1207	7918 / 123 / 442	10020 / 0 / 424	14249 / 1585 / 997
Goodness of fit	2.573	1.017	1.024	1.041
R_1 (I > 2σ (I))[a]	0.1682	0.0430	0.0353	0.0657
$_\omega R_2$ (all data)[b]	0.3974	0.0810	0.0821	0.1804

[a] $R_1 = \Sigma(||F0|-|Fc||)/\Sigma|F0|, F0 > 4s(F0)$. $_\omega R_2 = \{\Sigma[w(F02-Fc2)2/\Sigma[w(F02)^2]\}^{1/2}$

D

Bibliography

[1] S. Kobayashi, M. Sugiura, H. Kitagawa, W. W.-L. Lam, *Chem. Rev.* **2002**, *102*, 2227–2302.

[2] J. L. Luche, *J. Am. Chem. Soc.* **1978**, *100*, 2226–2227.

[3] P. Girard, J. L. Namy, H. B. Kagan, *J. Am. Chem. Soc.* **1980**, *102*, 2693–2698.

[4] S. Fukuzawa, K. Mutoh, T. Tsuchimoto, T. Hiyama, *J. Org. Chem.* **1996**, *61*, 5400–5405.

[5] M. Szostak, D. J. Procter, *Angew. Chem. Int. Ed.* **2012**, *51*, 9238–9256.

[6] M. Szostak, D. J. Procter, *Angew. Chem.* **2012**, *124*, 9372–9390.

[7] T. Imamoto, T. Kusumoto, Y. Tawarayama, Y. Sugiura, T. Mita, Y. Hatanaka, M. Yokoyama, *J. Org. Chem.* **1984**, *49*, 3904–3912.

[8] T. Imamoto, Y. Sugiura, N. Takiyama, *Tetrahedron Lett.* **1984**, *25*, 4233–4236.

[9] T. Imamoto, N. Takiyama, K. Nakamura, T. Hatajima, Y. Kamiya, *J. Am. Chem. Soc.* **1989**, *111*, 4392–4398.

[10] G. Bartoli, E. Marcantoni, M. Marcolini, L. Sambri, *Chem. Rev.* **2010**, *110*, 6104–6143.

[11] V. Nair, J. Mathew, J. Prabhakaran, *Chem. Soc. Rev.* **1997**, *26*, 127–132.

[12] V. Nair, A. Deepthi, *Tetrahedron* **2009**, *65*, 10745–10755.

[13] J. L. Namy, J. Souppe, J. Collin, H. B. Kagan, *J. Org. Chem.* **1984**, *49*, 2045–2049.

[14] T. Okano, M. Matsuoka, H. Konishi, J. Kiji, *Chem. Lett.* **1987**, *16*, 181–184.

[15] D. A. Evans, S. G. Nelson, M. R. Gagne, A. R. Muci, *J. Am. Chem. Soc.* **1993**, *115*, 9800–9801.

[16] C. F. de Graauw, J. A. Peters, H. van Bekkum, J. Huskens, *Synthesis* **1994**, *1994*, 1007–1017.

[17] Y. Nakano, S. Sakaguchi, Y. Ishii, *Tetrahedron Lett.* **2000**, *41*, 1565–1569.

[18] S. Fukuzawa, N. Nakano, T. Saitoh, *Eur. J. Org. Chem.* **2004**, *2004*, 2863–2867.

[19] H. M. Dietrich, K. W. Törnroos, R. Anwander, *J. Am. Chem. Soc.* **2006**, *128*, 9298–9299.

[20] R. Litlabø, M. Zimmermann, K. Saliu, J. Takats, K. W. Törnroos, R. Anwander, *Angew. Chem. Int. Ed.* **2008**, *47*, 9560–9564.

[21] R. Litlabø, M. Zimmermann, K. Saliu, J. Takats, K. W. Törnroos, R. Anwander, *Angew. Chem.* **2008**, *120*, 9702–9706.

[22] J. Scott, H. Fan, B. F. Wicker, A. R. Fout, M.-H. Baik, D. J. Mindiola, *J. Am. Chem. Soc.* **2008**, *130*, 14438–14439.

[23] J. Hong, L. Zhang, X. Yu, M. Li, Z. Zhang, P. Zheng, M. Nishiura, Z. Hou, X. Zhou, *Chem. – Eur. J.* **2011**, *17*, 2130–2137.

[24] W.-X. Zhang, Z. Wang, M. Nishiura, Z. Xi, Z. Hou, *J. Am. Chem. Soc.* **2011**, *133*, 5712–5715.

[25] S. Li, M. Wang, B. Liu, L. Li, J. Cheng, C. Wu, D. Liu, J. Liu, D. Cui, *Chem. - Eur. J.* **2014**, *20*, 15493–15498.

[26] D. Schädle, M. Meermann-Zimmermann, C. Maichle-Mössmer, C. Schädle, K. W. Törnroos, R. Anwander, *Dalton Trans.* **2015**, *44*, 18101–18110.

[27] J. Hong, H. Tian, L. Zhang, X. Zhou, I. del Rosal, L. Weng, L. Maron, *Angew. Chem. Int. Ed.* **2018**, *57*, 1062–1067.

[28] J. Hong, H. Tian, L. Zhang, X. Zhou, I. del Rosal, L. Weng, L. Maron, *Angew. Chem.* **2018**, *130*, 1074–1079.

[29] M. Yamashita, Y. Takemoto, E. Ihara, H. Yasuda, *Macromolecules* **1996**, *29*, 1798–1806.

[30] Y. Shen, Z. Shen, Y. Zhang, K. Yao, *Macromolecules* **1996**, *29*, 8289–8295.

[31]   H. Yasuda, E. Ihara, in *Met. Complex Catal. Supercrit. Fluid Polym. Supramol. Archit.* (Eds.: D.A. Canelas, J.M. DeSimone, A. Harada, E. Ihara, K. Mashima, A. Nakamura, Y. Nakayama, H. Yasuda), Springer, Berlin, Heidelberg, **1997**, pp. 53–101.

[32]   K. B. Aubrecht, K. Chang, M. A. Hillmyer, W. B. Tolman, *J. Polym. Sci. Part Polym. Chem.* **2001**, *39*, 284–293.

[33]   D. Barbier-Baudry, S. Heiner, M. M. Kubicki, E. Vigier, M. Visseaux, A. Hafid, *Organometallics* **2001**, *20*, 4207–4210.

[34]   Y. Matsuo, K. Mashima, K. Tani, *Organometallics* **2001**, *20*, 3510–3518.

[35]   H. Ma, T. P. Spaniol, J. Okuda, *Dalton Trans.* **2003**, 4770–4780.

[36]   Y. Satoh, N. Ikitake, Y. Nakayama, S. Okuno, H. Yasuda, *J. Organomet. Chem.* **2003**, *667*, 42–52.

[37]   P. Brignou, M. Priebe Gil, O. Casagrande, J.-F. Carpentier, S. M. Guillaume, *Macromolecules* **2010**, *43*, 8007–8017.

[38]   M. A. Sinenkov, G. K. Fukin, A. V. Cherkasov, N. Ajellal, T. Roisnel, F. M. Kerton, J.-F. Carpentier, A. A. Trifonov, *New J. Chem.* **2011**, *35*, 204–212.

[39]   C. Bakewell, T.-P.-A. Cao, N. Long, X. F. Le Goff, A. Auffrant, C. K. Williams, *J. Am. Chem. Soc.* **2012**, *134*, 20577–20580.

[40]   J.-F. Carpentier, *Organometallics* **2015**, *34*, 4175–4189.

[41]   C. Bakewell, A. J. P. White, N. J. Long, C. K. Williams, *Inorg. Chem.* **2015**, *54*, 2204–2212.

[42]   H. Yasuda, E. Ihara, *Macromol. Chem. Phys.* **1995**, *196*, 2417–2441.

[43]   T. Sato, M. Naruse, K. Toyosu, M. Seno, *Macromol. Chem. Phys.* **1996**, *197*, 3541–3554.

[44]   L. S. Boffa, B. M. Novak, *Tetrahedron* **1997**, *53*, 15367–15396.

[45]   M. Yousaf, J.-U. Huang, Z.-F. Feng, Y.-L. Qian, J.-Q. Sun, Z.-D. Pan, *Chin. J. Chem.* **2000**, *18*, 759–763.

[46]   H. Yasuda, M. Furo, H. Yamamoto, A. Nakamura, S. Miyake, N. Kibino, *Macromolecules* **1992**, *25*, 5115–5116.

[47]   G. Desurmont, T. Tokimitsu, H. Yasuda, *Macromolecules* **2000**, *33*, 7679–7681.

[48]   H. Yasuda, *J. Organomet. Chem.* **2002**, *647*, 128–138.

[49]   L. Wang, D. Cui, Z. Hou, W. Li, Y. Li, *Organometallics* **2011**, *30*, 760–767.

[50]   C. Yao, D. Liu, P. Li, C. Wu, S. Li, B. Liu, D. Cui, *Organometallics* **2014**, *33*, 684–691.

[51]   P. Falkowski, R. J. Scholes, E. Boyle, J. Canadell, D. Canfield, J. Elser, N. Gruber, K. Hibbard, P. Högberg, S. Linder, F. T. Mackenzie, B. Moore III, T. Pedersen, Y. Rosenthal, S. Seitzinger, V. Smetacek, W. Steffen, *Science* **2000**, *290*, 291–296.

[52]   S. Solomon, G.-K. Plattner, R. Knutti, P. Friedlingstein, *Proc. Natl. Acad. Sci.* **2009**, *106*, 1704–1709.

[53]   R. S. Haszeldine, *Science* **2009**, *325*, 1647–1652.

[54]   D. W. Keith, *Science* **2009**, *325*, 1654–1655.

[55]   N. von der Assen, P. Voll, M. Peters, A. Bardow, *Chem. Soc. Rev.* **2014**, *43*, 7982–7994.

[56]   D. V. Vitanova, F. Hampel, K. C. Hultzsch, *J. Organomet. Chem.* **2005**, *690*, 5182–5197.

[57]   D. Cui, M. Nishiura, Z. Hou, *Macromolecules* **2005**, *38*, 4089–4095.

[58]   B. B. Lazarov, F. Hampel, K. C. Hultzsch, *Z. Für Anorg. Allg. Chem.* **2007**, *633*, 2367–2373.

[59]   D. Cui, M. Nishiura, O. Tardif, Z. Hou, *Organometallics* **2008**, *27*, 2428–2435.

[60] Z. Zhang, D. Cui, X. Liu, *J. Polym. Sci. Part Polym. Chem.* **2008**, *46*, 6810–6818.

[61] A. Decortes, R. M. Haak, C. Martín, M. M. Belmonte, E. Martin, J. Benet-Buchholz, A. W. Kleij, *Macromolecules* **2015**, *48*, 8197–8207.

[62] B. Xu, P. Wang, M. Lv, D. Yuan, Y. Yao, *ChemCatChem* **2016**, *8*, 2466–2471.

[63] H. Yasuda, L.-N. He, T. Sakakura, *J. Catal.* **2002**, *209*, 547–550.

[64] J. Qin, P. Wang, Q. Li, Y. Zhang, D. Yuan, Y. Yao, *Chem. Commun.* **2014**, *50*, 10952–10955.

[65] C. Wang, X. Liu, Z. Dai, Y. Sun, N. Tang, J. Wu, *Inorg. Chem. Commun.* **2015**, *56*, 69–72.

[66] J. Martínez, J. Fernández-Baeza, L. F. Sánchez-Barba, J. A. Castro-Osma, A. Lara-Sánchez, A. Otero, *ChemSusChem* **2017**, *10*, 2886–2890.

[67] Z. Zhao, J. Qin, C. Zhang, Y. Wang, D. Yuan, Y. Yao, *Inorg. Chem.* **2017**, *56*, 4568–4575.

[68] A. Ion, V. Parvulescu, P. Jacobs, D. de Vos, *Appl. Catal. Gen.* **2009**, *363*, 40–44.

[69] O. Sodpiban, S. Del Gobbo, S. Barman, V. Aomchad, P. Kidkhunthod, S. Ould-Chikh, A. Poater, V. D'Elia, J.-M. Basset, *Catal. Sci. Technol.* **2019**, *9*, 6152–6165.

[70] F. A. LeBlanc, A. Berkefeld, W. E. Piers, M. Parvez, *Organometallics* **2012**, *31*, 810–818.

[71] A. Berkefeld, W. E. Piers, M. Parvez, L. Castro, L. Maron, O. Eisenstein, *Chem. Sci.* **2013**, *4*, 2152–2162.

[72] A. Nomoto, Y. Kojo, G. Shiino, Y. Tomisaka, I. Mitani, M. Tatsumi, A. Ogawa, *Tetrahedron Lett.* **2010**, *51*, 6580–6583.

[73] A. Prikhod'ko, O. Walter, T. A. Zevaco, J. Garcia-Rodriguez, O. Mouhtady, S. Py, *Eur. J. Org. Chem.* **2012**, *2012*, 3742–3746.

[74] K. Tomishige, K. Kunimori, *Appl. Catal. Gen.* **2002**, *237*, 103–109.

[75] M. Honda, M. Tamura, Y. Nakagawa, S. Sonehara, K. Suzuki, K. Fujimoto, K. Tomishige, *ChemSusChem* **2013**, *6*, 1341–1344.

[76] M. Honda, M. Tamura, Y. Nakagawa, K. Nakao, K. Suzuki, K. Tomishige, *J. Catal.* **2014**, *318*, 95–107.

[77] D. Stoian, F. Medina, A. Urakawa, *ACS Catal.* **2018**, *8*, 3181–3193.

[78] D. Esrafilzadeh, A. Zavabeti, R. Jalili, P. Atkin, J. Choi, B. J. Carey, R. Brkljača, A. P. O'Mullane, M. D. Dickey, D. L. Officer, D. R. MacFarlane, T. Daeneke, K. Kalantar-Zadeh, *Nat. Commun.* **2019**, *10*, DOI 10.1038/s41467-019-08824-8.

[79] D.-X. Xue, A. J. Cairns, Y. Belmabkhout, L. Wojtas, Y. Liu, M. H. Alkordi, M. Eddaoudi, *J. Am. Chem. Soc.* **2013**, *135*, 7660–7667.

[80] W. Mu, X. Huang, R. Zhong, W. Xia, J. Liu, R. Zou, *CrystEngComm* **2015**, *17*, 1637–1645.

[81] J. Ethiraj, F. Bonino, J. G. Vitillo, K. A. Lomachenko, C. Lamberti, H. Reinsch, K. P. Lillerud, S. Bordiga, *ChemSusChem* **2016**, *9*, 713–719.

[82] Y.-N. Gong, P. Xiong, C.-T. He, J.-H. Deng, D.-C. Zhong, *Inorg. Chem.* **2018**, *57*, 5013–5018.

[83] H. J. Heeres, M. Maters, J. H. Teuben, G. Helgesson, S. Jagner, *Organometallics* **1992**, *11*, 350–356.

[84] M. Allen, H. C. Aspinall, S. R. Moore, M. B. Hursthouse, A. I. Karvalov, *Polyhedron* **1992**, *11*, 409–413.

[85]   A. R. Crozier, K. W. Törnroos, C. Maichle-Mössmer, R. Anwander, *Eur. J. Inorg. Chem.* **2013**, *2013*, 409–414.

[86]   H. Schulz, H. Schultze, H. Reddmann, M. Link, H.-D. Amberger, *J. Organomet. Chem.* **1992**, *424*, 139–152.

[87]   Â. Domingos, N. Marques, A. Pires de Matos, M. G. Silva-Valenzuela, L. B. Zinner, *Polyhedron* **1993**, *12*, 2545–2549.

[88]   X. Zhou, H. Ma, Z. Wu, X. You, Z. Xu, Y. Zhang, X. Huang, *Acta Crystallogr. Sect. C* **1996**, *52*, 1875–1877.

[89]   X. Li, J. Hong, R. Liu, L. Weng, X. Zhou, *Organometallics* **2010**, *29*, 4606–4610.

[90]   W. J. Evans, C. H. Fujimoto, M. A. Johnston, J. W. Ziller, *Organometallics* **2002**, *21*, 1825–1831.

[91]   M. R. MacDonald, J. W. Ziller, W. J. Evans, *Inorg. Chem.* **2011**, *50*, 4092–4106.

[92]   K. Chang, X. Wang, Z. Fan, X. Xu, *Inorg. Chem.* **2018**, *57*, 8568–8580.

[93]   H. Yasuda, H. Yamamoto, K. Yokota, S. Miyake, A. Nakamura, *J. Am. Chem. Soc.* **1992**, *114*, 4908–4910.

[94]   D. Baudry, *J. Organomet. Chem.* **1997**, *547*, 157–165.

[95]   F. Basuli, J. Tomaszewski, J. C. Huffman, D. J. Mindiola, *Organometallics* **2003**, *22*, 4705–4714.

[96]   M. E. Burin, A. A. Logunov, N. O. Druzhkov, G. K. Fukin, M. N. Bochkarev, *Russ. Chem. Bull.* **2011**, *60*, 1586–1590.

[97]   T. A. Starostina, R. R. Shifrina, E. S. Petrov, *Zh Obs Khim* **1987**, *57*, 2402.

[98]   J. Arnold, C. G. Hoffman, D. Y. Dawson, F. J. Hollander, *Organometallics* **1993**, *12*, 3645–3654.

[99]   H. M. Dietrich, C. Meermann, K. W. Törnroos, R. Anwander, *Organometallics* **2006**, *25*, 4316–4321.

[100]   Y. Nakajima, J. Okuda, *Organometallics* **2007**, *26*, 1270–1278.

[101]   M. U. Kramer, D. Robert, S. Arndt, P. M. Zeimentz, T. P. Spaniol, A. Yahia, L. Maron, O. Eisenstein, J. Okuda, *Inorg. Chem.* **2008**, *47*, 9265–9278.

[102]   Y. Yang, D. Cui, X. Chen, *Dalton Trans.* **2010**, *39*, 3959.

[103]   G. B. Deacon, P. C. Junk, J. Wang, D. Werner, *Inorg. Chem.* **2014**, *53*, 12553–12563.

[104]   L. Xu, Y.-C. Wang, J. Wei, Y. Wang, Z. Wang, W.-X. Zhang, Z. Xi, *Chem. – Eur. J.* **2015**, *21*, 6686–6689.

[105]   M. R. Crimmin, A. J. P. White, *Chem. Commun.* **2012**, *48*, 1745–1747.

[106]   J. Scholz, H. Görls, H. Schumann, R. Weimann, *Organometallics* **2001**, *20*, 4394–4402.

[107]   A. V. Zabula, Y. Qiao, A. J. Kosanovich, T. Cheisson, B. C. Manor, P. J. Carroll, O. V. Ozerov, E. J. Schelter, *Chem. – Eur. J.* **2017**, *23*, 17923–17934.

[108]   C. Zhang, R. Liu, J. Zhang, Z. Chen, X. Zhou, *Inorg. Chem.* **2006**, *45*, 5867–5877.

[109]   C.-M. Zhang, R.-T. Liu, Z.-X. Chen, X.-G. Zhou, *Chin. J. Chem.* **2006**, *24*, 231–234.

[110]   C. Schoo, S. V. Klementyeva, M. T. Gamer, S. N. Konchenko, P. W. Roesky, *Chem. Commun.* **2016**, *52*, 6654–6657.

[111]   J. Chu, E. Lu, Z. Liu, Y. Chen, X. Leng, H. Song, *Angew. Chem. Int. Ed.* **2011**, *50*, 7677–7680.

[112]   J. Chu, E. Lu, Z. Liu, Y. Chen, X. Leng, H. Song, *Angew. Chem.* **2011**, *123*, 7819–7822.

[113]   D. Werner, G. B. Deacon, P. C. Junk, R. Anwander, *Eur. J. Inorg. Chem.* **2017**, *28*, 3419–3428.

[114]   W. Mao, L. Xiang, C. A. Lamsfus, L. Maron, X. Leng, Y. Chen, *Chin. J. Chem.* **2018**, *36*, 904–908.

[115]   Z. Hou, H. Yamazaki, Y. Fujiwara, H. Taniguchi, *Organometallics* **1992**, *11*, 2711–2714.

[116]   Z. Hou, T. Miyano, H. Yamazaki, Y. Wakatsuki, *J. Am. Chem. Soc.* **1995**, *117*, 4421–4422.

[117]   Z. Hou, A. Fujita, H. Yamazaki, Y. Wakatsuki, *J. Am. Chem. Soc.* **1996**, *118*, 7843–7844.

[118]   I. Nagl, M. Widenmeyer, S. Grasser, K. Köhler, R. Anwander, *J. Am. Chem. Soc.* **2000**, *122*, 1544–1545.

[119]   Z. Hou, A. Fujita, Y. Zhang, T. Miyano, H. Yamazaki, Y. Wakatsuki, *J. Am. Chem. Soc.* **1998**, *120*, 754–766.

[120]   Z. Hou, T. Koizumi, M. Nishiura, Y. Wakatsuki, *Organometallics* **2001**, *20*, 3323–3328.

[121]   I. Lopes, R. Dias, Â. Domingos, N. Marques, *J. Alloys Compd.* **2002**, *344*, 60–64.

[122]   Â. Domingos, I. Lopes, J. C. Waerenborgh, N. Marques, G. Y. Lin, X. W. Zhang, J. Takats, R. McDonald, A. C. Hillier, A. Sella, M. R. J. Elsegood, V. W. Day, *Inorg. Chem.* **2007**, *46*, 9415–9424.

[123]   D. Werner, X. Zhao, S. P. Best, L. Maron, P. C. Junk, G. B. Deacon, *Chem. – Eur. J.* **2017**, *23*, 2084–2102.

[124]   W. Clegg, K. Izod, P. O'Shaughnessy, C. Eaborn, J. D. Smith, *Angew. Chem. Int. Ed. Engl.* **1997**, *36*, 2815–2817.

[125]   T. Cheisson, L. Ricard, F. W. Heinemann, K. Meyer, A. Auffrant, G. Nocton, *Inorg. Chem.* **2018**, *57*, 9230–9240.

[126]   G. B. Deacon, C. M. Forsyth, D. L. Wilkinson, *Chem. – Eur. J.* **2001**, *7*, 1784–1795.

[127]   H. Lankamp, W. Th. Nauta, C. MacLean, *Tetrahedron Lett.* **1968**, *9*, 249–254.

[128]   N. S. Blom, G. Roelofsen, J. A. Kanters, *Cryst. Struct. Commun.* **1982**, *11*, 297.

[129]   O. Tardif, Z. Hou, M. Nishiura, T. Koizumi, Y. Wakatsuki, *Organometallics* **2001**, *20*, 4565–4573.

[130]   A. Sen, H. A. Stecher, A. L. Rheingold, *Inorg. Chem.* **1992**, *31*, 473–479.

[131]   J. R. Robinson, C. H. Booth, P. J. Carroll, P. J. Walsh, E. J. Schelter, *Chem. - Eur. J.* **2013**, *19*, 5996–6004.

[132]   D. Werner, G. B. Deacon, P. C. Junk, R. Anwander, *Chem. - Eur. J.* **2014**, *20*, 4426–4438.

[133]   D. Schneider, N. Harmgarth, F. T. Edelmann, R. Anwander, *Chem. – Eur. J.* **2017**, *23*, 12243–12252.

[134]   D. Werner, G. B. Deacon, P. C. Junk, R. Anwander, *Dalton Trans.* **2017**, *46*, 6265–6277.

[135]   D. Werner, U. Bayer, D. Schädle, R. Anwander, *Chem. - Eur. J.* **2020**, *26*, 12194–12205.

[136]   D. M. Kuzyaev, D. L. Vorozhtsov, N. O. Druzhkov, M. A. Lopatin, E. V. Baranov, A. V. Cherkasov, G. K. Fukin, G. A. Abakumov, M. N. Bochkarev, *J. Organomet. Chem.* **2012**, *698*, 35–41.

[137]   M. N. Bochkarev, A. A. Fagin, N. O. Druzhkov, V. K. Cherkasov, M. A. Katkova, G. K. Fukin, Y. A. Kurskii, *J. Organomet. Chem.* **2010**, *695*, 2774–2780.

[138]   N. J. C. van Velzen, S. Harder, *Organometallics* **2018**, *37*, 2263–2271.

[139]   M. Bochkarev, E. A. Fedorova, Y. F. Radkov, S. Ya, G. S. Kalinina, G. A. Razuvaev, *J. Organomet. Chem.* **1983**, *258*, C29–C33.

[140]   Y. F. Radkov, E. A. Fedorova, S. Y. Khorshev, G. S. Kalinina, M. N. Bochkarev, G. A. Razuvaev, *Zhur. Obshchei Khimii* **1986**, *56*, 386–389.

[141] H. Yin, P. J. Carroll, E. J. Schelter, *Chem. Commun.* **2016**, *52*, 9813–9816.

[142] M. A. S. Clair, B. D. Santarsiero, *Acta Cryst* **1989**, *C45*, 850–852.

[143] B. K. Campion, R. H. Heyn, T. D. Tilley, *Inorg. Chem.* **1990**, *29*, 4355–4356.

[144] H. Schumann, J. A. Meese-Marktscheffel, A. Dietrich, F. H. Görlitz, *J. Organomet. Chem.* **1992**, *430*, 299–315.

[145] W. J. Evans, C. A. Seibel, J. W. Ziller, R. J. Doedens, *Organometallics* **1998**, *17*, 2103–2112.

[146] W. J. Evans, J. M. Perotti, S. A. Kozimor, T. M. Champagne, B. L. Davis, G. W. Nyce, C. H. Fujimoto, R. D. Clark, M. A. Johnston, J. W. Ziller, *Organometallics* **2005**, *24*, 3916–3931.

[147] W. J. Evans, D. B. Rego, J. W. Ziller, A. G. DiPasquale, A. L. Rheingold, *Organometallics* **2007**, *26*, 4737–4745.

[148] J. Sun, D. J. Berg, B. Twamley, *Organometallics* **2008**, *27*, 683–690.

[149] W. J. Evans, T. J. Mueller, J. W. Ziller, *J. Am. Chem. Soc.* **2009**, *131*, 2678–2686.

[150] M. R. MacDonald, R. R. Langeslay, J. W. Ziller, W. J. Evans, *J. Am. Chem. Soc.* **2015**, *137*, 14716–14725.

[151] V. Goudy, M. Xémard, S. Karleskind, M. Cordier, C. Alvarez Lamsfus, L. Maron, G. Nocton, *Inorganics* **2018**, *6*, 82.

[152] D. W. Beh, W. E. Piers, I. del Rosal, L. Maron, B. S. Gelfand, C. Gendy, J.-B. Lin, *Dalton Trans.* **2018**, *47*, 13680–13688.

[153] I. Korobkov, S. Gambarotta, *Organometallics* **2009**, *28*, 4009–4019.

[154] J. Hong, L. Zhang, K. Wang, Z. Chen, L. Wu, X. Zhou, *Organometallics* **2013**, *32*, 7312–7322.

[155] F. Kong, M. Li, X. Zhou, L. Zhang, *RSC Adv.* **2017**, *7*, 29752–29761.

[156] X. Liu, L. Xiang, C. Wang, B. Wang, X. Leng, Y. Chen, *Chin. J. Chem.* **2020**, *38*, 247–253.

[157] F. A. LeBlanc, W. E. Piers, M. Parvez, *Angew. Chem. Int. Ed.* **2014**, *53*, 789–792.

[158] F. A. LeBlanc, W. E. Piers, M. Parvez, *Angew. Chem.* **2014**, *126*, 808–811.

[159] J. Zhou, T. Li, L. Maron, X. Leng, Y. Chen, *Organometallics* **2015**, *34*, 470–476.

[160] O. Tardif, D. Hashizume, Z. Hou, *J. Am. Chem. Soc.* **2004**, *126*, 8080–8081.

[161] O. T. Summerscales, C. M. Moore, B. L. Scott, M. P. Wilkerson, A. D. Sutton, *Organometallics* **2017**, *36*, 4682–4685.

[162] L. A. M. Steele, T. J. Boyle, R. A. Kemp, C. Moore, *Polyhedron* **2012**, *42*, 258–264.

[163] W. J. Evans, K. A. Miller, J. W. Ziller, *Inorg. Chem.* **2006**, *45*, 424–429.

[164] W. J. Evans, C. H. Fujimoto, J. W. Ziller, *Organometallics* **2001**, *20*, 4529–4536.

[165] U. Baisch, D. B. Dell' Amico, F. Calderazzo, L. Labella, F. Marchetti, D. Vitali, *J. Mol. Catal. Chem.* **2003**, *204–205*, 259–265.

[166] U. Bayer, D. Werner, C. Maichle-Mössmer, R. Anwander, *Angew. Chem. Int. Ed.* **2020**, *59*, 5830–5836.

[167] J. Hong, L. Zhang, K. Wang, Y. Zhang, L. Weng, X. Zhou, *Chem. – Eur. J.* **2013**, *19*, 7865–7873.

[168] E. N. Lapsheva, T. Cheisson, C. Á. Lamsfus, P. J. Carroll, M. R. Gau, L. Maron, E. J. Schelter, *Chem. Commun.* **2020**, *56*, 4781–4784.

[169] P. L. Arnold, Z. R. Turner, A. I. Germeroth, I. J. Casely, G. S. Nichol, R. Bellabarba, R. P. Tooze, *Dalton Trans* **2013**, *42*, 1333–1337.

[170] P. L. Arnold, I. A. Marr, S. Zlatogorsky, R. Bellabarba, R. P. Tooze, *Dalton Trans.* **2014**, *43*, 34–37.

[171] P. L. Arnold, R. W. F. Kerr, C. Weetman, S. R. Docherty, J. Rieb, F. L. Cruickshank, K. Wang, C. Jandl, M. W. McMullon, A. Pöthig, F. E. Kühn, A. D. Smith, *Chem. Sci.* **2018**, *9*, 8035–8045.

[172] T. Simler, T. J. Feuerstein, R. Yadav, M. T. Gamer, P. W. Roesky, *Chem. Commun.* **2019**, *55*, 222–225.

[173] W. J. Evans, C. A. Seibel, J. W. Ziller, *Inorg. Chem.* **1998**, *37*, 770–776.

[174] W. J. Evans, J. M. Perotti, J. C. Brady, J. W. Ziller, *J. Am. Chem. Soc.* **2003**, *125*, 5204–5212.

[175] L. Castro, D. P. Mills, C. Jones, L. Maron, *Eur. J. Inorg. Chem.* **2016**, *2016*, 792–796.

[176] J. Andrez, J. Pécaut, P.-A. Bayle, M. Mazzanti, *Angew. Chem. Int. Ed.* **2014**, *53*, 10448–10452.

[177] J. Andrez, J. Pécaut, P.-A. Bayle, M. Mazzanti, *Angew. Chem.* **2014**, *126*, 10616–10620.

[178] A. R. Willauer, D. Toniolo, F. Fadaei-Tirani, Y. Yang, M. Laurent, M. Mazzanti, *Dalton Trans.* **2019**, *48*, 6100–6110.

[179] W. J. Evans, S. E. Lorenz, J. W. Ziller, *Inorg. Chem.* **2009**, *48*, 2001–2009.

[180] D. H. Woen, G. P. Chen, J. W. Ziller, T. J. Boyle, F. Furche, W. J. Evans, *Angew. Chem. Int. Ed.* **2017**, *56*, 2050–2053.

[181] D. H. Woen, G. P. Chen, J. W. Ziller, T. J. Boyle, F. Furche, W. J. Evans, *Angew. Chem.* **2017**, *129*, 2082–2085.

[182] M. Fang, J. H. Farnaby, J. W. Ziller, J. E. Bates, F. Furche, W. J. Evans, *J. Am. Chem. Soc.* **2012**, *134*, 6064–6067.

[183] D. Min, S. W. Lee, *Inorg. Chem. Commun.* **2002**, *5*, 978–983.

[184] H. S. Huh, S. W. Lee, *Bull. Korean Chem. Soc.* **2006**, *27*, 1839–1843.

[185] S. P. Chen, Y. X. Ren, F. Fu, S. L. Gao, *Russ. J. Coord. Chem.* **2009**, *35*, 157–159.

[186] K. Gong, X. Zhao, T. Xiao, C. Zhao, Z. Han, H. Yu, X. Zhai, *J. Mol. Struct.* **2014**, *1068*, 270–274.

[187] N. W. Davies, A. S. P. Frey, M. G. Gardiner, J. Wang, *Chem. Commun.* **2006**, 4853.

[188] M. Xémard, V. Goudy, A. Braun, M. Tricoire, M. Cordier, L. Ricard, L. Castro, E. Louyriac, C. E. Kefalidis, C. Clavaguéra, L. Maron, G. Nocton, *Organometallics* **2017**, *36*, 4660–4668.

[189] M. Xémard, M. Cordier, E. Louyriac, L. Maron, C. Clavaguéra, G. Nocton, *Dalton Trans.* **2018**, *47*, 9226–9230.

[190] Y.-M. So, G.-C. Wang, Y. Li, H. H.-Y. Sung, I. D. Williams, Z. Lin, W.-H. Leung, *Angew. Chem. Int. Ed.* **2014**, *53*, 1626–1629.

[191] Y.-M. So, G.-C. Wang, Y. Li, H. H.-Y. Sung, I. D. Williams, Z. Lin, W.-H. Leung, *Angew. Chem.* **2014**, *126*, 1652–1655.

[192] G.-C. Wang, Y.-M. So, K.-L. Wong, K.-C. Au-Yeung, H. H.-Y. Sung, I. D. Williams, W.-H. Leung, *Chem. – Eur. J.* **2015**, *21*, 16126–16135.

[193] K. A. Grice, *Coord. Chem. Rev.* **2017**, *336*, 78–95.

[194] J. Huang, J. C. Worch, A. P. Dove, O. Coulembier, *ChemSusChem* **2020**, *13*, 469–487.

[195] P. P. Pescarmona, M. Taherimehr, *Catal. Sci. Technol.* **2012**, *2*, 2169–2187.

[196] X. Chen, Z. Shen, Y. Zhang, *Macromolecules* **1991**, *24*, 5305–5308.

[197] C.-S. Tan, T.-J. Hsu, *Macromolecules* **1997**, *30*, 3147–3150.

[198] T.-J. Hsu, C.-S. Tan, *Polymer* **2001**, *42*, 5143–5150.

[199] B. Liu, X. Zhao, X. Wang, F. Wang, *Polymer* **2003**, *44*, 1803–1808.

[200] Z. Quan, X. Wang, X. Zhao, F. Wang, *Polymer* **2003**, *44*, 5605–5610.

[201] Y. Hu, L. Qiao, Y. Qin, X. Zhao, X. Chen, X. Wang, F. Wang, *Macromolecules* **2009**, *42*, 9251–9254.

[202] Y. Dong, X. Wang, X. Zhao, F. Wang, *J. Polym. Sci. Part Polym. Chem.* **2012**, *50*, 362–370.

[203] J. Qin, B. Xu, Y. Zhang, D. Yuan, Y. Yao, *Green Chem.* **2016**, *18*, 4270–4275.

[204] H. Nagae, R. Aoki, S. Akutagawa, J. Kleemann, R. Tagawa, T. Schindler, G. Choi, T. P. Spaniol, H. Tsurugi, J. Okuda, K. Mashima, *Angew. Chem. Int. Ed.* **2018**, *57*, 2492–2496.

[205] H. Nagae, R. Aoki, S. Akutagawa, J. Kleemann, R. Tagawa, T. Schindler, G. Choi, T. P. Spaniol, H. Tsurugi, J. Okuda, K. Mashima, *Angew. Chem.* **2018**, *130*, 2518–2522.

[206] L. Hua, B. Li, C. Han, P. Gao, Y. Wang, D. Yuan, Y. Yao, *Inorg. Chem.* **2019**, *58*, 8775–8786.

[207] L. Qu, I. del Rosal, Q. Li, Y. Wang, D. Yuan, Y. Yao, L. Maron, *J. CO2 Util.* **2019**, *33*, 413–418.

[208] R. Xu, L. Hua, X. Li, Y. Yao, X. Leng, Y. Chen, *Dalton Trans.* **2019**, *48*, 10565–10573.

[209] H. Asaba, T. Iwasaki, M. Hatazawa, J. Deng, H. Nagae, K. Mashima, K. Nozaki, *Inorg. Chem.* **2020**, *59*, 7928–7933.

[210] Y.-C. Su, W.-L. Liu, C.-Y. Li, B.-T. Ko, *Polymer* **2019**, *167*, 21–30.

[211] C.-H. Ho, H.-J. Chuang, P.-H. Lin, B.-T. Ko, *J. Polym. Sci. Part Polym. Chem.* **2017**, *55*, 321–328.

[212] R. Zhang, L. Wang, C. Xu, H. Yang, W. Chen, G. Gao, W. Liu, *Dalton Trans.* **2018**, *47*, 7159–7165.

[213] G. A. Gurina, A. A. Kissel, D. M. Lyubov, L. Luconi, A. Rossin, G. Tuci, A. V. Cherkasov, K. A. Lyssenko, A. S. Shavyrin, A. M. Ob'edkov, G. Giambastiani, A. A. Trifonov, *Dalton Trans.* **2020**, *49*, 638–650.

[214] C. A. Huff, M. S. Sanford, *J. Am. Chem. Soc.* **2011**, *133*, 18122–18125.

[215] W.-Y. Chu, Z. Culakova, B. T. Wang, K. I. Goldberg, *ACS Catal.* **2019**, *9*, 9317–9326.

[216] R. Anwander, M. Dolg, F. T. Edelmann, *Chem. Soc. Rev.* **2017**, *46*, 6697–6709.

[217] J. Eppinger, M. Spiegler, W. Hieringer, W. A. Herrmann, R. Anwander, *J. Am. Chem. Soc.* **2000**, *122*, 3080–3096.

[218] A. R. Crozier, A. M. Bienfait, C. Maichle-Mössmer, K. W. Törnroos, R. Anwander, *Chem Commun* **2013**, *49*, 87–89.

[219] U. J. Williams, D. Schneider, W. L. Dorfner, C. Maichle-Mössmer, P. J. Carroll, R. Anwander, E. J. Schelter, *Dalton Trans* **2014**, *43*, 16197–16206.

[220] J. E. Kim, P. J. Carroll, E. J. Schelter, *Chem. Commun.* **2015**, *51*, 15047–15050.

[221] J. R. Levin, W. L. Dorfner, A. X. Dai, P. J. Carroll, E. J. Schelter, *Inorg. Chem.* **2016**, *55*, 12651–12659.

[222] J. R. Robinson, P. J. Carroll, P. J. Walsh, E. J. Schelter, *Angew. Chem. Int. Ed.* **2012**, *51*, 10159–10163.

[223] J. R. Robinson, P. J. Carroll, P. J. Walsh, E. J. Schelter, *Angew. Chem.* **2012**, *124*, 10306–10310.

[224] J. R. Robinson, Z. Gordon, C. H. Booth, P. J. Carroll, P. J. Walsh, E. J. Schelter, *J. Am. Chem. Soc.* **2013**, *135*, 19016–19024.

[225] I. J. Casely, S. T. Liddle, A. J. Blake, C. Wilson, P. L. Arnold, *Chem. Commun.* **2007**, 5037–5039.

[226] P. L. Arnold, I. J. Casely, S. Zlatogorsky, C. Wilson, *Helv. Chim. Acta* **2009**, *92*, 2291–2303.

[227] M. T. Huynh, C. W. Anson, A. C. Cavell, S. S. Stahl, S. Hammes-Schiffer, *J. Am. Chem. Soc.* **2016**, *138*, 15903–15910.

[228] T. Han, J. B. Petersen, Z.-H. Li, Y.-Q. Zhai, A. Kostopoulos, F. Ortu, E. J. L. McInnes, R. E. P. Winpenny, Y.-Z. Zheng, *Inorg. Chem.* **2020**, *59*, 7371–7375.

[229] Z. Guo, J. Luu, V. Blair, G. B. Deacon, P. C. Junk, *Eur. J. Inorg. Chem.* **2019**, *2019*, 1018–1029.

[230] P. B. Hitchcock, A. G. Hulkes, M. F. Lappert, Z. Li, *Dalton Trans.* **2004**, 129–136.

[231] D. Werner, U. Bayer, N. E. Rad, P. C. Junk, G. B. Deacon, R. Anwander, *Dalton Trans.* **2018**, *47*, 5952–5955.

[232] S. Yang, X. Zhu, S. Zhou, S. Wang, Z. Feng, Y. Wei, H. Miao, L. Guo, F. Wang, G. Zhang, X. Gu, X. Mu, *Dalton Trans* **2014**, *43*, 2521–2533.

[233] D. S. Levine, T. D. Tilley, R. A. Andersen, *Organometallics* **2017**, *36*, 80–88.

[234] J. Sampson, G. Choi, M. N. Akhtar, E. A. Jaseer, R. Theravalappil, N. Garcia, T. Agapie, *ACS Omega* **2019**, *4*, 15879–15892.

[235] H. Schumann, P. R. Lee, A. Dietrich, *Chem. Ber.* **1990**, *123*, 1331–1334.

[236] P. L. Arnold, T. Cadenbach, I. H. Marr, A. A. Fyfe, N. L. Bell, R. Bellabarba, R. P. Tooze, J. B. Love, *Dalton Trans.* **2014**, *43*, 14346–14358.

[237] U. Bayer, L. Bock, C. Maichle-Mössmer, R. Anwander, *Eur. J. Inorg. Chem.* **2020**, *2020*, 101–106.

[238] W. J. Evans, D. S. Lee, D. B. Rego, J. M. Perotti, S. A. Kozimor, E. K. Moore, J. W. Ziller, *J. Am. Chem. Soc.* **2004**, *126*, 14574–14582.

E

Publications

A Facile Route toward Ceric Precursor [Ce{N(SiHMe$_2$)$_2$}$_4$]

▌ Cerium(III) Oxidation | *Very Important Paper* |

VIP A Facile Route toward Ceric Silylamide [Ce{N(SiHMe$_2$)$_2$}$_4$]

Uwe Bayer,[a][‡] Lorenz Bock,[a][‡] Cäcilia Maichle-Mössmer,[a] and Reiner Anwander*[a]

Abstract: Treatment of the ate complex [Ce{N(SiHMe$_2$)$_2$}$_4$-Li(thf)] with neutral donor molecules (do) gave several solvent(do)-separated ion-pair complexes of the composition [Ce{N(SiHMe$_2$)$_2$}$_4$][Li(do)$_n$] (do = thf, pyridine, tmeda, dme, 12-crown-4). Their solid-state structures have been analyzed by X-ray diffraction and DRIFTS. Displacement of the [Li(do)$_n$] entity, resulting in a solvent-separated ion pair with a symmetric envi-

ronment around the Ce(III) center, was also revealed in solution by ^{7}Li NMR spectroscopy. The oxidation of [Ce{N(SiHMe$_2$)$_2$}$_4$]-[Li(do)$_n$] with 1,4-benzoquinone to afford homoleptic ceric [Ce{N(SiHMe$_2$)$_2$}$_4$] has been investigated and screened. Overall, the separated ion pairs [Ce{N(SiHMe$_2$)$_2$}$_4$][Li(do)$_n$] performed better than the intramolecular ate complex [Ce{N(SiHMe$_2$)$_2$}$_4$-Li(thf)], with pyridine as donor giving the best results.

Introduction

Molecular cerium chemistry is currently experiencing a veritable boom, which is documented by a number of review articles.[1] This is mainly due to the unique cerium redox chemistry featuring +3 and +4 as stable oxidation states of molecular compounds in many polar and apolar solvents.[1] Although ceric derivatives have long been a focus of scientific interest in metal-organic chemistry as well,[2] many of these compounds could only be fully characterized in recent years, because of their high sensitivity toward oxygen and moisture.[3]

With respect to the synthesis of molecular Ce(IV) compounds, ceric ammonium nitrate (CAN), (NH$_4$)$_2$Ce(NO$_3$)$_6$, has long been the precursor of choice.[1d,3a,4] More recently, synthesis protocols have also drawn on alternative ceric precursors such as triflate Ce(OTf)$_4$[5] or various alkoxides Ce(OR)$_4$.[1c,6] We and others have embarked on the silylamide [Ce{N(SiHMe$_2$)$_2$}$_4$] as a more versatile precursor en route to unprecedented Ce(IV) chemistry.[7,8] Solely judged by the proligand pK_a values, the more basic organoamides are supposed to display enhanced reactivity compared to, e.g. alkoxides,[2c,9] thus markedly extending the scope of potentially accessible Ce(IV) complexes.[7–10] The synthesis of the tetravalent homoleptic silylamide itself, however, has so far been impaired by several problems: the synthesis from [Ce{N(SiHMe$_2$)$_2$}$_3$(thf)$_2$] afforded only unsatisfactory yields (ca. 31 %) after a reaction time of 18 h, when oxidized with C$_2$Cl$_6$ or even 17 % for the oxidation with PhICl$_2$ respectively;[7] moreover, ca. 35 % of [Ce{N(SiHMe$_2$)$_2$}$_4$] (based on employed CeCl$_3$) were obtained in the presence of K[N(SiHMe$_2$)$_2$] via the potassium ate complex and oxidation with Ph$_3$CCl,[8b] and a still time-consuming synthesis (6 h sonication)

was involved when accessed more directly from CeCl$_3$(thf)$_{1.04}$ via the ate complex [Ce{N(SiHMe$_2$)$_2$}$_4$Li(thf)] and oxidized with C$_2$Cl$_6$.[8a]

We found that by adjusting the amount of the donor solvent in the above trivalent ate complex, including donor exchange the (solid-state) structure of the ate complex switched from intramolecular to that of an ion-separated compound of the general formula [Ce{N(SiHMe$_2$)$_2$}$_4$]$^-$[Li(do)$_n$]$^+$. The latter, when oxidized with 1,4-benzoquinone (bq), gave the desired [Ce{N(SiHMe$_2$)$_2$}$_4$] via an oxidative alkali-metal salt separation in a rapid and straightforward manner with only insoluble, easy-to-separate by-products (Scheme 1).
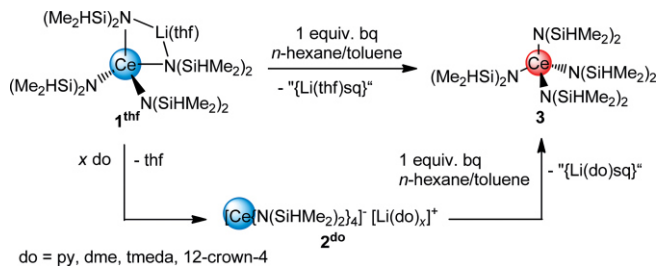
Scheme 1. Formation of [Ce{N(SiHMe$_2$)$_2$}$_4$] (**3**) via direct oxidation of ate complex [Ce{N(SiHMe$_2$)$_2$}$_4$Li(thf)] (**1**$^{\text{thf}}$) with 1,4-benzoquinone (bq) or by preceding donor exchange and subsequent oxidation of the formed solvent-separated ion pair [Ce{N(SiHMe$_2$)$_2$}$_4$][Li(do)$_n$] (**2**$^{\text{do}}$) (sq = 1,4-benzosemiquinolato).

Results and Discussion

Ate complex [Ce{N(SiHMe$_2$)$_2$}$_4$Li(thf)] (**1**$^{\text{thf}}$) was obtained as published previously by our group.[8a] Treatment of **1**$^{\text{thf}}$ with excess of different donor solvent molecules (pyridine, TMEDA, DME, 12-crown-4) and subsequent crystallization from either the donor solvent itself or from a mixture of it and *n*-hexane gave solvent-separated ion-pair complexes of the formula [Ce{N(SiHMe$_2$)$_2$}$_4$][Li(do)$_n$] (**2**$^{\text{do}}$). The crystal structures of **2**$^{\text{py}}$, **2**$^{\text{tmeda}}$ and **2**$^{\text{12-crown-4}}$ display anionic Ce(III) centers tetra-

[a] *Institut für Anorganische Chemie, University of Tübingen,*
   Auf der Morgenstelle 18, 72076 Tübingen, Germany
   E-mail: reiner.anwander@uni-tuebingen.de
   http://uni-tuebingen.de/syncat-anwander
[‡] These authors contributed equally to this publication.
   Supporting information and ORCID(s) from the author(s) for this article are
   available on the WWW under https://doi.org/10.1002/ejic.201901023.
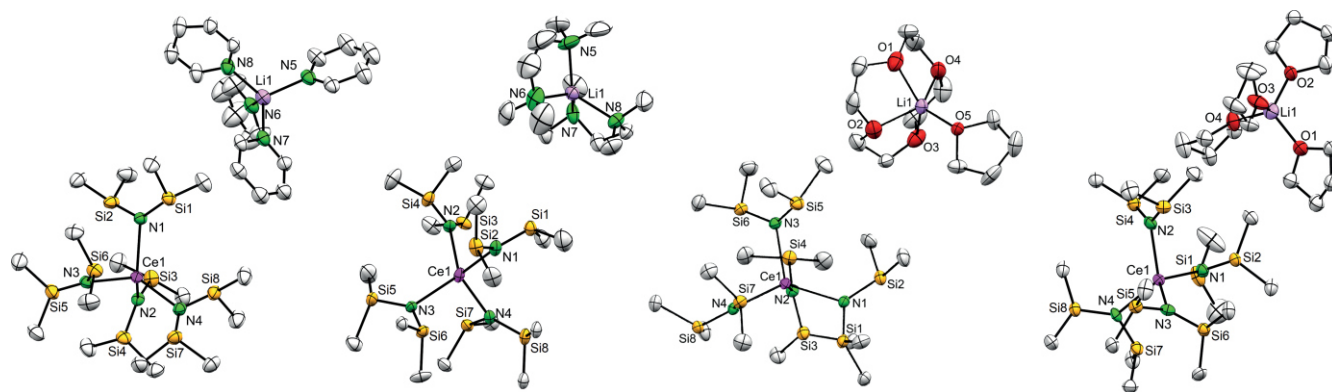
Figure 1. Crystal structures of [Ce{N(SiHMe$_2$)$_2$}$_4$][Li(py)$_4$] **2^{py}** (left), [Ce{N(SiHMe$_2$)$_2$}$_4$][Li(tmeda)$_2$] **2^{tmeda}** (center left), [Ce{N(SiHMe$_2$)$_2$}$_4$][Li(12-crown-4)(thf)] **2$^{12-crown-4}$** (center right) and [Ce{N(SiHMe$_2$)$_2$}$_4$][Li(thf)$_4$] **2^{thf}** (right). Ellipsoids are shown at either the 50 % (**2^{py}**, **2$^{12-crown-4}$**, **2^{thf}**) or the 30 % (**2^{tmeda}**) probability level. Hydrogen atoms as well as disorder in the silylamido ligands (**2^{py}**, **2^{tmeda}**, **2^{thf}**) and donor solvent molecules (**2^{py}**, **2^{tmeda}**) are omitted for clarity.

hedrally coordinated by four [N(SiHMe$_2$)$_2$] ligands. The lithium counterions are surrounded by either four molecules of pyridine, two molecules of TMEDA or one molecule of 12-crown-4 plus an additional molecule of THF (Figure 1).

As a result of the displacement of the lithium cation, the four Ce–N bonds are of equal length instead of two shortened and two elongated ones as found in the starting product **1^{thf}** (Table 1). As expected, the Ce–N bond lengths of the trivalent separated ion pairs **2^{py}** [2.397(4)-2.417(4) Å], **2^{tmeda}** [2.386(10)-2.438(6) Å] and **2$^{12-crown-4}$** [2.391(3)-2.436(3) Å] are elongated compared to the tetravalent target product [Ce{N(SiHMe$_2$)$_2$}$_4$] (**3**) [2.238(1)-2.257(1) Å].[7] For further comparison, the separated ion pair [Ce{N(SiMe$_3$)$_2$}$_4$][Na(thf)$_4$(Et$_2$O)] bearing the bulkier bis(trimethylsilyl) amido ligand exhibits slightly elongated Ce–N bond lengths in the range of 2.434(6)-2.448(6) Å.[11] As trivalent cerium is paramagnetic (4f^1), and due to solubility problems in common non-donating solvents (e.g. phase separation in toluene or benzene), the recorded ^{1}H NMR spectra were not very informative (Figure S4, Supporting Information). However, the chemical environment of lithium could be examined by ^{7}Li-NMR spectroscopy in a mixture of C$_6$D$_6$ and 1,2-difluorobenzene. The ^{7}Li-NMR spectra of the separated ion pairs **2^{py}**, **2^{tmeda}**, **2^{dme}** and **2$^{12-crown-4}$** revealed a singlet ranging from –1.44 to 2.45 ppm (Figure 2). In comparison and stark contrast, the intramolecular ate complex [Ce{N(SiHMe$_2$)$_2$}$_4$Li(thf)] (**1^{thf}**)

shows a broadened singlet at 84.04 ppm for the lithium center, reflecting the close proximity of the lithium to the paramagnetic Ce(III) center. Additionally, a signal at 1.10 ppm was
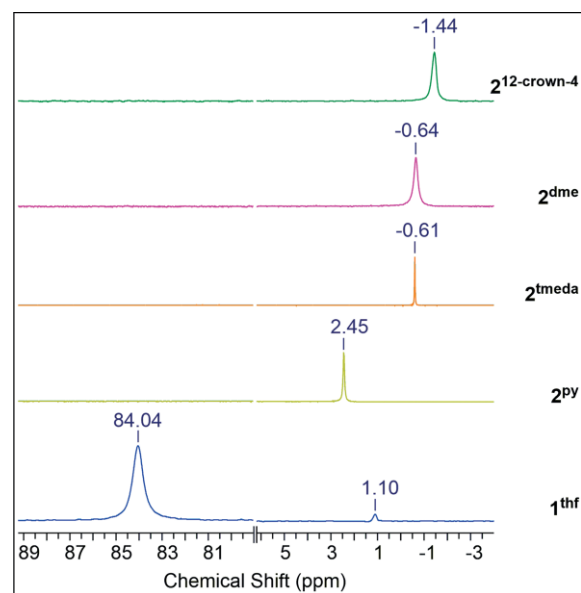
Figure 2. ^{7}Li NMR spectra of **1^{thf}** and **2do**.

Table 1. Bond lengths [Å] and angles [°] for **2^{py}**, **2^{tmeda}**, **2$^{12-crown-4}$**, **2^{thf}**, **1^{thf}**, and **3**

Bond	**2^{py}**	**2^{tmeda}**	**2$^{12-crown-4}$**	**2^{thf}**	**1^{thf}** [8a]	**3**[7]
Ce1–N1	2.398(4)	2.438(6)	2.412(3)	2.416(6)	2.388(5)	2.244(1)
Ce1–N2	2.397(4)	2.40(2)	2.408(3)	2.397(7)	2.386(4)	2.238(1)
Ce1–N3	2.404(4)	2.41(1)	2.391(3)	2.377(6)	2.523(4)	2.249(1)
Ce1–N4	2.417(4)	2.39(1)	2.436(3)	2.413(6)	2.532(5)	2.257(1)
Angle						
Ce1–N1–Si1	122.6(2)	129.0(3)	110.0(2)	123.0(3)	132.8(3)	108.68(5)
Ce1–N1–Si2	109.4(2)	107.2(4)	123.1(2)	105.7(3)	100.7(2)	122.41(6)
Ce1–N2–Si3	124.6(2)	122(1)	108.7(2)	109.9(3)	101.5(2)	125.73(6)
Ce1–N2–Si4	107.5(2)	110.1(8)	125.5(2)	120.7(4)	130.6(2)	106.60(5)
Ce1–N3–Si5	118.8(2)	129.4(6)	123.3(2)	111.1(3)	98.1(2)	105.64(5)
Ce1–N3–Si6	106.6(2)	106.2(6)	105.7(2)	121.3(3)	122.7(2)	124.74(6)
Ce1–N4–Si7	126.1(3)	104.1(4)	105.4(2)	102.8(3)	126.0(3)	126.08(6)
Ce1–N4–Si8	103.7(2)	132.3(5)	127.2(2)	130.8(3)	98.0(2)	106.23(5)

ChemPubSoc
Europe

EurJIC
European Journal
of Inorganic Chemistry

Full Paper

observed, indicating the presence of a solvent-separated ion-pair complex [Ce{N(SiHMe$_2$)$_2$}$_4$][Li(thf)$_x$] in a ratio of 3:97. This small amount of ion-pair complex may be a result of the small hyperstoichiometric amount of THF present when using Soxhlet-extracted/activated CeCl$_3$ with statistically 1.04 molecules of THF as donor for each cerium center.

Therefore, intramolecular ate complex **1^{thf}** was treated with stoichiometric amounts of THF to enhance the formation of the ion-separated complex [Ce{N(SiHMe$_2$)$_2$}$_4$][Li(thf)$_x$] (Figure S11, Supporting Information). Upon addition of five equivalents of THF, almost all of ate complex **1^{thf}** was consumed, whereas the signal for putative solvent-separated **2^{thf}** increased with the amount of THF added. Crystallization from a concentrated solution of **1^{thf}** in THF at –40 °C gave yellow crystals which were analyzed by X-ray diffraction confirming a compound of the composition [Ce{N(SiHMe$_2$)$_2$}$_4$][Li(thf)$_4$] (**2^{thf}**). The crystal structure of **2^{thf}** shows a 4-coordinate cerium center with equally long Ce–N bonds [2.377(6)-2.416(6) Å] as found for the other solvent(do)-separated ion pairs **2do** (Figure 1).

The Si–H-stretch vibration is another sensitive spectroscopic probe of metal–[N(SiHMe$_2$)$_2$] moieties.[12] While DRIFTS measurements of **1^{thf}** show two strong well-resolved absorption bands for the Si–H moieties at around 2000 cm^{-1}, the spectra of the ion pairs **2^{py}**, **2^{tmeda}**, **2^{dme}**, **2$^{12-crown-4}$**, and **2^{thf}** revealed one broad absorption band in this region supporting the formation of a highly symmetric environment around the cerium center (Figure 3). In the DRIFT spectrum of the oxidized species **3**, two distinct bands for the Si–H vibrations are visible again, which is generally attributed to the presence of β-H-agostic interactions.[7]

low yields with PhICl$_2$ or C$_2$Cl$_6$),[7] via potassium ate complex [Ce{N(SiHMe$_2$)$_2$}$_4$K] (with Ph$_3$CCl)[8b] or labor-intensive oxidations of **1^{thf}** using C$_2$Cl$_6$[8a] or Ph$_3$CCl, previously reported synthesis routes seemed not as straightforward as desired for an efficient precursor. Hence, 1,4-benzoquinone was chosen as an oxidant for the different trivalent cerium precursors **2do**, aiming at [Ce{N(SiHMe$_2$)$_2$}$_4$]. Benzoquinone reduction in non-polar solvents forms only insoluble by-products and therefore workup procedures should be easy.[6e,13] The oxidation of **1^{thf}** with 1,4-benzoquinone was already examined previously,[6e,8a,8e,13] however, was reported to afford low yields. Notwithstanding, the oxidizability of the different Ce(III) complexes was re-investigated. Accordingly, **1^{thf}** and **2do** were treated with one equivalent of benzoquinone for 15 min in a mixture of toluene and n-hexane. The use of an equimolar amount of benzoquinone was essential for an efficient oxidation, which favors the formation of lithium 1,4-benzosemiquinolate as the insoluble by-product. After filtration of the reaction mixture, the soluble parts were evaporated to dryness under reduced pressure. ^{1}H NMR spectra of the crude products were recorded to compare the different Ce(III) species' performance as precursors (Figure 4). While all crude products contained minor impurities, the ^{1}H NMR spectrum of the oxidation product of **2^{py}** shows only a doublet at 0.34 ppm for the methyl and a septet at 6.01 ppm for the Si–H moieties. Another important indicator for assessing the oxidation efficiency is the yield of the product. Therefore, yields of the crude products were determined, showing that the products with less impurities had lower yields of 54–59 %. Products of the oxidation of **2^{tmeda}** and **2$^{12-crown-4}$** revealed higher yields for the crude product, however, required recrystallization to remove impurities. The higher yields in the latter cases might be due to a more efficient shielding of the Li cation from re-associ-

Figure 3. Stacked DRIFT spectra of **1^{thf}** (black trace), **2^{py}** (red trace), **2^{tmeda}** (blue trace), **2^{dme}** (green trace), **2$^{12-crown-4}$** (pink trace), **2^{thf}** (yellow trace), and **3** (purple trace).
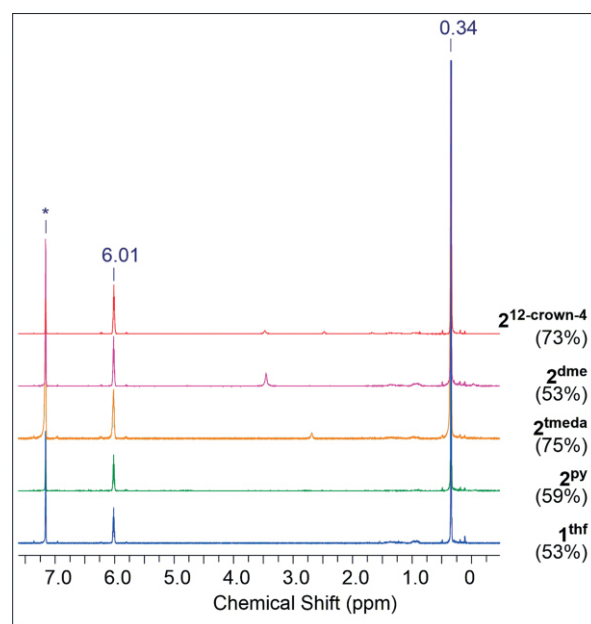
Figure 4. ^{1}H NMR spectra of the crude products of the oxidation reaction of **1^{thf}** and **2do** with 1,4-benzoquinone (yields are given in parentheses). Peaks at 0.34 and 6.01 ppm belong to [Ce{N(SiHMe$_2$)$_2$}$_4$] (**3**). Solvent signal is marked with *.

Due to different problems encountered with the oxidation of trivalent [Ce{N(SiHMe$_2$)$_2$}$_3$(thf)$_2$] with chlorinating oxidants (e.g.,

ChemPubSoc
Europe

EurJIC
European Journal
of Inorganic Chemistry

Full Paper

ating with the anionic cerous fragment. Only **2$^{\text{dme}}$** showed low yields and purity which makes it the least useful precursor for [Ce{N(SiHMe$_2$)$_2$}$_4$] (**3**). The impact of ligand reorganization on Ce(III) oxidation has been thoroughly examined for Shibasaki's heterobimetallic BINOLate complexes [M$_3$(thf)$_x$Ce(binolate)-(thf)$_y$][14] by the Schelter group.[15] It was shown that the presence of distinct alkali-metal ions in the secondary coordination sphere control such ligand reorganization and hence tune the redox behavior (involving alkali-metal salt elimination).

Conclusions

The synthesis of homoleptic ceric silylamide [Ce{N(SiHMe$_2$)$_2$}$_4$] in non-donating solvents can be improved/optimized by carefully fine-tuning the donor coordination in the trivalent precursor [Ce{N(SiHMe$_2$)$_2$}$_4$Li(thf)]. Supplying extra donor molecules (do) transforms the intramolecular ate complex into a separated ion pair of the type [Ce{N(SiHMe$_2$)$_2$}$_4$][Li(do)$_n$] that can undergo straightforward oxidation with 1,4-benzoquinone to [Ce{N(SiHMe$_2$)$_2$}$_4$]. The purest oxidation product could be obtained by applying pyridine adduct [Ce{N(SiHMe$_2$)$_2$}$_4$][Li(py)$_4$], while tmeda and 12-crown-4 donor molecules gave higher yields but at the expense of higher amounts of impurities. Furthermore, ^{7}Li NMR spectroscopy features a nice tool to distinguish between intramolecular ate complexes and separated ion pairs in the presence of paramagnetic metal centers. We have thereby uncovered a new, less tedious route toward [Ce{N(SiHMe$_2$)$_2$}$_4$], hopefully facilitating future endeavors in metalorganic Ce(IV) chemistry.

Experimental Section

General Experimental Procedures and Instrumentation: All operations were performed under rigorous exclusion of air and moisture using a glovebox (MBraun MB150B-G-II and MBraun UNIlab pro ECO; <1 ppm O$_2$, <1 ppm H$_2$O) and standard Schlenk techniques under argon atmosphere. Solvents (toluene, *n*-hexane and THF) were purchased from Merck (formerly Sigma-Aldrich), pre-treated with Grubbs-type columns (M. Braun MB SPS-800), and stored inside a glovebox. 1,2-Difluorobenzene was purchased from Merck, dried over P$_2$O$_5$, distilled, and stored in a glovebox over molecular sieves (3 Å) for at least one week before use. C$_6$D$_6$ and [D$_8$]toluene were obtained from Euriso-top, dried with NaK alloy for at least 24 h, and filtered before use. Donor solvents (TMEDA, DME and pyridine) were purchased from Merck and dried with NaH, then distilled and stored in a glovebox. 12-Crown-4 was purchased from Merck, stored inside a glovebox, and used as received. 1,4-Benzoquinone was purchased from Merck, sublimed, and stored inside a glovebox. CeCl$_3$ was activated prior to use by Soxhlet extraction with THF, giving CeCl$_3$(thf)$_{1.04}$. [Ce(N(SiHMe$_2$)$_2$)$_4$Li(thf)] (**1$^{\text{thf}}$**) was synthesized according to published procedures.[7,8] NMR spectra were measured on a Bruker AV+400, a Bruker DRX-250 and a Bruker Avance III HD 300 spectrometer, were referenced to internal solvent residual signals and are reported relative to tetramethylsilane (^{1}H, ^{13}C).[16] ^{7}Li spectra are reported relative to LiCl. Due to the high air and moisture sensitivity of all compounds, all NMR spectra were recorded using NMR tubes with J.-Young-type valves. DRIFT spectra were recorded using a NICOLET 6700 FTIR spectrometer (Thermo SCIENTIFIC) diluted to 5 wt.-% with dried KBr powder as a dilution matrix. The

sample was carefully homogenized with KBr in an agate mortar and transferred into a DRIFTS cell with KBr windows. The collected data were converted with the Kubelka–Munk refinement. Elemental analyses were carried out with an Elementar Vario MICRO Cube in the CHNS mode.

Syntheses

Synthesis of [Ce(N(SiHMe$_2$)$_2$)$_4$][Li(dme)$_3$] (2$^{\text{dme}}$): 1$^{\text{thf}}$ (246.6 mg, 0.33 mmol) was dissolved in *n*-hexane, DME (90.1 mg, 1.00 mmol, 3.00 equiv.) was mixed with *n*-hexane and added dropwise whilst stirring. The solution was stirred for 15 min, then the solvent was removed in vacuo, providing **2$^{\text{dme}}$** (290.4 mg, 0.31 mmol, 93 %) as a yellow-orange powder. ^{7}Li NMR (C$_6$D$_6$/C$_6$H$_4$F$_2$, 299 K, 116.6 MHz): δ = –0.64 ppm; DRIFTS: $\tilde{\nu}$ = 3008 (w), 2942 (s), 2892 (m), 2849 (w), 2829 (w), 2807 (vw), 2726 (vw), 2060 (s), 2014 (s), 1769 (vw, br), 1665 (vw, br), 1475 (w), 1453 (m), 1410 (vw), 1369 (m), 1276 (vw), 1239 (s), 1207 (vw), 1191 (m), 1157 (w), 1123 (m), 1079 (vs), 1029 (w), 938 (s), 894 (vs), 889 (vs), 831 (s), 778 (m), 758 (m), 676 (m), 622 (w), 592 (m), 434 (vw), 427 (vw) cm^{-1}; elemental analysis calcd. (%) for C$_{28}$H$_{86}$CeLiN$_4$O$_6$Si$_8$: C 35.52, H 9.16, N 5.92; found C 35.41, H 9.27, N 5.99.

Synthesis of [Ce(N(SiHMe$_2$)$_2$)$_4$][Li(tmeda)$_2$] (2$^{\text{tmeda}}$): 1$^{\text{thf}}$ (284.6 mg, 0.38 mmol) was dissolved in *n*-hexane, TMEDA (91.0 mg, 0.78 mmol, 2.05 equiv.) was mixed with *n*-hexane and added dropwise whilst stirring. The solution was stirred for 15 min, then the solvent was removed in vacuo, providing **2$^{\text{tmeda}}$** (336.0 mg, 0.37 mmol, 97 %) as a crystalline, greenish yellow material. Single crystals suitable for an X-ray structure analysis were obtained from a concentrated solution of **2$^{\text{tmeda}}$** in TMEDA and *n*-hexane at –35 °C. ^{7}Li NMR (C$_6$D$_6$/C$_6$H$_4$F$_2$, 299 K, 116.6 MHz): δ = –0.61 ppm; DRIFTS: $\tilde{\nu}$ = 2990 (m), 2954 (s), 2944 (s), 2891 (s), 2842 (m), 2800 (m), 2046 (s), 2017 (s), 1778 (w, br), 1664 (vw, br), 1470 (m), 1458 (s), 1409 (w), 1388 (vw), 1357 (m), 1288 (m), 1237 (s), 1182 (w), 1159 (m), 1127 (m), 1077 (s), 1068 (s), 1044 (s), 1013 (m), 942 (s), 895 (vs), 835 (s), 780 (s), 759 (s), 698 (w), 678 (m), 625 (m), 594 (m), 492 (w), 459 (vw), 437 (vw) cm^{-1}; elemental analysis calcd. (%) for C$_{28}$H$_{88}$CeLiN$_8$Si$_8$: C 37.01, H 9.76, N 12.33; found C 37.13, H 10.07, N 12.02.

Synthesis of [Ce(N(SiHMe$_2$)$_2$)$_4$][Li(py)$_4$] (2$^{\text{py}}$): 1$^{\text{thf}}$ (249.6 mg, 0.33 mmol) was dissolved in *n*-hexane, pyridine (107.7 mg, 1.36 mmol, 4.08 equiv.) was mixed with *n*-hexane and added dropwise whilst stirring. The solution was stirred for 15 min, then the solvent was removed in vacuo, providing **2$^{\text{py}}$** (298.6 mg, 0.30 mmol, 90 %) as a crystalline, yellow-orange material. Single crystals suitable for an X-ray structure analysis were acquired from a concentrated solution of **2$^{\text{py}}$** in a mixture of pyridine and *n*-hexane at –35 °C. ^{7}Li NMR (C$_6$D$_6$/C$_6$H$_4$F$_2$, 299 K, 116.6 MHz): δ = 2.45 ppm; DRIFTS: $\tilde{\nu}$ = 3088 (w), 3059 (w), 3045 (w), 3016 (vw), 2949 (s), 2894 (m), 2035 (s, br), 1776 (w, br), 1628 (vw), 1597 (m), 1574 (w), 1488 (w), 1442 (m), 1243 (s), 1216 (w), 1151 (m), 1051 (s), 1037 (s), 1004 (m), 970 (vw), 931 (m), 893 (vs), 834 (s), 784 (m), 761 (s), 751 (m), 701 (s), 679 (m), 624 (m), 594 (m), 421 (m), 401 (w) cm^{-1}; elemental analysis calcd. (%) for C$_{36}$H$_{76}$CeLiN$_8$Si$_8$: C 43.55, H 7.72, N 11.29; found C 43.11, H 7.52, N 11.13.

Synthesis of [Ce(N(SiHMe$_2$)$_2$)$_4$][Li(12-crown-4)(thf)] (2$^{\text{12-crown-4}}$): 1$^{\text{thf}}$ (50.0 mg, 0.067 mmol) was dissolved in *n*-hexane, 12-crown-4 (11.8 mg, 0.067 mmol, 1.00 equiv.) was mixed with *n*-hexane and added dropwise whilst stirring. The solution was stirred for 15 min, then the solvent was removed in vacuo, providing **2$^{\text{12-crown-4}}$** (57.7 mg, 0.062 mmol, 93 %) as a crystalline, yellow material. Single crystals suitable for an X-ray structure analysis were obtained from a concentrated solution of **2$^{\text{12-crown-4}}$** in *n*-hexane at –40 °C. ^{7}Li NMR (C$_6$D$_6$/C$_6$H$_4$F$_2$, 299 K, 116.6 MHz): δ = –1.44 ppm; DRIFTS: $\tilde{\nu}$ =

2941 (s), 2887 (m), 2018 (s), 1449 (w), 1363 (w), 1287 (w), 1239 (ws), 1133 (m), 1085 (ws), 1076 (s), 1024 (m), 938 (ws), 900 (ws), 889 (ws), 836 (ws), 781 (s), 771 (m), 758 (s), 676 (m), 625 (w), 588 (w) cm^{-1}; elemental analysis calcd. (%) for $C_{28}H_{80}CeLiN_4O_5Si_8$: C 36.37, H 8.72, N 6.06; found C 36.80, H 8.42, N 5.75.

Synthesis of [Ce(N(SiHMe₂)₂)₄][Li(thf)₄] (2^{thf}): Single crystals of **2^{thf}** suitable for an X-ray structure analysis were obtained from a saturated solution of **1^{thf}** in THF by keeping it at –40 °C until crystals formed. ^{7}Li NMR ($C_6D_6/C_6H_4F_2$, 299 K, 116.6 MHz): δ = 1.10 ppm; DRIFTS: $\tilde{v}$ = 2949 (s), 2890 (s), 2056 (s), 2029 (s), 1242 (s), 1077 (s), 1042 (s), 938 (s), 892 (vs), 835 (s), 780 (s), 760 (s), 679 (m), 626 (w), 590 (m) cm^{-1}; elemental analysis calcd. (%) for $C_{32}H_{88}CeLiN_4O_4Si_8$: C 39.84, H 9.19, N 5.81; found C 39.40, H 8.97, N 5.89.

Oxidation of 1^{thf} with 1,4-benzoquinone: **1^{thf}** (56.4 mg, 0.075 mmol) was dissolved in toluene, 1,4-benzoquinone (8.2 mg, 0.076 mmol) was dissolved in toluene and added dropwise to the solution of **1^{thf}** whilst stirring. An immediate color change to black was observed. After stirring for 15 min, solid by-products were removed by centrifugation and filtration. After removal of the toluene in vacuo, the resulting product was washed three times with cold *n*-hexane and any precipitate again removed by centrifugation and filtration. Finally, *n*-hexane was removed in vacuo to yield **3** (27.1 mg, 53 %) as a dark red solid.

Oxidation of 2^{dme} with 1,4-benzoquinone: **2^{dme}** (49.9 mg, 0.053 mmol) was dissolved in toluene, 1,4-benzoquinone (5.7 mg, 0.053 mmol) was dissolved in toluene and added dropwise to the solution of **2^{dme}** whilst stirring. An immediate color change to black was observed. After stirring for 15 min, solid by-products were removed by centrifugation and filtration. After removal of the toluene in vacuo, the resulting product was washed three times with cold *n*-hexane and any precipitate again removed by centrifugation and filtration. Finally, *n*-hexane was removed in vacuo to yield **3** (18.9 mg, 53 %) as a dark red solid.

Oxidation of 2^{tmeda} with 1,4-benzoquinone: **2^{tmeda}** (54.4 mg, 0.060 mmol) was dissolved in toluene, 1,4-benzoquinone (6.5 mg, 0.060 mmol) was dissolved in toluene and added dropwise to the solution of **2^{tmeda}** whilst stirring. An immediate color change to black was observed. After stirring for 15 min, solid by-products were removed by centrifugation and filtration. After removal of the toluene in vacuo, the resulting product was washed three times with cold *n*-hexane and any precipitate again removed by centrifugation and filtration. Finally, *n*-hexane was removed in vacuo to yield **3** (30.3 mg, 75 %) as a dark red solid.

Oxidation of 2^{py} with 1,4-benzoquinone: **2^{py}** (51.2 mg, 0.052 mmol) was dissolved in toluene, 1,4-benzoquinone (5.6 mg, 0.052 mmol) was dissolved in toluene and added dropwise to the solution of **2^{py}** whilst stirring. An immediate color change to black was observed. After stirring for 15 min, solid by-products were removed by centrifugation and filtration. After removal of the toluene in vacuo, the resulting product was washed three times with cold *n*-hexane and any precipitate again removed by centrifugation and filtration. Finally, *n*-hexane was removed in vacuo to yield **3** (20.4 mg, 59 %) as a dark red solid.

Oxidation of 2$^{12\text{-crown-4}}$ with 1,4-benzoquinone: **2$^{12\text{-crown-4}}$** (50.0 mg, 0.054 mmol) was dissolved in toluene, 1,4-benzoquinone (5.8 mg, 0.054 mmol) was dissolved in toluene and added dropwise to the solution of **2$^{12\text{-crown-4}}$** whilst stirring. An immediate color change to black was observed. After stirring for 15 min, solid by-products were removed by centrifugation and filtration. After removal of the toluene in vacuo, the resulting product was washed three times with cold *n*-hexane and any precipitate again removed

by centrifugation and filtration. Finally, *n*-hexane was removed in vacuo to yield **3** (20.0 mg, 73 %) as a dark red solid.

Crystal Data Collection, Structure Solution, and Refinement

Crystals for X-ray crystallography were grown using saturated solutions in THF (**2^{thf}**), a mixture of TMEDA and *n*-hexane (**2^{tmeda}**), a mixture of pyridine and *n*-hexane (**2^{py}**) or *n*-hexane (**2$^{12\text{-crown-4}}$**). All compounds are sensitive toward moisture and oxygen, while single crystals start to melt at ambient temperature (except **2$^{12\text{-crown-4}}$**). At ambient temperature "melting" of the crystals occurred immediately. Suitable crystals for the diffraction experiments were hand-picked in a glovebox, coated with Parabar 10312 and stored on microscope slides. Data collections were done on a *Bruker* APEX II Duo diffractometer by using QUAZAR optics and Mo-K_α (λ = 0.71073 Å). The data collection strategy was determined using COSMO[17] employing ω scans. Raw data were processed by APEX[18] and SAINT,[19] corrections for absorption effects were applied using SADABS.[20] The structures were solved by direct methods and refined against all data by full-matrix least-squares methods on F^2 using SHELXTL[21] and SHELXLE.[22] Disorder was found for **2^{py}**, **2^{thf}**, and **2^{tmeda}**, and restraints (RIGU, SIMU, EADP) were given for refining the crystal structures. Plots were generated by using Mercury 3.19.1. Further details regarding the refinement and crystallographic data are listed in Table S1 and in the CIF files.

CCDC 1954721 (for **2^{py}**), 1954722 (for **2$^{12\text{-crown-4}}$**), 1954723 (for **2^{tmeda}**), and 1954724 (for **2^{thf}**) contain the supplementary crystallographic data for this paper. These data can be obtained free of charge from The Cambridge Crystallographic Data Centre.

Supporting Information (see footnote on the first page of this article): NMR/DRIFT spectra.

Acknowledgments

[1] a) F. M. A. Sroor, F. T. Edelmann in *Tetravalent Cerium Chemistry*, (Ed. A. P. Izyumov, G.), Nova Science Publishers, Hauppauge, N. Y. **2012**, pp. 73–106; b) N. A. Piro, J. R. Robinson, P. J. Walsh, E. J. Schelter, *Coord. Chem. Rev.* **2014**, *260*, 21–36; c) R. Anwander, M. Dolg, F. T. Edelmann, *Chem. Soc. Rev.* **2017**, *46*, 6697-6709; d) Y.-M. So, W.-H. Leung, *Coord. Chem. Rev.* **2017**, *340*, 172–197; e) Y. Qiao, E. J. Schelter, *Acc. Chem. Res.* **2018**, *51*, 2926–2936.

[2] a) D. C. Bradley, A. K. Chatterjee, W. Wardlaw, *J. Chem. Soc.* **1956**, 2260–2264; b) D. C. Bradley, A. K. Chatterjee, W. Wardlaw, *J. Chem. Soc.* **1956**, 3469–3472; c) D. C. Bradley, A. K. Chatterjee, W. Wardlaw, *J. Chem. Soc.* **1957**, 2600–2604; d) A. Greco, S. Cesca, W. Bertolini, *J. Organomet. Chem.* **1976**, *113*, 321–330; e) G. B. Deacon, T. D. Tuong, D. G. Vince, *Polyhedron* **1983**, *2*, 969–970.

[3] For example, see: a) W. J. Evans, T. J. Deming, J. W. Ziller, *Organometallics* **1989**, *8*, 1581–1583; b) P. Toledano, F. Ribot, C. Sanchez, *Acta Crystallogr., Sect. C: Cryst. Struct. Commun.* **1990**, *46*, 1419–1422; c) E. Kurras, C, Kruger, *CSD Communication* **2004**; d) P. Dröse, A. R. Crozier, S. Lashkari, J. Gottfriedsen, S. Blaurock, C. G. Hrib, C. Maichle-Mössmer, C. Schädle, R. Anwander, F. T. Edelmann, *J. Am. Chem. Soc.* **2010**, *132*, 14046–14047; e) J. Schläfer, W. Tyrra, S. Mathur, *Inorg. Chem.* **2014**, *53*, 2751–2753; f) J. Friedrich, D. Schneider, L. Bock, C. Maichle-Mössmer, R. Anwander, *Inorg. Chem.* **2017**, *56*, 8114–8127.

[4] For example, see: a) P. S. Gradeff, F. G. Schreiber, K. C. Brooks, R. E. Sievers, *Inorg. Chem.* **1985**, *24*, 1110–1111; b) P. S. Gradeff, F. G. Schreiber, H. Mauermann, *J. Less-Common Met.* **1986**, *126*, 335–338; c) W. J. Evans, T. J. Deming, J. M. Olofson, J. W. Ziller, *Inorg. Chem.* **1989**, *28*, 4027–4034; d) V.

Nair, A. Deepthi, *Chem. Rev.* **2007**, *107*, 1862–1891; e) V. Nair, A. Deepthi, *Tetrahedron* **2009**, *65*, 10745–10755; f) A. R. Crozier, C. Schädle, C. Maichle-Mössmer, K. W. Törnroos, R. Anwander, *Dalton Trans.* **2013**, *42*, 5491–5499.

[5] T. Imamoto, Y. Koide, S. Hiyama, *Chem. Lett.* **1990**, *19*, 1445–1446.

[6] For example, see: a) P. S. Gradeff, H. Mauermann, F. G. Schreiber, *J. Less-Common Met.* **1989**, *149*, 87–94; b) L. G. Hubert-Pfalzgraf, N. El Khokh, J.-C. Daran, *Polyhedron* **1992**, *11*, 59–63; c) L. G. Hubert-Pfalzgraf, V. Abada, J. Vaissermann, *J. Chem. Soc., Dalton Trans.* **1998**, 3437–3442; d) S. Daniele, L. G. Hubert-Pfalzgraf, M. Perrin, *Polyhedron* **2002**, *21*, 1985–1990; e) P. L. Arnold, I. J. Casely, S. Zlatogorsky, C. Wilson, *Helv. Chim. Acta* **2009**, *92*, 2291–2303; f) E. M. Broderick, P. L. Diaconescu, *Inorg. Chem.* **2009**, *48*, 4701–4706; g) E. M. Broderick, P. S. Thuy-Boun, N. Guo, C. S. Vogel, J. Sutter, J. T. Miller, K. Meyer, P. L. Diaconescu, *Inorg. Chem.* **2011**, *50*, 2870–2877; h) P. Dröse, J. Gottfriedsen, C. G. Hrib, P. G. Jones, L. Hilfert, F. T. Edelmann, *Z. Anorg. Allg. Chem.* **2011**, *637*, 369–373; i) L. Li, F. Yuan, T. Li, Y. Zhou, M. Zhang, *Inorg. Chim. Acta* **2013**, *397*, 69–74; j) W. Huang, P. L. Diaconescu, *Inorg. Chem.* **2016**, *55*, 10013–10023; k) M. Paul, S. Shirase, Y. Morimoto, L. Mathey, B. Murugesapandian, S. Tanaka, S. Itoh, H. Tsurugi, K. Mashima, *Chem. Eur. J.* **2016**, *22*, 4008–4014.

[7] A. R. Crozier, A. M. Bienfait, C. Maichle-Mössmer, K. W. Törnroos, R. Anwander, *Chem. Commun.* **2013**, *49*, 87–89.

[8] a) D. Werner, G. B. Deacon, P. C. Junk, R. Anwander, *Chem. Eur. J.* **2014**, *20*, 4426–4438; b) U. J. Williams, D. Schneider, W. L. Dorfner, C. Maichle-Mössmer, P. J. Carroll, R. Anwander, E. J. Schelter, *Dalton Trans.* **2014**, *43*, 16197–16206; c) J. E. Kim, P. J. Carroll, E. J. Schelter, *Chem. Commun.* **2015**, *51*, 15047–15050; d) J. R. Levin, W. L. Dorfner, A. X. Dai, P. J. Carroll, E. J. Schelter, *Inorg. Chem.* **2016**, *55*, 12651–12659; e) D. Werner, G. B. Deacon, P. C. Junk, R. Anwander, *Dalton Trans.* **2017**, *46*, 6265–6277.

[9] D. Schneider, T. Spallek, C. Maichle-Mössmer, K. W. Törnroos, R. Anwander, *Chem. Commun.* **2014**, *50*, 14763–14766.

[10] P. B. Hitchcock, M. F. Lappert, A. V. Protchenko, *Chem. Commun.* **2006**, 3546–3548.

[11] W. J. Evans, D. S. Lee, D. B. Rego, J. M. Perotti, S. A. Kozimor, E. K. Moore, J. W. Ziller, *J. Am. Chem. Soc.* **2004**, *126*, 14574–14582.

[12] a) R. Anwander, O. Runte, J. Eppinger, G. Gerstberger, E. Herdtweck, M. Spiegler, *J. Chem. Soc., Dalton Trans.* **1998**, 847–858; b) I. Nagl, W. Scherer, M. Tafipolsky, R. Anwander, *Eur. J. Inorg. Chem.* **1999**, 1405–1407; c) J. Eppinger, M. Spiegler, W. Hieringer, W. A. Herrmann, R. Anwander, *J. Am. Chem. Soc.* **2000**, *122*, 3080–3096; d) C. Meermann, G. Gerstberger, M. Spiegler, K. W. Törnroos, R. Anwander, *Eur. J. Inorg. Chem.* **2008**, 2014–2023.

[13] For example, see: a) A. Sen, H. A. Stecher, A. L. Rheingold, *Inorg. Chem.* **1992**, *31*, 473–479; b) M. D. Walter, R. Fandos, R. A. Andersen, *New J. Chem.* **2006**, *30*, 1065; c) I. J. Casely, S. T. Liddle, A. J. Blake, C. Wilson, P. L. Arnold, *Chem. Commun.* **2007**, 5037–5039; d) M. D. Walter, C. H. Booth, W. W. Lukens, R. A. Andersen, *Organometallics* **2009**, *28*, 698–707; e) J. R. Robinson, C. H. Booth, P. J. Carroll, P. J. Walsh, E. J. Schelter, *Chem. Eur. J.* **2013**, *19*, 5996–6004; f) D. Schneider, N. Harmgarth, F. T. Edelmann, R. Anwander, *Chem. Eur. J.* **2017**, *23*, 12243–12252.

[14] H. Sasai, T. Suzuki, N. Itoh, K. Tanaka, T. Date, K. Okamura, M. Shibasaki, *J. Am. Chem. Soc.* **1993**, *115*, 10372–10373.

[15] a) J. R. Robinson, P. J. Carroll, P. J. Walsh, E. J. Schelter, *Angew. Chem. Int. Ed.* **2012**, *51*, 10159–10163; *Angew. Chem.* **2012**, *124*, 10306–10310; b) J. R. Robinson, Z. Gordon, C. H. Booth, P. J. Carroll, P. J. Walsh, E. J. Schelter, *J. Am. Chem. Soc.* **2013**, *135*, 19016–19024.

[16] G. R. Fulmer, A. J. M. Miller, N. H. Sherden, H. E. Gottlieb, A. Nudelman, B. M. Stoltz, J. E. Bercaw, K. I. Goldberg, *Organometallics* **2010**, *29*, 2176–2179.

[17] in *COSMO v. 1.61*, *Vol.* B. A. I., Madison, WI, **2012**.

[18] in *APEX 2 v. 2012.10_0*, *Vol.* B. A. I., Madison, WI, **2012**.

[19] a) in *SAINT v. 8.34A*, *Vol.* B. A. I., Madison, WI, **2013**; b) in *SAINT v. 8.37A*, *Vol.* Bruker AXS Inc., Madison, WI, **2015**.

[20] L. Krause, R. Herbst-Irmer, G. M. Sheldrick, D. Stalke, *J. Appl. Crystallogr.* **2015**, *48*, 3–10.

[21] G. M. Sheldrick, *Acta Crystallogr., Sect. C: Struct. Chem.* **2015**, *71*, 3–8.

[22] C. B. Hübschle, G. M. Sheldrick, B. Dittrich, *J. Appl. Crystallogr.* **2011**, *44*, 1281–1284.

A Facile Route toward Ceric Silylamide [Ce{N(SiHMe₂)₂}₄]

Uwe Bayer, Lorenz Bock, Cäcilia Maichle-Mössmer, and Reiner Anwander*

Table of Contents

1. NMR Spectra (solvent signals are marked with *)
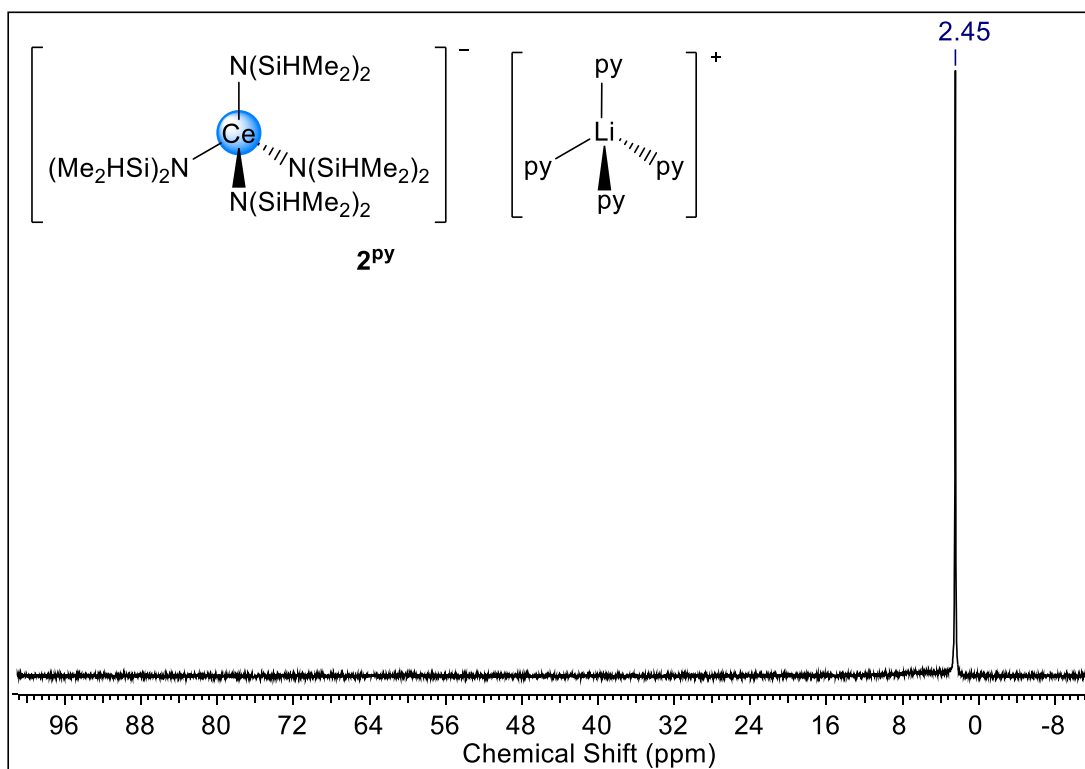
Figure S1. ^{7}Li NMR ($C_6D_6/C_6H_4F_2$, 299 K, 116.6 MHz) of [Ce{N(SiHMe$_2$)$_2$}$_4$][Li(py)$_4$] (**2^{py}**).
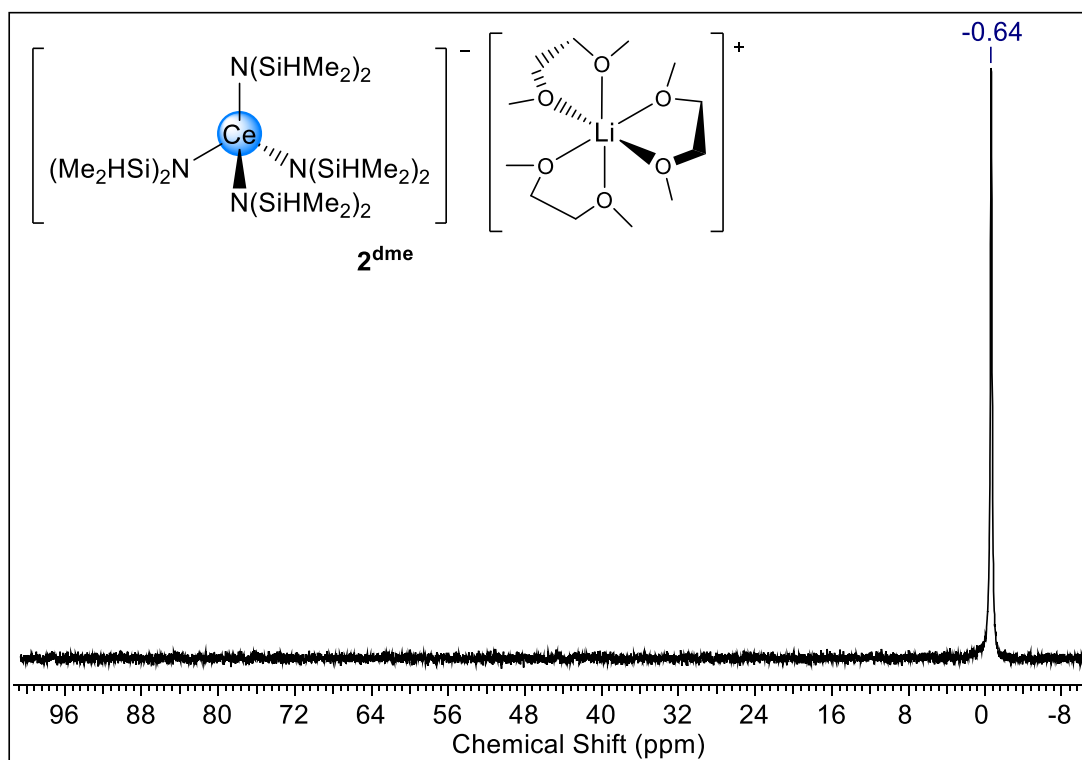
Figure S2. ^{7}Li NMR ($C_6D_6/C_6H_4F_2$, 299 K, 116.6 MHz) of [Ce{N(SiHMe$_2$)$_2$}$_4$][Li(dme)$_3$] (**2^{dme}**).
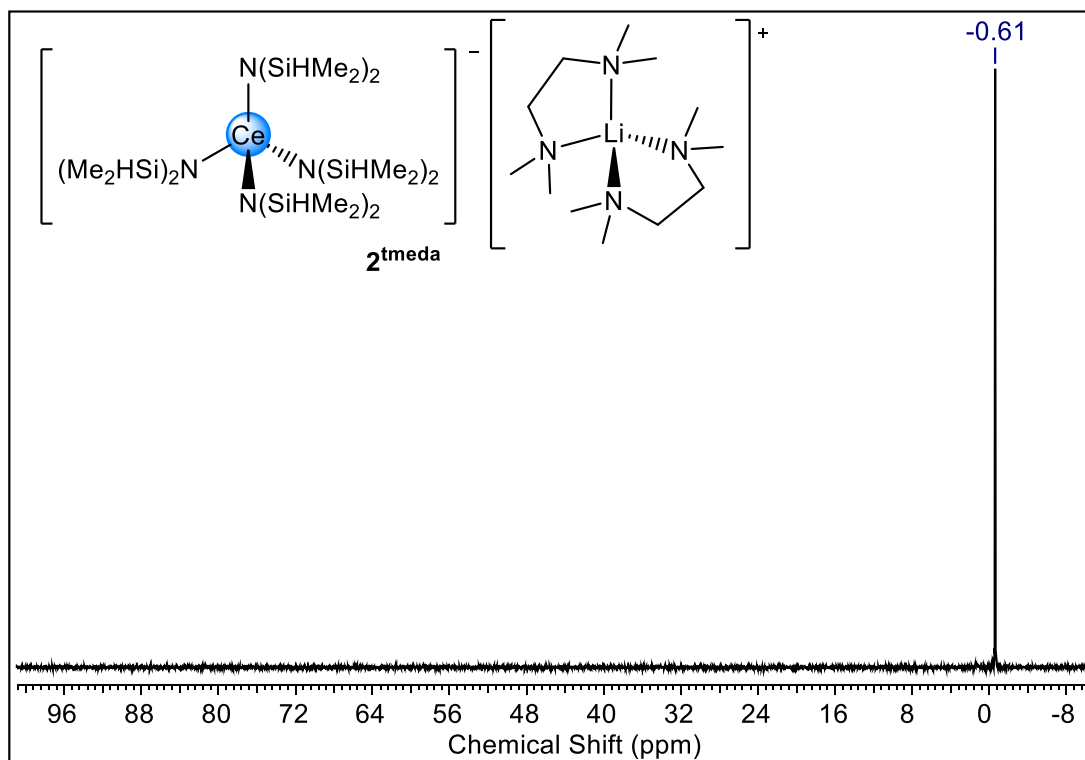
Figure S3. ^{7}Li NMR (C$_6$D$_6$/C$_6$H$_4$F$_2$, 299 K, 116.6 MHz) of [Ce{N(SiHMe$_2$)$_2$}$_4$][Li(tmeda)$_2$] (**2**^{tmeda}).
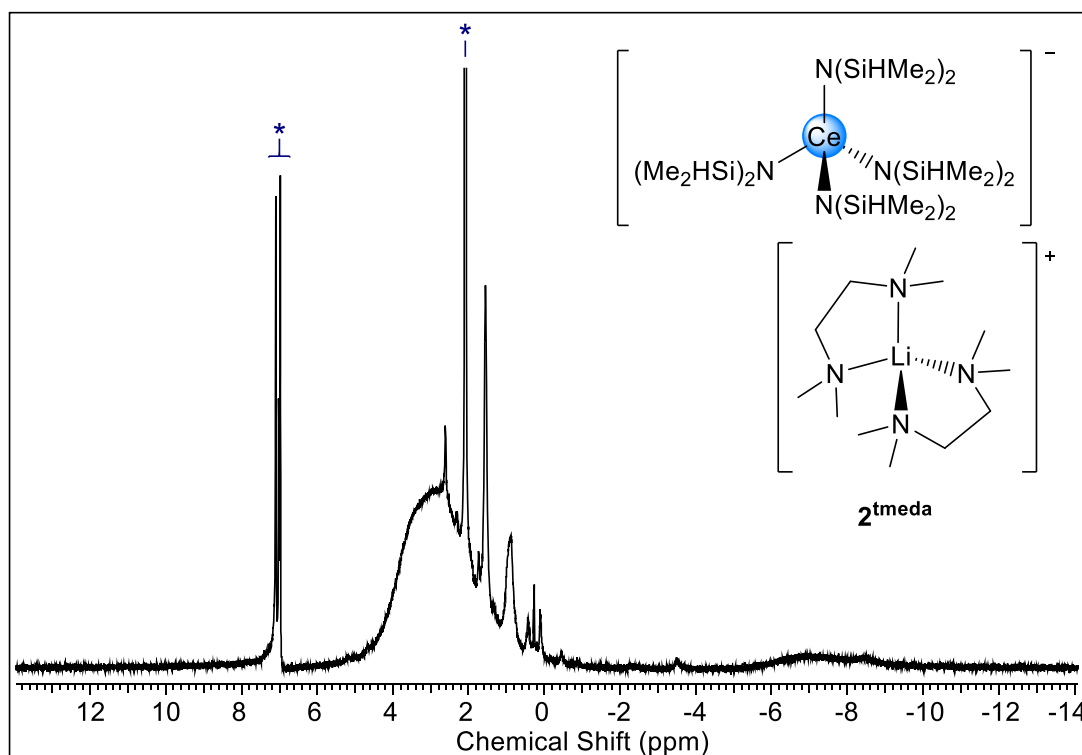
Figure S4. ^{1}H NMR (tol-d_8, 299 K, 250.1 MHz) of [Ce{N(SiHMe$_2$)$_2$}$_4$][Li(tmeda)$_2$] (**2**^{tmeda}).
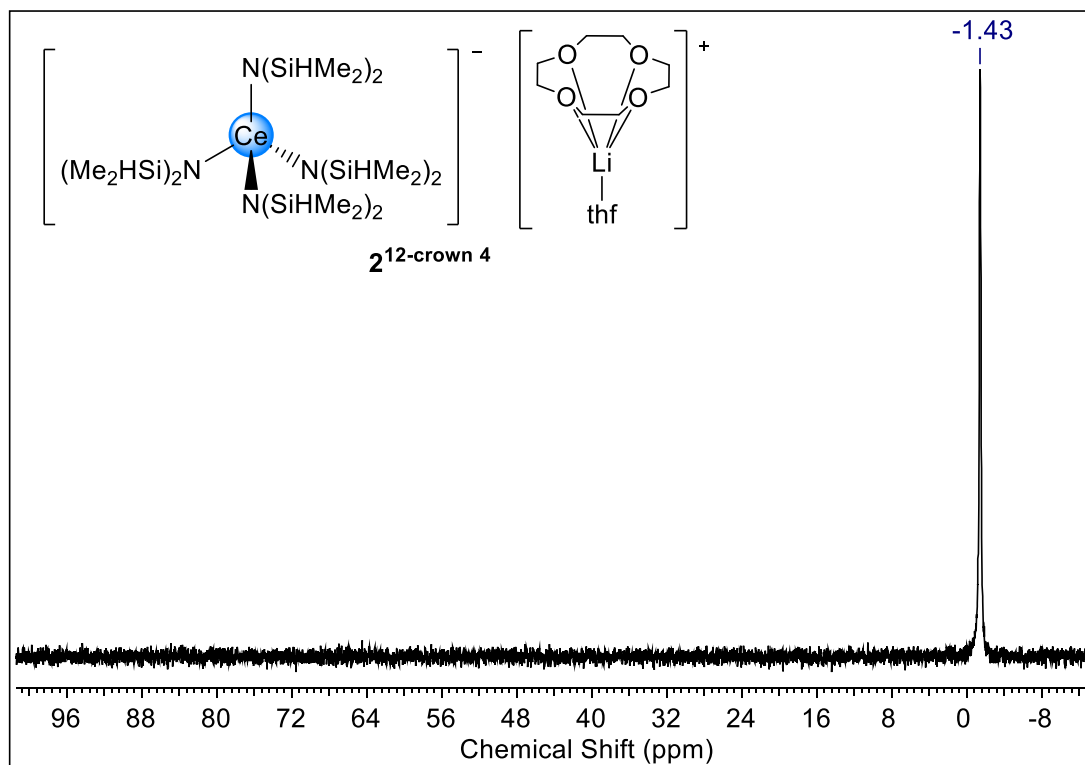
Figure S5. ^{7}Li NMR (C$_6$D$_6$/C$_6$H$_4$F$_2$, 299 K, 116.6 MHz) of [Ce{N(SiHMe$_2$)$_2$}$_4$][Li(12-crown-4)(thf)] (**2$^{12\text{-crown-4}}$**).
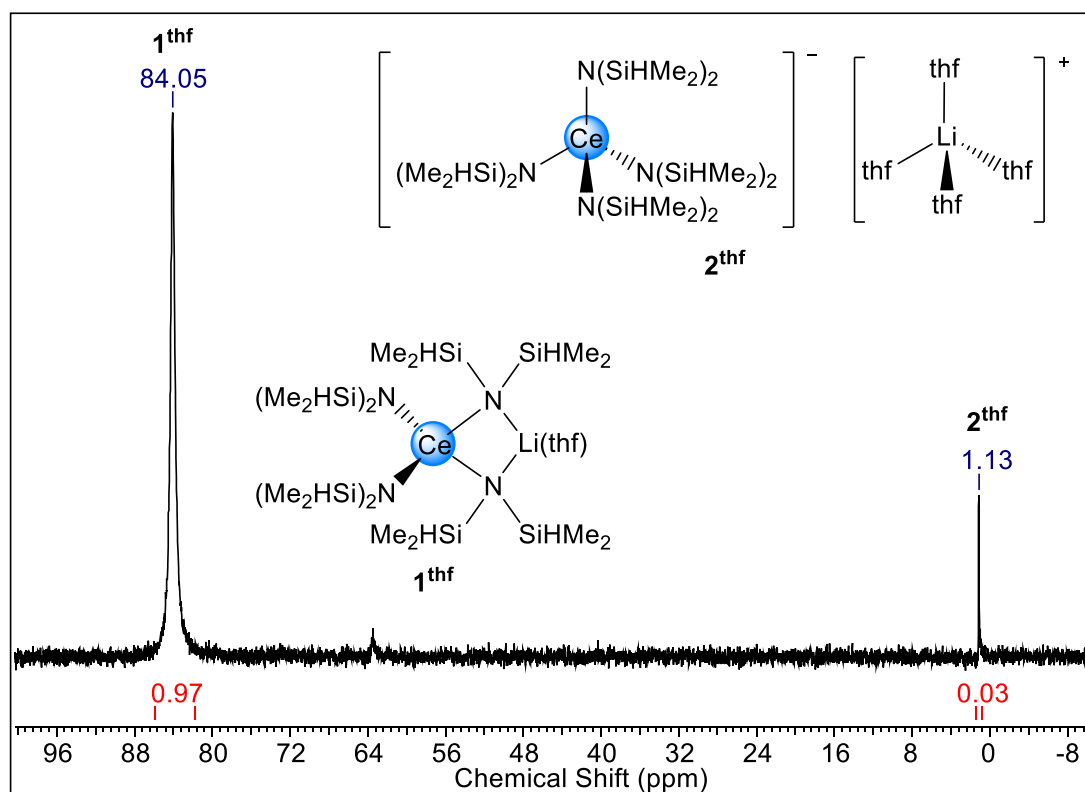
Figure S6. ^{7}Li NMR (C$_6$D$_6$/C$_6$H$_4$F$_2$, 299 K, 116.6 MHz) of [Ce{N(SiHMe$_2$)$_2$}$_4$Li(thf)] (**1^{thf}**).
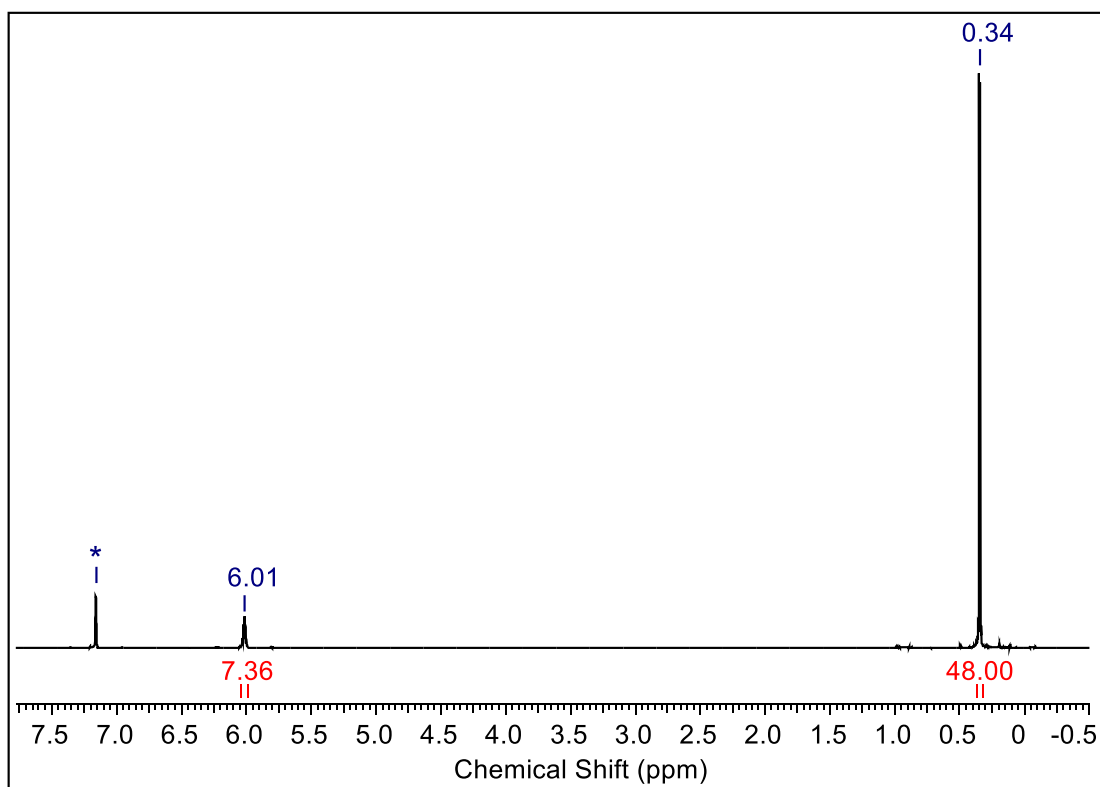
Figure S7. ^{1}H NMR (C_6D_6, 299 K, 400.1 MHz) of the crude product of the oxidation of [Ce{N(SiHMe$_2$)$_2$}$_4$][Li(py)$_4$] (**2^{py}**).
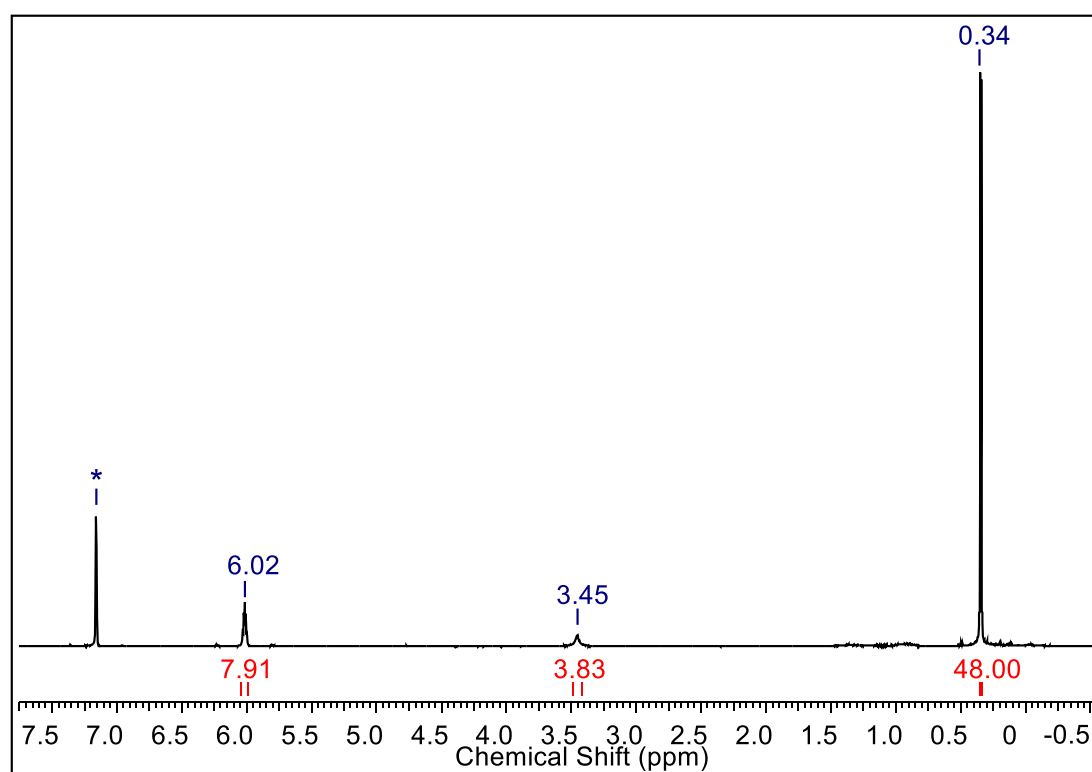
Figure S8. ^{1}H NMR (C_6D_6, 299 K, 400.1 MHz) of the crude product of the oxidation of [Ce{N(SiHMe$_2$)$_2$}$_4$][Li(dme)$_3$] (**2^{dme}**).
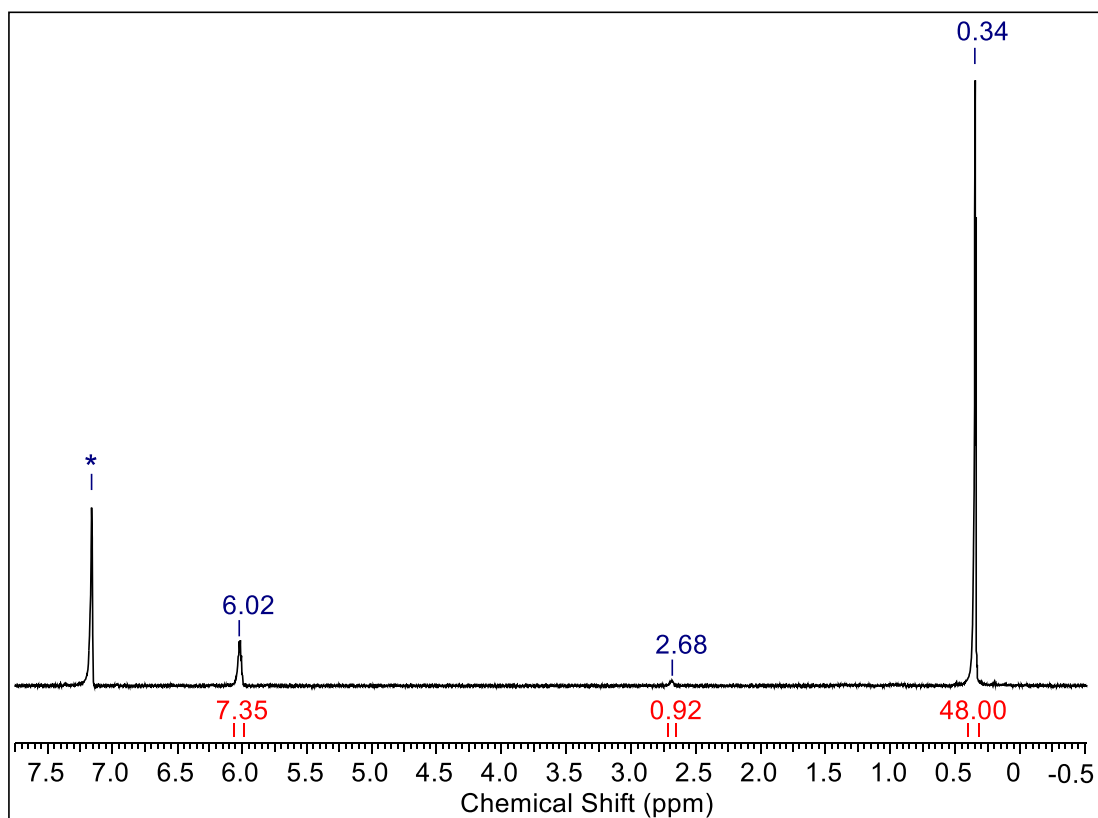
Figure S9. ^{1}H NMR (C$_6$D$_6$, 299 K, 400.1 MHz) of the crude product of the oxidation of [Ce{N(SiHMe$_2$)$_2$}$_4$][Li(tmeda)$_2$] (**2^{tmeda}**).
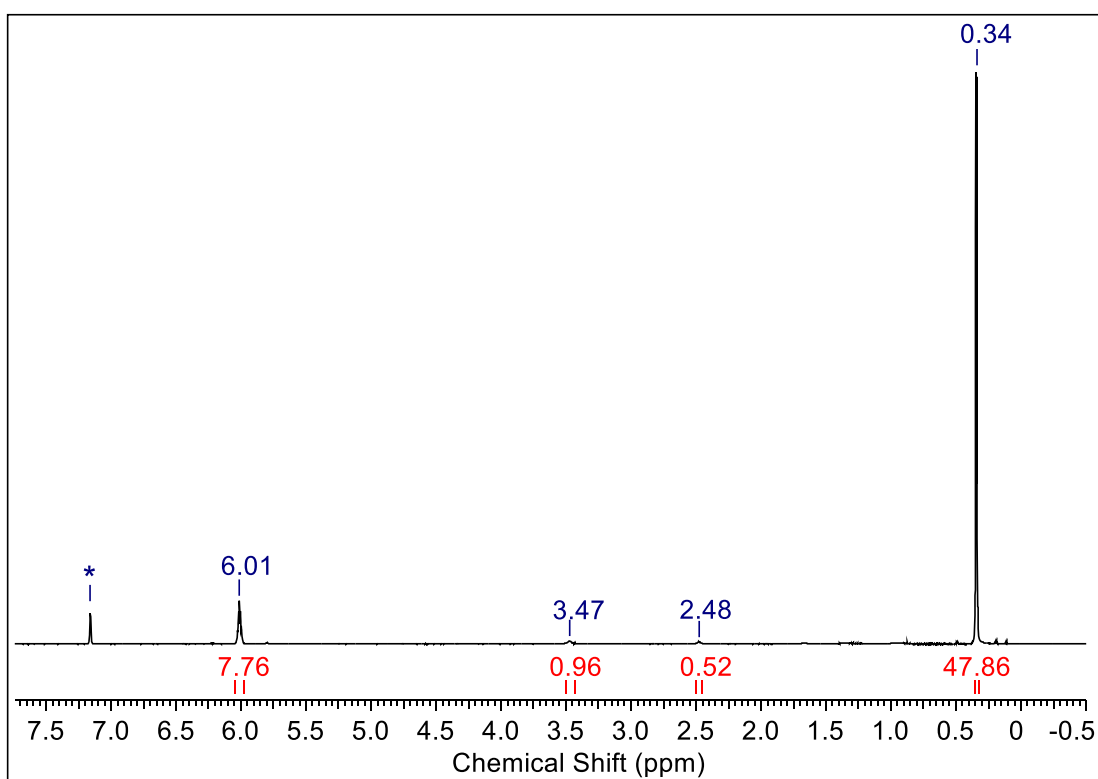
Figure S10. ^{1}H NMR (C$_6$D$_6$, 299 K, 400.1 MHz) of the crude product of the oxidation of [Ce{N(SiHMe$_2$)$_2$}$_4$][Li(12-crown-4)(thf)] (**2$^{12\text{-crown-4}}$**).
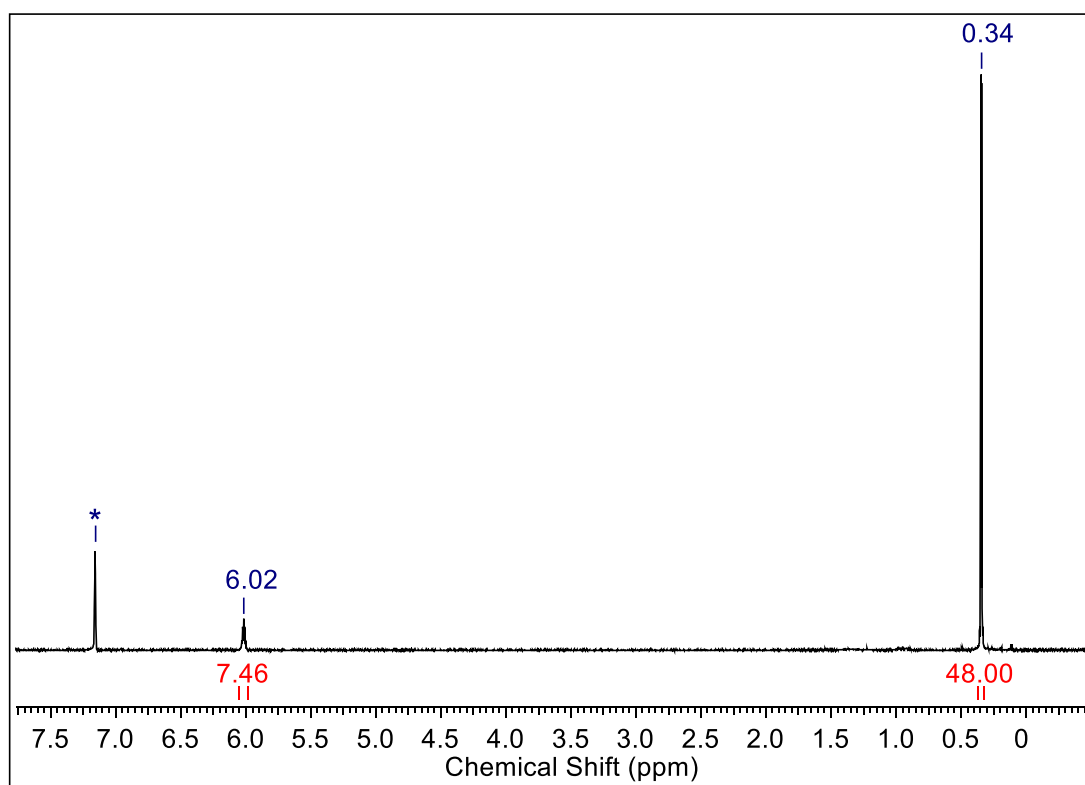
Figure S11. ^{1}H NMR (C$_6$D$_6$, 299 K, 400.1 MHz) of the crude product of the oxidation of [Ce{N(SiHMe$_2$)$_2$}$_4$Li(thf)] (**1^{thf}**).
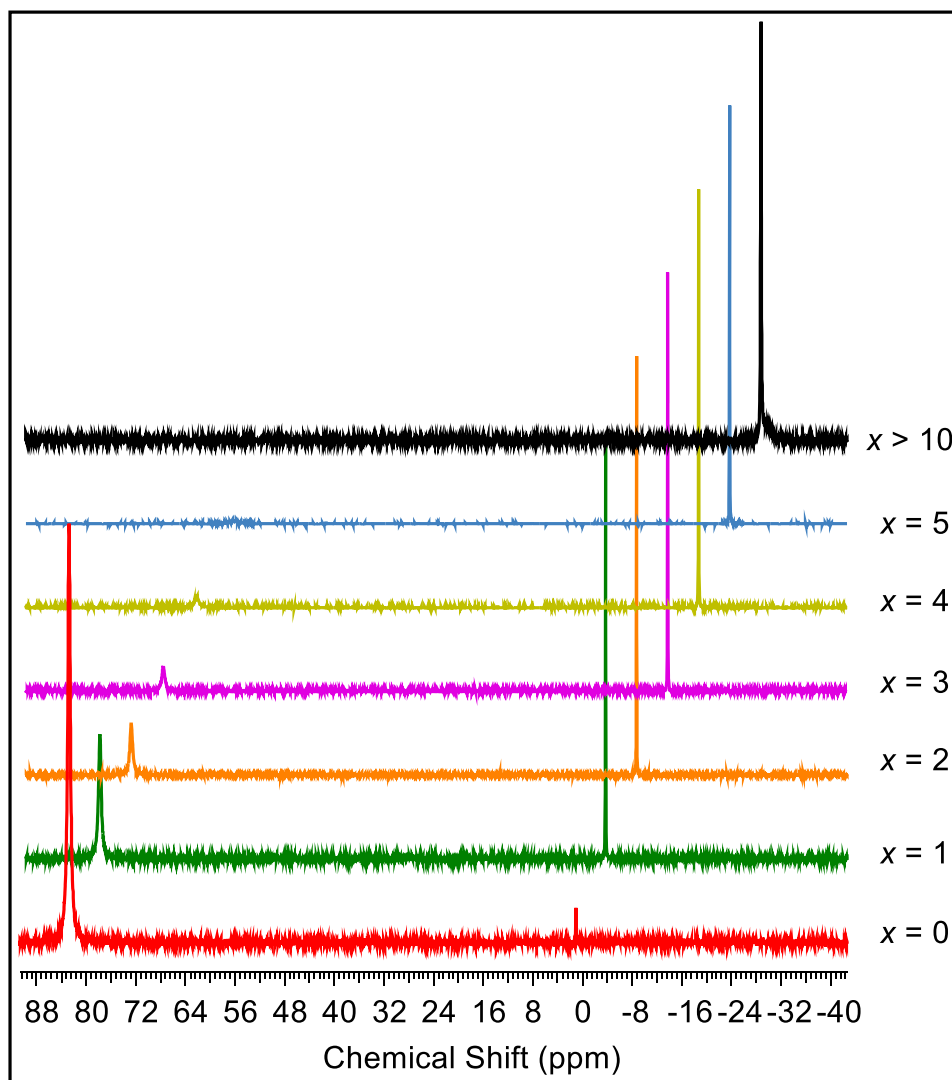
Figure S12. Stacked ^{7}Li NMR spectra of [Ce{N(SiHMe$_2$)$_2$}$_4$Li(thf)] (**1^{thf}**) with additional *x* equivalents of THF added.

2. DRIFT Spectra
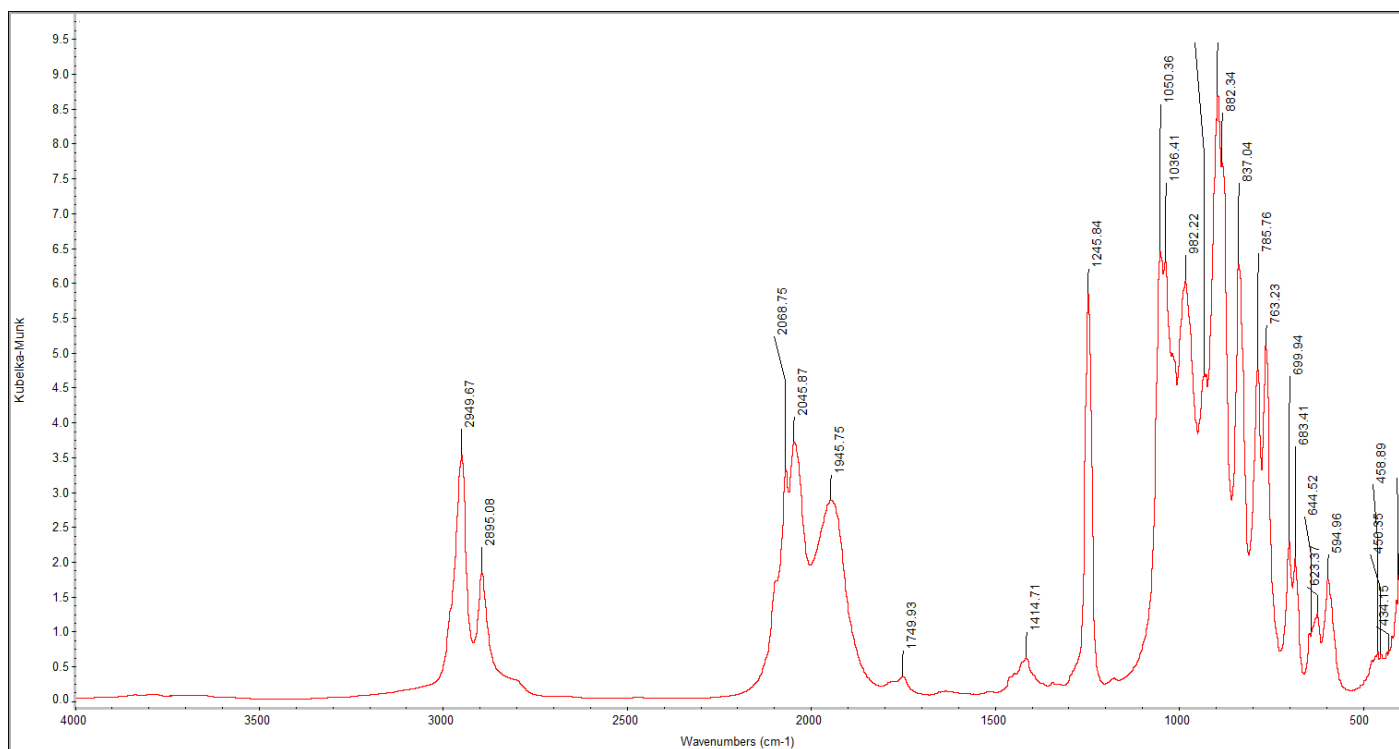
Figure S13. DRIFT spectrum of [Ce{N(SiHMe$_2$)$_2$}$_4$Li(thf)] (**1^{thf}**).
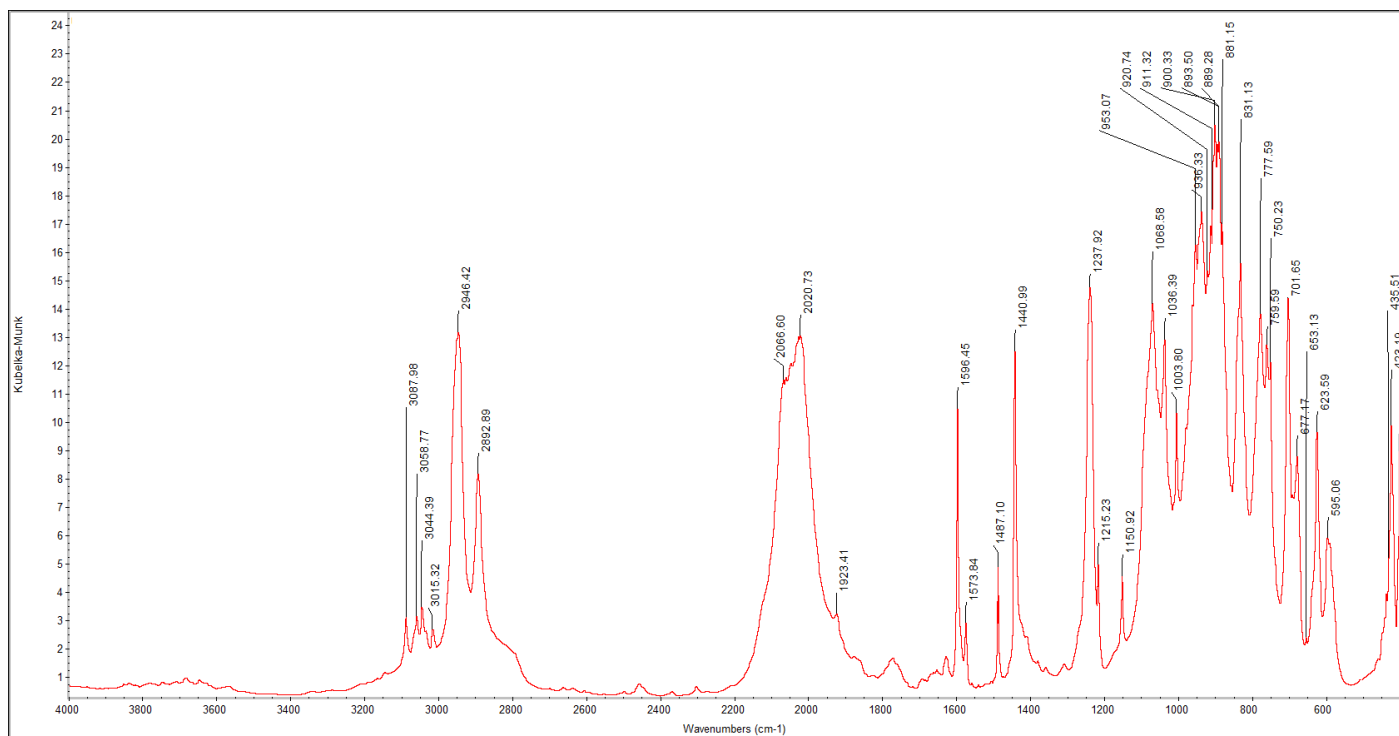
Figure S14. DRIFT spectrum of [Ce{N(SiHMe$_2$)$_2$}$_4$][Li(py)$_4$] (**2^{py}**).
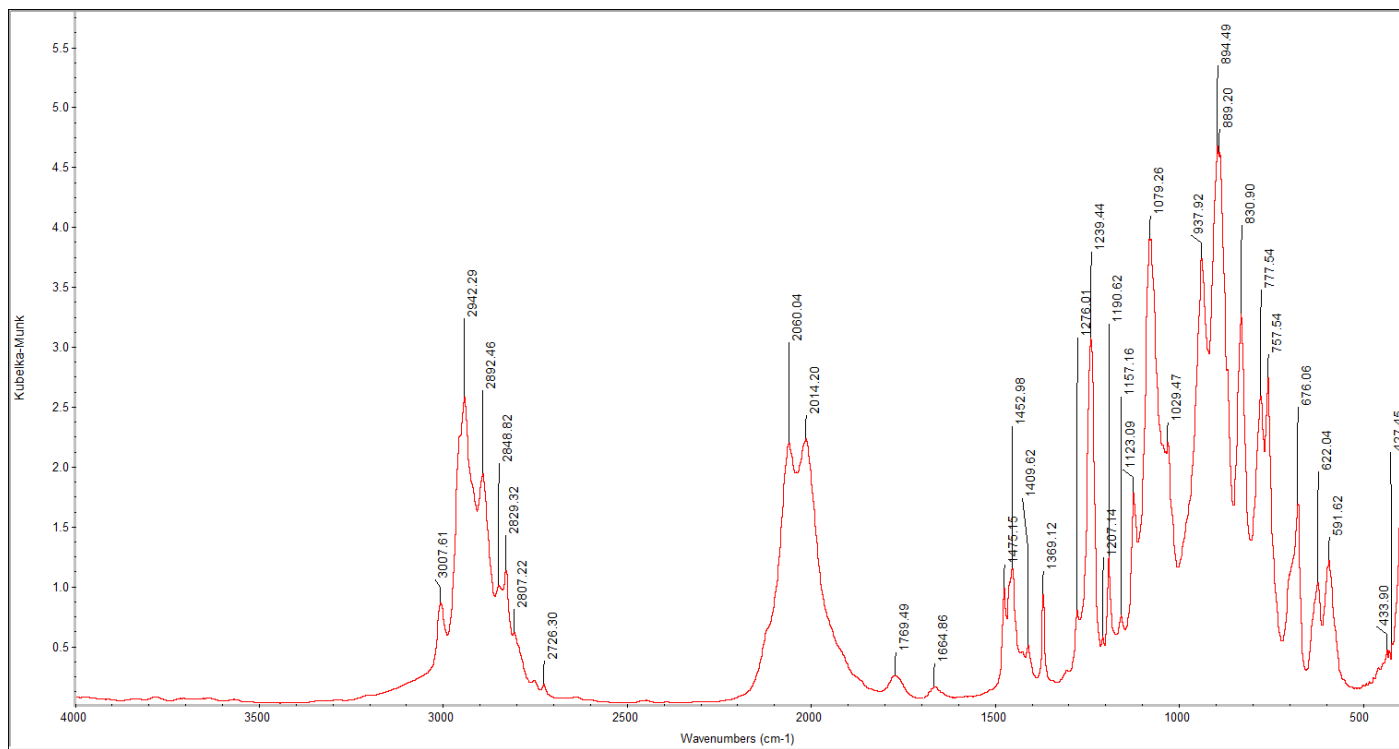
Figure S15. DRIFT spectrum of [Ce{N(SiHMe$_2$)$_2$}$_4$][Li(dme)$_3$] (**2^{dme}**).
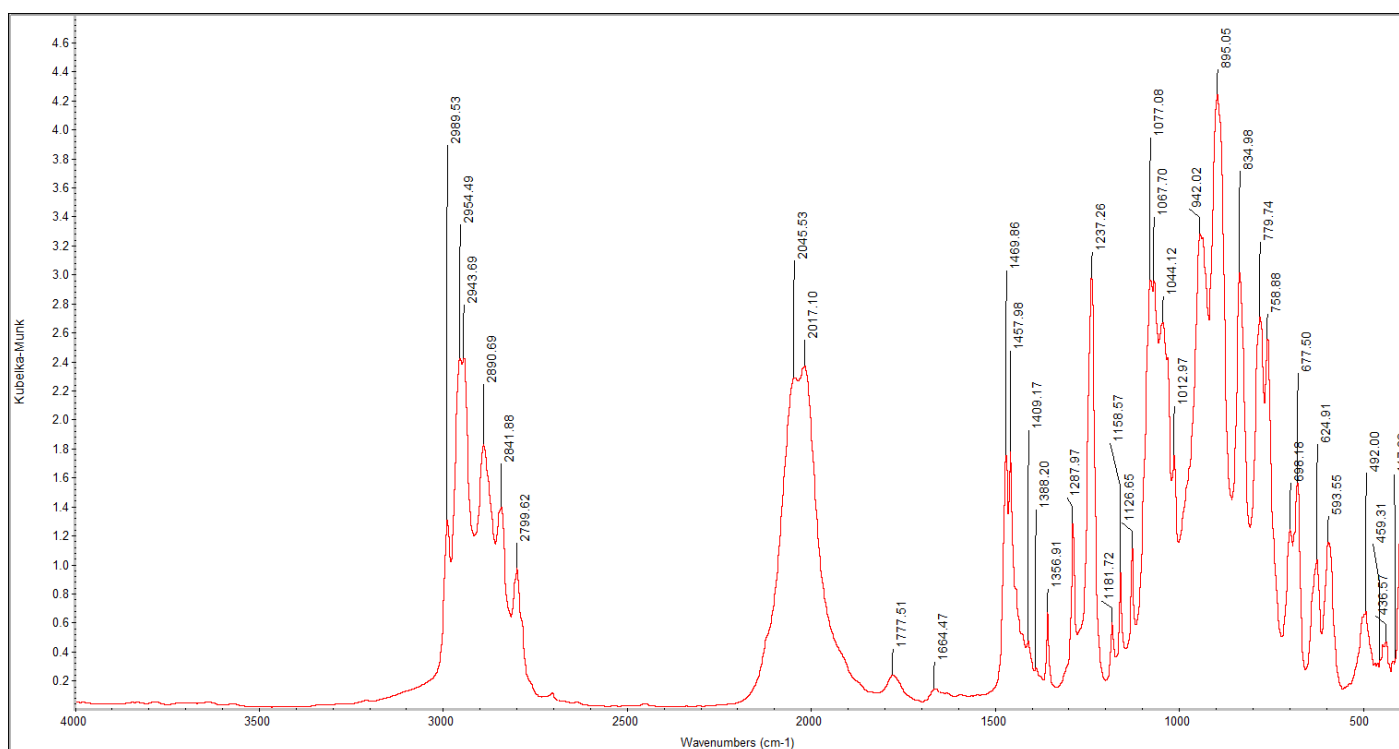
Figure S16. DRIFT spectrum of [Ce{N(SiHMe$_2$)$_2$}$_4$][Li(tmeda)$_2$] (**2^{tmeda}**).
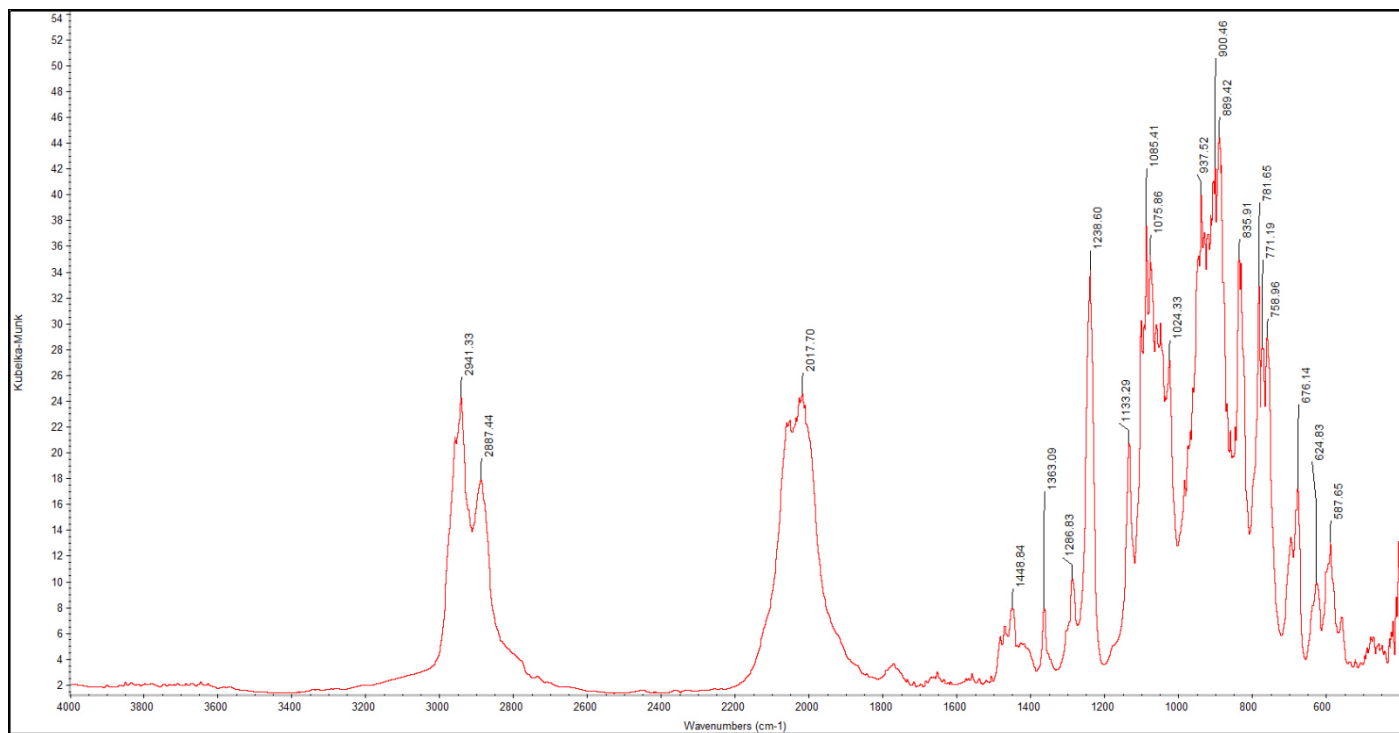
Figure S17. DRIFT spectrum of [Ce{N(SiHMe$_2$)$_2$}$_4$][Li(12-crown-4)(thf)] (**2$^{12\text{-crown-4}}$**).
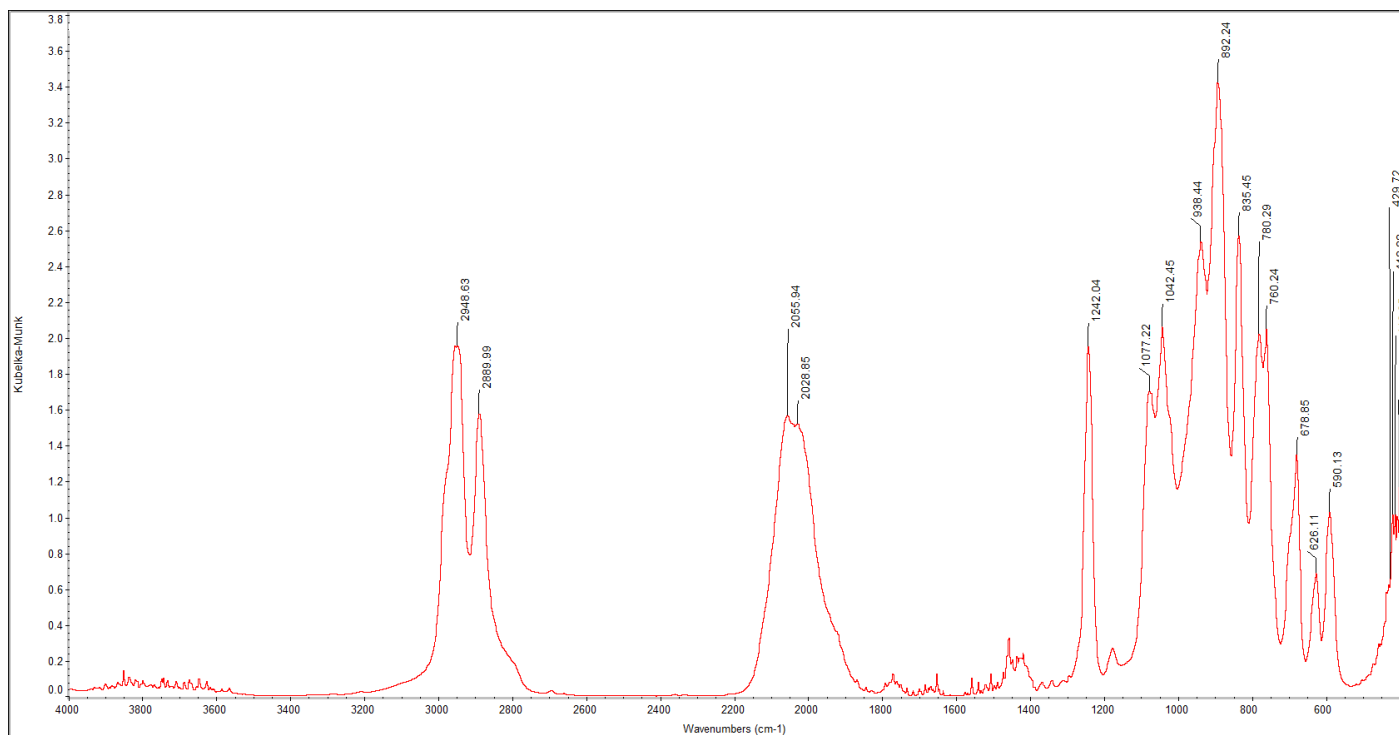
Figure S18. DRIFT spectrum of [Ce{N(SiHMe$_2$)$_2$}$_4$][Li(thf)$_4$] (**2^{thf}**).

3. Crystallographic Data

Table S1. Crystallographic data for compounds 2^{py}, 2^{tmeda}, $2^{12\text{-}crown\text{-}4}$, and 2^{thf}

	2^{py}	2^{tmeda}	$2^{12\text{-}crown\text{-}4}$	2^{thf}
CCDC	1954721	1954723	1954722	1954724
formula	$C_{36}H_{76}CeLiN_8Si_8$	$C_{28}H_{88}CeLiN_8Si_8$	$C_{28}H_{80}CeLiN_4O_5Si_8$	
M [g·mol^{-1}]	992.82	908.84	924.74	964.84
λ [Å]	0.71073	0.71073	0.71073	0.71073
color	yellow	orange	colorless	yellow
crystal dimensions [mm]	0.127 x 0.116 x 0.043	0.346 x 0.132 x 0.131	0.155 x 0.121 x 0.101	0.221 x 0.151 x 0.135
crystal system	Monoclinic	Monoclinic	Monoclinic	Triclinic
space group	P 2$_1$/c	P 2$_1$/c	P 2$_1$/c	P$\bar{1}$
a [Å]	14.5041(11)	16.2760(16)	19.025(4)	14.465(4)
b [Å]	16.1209(13)	14.9972(15)	11.663(2)	19.271(5)
c [Å]	24.568(2)	22.022(2)	23.592(5)	20.664(6)
α [°]	90	90	90	106.320(3)
β [°]	97.996(2)	96.301(2)	105.090(4)	94.712(3)
γ [°]	90	90	90	98.744(3)
V [Å³]	5688.7(8)	5343.0(9)	5054.2(17)	5416(2)
Z	4	4	4	4
F(000)	2084	1940	1956	2052
T [K]	180(2)	100(2)	100(2)	100(2)
ρ$_{calcd}$ [g·cm^{-3}]	1.159	1.130	1.215	1.183
μ[mm^{-1}]	0.999	1.057	1.123	1.050
Data / restraints / parameters	7924 / 556 / 580	13380 / 1524/ 714	10328 / 0 / 472	18575/996/1027
Goodness of fit	1.010	1.027	1.005	1.188
R$_1$ (I > 2σ (I))[a]	0.0422	0.0737	0.0409	0.0655
$_\omega$R$_2$ (all data)[b]	0.0982	0.2094	0.0971	0.1835

[a] $R_1 = \Sigma(||F0|-|Fc||)/\Sigma|F0|, F0> 4s(F0)$. $_\omega R_2 = \{\Sigma[w(F02-Fc2)2/\Sigma[w(F02)^2]\}^{1/2}$

Effective and Reversible Carbon Dioxide Insertion into Cerium Pyrazolates
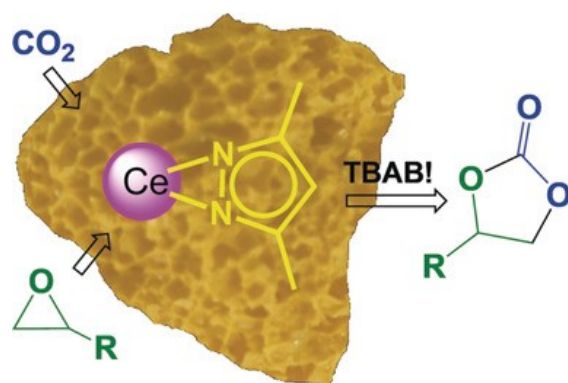
Carbon Dioxide Uptake

Effective and Reversible Carbon Dioxide Insertion into Cerium Pyrazolates

Uwe Bayer, Daniel Werner, Cäcilia Maichle-Mössmer, and Reiner Anwander*

Abstract: *The homoleptic pyrazolate complexes [Ce^{III}_4-(Me_2pz)$_{12}$] and [Ce^{IV}(Me_2pz)$_4$]$_2$ quantitatively insert CO_2 to give [Ce^{III}_4($Me_2pz\cdot CO_2$)$_{12}$] and [Ce^{IV}($Me_2pz\cdot CO_2$)$_4$], respectively ($Me_2pz = 3,5$-dimethylpyrazolato). This process is reversible for both complexes, as observed by in situ IR and NMR spectroscopy in solution and by TGA in the solid state. By adjusting the molar ratio, one molecule of CO_2 per [Ce^{IV}-(Me_2pz)$_4$] complex could be inserted to give trimetallic [Ce_3-(Me_2pz)$_9$($Me_2pz\cdot CO_2$)$_3$(thf)]. Both the cerous and ceric insertion products catalyze the formation of cyclic carbonates from epoxides and CO_2 under mild conditions. In the absence of epoxide, the ceric catalyst is prone to reduction by the co-catalyst tetra-n-butylammonium bromide (TBAB).*

Introduction

Inexorably rising CO_2 levels in the earth's atmosphere—and their consequential environmental impact—have spurred much interest in combating CO_2 build-up.[1] Capture technologies, such as carbon dioxide capture and storage (CCS) and direct air capture (DAC),[2] and CO_2 conversion into fuels or chemical feedstocks[3] appear promising. However, such tactics suffer from either a lack of appropriate storage and transportation of CO_2, or overcoming the high activation barrier of CO_2.[4] To date, the most effective sorbents for CCS/DAC are alkali-metal/alkaline-earth metal hydroxide solutions, inorganic salts (e.g. alkali-metal carbonates),[1,2] or high-surface supported polyamines (max. CO_2 sorption capacity ca. 3 mmol g^{-1} at 1 bar)[5] and magnesium-based metal-organic frameworks (ca. 35 wt% or 8 mmol CO_2 g^{-1} at 1 bar).[6]

Like alkaline-earth metals, rare-earth metals (Ln) feature a high affinity for carbon dioxide (cf. bastnaesite is the most important Ln^{III} deposit in the Earth's crust). Thus, metal-organic derivatives easily react with or insert CO_2, as initially demonstrated by Bochkarev et al. for homoleptic silylamides
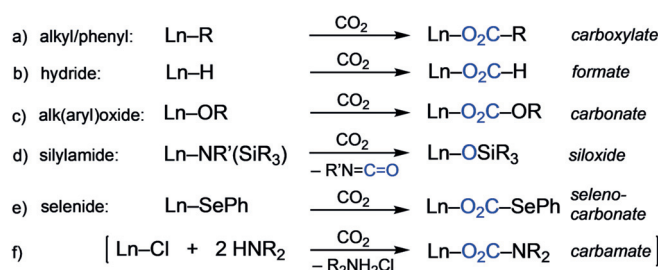
Scheme 1. Irreversible reaction of carbon dioxide with archetypal organo-rare-earth-metal complexes, with the exception of (e) as shown for (C_5Me_5)$_2$Sm(SePh)(thf).[22]

Ln[N(SiMe$_3$)$_2$]$_3$[7,8] and alkoxides [Ln(O*n*Bu)$_3$] (Scheme 1c,d).[9,10]

Similar archetypes (including Ln^{III} aryloxides) can also be used for chemical transformations, such as the catalytic conversion of a CO_2/epoxide mixture into cyclic carbonates[11] or copolymers.[10a,12,13] However, highly reactive organo-rare-earth-metal complexes such as alkyl[14] and hydride[10a,15] (Scheme 1a,b) or divalent derivatives[16] display irreversible CO_2 insertion or favor additional transformations through CO_2 post-activation (e.g. formation of CO, CO_3^{2-}, $C_2O_4^{2-}$).[16] Recently, cerium, the most abundant rare-earth element, has gained attention for CO_2 activation.[8,17–19] For example, while the hydrogen-bonded Ce^{IV} oxo complex [(L_{OEt})$_2$Ce=O-(H_2O)]·MeC(O)NH$_2$ (L_{OEt}^- = [Co(η^5-C_5H_5){P(O)(OEt)$_2$}$_3$]$^-$) was shown to form the tetravalent carbonate species [(L_{OEt})$_2$Ce(CO_3)],[17] *ortho*-NHC-substituted aryloxide Ce^{III} complexes (NHC = N-heterocyclic carbene) insert CO_2 into the Ce−C$_{NHC}$ bond in a semireversible manner, and catalytically form propylene carbonate from propylene oxide.[18,19]

Bulky cyclopentadienyl (Cp) derivatives (e.g. Ln-(C_5Me_5)$_3$) were shown to accommodate CO_2 insertion in a unidirectional manner, thereby forming very stable carboxylato moieties through a η^5-to-η^1 switch in the C_5Me_5 coordination (cf. Scheme 1a).[20] Pyrazolates (pz), on the other hand, are dinitrogen-derived Cp counterparts, where the putative N−CO_2 bond may tolerate a more reversible insertion process, as seen for other CO_2-heteroatom bonds (Scheme 1e).[21,22] As the tetravalent [Ce(Me_2pz)$_4$]$_2$ complex was recently shown to undergo reversible insertion of ketones into the Ce−N bond,[23] we extended the study toward CO_2. Quantitative insertion of CO_2 into the Ce−N(Me_2pz) bond was observed for both tetravalent and trivalent cerium Me_2pz complexes, and intriguingly the insertion process was found to be fully reversible.

[*] U. Bayer, Dr. D. Werner, Dr. C. Maichle-Mössmer,
Prof. Dr. R. Anwander
Institut für Anorganische Chemie
Eberhard Karls Universität Tübingen
Auf der Morgenstelle 18, 72076 Tübingen (Germany)
E-mail: reiner.anwander@uni-tuebingen.de

Supporting information and the ORCID identification numbers for some of the authors of this article can be found under:
https://doi.org/10.1002/anie.201916483.

Results and Discussion

Carbon Dioxide Insertion into a Ceric Pyrazolate: Treatment of $[Ce(Me_2pz)_4]_2$ (**1**) with excess CO_2 in either toluene or thf (under 1 bar CO_2 pressure) led to a color change from dark red to orange within 5 minutes (Scheme 2). Crystallization from concentrated toluene or thf solutions at $-40\,°C$ gave orange crystals of $[Ce(Me_2pz·CO_2)_4]$ with either toluene (**2·toluene**, 54%) or thf (**2·thf**, 64%) within the lattice. Discounting the lattice solvent, this accounts for about 25 wt% CO_2 or 5.7 mmol CO_2 per gram.
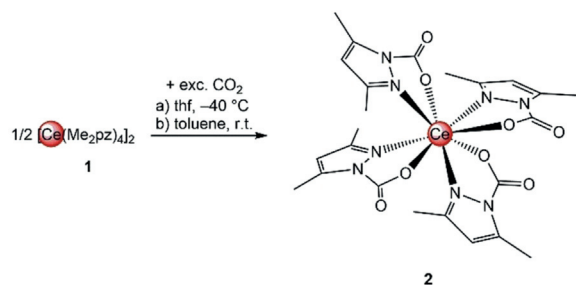
Scheme 2. Insertion of CO_2 into the Ce–$N(Me_2pz)$ bond of [Ce-$(Me_2pz)_4]_2$ at: a) $-40\,°C$ in thf or b) ambient temperature in toluene.

The molecular structure of **2·toluene** revealed an 8-coordinate cerium(IV) center with four $\kappa^2(N,O)$-coordinating $Me_2pz·CO_2$ ligands (Figure 1), in contrast to the $\kappa^2(O,O)$ modes in carboxylates and related carbamates. The Ce–N and Ce–O bond lengths average 2.528 Å and 2.255 Å, respectively, thus matching the values found in the benzophenone-inserted product $[Ce(Me_2pz)_2(pdpm)_2]$ (Ce1–N1 2.564 Å, Ce1–O1 2.173 Å; pdpm = (3,5-dimethylpyrazol-1-yl)diphenylmethanolate).[23] Other homoleptic Ce^{IV} complexes, [Ce-$(L)_4$] (with L as a donor-functionalized alkoxy ligand engaged in a 5-membered chelate to cerium), also have similar Ce–O bond lengths as those in **2**, thus highlighting a common chelating coordination motif.[24,25] Seemingly, no delocalization occurs across the O=C–O fragment, which exhibits average C–O bond lengths of 1.207 Å (terminal) and 1.291 Å (bridging). Support for the localization of the C–O double bond came from DRIFTS measurements of **2·toluene** and
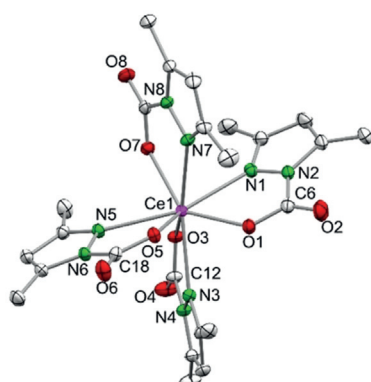
2·thf, which showed the presence of a strong absorption band at $\tilde{\nu} = 1732$ and $1718\,cm^{-1}$, respectively, for the CO stretching of the C–O double bond as well as a strong absorption band at $\tilde{\nu} = 1336\,cm^{-1}$ for the CO stretching of the C–O single bond.

The structure was also supported by NMR spectroscopic measurements. The ^1H NMR spectrum recorded in $[D_8]$toluene at ambient temperature revealed two distinct methyl group environments for all the pyrazolato ligands, indicative of ligand asymmetry and complete consumption of $[Ce(Me_2pz)_4]_2$. The ^{13}C signal of the inserted CO_2 was detected at $\delta = 149.9$ ppm, a region where pyrazolate N-CO_2R signals are expected.[26] ^1H NMR measurements on **2·thf** in $[D_8]$THF at ambient temperature showed a mixture of products, which could not be assigned. Cooling the solution to $-40\,°C$ under 1 bar CO_2 pressure led to a color change from red to orange and both the ^1H and ^{13}C NMR spectra recorded at $-40\,°C$ showed similar signals as **2·toluene** in $[D_8]$toluene.

Variable-temperature (VT) NMR studies of **2·toluene** and **2·thf** in $[D_8]$toluene and $[D_8]$THF were conducted to investigate the reversibility of CO_2 insertion (Scheme 3). In $[D_8]$toluene, the formation of a new species at $40\,°C$ was revealed and no further liberation of CO_2 was observed even after heating above $60\,°C$ (see Figure S6 in the Supporting Information). The ^1H NMR spectrum recorded at $40\,°C$ shows two sets of signals for different Me_2pz moieties in a 1:1 ratio, which suggests the formation of putative compound $[Ce-(Me_2pz)_2(Me_2pz·CO_2)_2]$.

Recooling the solution did not reform **2·toluene** quantitatively, likely because some of the liberated CO_2 was no longer within the reaction medium, but the addition of fresh CO_2 quantitatively reformed **2·toluene**. The $[D_8]$THF VT NMR experiment of compound **2·thf** showed a different CO_2-deinsertion behavior (see Figure S10). As a consequence of competitive thf coordination, displacement of CO_2 starts at $10\,°C$ and is complete at $60\,°C$, with formation of $[Ce(Me_2pz)_4-(thf)]$. As seen in the experiment in $[D_8]$toluene, this reaction is fully reversible by recooling the sample and subsequently

Figure 1. Crystal structure of $[Ce(Me_2pz·CO_2)_4]$ (**2·toluene**). Ellipsoids are shown at the 50% probability level. Hydrogen atoms and lattice toluene are omitted for clarity. Selected bond lengths/angles are listed in the Supporting Information.
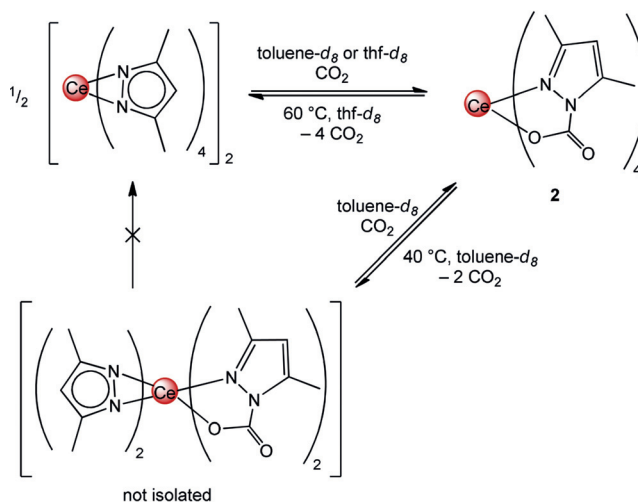
Scheme 3. Reversible insertion of CO_2 into the Ce–$N(Me_2pz)$ bond. The process is completely reversible in $[D_8]$thf and partially reversible in $[D_8]$toluene. The product arising from the elimination of CO_2 in $[D_8]$toluene has not been isolated; the structure is based on ^1H NMR spectroscopic analysis at $40\,°C$.
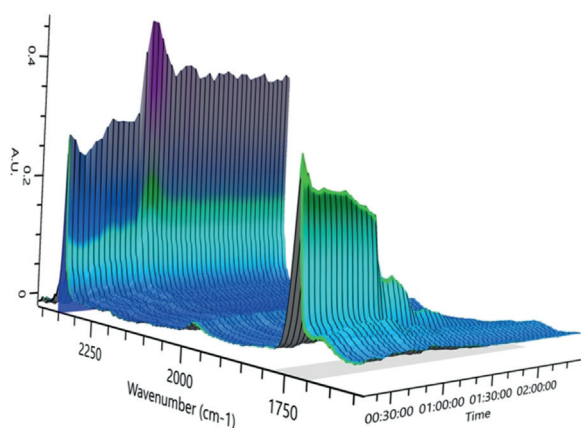
Figure 2. In situ IR spectroscopy of **2·thf** at 60 °C in the range of $\tilde{\nu} = 1700$ to 2350 cm^{-1}. Normalized intensities are shown. Spectra were recorded every minute.

Scheme 4. Insertion of one equivalent of CO_2 into the Ce–N(Me$_2$pz) bond of [Ce(Me$_2$pz)$_4$(thf)].

Figure 3. Crystal structure of [Ce$_3$(Me$_2$pz)$_9$(Me$_2$pz·CO$_2$)$_3$(thf)] (**3**). Ellipsoids are shown at the 50% probability level. Hydrogen atoms and lattice *n*-hexane are omitted for clarity. Selected bond lengths/angles are listed in the Supporting Information.

introducing CO_2. Additionally, in situ IR measurements were performed at 60 °C, which showed complete loss of inserted CO_2 and formation of free CO_2 (Figure 2 and see also Figure S58).

In the solid state, **2·toluene** is stable for several weeks at −40 °C, but at ambient temperature it partially loses CO_2 over a few days or when it is exposed to vacuum, as indicated by a color change from orange to dark red. A thermogravimetric analysis (TGA), performed under a flow of Ar and heating the sample slowly from 28 °C to 250 °C, indicated an initial loss of mostly lattice toluene. The liberation of CO_2 and small amounts of lattice toluene was dominant between 55 and 95 °C, as revealed by a step of 21.92% (theoretical proportion of CO_2 in **2·toluene** 19.98%). At 250 °C, only nonvolatile parts of **2·toluene** remain, leaving a mass of 49.79% of the initial weight (theoretical value 51.61%; see Figure S59). Although the deinsertion of carbon dioxide was achieved in the solid state, bulk compound **1** did not insert any carbon dioxide when stored under 1 bar CO_2 pressure for three days. Moreover, compound **1** was hydrolyzed upon exposure to air within one hour (DRIFT spectrum, see Figure S57).

[Ce(Me$_2$pz)$_4$(thf)] (**1·thf**) was treated with stoichiometric amounts of CO_2 to generate the putative [Ce-(Me$_2$pz)$_2$(Me$_2$pz·CO$_2$)$_2$] (Scheme 3). Although this species could not be isolated, it was possible to generate mono-inserted [Ce$_3$(Me$_2$pz)$_9$(Me$_2$pz·CO$_2$)$_3$(thf)] (**3**) in moderate yields of 46% (Scheme 4). The crystal structure of ceric **3** shows a ring motif with two distinct 9-coordinate and one 10-coordinate cerium atoms (Figure 3). Although all the cerium centers are coordinated by three Me$_2$pz ligands in an $\eta^2(N,N')$ fashion, Ce1 connects further to two oxygen atoms of neighboring Me$_2$pz·CO$_2$ ligands as well as an additional thf molecule, 10-coordinate Ce2 is surrounded by two κ^2:(N,O)-chelating Me$_2$pz·CO$_2$ ligands, and Ce3 exhibits additional contacts to one κ^2:(N,O)-Me$_2$pz·CO$_2$ ligand and an oxygen atom of a neighboring Me$_2$pz·CO$_2$ ligand.

Each Me$_2$pz·CO$_2$ ligand bridges between two cerium atoms. In contrast to homoleptic **2**, all the oxygen atoms are engaged in cerium bonding, which implies delocalized O–C–O bonds (av. C–O, 1.247 Å). The $\eta^2(N,N')$-Ce–N(Me$_2$pz)
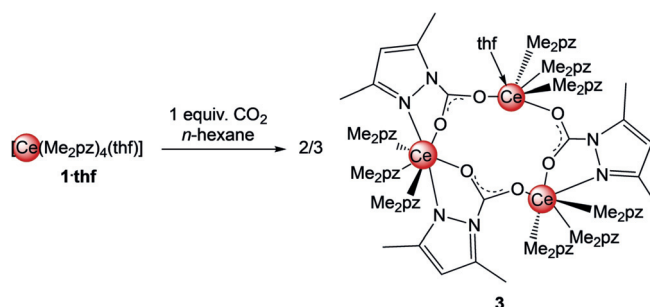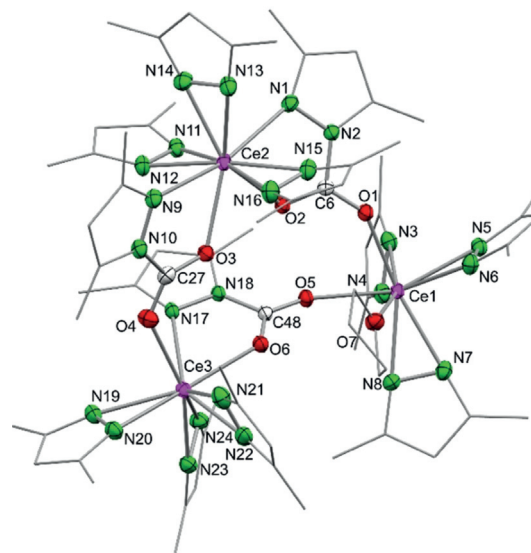
bond lengths are in the expected range.[24,27] According to VT NMR studies carried out in [D$_8$]toluene, the trimetallic entity **3** is retained in solution at low temperatures, with every dimethylpyrazolato ligand showing a distinct signal set in the proton NMR spectrum at −80 °C (see Figure S12). The signals for the protons of the bridging Me$_2$pz·CO$_2$ ligands are shifted upfield compared to those of the terminal $\eta^2(N,N')$-Me$_2$pz ligands. As a consequence of the equilibrium between potential alternative oligomers formed in the presence of only one equivalent of CO_2 per cerium, the interpretation of the ambient-temperature NMR spectrum was difficult. This was already experienced for the insertion of benzophenone into the Ce–N(Me$_2$pz) bond.[23] Upon heating to 90 °C, CO_2 was liberated and [Ce(Me$_2$pz)$_4$] re-formed (see Figure S14). After cooling to ambient temperature, a partial reinsertion of CO_2 was observed, as was found in the VT NMR experiments on **2·toluene** and **2·thf**.

Carbon Dioxide Insertion into a Cerous Pyrazolate: To examine the role of the oxidation state of cerium (Ce^{IV} versus Ce^{III}) and, therefore, the impact of its Lewis acidity, cerous donor-free [Ce$_4$(Me$_2$pz)$_{12}$][28] (**4**) was used as a precursor for CO_2 insertion (Scheme 5). Remarkably, while retaining the

Ce_4 nuclearity, all of the $Ce-N(Me_2pz)$ moieties engaged in CO_2 insertion, leading to the complex $[Ce_4(Me_2pz\cdot CO_2)_{12}]$ (**5**; Figure 4). Compared to the six different coordination modes of the pyrazolato moieties in starting material **4**,[28] the crystal structure of **5** revealed only three. Ce2, Ce3, and Ce4 form a nearly equilateral triangle bridged by μ_3-$1\kappa^2(N,O)$:$2\kappa(O)$:3κ-(O')-$Me_2pz\cdot CO_2$. Each of the 9-coordinate cerium centers (Ce2, Ce3, and Ce4) is also surrounded by two terminal $Me_2pz\cdot CO_2$ groups in a $\kappa^2(N,O)$ coordination mode and two oxygen atoms in a $\kappa^2(O,O')$ fashion (Figure S66). This triangle is capped by 9-coordinate Ce1, which is coordinated to three $Me_2pz\cdot CO_2$ ligands in a $\kappa^2(N,O)$ manner (Ce1$-N_{avg}$ 2.710 Å, Ce1$-O_{avg}$ 2.395 Å) and to three bridging oxygen atoms. The $Ce-O$ bond lengths are similar to those found in $[Ce\text{-}(L^R\cdot CO_2)_3]$ ($L^R = 2$-O-$3,5$-tBu_2-$C_6H_2(1$-$C\{N(CH)_2N(R)\})$) and $R = iPr$ and Mes) reported by Arnold et al. with $Ce-O$ bond lengths of 2.466(6)–2.482(6) Å.[18b] The O$-$C$-$O bond lengths
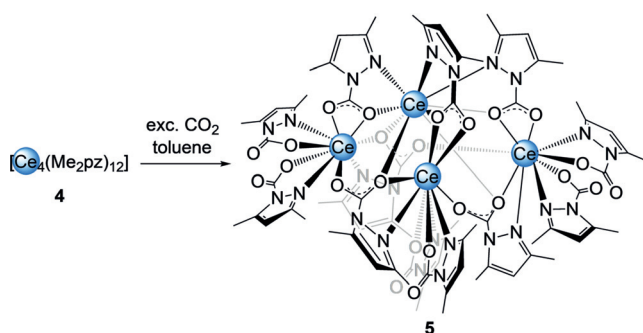
Scheme 5. Insertion of of CO_2 into the $Ce-N(Me_2pz)$ bonds of cerous $[Ce_4(Me_2pz)_{12}]$.
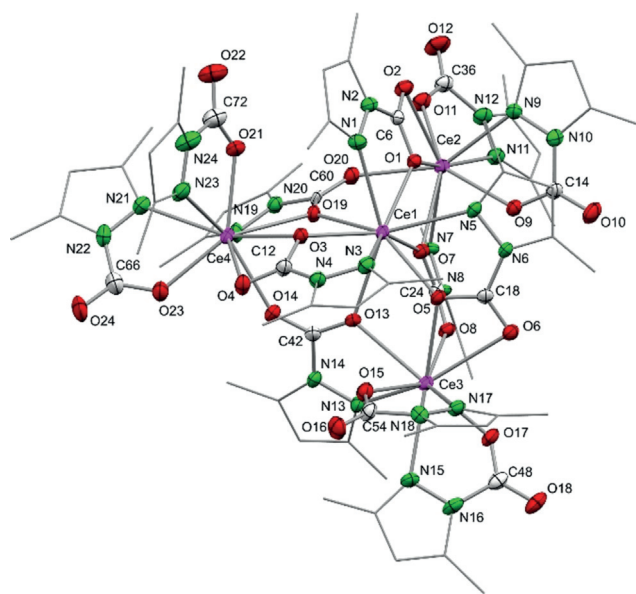
Figure 4. Crystal structure of $[Ce_4(Me_2pz\cdot CO_2)_{12}]$ (**5**). Ellipsoids are shown at the 50% probability level. Hydrogen atoms and lattice toluene (ten molecules) are omitted for clarity. Cutouts of the crystal structure of **5** and a schematic view of different $Me_2Pz\cdot CO_2$ binding modes, as well as selected bond lengths/angles are shown in the Supporting Information.

indicate delocalization of the bridging $Me_2pz\cdot CO_2$ ligands, with two C$-$O bond lengths in the same region (1.235(9)–1.264(9) Å) and rather localized C$-$O single (1.26(1)–1.301-(9) Å) and C$-$O double bonds (1.21(1)–1.229(9) Å) for the capping and terminal $Me_2pz\cdot CO_2$ ligands. For further comparison, the cerous carbamate $[Ce_4(O_2CNiPr_2)_{12}]$ features a lozenged arrangement of one 8-coordinate and three 7-coordinate Ce^{III} centers with $Ce-O$ bond lengths in the range 2.322(7)–2.746(7) Å (no Ce-N interaction).[29] The latter complex was obtained from the reaction of $CeCl_3(DME)$ with $HNiPr_2$ and CO_2 (Scheme 1f). In accordance with the crystal structure of cluster **5**, DRIFTS measurements show strong absorption bands for both the C$-$O single bonds ($\tilde{\nu} = 1250$–1350 cm^{-1}) and C$-$O double bonds ($\tilde{\nu} = 1600$–1750 cm^{-1}). ^{1}H DOSY NMR measurements on **5** in $[D_8]$toluene, $[D_8]$THF, or a $[D_8]$toluene/3,3-dimethyl-1,2-butylene oxide mixture revealed distinct diffusion coefficients (see Figures S17–S20) for the solvents employed and only one additional peak corresponding to a much larger species but correlating with every other signal in the proton NMR spectra. Calculation of the molar mass of this compound ($[D_8]$toluene: $M_r = 1989$ $g\,mol^{-1}$; $[D_8]$THF: $M_r = 1643$ $g\,mol^{-1}$; $[D_8]$toluene + 3,3-dimethyl-1,2-butyleneoxide: $M_r = 2357$ $g\,mol^{-1}$) as a compact sphere-like molecule[30] suggests it exists as a tetrametallic ($M_r = 2242$ $g\,mol^{-1}$) or a non-monometallic species in solution. Treating $[Ce(Me_2pz)_3(thf)]_2$ with CO_2 in $[D_8]$THF gave the same NMR spectrum as that of **5·toluene**, thus indicating the formation of a multimetallic compound also in donor solvents (see Figure S16). TGA of **5·toluene** also showed an initial loss of toluene (cf. **2·toluene**), followed by a pronounced step (21.39% weight loss) in the range from 52 to 90 °C, consistent with the release of CO_2 (theoretical value: 16.75%) and some lattice toluene (Figure S60). At 250 °C, only the nonvolatile parts of **5·toluene** remain and a total loss of 46.82 wt% compared to the starting material fits well with the theoretical value of 45.99% for 10 molecules of toluene and 12 molecules of CO_2 eliminated from $[Ce_4(Me_2pz\cdot CO_2)_{12}]\cdot 10$ toluene (**5·toluene**).
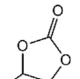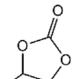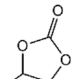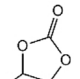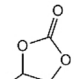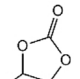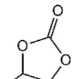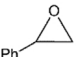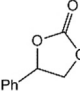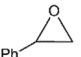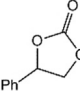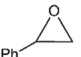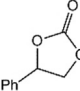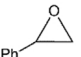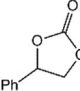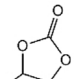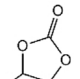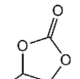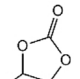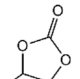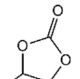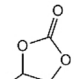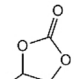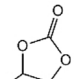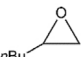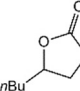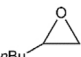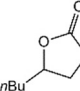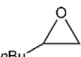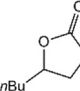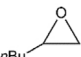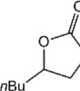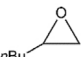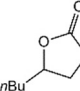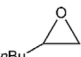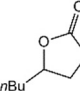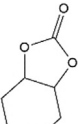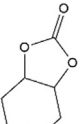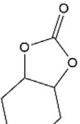
Catalytic Formation of Cyclic Carbonates from CO_2 and Oxiranes: Having established the efficiency and reversibility of CO_2 insertion into $Ce-N(Me_2pz)$ bonds, we were interested in any catalytic utilization. Accordingly, pyrazolate complexes **1** and **4** were probed as catalysts for the generation of cyclic carbonates from CO_2 and oxiranes. In the absence of CO_2, compound **1** interacts with epoxides, as indicated by a noticeable shift in the ^{1}H NMR spectrum upon addition of one equivalent of 3,3-dimethyl-1,2-butylene oxide (see Figure S24). This is most likely due to formation of a donor adduct, which is considered a crucial step in Lewis-acid-catalyzed cycloaddition reactions. Even though such donor adducts were shown to be isolable (e.g. $Tp^{tBu}Ca(O$-$2,6$-$iPr_2C_6H_3)\cdot(PO)$; $Tp^{tBu} = tris(3$-tBu-pyrazolyl)borato, PO = propylene oxide[31]), the putative $[Ce(Me_2pz)_4(PO)]$ (**1-PO**) could not be isolated. Tetra-n-butylammonium bromide (TBAB) was employed as a co-catalyst, since it was shown to promote the highest activities in such cycloaddition reactions.[11b,32] The reaction was optimized for propylene oxide, which gave almost quantitative conversion after 24 h under mild conditions. Using 0.5 mol% **1** or 0.25 mol% **4** and

1 mol% TBAB without solvent at ambient temperature and 1 bar CO_2 pressure gave 93% conversion for the tetravalent catalyst **1** and 98% for its trivalent counterpart (Table 1, entries 1 and 3). The CO_2-insertion complexes **2** and **5** displayed similar catalytic activity (entries 2 and 4). The conversion dropped drastically on increasing the steric bulk of the substituent on the epoxides. As a result, styrene oxide, and 3,3-dimethyl-1,2-butylene oxide showed only very low conversions (entry 21) for ceric **1** and almost no conversion in the case of trivalent catalyst **4** (entry 22). Moderate conversion was observed for 1,2-*n*-hexylene oxide with the tetravalent catalyst **1** (entry 13). Conducting the catalysis at higher

Table 1: Catalytic formation of cyclic carbonates from epoxides and CO_2.[a]

Entry	Catalyst	Substrate	Product	Conversion [%]	TON/Ce
1	**1**			93	93
2	**2**			93	93
3	**4**			98	98
4	**5**			96	96
5	**1**[i]			98	196
6	**1**			20	20
7	**1**[b]			4	8
8	**4**			13	13
9	**4**[c]	Ph	Ph	6	12
10	**4·thf**			13	13
11	**4·thf**[c]			7	14
12	**1**[i]			12	24
13	**1**			61	61
14	**4**			25	25
15	**1**[d]			98	98
16	**4**[e]			96	96
17	**1**[f]	*n*Bu	*n*Bu	25	25
18	**1**[g]			76	76
19	**6**			3	3
20	**1**[i]			49	98
21	**1**			12	12
22	**4**			3	3
23	**1**[g]			9	9
24	**1**[h]	*t*Bu	*t*Bu	84	168
25	**1**[i]			14	28
26	**1**[j]			60	300
27	**1**			2	2
28	**1**[h]			77	154
29	**1**[j]			35	175

[a] Reaction conditions if not otherwise noted: 1 bar CO_2 pressure and 0.5 mol% catalyst (1 mol% for **2** and **6**; 0.25 mol% for **4** and **5**) and 1 mol% co-catalyst for 24 h at ambient temperature in neat epoxide. [b] 0.25 mol% catalyst **1** and 0.5 mol% TBAB, 24 h. [c] 0.125 mol% catalyst **4** and 0.5 mol% TBAB, 24 h. [d] 0.5 mol% catalyst **1** and 1 mol% TBAB, 24 h, 90°C. [e] 0.25 mol% catalyst **4** and 1 mol% TBAB, 24 h, 90°C. [f] At 90°C without TBAB as a co-catalyst. [g] 0.5 mol% catalyst **1** and 1 mol% TBAB, 24 h, 10 bar CO_2 pressure. [h] 0.25 mol% catalyst **1** and 0.5 mol% TBAB, 24 h, 90°C, 10 bar CO_2 pressure. [i] 0.25 mol% catalyst **1** and 0.5 mol% TBAB, 1 h, 90°C, 10 bar CO_2 pressure. [j] 0.1 mol% catalyst **1** and 0.2 mol% TBAB, 24 h, 90°C, 10 bar CO_2 pressure.

temperature increased the TONs with both catalysts **1** and **4**, and resulted in nearly quantitative conversion for both systems (entries 15 and 16). Without co-catalyst TBAB, **1** showed moderate catalytic activity at 90°C (entry 17). In almost all cases, tetravalent **1** showed higher catalytic activity than cerous **4**, which most likely results from the higher Lewis acidity of Ce[IV] versus Ce[III]. To further evaluate the catalytic reaction with catalyst **1** and propylene oxide, the TOFs at different stages of the catalysis were determined (see Table S1). After a short induction period, most likely corresponding to the insertion of CO_2 into **1**, the TOF reached a maximum of 11 h^{-1} within the first 3 h. For comparison, a TOF of 155 h^{-1} was reported by Yao and co-workers when performing the reaction under 10 bar CO_2 pressure.[11a] Increasing the CO_2 pressure did not significantly affect the catalytic activity of compound **1** (entries 13 vs. 18 and 21 vs. 23). However, a simultaneous increase of the temperature to 90°C and the CO_2 pressure to 10 bar led to a marked improvement in the catalytic activity, resulting in TONs of up to 300 for the sterically demanding 3,3-dimethyl-1,2-butylene oxide (entries 24 and 26). The latter conditions were also applicable for the cycloaddition of CO_2 and cyclohexene oxide, an internal epoxide (entries 27–29). Having optimized the reaction conditions, we determined the initial turnover frequencies for the different epoxides (entries 5, 12, 20, and 25). As expected, the TOFs increased as the steric of the substituents bulk decreased, ranging from 24 to 196 h^{-1} and giving almost quantitative conversion of propylene oxide after a reaction time of one hour (entry 5). Compared to the other catalyst systems based on rare-earth metals reported by Yao and co-workers (TOFs up to 440 h^{-1}) or by Otero and co-workers (3167 h^{-1}), our system shows only moderate catalytic activity under comparable conditions.[11a,b]

The mechanism of the cycloaddition of CO_2 and epoxides using tetraalkylammonium salts as co-catalysts has been discussed in detail.[32,33] It is generally accepted that the epoxide is activated by coordination to a Lewis-acidic metal center followed by a nucleophilic ring-opening attack of the bromide to form a metal-alkoxy bond (Scheme 6). Subsequently, the alkoxide reacts with CO_2 and cyclizes to produce a cyclic carbonate. Hints that the mechanisms for the cycloaddition differ using ceric **1** or cerous **4** as the catalyst could be found when conducting the reactions with different amounts of catalyst loading (entries 7 and 9). This results in a change in the TONs for the tetravalent catalyst **1**, whereas the TONs remained the same for trivalent complex **4**. The occurrence of distinct reaction mechanisms is not surprising, as **1** is a monometallic complex while **4** is a tetrametallic compound in the solid state and in solution (for a more detailed possible mechanism see Scheme S1). Such a mechanism, involving multiple metal centers, was previously proposed for the bimetallic complex [Al(salen)]$_2$O by North and co-workers.[32] However, any detailed information about the mechanism could not be retrieved from our catalyst system as the TOFs decreased enormously when the reactions were conducted in propylene carbonate (no significant conversion at ambient temperature after 24 h and ca. 10% conversion after 20 h at 90°C) or any other solvent, which makes kinetic studies unfeasible.
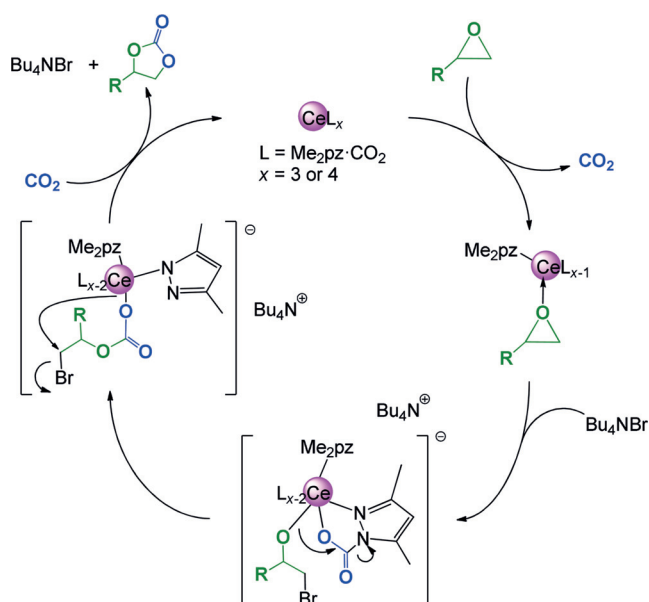
Scheme 6. Proposed overall mechanism for the coupling of CO_2 with epoxides.

dioxide with TBAB as a co-catalyst under mild conditions. We are currently investigating the carbon dioxide capture performance of silica-grafted variants of Ce-pyrazolates,[34] and our findings might also stimulate research in the area of cerium-dipyrazolate-based CO_2-"breathable"/expandable MOFs.[35,36]

Conflict of interest

The authors declare no conflict of interest.

Complex **2** underwent a reductive side reaction in the presence of TBAB to afford cerous species [Ce(Me$_2$pz·CO$_2$)$_4$][NBu$_4$] (**6**). This side reaction occurred during the catalytic studies and when combining **1** and TBAB in stoichiometric amounts in [D$_8$]toluene under 1 bar CO_2 pressure. Although **2** is very stable in toluene solution under these conditions (no color change was observed after several days), it underwent reduction in the presence of TBAB within hours, as evidenced by decolorization of the orange solution. Most probably bromine is formed as an oxidation product; however, no brominated product could be detected in the reaction mixture (see Figure S23). The use of epoxides as a solvent seems to stabilize the tetravalent **2**, as no paramagnetic signals were found in the ^{1}H NMR spectra of the catalytic reactions. The crystal structure of **6** revealed the same motif as seen in **2·toluene** and **2·thf** (see Figure S67). The 8-coordinate cerium center bears four $\kappa^2(N,O)$ Me$_2$pz·CO$_2$ ligands with elongated Ce−N and Ce−O bonds compared to ceric **2·toluene** and **2·thf**, as would be expected for a cerium(III) center. Cerous **6** displays poor catalytic activity compared to tetravalent **1** (Table 1, entry 19), thus underlining that it is a side product and not the active catalyst.

Conclusion

We have shown that carbon dioxide easily inserts into the Ce−N(Me$_2$pz) bond of both ceric [Ce(Me$_2$pz)$_4$]$_2$ and cerous [Ce$_4$(Me$_2$pz)$_{12}$] at an amount equivalent to 5.7 mmol CO_2 per gram complex and via the controlled activation of 12 molecules of CO_2 within one complex, respectively. The insertion process is reversible both in solution and in the solid state, with CO_2 desorption being complete at < 100 °C. Both trivalent and tetravalent cerium pyrazolate complexes are active catalysts for the cycloaddition of epoxides and carbon

[1] a) P. Falkowski et al., *Science* **2000**, *290*, 291–296; b) S. Solomon, G.-K. Plattner, R. Knutti, P. Friedlingstein, *Proc. Natl. Acad. Sci. USA* **2009**, *106*, 1704–1709; c) R. S. Haszeldine, *Science* **2009**, *325*, 1647–1652; d) D. W. Keith, *Science* **2009**, *325*, 1654–1655; e) N. von der Assen, P. Voll, M. Peters, A. Bardow, *Chem. Soc. Rev.* **2014**, *43*, 7982–7994.

[2] For review articles, see a) D. M. D'Alessandro, B. Smit, J. R. Long, *Angew. Chem. Int. Ed.* **2010**, *49*, 6058–6082; *Angew. Chem.* **2010**, *122*, 6194–6219; b) C.-H. Yu, C.-H. Huang, C.-S. Tan, *Aerosol Air Qual. Res.* **2012**, *12*, 745–769; c) K. Sumida, D. L. Rogow, J. A. Mason, T. M. McDonald, E. D. Bloch, Z. R. Herm, T.-H. Bae, J. R. Long, *Chem. Rev.* **2012**, *112*, 724–781; d) E. S. Sanz-Pérez, C. R. Murdock, S. A. Didas, C. W. Jones, *Chem. Rev.* **2016**, *116*, 11840–11876; e) Y. Lin, C. Kong, Q. Zhang, L. Chen, *Adv. Energy Mater.* **2017**, *7*, 1601296.

[3] For review articles, see a) T. Sakakura, J.-C. Choi, H. Yasuda, *Chem. Rev.* **2007**, *107*, 2365–2387; b) G. Centi, S. Perathoner, *Catal. Today* **2009**, *148*, 191–205; c) M. Cokoja, C. Bruckmeier, B. Rieger, W. A. Herrmann, F. E. Kühn, *Angew. Chem. Int. Ed.* **2011**, *50*, 8510–8537; *Angew. Chem.* **2011**, *123*, 8662–8690; d) M. Aresta, A. Dibenedetto, A. Angelini, *Chem. Rev.* **2014**, *114*, 1709–1742; e) Q. Liu, L. Wu, R. Jackstell, M. Beller, *Nat. Commun.* **2015**, *6*, 5933; f) J. Artz, T. E. Müller, K. Thenert, J. Kleinekorte, R. Meys, A. Sternberg, A. Bardow, W. Leitner, *Chem. Rev.* **2018**, *118*, 434–504.

[4] A. Paparo, J. Okuda, *Coord. Chem. Rev.* **2017**, *334*, 136–149.

[5] a) A. Goeppert, M. Czaun, R. B. May, G. K. S. Prakash, G. A. Olah, S. R. Narayanan, *J. Am. Chem. Soc.* **2011**, *133*, 20164–20167; b) F. Inagaki, C. Matsumoto, T. Iwata, C. Mukai, *J. Am. Chem. Soc.* **2017**, *139*, 4639–4642.

[6] a) S. R. Caskey, A. G. Wong-Foy, A. J. Matzger, *J. Am. Chem. Soc.* **2008**, *130*, 10870–10871; b) T. M. McDonald et al., *Nature* **2015**, *519*, 303–308.

[7] Y. F. Radkov, E. A. Fedorova, S. Y. Khorshev, G. S. Kalinina, M. N. Bochkarev, G. A. Razuvaev, *Zhur. Obshchei Khimii* **1986**, *56*, 386–389.

[8] For a recent study on Ce^III silylamides, see H. Yin, P. J. Carroll, E. J. Schelter, *Chem. Commun.* **2016**, *52*, 9813–9816.

[9] M. N. Bochkarev, E. A. Fedorova, Y. F. Radkov, S. Y. Khorshev, G. S. Kalinina, G. A. Razuvaev, *J. Organomet. Chem.* **1983**, *258*, C29–C33.

[10] For examples of CO₂ insertion into Ln^III–aryloxy bonds, see a) D. Cui, M. Nishiura, O. Tardif, Z. Hou, *Organometallics* **2008**, *27*, 2428–2435; b) L. A. M. Steele, T. J. Boyle, R. A. Kemp, C. Moore, *Polyhedron* **2012**, *42*, 258–264.

[11] a) J. Qin, P. Wang, Q. Li, Y. Zhang, D. Yuan, Y. Yao, *Chem. Commun.* **2014**, *50*, 10952–10955; b) J. Martínez, J. Fernández-Baeza, L. F. Sánchez-Barba, J. A. Castro-Osma, A. Lara-Sánchez, A. Otero, *ChemSusChem* **2017**, *10*, 2886–2890; c) Z. Zhao, J. Qin, C. Zhang, Y. Wang, D. Yuan, Y. Yao, *Inorg. Chem.* **2017**, *56*, 4568–4575.

[12] a) D. Cui, M. Nishiura, Z. Hou, *Macromolecules* **2005**, *38*, 4089–4095; b) D. V. Vitanova, F. Hampel, K. C. Hultzsch, *J. Organomet. Chem.* **2005**, *690*, 5182–5197; c) B. B. Lazarov, F. Hampel, K. C. Hultzsch, *Z. Anorg. Allg. Chem.* **2007**, *633*, 2367–2373; d) Z. Zhang, D. Cui, X. Liu, *J. Polym. Sci. Part A* **2008**, *46*, 6810–6818; e) A. Decortes, R. M. Haak, C. Martín, M. M. Belmonte, E. Martin, J. Benet-Buchholz, A. W. Kleij, *Macromolecules* **2015**, *48*, 8197–8207; f) J. Qin, B. Xu, Y. Zhang, D. Yuan, Y. Yao, *Green Chem.* **2016**, *18*, 4270–4275.

[13] For the use of organoscandium(III) complexes in the catalytic hydrosilylation of CO₂, see a) A. Berkefeld, W. E. Piers, M. Parvez, L. Castro, L. Maron, O. Eisenstein, *Chem. Sci.* **2013**, *4*, 2152–2162; b) F. A. LeBlanc, W. E. Piers, M. Parvez, *Angew. Chem. Int. Ed.* **2014**, *53*, 789–792; *Angew. Chem.* **2014**, *126*, 808–811.

[14] a) M. A. St. Clair, B. D. Santarsiero, *Acta Crystallogr. Sect. C* **1989**, *45*, 850–852; b) H. Schumann, J. A. Meese-Marktscheffel, A. Dietrich, F. H. Görlitz, *J. Organomet. Chem.* **1992**, *430*, 299–315; c) W. J. Evans, C. A. Seibel, J. W. Ziller, R. J. Doedens, *Organometallics* **1998**, *17*, 2103–2112; d) F. A. LeBlanc, A. Berkefeld, W. E. Piers, M. Parvez, *Organometallics* **2012**, *31*, 810–818.

[15] a) O. T. Summerscales, C. M. Moore, B. L. Scott, M. P. Wilkerson, A. D. Sutton, *Organometallics* **2017**, *36*, 4682–4685; b) D. W. Beh, W. E. Piers, I. del Rosar, L. Maron, B. S. Gelfand, C. Gendy, J.-B. Lin, *Dalton Trans.* **2018**, *47*, 13680–13688.

[16] a) W. J. Evans, C. A. Seibel, J. W. Ziller, *Inorg. Chem.* **1998**, *37*, 770–776; b) W. J. Evans, J. M. Perotti, J. C. Brady, J. W. Ziller, *J. Am. Chem. Soc.* **2003**, *125*, 5204–5212; c) N. W. Davies, A. S. P. Frey, M. G. Gardinier, J. Wang, *Chem. Commun.* **2006**, 4853–4855; d) J. Andrez, J. Pécaut, P.-A. Bayle, M. Mazzanti, *Angew. Chem. Int. Ed.* **2014**, *53*, 10448–10452; *Angew. Chem.* **2014**, *126*, 10616–10620; e) M. Xémard, V. Goudy, A. Braun, M. Tricoire, M. Cordier, L. Ricard, L. Castro, E. Louyriac, C. E. Kefalidis, C. Clavaguéra, L. Maron, G. Nocton, *Organometallics* **2017**, *36*, 4660–4668; f) A. R. Willauer, D. Toniolo, F. Fadaei-Tirani, Y. Yang, M. Laurent, M. Mazzanti, *Dalton Trans.* **2019**, *48*, 6100–6110.

[17] a) Y.-M. So, G.-C. Wang, Y. Li, H. H. Y. Sung, I. D. Williams, Z. Lin, W.-H. Leung, *Angew. Chem. Int. Ed.* **2014**, *53*, 1626–1629; *Angew. Chem.* **2014**, *126*, 1652–1655; b) G.-C. Wang, Y.-M. So, Y. Li, K.-L. Wong, K.-C. Au-Yeung, H. H. Y. Sung, I. D. Williams, W.-H. Leung, *Chem. Eur. J.* **2015**, *21*, 16126–16135.

[18] a) P. L. Arnold, Z. R. Turner, A. I. Germeroth, I. J. Casely, G. S. Nichol, R. Bellabarba, R. P. Tooze, *Dalton Trans.* **2013**, *42*, 1333–1337; b) P. L. Arnold, R. W. F. Kerr, C. Weetman, S. R. Docherty, J. Rieb, F. L. Cruickshank, K. Wang, C. Jandl, M. W. McMullon, A. Pöthig, et al., *Chem. Sci.* **2018**, *9*, 8035–8045.

[19] For further examples of CO₂ insertion into Ln–NHC bonds, see a) P. L. Arnold, I. A. Marr, S. Zlatogorsky, R. Bellabarba, R. P. Tooze, *Dalton Trans.* **2014**, *43*, 34–37; b) T. Simler, T. J.

Feuerstein, R. Yadav, M. T. Gamer, P. W. Roesky, *Chem. Commun.* **2019**, *55*, 222–225.

[20] W. J. Evans, J. M. Perroti, S. A. Kozimor, T. M. Champagne, B. I. Davis, G. W. Nyce, C. H. Fujimoto, R. D. Clark, M. A. Johnston, J. W. Ziller, *Organometallics* **2005**, *24*, 3916–3931.

[21] For an irreversible insertion of [Me₂SiO] into a Yb–Me₂pz bond, see X. Zhou, H. Ma, X. Huang, X. You, *J. Chem. Soc. Chem. Commun.* **1995**, 2483–2484.

[22] a) For a reversible CO₂ insertion into a Sm–EPh bond (E = S, Se), see W. J. Evans, K. A. Miller, J. W. Ziller, *Inorg. Chem.* **2006**, *45*, 424–429; b) a scandium(III)-bonded β-diketiminato ("nannac")ligand framework was shown to reversibly capture CO₂: Ref. [14b].

[23] D. Werner, G. B. Deacon, P. C. Junk, R. Anwander, *Eur. J. Inorg. Chem.* **2017**, 3419–3428.

[24] H. C. Aspinall, J. Bacsa, A. C. Jones, J. S. Wrench, K. Black, P. R. Chalker, P. J. King, P. Marshall, M. Werner, H. O. Davies, et al., *Inorg. Chem.* **2011**, *50*, 11644–11652.

[25] J. A. Bogart, A. J. Lewis, S. A. Medling, N. A. Piro, P. J. Carroll, C. H. Booth, E. J. Schelter, *Inorg. Chem.* **2013**, *52*, 11600–11607.

[26] M. Begtrup, J. Elguero, R. Faure, P. Camps, C. Estopá, D. Ilavský, A. Fruchier, C. Marzin, J. de Mendoza, *Magn. Reson. Chem.* **1988**, *26*, 134–151.

[27] D. Werner, G. B. Deacon, P. C. Junk, R. Anwander, *Dalton Trans.* **2017**, *46*, 6265–6277.

[28] D. Werner, U. Bayer, N. E. Rad, P. C. Junk, G. B. Deacon, R. Anwander, *Dalton Trans.* **2018**, *47*, 5952–5955.

[29] U. Baisch, D. B. Dell'Amico, F. Calderazzo, L. Labella, F. Marchetti, D. Vitali, *J. Mol. Catal.* **2003**, *204–205*, 259–265.

[30] S. Bachmann, B. Gernert, D. Stalke, *Chem. Commun.* **2016**, *52*, 12861–12864.

[31] M. H. Chisholm, J. C. Gallucci, K. Phomphrai, *Inorg. Chem.* **2004**, *43*, 6717–6725.

[32] W. Clegg, R. W. Harrington, M. North, R. Pasquale, *Chem. Eur. J.* **2010**, *16*, 6828–6843.

[33] a) D. J. Darensbourg, M. W. Holtcamp, *Coord. Chem. Rev.* **1996**, *153*, 155–174; b) H. Jing, T. Chang, L. Jin, M. Wu, W. Qiu, *Catal. Commun.* **2007**, *8*, 1630–1634; c) J. Meléndez, M. North, R. Pasquale, *Eur. J. Inorg. Chem.* **2007**, 3323–3326; d) F. Jutz, J.-D. Grunwaldt, A. Baiker, *J. Mol. Catal. A* **2008**, *279*, 94–103; e) F. Jutz, J.-D. Grunwaldt, A. Baiker, *J. Mol. Catal. A* **2009**, *297*, 63–72; f) M. North, R. Pasquale, *Angew. Chem. Int. Ed.* **2009**, *48*, 2946–2948; *Angew. Chem.* **2009**, *121*, 2990–2992.

[34] Y. Liang, R. Anwander, *Dalton Trans.* **2013**, *42*, 12521–12545.

[35] For Ce^IV carboxylate MOFs, see a) P. Ji, T. Sawano, Z. Lin, A. Urban, D. Bours, W. Lin, *J. Am. Chem. Soc.* **2016**, *138*, 14860–14863; b) X.-P. Wu, L. Gagliardi, D. G. Truhlar, *J. Am. Chem. Soc.* **2018**, *140*, 7904–7912.

[36] For examples of dipyrazolyl-based MOFs, see a) H. J. Choi, M. Dinca, J. R. Long, *J. Am. Chem. Soc.* **2008**, *130*, 7848–7850; b) M. Tonigold, Y. Lu, B. Bredenkötter, B. Rieger, S. Bahnmüller, J. Hitzbleck, G. Langstein, D. Volkmer, *Angew. Chem. Int. Ed.* **2009**, *48*, 7546–7550; *Angew. Chem.* **2009**, *121*, 7682–7687; c) N. M. Padial, E. Q. Procopio, C. Montoro, E. López, J. E. Oltra, V. Colombo, A. Maspero, N. Masciocchi, S. Galli, I. Senkovska, S. Kaskel, E. Barea, J. A. R. Navarro, *Angew. Chem. Int. Ed.* **2013**, *52*, 8290–8294; *Angew. Chem.* **2013**, *125*, 8448–8452; d) Z. R. Herm, B. M. Wiers, J. A. Mason, M. R. Hudson, P. Zajdel, C. M. Brown, N. Masciocchi, R. Krishna, J. R. Long, *Science* **2013**, *340*, 960–964; e) J. A. Mason, J. Oktawiec, M. K. Taylor, M. R. Hudson, J. Rodriguez, J. E. Bachman, M. I. Gonazalez, A. Cervellino, A. Guagliardi, C. M. Brown, P. L. Llewellyn, N. Masciocchi, J. R. Long, *Nature* **2015**, *527*, 357–363.

Angewandte Chemie

Eine Zeitschrift der Gesellschaft Deutscher Chemiker

Supporting Information

Effective and Reversible Carbon Dioxide Insertion into Cerium Pyrazolates

Uwe Bayer, Daniel Werner, Cäcilia Maichle-Mössmer, and Reiner Anwander*

anie_201916483_sm_miscellaneous_information.pdf

Supporting Information

Table of Contents

Experimental Section

General Procedures. All manipulations were performed under an inert atmosphere (Ar) using a glovebox (*MBraun* 200B; <0.1 ppm O_2, <0.1 ppm H_2O), or according to standard Schlenk techniques in oven-dried glassware. The solvents were purified with Grubbs columns (MBraun SPS, solvent purification system) and stored in a glovebox. [Ce(Me$_2$pz)$_4$]$_2$, [Ce(Me$_2$pz)$_3$(thf)]$_2$ and [Ce(Me$_2$pz)$_3$]$_4$ were synthesized according to published procedures.[1-3] Cyclohexane was pre-dried over NaK alloy. Benzene-d_6 (C_6D_6), toluene-d_8, and thf-d_8 were purchased from *Euriso-top*, pre-dried over NaK alloy, and filtered off prior use, thf-d_8 was re-condensed. Chloroform-$d3$ was purchased from *Euriso-top* and used as received. NMR spectra were recorded at 26 °C with either a Bruker AVII+400 (^{1}H: 400.13 MHz, ^{13}C: 100.16 MHz), a Bruker DRX-250 (^{1}H: 250.00 MHz, ^{13}C: 62.86 MHz) or a Bruker-Avance II 500 (^{1}H: 500.13 MHz, ^{13}C: 125.76 MHz) using J. Young valve NMR spectroscopy tubes. ^{1}H and ^{13}C NMR shifts are referenced to a solvent resonance and reported in parts per million (ppm) relative to tetramethylsilane.[4] Analyses of NMR spectra were performed with ACD/NMR Processor Academic Edition (product version: 12.01). Infrared spectra were recorded on a *ThermoFisher Scientific* NICOLET 6700 FTIR ($\tilde{v}$= 4000 – 400 cm^{-1}) spectrometer using a DRIFTS chamber with dry KBr/sample mixtures and KBr windows. Elemental analysis (C, H, N) was performed on an *Elementar vario MICRO cube*. *In situ* IR spectra were recorded on a METTLER TOLEDO ReactIR 15. Thermogravimetric analyses (DTA) were performed under argon flow (60 l min^{-1}) heating from ambient temperature to 250 °C at a rate of 0.5 K min^{-1} in corundum crucibles on a Netzsch STA 449 F3 Jupiter.

Synthesis

[Ce(Me$_2$pz)$_4$(thf)] (1-thf). [Ce{N(SiHMe$_2$)$_2$}$_4$] (46.9 mg, 0.079 mmol) was dissolved in cyclohexane (2 mL), and added to a THF (~0.5 mL) solution of Me$_2$pzH (26.5 mg, 0.28 mmol). The mixture was shaken for 30 seconds before immediate exposure to vacuum, giving a bright red powder of crude [Ce(Me$_2$pz)$_4$(thf)] (**2a**). Crystallization from *n*-hexane yielded red blocks of **2a** (25 mg, 62%). ^{1}H NMR (26 °C, 250.00 MHz, C_6D_6): δ = 6.13 (s, 4 H, CH), 3.31 (m, 4 H, *α*-CH thf), 2.34 (s, 24 H, CH$_3$), 0.94 (m, 4 H, *β*-CH thf) ppm; ^{13}C NMR (26 °C, 62.86 MHz, C_6D_6): δ = 144.6 (CCH$_3$), 112.6 (CH), 70.3 (*α*-CH thf), 25.2 (*β*-CH thf), 13.5 (CH$_3$) ppm; IR (DRIFT): v = 3099 (w), 3024 (w), 3013 (s), 2942 (s), 2878 (s), 2859 (m), 1517 (vs), 1474 (w), 1470 (w), 1455 (w), 1444 (m), 1432 (vs), 1417 (s), 1364 (m), 1315 (w), 1301 (w), 1106 (w), 1050 (w), 1028 (w), 1006 (m), 959 (w), 921 (w), 871 (m), 806 (w), 781 (w), 728 (w) cm^{-1}; elemental analysis calcd. (%) for C$_{24}$H$_{36}$CeN$_8$O (592.71 g mol^{-1}, performed on crystalline **2a**): C 48.63, H 6.12, N 18.91; found: C 47.89, H 5.78, N 19.37.

[Ce(Me$_2$pz·CO$_2$)$_4$]·2 toluene (2·toluene). [Ce(Me$_2$pz)$_4$]$_2$ (**1**) (0.043 g, 0.042 mmol) was dissolved in toluene (2 mL) and stirred under 1 bar CO_2 pressure. After 5 min the dark red solution turned orange and was stored at −40 °C. After 1 day the supernatant solution was separated and the crystalline orange material was dried with a paper towel and subsequently under reduced pressure at −40 °C, leaving [Ce(Me$_2$pz·CO$_2$)$_4$]·2 toluene (**2·toluene**) as orange crystals. Yield 0.040 g (0.045 mmol, 54%). ^{1}H NMR (26 °C, 400.13 MHz, toluene-d_8) δ: 5.09 (4 H, s, CH), 2.81 (12 H, s, CH$_3$), 2.04 (12 H, s, CH_3) ppm. ^{13}C{^{1}H} NMR (26 °C, 100.16 MHz toluene-d_8) δ: 152.7 (CCH$_3$), 149.9 (OCO), 144.2 (CCH$_3$), 109.9 (CH), 14.0 (CH$_3$), 12.6 (CH$_3$) ppm. DRIFTS: $\tilde{v}$ = 3129

(vw), 3093 (vw), 2979 (vw), 2931 (vw), 1788 (vw), 1732 (vs), 1558 (m), 1496 (vw), 1457 (m), 1416 (w), 1385 (w), 1336 (s), 1292 (m), 1258 (s), 1213 (w), 1164 (w), 1156 (w), 1122 (s), 1042 (m), 983 (w), 838 (m), 817 (w), 778 (w), 769 (w), 741 (vw), 455 (m), 409 (vw) cm^{-1}. Elemental analysis calc. (%) $C_{38}H_{44}CeN_8O_8$ (880.93 g mol^{-1}) C 51.81, H 5.03, N 12.72; found C 51.85, H 4.71, N 12.79.

[Ce(Me$_2$pz·CO$_2$)$_4$]·2 thf (2·thf). [Ce(Me$_2$pz)$_4$]$_2$ (**1**) (0.254 g, 0.244 mmol) was dissolved in thf (2 mL) and stirred under 1 bar CO_2 pressure at 0 °C. After 5 min the dark red solution turned orange and was stored at −40 °C. After 1 day the supernatant solution was separated and the crystalline orange material was dried with a paper towel and subsequently at −40 °C under reduced pressure, leaving [Ce(Me$_2$pz·CO$_2$)$_4$]·2 thf (**2·thf**) as orange crystals. Yield 0.264 g (0.313 mmol, 64%). ^{1}H NMR (−20 °C, 500.13 MHz, thf-d_8) δ: 6.09 (4 H, s, CH), 2.63 (12 H, s, CH$_3$), 2.40 (12 H, s, CH$_3$) ppm. ^{13}C{^{1}H} NMR (−20 °C, 125.76 MHz, thf-d_8) δ: 152.4 (CCH$_3$), 152.4 (CCH3), 150.2 (OCO), 144.4 (CCH3), 110.2 (CH), 13.8 (CH3), 13.2 (CH$_3$) ppm. DRIFTS: $\tilde{v}$ = 3138 (vw), 2975 (w), 2865 (w), 1792 (vw), 1718 (vs), 1559 (m), 1458 (m), 1414 (m), 1379 (w), 1336 (s), 1293 (m), 1255 (m), 1168 (w), 1045 (m), 986 (w), 912 (vw), 822 (m), 777 (w), 768 (w), 628 (vw), 457 (m) cm^{-1}. Elemental analysis calc. (%) $C_{32}H_{44}CeN_8O_{10}$ (840.87 g mol^{-1}) C 45.70, H 5.27, N 13.33; found C 45.29, H 5.11, N 13.66.

[Ce$_3$(Me$_2$pz)$_9$(Me$_2$pzCO$_2$)$_3$(thf)] (3). [Ce(Me$_2$pz)$_4$(thf)] (0.050 g, 0.084 mmol) was stirred in *n*-hexane (3 mL), and CO_2 (2.1 mL, 0.084 mmol) was admitted. The reaction was stirred for 5 min at ambient temperature and then stored at −35 °C. After 2 days the supernatant solution was removed and the crystals were allowed to evaporate to dryness in the atmosphere of the glovebox, leaving [Ce$_3$(Me$_2$Pz)$_9$(Me$_2$pz·CO$_2$)$_3$(thf)] as dark red crystals. Yield: 0.023 g (0.013 mmol, 46%). ^{1}H NMR (−80 °C, 400.13 MHz, toluene-d_8) δ: 6.30 (s, 1H, C4-H Me$_2$pz), 6.29 (s, 1H, C4-H Me$_2$pz), 6.27 (s, 1H, C4-H Me$_2$pz), 6.24 (s, 1H, C4-H Me$_2$pz), 6.22 (s, 1H, C4-H Me$_2$pz), 6.20 (s, 1H, C4-H Me$_2$pz), 6.12 (s, 1H, C4-H Me$_2$pz), 6.04 (s, 1H, C4-H Me$_2$pz), 5.97 (s, 1H, C4-H Me$_2$pz), 5.26 (s, 1H, C4-H Me$_2$pzCO$_2$), 5.24 (s, 1H, C4-H Me$_2$pzCO$_2$), 5.15 (s, 1H, C4-H Me$_2$pzCO$_2$), 3.91 (bs, 2H, α-CH thf), 3.69 (bs, 2H, α-CH thf), 2.53, 2.43, 2.39, 2.33, 2.21, 2.04, 1.97, 1.91, 1.83, 1.82, 1.28, 1.25, 1.21, 1.18 ppm. Signals 1.18 – 2.53 ppm show singlets for CH$_3$ Me$_2$pz and β-CH thf. Elemental analysis calc. (%) for $C_{67}H_{92}Ce_3N_{24}O_7$ (1764.47 g mol^{-1}) C 45.57, H 5.25, N 19.04, found C 45.45, H 5.26, N 19.28.

[Ce$_4$(Me$_2$pz·CO$_2$)$_{12}$]·10 toluene (5·toluene). [Ce$_4$(Me$_2$pz)$_{12}$] (**4**) (0.285 g, 0.167 mmol) was dissolved in toluene (5 mL) and stirred under 1 bar CO_2 pressure at ambient temperature. After 5 min the light yellow solution turned colorless and was stored at −40 °C. After 3 d the supernatant solution was separated and the crystalline orange material was dried with a paper towel and subsequently at −40 °C under reduced pressure, leaving [Ce$_4$(Me$_2$pz·CO$_2$)$_{12}$]·10 toluene (**5·toluene**) as colorless crystals. Yield 0.430 g (0.136 mmol, 82 %). ^{1}H NMR (26 °C, 400.13 MHz, toluene-d_8) δ: 6.42 (s), 6.30 (s), 5.83 (s), 4.16 (s), 1.84 (s), 1.61 (s), 0.50 (s), 0.27 (s), −1.32 (s), −2.39 (s), −3.00 (s), −5.03 (s), −7.15 (s), ppm. DRIFTS: $\tilde{v}$ = 2976 (vw), 2926 (vw), 1725 (vs), 1683 (vs), 1570 (w), 1558 (w), 1516 (vw), 1466 (m), 1416 (m), 1378 (vs), 1347 (vs), 1286 (s), 1206 (w), 1157 (vw), 1127 (m), 1037 (w), 980 (w), 862 (w), 824 (w), 791 (w), 759 (w), 731 (vw) cm^{-1}. Elemental analysis calc. (%) for $C_{142}H_{164}Ce_4N_{24}O_{24}$ (3151.48 g mol^{-1}) C 54.12, H 5.25, N 10.67 found C 52.08, H 4.82, N 11.55. Low carbon and hydrogen values as well as the high nitrogen value indicate loss of toluene.

Attempted synthesis of [Ce(Me$_2$pz·CO$_2$)$_4$][NBu$_4$] (6). [Ce(Me$_2$pz)$_4$]$_2$ (**1**) (0.096 g, 0.096 mmol) was dissolved in toluene (10 mL) and tetra-*n*-butylammonium bromide (TBAB) (61.8 mg, 0.192 mmol) was added and stored under 1 bar CO$_2$ pressure for 16 h. The dark red solution turned yellow and a yellow precipitate formed. The supernatant solution was separated and the yellow residue was dried at −40 °C under reduced pressure. Yield 0.103 g. Analysis of the yellow powder revealed a poorly fitting elemental anaylsis and an inconclusive ^{1}H NMR spectrum (Figure SX). Elemental analysis calc. (%) for C$_{40}$H$_{64}$CeN$_9$O$_8$ (939.12 g mol^{-1}) C 51.16, H 6.87, N 13.42 found C 51.73, H 6.53, N 11.22.

Catalytic studies

General procedure for the synthesis of cyclic carbonates for [Ce(Me$_2$pz)$_4$]$_2$ (1)

[Ce(Me$_2$pz)$_4$]$_2$ (**1**, 10.0 mg, 9.60 *μ*mol) and tetra-*n*-butylammonium bromide (TBAB) (6.20 mg, 19.2 μmol) were dissolved in 1.92 mmol of epoxide and stirred under 1 bar CO$_2$ pressure. After 24 h the mixture was dissolved in chloroform-*d* to determine the conversion of epoxide to cyclic carbonate *via* ^{1}H NMR spectroscopy.

General procedure for the synthesis of cyclic carbonates for [Ce$_4$(Me$_2$pz)$_{12}$] (4)

[Ce$_4$(Me$_2$pz)$_{12}$] (**4**, 6.1 mg, 14.3 *μ*mol) and tetra-*n*-butylammonium bromide (TBAB) (4.60 mg, 14.3 μmol) were dissolved in 1.43 mmol of epoxide and stirred under 1 bar CO$_2$ pressure. After 24 h the mixture was dissolved in chloroform-*d* to determine the conversion of epoxide to cyclic carbonate *via* ^{1}H NMR spectroscopy.

Table S1. TOFs for complex **1** under 1 bar CO_2 pressure[a]

Entry	Time [h]	Conversion [%]	TOF [h^{-1}]
1	1/12	0	0
2	1/2	4	8
3	1	10	10
4	2	21	10.5
5	3	33	11
6	4	38	9.5
7	12	79	6.6
8	18	86	4.8
9	24	93	3.9

[a] Reaction conditions: 1 bar CO_2 pressure and 0.5 mol% of catalyst **1** and 1 mol% of cocatalyst TBAB at ambient temperature in neat propylene oxide.
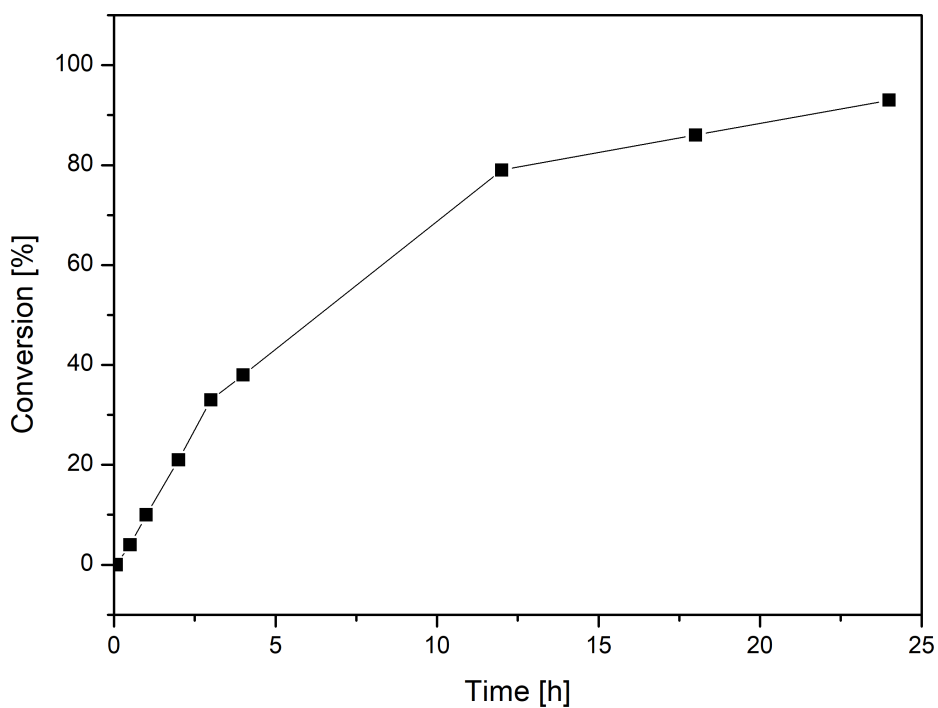
Figure S1. Conversion of propylene oxide and CO_2 catalyzed by **1** and TBAB at 1 bar CO_2 pressure plotted against the reaction time.

NMR Spectra (solvent signals are marked with *)
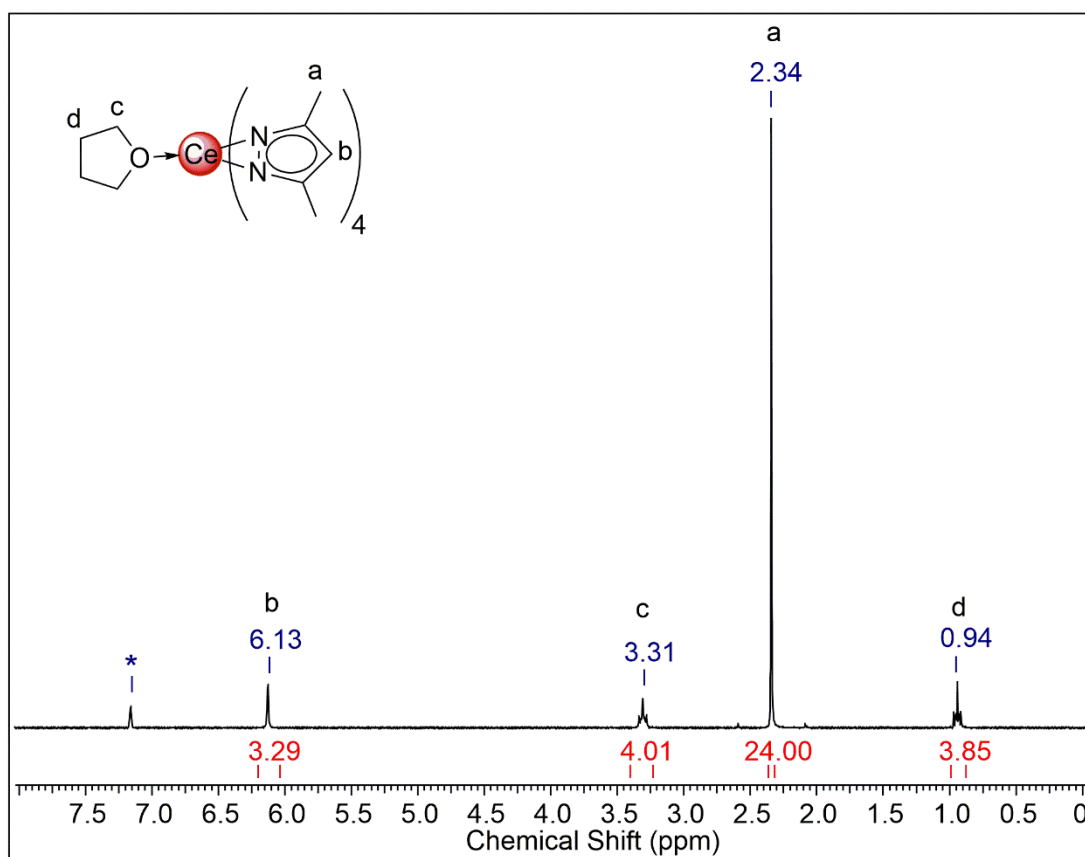
Figure S2. ^1H NMR spectrum (26 °C, 250.00 MHz, C_6D_6) of [Ce(Me$_2$pz)$_4$(thf)] (**1-thf**).
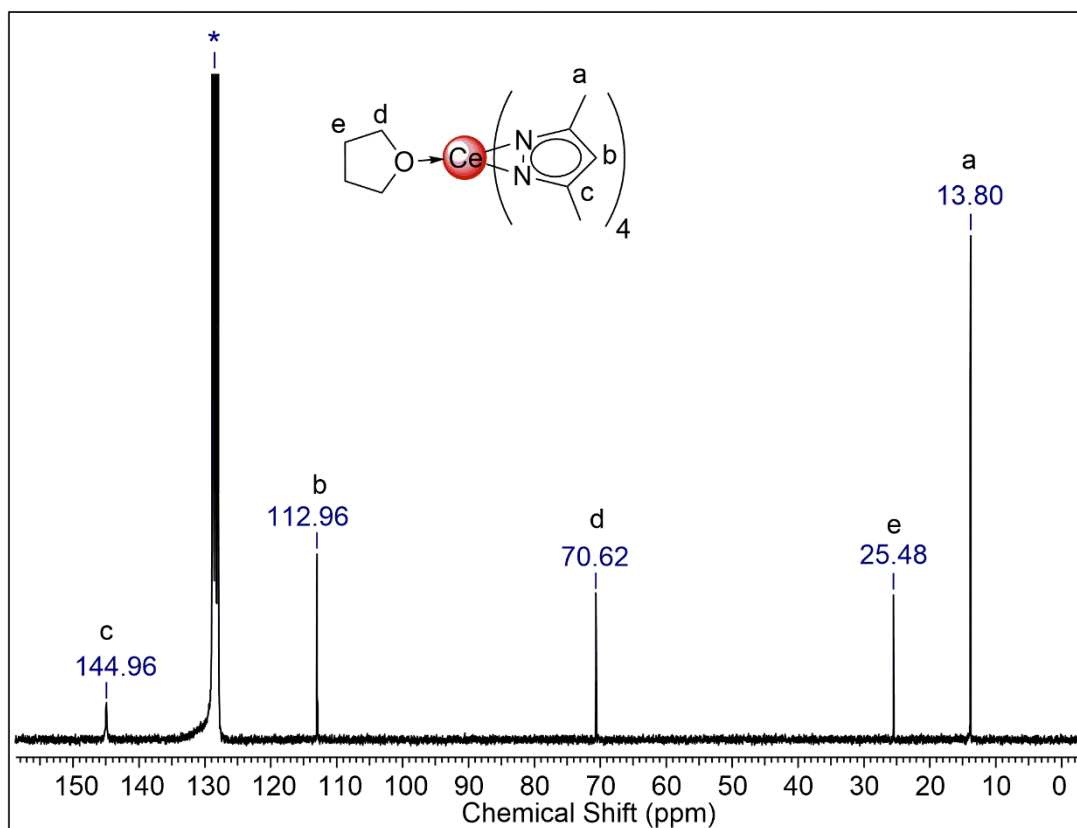
Figure S3. ^{13}C NMR spectrum (26 °C, 62.86 MHz, C_6D_6) of [Ce(Me$_2$pz)$_4$(thf)] (**1-thf**).
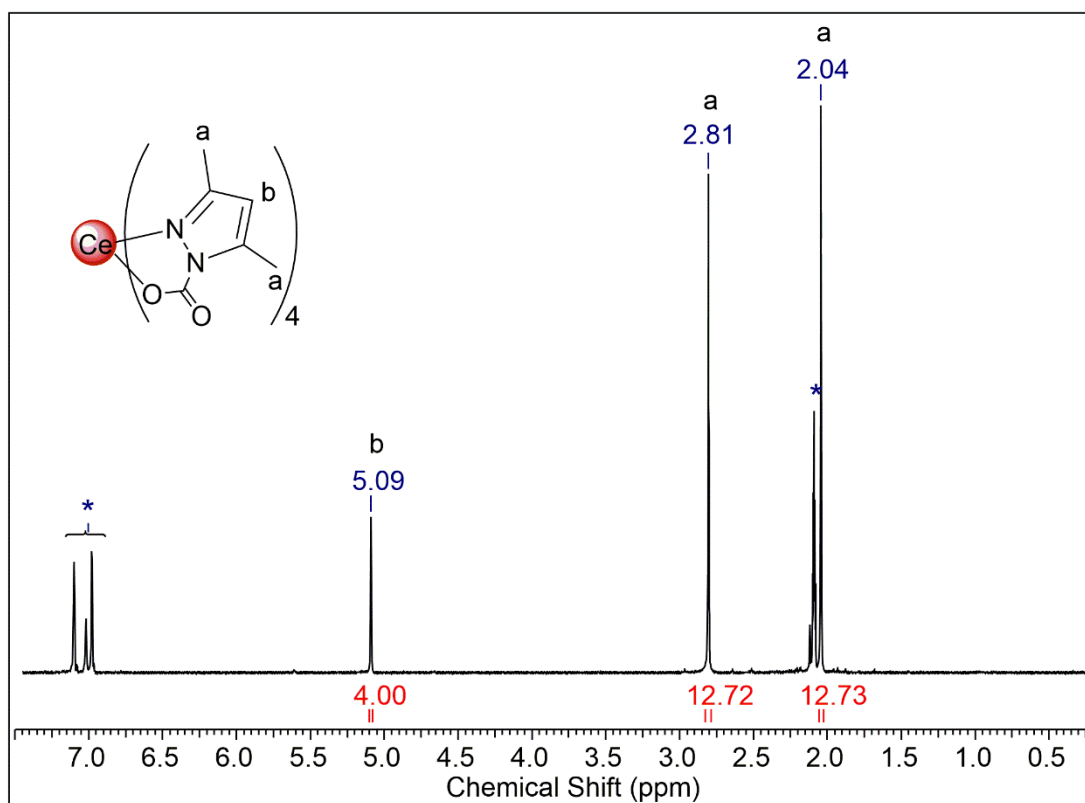
Figure S4. ^{1}H NMR spectrum (26 °C, 400.13 MHz, toluene-d_8) of [Ce(Me$_2$pz·CO$_2$)$_4$]·2 toluene (**2·toluene**).
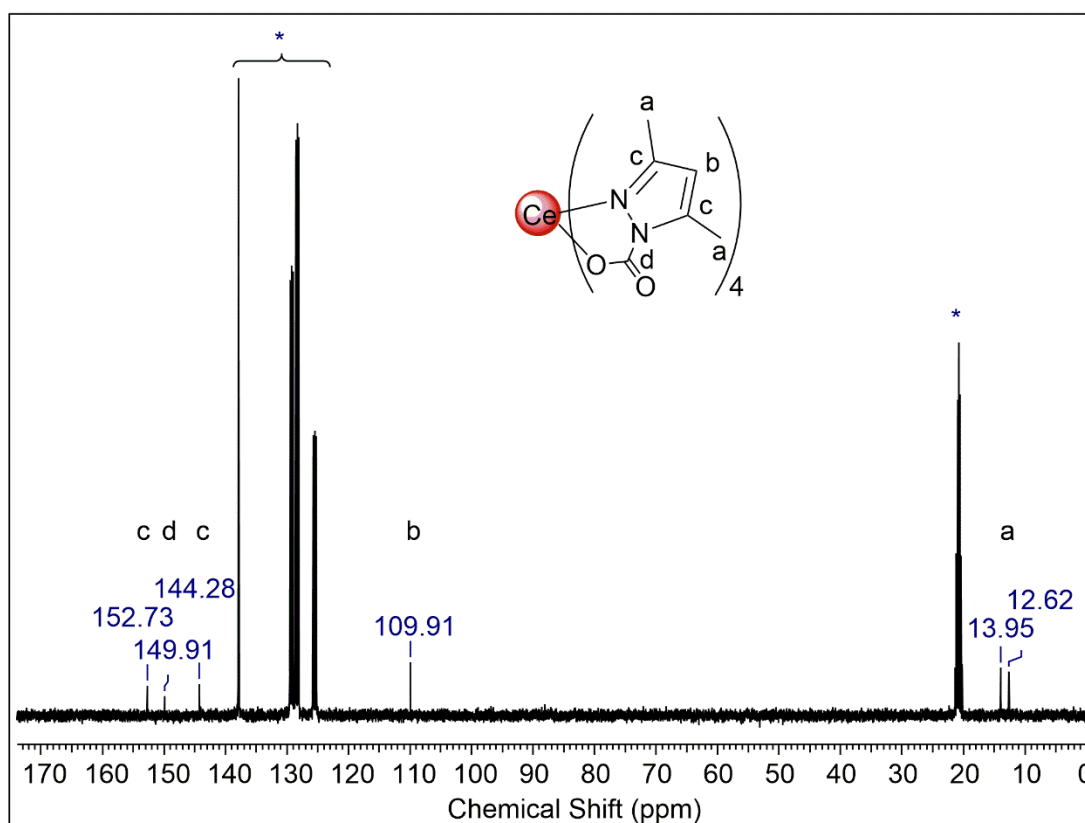
Figure S5. ^{13}C{^{1}H} NMR spectrum (26 °C, 100.16 MHz, toluene-d_8) of [Ce(Me$_2$pz·CO$_2$)$_4$]·2 toluene (**2·toluene**).
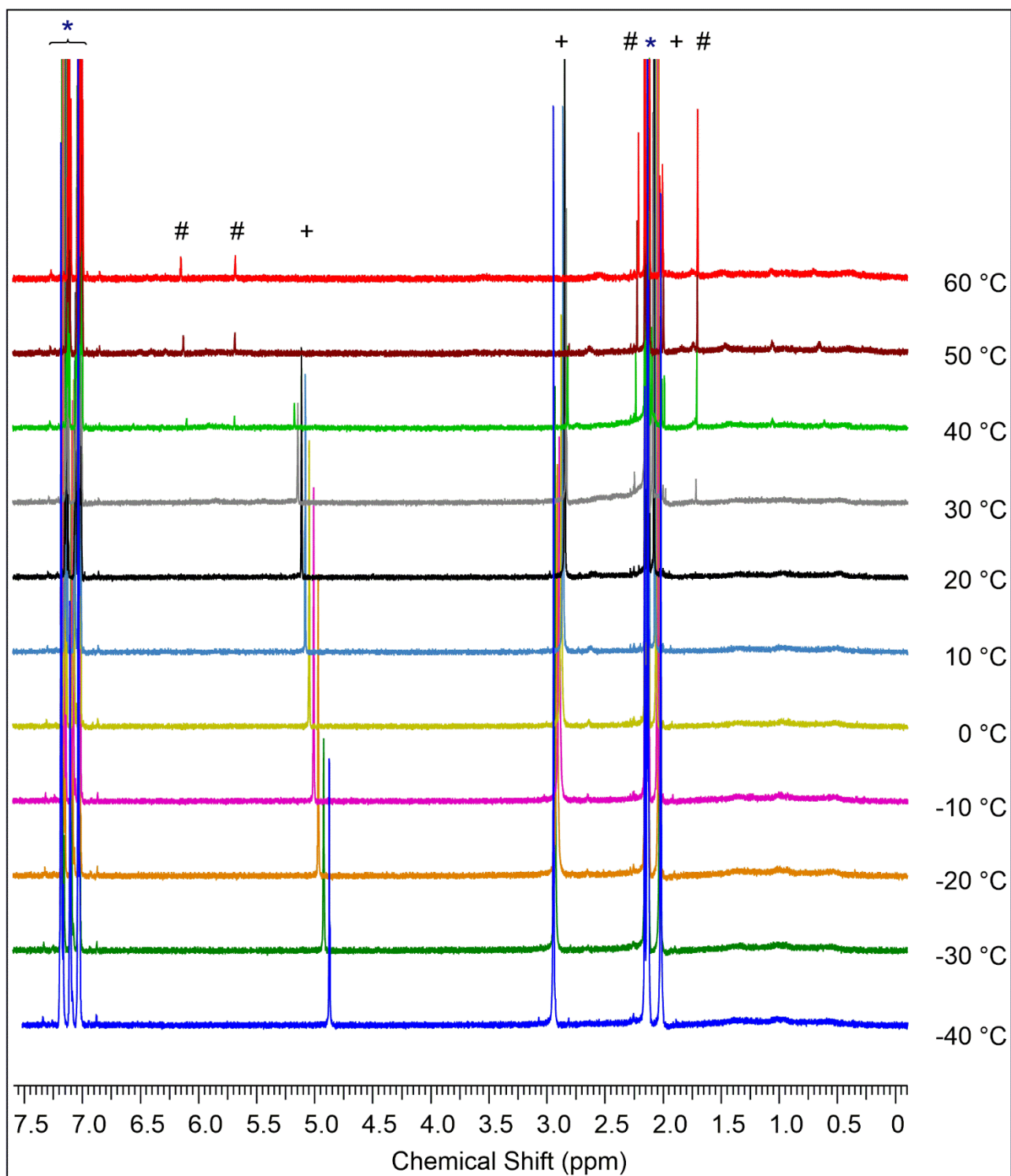
Figure S6. VT ^{1}H NMR spectra (500.13 MHz, toluene-d_8) of [Ce(Me$_2$pz·CO$_2$)$_4$]·2 toluene (**2·tolene**) in the range from −40 to 60 °C. Signals for **2·toluene** are marked with + and putative [Ce(Me$_2$pz)$_2$(Me$_2$pz·CO$_2$)$_2$] with #.
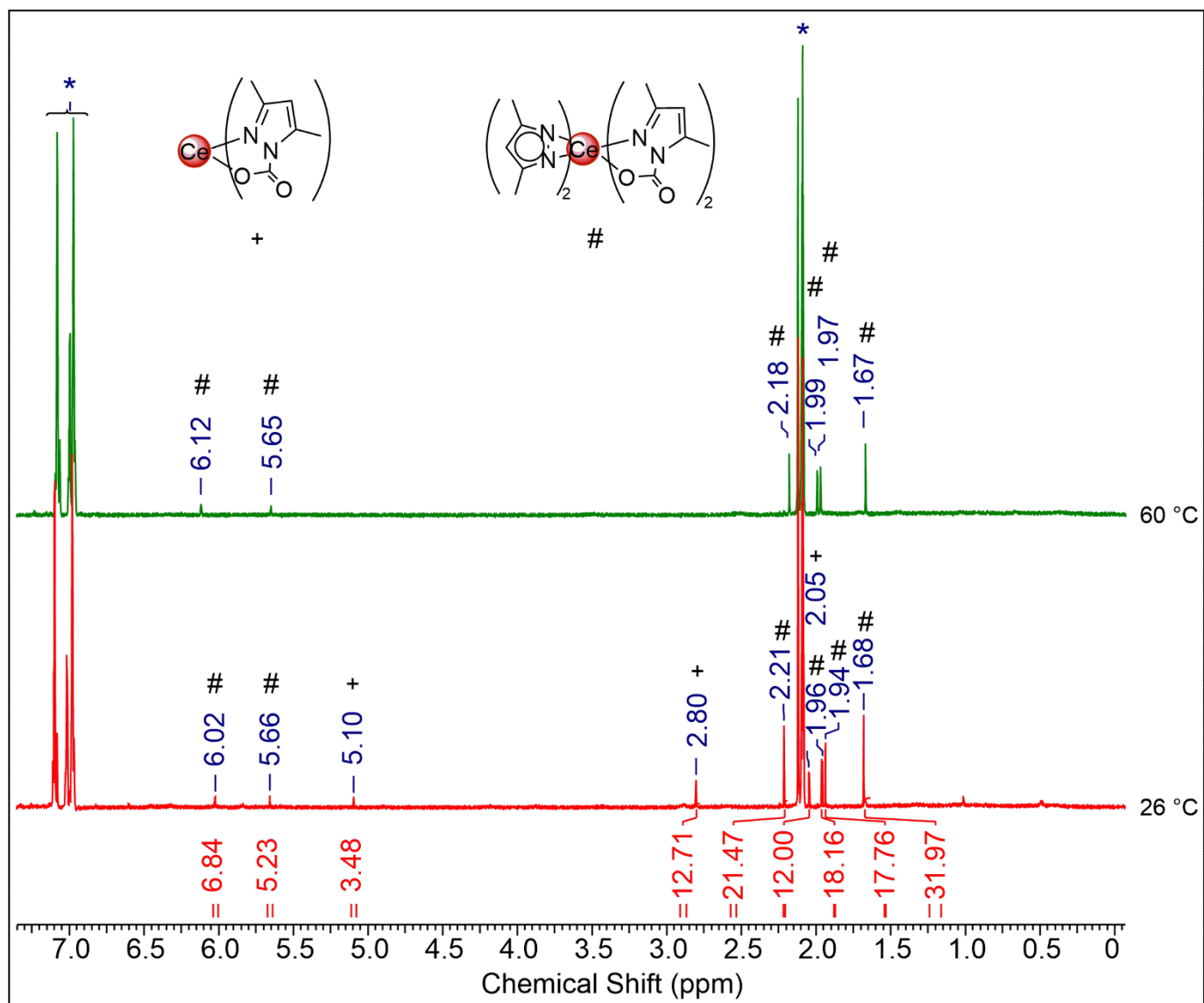
Figure S7. ^{1}H NMR spectra of $[Ce(Me_2pz \cdot CO_2)_4] \cdot 2$ toluene (**2·toluene**) in toluene-d_8 at 60 °C and after cooling to 26 °C. Signals for **2·toluene** are marked with + and putative $[Ce(Me_2pz)_2(Me_2pz \cdot CO_2)_2]$ with #.
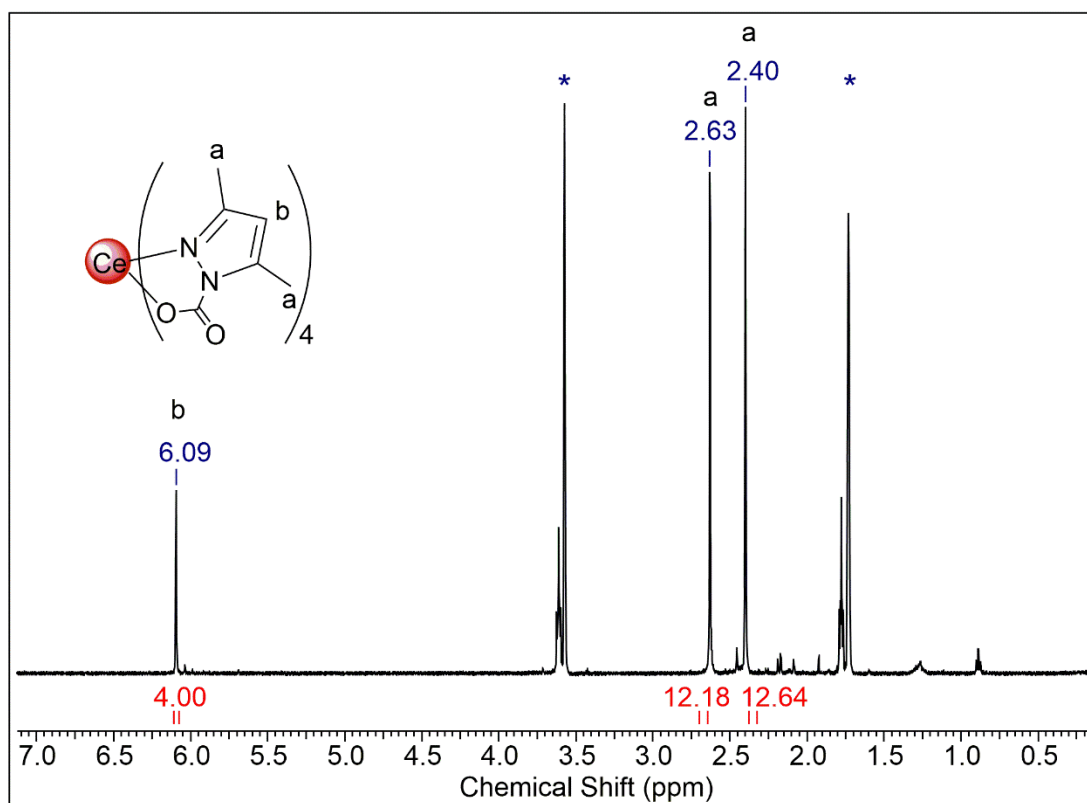
Figure S8. ^{1}H NMR spectrum (−20 °C, 500.13 MHz, thf-d_8) of [Ce(Me$_2$pz·CO$_2$)$_4$]·2 thf (**2·thf**).
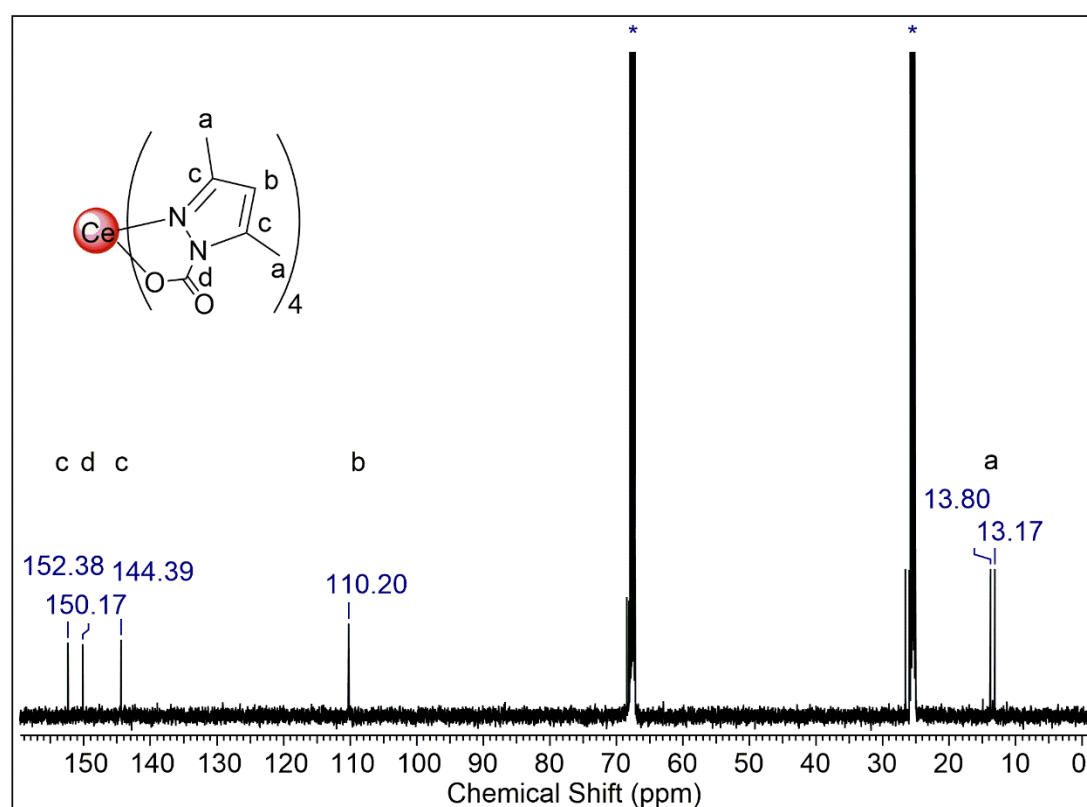
Figure S9. ^{13}C{^{1}H} NMR spectrum (−20 °C, 100.16 MHz, thf-d_8) of [Ce(Me$_2$pz·CO$_2$)$_4$]·2 thf (**2·thf**).
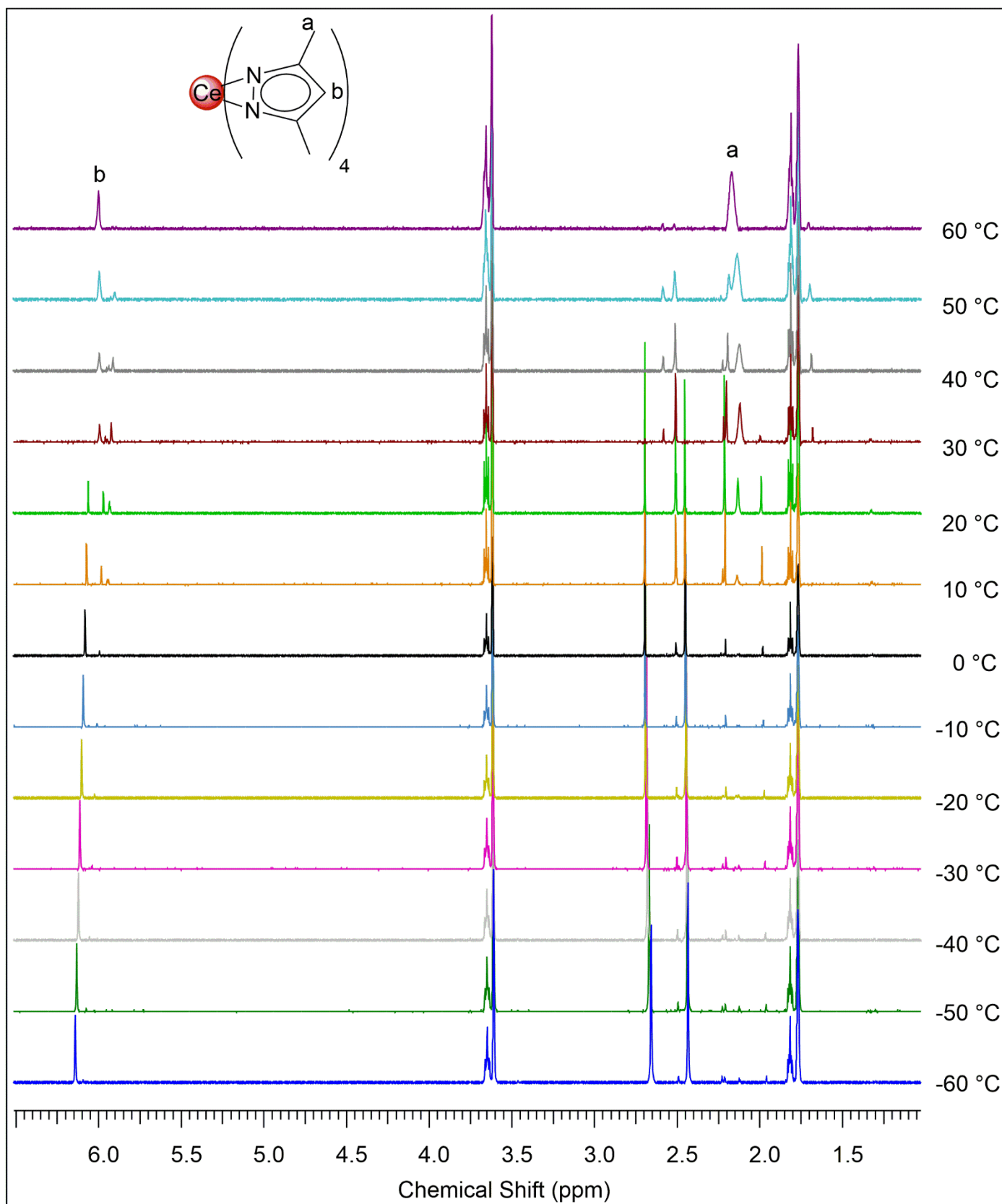
Figure S10. VT ^{1}H NMR spectra (500.13 MHz, thf-d_8) of [Ce(Me$_2$pz·CO$_2$)$_4$]·2 thf (**2·thf**) in the range from −60 to 60 °C showing the formation of [Ce(Me$_2$pz)$_4$]$_2$ (**1**) at 60 °C.
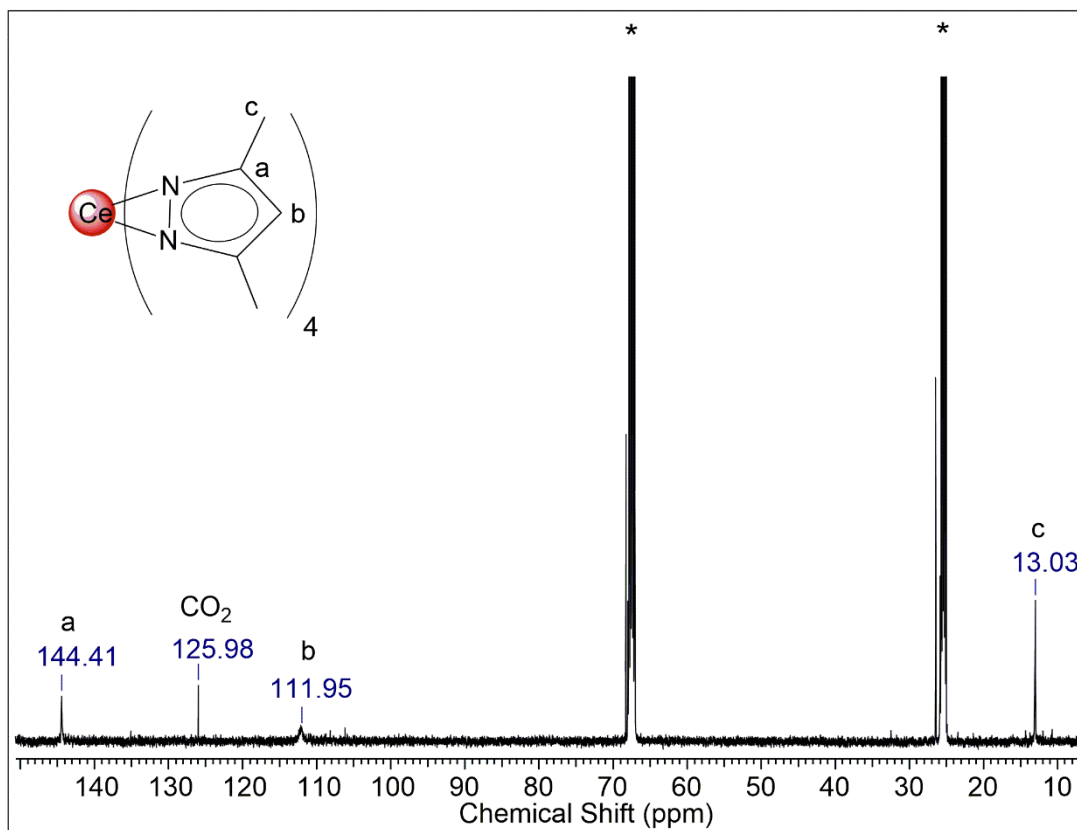
Figure S11. $^{13}C\{^1H\}$ NMR spectrum (60 °C, 100.16 MHz, thf-d_8) of [Ce(Me$_2$pz·CO$_2$)$_4$]·2 thf (**2·thf**).
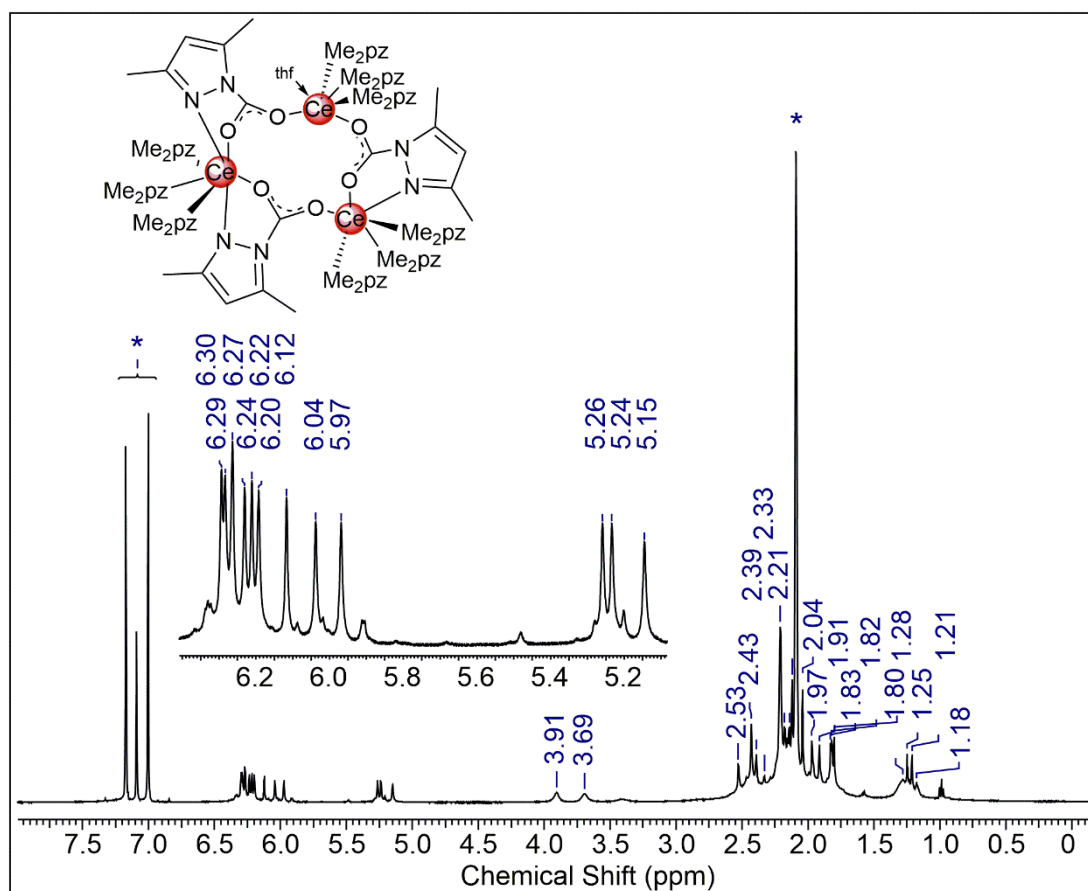
Figure S12. ^{1}H NMR spectrum (−80 °C, 500.13 MHz, toluene-d_8) of [Ce$_3$(Me$_2$pz)$_9$(Me$_2$pz·CO$_2$)$_3$(thf)] (**3**).
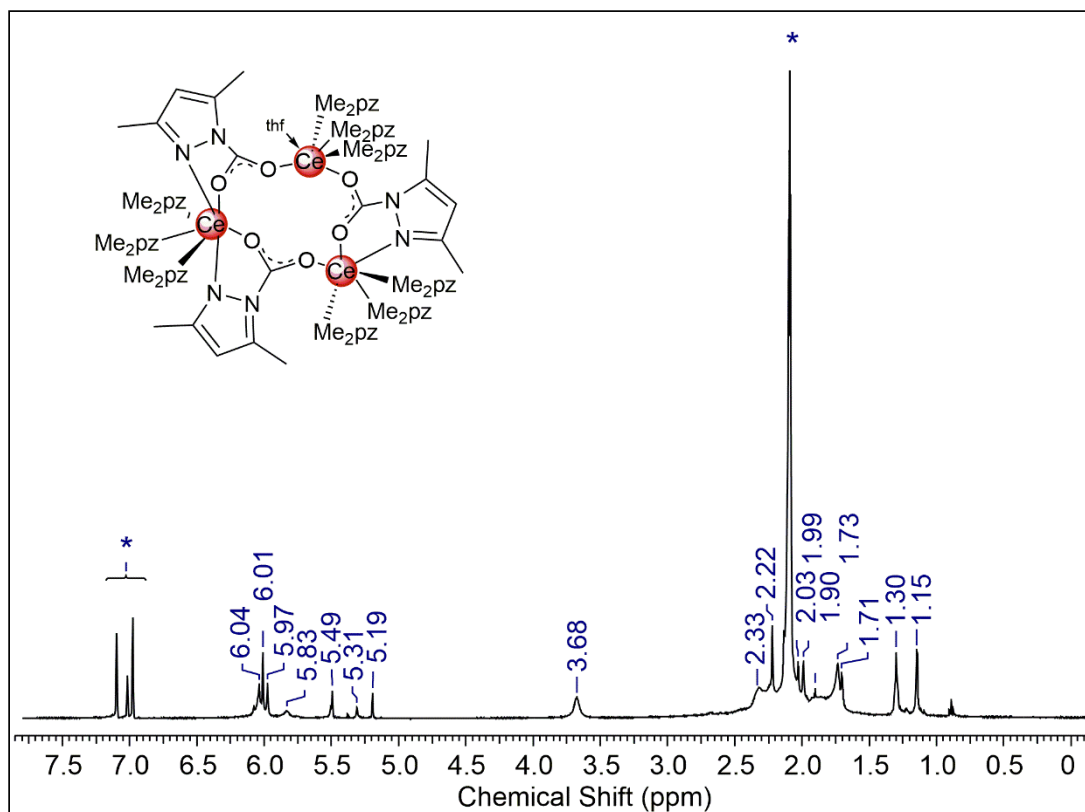
Figure S13. ^{1}H NMR spectrum (26 °C, 500.13 MHz, toluene-d_8) of [Ce$_3$(Me$_2$pz)$_9$(Me$_2$pz·CO$_2$)$_3$(thf)] (**3**).
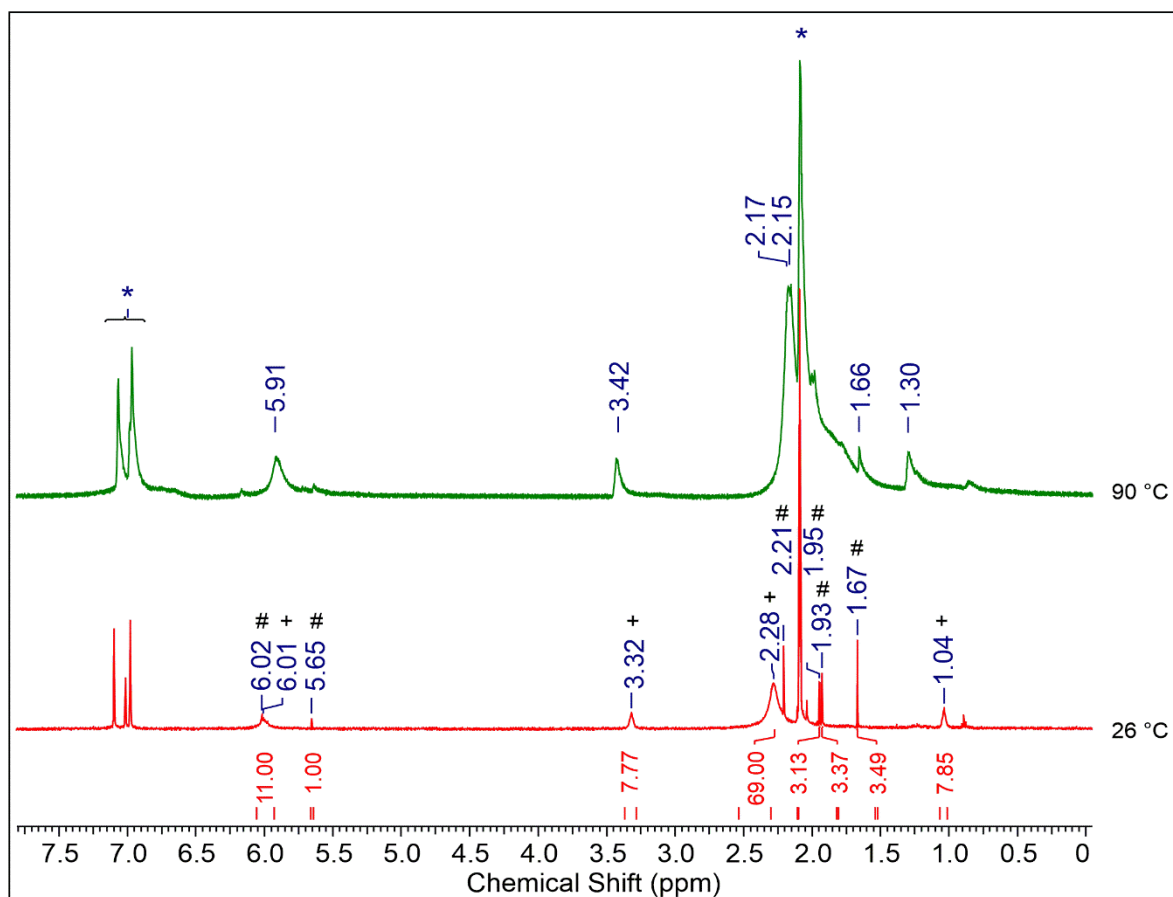
Figure S14. ^{1}H NMR spectra of [Ce$_3$(Me$_2$pz)$_9$(Me$_2$pz·CO$_2$)$_3$(thf)] (**3**) in toluene-d_8 at 90 °C and after cooling to 26 °C. Signals for [Ce(Me$_2$pz)$_4$(thf)] are marked with + and unknown other product with #.
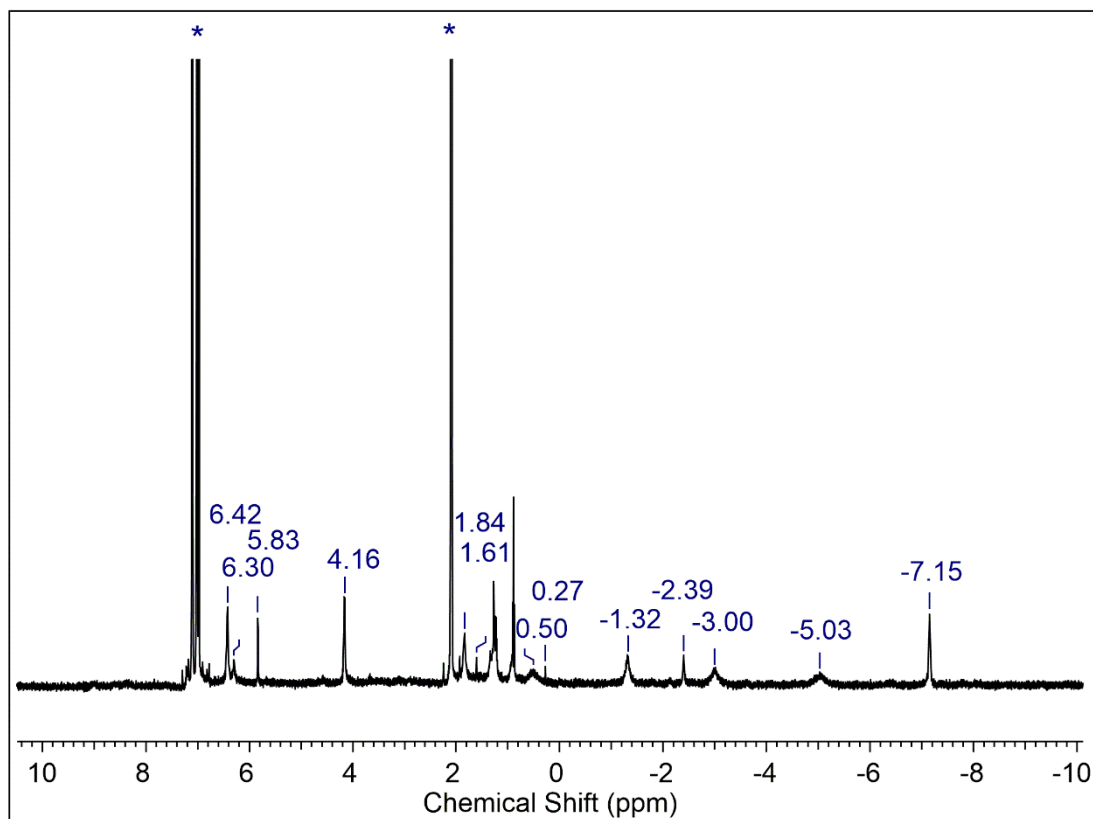
Figure S15. ^{1}H NMR spectrum (26 °C, 400.13 MHz, toluene-d_8) of [Ce$_4$(Me$_2$pz·CO$_2$)$_{12}$]·10 toluene (**5·toluene**).
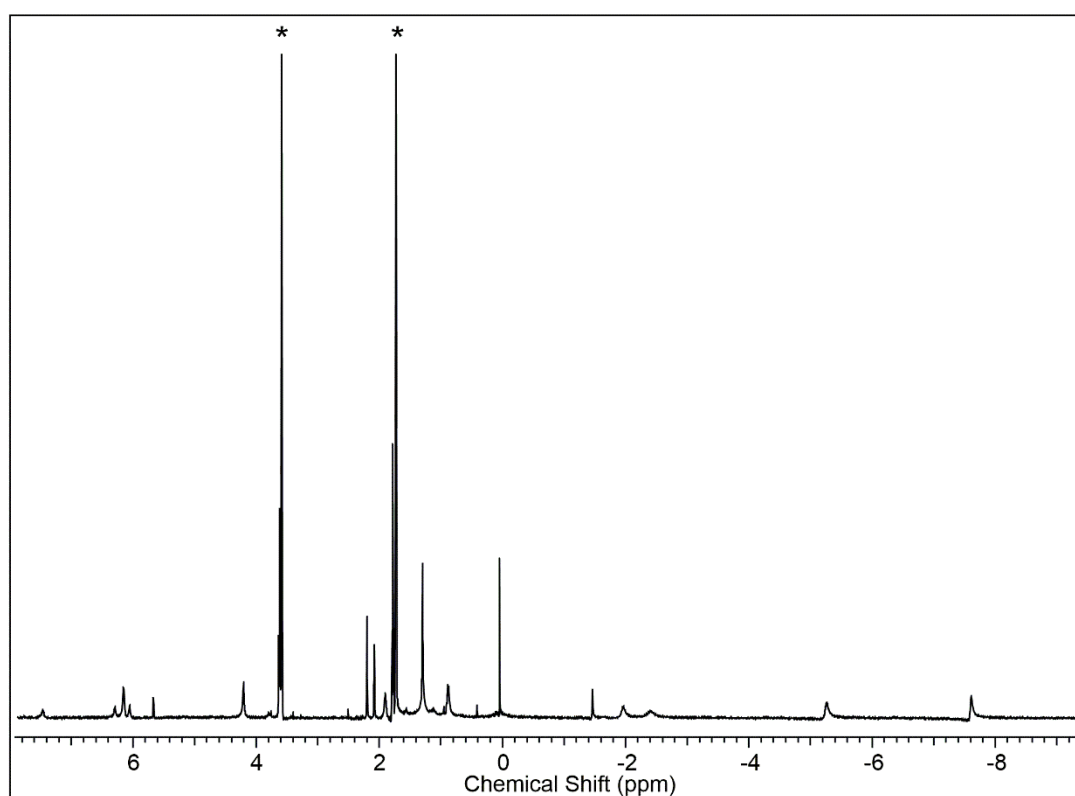
Figure S16. ^{1}H NMR spectrum (26 °C, 400.13 MHz, thf-d_8) of the reaction of [Ce(Me$_2$pz)$_3$(thf)$_2$] with CO$_2$ in thf-d_8.
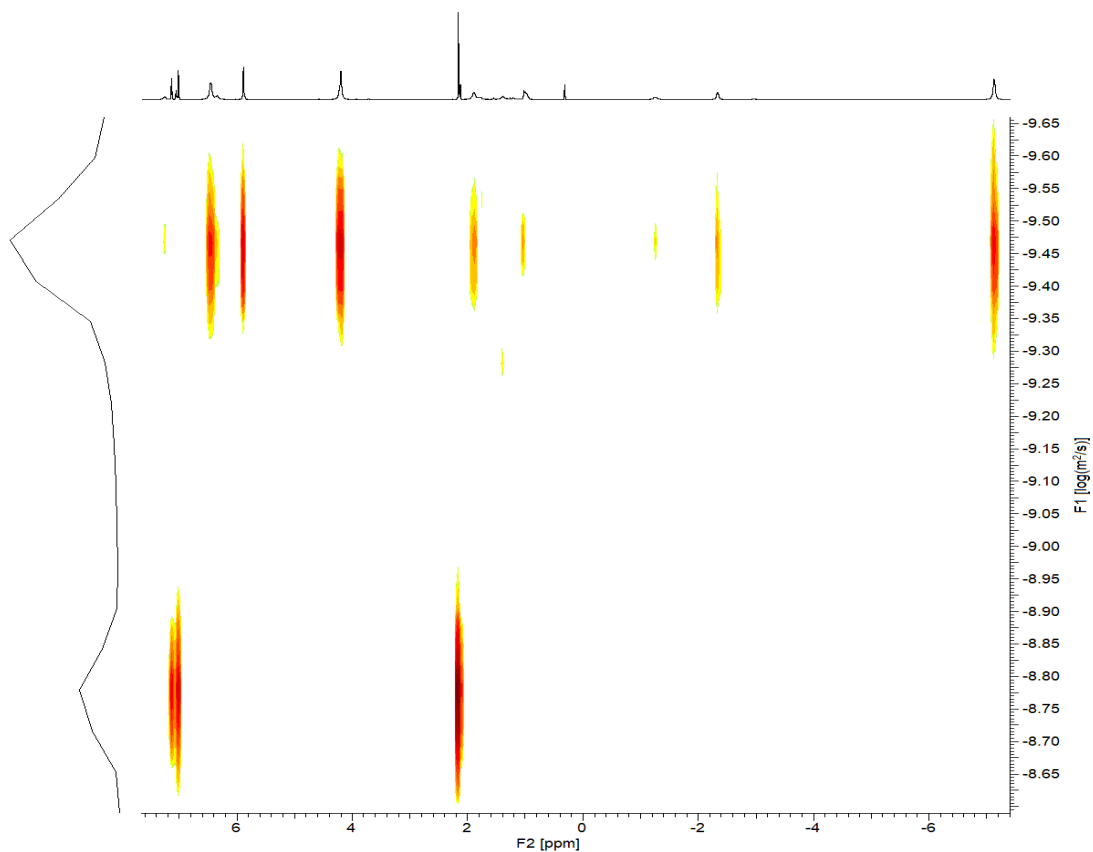
Figure S17. ^{1}H DOSY NMR spectrum (26 °C, 600.13 MHz, toluene-d_8) of [Ce$_4$(Me$_2$pz$^:$CO$_2$)$_{12}$]·10 toluene (**5·toluene**) showing toluene at −8.78 and [Ce$_4$(Me$_2$pz$^:$CO$_2$)$_{12}$] at −9.47 log(m^2/s) (M = 1989 g·mol^{-1}).
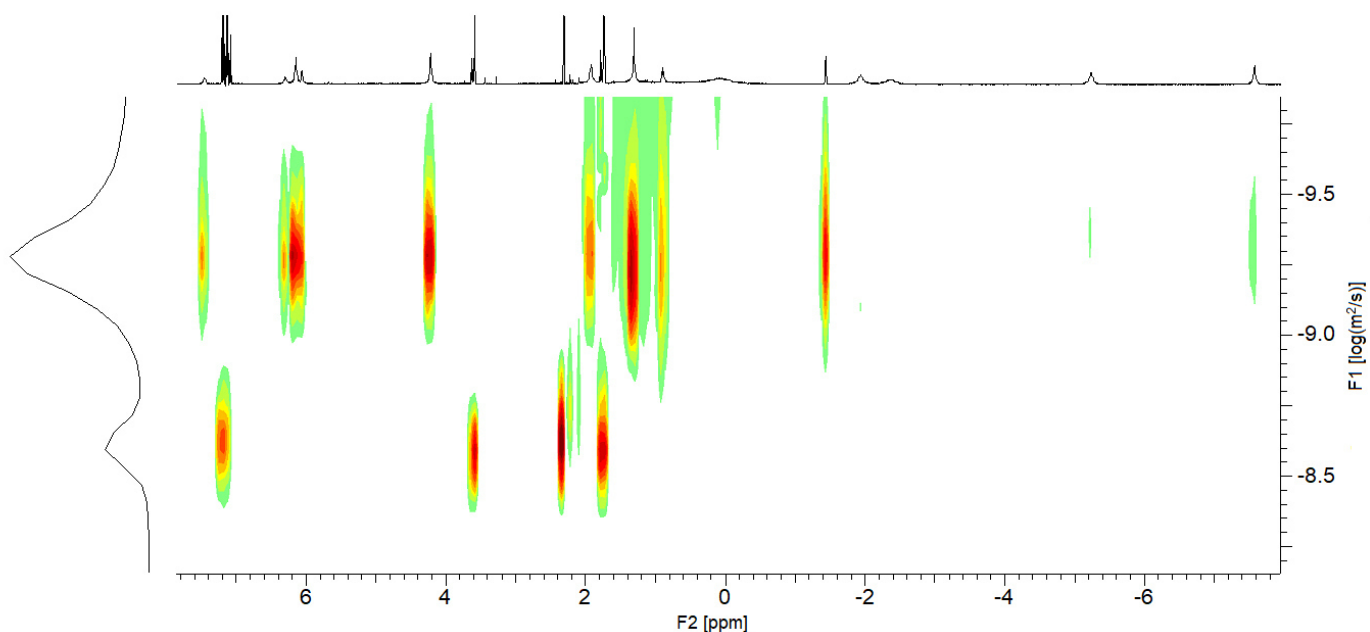
Figure S18. ^{1}H DOSY NMR spectrum (26 °C, 500.13 MHz, thf-d_8) of [Ce$_4$(Me$_2$pz$^:$CO$_2$)$_{12}$]·10 toluene (**5·toluene**) showing thf-d_8 at −8.587, toluene at −8.620 (M = 75 g·mol^{-1}) and [Ce$_4$(Me$_2$pz$^:$CO$_2$)$_{12}$] at −9.282 log(m^2/s) (M = 1643 g·mol^{-1}).
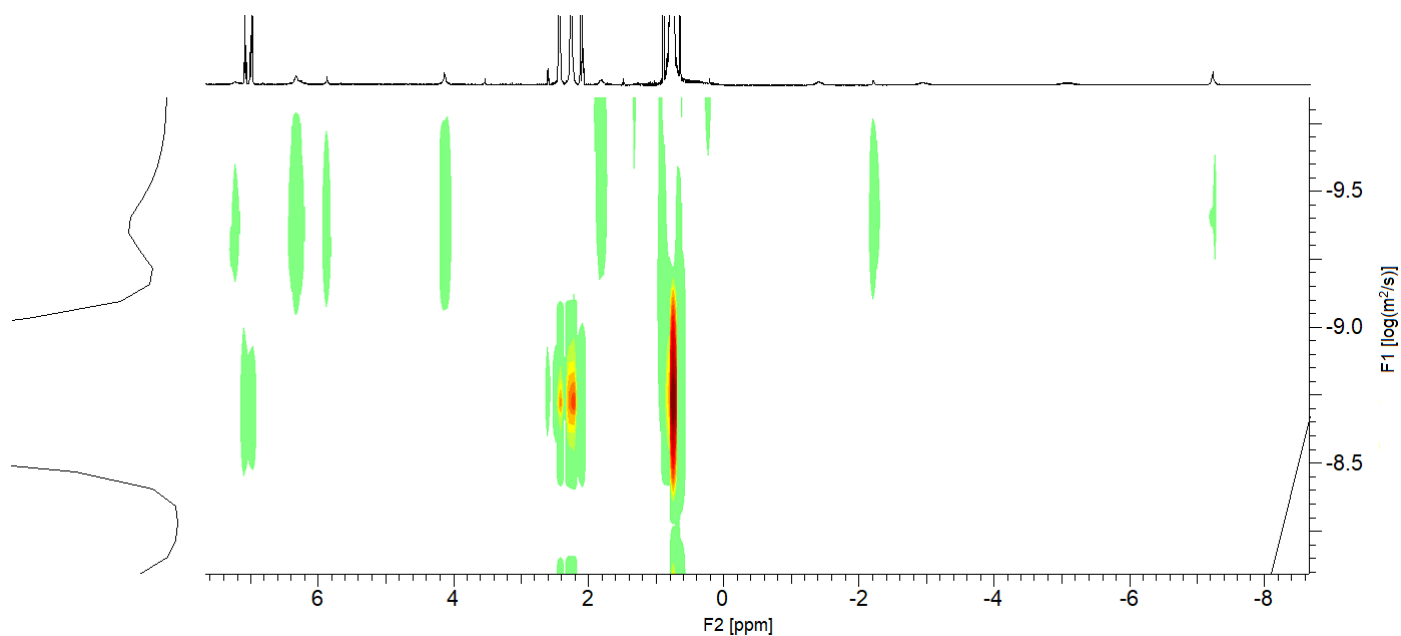
Figure S19. ^{1}H DOSY NMR spectrum (26 °C, 500.13 MHz, toluene-d_8) of [Ce$_4$(Me$_2$pz$^\cdot$CO$_2$)$_{12}$]·10 toluene (**5·toluene**) + excess of 3,3-dimethyl-1,2-butene oxide showing toluene-d_8 at −8.658, 3,3-dimethyl-1,2-butene oxide at −8.722 (M = 114 g·mol^{-1}) and [Ce$_4$(Me$_2$pz$^\cdot$CO$_2$)$_{12}$] at −9.382 log(m^2/s) (M = 2357 g·mol^{-1}).
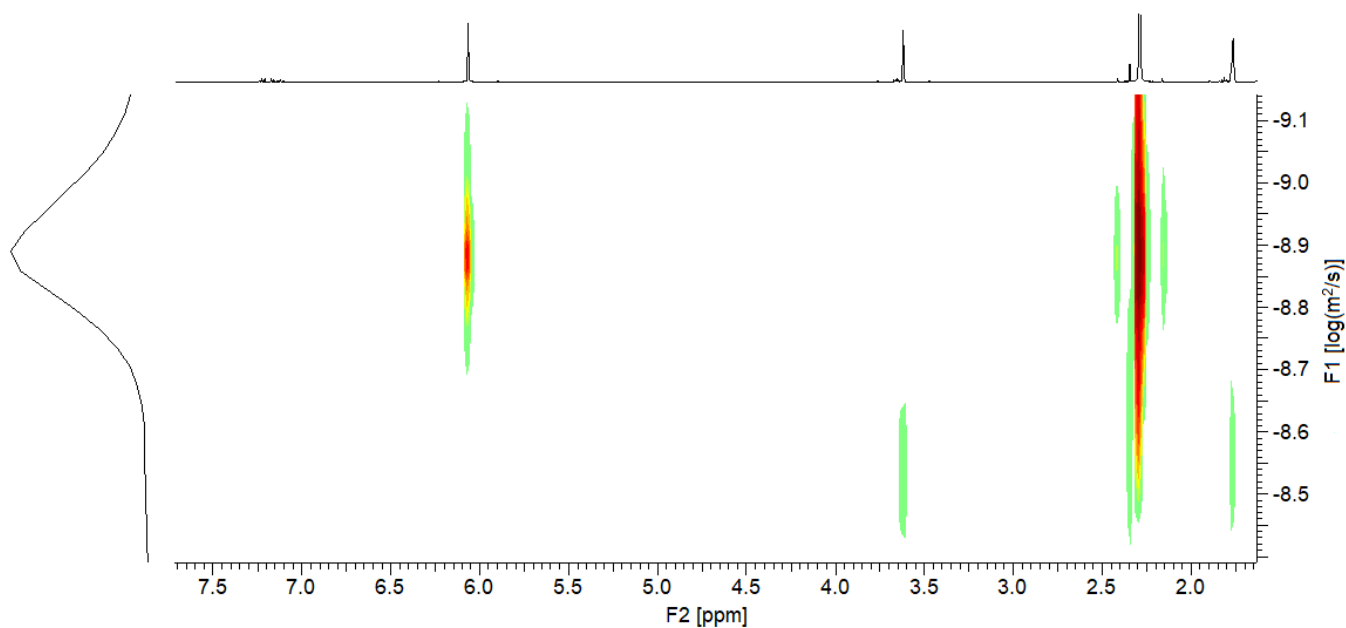
Figure S20. ^{1}H DOSY NMR spectrum (26 °C, 500.13 MHz, thf-d_8) of [Ce(Me$_2$pz)$_4$(thf)]·(**1·thf**) showing thf-d_8 at −8.530 and [Ce(Me$_2$pz)$_4$(thf)] at −8.896 log(m^2/s) (M = 354 g·mol^{-1}).
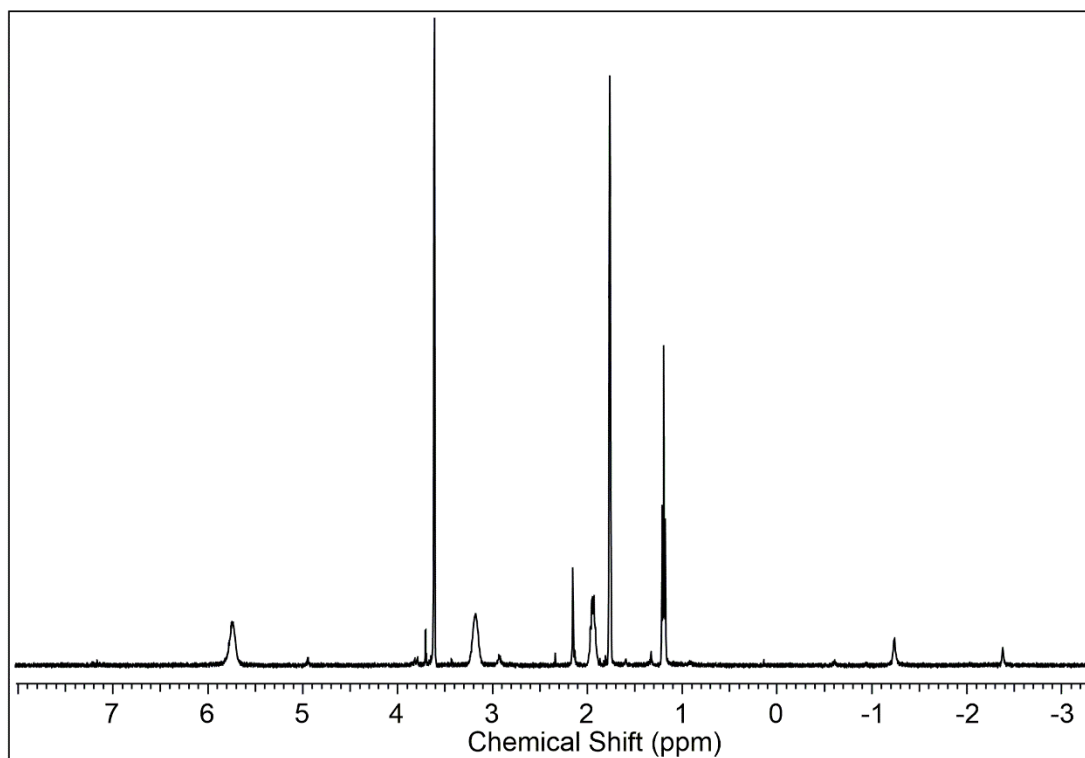
Figure S21. ^{1}H NMR spectrum (26 °C, 400.13 MHz, thf-d_8) of the reduction of [Ce(Me$_2$pz·CO$_2$)$_4$] (**2**) with TBAB.
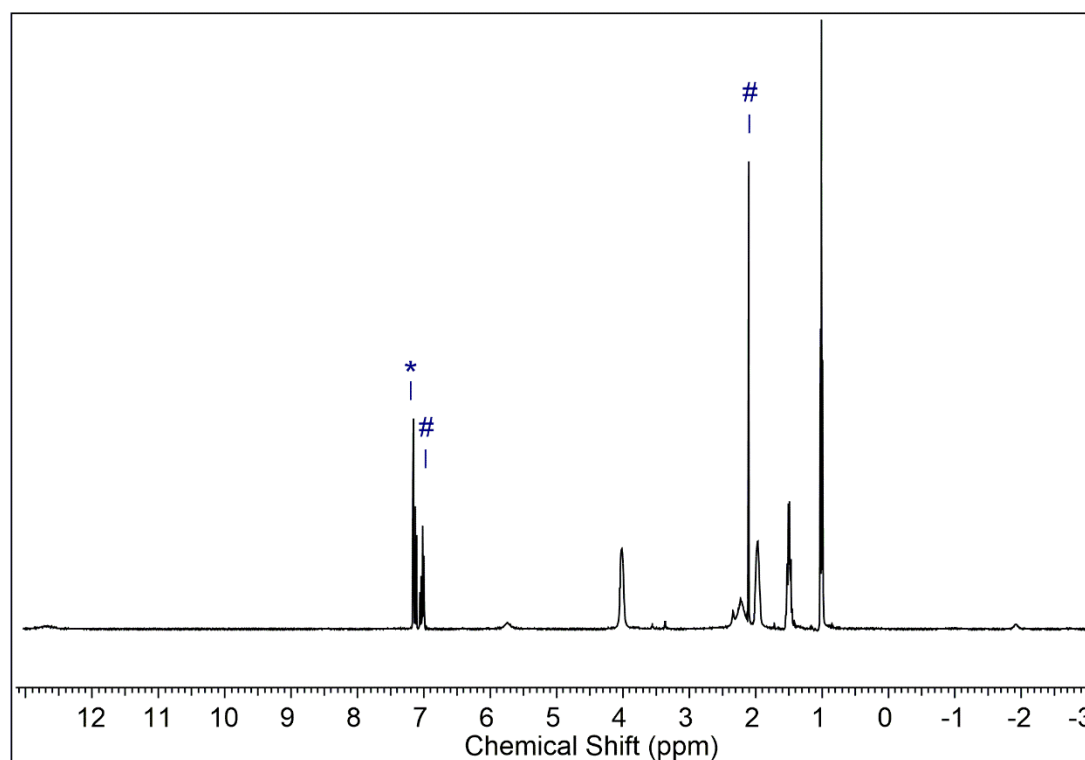
Figure S22. ^{1}H NMR spectrum (26 °C, 400.13 MHz, benzene-d_6) of the supernatant of the reduction of [Ce(Me$_2$pz·CO$_2$)$_4$] (**2**) together with TBAB. Toluene signals are marked with #.

S18
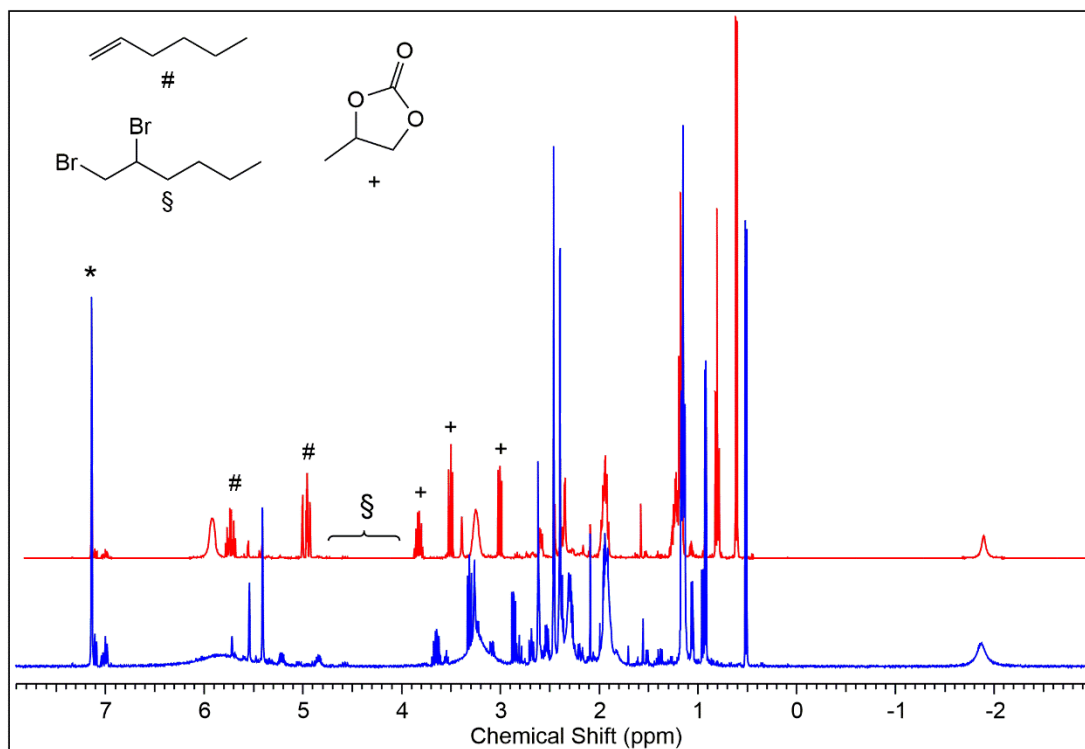
Figure S23. ^{1}H NMR spectrum (26 °C, 400.13 MHz, benzene-d_6) of the reaction of [Ce(Me$_2$pz·CO$_2$)$_4$] (**2**) with TBAB, CO$_2$ and propylene oxide (blue trace) and [Ce(Me$_2$pz·CO$_2$)$_4$] (**2**) with TBAB, CO$_2$, propylene oxide and 1-n-hexene (red trace). Signals for 1,2-dibromohexane would be expected in the region marked with §.
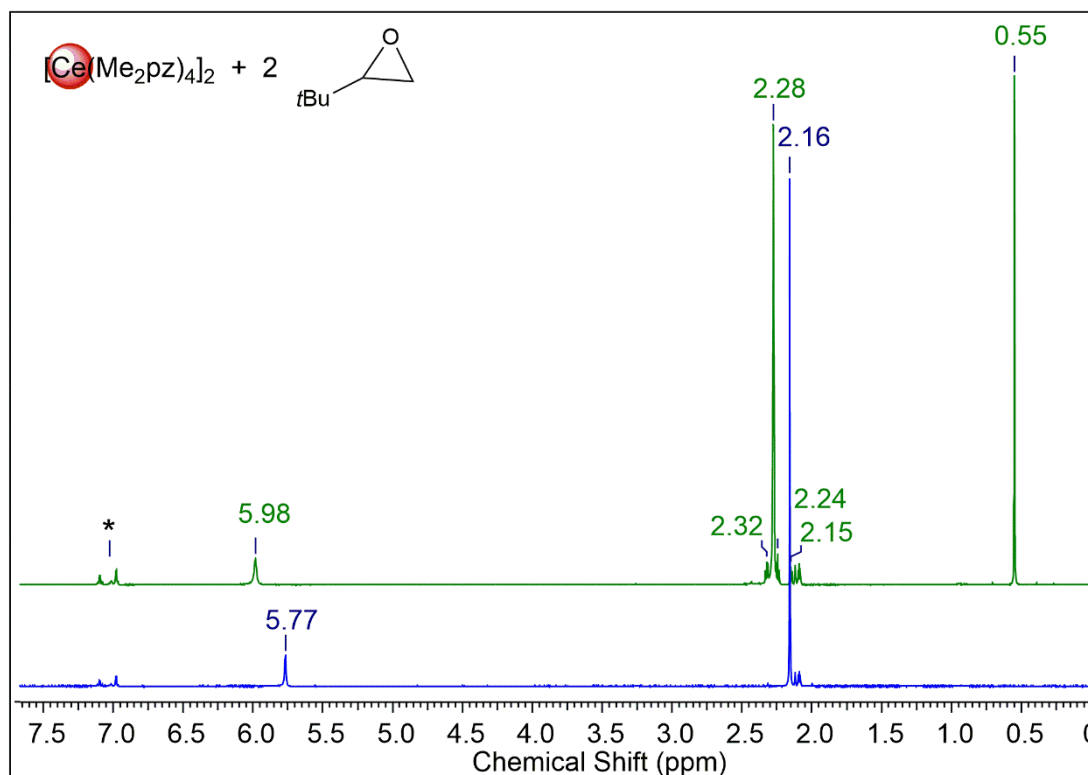
Figure S24. ^{1}H NMR spectrum (26 °C, 400.13 MHz, toluene-d_8) of [Ce(Me$_2$pz)$_4$]$_2$·(blue trace) and [Ce(Me$_2$pz)$_4$]$_2$ plus 3,3-dimethyl-1,2-butene oxide (green trace).
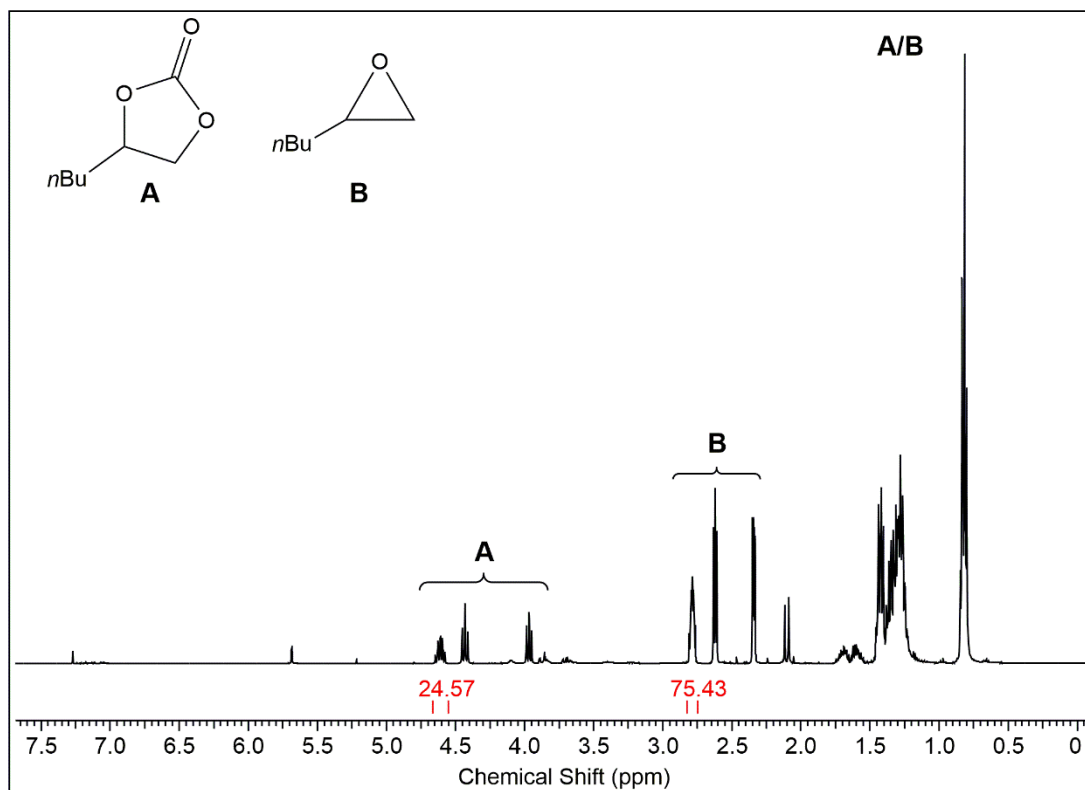
S19
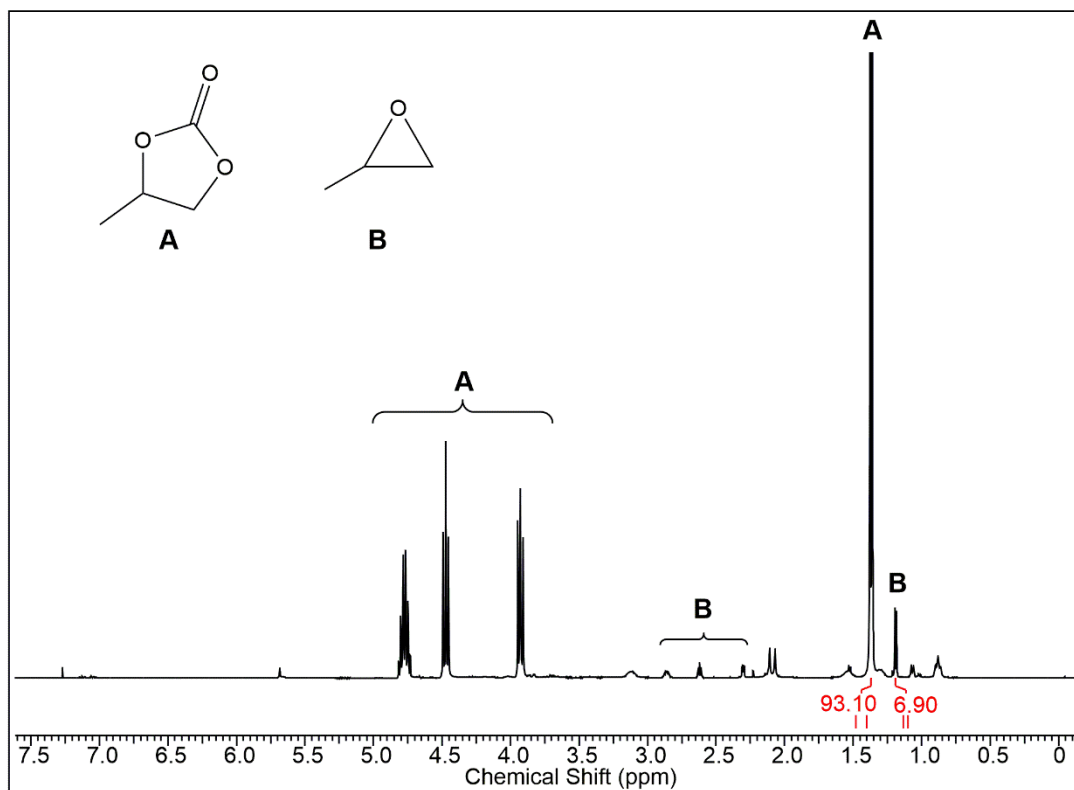
Figure S25. ^{1}H NMR (26 °C, 400.13 MHz, chloroform-*d*) of the product mixture of the catalytic formation of propylene carbonate using 0.5 mol% [Ce(Me2pz)4]2 (**1**) as a catalyst. The conversion was determined by the integral ratio of the methyl protons in propylene oxide and propylene carbonate.
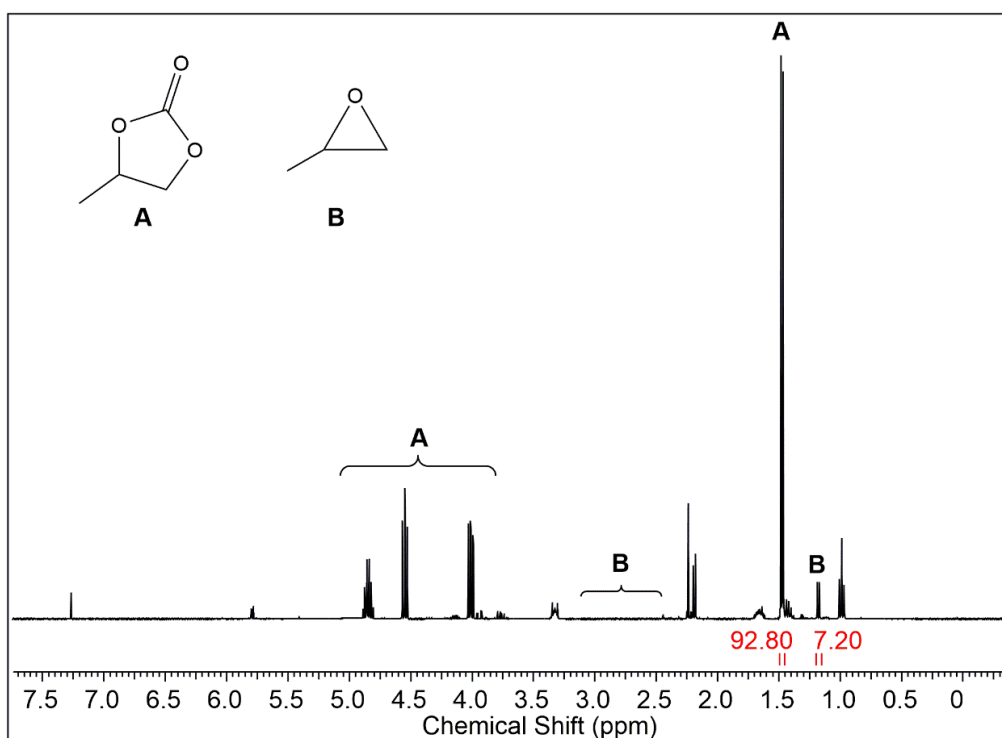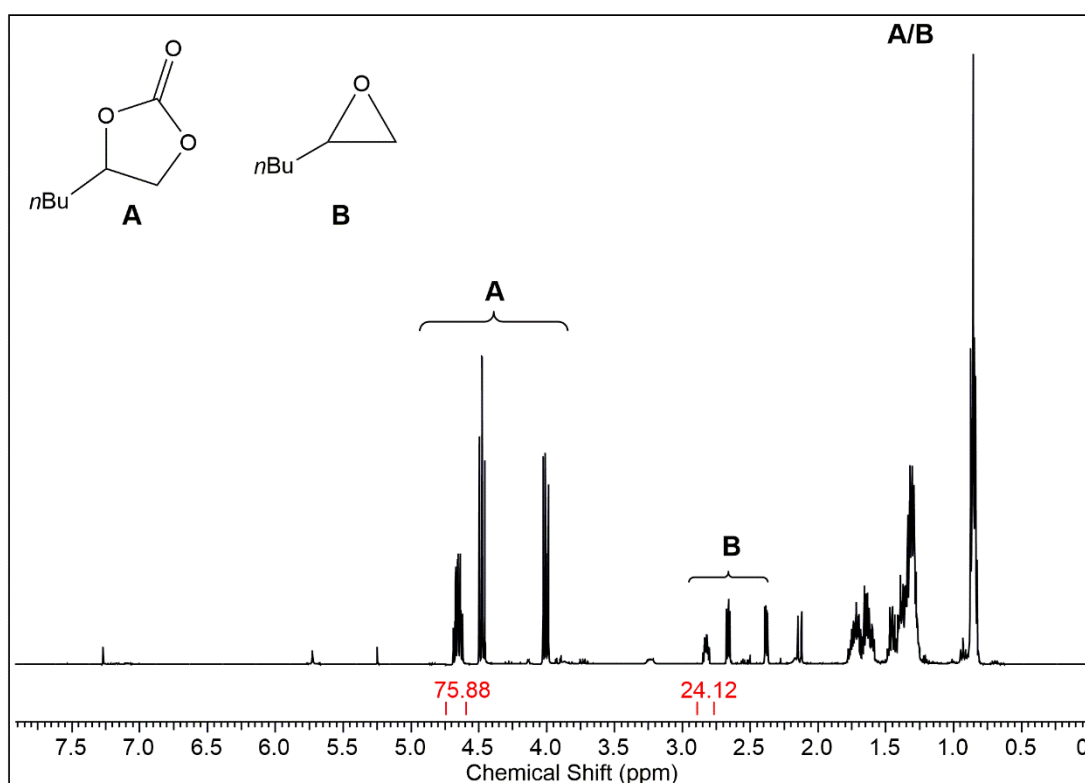

Figure S26. ^{1}H NMR (26 °C, 400.13 MHz, chloroform-*d*) of the product mixture of the catalytic formation of propylene carbonate using 1 mol% [Ce(Me2pz·CO2)4]·2 thf (**2·thf**) as a catalyst. The conversion was determined by the integral ratio of the methyl protons in propylene oxide and propylene carbonate.
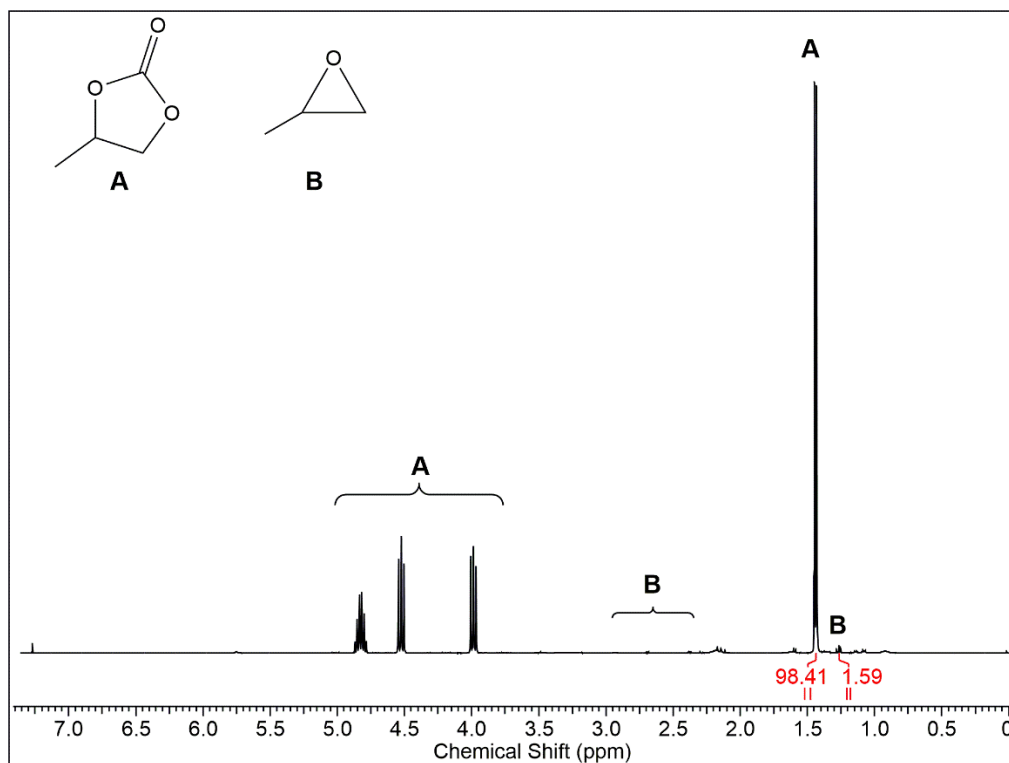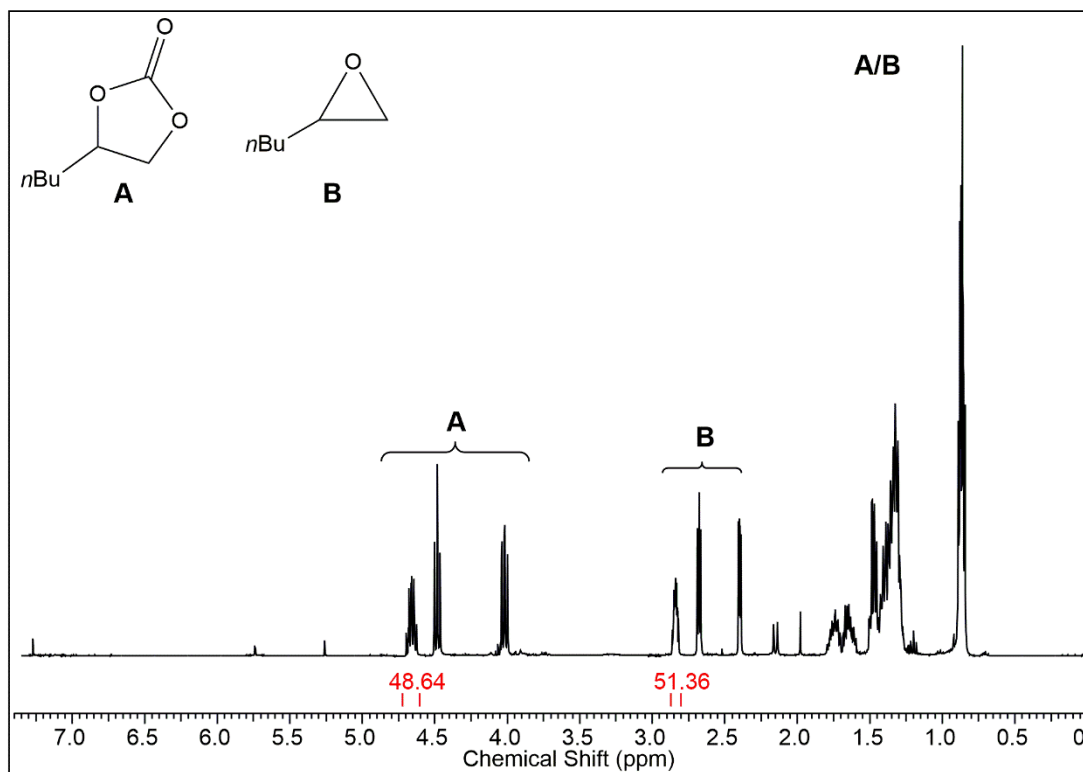
Figure S27. ^{1}H NMR (26 °C, 400.13 MHz, chloroform-*d*) of the product mixture of the catalytic formation of propylene carbonate using 0.25 mol% [Ce(Me$_2$pz)$_4$]$_2$ (**1**) as a catalyst at 90 °C and 10 bar CO$_2$ pressure for 1 hour. The conversion was determined by the integral ratio of the methyl protons in propylene oxide and propylene carbonate.
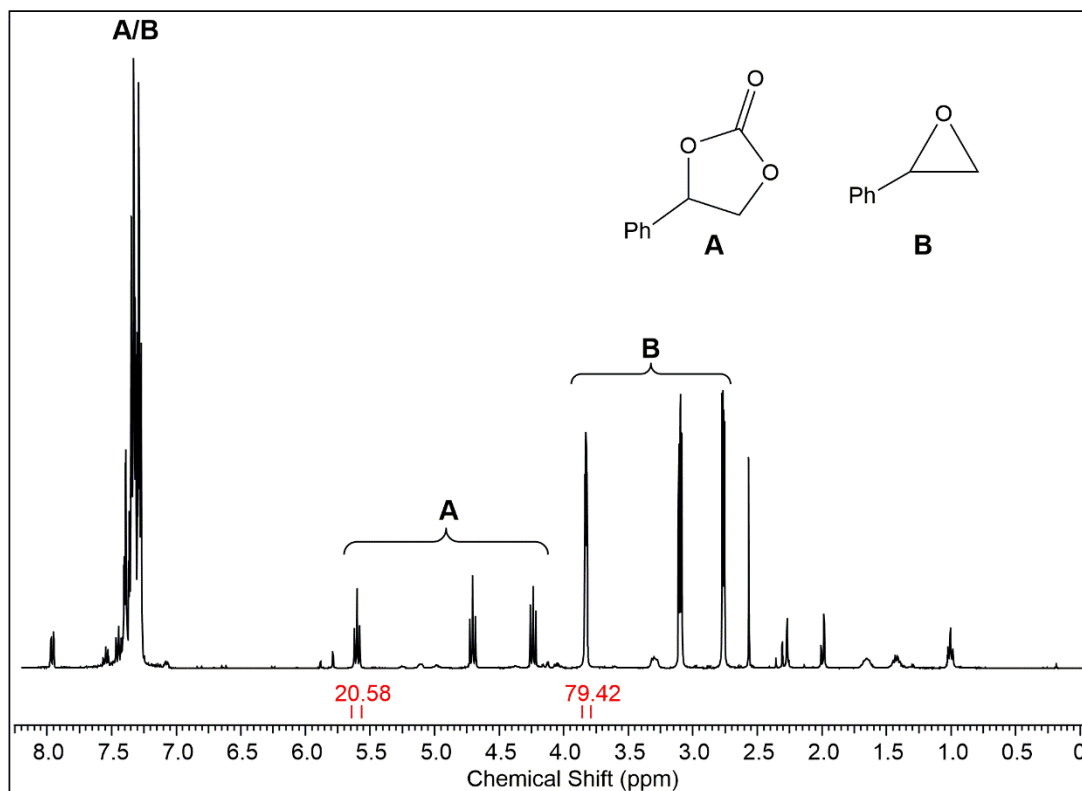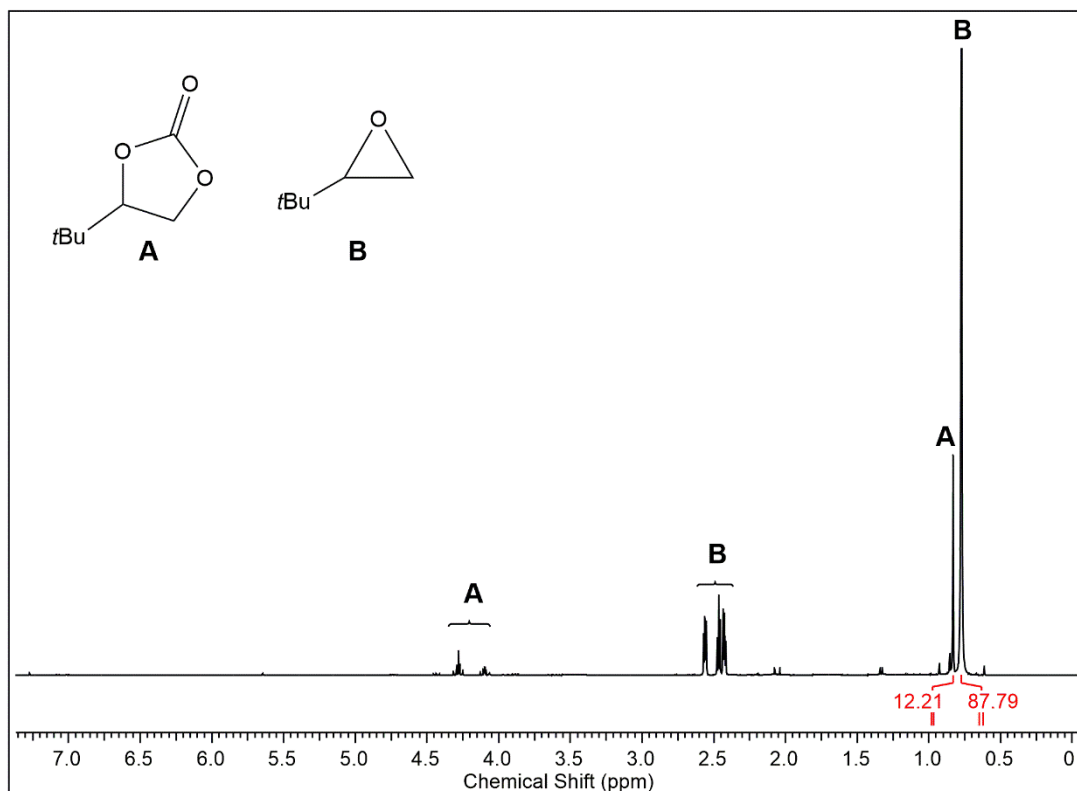

Figure S28. ^{1}H NMR (26 °C, 400.13 MHz, chloroform-*d*) of the product mixture of the catalytic formation of styrene carbonate using 0.5 mol% [Ce(Me$_2$pz)$_4$]$_2$ (**1**) as a catalyst. The conversion was determined by the integral ratio of the protons in α-position in styrene oxide and styrene carbonate.

S21
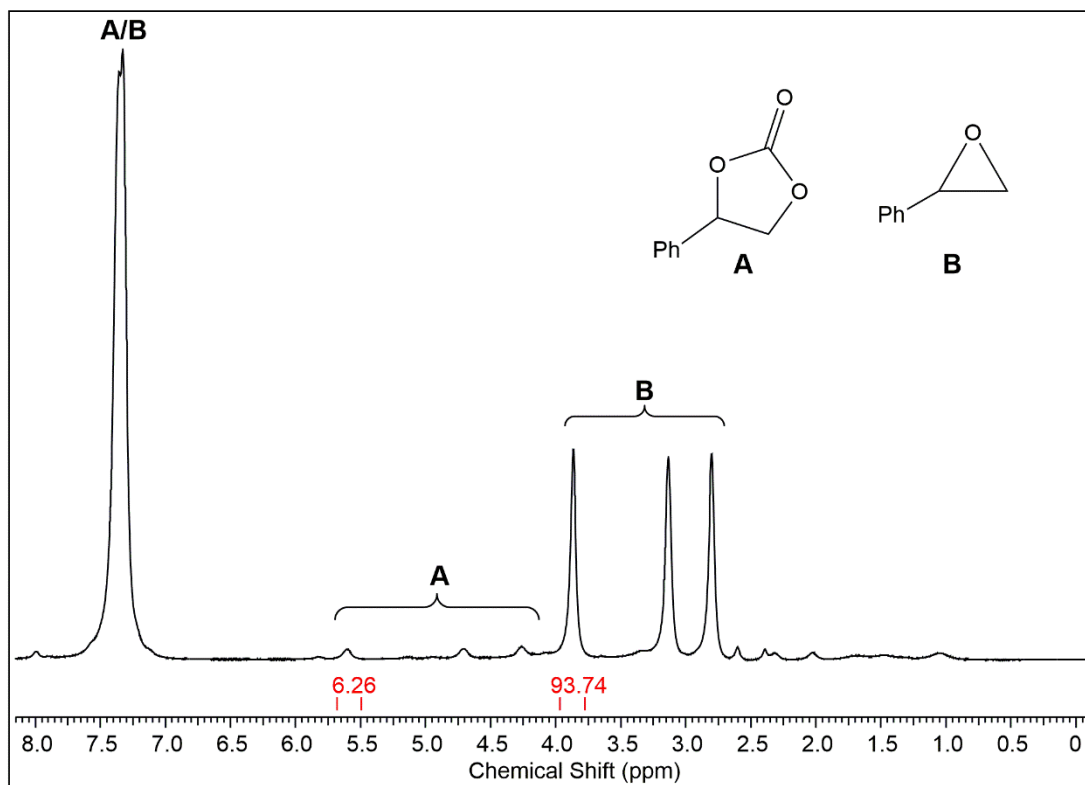
Figure S29. ^{1}H NMR (26 °C, 400.13 MHz, chloroform-*d*) of the product mixture of the catalytic formation of styrene carbonate using 0.25 mol% [Ce(Me$_2$pz)$_4$]$_2$ (**1**) as a catalyst. The conversion was determined by the integral ratio of the protons in α-position in styrene oxide and styrene carbonate.
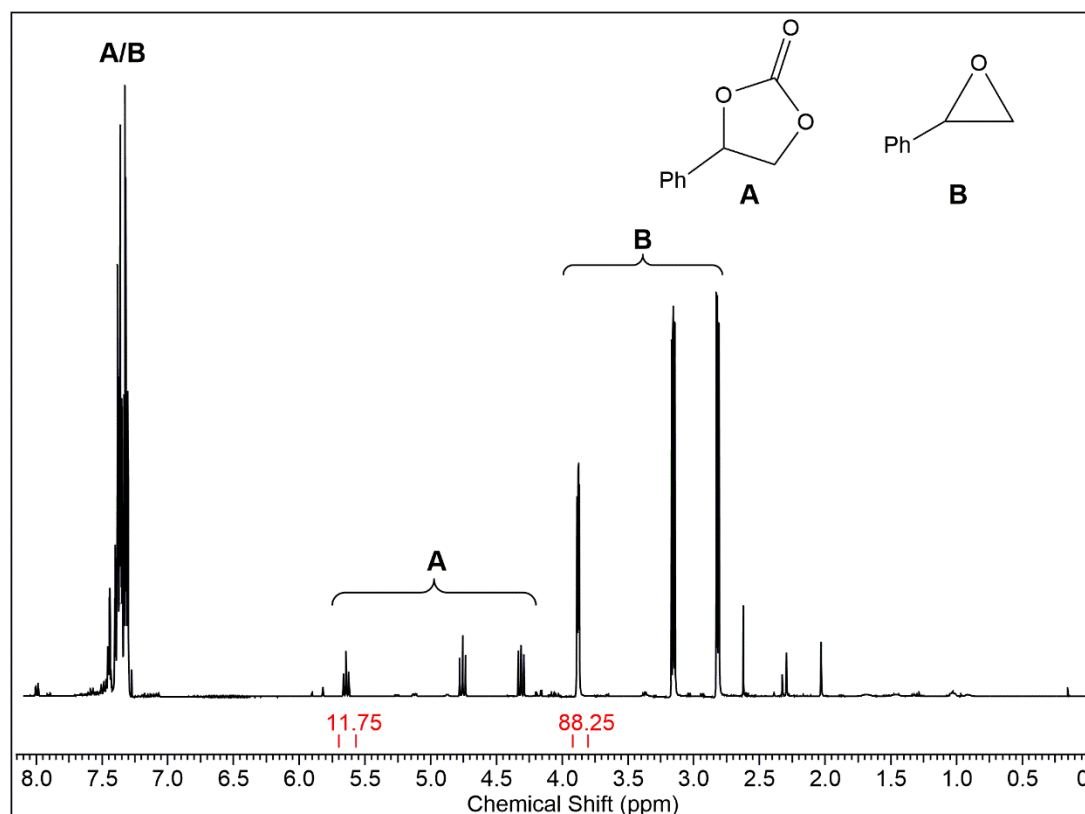
Figure S30. ^{1}H NMR (26 °C, 400.13 MHz, chloroform-*d*) of the product mixture of the catalytic formation of styrene carbonate using 0.25 mol% [Ce(Me$_2$pz)$_4$]$_2$ (**1**) as a catalyst at 90 °C and 10 bar CO$_2$ pressure. The conversion was determined by the integral ratio of the protons in α-position in styrene oxide and styrene carbonate.
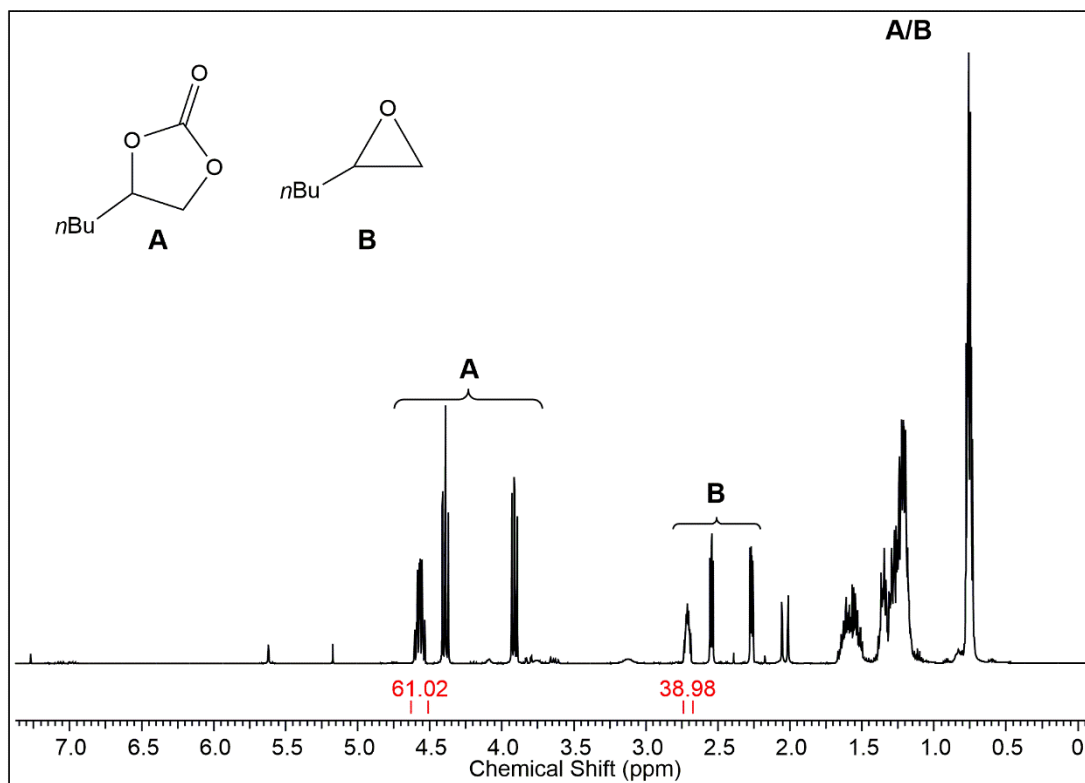
Figure S31. ^{1}H NMR (26 °C, 400.13 MHz, chloroform-*d*) of the product mixture of the catalytic formation of 1,2-*n*-hexylene carbonate using 0.5 mol% [Ce(Me$_2$pz)$_4$]$_2$ (**1**) as a catalyst. The conversion was determined by the integral ratio of the protons in α-position in 1,2-*n*-hexylene oxide and 1,2-*n*-hexylene carbonate.
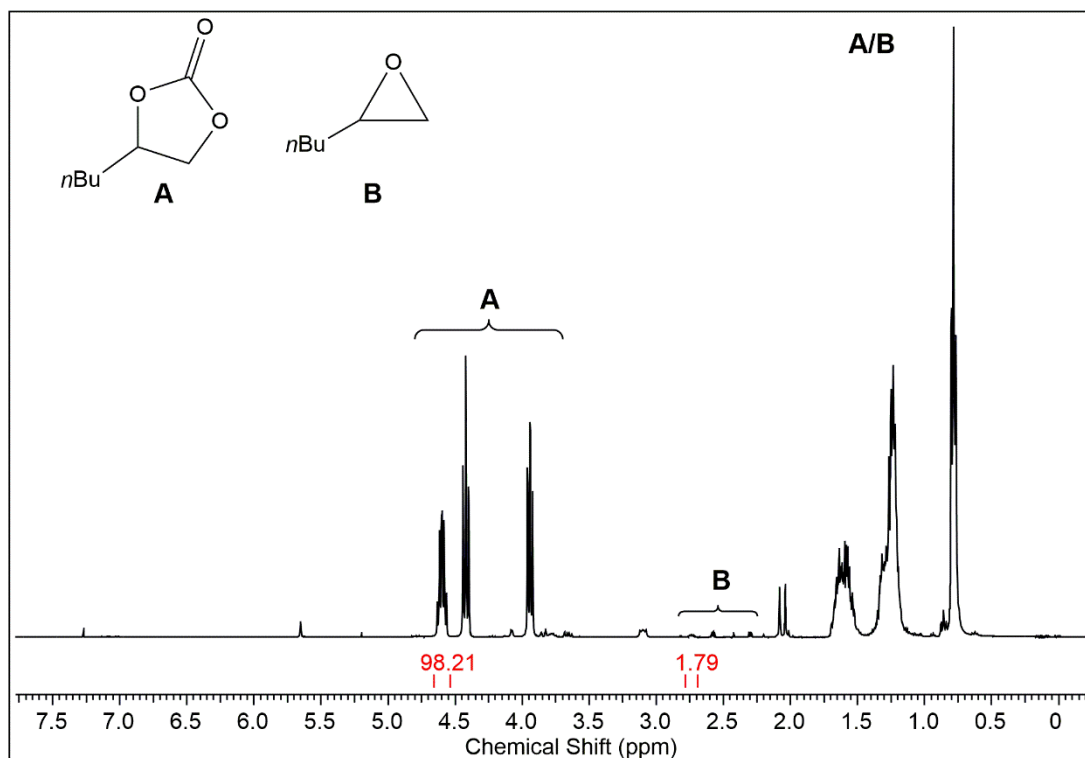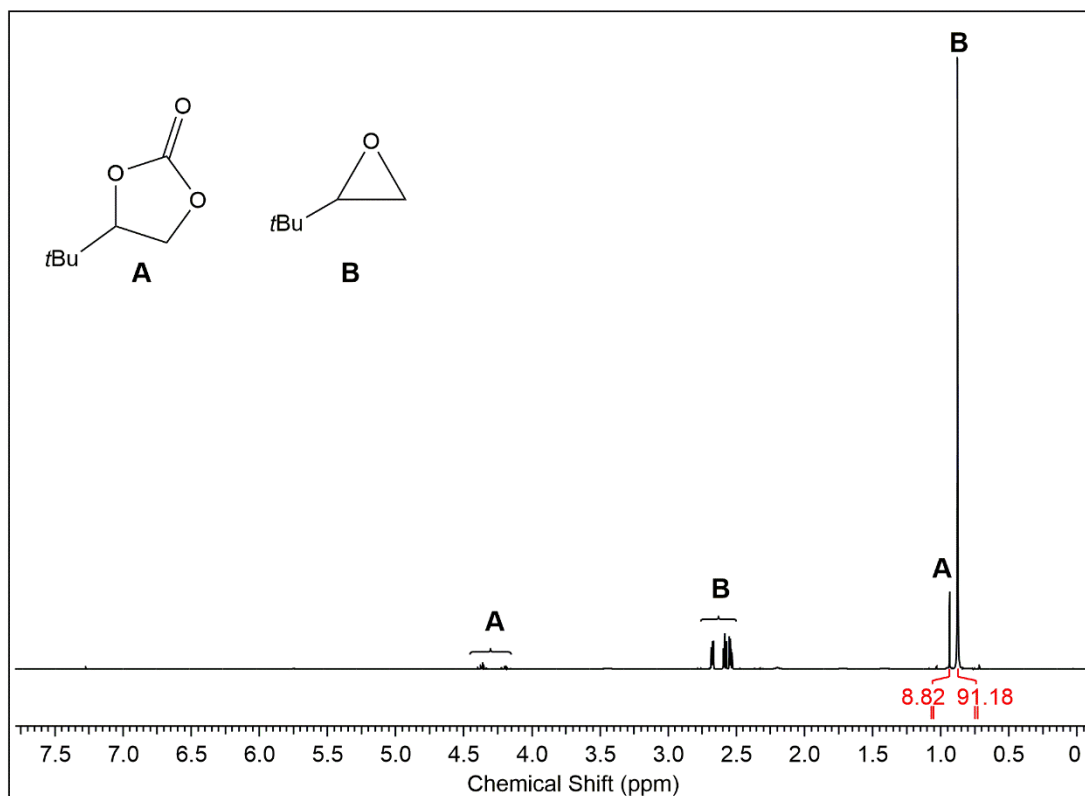

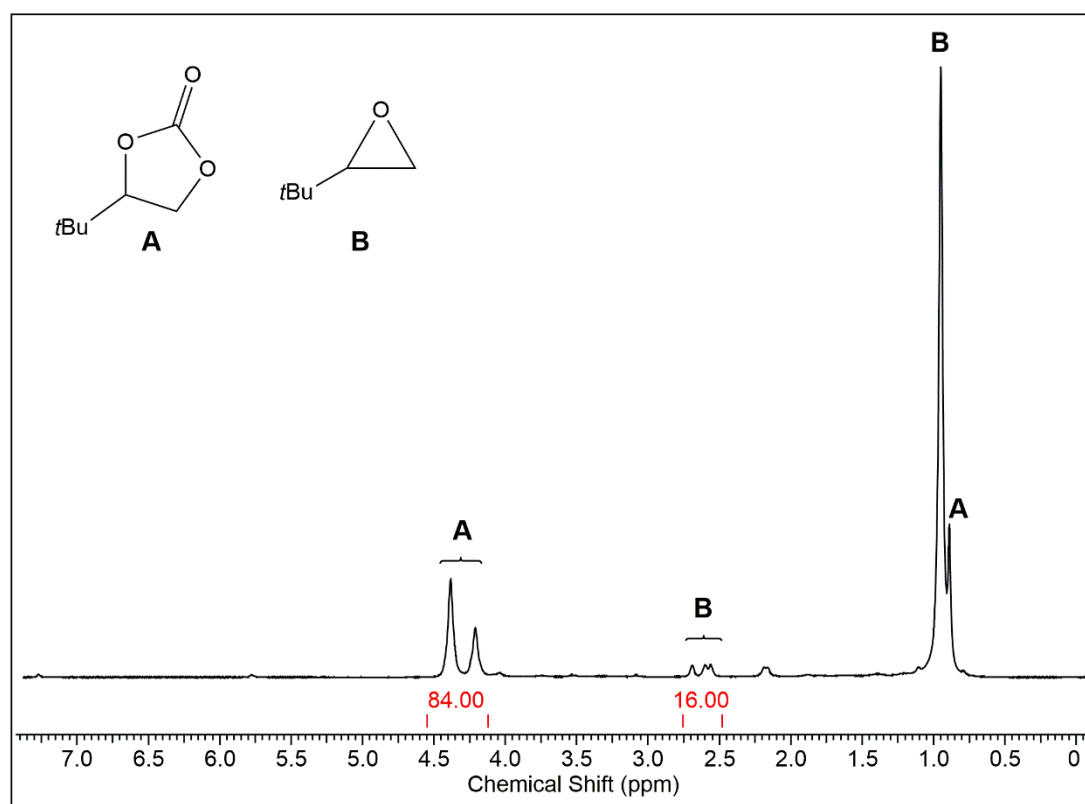**Figure S32.** ^{1}H NMR (26 °C, 400.13 MHz, chloroform-*d*) of the product mixture of the catalytic formation of 1,2-*n*-hexylene carbonate using 0.5 mol% [Ce(Me$_2$pz)$_4$]$_2$ (**1**) as a catalyst at 90 °C. The conversion was determined by the integral ratio of the protons in α-position in 1,2-*n*-hexylene oxide and 1,2-*n*-hexylene carbonate.
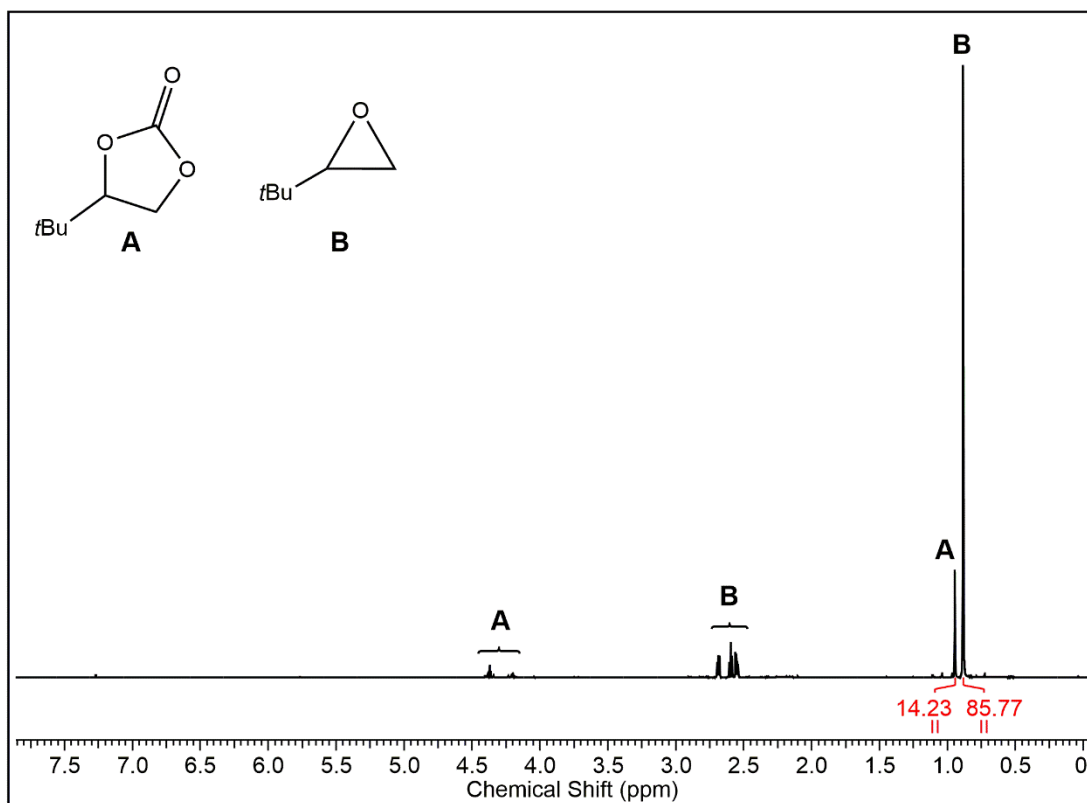
S23

Figure S33. ^{1}H NMR (26 °C, 400.13 MHz, chloroform-*d*) of the product mixture of the catalytic formation of 1,2-*n*-hexylene carbonate using 0.5 mol% [Ce(Me₂pz)₄]₂ (**1**) as a catalyst without TBAB as cocatalyst at 90 °C. The conversion was determined by the integral ratio of the protons in α-position in 1,2-*n*-hexylene oxide and 1,2-*n*-hexylene carbonate.
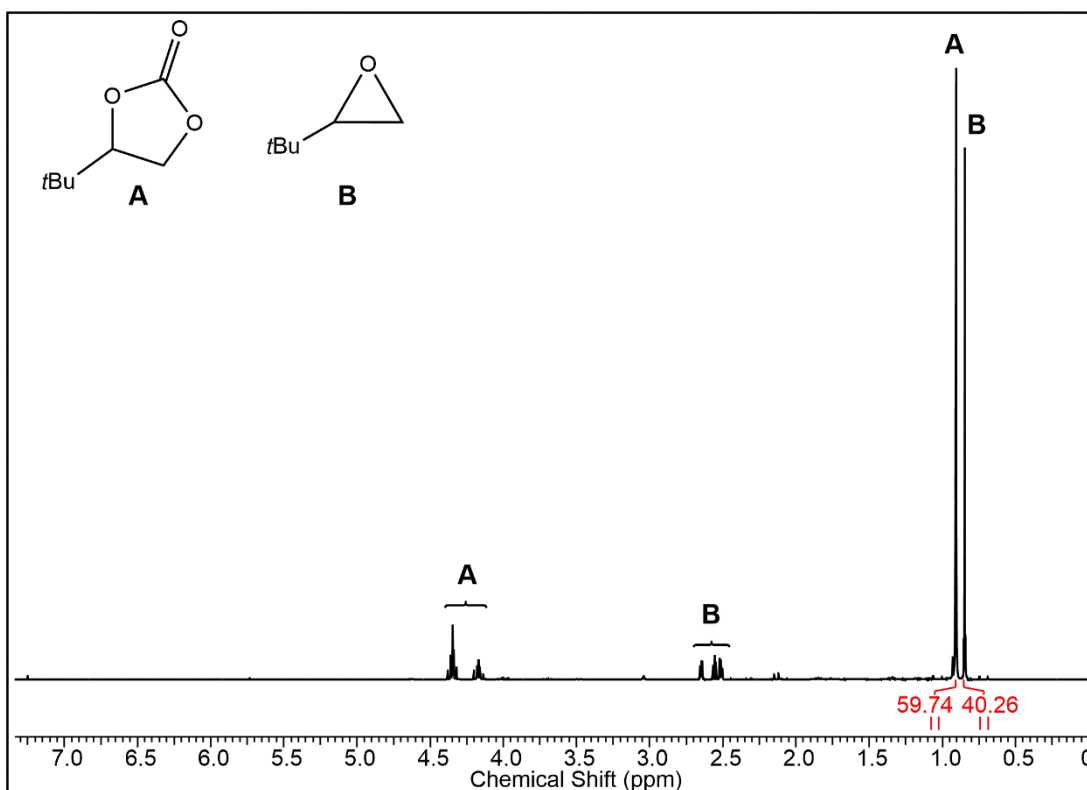

Figure S34. ^{1}H NMR (26 °C, 400.13 MHz, chloroform-*d*) of the product mixture of the catalytic formation of 1,2-*n*-hexylene carbonate using 0.5 mol% [Ce(Me₂pz)₄]₂ (**1**) as a catalyst at 10 bar CO₂ pressure. The conversion was determined by the integral ratio of the protons in α-position in 1,2-*n*-hexylene oxide and 1,2-*n*-hexylene carbonate.
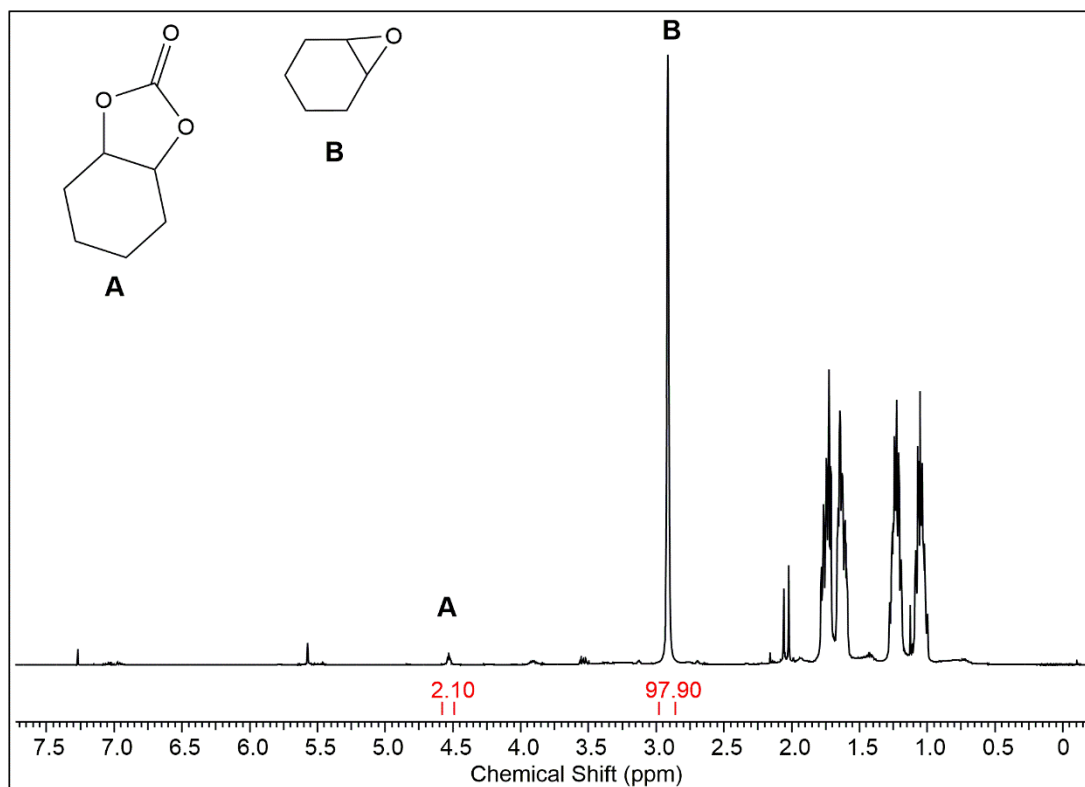
Figure S35. ^{1}H NMR (26 °C, 400.13 MHz, chloroform-*d*) of the product mixture of the catalytic formation of 1,2-*n*-hexylene carbonate using 0.25 mol% [Ce(Me$_2$pz)$_4$]$_2$ (**1**) as a catalyst at 90°C and 10 bar CO_2 pressure for 1 hour. The conversion was determined by the integral ratio of the protons in α-position in 1,2-*n*-hexylene oxide and 1,2-*n*-hexylene carbonate.
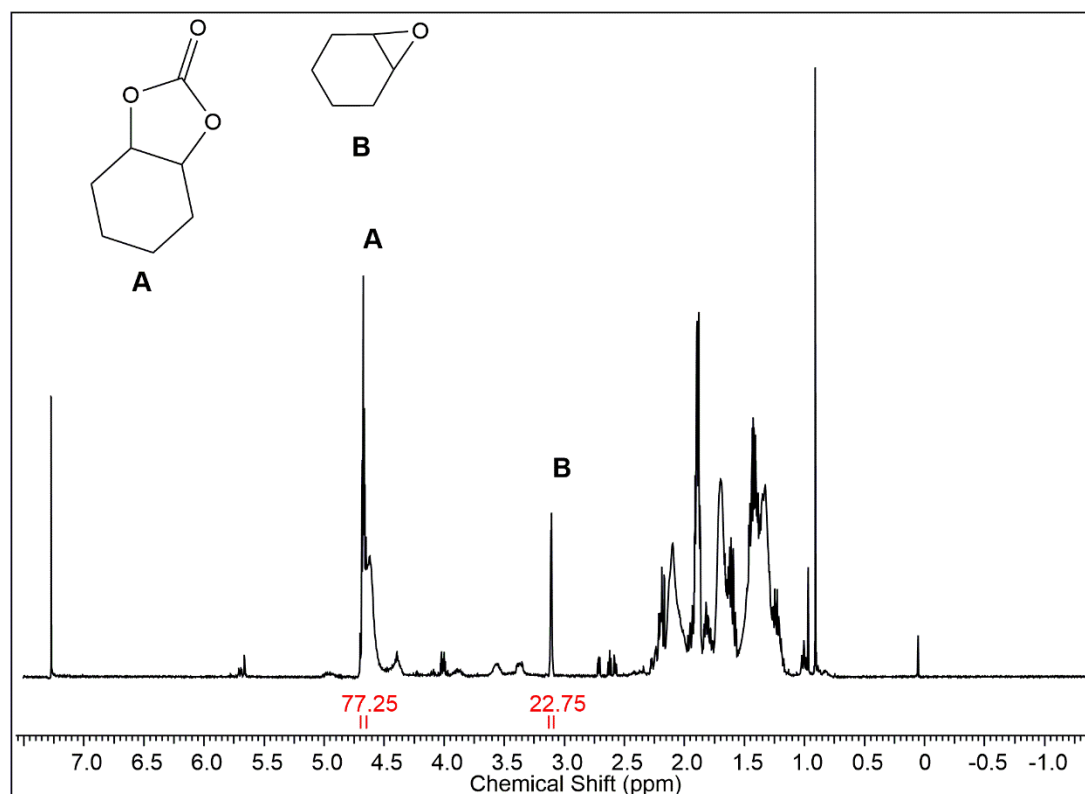

Figure S36. ^{1}H NMR (26 °C, 400.13 MHz, chloroform-*d*) of the product mixture of the catalytic formation of 3,3-dimethyl-1,2-butene carbonate using 0.5 mol% [Ce(Me$_2$pz)$_4$]$_2$ (**1**) as a catalyst. The conversion was determined by the integral ratio of the *tert*-butyl protons in 3,3-dimethyl-1,2-butene oxide and 3,3-dimethyl-1,2-butylene carbonate.

Figure S37. ^{1}H NMR (26 °C, 400.13 MHz, chloroform-d) of the product mixture of the catalytic formation of 3,3-dimethyl-1,2-butene carbonate using 0.5 mol% [Ce(Me$_2$pz)$_4$]$_2$ (**1**) as a catalyst at 10 bar CO$_2$ pressure. The conversion was determined by the integral ratio of the *tert*-butyl protons in 3,3-dimethyl-1,2-butene oxide and 3,3-dimethyl-1,2-butylene carbonate.
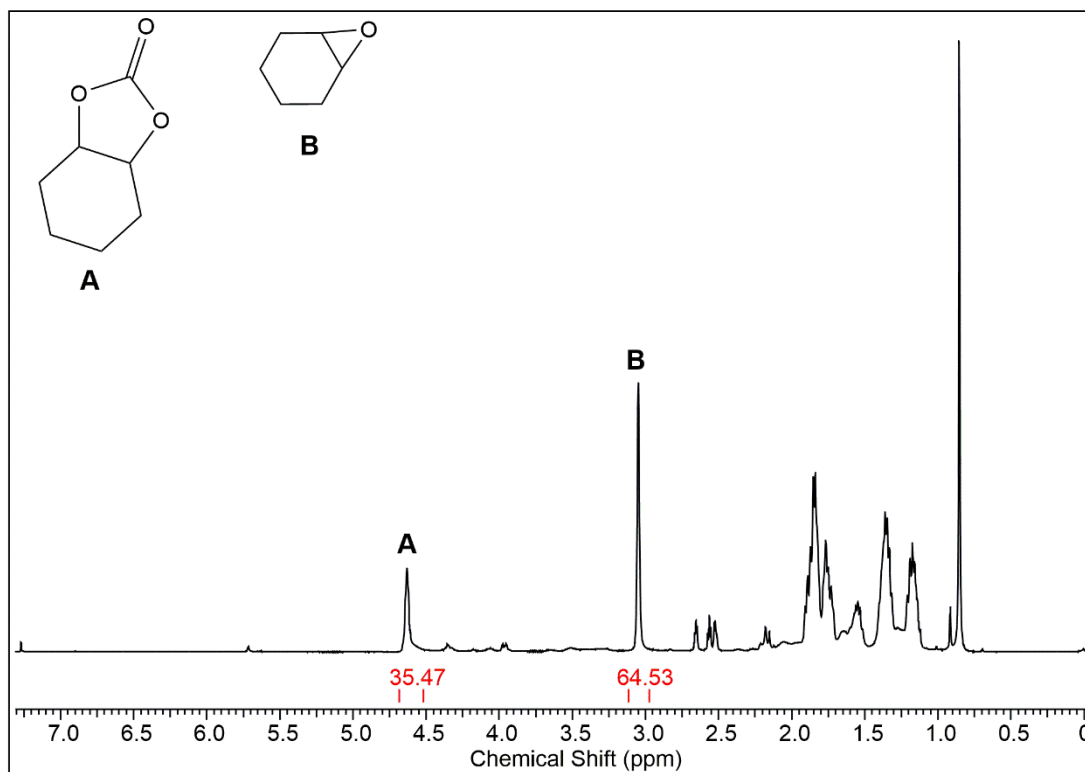

Figure S38. ^{1}H NMR (26 °C, 400.13 MHz, chloroform-d) of the product mixture of the catalytic formation of 3,3-dimethyl-1,2-butene carbonate using 0.25 mol% [Ce(Me$_2$pz)$_4$]$_2$ (**1**) as a catalyst at 90 °C and 10 bar CO$_2$ pressure. The conversion was determined by the integral ratio of the protons in α- and β-position in 3,3-dimethyl-1,2-butene oxide and 3,3-dimethyl-1,2-butylene carbonate.

Figure S39. ^{1}H NMR (26 °C, 400.13 MHz, chloroform-*d*) of the product mixture of the catalytic formation of 3,3-dimethyl-1,2-butene carbonate using 0.25 mol% [Ce(Me$_2$pz)$_4$]$_2$ (**1**) as a catalyst at 90 °C and 10 bar CO$_2$ pressure after 1 hour. The conversion was determined by the integral ratio of the *tert*-butyl protons in 3,3-dimethyl-1,2-butene oxide and 3,3-dimethyl-1,2-butylene carbonate.
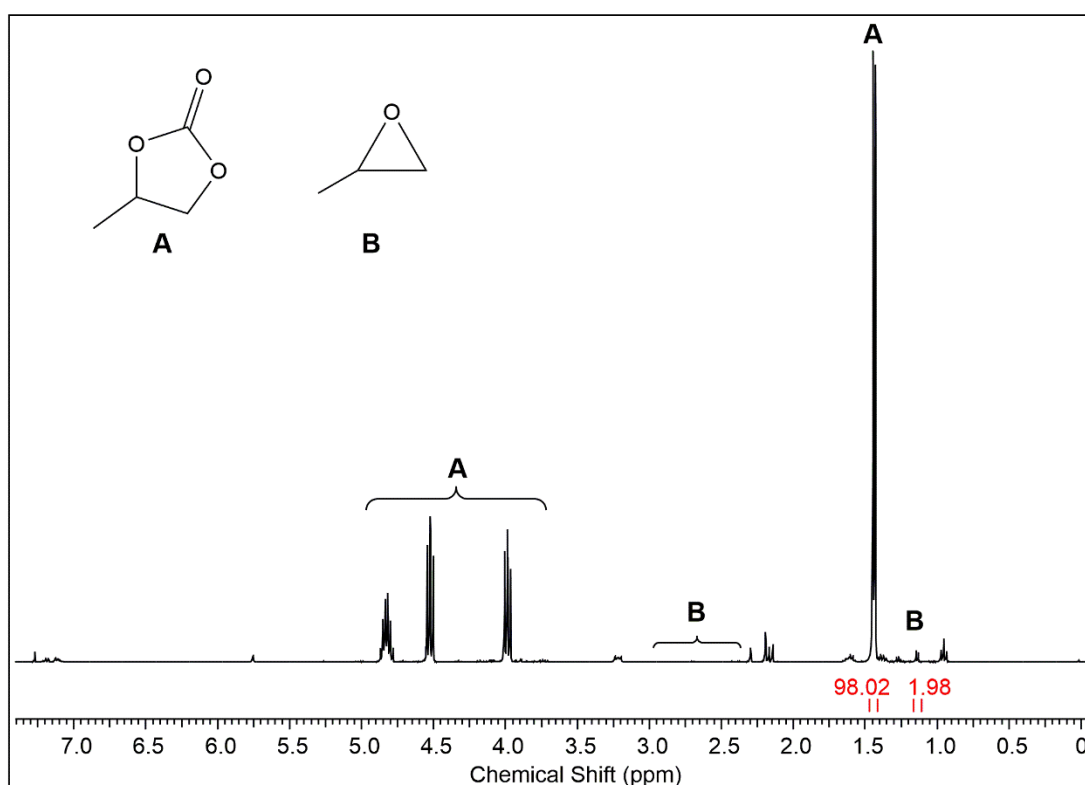

Figure S40. ^{1}H NMR (26 °C, 400.13 MHz, chloroform-*d*) of the product mixture of the catalytic formation of 3,3-dimethyl-1,2-butene carbonate using 0.1 mol% [Ce(Me$_2$pz)$_4$]$_2$ (**1**) as a catalyst at 90 °C and 10 bar CO$_2$ pressure after 1 hour. The conversion was determined by the integral ratio of the *tert*-butyl protons in 3,3-dimethyl-1,2-butene oxide and 3,3-dimethyl-1,2-butylene carbonate.

Figure S41. ^{1}H NMR (26 °C, 400.13 MHz, chloroform-*d*) of the product mixture of the catalytic formation of cyclohexene carbonate using 0.5 mol% [Ce(Me$_2$pz)$_4$]$_2$ (**1**) as a catalyst. The conversion was determined by the integral ratio of the protons in α-position in cyclohexene oxide and cyclohexene carbonate.
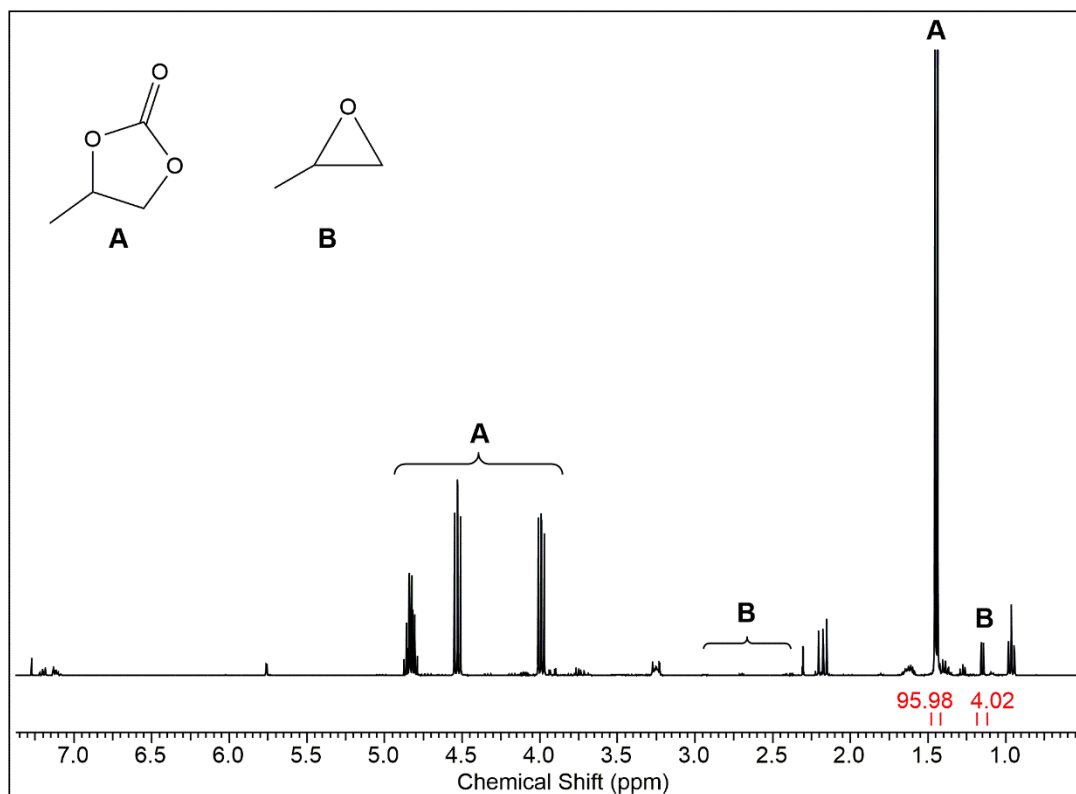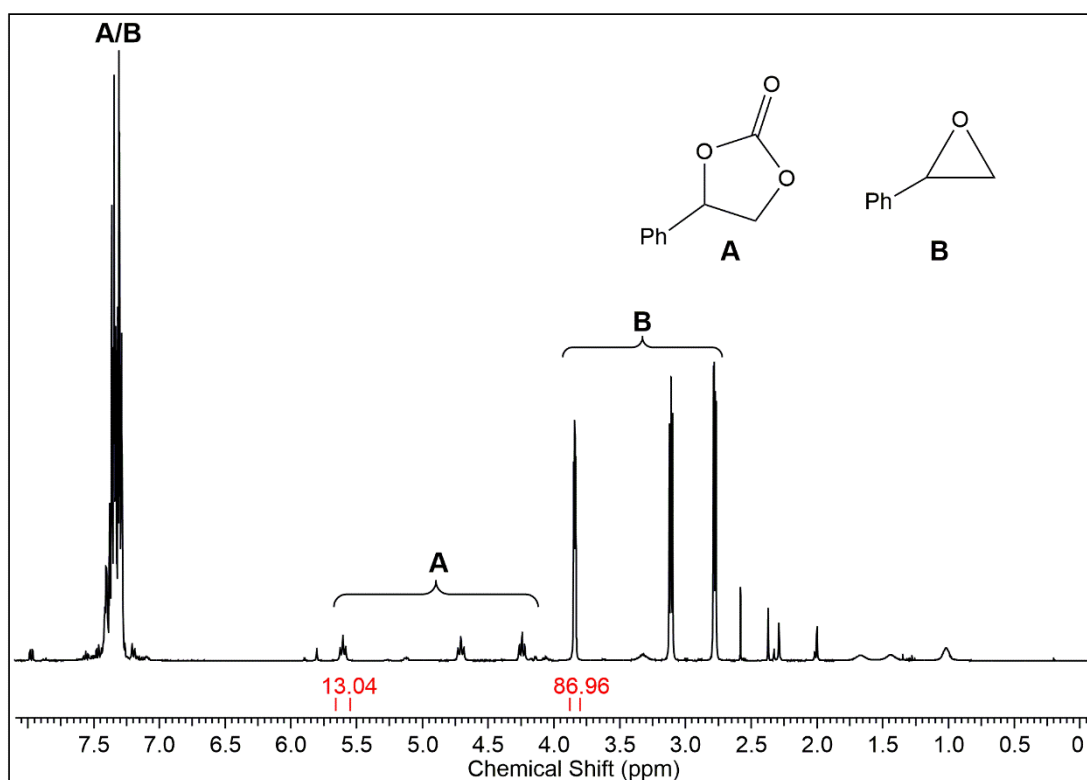

Figure S42. ^{1}H NMR (26 °C, 400.13 MHz, chloroform-*d*) of the product mixture of the catalytic formation of cyclohexene carbonate using 0.25 mol%[Ce(Me$_2$pz)$_4$]$_2$ (**1**) as a catalyst at 90 °C and 10 bar CO$_2$ pressure. The conversion was determined by the integral ratio of the protons in α-position in cyclohexene oxide and cyclohexene carbonate.
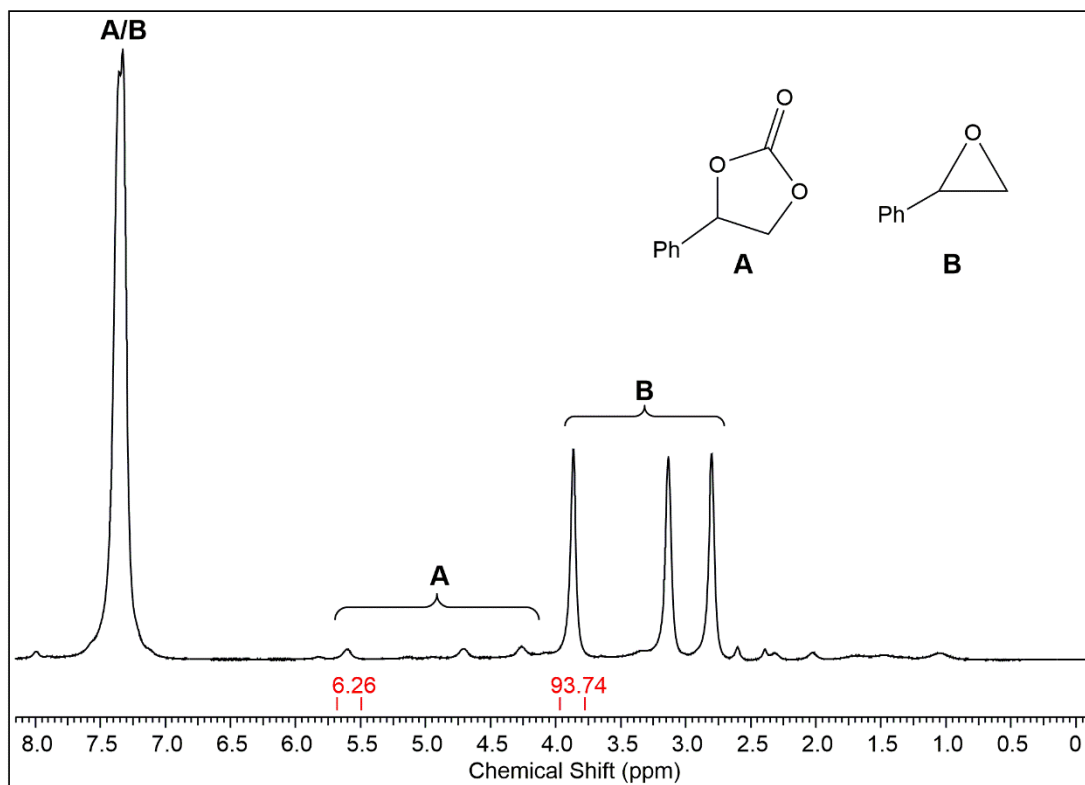
Figure S43. ¹H NMR (26 °C, 400.13 MHz, chloroform-*d*) of the product mixture of the catalytic formation of cyclohexene carbonate using 0.1 mol%[Ce(Me₂pz)₄]₂ (**1**) as a catalyst at 90 °C and 10 bar CO_2 pressure. The conversion was determined by the integral ratio of the protons in α-position in cyclohexene oxide and cyclohexene carbonate.

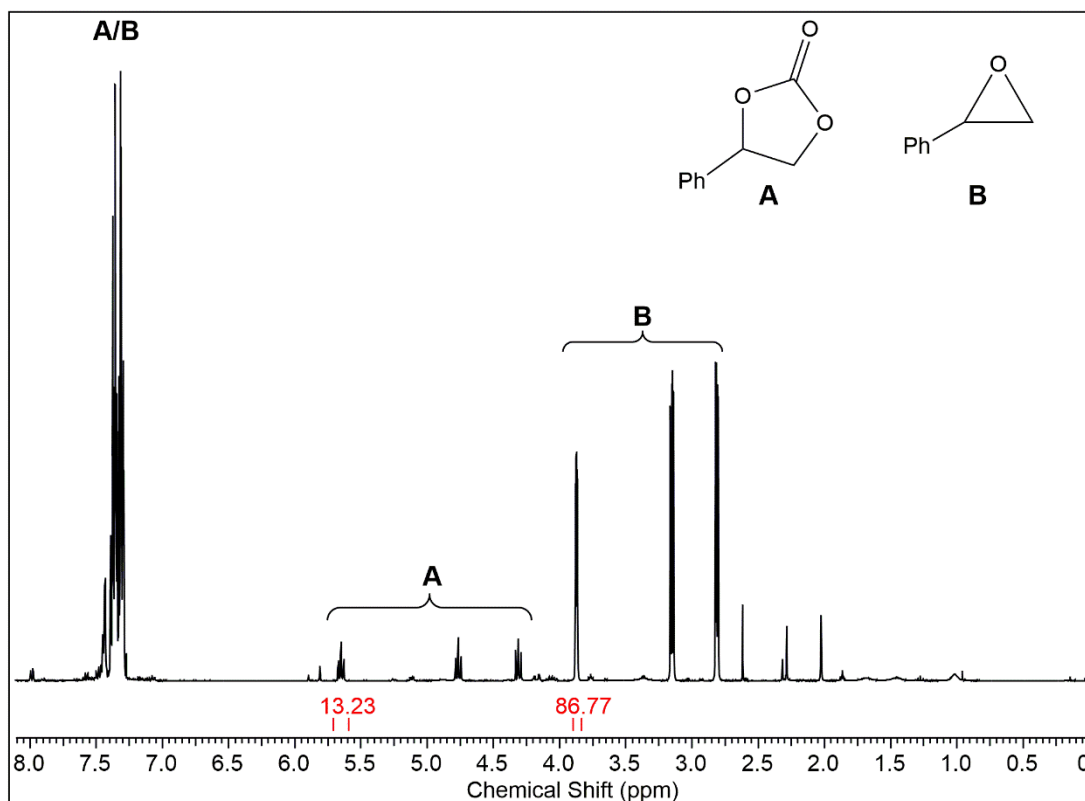

Figure S44. ¹H NMR (26 °C, 400.13 MHz, chloroform-*d*) of the product mixture of the catalytic formation of propylene carbonate using 0.25 mol% [Ce₄(Me₂pz)₁₂] (**4**) as a catalyst. The conversion was determined by the integral ratio of the methyl protons in propylene oxide and propylene carbonate.

Figure S45. ^{1}H NMR (26 °C, 400.13 MHz, chloroform-*d*) of the product mixture of the catalytic formation of propylene carbonate using 0.25 mol% $[Ce_4(Me_2pz^:CO_2)_{12}] \cdot 10$ toluene (**5·toluene**) as a catalyst. The conversion was determined by the integral ratio of the methyl protons in propylene oxide and propylene carbonate.
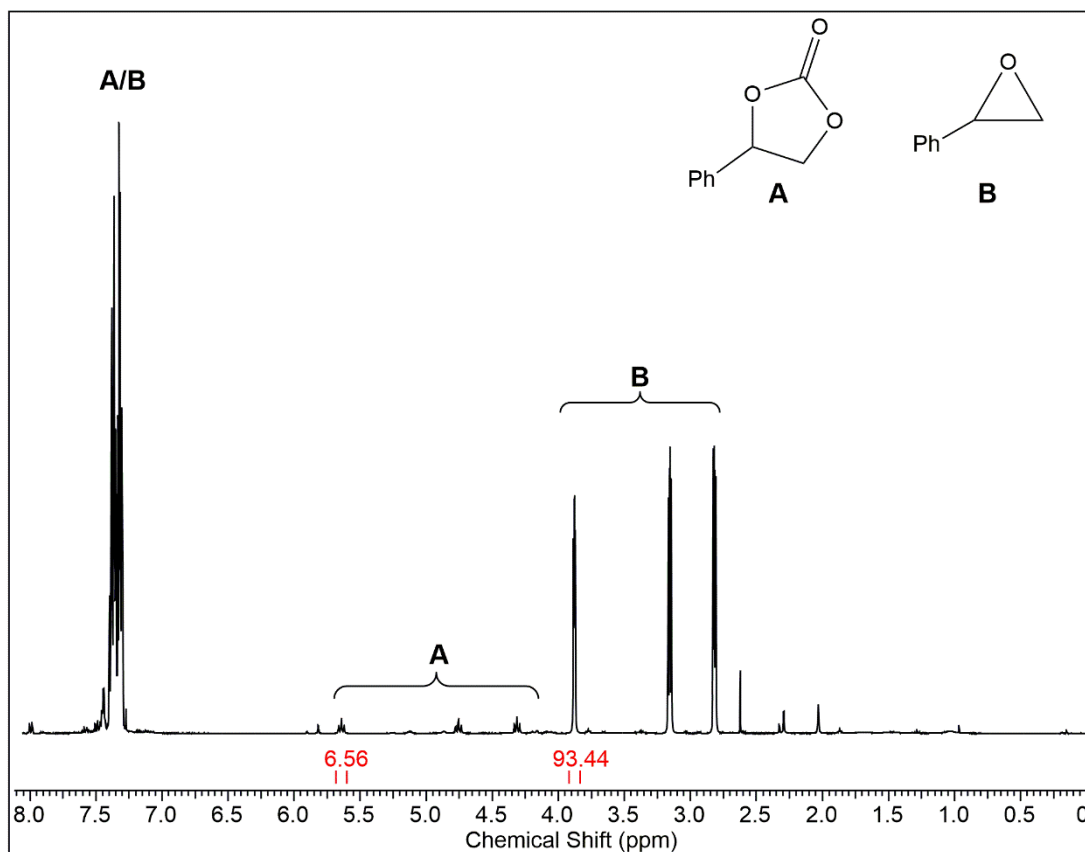

Figure S46. ^{1}H NMR (26 °C, 400.13 MHz, chloroform-*d*) of the product mixture of the catalytic formation of styrene carbonate using 0.25 mol% $[Ce_4(Me_2pz)_{12}]$ (**4**) as a catalyst. The conversion was determined by the integral ratio of the protons in α-position in styrene oxide and styrene carbonate.
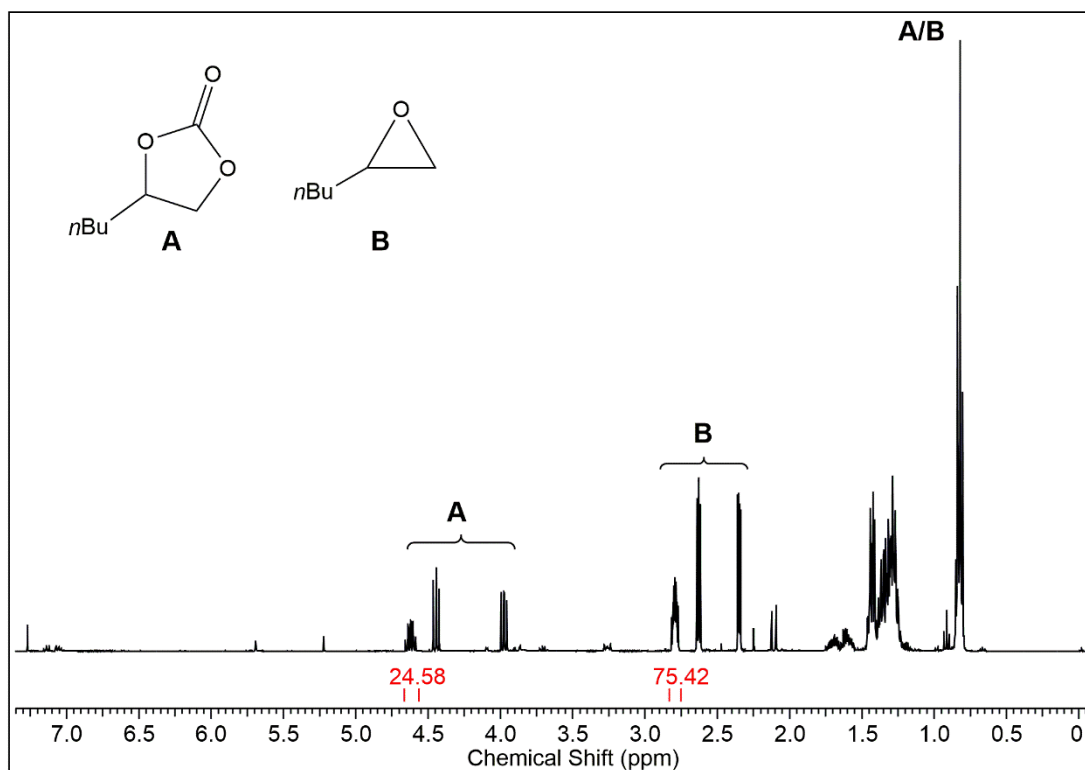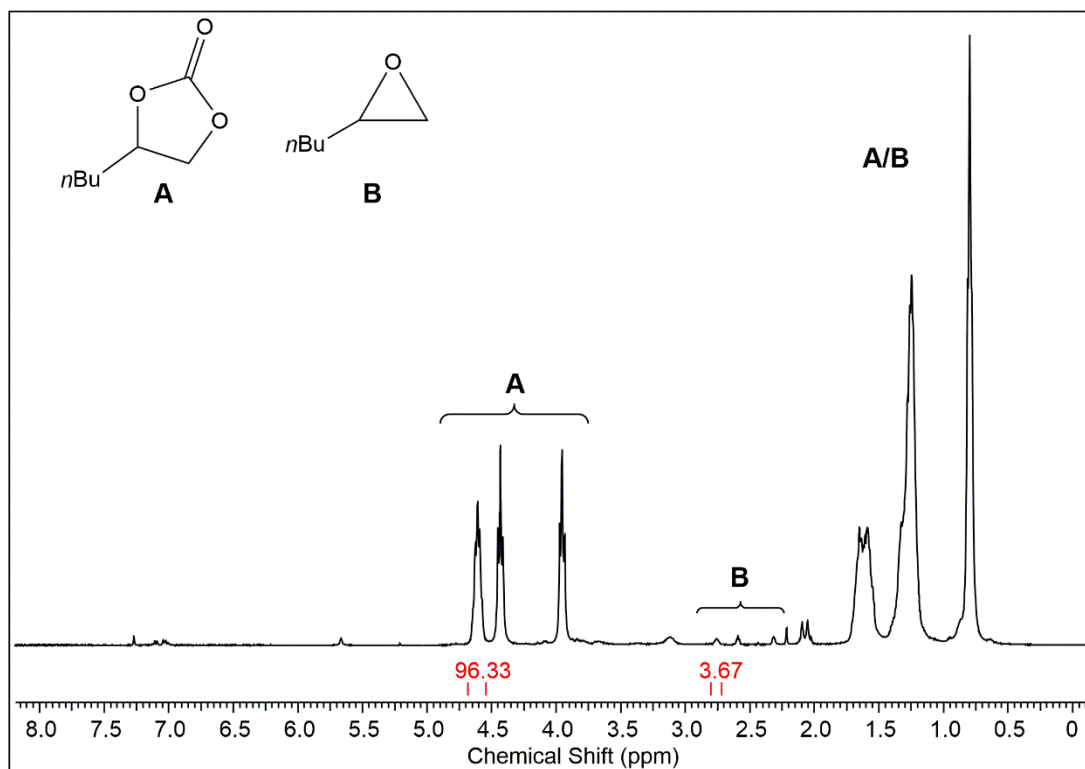
Figure S47. ^{1}H NMR (26 °C, 400.13 MHz, chloroform-*d*) of the product mixture of the catalytic formation of styrene carbonate using 0.125 mol% [Ce$_4$(Me$_2$pz)$_{12}$] (**4**) as a catalyst. The conversion was determined by the integral ratio of the protons in α-position in styrene oxide and styrene carbonate.

Figure S48. ^{1}H NMR (26 °C, 400.13 MHz, chloroform-*d*) of the product mixture of the catalytic formation of styrene carbonate using 0.5 mol% [Ce(Me$_2$pz)$_3$(thf)]$_2$ (**4·thf**) as a catalyst. The conversion was determined by the integral ratio of the protons in α-position in styrene oxide and styrene carbonate.
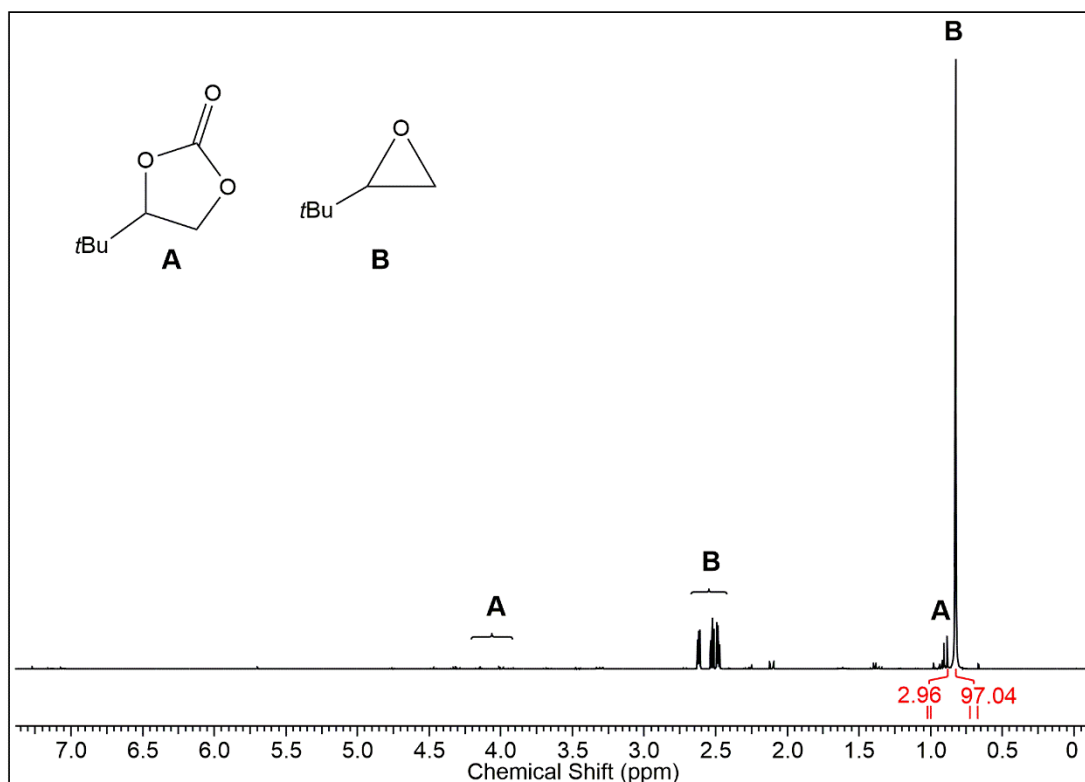
Figure S49. ^{1}H NMR (26 °C, 400.13 MHz, chloroform-*d*) of the product mixture of the catalytic formation of styrene carbonate using 0.25 mol% [Ce(Me$_2$pz)$_3$(thf)]$_2$ (**4·thf**) as a catalyst. The conversion was determined by the integral ratio of the protons in α-position in styrene oxide and styrene carbonate.

Figure S50. ^{1}H NMR (26 °C, 400.13 MHz, chloroform-*d*) of the product mixture of the catalytic formation of 1,2-*n*-hexylene carbonate using 0.25 mol% [Ce$_4$(Me$_2$pz)$_{12}$] (**4**) as a catalyst. The conversion was determined by the integral ratio of the protons in α-position in 1,2-*n*-hexylene oxide and 1,2-*n*-hexylene carbonate.
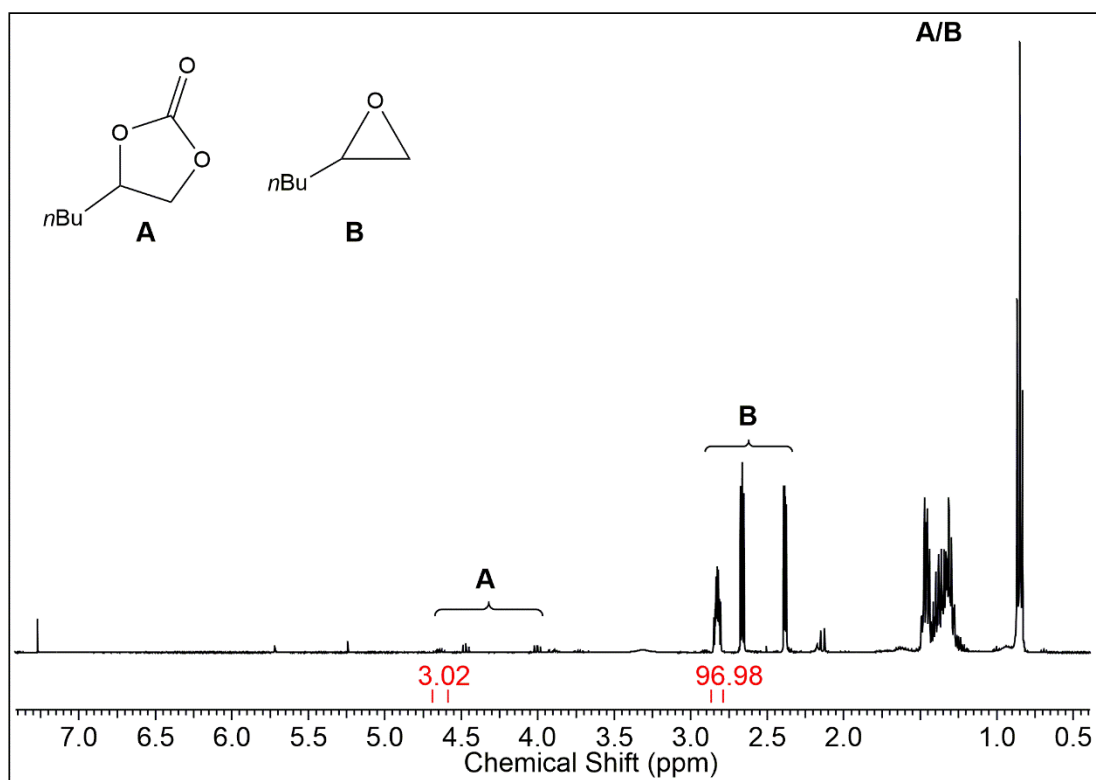
Figure S51. ^{1}H NMR (26 °C, 400.13 MHz, chloroform-*d*) of the product mixture of the catalytic formation of 1,2-*n*-hexylene carbonate using 0.25 mol% [Ce$_4$(Me$_2$pz)$_{12}$] (**4**) as a catalyst at 90 °C. The conversion was determined by the integral ratio of the protons in α-position in 1,2-*n*-hexylene oxide and 1,2-*n*-hexylene carbonate.


Figure S52. ^{1}H NMR (26 °C, 400.13 MHz, chloroform-*d)* of the product mixture of the catalytic formation of 3,3-dimethyl-1,2-butene carbonate using 0.25 mol% [Ce$_4$(Me$_2$pz)$_{12}$] (**4**) as a catalyst. The conversion was determined by the integral ratio of the *tert*-butyl protons in 3,3-dimethyl-1,2-butene oxide and 3,3-dimethyl-1,2-butylene carbonate.

Figure S53. ^{1}H NMR (26 °C, 400.13 MHz, chloroform-*d*) of the product mixture of the catalytic formation of 1,2-*n*-hexylene carbonate using 1 mol% [Ce(Me$_2$pz)$_4$][NBu$_4$] (**6**) as a catalyst. The conversion was determined by the integral ratio of the protons in α-position in 1,2-*n*-hexylene oxide and 1,2-*n*-hexylene carbonate.
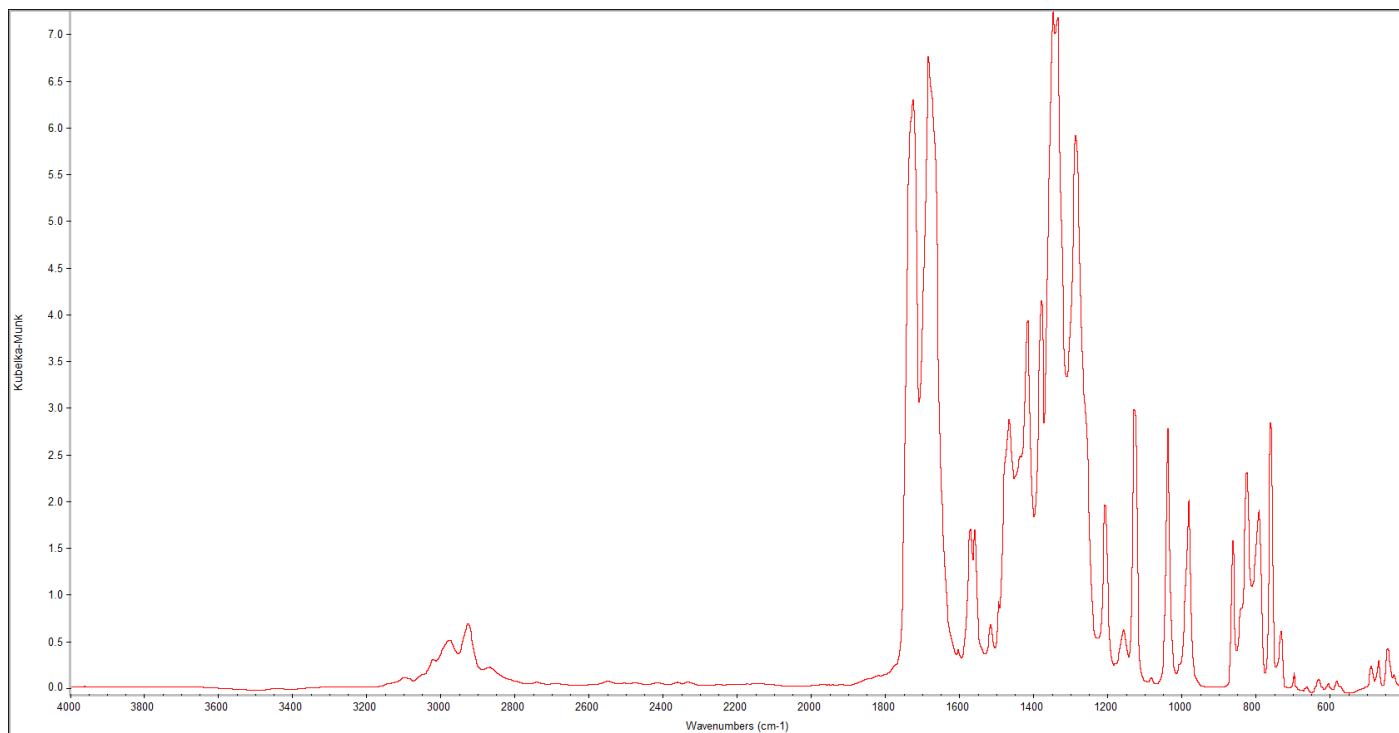
IR Spectra
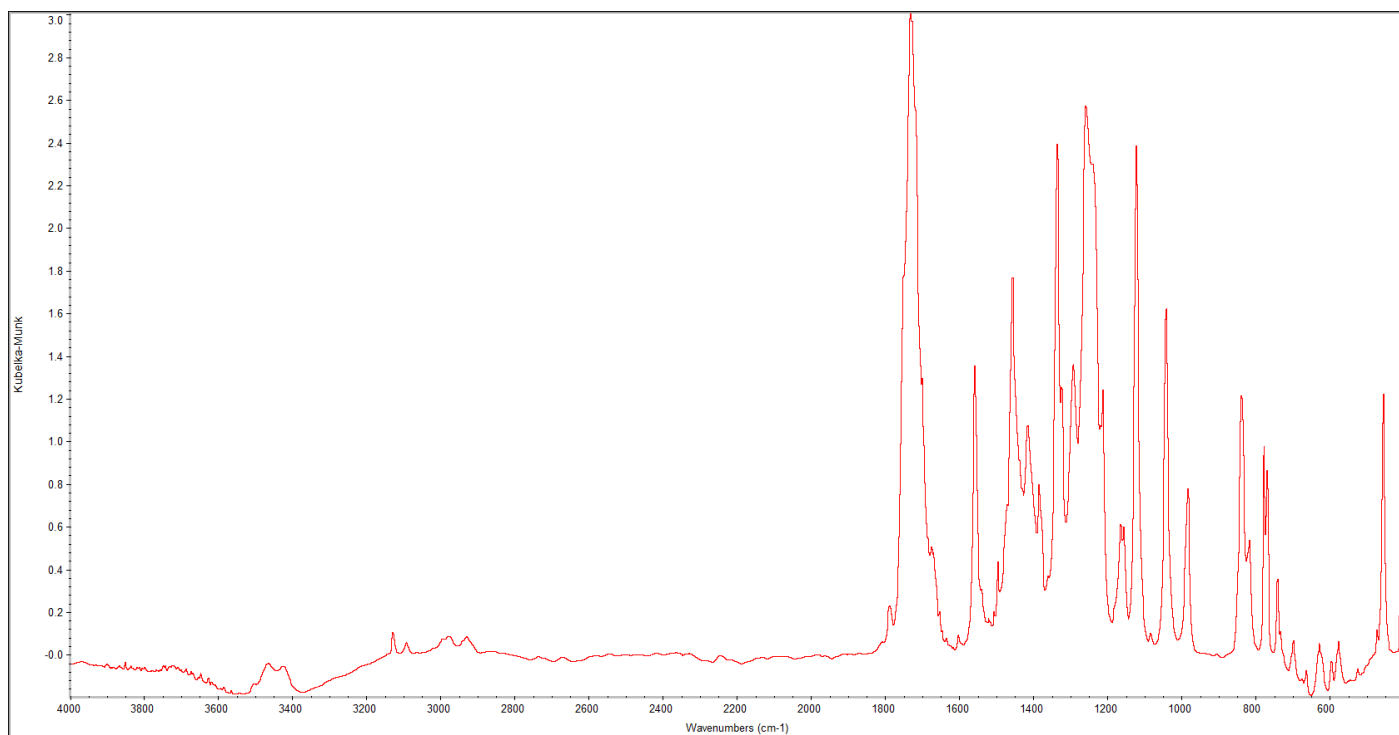
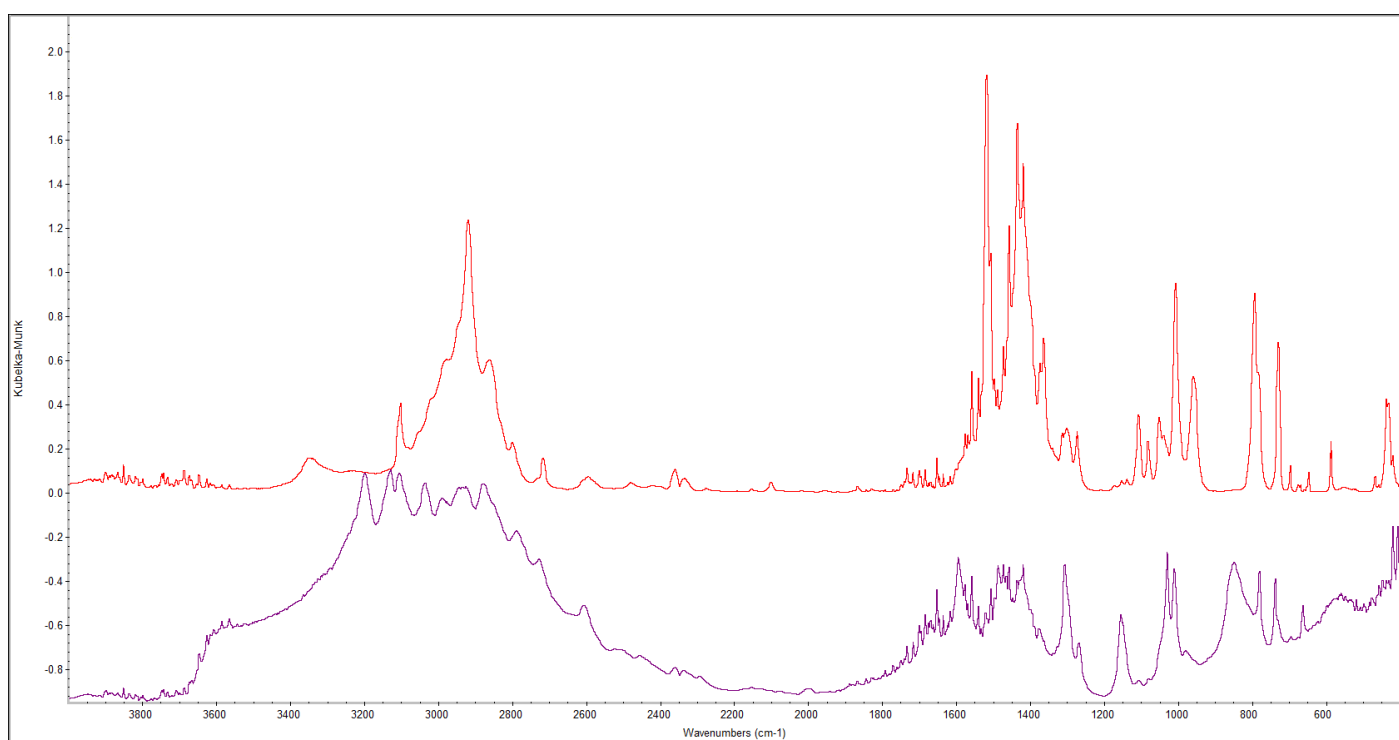**Figure S54.** DRIFT spectrum of [Ce(Me$_2$pz·CO$_2$)$_4$]·2 tol (**2·toluene**) at 25 °C.
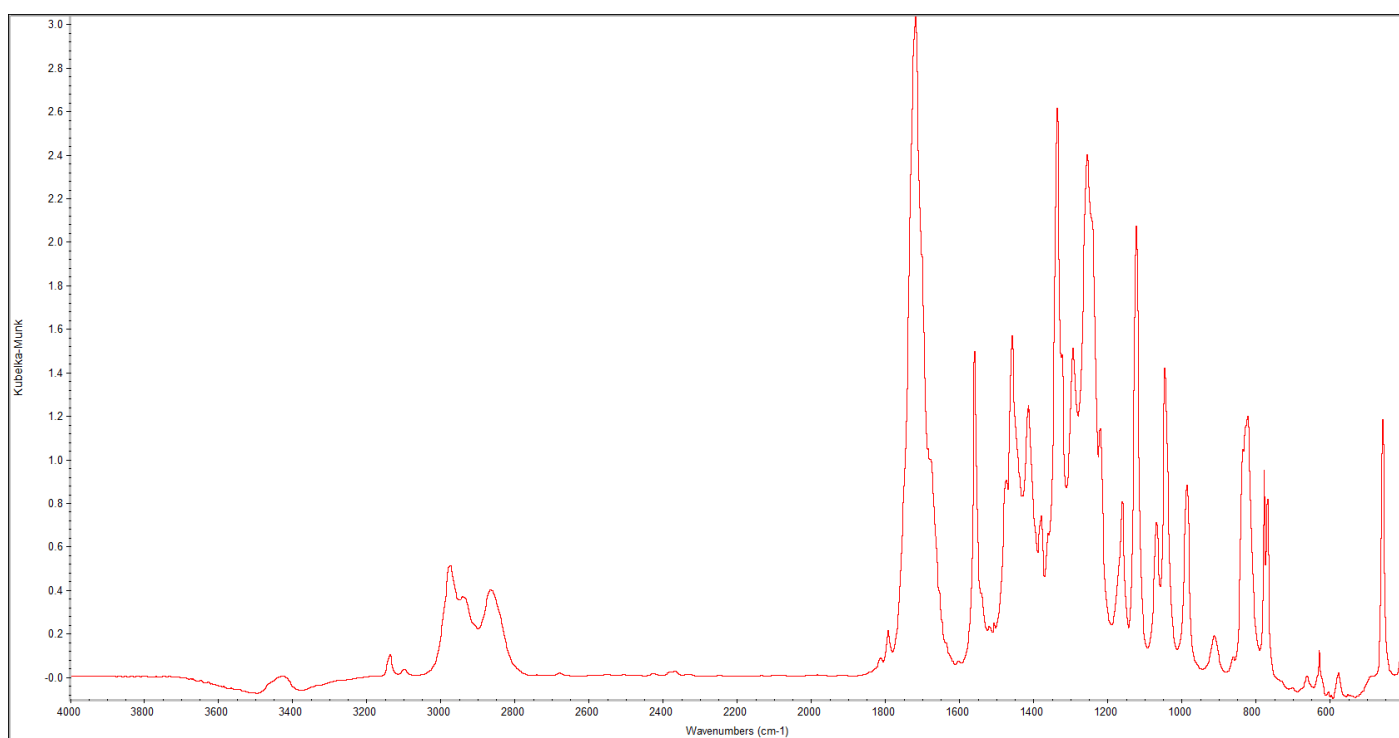
Figure S55. DRIFT spectrum of [Ce(Me$_2$pz·CO$_2$)$_4$]·2 thf (**2·thf**) at 25 °C.
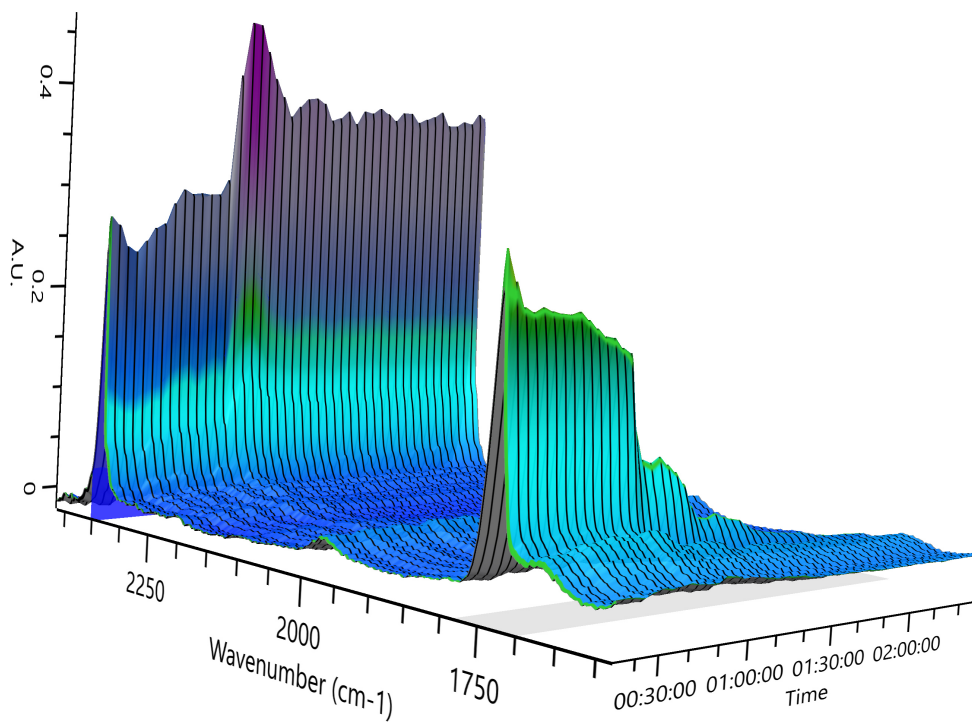
Figure S56. DRIFT spectrum of $[Ce_4(Me_2pz \cdot CO_2)_{12}] \cdot 10$ toluene (**5·toluene**) at 25 °C.
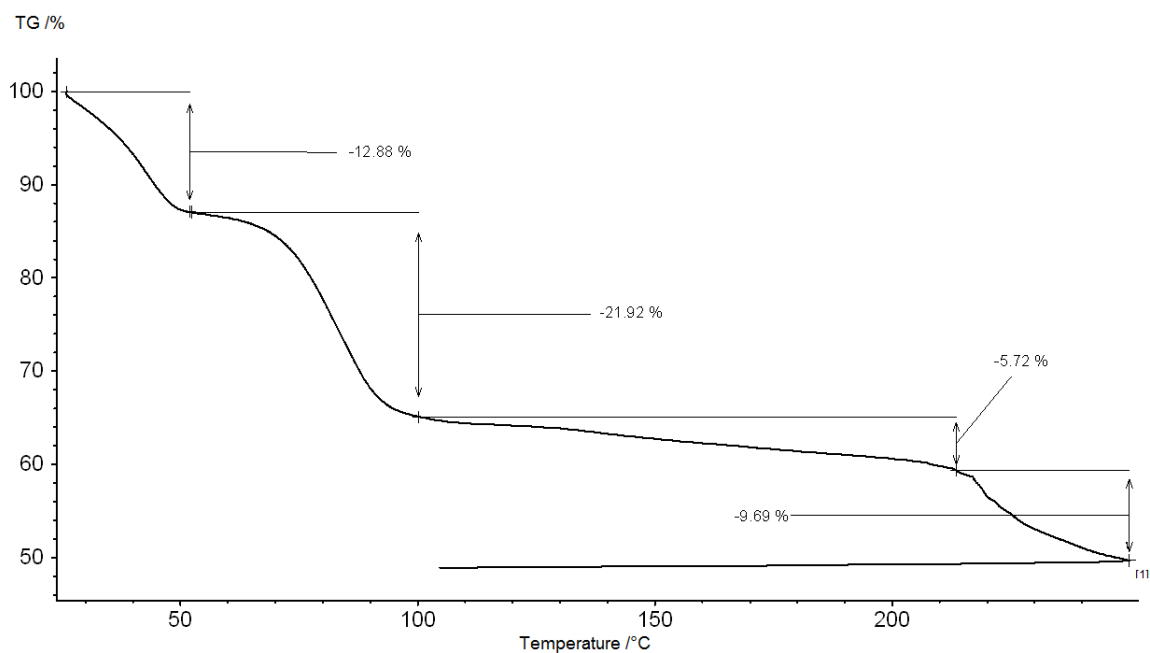

Figure S57. DRIFT spectra of $[Ce(Me_2pz)_4]_2$ stored for 3 days under 1 bar CO2 pressure (red trace) and $[Ce(Me_2pz)_4]_2$ after 30 min at ambient conditions (purple trace) at 25 °C.
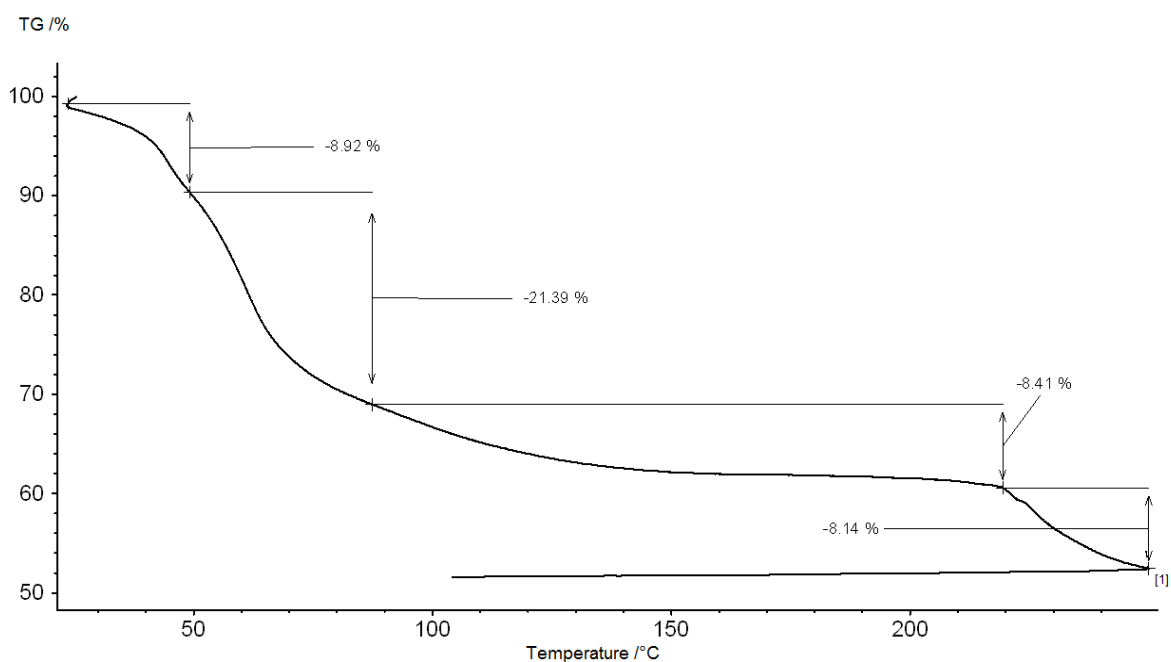
Figure S58. Stacked IR spectra of **2·thf** at 60 °C in the range of 1700 and 2350 cm^{-1}. Spectra were recorded every minute.

Thermogravimetric Analysis (TGA)

Figure S59. TGA of [Ce(Me$_2$pz·CO$_2$)$_4$]·tol (**2·toluene**). Sample was heated from 28 °C to 250 °C with a heating rate of 0.5 K min^{-1} than cooled to ambient temperature with 10 K min^{-1}.

Figure S60. TGA of [Ce(Me$_2$pz·CO$_2$)$_3$]$_4$·10 toluene (**5·toluene**). Sample was heated from 28 °C to 250 °C with a heating rate of 0.5 K min^{-1} than cooled to ambient temperature with 10 K min^{-1}.

Proposed Mechanisms of the Cycloaddition of CO₂ with Epoxides
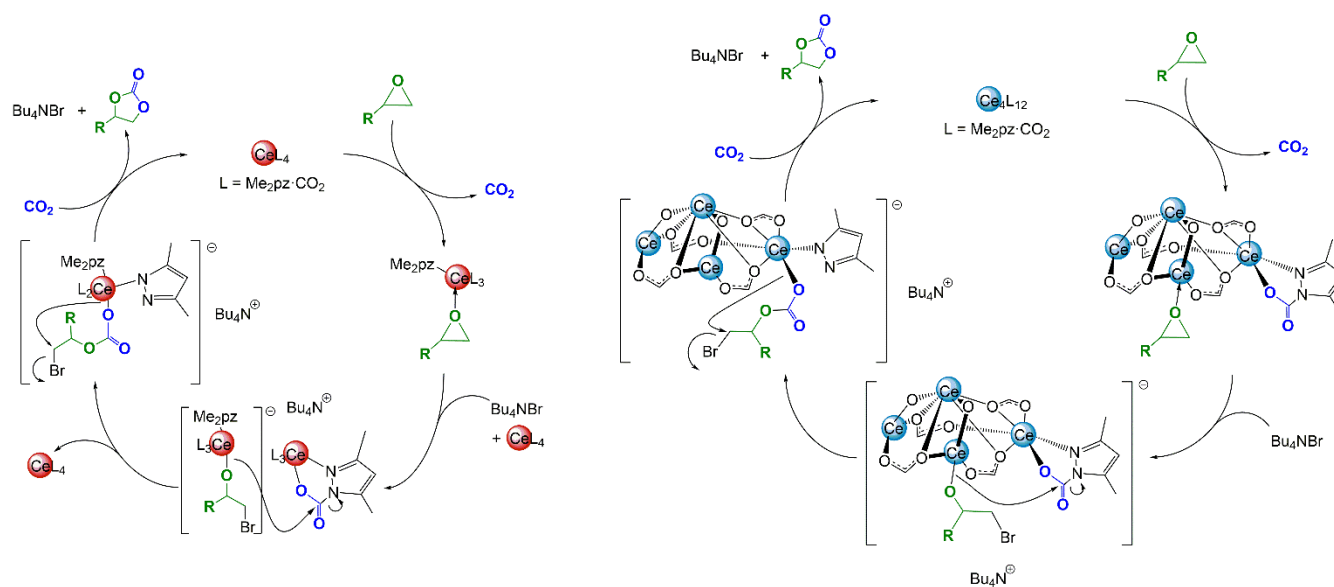
Scheme S1. Proposed mechanism for the cycloaddition of epoxides and carbon dioxide with tetravalent [Ce(Me₂pz·CO₂)₄] **2** (left) and trivalent [Ce₄(Me₂pz·CO₂)₁₂] **5** (right) as catalysts and TBAB as a cocatalyst.

Crystallography

Crystals for X-ray structure analysis were grown using saturated solutions of toluene (**2·toluene**, **3**), thf (**1·thf**, **2·thf**) or *n*-hexane (**5·toluene**) or a mixture of propylene oxide and propylene carbonate (**6**). Suitable crystals for were handpicked in a glovebox, coated with Parabar 10312 and stored on microscope slides and mounted rapidly outside the box onto a microloop Data collection were done on a *Bruker* APEX II Duo diffractometer by using QUAZAR optics and Mo K_α (λ = 0.71073 Å). The data collection strategy was determined using COSMO[5] employing ω scans. Raw data were processed by APEX 3[6] and SAINT,[7] corrections for absorption effects were applied using SADABS.[7] The structures were solved by direct methods and refined against all data by full-matrix least-squares methods on F^2 using SHELXTL[9] and SHELXLE or OLEX 2.[10,11] All atoms were refined anisotropically. The disorders of the solvent molecules were modelled using DSR,[12] a program to refinement of disordered structures with SHELXL. For compound **5** a global restrain (RIGU) was applied to all atoms to achieve a more chemically reasonable model. There are six disordered solvent toluenes in the asymmetric unit. Twinning was found for complex **6** and refinement in hklf 5 format was done. Plots were generated by using CCDC Mercury 3.19.1.[13] Further details regarding the refinement and crystallographic data are listed in Table S2 and in the CIF files.

Table S2. Crystallographic data for compounds **1·thf**, **2·toluene**, **2·thf**, **3, 5·toluene**, and **6**

	1-thf	2·toluene	2·toluene	2·thf
CCDC	1540353	1959858	1959855	1959856
formula	$C_{24}H_{36}CeN_8O$	$C_{31}H_{36}CeN_8O_8$	$C_{24}H_{28}CeN_8O_8$	$C_{32}H_{44}CeN_8O_{10}$
M [g·mol^{-1}]	592.73	788.80	696.66	840.87
λ [Å]	0.71073	0.71073	0.71073	0.71073
color	red/ block	red/ block	yellow/ plate	yellow/ plate
crystal dimensions [mm]	0.3 × 0.3 × 0.3	0.199 × 0.174 × 0.143	0.218 × 0.146 × 0.089	0.206 × 0.204 × 0.113
crystal system	monoclinic	orthorhombic	orthorhombic	orthorhombic
space group	$P2_1/m$	$P2_12_12_1$	Aba2	Aba2
a [Å]	8.5694(16)	14.4389(3)	12.4084(14)	12.4385(8)
b [Å]	17.879(3)	14.8511(3)	12.5664(14)	12.9350(9)
c [Å]	8.7521(15)	15.5578(3)	25.508(3)	22.6128(15)
β [°]	91.013(3)			
V [Å^3]	1340.7(4)	3336.11(12)	3977.4(8)	3638.2(4)
Z	2	4	4	4
F(000)	604	1600	1400	1720
T [K]	100(2)	100(2)	180(2)	150(2)
ρ$_{calcd}$ [g·cm^{-3}]	1.468	1.570	1.163	1.535
μ[mm^{-1}]	1.729	1.426	1.188	1.317
Data / restraints / parameters	2447 / 12 / 182	11095 / 0 / 442	4880 / 1 / 190	5067 / 214 / 282
Goodness of fit	1.055	1.042	0.988	1.034
R$_1$ (I > 2σ (I))[a]	0.0311	0.0186	0.0233	0.0273
$_ω$R$_2$ (all data)[b]	0.0685	0.0439	0.0596	0.0789

[a] $R_1 = \Sigma(||F0|-|Fc||)/\Sigma|F0|, F0> 4s(F0)$. $_ωR_2 = \{\Sigma[w(F02-Fc2)2/\Sigma[w(F02)^2]\}^{1/2}$

Table S2 continued**:**

	3	5	6
CCDC	1959857	1959860	1959859
formula	$C_{73}H_{106}Ce_3N_{24}O_7$	$C_{142}H_{164}Ce_4N_{24}O_{24}$	$C_{40}H_{64}CeN_9O_8$
M [g·mol^{-1}]	1852.18	3151.44	939.12
λ [Å]	0.71073	0.71073	0.71073
color	red/ block	colorless/ block	colorless/ block
crystal dimensions [mm]	0.21 × 0.19 × 0.18	0.311 × 0.211 × 0.078	0.063 × 0.047 × 0.038
crystal system	triclinic	monoclinic	triclinic
space group	P$\bar{1}$	P2$_1$/n	P1
a [Å]	14.463(2)	15.5082(12)	9.725(18)
b [Å]	14.757(2)	47.275(4)	9.843(18)
c [Å]	22.630(3)	19.4079(15)	13.02(2)
α [°]	106.365(2)	90	106.19(2)
β [°]	95.252(2)	94.6410(10)	108.52(2)
γ [°]	110.714(2)	90	90.58(2)
V [Å³]	4235.2(11)	14182.3(19)	1128(4)
Z	2	4	1
F(000)	1884	6432	489
T [K]	100(2)	100(2)	100(2)
ρ$_{calcd}$ [g·cm^{-3}]	1.452	1.476	1.383
μ[mm^{-1}]	1.648	1.336	1.067
Data / restraints / parameters	21905 / 6 / 990	29142 / 9288 / 2151	6581 / 537 / 536
Goodness of fit	1.019	1.293	1.034
R$_1$ (I > 2σ (I))[a]	0.0305	0.0852	0.0683
ωR$_2$ (all data)[b]	0.0698	0.1636	0.1792

[a] $R_1 = \Sigma(||F0|-|Fc||)/\Sigma|F0|, F0 > 4s(F0)$. $_\omega R_2 = \{\Sigma[w(F02-Fc2)2/\Sigma[w(F02)^2]\}^{1/2}$
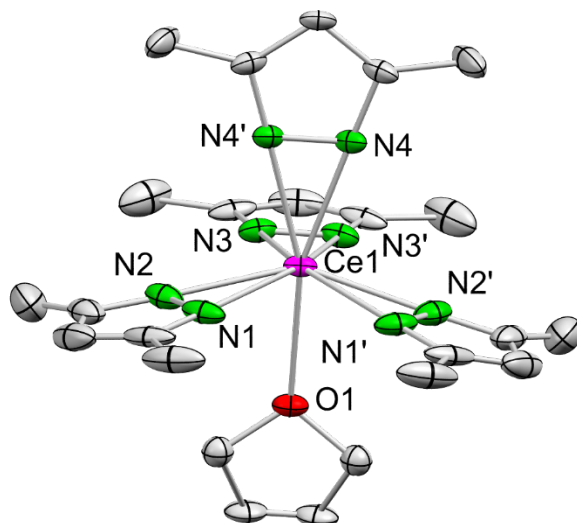
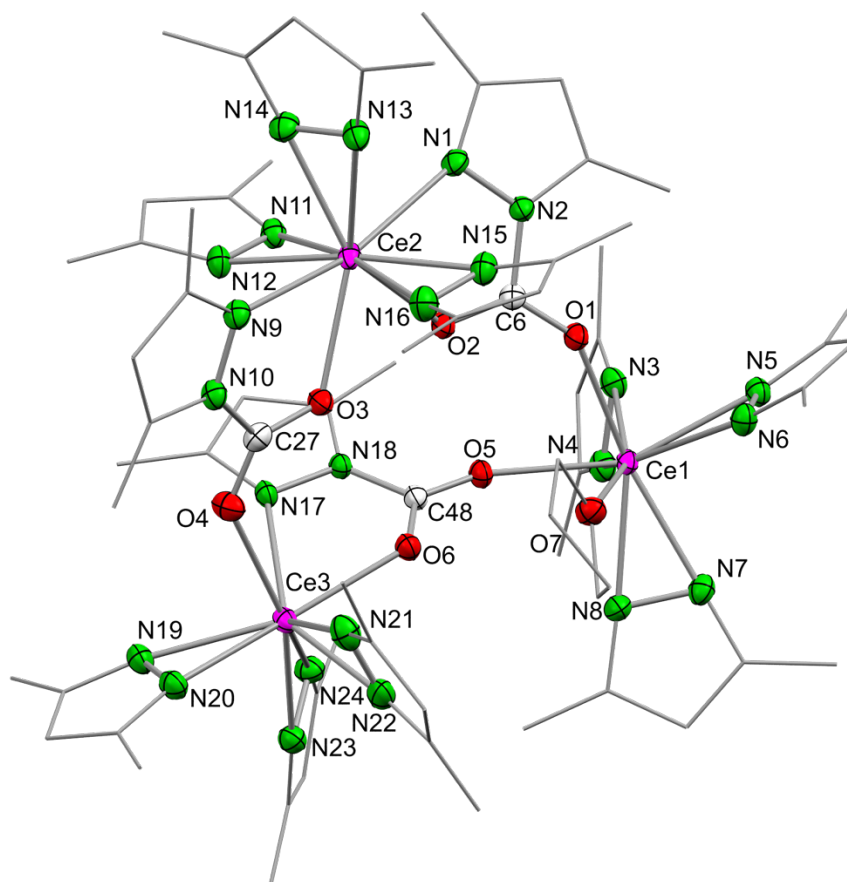**Figure S61.** Crystal structure of [Ce(Me$_2$pz)$_4$(thf)] (**1-thf**). Ellipsoids are shown at the 50 % probability level. Hydrogen atoms and disordered thf are omitted for clarity. Selected bond lengths [Å]: Ce1–N1 2.384(3), Ce1–N2 2.367(3), Ce1–N3 2.364(3), Ce1–N4 2.356(3), Ce1–O1 2.494(4).
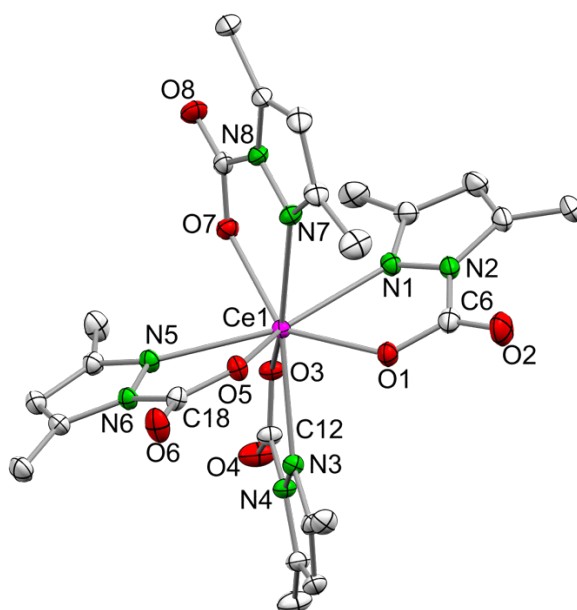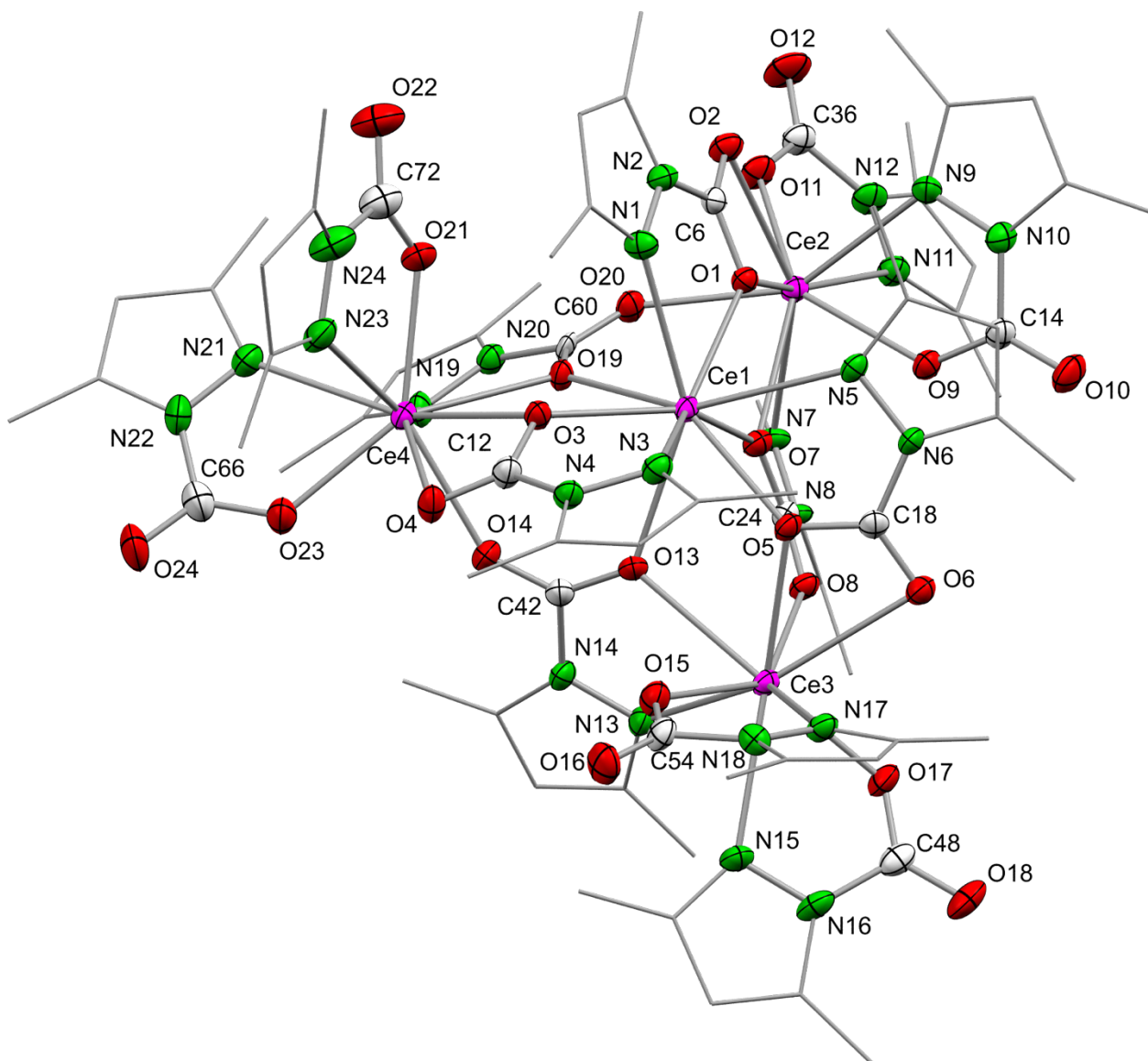

Figure S62. Crystal structure of [Ce(Me$_2$pz·CO$_2$)$_4$] (**2·toluene**). Ellipsoids are shown at the 50 % probability level. Hydrogen atoms and toluene are omitted for clarity. Selected bond lengths [Å]: Ce1–N1 2.530(2), Ce1–N3 2.539(2), Ce1–N5 2.504(2), Ce1–N7 2.538(2), Ce1–O1 2.247(1), Ce1–O3 2.263(1), Ce1–O5 2.244(2), Ce1–O7 2.265(1), C6–O1 1.293(2), C6–O2 1.201(3), C12–O3 1.293(2), C12–O4 1.209(3), C18–O5 1.289(2), C18–O6 1.204(3), C24–O7 1.289(3), C24–O8 1.212(3). Selected angles [°]: O-Ce-N (bite) 64.06(5)-64.68(5).
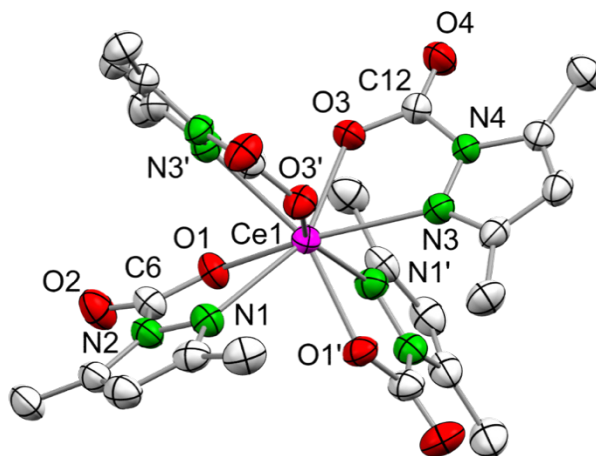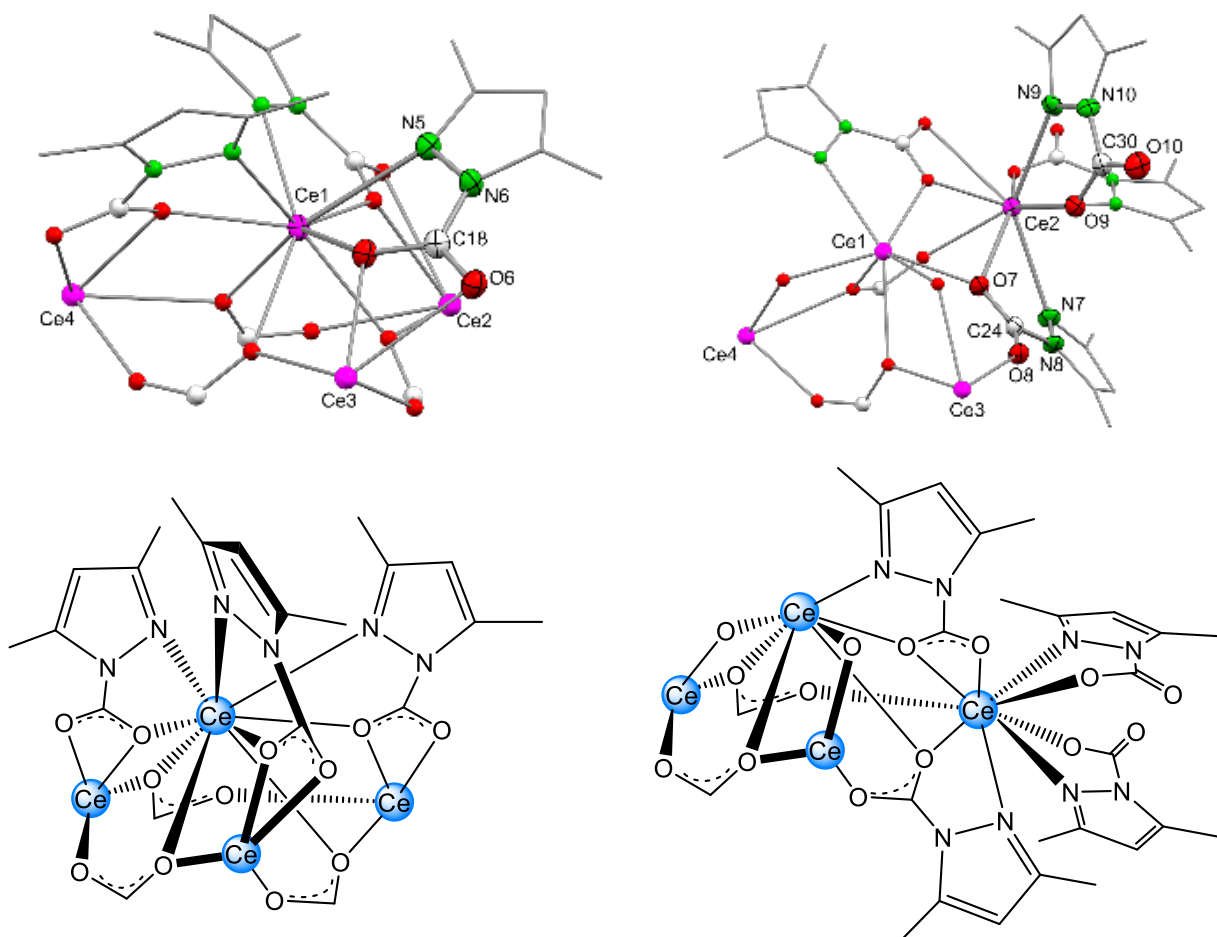
Figure S63. Crystal structure of [Ce(Me$_2$pz·CO$_2$)$_4$]·2 thf (**2·thf**). Ellipsoids are shown at the 50 % probability level. Hydrogen atoms and toluene are removed for clarity. Selected bond lengths [Å]: Ce1–N1 2.516(4), Ce1–N3 2.521(4), Ce1–O1 2.256(4), Ce1–O3 2.246(4), C6–O1 1.312(6), C6–O2 1.188(6), C12–O3 1.308(6), C12–O4 1.190(6). Selected angles [°]: O-Ce-N (bite) 64.95(13)-64.98(13).

Figure S64. Crystal structure of [Ce$_3$(Me$_2$pz)$_9$(Me$_2$pz·CO$_2$)$_3$(thf)] (**3**). Ellipsoids are shown at the 50 % probability level. Hydrogen atoms and *n*-hexane are omitted for clarity. Selected bond lengths [Å]: Ce1–O1 2.374(2), Ce1–O5 2.360(2), Ce1–N3-8 2.356(2)–2.399(2), Ce2–O2 2.436(2), Ce2–O3 2.394(2), Ce2–N1 2.659(2), Ce2–N9 2.645(2), Ce2–N11-16 2.355(2)–2.442(2), Ce3–O4 2.381(2), Ce3–O6 2.372(2), Ce3–N17 2.588(2), Ce3–N19-24 2.327(2)–2.411(2), C6–O1 1.252(3), C6–O2 1.244(3), C27–O3 1.243(3), C27–O4 1.247(3), C48–O5 1.244(3), C48–O6 1.252(3). Selected angles [°]: O-Ce-N bite 61.72(6)-63.69(6).

Figure S65. Crystal structure of [Ce$_4$(Me$_2$pz·CO$_2$)$_{12}$] (**5**). Ellipsoids are shown at the 50 % probability level. Hydrogen atoms and toluene are omitted for clarity. Selected bond lengths [Å]: Ce1–O1/O3/O5 2.386(5)–2.399(5), Ce1–O7/O13/O19 2.579(6)–2.625(5), Ce1–N1/N3/N5 2.688(7)–2.724(7), Ce2–O1/O20 2.473(6)–2.515(5), Ce2–O2/O7 2.675(5) - 2.771(6), Ce2–O9/O11 2.373(5)–2.387(5), Ce2–N7/N9/N11 2.617(7)–2.673(7), Ce3–O5/O8 2.495(6)–2.503(5), Ce3–O6/O13 2.661(5)–2.750(6), Ce3–O15/O17 2.366(5)–2.386(6), Ce3–N13/N15/N17 2.636(7)–2.671(7), Ce4–O3/O14 2.474(6)–2.524(5), Ce4–O4/O19 2.665(5)–2.743(6), Ce4–O21/O23 2.364(6)–2.389(6), Ce4–N19/N21/N23 2.614(8)–2.658(7). Selected angles [°]: O-Ce-N bite 59.43(19)-63.1(2).

Figure S66. Top: Cutouts of the crystal structure of $[Ce_4(Me_2pz \cdot CO_2)_{12}]_4$ (**5**), showing the surrounding of Ce1 and Ce2. Bottom: Schematic view of different $Me_2Pz \cdot CO_2$ binding modes in complex **5**.
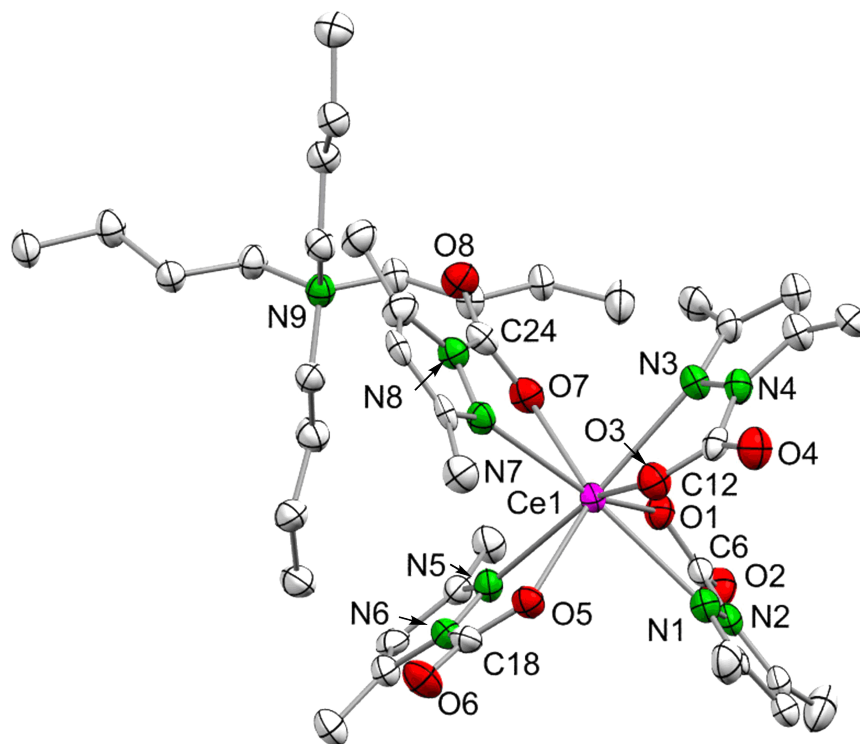
Figure S67. Crystal structure of [Ce(Me$_2$pz·CO$_2$)$_4$][NBu$_4$] (**6**). Ellipsoids are shown at the 50 % probability level. Hydrogen atoms and toluene are omitted for clarity. Selected bond lengths [Å]: Ce1–N1 2.64(2), Ce1–N3 2.62(2), Ce1–N5 2.65(2), Ce1–N7 2.61(2), Ce1–O1 2.40(1), Ce1–O3 2.41(2), Ce1–O5 2.40(1), Ce1–O7 2.40(1), C6–O1 1.27(2), C6–O2 1.21(2), C12–O3 1.26(2), C12–O4 1.20(2), C18–O5 1.26(2), C18–O6 1.22(2), C24–O7 1.29(3), C24–O8 1.20(2). Selected angles [°]: O-Ce-N bite 61.6(5)-62.3(5).
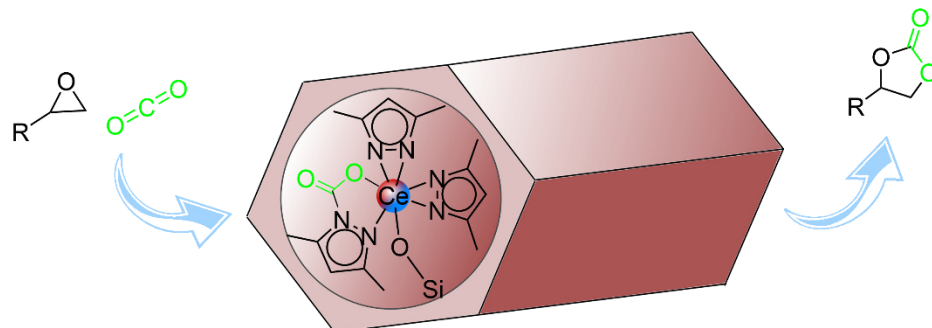
References

[1]   D. Werner, G. B. Deacon, P. C. Junk, R. Anwander, *Dalton Trans.* **2017**, *46*, 6265–6277.

[2]   G.B. Deacon, R. Harika, P.C. Junk, B.W. Skelton, D. Werner, A.H. White, *Eur. J. Inorg. Chem.* **2014**, 2412-2419.

[3]   D. Werner, U. Bayer, N. E. Rad, P. C. Junk, G. B. Deacon, R. Anwander, *Dalton Trans.* **2018**, *47*, 5952–5955.

[4]   G. R. Fulmer, A. J. M. Miller, N. H. Sherden, H. E. Gottlieb, A. Nudelman, B. M. Stoltz, J. E. Bercaw, K. I. Goldberg, *Organometallics* **2010**, *29*, 2176–2179.

[5]   COSMO, v. 1.61; Bruker AXS Inc., Madison, WI, 2012.

[6]   APEX 3, v. 2016.5-0; Bruker AXS Inc., Madison, WI, 2012.

[7]   SAINT, v. 8.34A; Bruker AXS Inc., Madison, WI, 2010.

[8]   L. Krause, R. Herbst-Irmer, G. M. Sheldrick, D. Stalke, *J. Appl. Cryst.* **2015**, *48*, 3-10.

[9]   a) G. M. Sheldrick, *SHELXS: Acta Cryst.* **2008**, *A64*, 112-122; b) G. M. Sheldrick, *Acta Crystallogr.*, Sect. A **2015**, *71*, 3-8.

[10]   C. B. Hübschle, G. M. Sheldrick, B. J. Dittrich, *J. Appl. Cryst.* **2011**, *44*, 1281-1284.

[11]   O. V. Dolomanov, L. J. Bourhis, R. J. Gildea, J. A. K. Howard, H. Puschmann, *J. Appl. Cryst.* **2009**, *42*, 339-341.

[12]   D. Kratzert, J. J. Holstein, I. Krossing, DSR: enhanced modelling and refinement of disordered structures with SHELXL. *J. Appl. Cryst.* **2015,** *48*, 933-938.

[13]   C. F. Macrae, I. J. Bruno, J. A. Chisholm, P. R. Edgington, P. McCabe, E. Pidcock, L. Rodriguez-Monge, R. Taylor, J. van de Streek, P. A. Wood, *J. Appl. Cryst.* **2008**, *41*, 466-470.

Cerium Pyrazolates Grafted onto Mesoporous Silica SBA-15: Reversible CO₂ Uptake and Catalytic Cycloaddition of Epoxides and Carbon Dioxide

Cerium Pyrazolates Grafted onto Mesoporous Silica SBA-15: Reversible CO_2 Uptake and Catalytic Cycloaddition of Epoxides and Carbon Dioxide

Uwe Bayer, Yucang Liang, and Reiner Anwander*

ABSTRACT: The activation and catalytic conversion of CO_2 is a current topic relating to molecular chemistry and materials science alike. As a transdisciplinary field of research, surface organometallic chemistry (SOMC) might be applicable to perform synergistically, thus striking a new path in sustainable chemistry. Both ceric and cerous rare-earth-metal pyrazolates, which were recently shown to reversibly insert CO_2 and to promote the catalytic cycloaddition of epoxides and carbon dioxide, were grafted onto large-pore mesoporous silica SBA-15$_{500}$, thermally pretreated at 500 °C. The obtained hybrid materials $[Ce(Me_2pz)_4]_2$@SBA-15$_{500}$, $Ce(Me_2pz)_4(thf)$@SBA-15$_{500}$, $Ce_4(Me_2pz)_{12}$@SBA-15$_{500}$, and $[Ce(Me_2pz)_3(thf)]_2$@SBA-15$_{500}$ (Me_2pz = 3,5-dimethylpyrazolato) were characterized by DRIFTS (diffuse reflectance infrared Fourier transform spectroscopy), solid-state $^1H/^{13}C$ NMR spectroscopy, elemental analysis, ICP/OES, and N_2 physisorption. The lanthanum(III)-based material $[La(Me_2pz)_3(thf)]_2$@SBA-15$_{500}$ was synthesized for better assessment of the cerous materials being highly sensitive to oxidation. To mimic ceric surface species, $Ce[OSi(OtBu)_3]_3Cl$ was treated with 1 equiv of $K(Me_2pz)$, generating the mixed pyrazolyl/siloxy complex $KCe[OSi(OtBu)_3]_4(Me_2pz)$ featuring a cerium(IV)-bonded terminal pyrazolato ligand. All hybrid materials show efficient and reversible carbon dioxide uptake of maximum 20 wt % in the solid state. When combined with tetra-n-butylammonium bromide (TBAB), the hybrid materials catalyze the cycloaddition of CO_2 and epoxides, displaying good conversion of various epoxides and reusability.
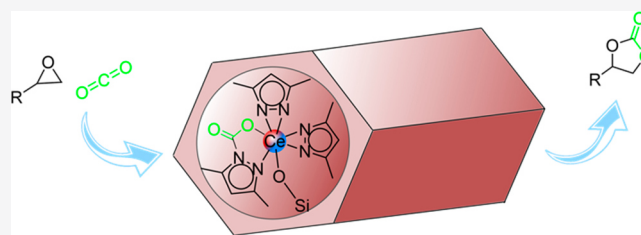
INTRODUCTION

Even though or precisely because carbon dioxide is the most notorious greenhouse gas, it is currently assessed as a cheap, abundant, and nontoxic C1 building block.[1] As a result, the utilization of CO_2 in organic synthesis emerged as an important target of sustainable chemistry.[2] Auspicious approaches are capturing and storing of carbon dioxide[3] as well as its conversion into more valuable organic molecules/feedstocks.[4] A prominent catalytic transformation features the reaction of CO_2 with epoxides to generate either polycarbonates[5] or cyclic carbonates.[6] Compared to the vast number of transition-metal complexes employed for catalytic CO_2 transformations, especially derived from zinc and cobalt,[6d] the count of active rare-earth-metal-based complexes seems small. One reason for this might be the lower catalytic activities observed until now in comparison to transition-metal-derived systems. Nevertheless, several rare-earth-metal complexes are known to catalyze the formation of cyclic carbonates with good turnover numbers and frequencies.[7]

Surface organometallic chemistry (SOMC) is a concept bearing several advantages compared to organometallic homogeneous catalysis.[8,9] By immobilizing metal complexes onto supports with a large surface area, e.g., periodic mesoporous silica,[10] the generation of well-defined, highly active surface species can be achieved. Through direct metal–support "covalent" bonding, these surface species are favorably protected from deactivation, while isolated metal sites in general increase the activity of the catalytic system via surface (and pore) confinement.[8b,c] Additionally, the grafting of organometallics can suppress oligomerization and therefore promote monomerization or at least formation of smaller aggregated surface species.[8b,c,10]

We have recently reported on homoleptic 3,5-dimethyl pyrazolates $[Ce(Me_2pz)_4]_2$ and $Ce_4(Me_2pz)_{12}$ capable of inserting carbon dioxide efficiently and reversibly and of promoting the catalytic cycloaddition of CO_2 and epoxides.[11] Applying the pK_a criterion,[12] metal pyrazolates are supposed to display suitable candidates for SOMC.[13] In light of this, we have now embarked on a strategy using grafted variants of such rare-earth-metal pyrazolates for carbon dioxide capture and conversion.
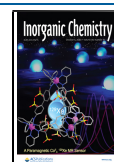
Table 1. Characterization Data of Support and Hybrid Materials

material	a_{BET}[a] (m^2 g^{-1})	V_{pore}[b] (cm^3 g^{-1})	d_{pore}[c] (nm)	$c_{surface\ SiOH}$[d] (mmol g^{-1})	wt % metal[e]
SBA-15$_{500}$	887	0.96	6.8	3.086	
[Ce(Me$_2$pz)$_4$]$_2$@SBA-15$_{500}$ (**H1**)	459	0.55	5.2		10.80
Ce(Me$_2$pz)$_4$(thf)@SBA-15$_{500}$ (**H2**)	353	0.42	5.2		9.96
Ce$_4$(Me$_2$pz)$_{12}$@SBA-15$_{500}$ (**H3**)	163	0.19	4.9		22.19
[Ce(Me$_2$pz)$_3$(thf)]$_2$@SBA-15$_{500}$ (**H4**)	159	0.19	4.9		20.27
[La(Me$_2$pz)$_3$(thf)]$_2$@SBA-15$_{500}$ (**H5**)	160	0.19	5.0		21.05

[a]BET surface area calculated between p/p_0 0.07 and 0.15. [b]BJH desorption cumulative pore volume between 2.0 and 10 nm. [c]Maximum pore diameter from the BJH desorption branch. [d]Calculated according to published procedures.[16] [e]Metal content determined by ICP-OES.

RESULTS AND DISCUSSION

SOMC Precursors. A large-pore mesoporous silica SBA-15[14] was chosen as a support material to allow for an exhaustive surface grafting of comparatively large pyrazolate complexes.[15] Concomitantly, any diffusion limitations during the envisaged catalytic transformation ought to be minimized. Silylation/grafting experiments[16] and N$_2$ physisorption measurements of the parent support material were conducted after activation at 500 °C and 10^{-3} mbar (denoted by SBA-15$_{500}$). The Si−OH surface population and the (mostly uniform) pore diameter were determined to be 2.1 sites per nm^2 and ca. 7 nm (Table 1). The presence of isolated Si−OH groups was also supported by DRIFTS measurements (Figure 1). Homoleptic
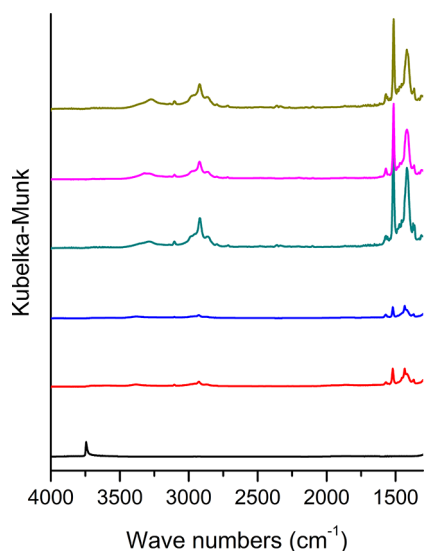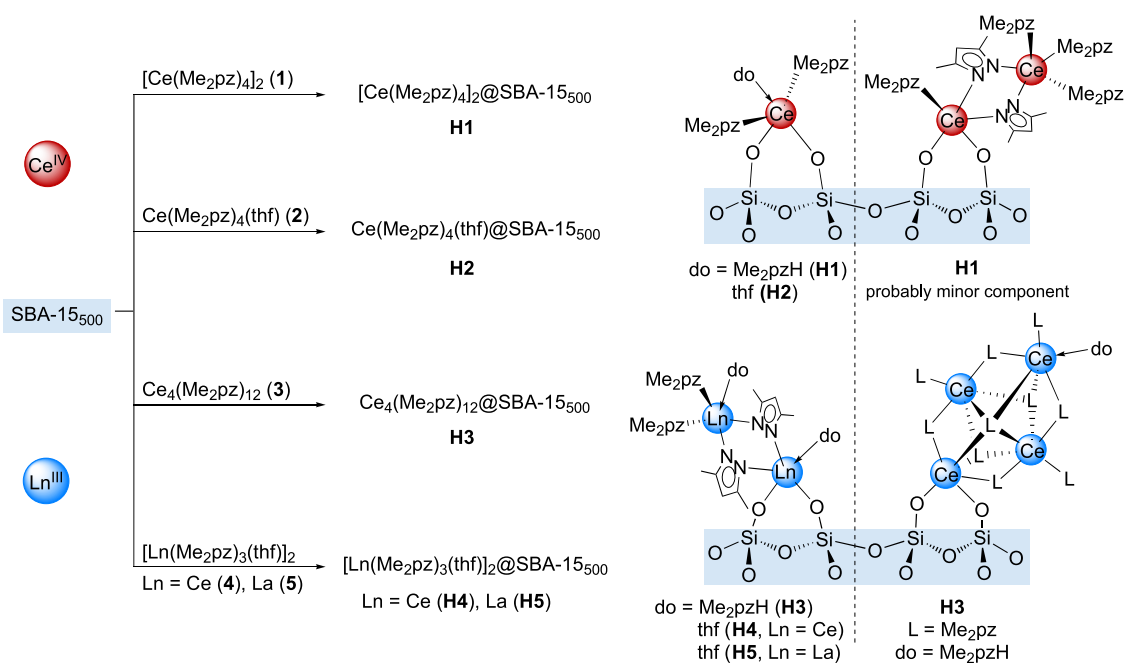

Figure 1. DRIFT spectra of support material SBA-15$_{500}$ (black), [Ce(Me$_2$pz)$_4$]$_2$@SBA-15$_{500}$ (**H1**) (red), Ce(Me$_2$pz)$_4$(thf)@SBA-15$_{500}$ (**H2**) (blue), Ce$_4$(Me$_2$pz)$_{12}$@SBA-15$_{500}$ (**H3**) (teal), [Ce(Me$_2$pz)$_3$(thf)]$_2$@SBA-15$_{500}$ (**H4**) (pink), and [La(Me$_2$pz)$_3$(thf)]$_2$@SBA-15$_{500}$ (**H5**) (yellow) from bottom to top.

and donor-coordinated ceric and cerous pyrazolates [Ce-(Me$_2$pz)$_4$]$_2$ (**1**), Ce(Me$_2$pz)$_4$(thf) (**2**), Ce$_4$(Me$_2$pz)$_{12}$ (**3**), and [Ce(Me$_2$pz)$_3$(thf)]$_2$ (**4**) were selected as molecular grafting precursors and synthesized according to literature-known procedures.[11,12,17] Having in mind the extreme redox sensitivity of silica-grafted cerous surface species,[18] the SOMC was additionally performed with the lanthanum derivative [La(Me$_2$pz)$_3$(thf)]$_2$ (**5**). We refrained from a sequential grafting approach, that is, treatment of putative hybrid material Ce[N(SiHMe$_2$)$_2$]$_4$@SBA-15 with pyrazole Me$_2$pzH, due to the likely occurrence of side-reactions.[18b]

Ln−Me$_2$pz@SBA-15$_{500}$. The pyrazolates **1−5** were reacted with dehydrated SBA-15$_{500}$ in *n*-hexane by using super-stoichiometric amounts of the metal−organic complexes (Scheme 1). Successful grafting experiments were supported by DRIFTS measurements. The complete consumption of the isolated surface hydroxy groups was evidenced by the disappearance of the Si−OH stretching vibration at 3743 cm^{-1} (Figure 1). NMR spectroscopic analysis of the supernatants collected from the grafting reactions of tetravalent **1** and **2** revealed the formation of pyrazole-coordinated complex Ce(Me$_2$pz)$_4$(Me$_2$pzH), further corroborating the release of Me$_2$pzH during the protonolysis reaction (Figure S6, Supporting Information). This also implies that with proceeding reaction time the grafting of monometallic complex Ce(Me$_2$pz)$_4$(Me$_2$pzH) prevails. Moreover, continued release of proligand Me$_2$pzH might deoligomerize initially formed dimetallic pyrazolato-bridged ceric surface species. Likewise, any signals for Me$_2$pzH have been absent in the supernatants examined from the grafting experiments of cerous pyrazolates **3−5**, clearly suggesting the formation of donor-stabilized surface species. Such donor stabilization through "free" pyrazoles is well-known for pyrazolate complexes, e.g., Hf(Me$_2$pz)$_4$(Me$_2$pzH) or Ce(Me$_2$pz)$_4$(Me$_2$pzH).[19] ICP-OES measurements and elemental analyses of the hybrid materials revealed high metal contents as well as high CHN values. Strikingly, the metal content of the trivalent hybrid materials **H3**, **H4**, and **H5** (∼20%) is approximately twice as high as detected for the tetravalent materials **H1** and **H2**, most likely due to grafting of bimetallic or even tetrametallic species. For a better overview, the proposed surface species depicted in Scheme 1 consider only a bipodal surface attachment; distinguishing between surface-bound (≡SiO)[Ce(Me$_2$pz)$_3$] and (≡SiO)$_2$[Ce(Me$_2$pz)$_2$(Me$_2$pzH)] is hardly possible. Nevertheless, calculations of the maximum metal content for exclusively monopodal (17.1% for a monometallic tetravalent surface species in **H2**, 22.9% for dimetallic trivalent surface species in **H4** and **H5**) and bipodal grafting (13.3% for **H2**, 19.3% for **H4** and **H5**) suggest a significant amount of bipodally grafted complex. Because of the unknown quantity of pyrazole donor ligands, only THF coordinated materials were calculated. However, all these calculations can only give hints about the nature of the surface bound species, as the exact amount of coordinated pyrazole and THF is hardly to be determined.

The formation of dimetallic cerium and lanthanum surface complexes upon grafting of trivalent **3** to **5** was also suggested by ^{13}C CP/MAS (magic angle spinning) NMR spectroscopy (Figure 2). The spectra of ceric hybrid materials **H1** and **H2** are quite similar, suggesting the presence of one Ce−Me$_2$pz environment and, hence, the existence of monometallic surface species (Scheme 1). In contrast, the spectrum of the likewise

Scheme 1. Direct Grafting Approach of Rare-Earth-Metal 3,5-Dimethyl Pyrazolates on SBA-15$_{500}$ and Proposed Bipodal Surface Species[a]

[a]Left: most likely formed surface species based on spectral data; right: other possible surface species which can be formed.
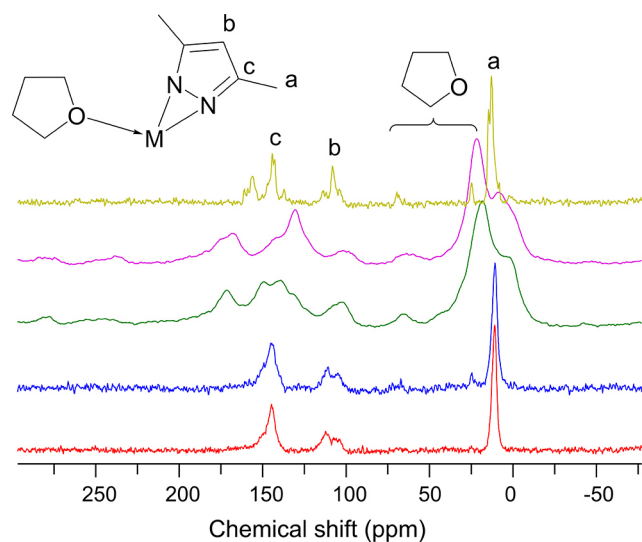

Figure 2. ^{13}C CP/MAS NMR spectra of $[Ce(Me_2pz)_4]_2$@SBA-15$_{500}$ (**H1**) (red), $Ce(Me_2pz)_4(thf)$@SBA-15$_{500}$ (**H2**) (blue), $Ce_4(Me_2pz)_{12}$@SBA-15$_{500}$ (**H3**) (green), $[Ce(Me_2pz)_3(thf)]_2$@SBA-15$_{500}$ (**H4**) (pink), and $[La(Me_2pz)_3(thf)]_2$@SBA-15$_{500}$ (**H5**) (yellow) from bottom to top.

diamagnetic material $[La(Me_2pz)_3(thf)]_2$@SBA-15$_{500}$ (**H5**) shows two signal sets for the grafted La−Me$_2$pz moieties. The respective cerous material $[Ce(Me_2pz)_3(thf)]_2$@SBA-15$_{500}$ (**H4**) gave a spectrum with paramagnetically broadened (and slightly shifted) signals, but a peak pattern reminiscent of that of the lanthanum derivative. The ^{13}C CP/MAS NMR spectrum of material **H3**, derived from the cerous cluster $Ce_4(Me_2pz)_{12}$, exhibits a distinct peak pattern at around 150 ppm, indicating more diverse Ce−Me$_2$pz environments, in line with surface cluster species. Additionally, the spectra of hybrid materials **H2**−**H5** display signals for coordinated THF.

N$_2$ physisorption measurements were conducted to investigate the influence of the grafting reactions on the surface area and pore size (Figure 3). To this end, the hybrid materials have been degassed at ambient temperature for 12 h. Because of their high sensitivity, degassing at higher temperatures was not possible. However, the cerium hybrid materials **H1** to **H4** showed evidence for decomposition (donor molecule displacement) during the degas processes as indicated by a color change from red/orange to yellow for **H1** and **H2** and from colorless to yellow for **H3** and **H4**, respectively. No color change was observed for lanthanum hybrid material **H5**. Because the physisorption isotherms of hybrid materials **H4** (cerium) and **H5** (lanthanum), and the surface/pore data derived therefrom, differ only marginally, the extent of decomposition seemed minor. Assuming decomposition at high vacuum, hybrid material **H4** was exposed to high vacuum (<9 × 10^{-5} mbar). In doing so, a color change from colorless to pale yellow was observed after 30 min, which strengthened in intensity with increasing evacuation time (Figure S3). Although information from the physisorption measurements must be treated carefully, the results support previous findings.[18b] The pore diameter and pore volume as well as the surface area of the hybrid materials are drastically reduced compared to the parent material (Table 1), indicating successful grafting. Striking are the extremely decreased surface areas and pore volumes of the trivalent hybrid materials, suggesting the presence of larger (multi)dimetallic surface complexes. Such pronounced filling of the mesopores with trivalent pyrazolates is also evidenced by the high metal contents.

A Mixed Pyrazolyl/Siloxy Ce^{IV} Model Complex. Tris-*tert*-butoxysiloxy moieties are routinely used as a molecular model for silica surfaces.[20] Accordingly, homoleptic [Ce-(Me$_2$pz)$_4$]$_2$ (**1**) was treated with 1 equiv of HOSi(O*t*Bu)$_3$ targeting a mixed pyrazolyl/siloxy complex. However, the ^{1}H
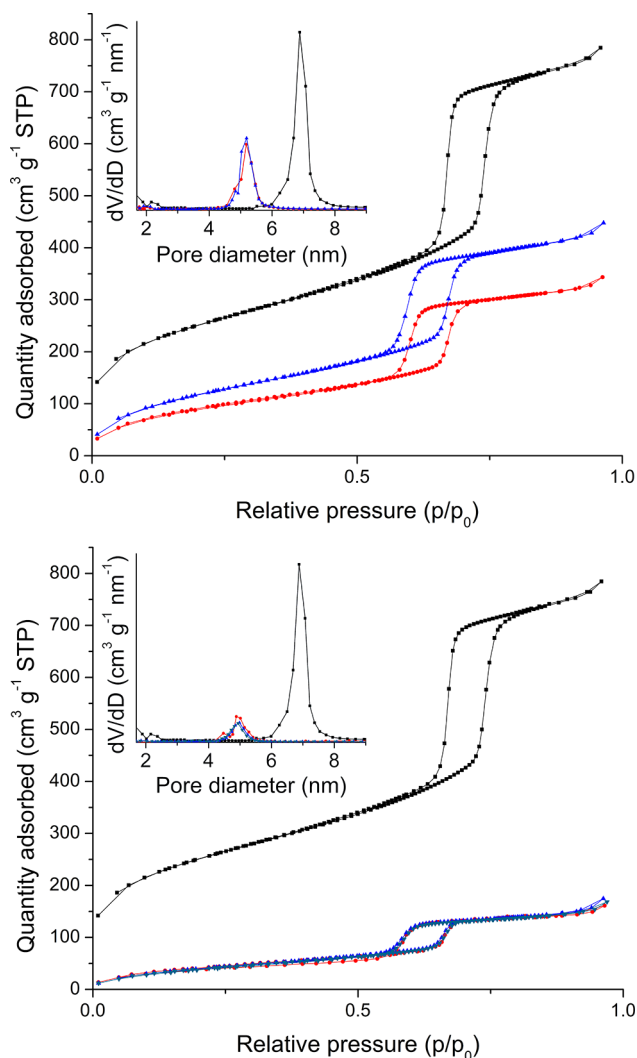
Figure 3. N₂ physisorption isotherms and pore size distribution. Top: parent material SBA-15$_{500}$ (black) and ceric [Ce(Me₂pz)₄]₂@SBA-15$_{500}$ (**H1**) (blue) and Ce(Me₂pz)₄(thf)@SBA-15$_{500}$ (**H2**) (red). Bottom: parent material SBA-15$_{500}$ (black) and cerous Ce₄(Me₂pz)₁₂@SBA-15$_{500}$ (**H3**) (teal), [Ce(Me₂pz)₃(thf)]₂@SBA-15$_{500}$ (**H4**) (red), and [La(Me₂pz)₃(thf)]₂@SBA-15$_{500}$ (**H5**) (blue).

Scheme 2. Reaction of Ce[OSi(OtBu)₃]₃Cl with K(Me₂pz) Giving KCe[OSi(OtBu)₃]₄(Me₂pz) (6) and K[OSi(OtBu)₃](Me₂pzH)(Et₂O) as well as Other Unidentified Products
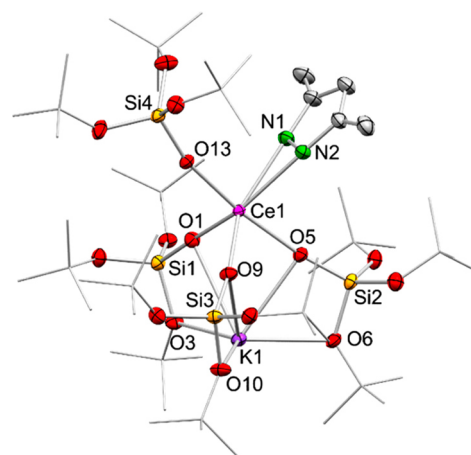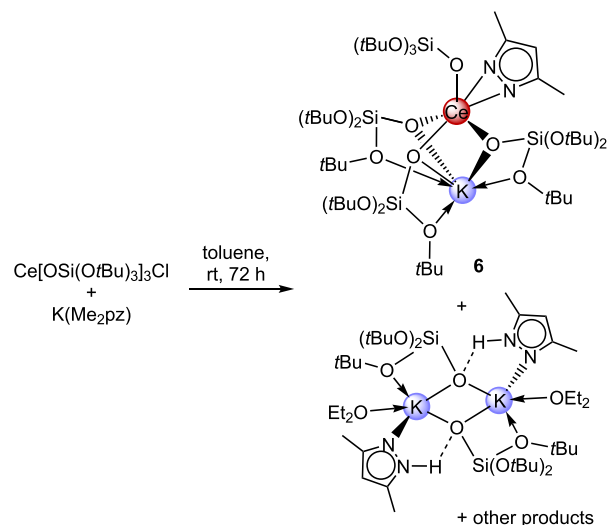
Figure 4. Crystal structure of KCe[OSi(OtBu)₃]₄(Me₂pz) (**6**). Ellipsoids are shown at the 50% probability level. Hydrogen atoms are omitted for clarity. Selected bond lengths [Å] and angles [deg]: Ce1−O1 2.1814(11), Ce1−O5 2.2126(11), Ce1−O9 2.1626(11), Ce1−O13 2.1545(11), Ce1−N1 2.3996(14), Ce1−N2 2.4084(14), Ce1−O13−Si4 166.33(7).

NMR spectrum of this reaction indicated the formation of the ceric pyrazole adduct Ce(Me₂pz)₄(Me₂pzH). Clearly, the pyrazole proligand is formed via protonolysis of **1**, but the formation of a ceric siloxy derivative like Ce[OSi(OtBu)₃]₄, via ligand redistribution, was not observed (Figure S7). As an alternative synthesis pathway to access a mixed pyrazolyl/siloxy Ce^{IV} complex, the literature-known complex Ce[OSi-(OtBu)₃]₃Cl[21] was treated with 1 equiv of K(Me₂pz) in toluene (Scheme 2). A color change from light yellow to orange and a concomitant precipitation of a colorless solid were indicative of a successful salt metathesis reaction.

Regrettably, crystallization from a 1:1 *n*-pentane/Et₂O mixture afforded two different sorts of crystals: colorless crystals of K[OSi(OtBu)₃](Me₂pzH)(Et₂O) (Figure S18) and orange crystals which were identified as ceric KCe[OSi-(OtBu)₃]₄(Me₂pz) (**6**). The crystal structure of **6** revealed a six-coordinated cerium center surrounded by a terminal η²-Me₂pz ligand and four tris-*tert*-butoxysiloxy ligands. Three of the latter siloxy ligands additionally embed a potassium atom (Figure 4). The Ce1−O$_{term}$ (2.1545(11) Å) and especially

Ce1−O$_{bridging}$ (2.1626(11)−2.2126(11) Å) distances are slightly elongated compared to the THF-donor adduct of the used precursor Ce[OSi(OtBu)₃]₃Cl(thf)₂ (2.096(4)−2.121(3) Å) due to bridging to the potassium atom.[21] Similarly, other Ce^{IV} siloxides such as Ce[OSi(OtBu)₃]₄ (2.089(2)−2.157(2) Å[21] and 2.084(2)−2.160(2) Å[22]) or Ce(OSiPh₃)₄(dme) (2.098(1)−2.133(1) Å)[23] exhibit shorter Ce−O$_{term}$ distances. The Ce1−N distances (2.3996(14)−2.4084(14) Å) compare well to other terminal Ce^{IV}−N(pz) bonds (Ce(tBu₂pz)₄: 2.322(4)−2.365(4) Å; **1**: 2.319(3)−2.384(2) Å; **2**: 2.356(3)−2.384(3) Å).[11,12] Interestingly, the pyrazolylato ligand does not adopt a bridging position by linking to the alkali metal as observed in ceric ate complex LiCe(Me₂pz)₉.[19b] Nonetheless, the coordination behavior of the potassium metal center was found to be similar to those in cerous ate complexes KCe[OSi(OtBu)₃]₄ and KCe[OSi(OtBu)₃]₄(thf)₂.[22,24]
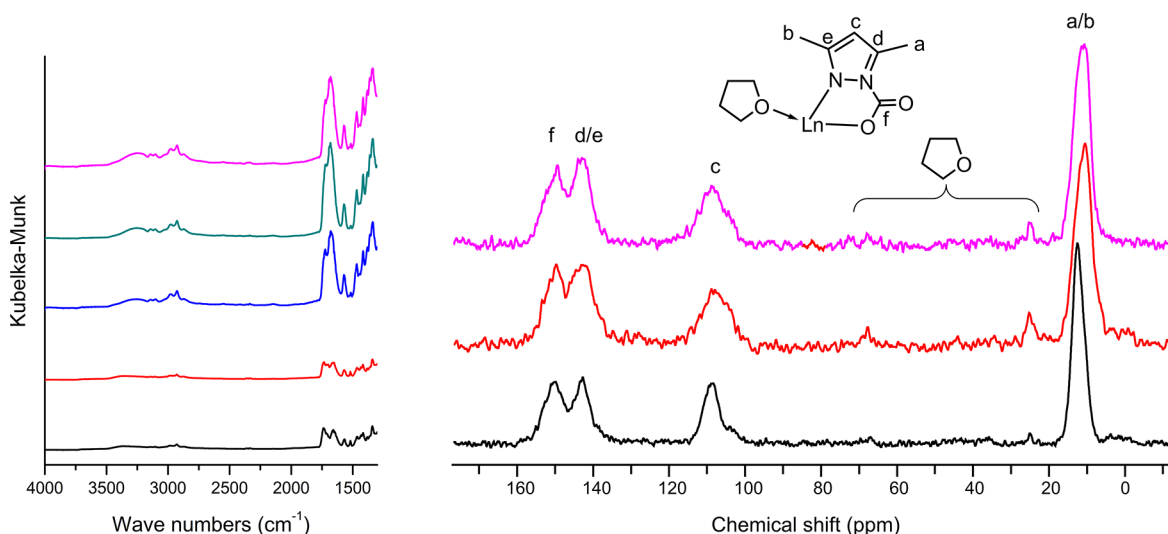
Figure 5. Left: DRIFT spectra of $CO_2@[Ce(Me_2pz)_4]_2@SBA-15_{500}$ (**H1^{CO2}**) (black), $CO_2@Ce(Me_2pz)_4(thf)@SBA-15_{500}$ (**H2^{CO2}**) (red), $CO_2@$ $Ce_4(Me_2pz)_{12}@SBA-15_{500}$ (**H3^{CO2}**) (blue), $CO_2@[Ce(Me_2pz)_3(thf)]_2@SBA-15_{500}$ (**H4^{CO2}**) (teal), and $CO_2@[La(Me_2pz)_3(thf)]_2@SBA-15_{500}$ (**H5^{CO2}**) (pink). Right: ^{13}C CP/MAS NMR spectra of $CO_2@[Ce(Me_2pz)_4]_2@SBA-15_{500}$ (**H1^{CO2}**) (black), $CO_2@Ce(Me_2pz)_4(thf)@SBA-15_{500}$ (**H2^{CO2}**) (red), and $CO_2@[La(Me_2pz)_3(thf)]_2@SBA-15_{500}$ (**H5^{CO2}**) (pink) from bottom to top.

A ^1H NMR spectroscopic investigation in toluene-d_8 of the crude product revealed the formation of two species in a 2:1 ratio supporting the presence of both $K[OSi(OtBu)_3]$-$(Me_2pzH)(Et_2O)$ and **6**. As the signals assigned to the siloxy groups both exhibit almost the same chemical shift (1.50 ppm), any unambiguous integration or definite statement for the ratio of siloxy to pyrazolyl groups of the respective complex was not possible. Also, because of cocrystallization of the two products, further analytics were inconclusive.

However, treatment of the crude product with 1 bar of CO_2 in toluene-d_8 gave a color change from orange to colorless within 5 min, and the ^1H NMR spectrum displayed new signal sets, indicative of a successful reaction with CO_2 (Figure S9). A splitting of the two methyl group resonances of the Me_2pz ligand suggests the formation of a $Me_2pz·CO_2$ moiety resulting from carbon dioxide insertion as it was previously observed for **1** and **2**.[11] Unfortunately, the CO_2-inserted product could not be obtained in single-crystalline form.

Carbon Dioxide Fixation. High surface mesoporous silica-supported polyamines belong to the most effective sorbents for carbon dioxide capture and storage (e.g., 3N-APS@SBA-15, anhydrous conditions: 2.41 mmol CO_2 g^{-1} at 1 atm $\triangleq$ 10.6 wt %; 3N-APS = N-[(3-trimethoxysilyl)propyl]-diethylenetriamine).[3b,25] Therefore, and because of the efficient CO_2 uptake of rare-earth-metal pyrazolates,[11] hybrid materials **H1** to **H5** have been investigated for their reactivity toward CO_2. Thus, the materials were stored under 1 bar CO_2 pressure for 16 h. The tetravalent cerium materials **H1** and **H2** gave a color change from red/orange to pale orange and an increase in weight of ~10 wt %. No color change was observed for the trivalent congeners, but an increase in weight of ~20 wt % ($\triangleq$ 4.54 mmol CO_2 g^{-1}) was found. This was indicative of a successful chemisorption of carbon dioxide and the formation of materials of composition $CO_2@[Ce(Me_2pz)_4]_2@SBA-15_{500}$ (**H1^{CO2}**), $CO_2@Ce(Me_2pz)_4(thf)@SBA-15_{500}$ (**H2^{CO2}**), $CO_2@Ce_4(Me_2pz)_{12}@SBA-15_{500}$ (**H3^{CO2}**), $CO_2@[Ce-(Me_2pz)_3(thf)]_2@SBA-15_{500}$ (**H4^{CO2}**), and $CO_2@[La-(Me_2pz)_3(thf)]_2@SBA-15_{500}$ (**H5^{CO2}**). DRIFTS measurements supported the insertion of CO_2, showing strong absorption

bands at around 1600−1750 cm^{-1} for the C−O stretch vibrations (Figure 5). The ^{13}C CP/MAS NMR spectra of diamagnetic **H1^{CO2}**, **H2^{CO2}**, and **H5^{CO2}** displayed signals at about 150 ppm, unequivocally confirming the insertion of CO_2 into the Ln−pyrazolato moieties. Furthermore, a splitting of the Me_2pz methyl signal in accordance with the asymmetry induced by the carbon dioxide insertion is indicated (Figure 5: two methyl signals for **H5^{CO2}** at 11.4/10.8 ppm and a shoulder for **H2^{CO2}**). Comparing **H5** and **H5^{CO2}**, the ^{13}C CP/MAS NMR spectrum of **H5^{CO2}** shows only one set of signals suggesting the formation of a more symmetric surface species. Note that CO_2 insertion might not only occur into Ce−pyrazolato moieties but also involve the Ln−pyrazole adduct bonding.[26]

To investigate into the reversibility of carbon dioxide insertion, thermogravimetric analyses (TGA) were performed under constant argon flow and slowly heating the sample to 350 °C (Figure S17). Unfortunately, the cerium-based hybrid materials turned out to be too sensitive for the measurements, and therefore no reliable TGA could be obtained. For the lanthanum-based hybrid material **H5^{CO2}**, a weight decrease of ~15 wt % was found to occur in three steps, starting at ~50 °C, then at ~100 °C, and finally at ~150 °C. An accurate value could not be determined for each step. At 220−230 °C another weight loss of ~11 wt % was observed. These numbers would fit well to the 14.5 wt % for inserted CO_2 and 12.7 wt % for coordinated THF. (For the calculation of the THF amount $[\{La(Me_2pz·CO_2)_2(thf)\}\{La(Me_2pz·CO_2)_3(thf)\}]^+$ was assumed as the only surface species.) Noteworthy, sublimation attempts of **1** at 200 °C gave both sublimed **1** and decomposition products, indicating thermal instability of rare-earth-metal pyrazolates at temperatures of 200 °C and higher. Therefore, a progressive decomposition of the surface pyrazolate complexes during the TGA measurements at temperatures higher than 200 °C cannot be ruled out.

Cycloaddition of CO_2 and Epoxides. Studies on the catalytic cycloaddition of CO_2 and epoxides were conducted by using hybrid materials **H1** to **H5** and TBAB (tetra-n-butylammonium bromide) as a catalyst system. To determine

the most active system, **H1** to **H5** were prescreened by combining each 0.1 mol % with TBAB in propylene oxide in the absence of a solvent and admittance of CO_2 (10 bar). After the reaction mixture was stirred at 90 °C for 24 h, the progress of the reaction was determined by ^1H NMR spectroscopy. In contrast to the homogeneous catalysts, these hybrid materials showed no significant difference in the catalytic activity regarding the oxidation state of the metal (Figure S10, conversions between 66% and 77%). The mechanism of the rare-earth-metal pyrazolate-catalyzed cycloaddition of CO_2 and epoxides was considered previously and includes (1) coordination of the epoxide to the rare-earth-metal center, (2) nucleophilic ring-opening attack of the bromide (TBAB) and formation of an alkoxy species, (3) nucleophilic attack of the alkoxy moiety at the pyrazolyl-inserted "activated" CO_2, and (4) ring-closure and displacement of the cyclic carbonate and TBAB by CO_2.[11,27] As the nucleophilic ring-opening of the epoxide is the rate-determining step,[6a] and its efficacy ascribed to the degree of Lewis acidity of the rare-earth metal cation, it is noteworthy that this behavior seems less pronounced for cerium-grafted materials (Ce[III] vs Ce[IV]). Therefore, thf-free hybrid material **H1** was chosen to further investigate the catalytic formation of other cyclic carbonates. To obtain full conversion, the catalyst loading was increased to 0.5 mol %.

As observed for the homogeneous catalytic cycloaddition of epoxides and CO_2, the conversions decrease with increasing steric bulk of the substituent at the epoxide.[11] Therefore, conversions of >90% were obtained for propylene oxide, 1,2-epoxyhexane, and styrene oxide, and a slightly lower conversion of 66% for 3,3-dimethyl-1,2-epoxybutane (Scheme 3). By varying the amount of catalyst and cocatalyst, we

Scheme 3. Catalytic Conversion of Epoxides and CO_2 Using 0.5 mol % [Ce] and TBAB as a Catalyst System[a]
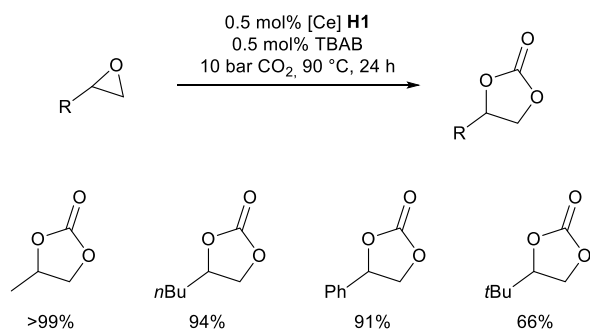
[a] Yields are given for the respective cyclic carbonate.

increased the TONs for the catalytic formation of propylene carbonate to 355 using 0.1 mol % [Ce] and TBAB. Overall, the catalytic activity of the hybrid materials is similar to that reported for the homogeneous catalytic systems.[11] The absence of any increase in catalytic activity is most likely due to pore confinement issues as the reaction involves four different reaction partners. However, these numbers compare also well with other silica-based heterogeneous catalysts, like $YCl_3(thf)_{3.5}@SiO_2$, giving a TON of 146 by using atmospheric CO_2 pressure.[28] Note that the formation of polycarbonates was not observed. This might be attributed to the use of TBAB as a cocatalyst. TBAB represents a suitable nucleophile for the ring opening of the epoxide and a good leaving group for the subsequent ring closure of the carbonate formation.[6a]

Being one of the main advantages of SOMC (and heterogeneous catalysis in general), we also investigated into the ease of catalyst separation and recyclability of one of our hybrid materials. To this end, 0.5 mol % of material **H2** and TBAB were used as a catalyst system, and the catalytic cycloaddition of propylene oxide was performed under 1 bar CO_2 pressure at ambient temperature. The hybrid material **H2** was chosen since its cerium surface species are considered to be exclusively monometallic. By use of **H1**, where dimetallic surface species cannot be ruled out, addition of a donor molecule (propylene oxide) might lead to the cleavage of the dimetallic species and therefore metal leakage after the first run. After 24 h the material was filtered off and washed with diethyl ether after each run. The first two runs gave a conversion of 70% which decreased to ~50% for the third and fourth runs (Figure 6). This decrease in conversion might be assigned to a loss of hybrid material during the filtering or washing process.
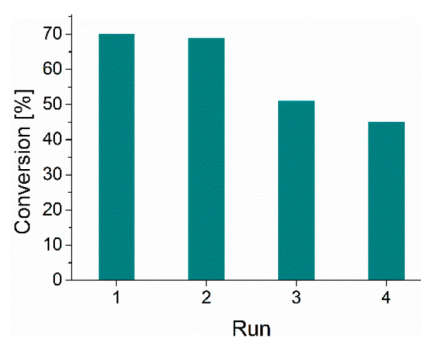
Figure 6. Conversion of the catalytic cycloaddition of propylene oxide and CO_2 using 0.5 mol % of hybrid material **H2** and TBAB as a catalyst system at 1 bar CO_2 pressure and ambient temperature. After each run, the material was filtered off, washed, and reused.

■ CONCLUSIONS

Large-pore mesoporous silica SBA-15 (pore diameter ca. 7 nm) seems ideally suited for efficiently accommodating large, multimetallic metal−organic compounds such as 3,5-dimethyl pyrazolates $[Ce(Me_2pz)_4]_2$ and $Ce_4(Me_2pz)_{12}$ via surface organometallic chemistry (SOMC). The resulting mesoporous hybrid materials (pore diameter ca. 5 nm) display high metal contents of up to 20% with an overall increase in materials weight of ca. 200%. Such high surface complex loading allows for extensive and reversible CO_2 insertion, implying a maximum increase in weight of ~20 wt % for $CO_2@[Ce(Me_2pz)_3(thf)]_2@SBA-15_{500}$. When combined with tetra-n-butylammonium bromide (TBAB), the hybrid materials also act as catalyst for the cycloaddition of CO_2 and epoxides. Though the catalytic activities are somewhat lower than those observed for the homogeneous congeners, such heterogenized catalysts are easily recyclable and can be reused without substantial loss of catalytic activity.

■ EXPERIMENTAL SECTION

General Procedures. All grafting reactions were performed under an inert atmosphere (Ar) by using a glovebox (MBraun 200B; <0.1 ppm of O_2, <0.1 ppm of H_2O) or according to standard Schlenk techniques in oven-dried glassware. The solvents were purified with Grubbs-type columns (MBraun SPS, solvent purification system) and stored in a glovebox. $[Ce(Me_2pz)_4]_2$ (**1**), $Ce(Me_2pz)_4(thf)$ (**2**),

$Ce_4(Me_2pz)_{12}$ (**3**), $[Ce(Me_2pz)_3(thf)]_2$ (**4**), $[La(Me_2pz)_3(thf)]_2$ (**5**), and $Ce[OSi(OtBu)_3]_3Cl$ were synthesized according to published procedures.[11,12,17,21] Propylene oxide purchased from Acros, 1,2-epoxyhexane and 3,3-dimethyl-1,2-epoxybutane from Alfa Aeser, and styrene oxide from VWR were dried and degassed before use. TBAB was purchased from Sigma-Aldrich and recrystallized from acetone/diethyl ether mixtures prior to use. Pluronic 123 was purchased from Sigma-Aldrich and used as received. $CDCl_3$ was purchased from Euriso-top and used as received. Solution NMR spectra were recorded at 26 °C on either a Bruker AVII+400 (^{1}H: 400.13 MHz; ^{13}C: 100.16 MHz) or a Bruker Avance II 500 (^{1}H: 500.13 MHz; ^{13}C: 125.76 MHz) using J. Young valve NMR spectroscopy tubes. ^{1}H and ^{13}C NMR shifts are referenced to a solvent resonance and reported in parts per million (ppm) relative to tetramethylsilane.[29] Solid-state NMR spectra were recorded on a Bruker ASX 300 (^{1}H 300.13 MHz, ^{13}C 75.47 MHz, and ^{29}Si 59.62 MHz) using a ZrO_2 rotor (4 mm diameter). Analyses of spectral data were performed with ACD/NMR Processor Academic Edition (product version: 12.01). Infrared spectra were recorded on a ThermoFisher Scientific NICOLET 6700 FTIR ($\tilde{\nu} = 4000-400$ cm^{-1}) spectrometer by using a DRIFT chamber with dry KBr/sample mixtures and KBr windows. Elemental analysis was performed on an Elementar vario MICRO cube in CHNS mode. Metal contents were determined by ICP-OES measurements on a Thermo Scientific iCAP 7000 Series. N_2-physisorption measurements were performed on an ASAP2020 volumetric adsorption apparatus (Micromeritics Instrument Corp.) at 77 K ($a_m(N_2, 77$ K$) = 0.162$ nm^2). The samples were degassed at <5 μmHg prior to analysis, in the case of the pure silica materials at 298 K for 2 h, and in the case of the hybrid materials at 298 K for 12 h to avoid degradation of the grafted organometallics. The Brunauer−Emmett−Teller (BET) specific surface area was calculated from the nitrogen adsorption branch of the isotherm in the relative pressure range of 0.07−0.15 for the pure SiO_2 materials and the hybrid materials.[30] Pore size distributions (dV/dD) were calculated from the nitrogen desorption branch by using the Barrett−Joyner−Halenda (BJH) method.[31] The low-angle powder X-ray diffraction (PXRD) pattern was recorded on a Bruker Advance D8 instrument using monochromatic Cu Kα radiation ($\lambda = 1.5406$ Å) in the 2θ range of 0.50°−9.99° with a scan speed of 2 s per step. The SEM/TEM images were obtained on a Hitachi SU8030 operated at 30 kV.

Parent Material. SBA-15$_{500}$. According to a previously reported method with slight modifications.[14] Pluronic P123 (6.99 g) was dissolved in a solution mixture containing 41.40 g of 37% concentrated hydrochloric acid and 184.3 g of water, and the solution was stirred at 40 °C for 1 h. Then TEOS (14.58 g) was added dropwise to the solution under vigorous stirring, and the stirring was continued at 40 °C for 24 h. Then the suspension was aged at 100 °C for 24 h. The precipitate was separated by suction filtration and washed with water several times. The surfactant was removed by calcination at 540 °C for 4 h with a temperature-controlled program. Finally, the calcined surfactant-free SBA-15 was further activated at 500 °C for 4 h under high vacuum and stored as **SBA-15$_{500}$** in a glovebox under an argon atmosphere for use. a_{BET} 887 m^2 g^{-1}, V_{pore} 0.96 cm^3 g^{-1}, and d_{pore} 6.8 nm. DRIFTS: $\tilde{\nu} = 3743$ (w, Si−OH), 3103 (vw), 1098 (vs), 1060 (vs), 818 (m), 467 (m), 446 (s), 426 (s) cm^{-1}.

Grafting Reactions. [Ce(Me$_2$pz)$_4$]$_2$@SBA-15$_{500}$ (H1). SBA-15$_{500}$ (276.4 mg, 0.853 mmol of SiOH) was suspended in n-hexane and $[Ce(Me_2pz)_4]_2$ (341.0 mg, 0.327 mmol, 0.654 mmol of [Ce]) in n-hexane was added. After the suspension was stirred for 16 h the hybrid material was separated via centrifugation and subsequently washed two times with toluene (5 mL) and five times with n-hexane (5 mL) until the red color of the supernatant vanished. Then the residual solvent was removed under reduced pressure to yield 426.9 mg of $[Ce(Me_2pz)_4]_2$@SBA-15$_{500}$ (**H1**) as a pale red powder. The supernatant was filtered and dried under reduced pressure. ^{1}H NMR spectroscopic analysis showed the formation of $[Ce(Me_2pz)_4(Me_2pzH)]$ as a result of the Me$_2$pzH formation during the grafting process. Elemental analysis found: Ce 10.80 (ICP-OES); C 16.85, H 2.11, N 7.59. a_{BET} 459 m^2 g^{-1}, V_{pore} 0.55 cm^3 g^{-1}, d_{pore} 5.2 nm. DRIFTS: $\tilde{\nu} = 3381$ (vw), 3101 (vw), 2927 (vw), 1569 (vw), 1520

(w), 1433 (w), 1369 (vw), 1072 (vs), 1031 (vs), 794 (m), 725 (vw), 453 (m), 428 (w) cm^{-1}.

Ce(Me$_2$pz)$_4$(thf)@SBA-15$_{500}$ (H2). SBA-15$_{500}$ (197.0 mg, 0.608 mmol of SiOH) was suspended in n-hexane and Ce(Me$_2$pz)$_4$(thf) (201.7 mg, 0.340 mmol, 0.340 mmol of [Ce]) in n-hexane was added. After the suspension was stirred for 16 h the hybrid material was separated via centrifugation and subsequently washed two times with toluene (5 mL) and five times with n-hexane (5 mL) until the red color of the supernatant vanished. Then the residual solvent was removed under reduced pressure to yield 322.7 mg of Ce(Me$_2$pz)$_4$(thf)@SBA-15$_{500}$ (**H2**) as a pale red powder. The supernatant was filtered and dried under reduced pressure. ^{1}H NMR spectroscopic analysis showed the formation of $[Ce(Me_2pz)_4(Me_2pzH)]$ as a result of the Me$_2$pzH formation during the grafting process. Elemental analysis found: Ce 9.96 (ICP-OES); C 16.80, H 2.16, N 7.11. a_{BET} 353 m^2 g^{-1}, V_{pore} 0.42 cm^3 g^{-1}, d_{pore} 5.2 nm. DRIFTS: $\tilde{\nu} = 3383$ (vw), 3105 (vw), 2927 (vw) 1571 (vw), 1519 (w), 1433 (w), 1369 (vw), 1096 (vs), 1057 (vs), 793 (m), 727 (w), 478 (m), 444 (vs), 431 (vs), 422 (vs) cm^{-1}.

Ce$_4$(Me$_2$pz)$_{12}$@SBA-15$_{500}$ (H3). SBA-15$_{500}$ (75.6 mg, 0.233 mmol of SiOH) was suspended in n-hexane, and Ce$_4$(Me$_2$pz)$_{12}$ (265.0 mg, 0.155 mmol, 0.620 mmol of [Ce]) in n-hexane was added. After the suspension was stirred for 16 h, the hybrid material was separated via centrifugation and subsequently washed two times with toluene (5 mL) and five times with n-hexane (5 mL). Then the residual solvent was removed under reduced pressure to yield 196.7 mg of Ce$_4$(Me$_2$pz)$_{12}$@SBA-15$_{500}$ (**H3**) as a colorless powder. The supernatant was filtered and dried under reduced pressure to recover any starting material (40.0 mg). Elemental analysis found: Ce 22.19 (ICP-OES); C 30.26, H 3.76, N 13.70. a_{BET} 163 m^2 g^{-1}, V_{pore} 0.19 cm^3 g^{-1}, d_{pore} 4.9 nm. DRIFTS: $\tilde{\nu} = 3292$ (vw), 3104 (vw), 2919 (w), 2865 (vw), 1571 (vw), 1516 (vs), 1416 (s), 1287 (vw), 1071 (vs), 1007 (vs), 955 (vw), 793 (m), 728 (w), 588 (vw), 431 (m) cm^{-1}.

[Ce(Me$_2$pz)$_3$(thf)]$_2$@SBA-15$_{500}$ (H4). SBA-15$_{500}$ (66.0 mg, 0.203 mmol of SiOH) was suspended in n-hexane, and $[Ce(Me_2pz)_3(thf)]_2$ (219.2 mg, 0.220 mmol, 0.440 mmol of [Ce]) in n-hexane was added. After the suspension was stirred for 16 h, the hybrid material was separated via centrifugation and subsequently washed two times with toluene (5 mL) and five times with n-hexane (5 mL). Then the residual solvent was removed under reduced pressure to yield 222.2 mg of $[Ce(Me_2pz)_3(thf)]_2$@SBA-15$_{500}$ (**H4**) as a colorless powder. The supernatant was filtered and dried under reduced pressure to recover the starting material (37.2 mg). Elemental analysis found: Ce 20.27 (ICP-OES); C 30.60, H 3.90, N 13.54. a_{BET} 159 m^2 g^{-1}, V_{pore} 0.19 cm^3 g^{-1}, d_{pore} 4.9 nm. DRIFTS: $\tilde{\nu} = 3321$ (vw), 3103 (vw), 2922 (w), 2866 (vw), 1570 (vw), 1514 (m), 1418 (m), 1365 (vw), 1311 (vw), 1072 (vs), 1009 (vs), 787 (m), 730 (w), 658 (vw), 587 (vw), 466 (s), 435 (s) cm^{-1}.

[La(Me$_2$pz)$_3$(thf)]@SBA-15$_{500}$ (H5). SBA-15$_{500}$ (90.0 mg, 0.278 mmol of SiOH) was suspended in n-hexane, and $[La(Me_2pz)_3(thf)]_2$ (303.3 mg, 0.306 mmol, 0.612 mmol of [La]) in n-hexane was added. After the suspension was stirred for 16 h, the hybrid material was separated via centrifugation and subsequently washed two times with toluene (5 mL) and five times with n-hexane (5 mL). Then the residual solvent was removed under reduced pressure to yield 322.5 mg of $[La(Me_2pz)_3(thf)]_2$@SBA-15$_{500}$ (**H5**) as a colorless powder. The supernatant was filtered and dried under reduced pressure to recover the starting material (43.6 mg). Elemental analysis found: La 21.05 (ICP-OES); C 30.99, H 3.85, N 13.58. a_{BET} 160 m^2 g^{-1}, V_{pore} 0.19 cm^3 g^{-1}, d_{pore} 5.0 nm. DRIFTS: $\tilde{\nu} = 3273$ (w), 3103 (vw), 2921 (w), 2867 (vw), 1570 (vw), 1514 (s), 1418 (m), 1365 (vw), 1313 (vw), 1068 (vs), 1008 (vs), 787 (w), 730 (w), 678 (vw), 447 (m) cm^{-1}.

Mixed Pyrazolyl/Siloxy Ce^{IV} Model Complex 6. KCe[OSi(OtBu)$_3$]$_4$(Me$_2$pz) (6). Ce[OSi(OtBu)$_3$]$_3$Cl (78.9 mg, 0.0818 mmol) was dissolved in toluene (3 mL), and K(Me$_2$pz) (10.9 mg, 0.0818 mmol) in toluene (2 mL) was added. After being stirred for 72 h, a color change from light yellow to orange and precipitation of a colorless solid was observed. The colorless precipitate was removed via filtration, and the supernatant was dried under reduced pressure.

Crystallization from *n*-pentane/Et$_2$O mixtures yielded two sorts of crystals: colorless crystals of K[OSi(OtBu)$_3$](Me$_2$pzH)(Et$_2$O) and orange crystals of KCe[OSi(OtBu)$_3$]$_4$(Me$_2$pz) (6), which have been identified by X-ray crystallography.

Carbon Dioxide Insertion. *CO$_2$@[Ce(Me$_2$pz)$_4$]$_2$@SBA-15$_{500}$ (H1^{CO2}).* [Ce(Me$_2$pz)$_4$]$_2$@SBA-15$_{500}$ (**H1**) (100.0 mg) was stored under 1 bar CO$_2$ pressure for 16 h, yielding CO$_2$@[Ce(Me$_2$pz)$_4$]$_2$@SBA-15$_{500}$ (**H1^{CO2}**) (110.6 mg) as a pale brown/orange powder. DRIFTS: $\tilde{\nu}$ = 3251 (vw), 2928 (vw), 1737 (w), 1658 (w), 1566 (vw), 1519 (vw), 1416 (w), 1341 (w), 1060 (vs), 795 (w), 438 (s) cm^{-1}.

CO$_2$@Ce(Me$_2$Pz)$_4$(thf)@SBA-15$_{500}$ (H2^{CO2}). Ce(Me$_2$pz)$_4$(thf)@SBA-15$_{500}$ (**H2**) (100.0 mg) was stored under 1 bar CO$_2$ pressure for 16 h, yielding CO$_2$@Ce(Me$_2$pz)$_4$(thf)@SBA-15$_{500}$ (**H2^{CO2}**) (108.6 mg) as a pale orange powder. DRIFTS: $\tilde{\nu}$ = 2929 (vw), 1733 (w), 1661 (w), 1568 (vw), 1519 (vw), 1417 (w), 1340 (w), 1064 (vs), 794 (w), 725 (w), 446 (s) cm^{-1}.

CO$_2$@Ce$_4$(Me$_2$pz)$_{12}$@SBA-15$_{500}$ (H3^{CO2}). Ce$_4$(Me$_2$pz)$_{12}$@SBA-15$_{500}$ (**H3**) (50.0 mg) was stored under 1 bar CO$_2$ pressure for 16 h, yielding CO$_2$@Ce$_4$(Me$_2$pz)$_{12}$@SBA-15$_{500}$ (**H2^{CO2}**) (59.6 mg) as a colorless powder. DRIFTS: $\tilde{\nu}$ = 3251 (vw), 2927 (vw), 1723 (m), 1679 (s), 1571 (w), 1468 (w), 1415 (m), 1338 (s), 1289 (m), 1208 (m), 1127 (s), 1057 (vs), 1038 (vs), 981 (m), 8276(m), 795 (m), 760 (m), 461 (m) cm^{-1}.

CO$_2$@[Ce(Me$_2$pz)$_3$(thf)]$_2$@SBA-15$_{500}$ (H4^{CO2}). [Ce(Me$_2$pz)$_3$(thf)]$_2$@SBA-15$_{500}$ (**H4**) (50.0 mg) was stored under 1 bar CO$_2$ pressure for 16 h, yielding CO$_2$@[Ce(Me$_2$pz)$_3$(thf)]$_2$@SBA-15$_{500}$ (**H4^{CO2}**) (60.2 mg) as a colorless powder. DRIFTS: $\tilde{\nu}$ = 3248 (vw), 2927 (vw), 1681 (s), 1571 (w), 1468 (w), 1415 (m), 1338 (s), 1128 (s), 1062 (vs), 1040 (vs), 982 (m), 827 (m), 794 (m), 760 (m), 452 (m) cm^{-1}.

CO$_2$@[La(Me$_2$pz)$_3$(thf)]$_2$@SBA-15$_{500}$ (H5^{CO2}). [La(Me$_2$pz)$_3$(thf)]$_2$@SBA-15$_{500}$ (**H5**) (100.0 mg) was stored under 1 bar CO$_2$ pressure for 16 h, yielding CO$_2$@[La(Me$_2$pz)$_3$(thf)]$_2$@SBA-15$_{500}$ (**H5^{CO2}**) (117.0 mg) as a colorless powder. DRIFTS: $\tilde{\nu}$ = 3251 (vw), 2926 (vw), 1679 (s), 1571 (w), 1468 (w), 1415 (m), 1337 (s), 1206 (m), 1128 (s), 1067 (vs), 1039 (vs), 981 (m), 825 (m), 795 (m), 759 (m), 447 (m) cm^{-1}.

Catalytic Reactions. *Catalysis under High Pressure and Elevated Temperatures.* [Ce(Me$_2$pz)$_4$]$_2$@SBA-15$_{500}$ (**H1**) (8.0 mg, 6.20 μmol [Ce]) and TBAB (2.0 mg, 6.20 μmol) were combined in a vial with a stirring bar, and an epoxide (1.24 mmol) was added. The vial was placed in a stainless-steel reactor, 10 bar of CO$_2$ was added, and the reaction mixture was stirred at 90 °C. After 24 h, CDCl$_3$ was added, and the material was removed via filtration. The conversion was determined by ^{1}H NMR spectroscopy.

Catalysis under Atmospheric Pressure and Reusability Study. Ce(Me$_2$pz)$_4$(thf)@SBA-15$_{500}$ (**H2**) (30.2 mg, 21.4 μmol [Ce]) and TBAB (6.9 mg, 21.4 μmol) were combined in a Schlenk flask, and 300 μL of propylene oxide was added. The reaction mixture was stirred under 1 bar CO$_2$ pressure for 24 h. Afterward, the supernatant was decanted, and the conversion was determined by ^{1}H NMR spectroscopy. The material was washed five times with diethyl ether (1 mL) and dried under reduced pressure before adding new TBAB and propylene oxide.

ASSOCIATED CONTENT

ⓈI Supporting Information

The Supporting Information is available free of charge at https://pubs.acs.org/doi/10.1021/acs.inorgchem.0c02502.

PXRD pattern, SEM/TEM images of parent material SBA-15; NMR spectra of grafted materials, modeling study, and catalytic reactions; TGA of hybrid material CO$_2$@[La(Me$_2$pz)$_3$(thf)]$_2$@SBA-15$_{500}$ (Figures S1–S17); X-ray crystallographic data for **6** and K[OSi-(OtBu)$_3$](Me$_2$pzH)(Et$_2$O) (Table S1, Figure S18, CCDCs 2023872 and 2023873) (PDF)

AUTHOR INFORMATION

Corresponding Author

 Reiner Anwander − *Institut für Anorganische Chemie, Eberhard Karls Universität Tübingen, 72076 Tübingen, Germany;* ⓞ orcid.org/0000-0002-1543-3787; Email: reiner.anwander@uni-tuebingen.de

Authors

 Uwe Bayer − *Institut für Anorganische Chemie, Eberhard Karls Universität Tübingen, 72076 Tübingen, Germany*
 Yucang Liang − *Institut für Anorganische Chemie, Eberhard Karls Universität Tübingen, 72076 Tübingen, Germany;* ⓞ orcid.org/0000-0003-1683-5486

Complete contact information is available at:
https://pubs.acs.org/10.1021/acs.inorgchem.0c02502

Notes

The authors declare no competing financial interest.

REFERENCES

(1) (a) Falkowski, P.; Scholes, R. J.; Boyle, E.; Canadell, J.; Canfield, D.; Elser, J.; Gruber, N.; Hibbard, K.; Högberg, P.; Linder, S.; Mackenzie, F. T.; Moore, B., III; Pedersen, T.; Rosenthal, Y.; Seitzinger, S.; Smetacek, V.; Steffen, W. The Global Carbon Cycle: A Test of Our Knowledge of Earth as a System. *Science* **2000**, *290*, 291−296. (b) Aresta, M.; Dibenedetto, A. Utilisation of CO$_2$ as a chemical feedstock: opportunities and challenges. *Dalton Trans.* **2007**, 2975−2992. (c) Solomon, S.; Plattner, G.-K.; Knutti, R.; Friedlingstein, P. Irreversible climate change due to carbon dioxide emissions. *Proc. Natl. Acad. Sci. U. S. A.* **2009**, *106*, 1704−1709.

(2) (a) Haszeldine, R. S. Carbon Capture and Storage: How Green Can Black Be? *Science* **2009**, *325*, 1647−1652. (b) von der Assen, N.; Voll, P.; Peters, M.; Bardow, A. Life cycle assessment of CO$_2$ capture and utilization: a tutorial review. *Chem. Soc. Rev.* **2014**, *43*, 7982−7994.

(3) (a) D'Alessandro, D. M.; Smit, B.; Long, J. R. Carbon Dioxide Capture: Prospects for New Materials. *Angew. Chem., Int. Ed.* **2010**, *49*, 6058−6082. (b) Yu, C.-H.; Huang, C.-H.; Tan, C.-S. A Review of CO$_2$ Capture by Absorption and Adsorption. *Aerosol Air Qual. Res.* **2012**, *12*, 745−769. (c) Sumida, K.; Rogow, D. L.; Mason, J. A.; McDonald, T. M.; Bloch, E. D.; Herm, Z. R.; Bae, T.-H.; Long, J. R. Carbon Dioxide Capture in Metal−Organic Frameworks. *Chem. Rev.* **2012**, *112*, 724−781. (d) Sanz-Pérez, E. S.; Murdock, C. R.; Didas, S. A.; Jones, C. W. Direct Capture of CO$_2$ from Ambient Air. *Chem. Rev.* **2016**, *116*, 11840−11876. (e) Lin, Y.; Kong, C.; Zhang, Q.; Chen, L. Metal-Organic Frameworks for Carbon Dioxide Capture and Methane Storage. *Adv. Energy Mater.* **2017**, *7*, 1601296.

(4) (a) Sakakura, T.; Choi, J.-C.; Yasuda, H. Transformation of Carbon Dioxide. *Chem. Rev.* **2007**, *107*, 2365−2387. (b) Centi, G.; Perathoner, S. Opportunities and prospects in the chemical recycling

of carbon dioxide to fuels. *Catal. Today* **2009**, *148*, 191−205. (c) Cokoja, M.; Bruckmeier, C.; Rieger, B.; Herrmann, W. A.; Kühn, F. E. Transformation of Carbon Dioxide with Homogeneous Transition-Metal Catalysts: A Molecular Solution to a Global Challenge? *Angew. Chem., Int. Ed.* **2011**, *50*, 8510−8537. (d) Aresta, M.; Dibenedetto, A.; Angelini, A. Catalysis for the Valorization of Exhaust Carbon: from CO_2 to Chemicals, Materials, and Fuels. Technological Use of CO_2. *Chem. Rev.* **2014**, *114*, 1709−1742. (e) Artz, J.; Müller, T. E.; Thenert, K.; Kleinekorte, J.; Meys, R.; Sternberg, A.; Bardow, A.; Leitner, W. Sustainable Conversion of Carbon Dioxide: An Integrated Review of Catalysis and Life Cycle Assessment. *Chem. Rev.* **2018**, *118*, 434−504. (f) Modak, A.; Bhanja, P.; Dutta, S.; Chowdhury, B.; Bhaumik, A. Catalytic reduction of CO_2 into fuels and fine chemicals. *Green Chem.* **2020**, *22*, 4002−4033.

(5) (a) Darensbourg, D. J.; Holtcamp, M. W. Catalysts for the reactions of epoxides and carbon dioxide. *Coord. Chem. Rev.* **1996**, *153*, 155−174. (b) Darensbourg, D. J.; Wilson, S. J. What's new with CO_2? Recent advances in its copolymerization with oxiranes. *Green Chem.* **2012**, *14*, 2665−2671. (c) Paul, S.; Zhu, Y.; Romain, C.; Brooks, R.; Saini, P. K.; Williams, C. K. Ring-opening copolymerization (ROCOP): synthesis and properties of polyesters and polycarbonates. *Chem. Commun.* **2015**, *51*, 6459−6479. (d) Huang, J.; Worch, J. C.; Dove, A. P.; Coulembier, O. Update and Challenges in Carbon Dioxide-Based Polycarbonate Synthesis. *ChemSusChem* **2020**, *13*, 469−487.

(6) (a) Pescarmona, P. P.; Taherimehr, M. Challenges in the catalytic synthesis of cyclic and polymeric carbonates from epoxides and CO_2. *Catal. Sci. Technol.* **2012**, *2*, 2169−2187. (b) Martín, C.; Fiorani, G.; Kleij, A. W. Recent Advances in the Catalytic Preparation of Cyclic Organic Carbonates. *ACS Catal.* **2015**, *5*, 1353−1370. (c) Yu, B.; He, L.-N. Upgrading Carbon Dioxide by Incorporation into Heterocycles. *ChemSusChem* **2015**, *8*, 52−62. (d) Grice, K. A. Carbon dioxide reduction with homogenous early transition metal complexes: Opportunities and challenges for developing CO_2 catalysis. *Coord. Chem. Rev.* **2017**, *336*, 78−95.

(7) (a) Qin, J.; Wang, P.; Li, Q.; Zhang, Y.; Yuan, D.; Yao, Y. Catalytic production of cyclic carbonates mediated by lanthanide phenolates under mild conditions. *Chem. Commun.* **2014**, *50*, 10952−10955. (b) Xu, B.; Wang, P.; Lv, M.; Yuan, D.; Yao, Y. Transformation of Carbon Dioxide into Oxazolidinones and Cyclic Carbonates Catalyzed by Rare-Earth-Metal Phenolates. *ChemCatChem* **2016**, *8*, 2466−2471. (c) Martínez, J.; Fernández-Baeza, J.; Sánchez-Barba, L. F.; Castro-Osma, J. A.; Lara-Sánchez, A.; Otero, A. An Efficient and Versatile Lanthanum Heteroscorpionate Catalyst for Carbon Dioxide Fixation into Cyclic Carbonates. *ChemSusChem* **2017**, *10*, 2886−2890. (d) Zhao, Z.; Qin, J.; Zhang, C.; Wang, Y.; Yuan, D.; Yao, Y. Recyclable Single-Component Rare-Earth Metal Catalysts for Cycloaddition of CO_2 and Epoxides at Atmospheric Pressure. *Inorg. Chem.* **2017**, *56*, 4568−4575. (e) Han, Q.; Wang, L.; Shi, Z.; Xu, C.; Dong, Z.; Mou, Z.; Liu, W. Self-Assembly of Luminescent Lanthanide Mesocates as Efficient Catalysts for Transforming Carbon Dioxide into Cyclic Carbonates. *Chem. - Asian J.* **2017**, *12*, 1364−1373.

(8) (a) Basset, J. M.; Choplin, A. Surface organometallic chemistry: A new approach to heterogeneous Catalysis? *J. Mol. Catal.* **1983**, *21*, 95−108. (b) Samantaray, M. K.; Pump, E.; Bendjeriou-Sedjerari, A.; D'Elia, V.; Pelletier, J. D. A.; Guidotti, M.; Psaro, R.; Basset, J.-M. Surface organometallic chemistry in heterogeneous catalysis. *Chem. Soc. Rev.* **2018**, *47*, 8403−8437. (c) Copéret, C.; Héroguel, F. In *Applied Homogeneous Catalysis with Organometallic Compounds*; John Wiley & Sons, Ltd.: 2017; pp 1069−1084.

(9) (a) Copéret, C.; Comas-Vives, A.; Conley, M. P.; Estes, D. P.; Fedorov, A.; Mougel, V.; Nagae, H.; Núñez-Zarur, F.; Zhizhko, P. A. Surface Organometallic and Coordination Chemistry toward Single-Site Heterogeneous Catalysts: Strategies, Methods, Structures, and Activities. *Chem. Rev.* **2016**, *116*, 323−421. (b) Copéret, C.; Allouche, F.; Chan, K. W.; Conley, M. P.; Delley, M. F.; Fedorov, A.; Moroz, I. B.; Mougel, V.; Pucino, M.; Searles, K.; Yamamoto, K.; Zhizhko, P. A.

Bridging the Gap between Industrial and Well-Defined Supported. *Angew. Chem., Int. Ed.* **2018**, *57*, 6398−6440.

(10) (a) Anwander, R. SOMC@PMS. Surface Organometallic Chemistry at Periodic Mesoporous Silica. *Chem. Mater.* **2001**, *13*, 4419−4438. (b) Liang, Y.; Anwander, R. Nanostructured catalysts via metal amide-promoted smart grafting. *Dalton Trans.* **2013**, *42*, 12521−12545.

(11) Bayer, U.; Werner, D.; Maichle-Mössmer, C.; Anwander, R. Effective and Reversible Carbon Dioxide Insertion into Cerium Pyrazolates. *Angew. Chem., Int. Ed.* **2020**, *59*, 5830−5836.

(12) Werner, D.; Deacon, G. B.; Junk, P. C.; Anwander, R. Pyrazolates advance cerium chemistry: a Ce^{III}/Ce^{IV} redox equilibrium with benzoquinone. *Dalton Trans.* **2017**, *46*, 6265−6277.

(13) Gajan, D.; Rendón, N.; Wampler, K. M.; Basset, J.-M.; Copéret, C.; Lesage, A.; Emsley, L.; Schrock, R. R. Synthesis and reactivity of molybdenum imido alkylidene bis-pyrazolide complexes. *Dalton Trans.* **2010**, *39*, 8547−8551.

(14) Tsai, C.-T.; Pan, Y.-C.; Ting, C.-C.; Vetrivel, S.; Chiang, A. S. T.; Fey, G. T. K.; Kao, H.-M. A simple one-pot route to mesoporous silicas SBA-15 functionalized with exceptionally high loadings of pendant carboxylic acid groups. *Chem. Commun.* **2009**, 5018−5020.

(15) (a) Le Roux, E.; Liang, Y.; Storz, M. P.; Anwander, R. Intramoecular Hydroamination/Cyclization of Aminoalkenes Catalyzed by $Ln[N(SiMe_3)_2]_3$ Grafted onto Periodic Mesoporous Silicas. *J. Am. Chem. Soc.* **2010**, *132*, 16368−16371. (b) Le Roux, E.; Liang, Y.; Anwander, R. Silica-Grafted Neodymium Catalysts for the Production of Ultra-High Molecular Weight *cis*-1,4-Polyisoprene. *ChemCatChem* **2018**, *10*, 1905−1911.

(16) Anwander, R.; Nagl, I.; Widenmeyer, M.; Engelhardt, G.; Groeger, O.; Palm, C.; Röser, T. Surface Characterization and Functionalization of MCM-41 Silicas via Silazane Silylation. *J. Phys. Chem. B* **2000**, *104*, 3532−3544.

(17) Deacon, G. B.; Harika, R.; Junk, P. C.; Skelton, B. W.; Werner, D.; White, A. H. The Synthesis, Structures and Polymorphism of the Dimeric Trivalent Rare-Earth 3,5-Dimethylpyrazolate Complexes $[Ln(Me_2pz)_3(thf)]_2$. *Eur. J. Inorg. Chem.* **2014**, *2014*, 2412−2419.

(18) (a) Crozier, A. R.; Schädle, C.; Maichle-Mössmer, C.; Törnroos, K. W.; Anwander, R. Synthesis and grafting of CAN-derived tetravalent cerium alkoxide silylamide precursors onto mesoporous silica MCM-41. *Dalton Trans.* **2013**, *42*, 5491−5499. (b) Bock, L.; Tran, X.; Liang, Y.; Kramer, M.; Maichle-Mössmer, C.; Anwander, R. SOMC@Periodic Mesoporous Silica Nanoparticles: Meerwein−Ponndorf−Verley Reduction Promoted by Immobilized Rare-Earth-Metal Alkoxides. *Organometallics* **2020**, *39*, 1046−1058.

(19) (a) Sebe, E.; Guzei, I. A.; Heeg, M. J.; Liable-Sands, L. M.; Rheingold, A. L.; Winter, C. H. Synthesis, Structure, and Properties of Zirconium and Hafnium Complexes Containing η^2-Pyrazolato Ligands. *Eur. J. Inorg. Chem.* **2005**, *2005*, 3955−3961. (b) Werner, D.; Bayer, U.; Schädle, D.; Anwander, R. Emergence of a New [NNN] Pincer Ligand via Si-H-Bond Activation and β-Hydride Abstraction at Tetravalent Cerium. *Chem. - Eur. J.* **2020**, *26*, 12194−12205.

(20) (a) Fischbach, A.; Klimpel, M. G.; Widenmeyer, M.; Herdtweck, E.; Scherer, W.; Anwander, R. Stereospecific Polymerization of Isoprene with Molecular and MCM-48-Grafted Lanthanide-(III) Tetraalkylaluminates. *Angew. Chem., Int. Ed.* **2004**, *43*, 2234−2239. (b) Blanc, F.; Copéret, C.; Thivolle-Cazat, J.; Basset, J.-M.; Lesage, A.; Emsley, L.; Sinha, A.; Schrock, R. R. Surface versus Molecular Siloxy Ligands in Well-Defined Olefin Metathesis Catalysts: $[\{(RO)_3SiO\}Mo(=NAr)(=CHtBu)(CH_2tBu)]$. *Angew. Chem., Int. Ed.* **2006**, *45*, 1216−1220. (c) Zimmermann, M.; Frøystein, N. Å.; Fischbach, A.; Sirsch, P.; Dietrich, H. M.; Törnroos, K. W.; Herdtweck, E.; Anwander, R. Homoleptic Rare-Earth Metal(III) Tetramethylaluminates: Structural Chemistry, Reactivity, and Performance in Isoprene Polymerization. *Chem. - Eur. J.* **2007**, *13*, 8784−8800. (d) Gauvin, R. M.; Buch, F.; Delevoye, L.; Harder, S. Well-Defined Silica-Supported Calcium Reagents: Control of Schlenk Equilibrium by Grafting. *Chem. - Eur. J.* **2009**, *15*, 4382−4393. (e) Dettenrieder, N.; Dietrich, H. M.; Maichle-Mössmer,

C.; Anwander, R. Yttrium Siloxide Complexes Bearing Terminal Methyl Ligands: Molecular Models for Ln−CH3 Terminated Silica Surfaces. *Chem. - Eur. J.* **2016**, *22*, 13189−13200.

(21) Friedrich, J.; Maichle-Mössmer, C.; Anwander, R. Synthesis and derivatisation of ceric tris(*tert*-butoxy)siloxides. *Chem. Commun.* **2017**, *53*, 12044−12047.

(22) Kelly, R. P.; Maron, L.; Scopelliti, R.; Mazzanti, M. Reduction of a Cerium(III) Siloxide Complex To Afford a Quadruple-Decker Arene-Bridged Cerium(II) Sandwich. *Angew. Chem., Int. Ed.* **2017**, *56*, 15663−15666.

(23) Gradeff, P. S.; Yunlu, K.; Gleizes, A.; Galy, J. Synthesis and X-ray crystal structure of a novel cerium(IV) arylsiloxide. *Polyhedron* **1989**, *8*, 1001−1005.

(24) Friedrich, J.; Qiao, Y.; Maichle-Mössmer, C.; Schelter, E. J.; Anwander, R. Redox-enhanced hemilability of a tris(*tert*-butoxy)siloxy ligand at cerium. *Dalton Trans.* **2018**, *47*, 10113−10123.

(25) Chang, F.-Y.; Chao, K.-J.; Cheng, H.-H.; Tan, C.-S. Adsorption of CO_2 onto amine-grafted mesoporous silicas. *Sep. Purif. Technol.* **2009**, *70*, 87−95.

(26) Arnold, P. L.; Marr, I. A.; Zlatogorsky, S.; Bellabarba, R.; Tooze, R. P. Activation of carbon dioxide and carbon disulfide by a scandium N-heterocyclic carbene complex. *Dalton Trans.* **2014**, *43*, 34−37.

(27) North, M.; Pasquale, R. Mechanism of Cyclic Carbonate Synthesis from Epoxides and CO_2. *Angew. Chem., Int. Ed.* **2009**, *48*, 2946−2948.

(28) Sodpiban, O.; Del Gobbo, S.; Barman, S.; Aomchad, V.; Kidkhunthod, P.; Ould-Chikh, S.; Poater, A.; D'Elia, V.; Basset, J.-M. Synthesis of well-defined yttrium-based Lewis acids by capturing a reaction intermediate and catalytic application for cycloaddition of CO_2 to epoxides under atmospheric pressure. *Catal. Sci. Technol.* **2019**, *9*, 6152−6165.

(29) Fulmer, G. R.; Miller, A. J. M.; Sherden, N. H.; Gottlieb, H. E.; Nudelman, A.; Stoltz, B. M.; Bercaw, J. E.; Goldberg, K. I. NMR Chemical Shifts of Trace Impurities: Common Laboratory Solvents, Organics, and Gases in Deuterated Solvents Relevant to the Organometallic Chemist. *Organometallics* **2010**, *29*, 2176−2179.

(30) Brunauer, S.; Emmett, P. H.; Teller, E. Adsorption of Gases in Multimolecular Layers. *J. Am. Chem. Soc.* **1938**, *60*, 309−319.

(31) Barrett, E. P.; Joyner, L. G.; Halenda, P. P. The Determination of Pore Volume and Area Distributions in Porous Substances. I. Computations from Nitrogen Isotherms. *J. Am. Chem. Soc.* **1951**, *73*, 373−380.

Cerium Pyrazolates Grafted onto Mesoporous Silica SBA-15: Reversible CO_2 Uptake and Catalytic Cycloaddition of Epoxides and Carbon Dioxide

Uwe Bayer, Yucang Liang, and Reiner Anwander*

Institut für Anorganische Chemie, Eberhard Karls Universität Tübingen, Auf der Morgenstelle 18, 72076 Tübingen, Germany

E-Mail: reiner.anwander@uni-tuebingen.de

Table of Contents

Powder X-Ray Diffraction (PXRD)
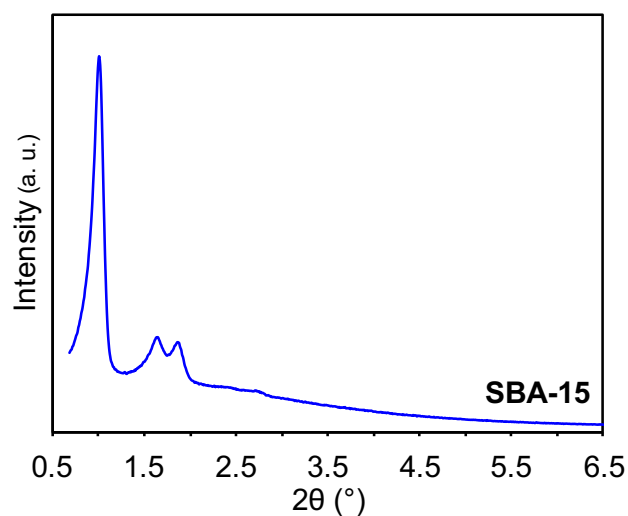
Figure S1. Low-angle PXRD pattern of parent SBA-15.

Scanning/Transmission Electron Microscopy (S/TEM)
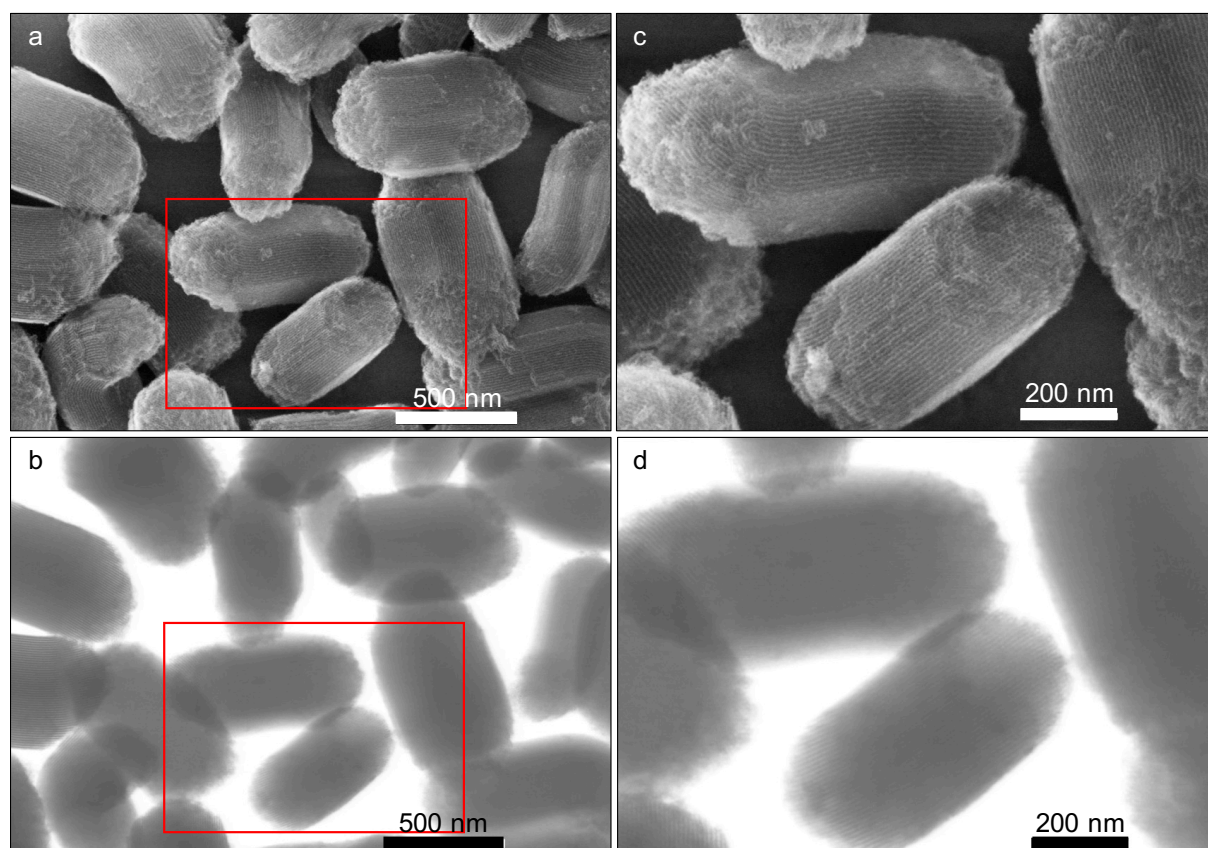
Figure S2. SEM (a,c) and TEM (b,d) images of parent SBA-15; (c) and (d) are magnified views of the red-marked areas in (a) and (b), respectively.
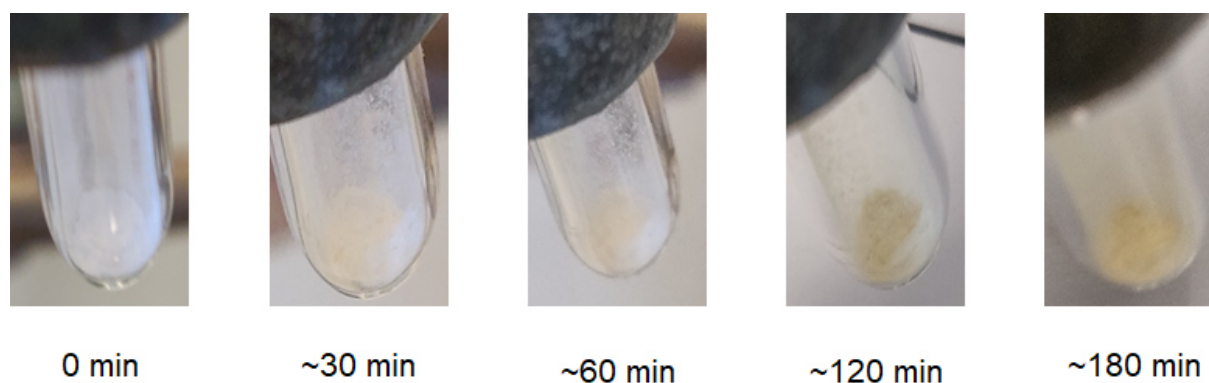
Figure S3. Color change during evacuation of a [Ce(Me$_2$pz)$_3$(thf)]$_2$@SBA-15$_{500}$ sample at high vacuum (p < 9·10^{-5} mbar) indicating decomposition under reduced pressure.

NMR Spectra (solvent signals are marked with *)
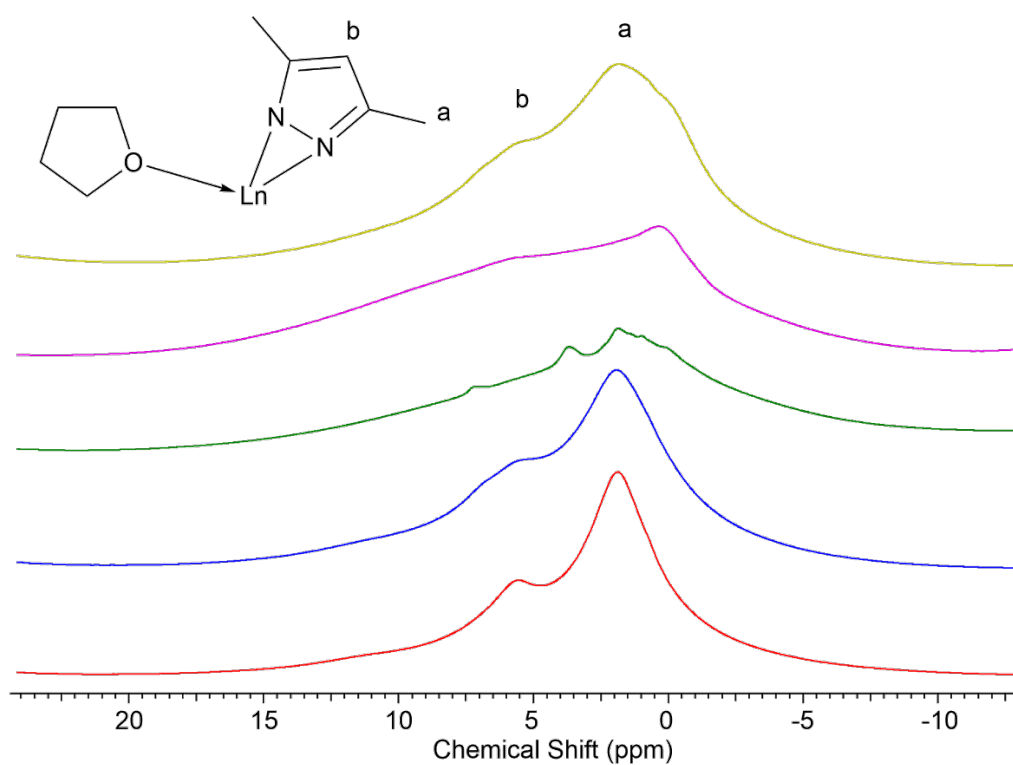
Figure S4. ^{1}H MAS NMR spectra of of [Ce(Me$_2$pz)$_4$]$_2$@SBA-15$_{500}$ (**H1**) (red), Ce$_4$(Me$_2$pz)$_4$(thf)@SBA-15$_{500}$ (**H2**) (blue), Ce$_4$(Me$_2$pz)$_{12}$@SBA-15$_{500}$ (**H3**) (green), [Ce(Me$_2$pz)$_3$(thf)]$_2$@SBA-15$_{500}$ (**H4**) (pink), and [La(Me$_2$pz)$_3$(thf)]$_2$@SBA-15$_{500}$ (**H5**) (yellow), from bottom to top.
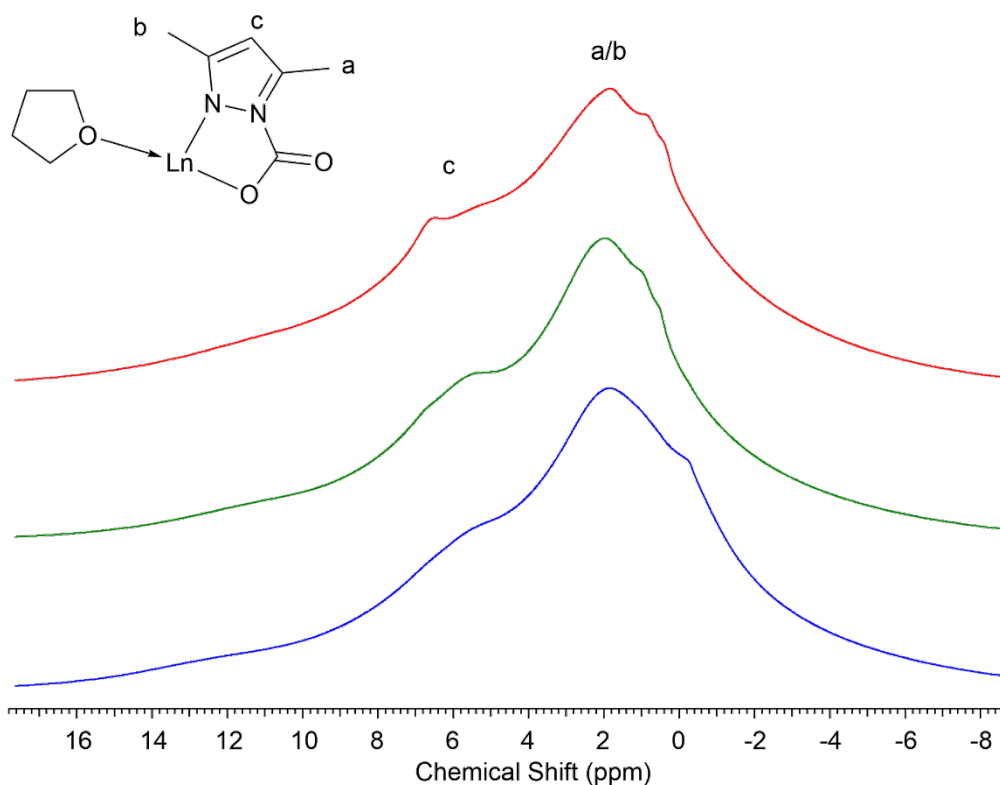
Figure S5. ^{1}H MAS NMR spectra of CO_2@[Ce(Me$_2$pz)$_4$]$_2$@SBA-15$_{500}$ (**H1^{CO2}**) (blue), CO_2@Ce(Me$_2$pz)$_4$(thf)@SBA-15$_{500}$ (**H2^{CO2}**) (green), and CO_2@[La(Me$_2$pz)$_3$(thf)]$_2$@SBA-15$_{500}$ (**H5^{CO2}**) (red) from bottom to top.
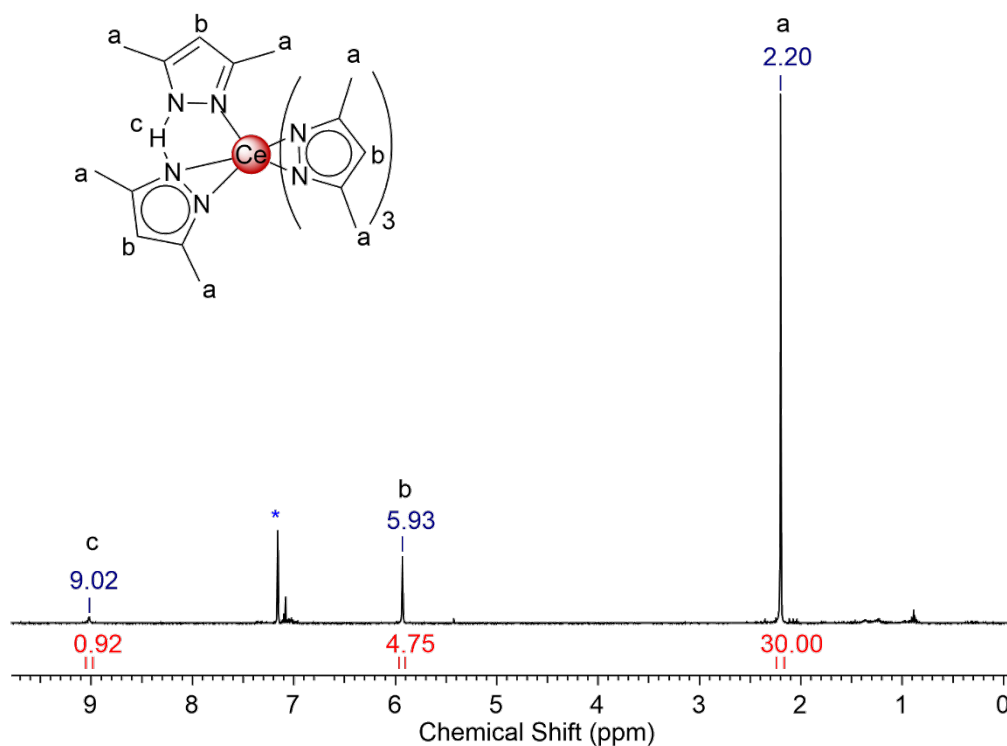
Figure S6. ^{1}H NMR spectrum (C$_6$D$_6$, 400.13 MHz, 26 °C) of the non-volatile compounds of the supernatant after grafting of Ce(Me$_2$pz)$_4$(thf) (**H2**). The spectrum shows minor impurities of *n*-hexane and toluene. Solvent signal is marked with an asterisk. Signals are in accordance with literature known Ce(Me$_2$pz)$_4$(Me$_2$pzH).[1]
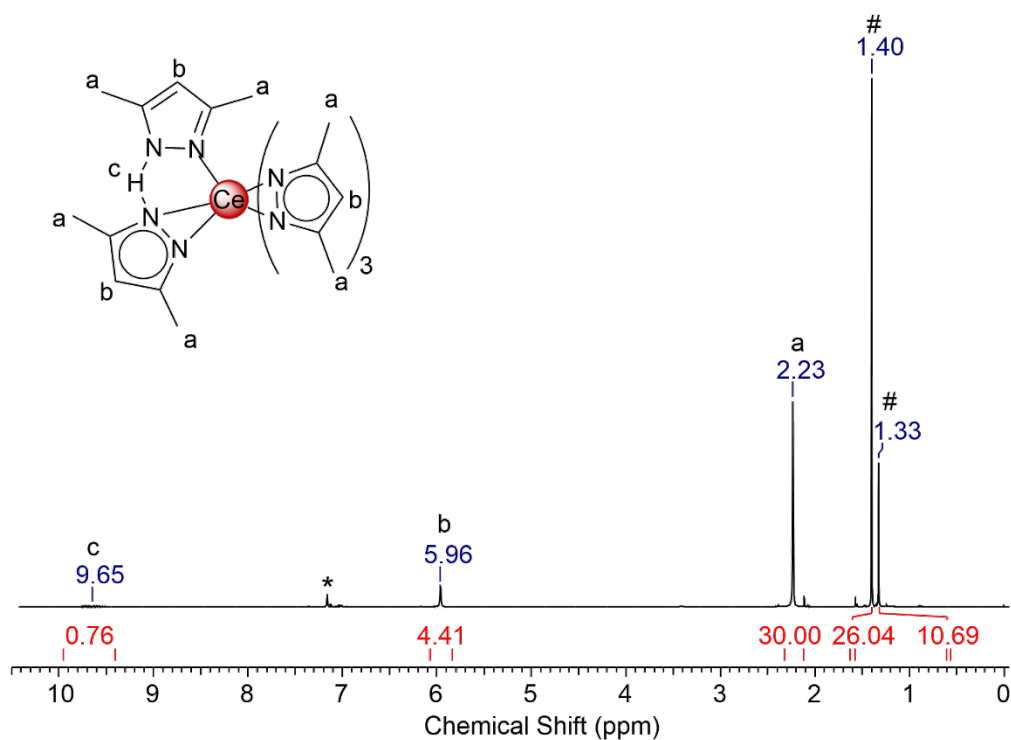
Figure S7. ^{1}H NMR spectrum (C$_6$D$_6$, 400.13 MHz, 26 °C) of the reaction mixture of [Ce(Me$_2$pz)$_4$]$_2$ and HOSi(O*t*Bu)$_3$ yielding Ce(Me$_2$pz)$_4$(Me$_2$pzH) and an unknown tris-*tert*-butoxysiloxy species (marked with #).
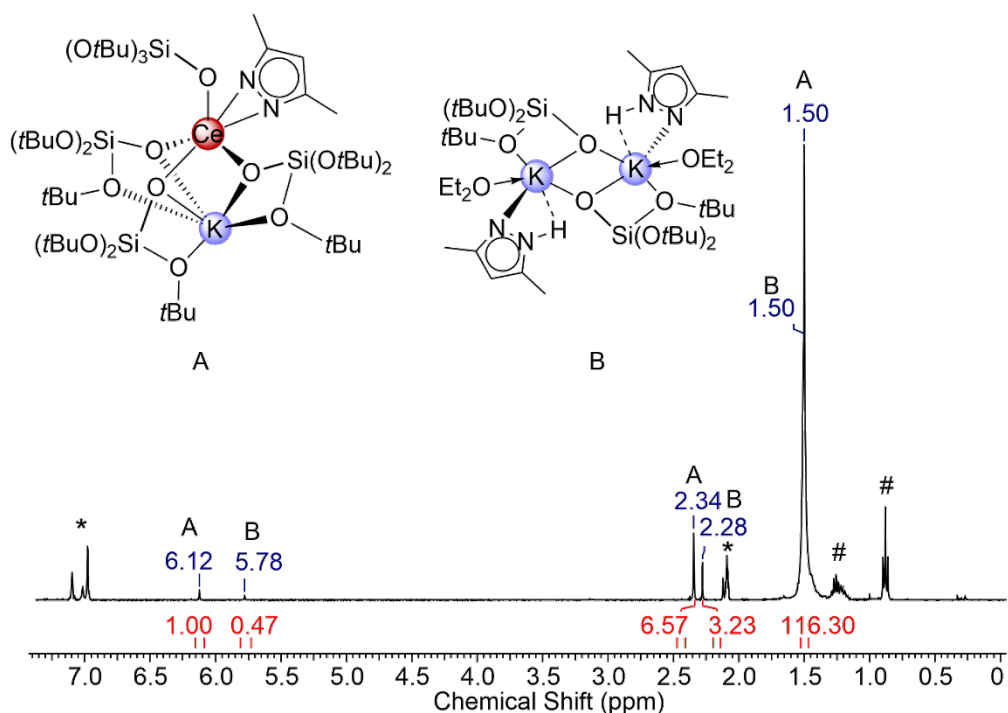
Figure S8. ^{1}H NMR spectrum (toluene-*d*$_8$, 400.13 MHz, 26 °C) of a mixture of KCe[OSi(OBu)$_3$]$_4$(Me$_2$pz) (**6**) and K[OSi(O*t*Bu)$_3$](Me$_2$pzH)(Et$_2$O). Impurities of *n*-pentane are marked with #.
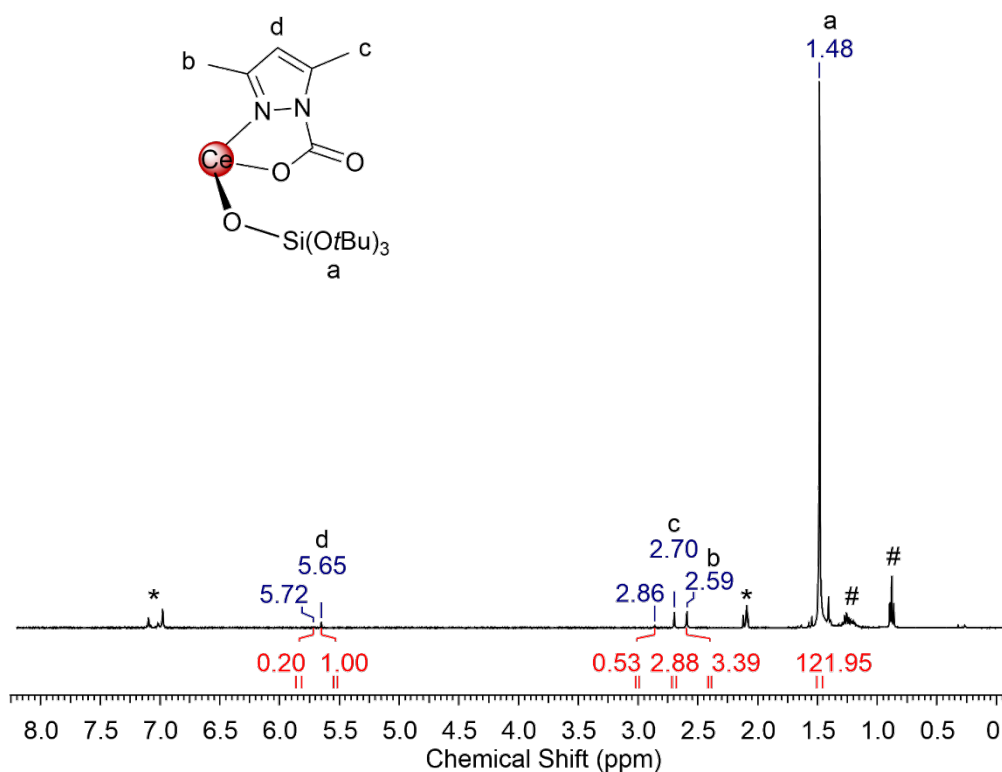
Figure S9. ^{1}H NMR spectrum (toluene-d_8, 400.13 MHz, 26 °C) of the reaction of CO_2 with the mixture KCe[OSi(OBu)$_3$]$_4$(Me$_2$pz) (**6**)/K[OSi(OtBu)$_3$](Me$_2$pzH)(Et$_2$O). Impurities of n-pentane are marked with #.
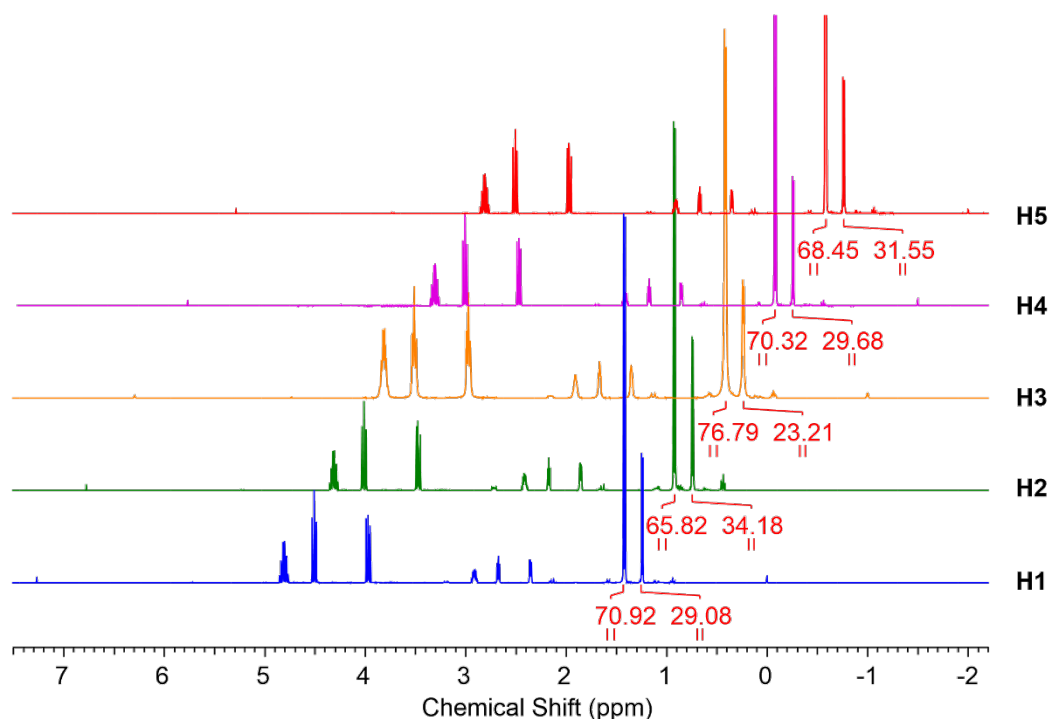
Figure S10. Stacked ^{1}H NMR spectra (CDCl$_3$, 400.13 MHz, 26 °C) of the product mixture of the catalytic formation of propylene carbonate using 0.1 mol% of [Ce(Me$_2$pz)$_4$]$_2$@SBA-15$_{500}$ (**H1**), Ce(Me$_2$pz)$_4$(thf)@SBA-15$_{500}$ (**H2**), Ce$_4$(Me$_2$pz)$_{12}$@SBA-15$_{500}$ (**H3**), [Ce(Me$_2$pz)$_3$(thf)]$_2$@SBA-15$_{500}$ (**H4**), or [La(Me$_2$pz)$_3$(thf)]$_2$@SBA-15$_{500}$ (**H5**) and TBAB as a catalyst system. The conversion was determined by the integral ratio of the methyl protons in propylene oxide and propylene carbonate.
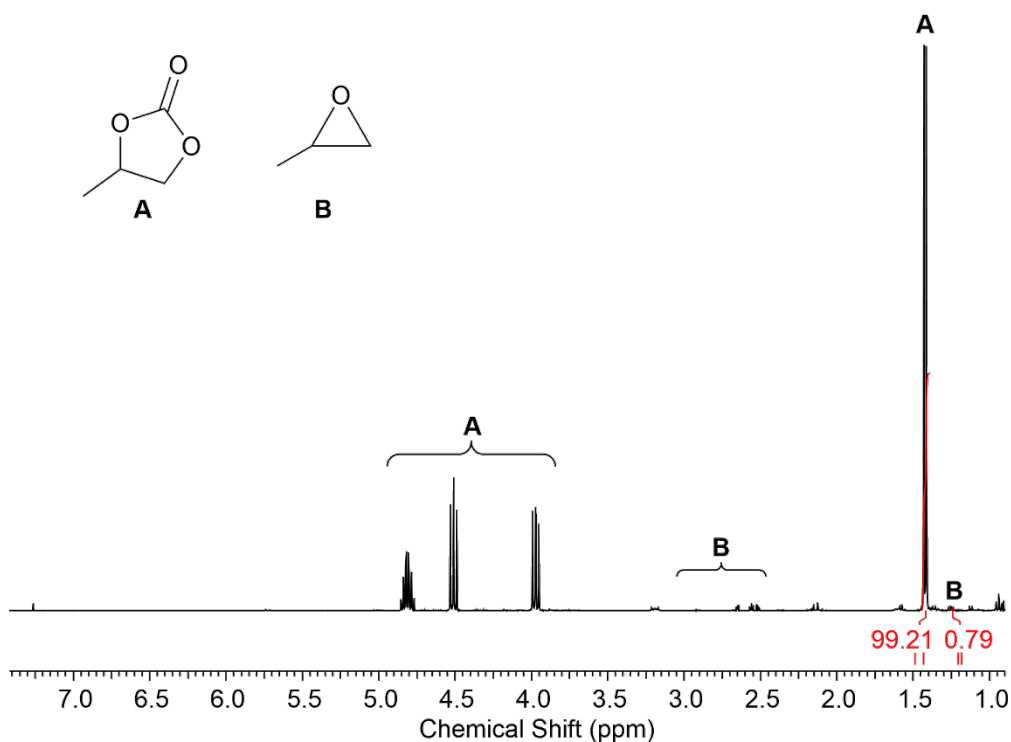
Figure S11. ^{1}H NMR (26 °C, 400.13 MHz, chloroform-*d*) of the product mixture of the catalytic formation of propylene carbonate using 0.5 mol% of [Ce(Me$_2$pz)$_4$]$_2$@SBA-15$_{500}$ (**H1**) and TBAB as a catalyst system. The conversion was determined by the integral ratio of the methyl protons in propylene oxide and propylene carbonate.
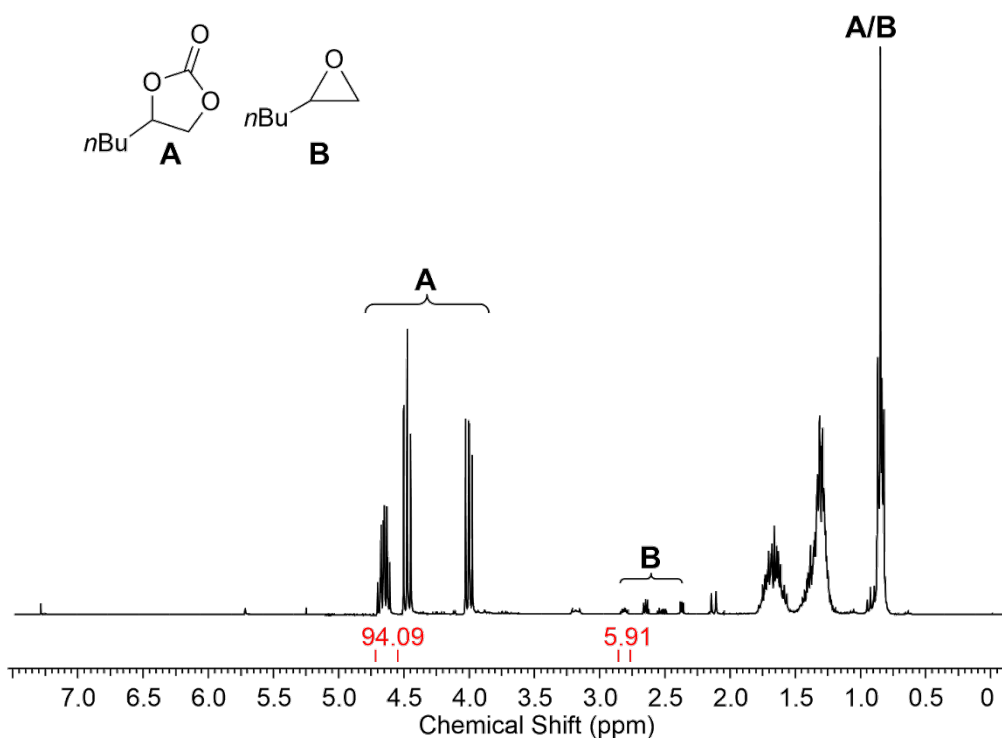
Figure S12. ^{1}H NMR (26 °C, 400.13 MHz, chloroform-*d*) of the product mixture of the catalytic formation of 1,2-*n*-hexylene carbonate using 0.5 mol% of [Ce(Me$_2$pz)$_4$]$_2$@SBA-15$_{500}$ (**H1**) and TBAB as a catalyst system. The conversion was determined by the integral ratio of the protons in *α*-position in 1,2-*n*-hexylene oxide and 1,2-*n*-hexylene carbonate.
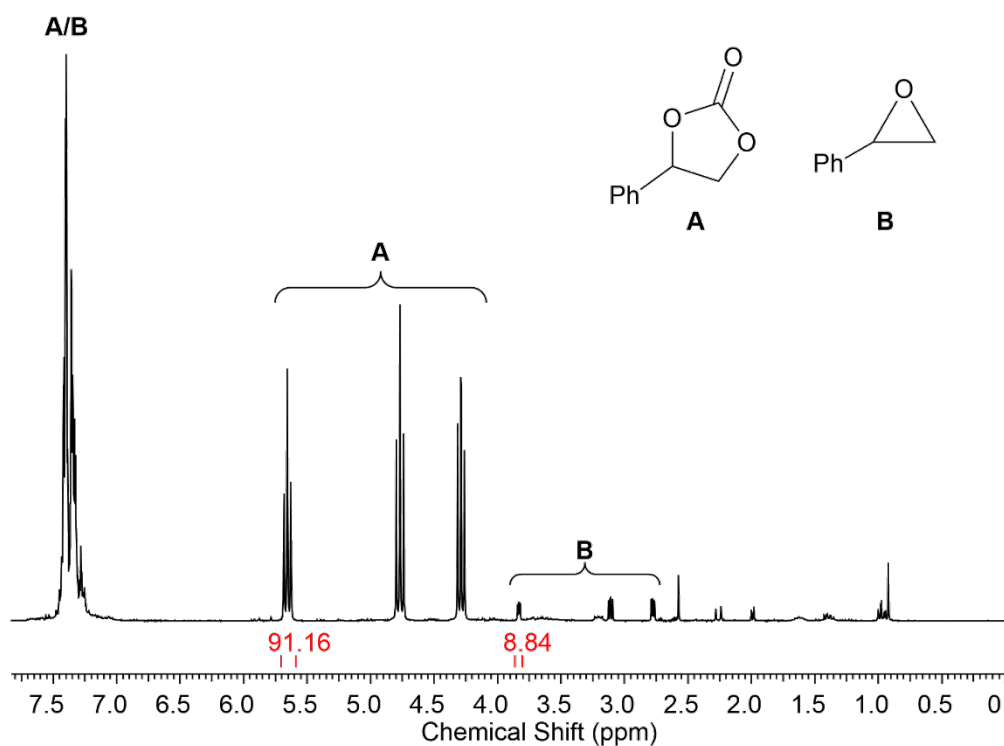
Figure S13. ^{1}H NMR (26 °C, 400.13 MHz, chloroform-*d*) of the product mixture of the catalytic formation of styrene carbonate using 0.5 mol% of [Ce(Me$_2$pz)$_4$]$_2$@SBA-15$_{500}$ (**H1**) and TBAB as a catalyst system. The conversion was determined by the integral ratio of the protons in *α*-position in styrene oxide and styrene carbonate.
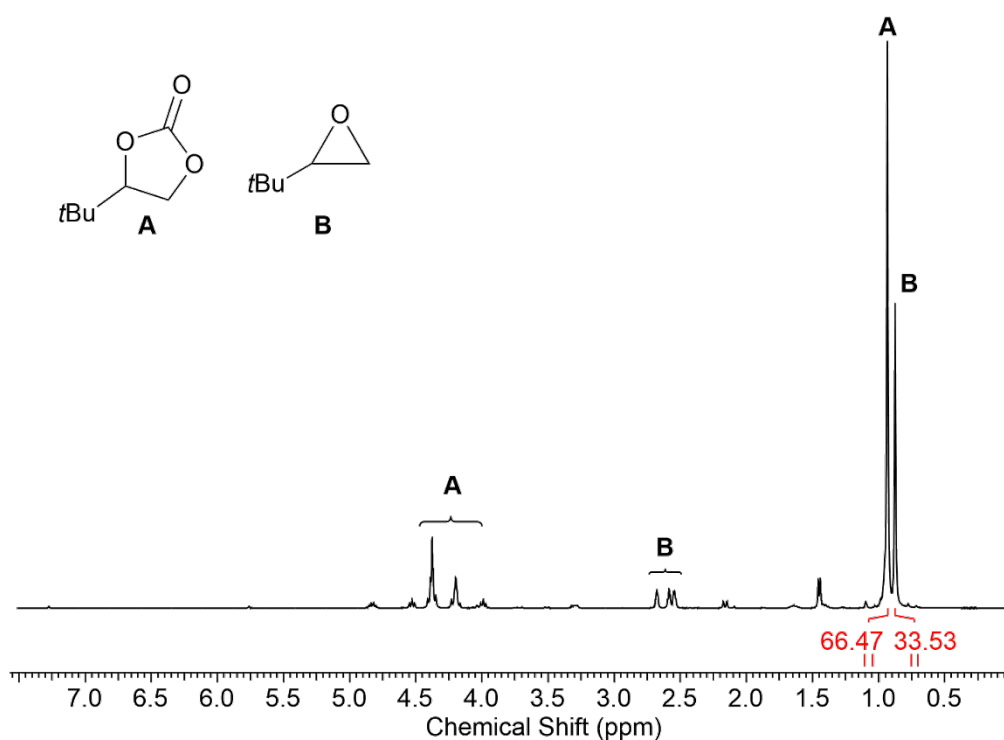
Figure S14. ^{1}H NMR (26 °C, 400.13 MHz, chloroform-*d*) of the product mixture of the catalytic formation of 3,3-dimethyl-1,2-butylene carbonate using 0.5 mol% of [Ce(Me$_2$pz)$_4$]$_2$@SBA-15$_{500}$ (**H1**) and TBAB as a catalyst system. The conversion was determined by the integral ratio of the *tert*-butyl protons in 3,3-dimethyl-1,2-butene oxide and 3,3-dimethyl-1,2-butylene carbonate.
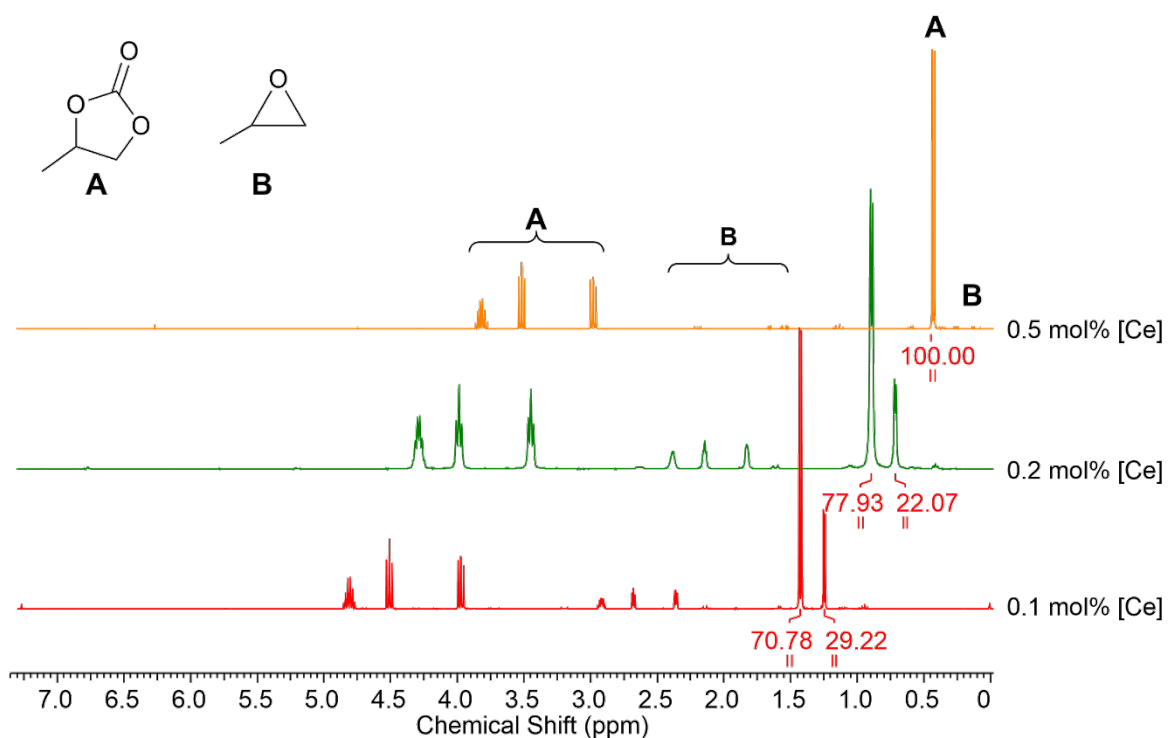
Figure S15. Stacked ^1H NMR spectra (CDCl$_3$, 400.13 MHz, 26 °C) of the product mixture of the catalytic formation of propylene carbonate using different amounts of [Ce(Me$_2$pz)$_4$]$_2$@SBA-15$_{500}$ (**H1**) and TBAB as a catalyst system. The conversion was determined by the integral ratio of the methyl protons in propylene oxide and propylene carbonate.
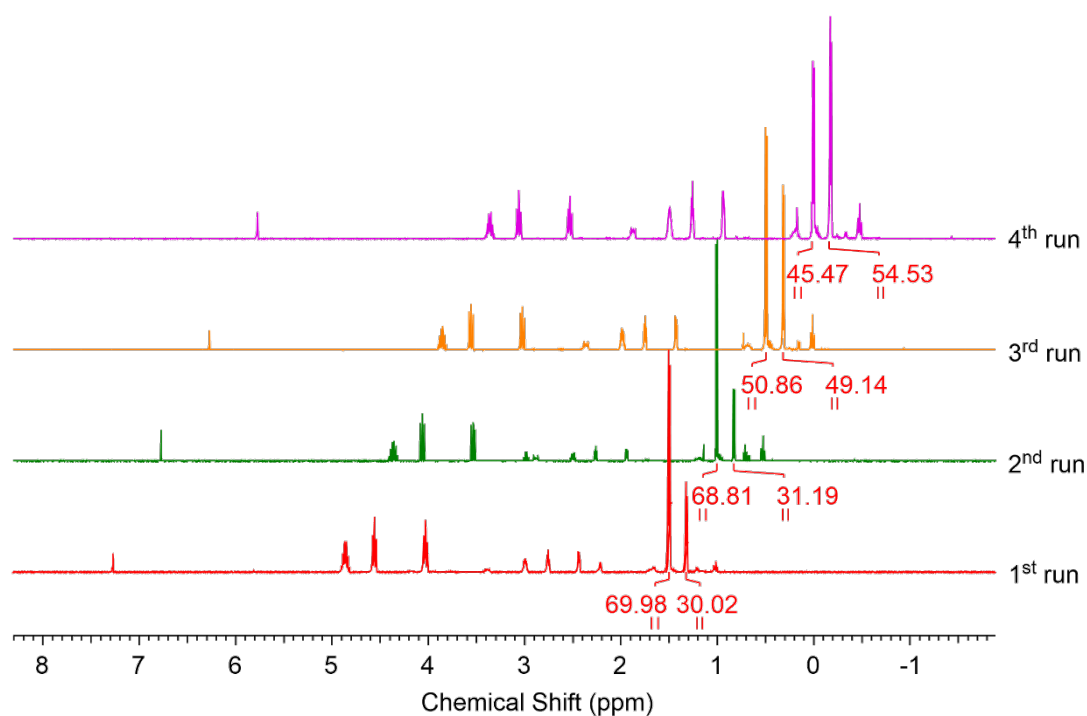
Figure S16. Stacked ^1H NMR spectra (CDCl$_3$, 400.13 MHz, 26 °C) of the product mixture of the catalytic formation of propylene carbonate using 0.5 mol% of Ce(Me$_2$pz)$_4$(thf)@SBA-15$_{500}$ (**H2**) and TBAB as a catalyst system. The conversion was determined by the integral ratio of the methyl protons in propylene oxide and propylene carbonate.

TGA
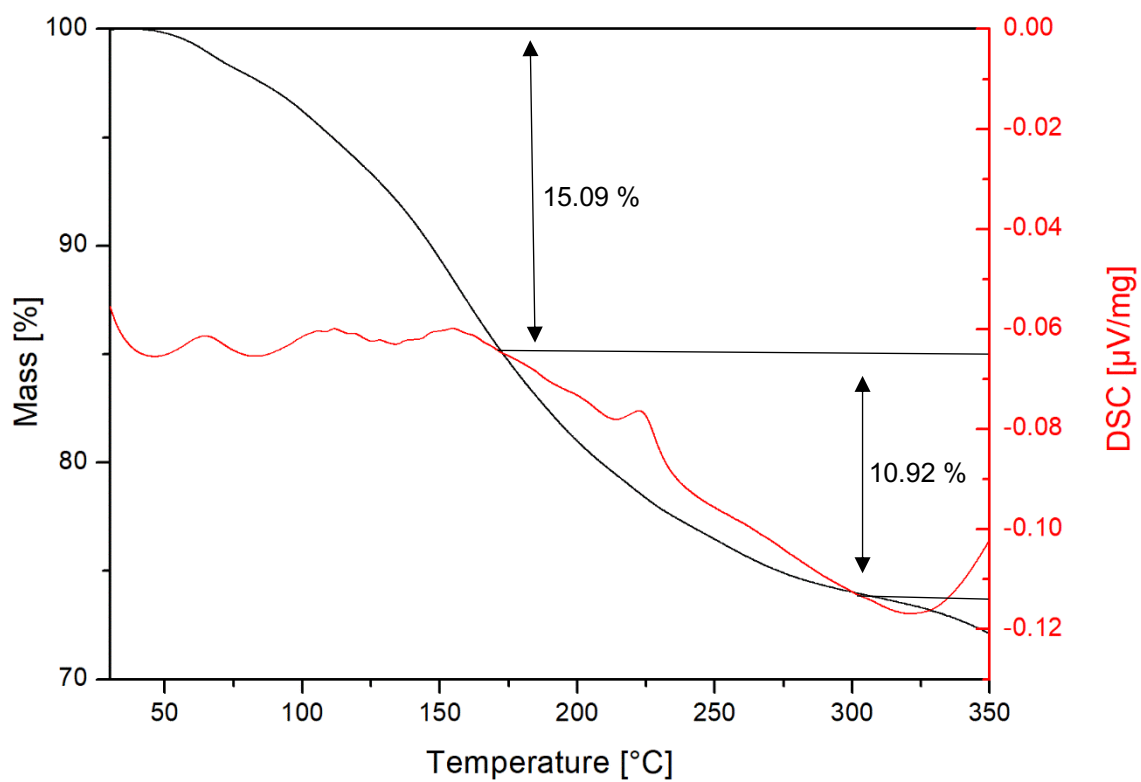
Figure S17. Thermogravimetric analysis (red) and differential scanning calorimetry (red) of $CO_2@[La(Me_2pz)_3(thf)]_2@SBA-15_{500}$ (**H5^{CO2}**).

Crystallographic Data

Crystals for X-ray crystallography were grown using saturated solutions of mixtures of *n*-pentane / Et_2O (**6** and $K[OSi(OtBu)_3](Me_2pzH)(Et_2O)$). Suitable crystals for X-ray analysis were handpicked in a glovebox, coated with Parabar 10312 and stored on microscope slides. Data collection was done on a *Bruker* APEX II Duo diffractometer by using QUAZAR optics and Mo K_α (λ = 0.71073 Å). The data collection strategy was determined using COSMO[2] employing ω scans. Raw data were processed by APEX and SAINT,[3,4] corrections for absorption effects were applied using SADABS.[5] The structures were solved by direct methods and refined against all data by full-matrix least-squares methods on F^2 using SHELXTL and SHELXLE.[6,7] All non-hydrogen atoms were refined anisotropically. Plots were generated by using CCDC Mercury 3.19.1.[8] Further details regarding the refinement and crystallographic data are listed in Table S1 and in the CIF files.

Table S1. Crystallographic data for compounds **6** and K[OSi(O*t*Bu)₃](Me₂pzH)(Et₂O)

	6	K[OSi(O*t*Bu)₃](Me₂pzH)(Et₂O)
CCDC	2023873	2023872
formula	$C_{53}H_{115}CeKN_2O_{16}Si_4$	$C_{42}H_{90}K_2N_4O_{10}Si_2$
M [g·mol⁻¹]	1328.04	945.55
λ [Å]	0.71073	0.71073
color	orange-yellow	colorless
crystal dimensions [mm]	0.379 × 0.254 × 0.114	0.512 × 0.299 × 0.292
crystal system	monoclinic	triclinic
space group	P2₁/n	P$\bar{1}$
a [Å]	16.7561(7)	11.5002(5)
b [Å]	19.8676(9)	12.0299(5)
c [Å]	21.7572(9)	12.7116(5)
α [°]	90	115.5620(10)
β [°]	98.9390(10)	96.0850(10)
γ [°]	90	113.5980(10)
V [Å³]	7155.1(5)	1368.67(10)
Z	4	1
F(000)	2832	516
T [K]	100(2)	100(2)
ρ$_{calcd}$ [g·cm⁻³]	1.233	1.147
μ[mm⁻¹]	0.818	0.268
Data / restraints / parameters	20044 / 18 / 732	9093 / 0 / 288
Goodness of fit	1.038	1.042
R₁ (I > 2σ (I))[a]	0.0281	0.0289
ωR₂ (all data)[b]	0.0719	0.0808

[a] $R_1 = \Sigma(||F0|-|Fc||)/\Sigma|F0|, F0> 4s(F0)$. $\omega R_2 = \{\Sigma[w(F02-Fc2)2/\Sigma[w(F02)^2]\}^{1/2}$
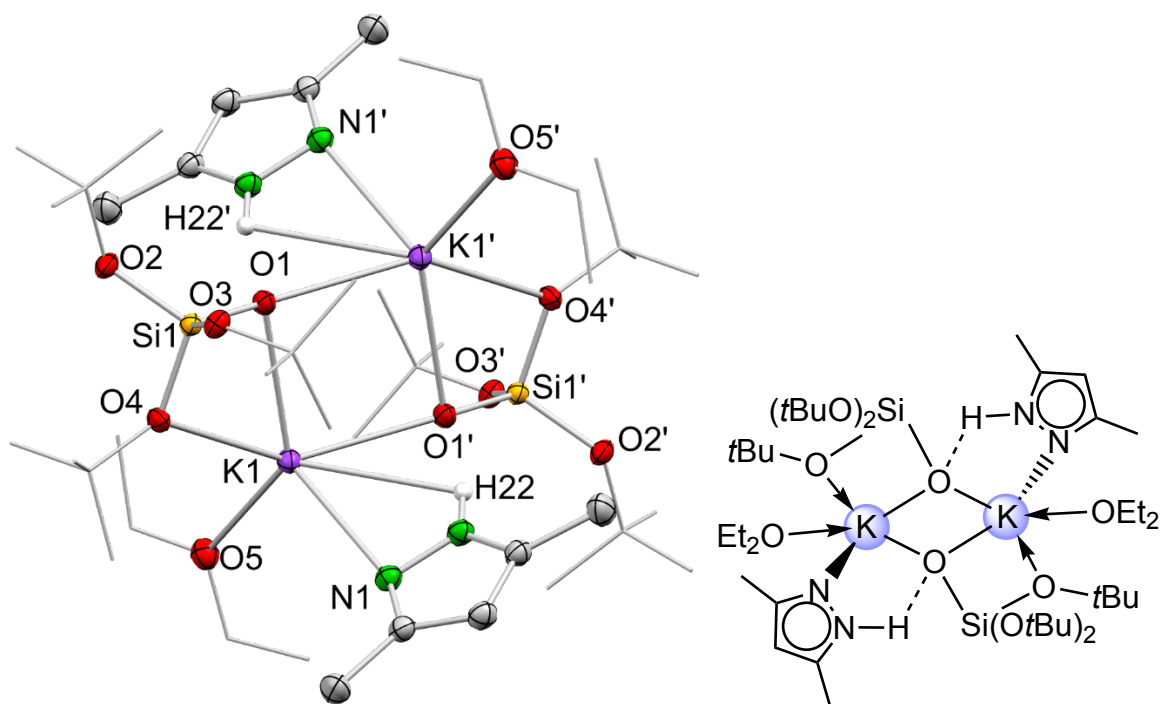
Figure S18. Crystal structure and structural representation of K[OSi(O*t*Bu)₃](Me₂pzH)(Et₂O). Ellipsoids are shown at the 50% probability level. Hydrogen atoms are omitted for clarity. Selected bond lengths [Å]: K1−O1 2.7686(6), K1−O4 2.7338(6), K1−O1' 2.6308(6), K1−N1 2.8604(7), K1−H22 2.902(14).

References

(1) Werner, D.; Bayer, U.; Schädle, D.; Anwander, R. Emergence of a New [NNN] Pincer Ligand via Si-H-Bond Activation and β-Hydride Abstraction at Tetravalent Cerium. *Chem. - Eur. J.* **2020**, *26*, 12194–12205.

(2) *COSMO, v. 1.61*; Bruker AXS Inc.: Madiso, Wi, **2012**.

(3) *APEX 3, v. 2016.5-0*; Bruker AXS Inc.: Madison, Wi, **2012**.

(4) *Saint, v. 8.34A*; Bruker AXS Inc.: Madison, Wi, **2012**.

(5) Krause, L.; Herbst-Irmer, R.; Sheldrick, G. M.; Stalke, D. Comparison of Silver and Molybdenum Microfocus X-Ray Sources for Single-Crystal Structure Determination. *J. Appl. Crystallogr.* **2015**, *48*, 3–10.

(6) Sheldrick, G. M. *SHELXT* – Integrated Space-Group and Crystal-Structure Determination. *Acta Crystallogr. Sect. Found. Adv.* **2015**, *71*, 3–8.

(7) Hübschle, C. B.; Sheldrick, G. M.; Dittrich, B. *ShelXle* : A Qt Graphical User Interface for *SHELXL*. *J. Appl. Crystallogr.* **2011**, *44*, 1281–1284.

(8) Macrae, C. F.; Bruno, I. J.; Chisholm, J. A.; Edgington, P. R.; McCabe, P.; Pidcock, E.; Rodriguez-Monge, L.; Taylor, R.; van de Streek, J.; Wood, P. A. *Mercury CSD 2.0* – New Features for the Visualization and Investigation of Crystal Structures. *J. Appl. Crystallogr.* **2008**, *41*, 466–470.

The cerium–quinone redox couples put under scrutiny
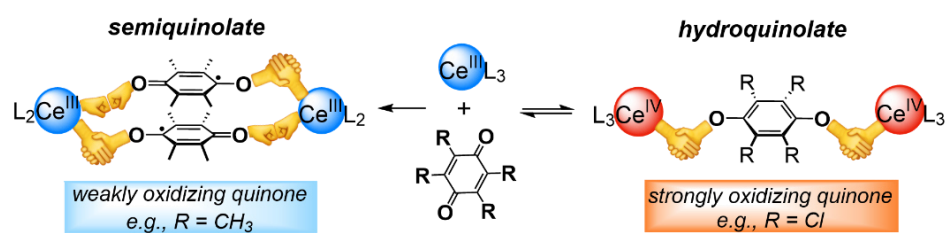
EDGE ARTICLE

Cerium–quinone redox couples put under scrutiny†

Uwe Bayer, [ID] Daniel Werner, Andreas Berkefeld, Cäcilia Maichle-Mössmer [ID] and Reiner Anwander [ID] *

Homoleptic cerous complexes $Ce[N(SiMe_3)_2]_3$, $[Ce\{OSi(OtBu)_3\}_3]_2$ and $[Ce\{OSi^iPr_3\}_3]_2$ were employed as thermally robust, weakly nucleophilic precursors to assess their reactivity towards 1,4-quinones in non-aqueous solution. The strongly oxidizing quinones 2,3-dichloro-5,6-dicyano-1,4-benzoquinone (DDQ) or tetrachloro-1,4-benzoquinone (Cl_4BQ) readily form hydroquinolato-bridged ceric complexes of the composition $[(Ce^{IV}L_3)_2(\mu_2-O_2C_6R_4)]$. Less oxidising quinones like 2,5-di-*tert*-butyl-1,4-benzoquinone (tBu_2BQ) tend to engage in redox equilibria with the ceric hydroquinolato-bridged form being stable only in the solid state. Even less oxidising quinones such as tetramethyl-1,4-benzoquinone (Me_4BQ) afford cerous semiquinolates of the type $[(Ce^{III}L_2(thf)_2)(\mu_2-O_2C_6Me_4)]_2$. All complexes were characterised by X-ray diffraction, ^1H, $^{13}C\{^1H\}$ and ^{29}Si NMR spectroscopy, DRIFT spectroscopy, UV-Vis spectroscopy and CV measurements. The species putatively formed during the electrochemical reduction of $[Ce^{IV}\{N(SiMe_3)_2\}_3]_2(\mu_2-O_2C_6H_4)$ could be mimicked by chemical reduction with $Co^{II}Cp_2$ yielding $[(Ce^{III}\{N(SiMe_3)_2\}_3)_2(\mu_2-O_2C_6H_4)][Co^{III}Cp_2]_2$.

Introduction

Quinones are multifunctional organic molecules exhibiting intriguing redox behaviour.[1,2] Of particular note is their importance in biological electron–transfer processes (photosynthesis, respiration)[3] and in industrial catalysis (anthraquinone process for hydrogen peroxide production).[4] Quinones can engage in one or two electron redox processes involving the formation of either semiquinolates or hydroquinolates.[5] Strikingly, the reduction potential of 1,4-benzoquinones (*para*-benzoquinones) can easily be modified by introducing electron-withdrawing or donating substituents into the benzene ring.[5,6] As a consequence, tetrachloro-1,4-benzoquinone (chloranil, Cl_4BQ) and even more so 2,3-dichloro-5,6-dicyano-1,4-benzoquinone (DDQ) emerged as efficient oxidants in organic synthesis.[7] DDQ has been further successfully applied in photoredox catalysis.[8] Moreover, anionic η^4-1,4-benzoquinone manganese tricarbonyl features a quinoid π-complex, broadly used for the fabrication of supramolecular metal–organometallic coordination networks.[9] Relatedly, deprotonated variants of 2,5-dihydroxy-1,4-benzoquinone (DHBQ) were shown to act

as rigid ditopic linkers,[10] *e.g.*, to support the formation of pentagonal dodecahedral $Ce_2(H_2O)_{18}$ cages or in permanently porous aluminium frameworks.[11] DHBQ was also probed as a bridging redox-active ligand in bimetallic $[LnCl_2(thf)_3]_2(\mu\text{-}bobq)$ (Ln = Y, Dy; bobq = 2,5-bisoxide-1,4-benzoquinolato) to build single-molecule magnets.[12] More recently, the related semiquinolato radical-bridged dimeric complexes $[LnCl_2(thf)_3(\mu\text{-}Me_4sq)_2]_2$ (Ln = Y, Gd) were obtained by oxidation of the corresponding *in situ* formed hydroquinolate complexes with $FeCl_3$.[13] Semiquinolato-bridged scandium(III) species were reported to promote self-organised electron transfer from d-transition metals (Ir, Fe) to 1,4-quinones.[14,15]

Targeted metal-redox chemistry with quinones has been a recurring issue for the rare-earth-metal couples Ln(II)/Ln(III)[16] and Ce(III)/Ce(IV).[17] Especially in the case of molecular cerium chemistry,[17] its unique single-electron-transfer (SET) pathway has recently been extended beyond the traditional application of ceric ammonium nitrate (CAN; redox potential of 1.61 V *vs.* NHE) in organic synthesis[18] to photoredox catalysis.[19] On the other hand, redox protocols are known to provide efficient access to metalorganic Ce^{IV} complexes. Typically, such $Ce^{III} \rightarrow Ce^{IV}$ transformations are promoted by halogenating oxidants (*e.g.* C_2Cl_6, Ph_3CCl, $PhICl_2$, $TeCl_4$, $FcPF_6$, $FcBF_4$, Ph_3CBF_4, Ph_3CPF_6, I_2),[20] silver salts (AgX, X = F, I, BF_4, OTf)[21] or dioxygen.[20b,22] Archetypical 1,4-benzoquinone (BQ) has been established as a versatile oxidant for the synthesis of homoleptic ceric complexes CeL_4 from cerous ate complexes $[CeL_4M(do)_x]$ *via* tandem oxidation-ligand redistribution protocols (L =

Institut für Anorganische Chemie, Eberhard Karls Universität Tübingen (EKUT), Auf der Morgenstelle 18, 72076 Tübingen, Germany. E-mail: reiner.anwander@uni-tuebingen.de; Web: [http://uni-tuebingen.de/syncat-anwander]
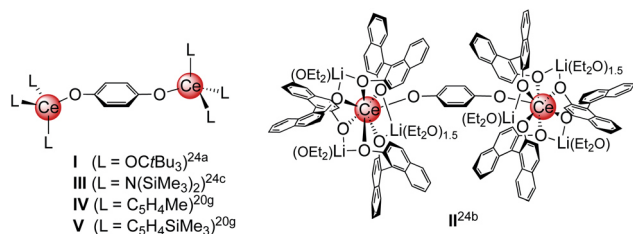
Chart 1 Structurally characterised dicerium(IV) hydroquinolate complexes (I–V),[20g,24] obtained *via* oxidation of cerous precursor with BQ.

monoanionic ligand, M = alkali metal and do = donor solvent; separation of an alkali-metal hydro-/semiquinolate).[23] In the presence of sterically demanding ligands L, BQ was also shown to form hydroquinolato (hq)–bridged ceric complexes of the general composition [L₃Ce–OC₆H₄O–CeL₃].[20g,24] This very Ce^III → Ce^IV transformation was pioneered by Sen *et al.* in 1992, resulting in the isolation of [(*t*Bu₃CO)₃Ce(OC₆H₄O)Ce(OC*t*Bu₃)₃] (Chart 1, **I**).[24a] In the same paper, the oxidation of Ce(OC*t*Bu₃)₃ with 2,6-di-*tert*-butyl-1,4-benzoquinone to the terminal Ce^IV-semiquinolate radical (*t*Bu₃CO)₃Ce(O₂C₆H₂*t*Bu₂) was described as evidenced by ¹H NMR and EPR spectroscopic measurements.[24a] More recently, Schelter *et al.* reported on hq-bridged complex **II** resulting from the oxidation of cerous Ce(BINOlate)₃(thf)Li₃(thf)₄ with 0.5 equivalents of BQ.[24b] Similarly, our group synthesized [Ce{N(SiMe₃)₂}₃]₂(μ₂-O₂C₆H₄)[24c] (**III**) and (CeCp^R₃)₂(μ₂-O₂C₆H₄) (Cp^R = C₅H₄Me (**IV**) and C₅H₄(SiMe₃) (**V**)).[20g] In contrast, the reaction of BQ with [Ce(Me₂pz)₃]ₓ featuring the sterically less demanding and increasingly nucleophilic 3,5-dimethylpyrazolato ligand (Me₂pz) led in fact to a transient Ce^IV hydroquinolate species (as indicated by the characteristic colour change), which, however, at ambient temperature was converted into the isolable trimetallic Ce^III

complex Ce₃(pchd)₂(Me₂pz)₅(thf)₂ (pchd = 1,4-bis(3,5-dime-thylpyrazol-1-yl)cyclohex-2,5-diene-1,4-diolato).[23c] Apparently, the new pchd ligand formed *via* 1,4-nucleophilic attack at bq by two adjacent Me₂pz ligands. This nucleophilic reaction pathway could be prevented by using bulky *t*Bu groups on the pz ligand, but homolpetic Ce(*t*Bu₂pz)₄ was formed as the main ceric product *via* irreversible ligand rearrangement.[23c]

As such, cerium–1,4-benzoquinone couples have revealed distinct redox chemistry, we became curious about as to what extent such redox transformations are affected by both the type of 1,4-benzoquinone oxidant and the molecular Ce^III precursor. The present study uncovers some unexpected correlation between Ce^IV–hydroquinolato stabilisation and quinone oxidant strength, as well as a new path to *p*-semiquinolato–radical-bridged rare-earth-metal complexes.

Results and discussion

Molecular redox precursors

The quinones used in this study comprise 2,3-dichloro-5,6-dicyano-1,4-benzoquinone (DDQ), tetrachloro-1,4-benzoquinone (Cl₄BQ), 1,4-benzoquinone (BQ), tetramethyl-1,4-benzoquinone (Me₄BQ), 2,5-di-*tert*-butyl-1,4-benzoquinone (*t*Bu₂BQ), 1,4-naphthoquinone (NQ), and 9,10-anthraquinone (AQ). All are commercially available and were selected according to their reduction potentials spanning a E^0 range of 89 to 887 mV (2e⁻/2H⁺, *vs.* NHE, *cf.*, Scheme 1).[5,25] The cerous precursors were chosen according to the criteria solubility, weak nucleophilicity, proven access to the tetravalent state, and a stabilizing effect on the latter. Furthermore, the use of sterically bulky ligands was assumed to minimise the occurrence of ligand redistribution reactions. Accordingly, homoleptic Ce[N(SiMe₃)₂]₃ (**1**) appeared to be an ideal benchmark system.[24c] After additional investigations into the respective pyrazolate
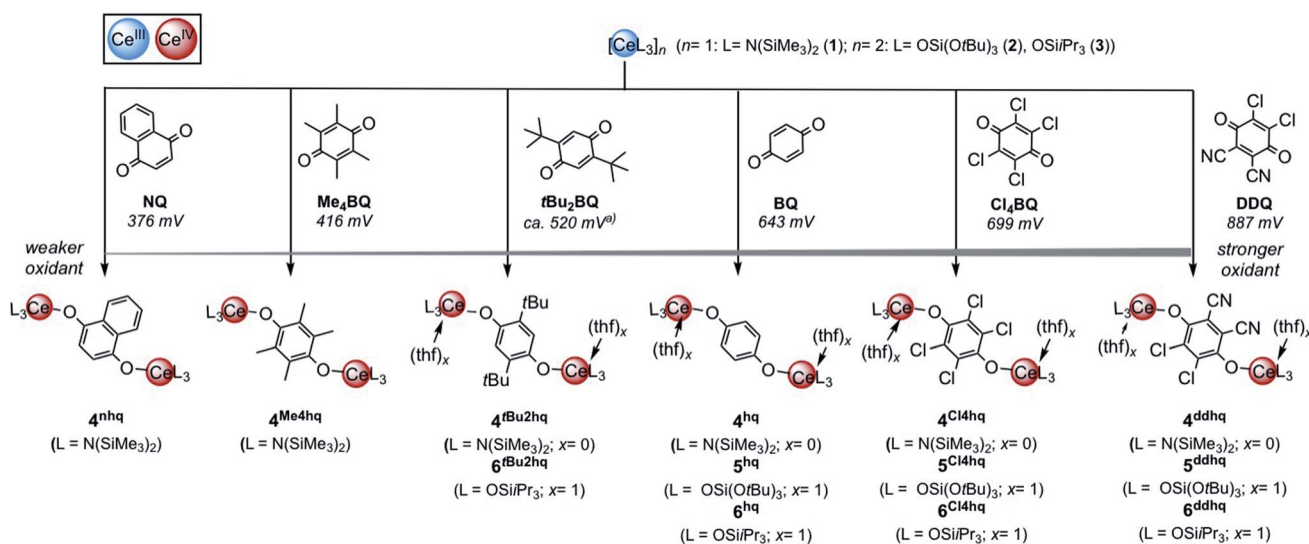
Scheme 1 Oxidation of trivalent cerium complexes with 1,4-quinone derivatives under formation of hydroquinolato-bridged ceric complexes. To enable better assessment of the relative oxidation ability 2e⁻/2H⁺ reductions potentials are given in mV *versus* NHE according to ref. 5. (*a*) Calculated value.
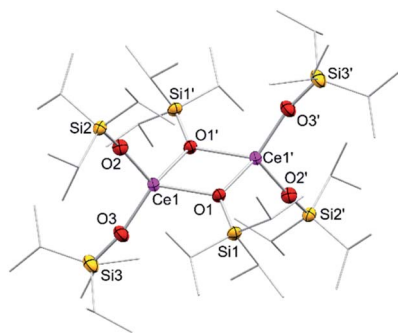
Fig. 1 Crystal structure of $[Ce\{OSi^iPr_3\}_3]_2$ (**3**). Ellipsoids are shown at the 50% probability level. Hydrogen atoms are omitted for clarity. Selected interatomic distances [Å] and angles [°]: Ce1–O1 2.3951(12), Ce1–O2 2.1659(14), Ce1–O3 2.1671(14); Ce1–O2–Si2 163.03(9), Ce1–O3–Si3 167.40(10).

chemistry, the abovementioned $[Ce(R_2pz)_3]$ (R = Me, tBu) were discarded because of persisting alternative reaction pathways like 1,4-nucleophilic attack of BQ by Me_2pz and ligand redistribution (formation of $Ce(tBu_2pz)_4$).[23c] The new pyrazolate studies clearly confirmed that steric hindrance of both the pyrazolato ligand and the 1,4-benzoquinone can minimise/counteract such undesired reactions, but the formation of product mixtures seems inevitable. Products crystallised from these reactions include minor amounts of ceric $[Ce(tBu_2pz)_3(-thf)]_2(Me_4hq)$ or a cerous product of partial pyrazolyl-promoted nucleophilic attack $Ce_3(bpad)(pasq)(Me_2pz)_6(thf)$ (bpad = 1,4-bis(3,5-dimethylpyrazol-1-yl)anthra-1,4-diolato; pasq = 1-(3,5-dimethylpyrazol-1-yl)anthra-1,4-semiquinolato) (84%) mixed with semiquinolate $[Ce(Me_2pz)_2(thf)_2(asq)]_2$ (asq = anthra-semiquinolato; *cf.* ESI† for structural details). The use of Ce^{III} halides was discarded mainly for solubility issues.

In addition to silylamide **1**, the siloxide derivatives $[Ce\{OSi(OtBu)_3\}_3]_2$ (**2**)[21d,26] and $[Ce\{OSi^iPr_3\}_3]_2$ (**3**) were assessed as suitable cerous precursors. Complexes **2** and **3**, with and without intramolecular donor site, respectively, were readily obtained in pure form *via* protonolysis of **1** with the corresponding silanol.[26] The crystal structure of the new complex **3** revealed a dimeric arrangement with two μ_2-bridging and four terminal siloxy groups (Fig. 1), similar to that found for tris(*tert*-butoxy)siloxy congener **2** or $[Ce(OSiPh_3)_3]_2$ [27] or $[Ce(OCHtBu_2)_3]_2$.[28] The Ce–$O_{terminal}$ (2.1659(14) and 2.1671(14) Å) and the Ce–O_{μ_2} distances (2.3951(12) and 2.4030(12) Å) of **3** are slightly shorter than those in **2** (Ce–$O_{terminal}$ 2.202(3), 2.186(3) Å; Ce–$O_{\mu2}$ 2.532(2) Å) and $[Ce(OSiPh_3)_3]_2$ (Ce–$O_{terminal}$ 2.141(7), 2.185(6) Å; Ce–$O_{\mu2}$ 2.345(6), 2.583(5) Å) reflecting the lower coordination number (CN 4 *vs.* 5), but slightly longer than in $[Ce(OCHtBu_2)_3]_2$ (Ce–$O_{terminal}$ 2.142(2), 2.152(3) Å; Ce–$O_{\mu2}$ 2.363(3) Å).[28] The ^{1}H NMR spectrum of **3** in C_6D_6 shows two singlets at −28.82 and −17.23 ppm for the μ_2-OSi^iPr_3 groups and two singlets at 6.46 and 9.09 ppm for the terminal siloxy ligands indicating a non-fluxional dimeric species in non-coordinating solvents. When recorded in THF-d_8, only two signals for the OSi^iPr_3 groups appeared, in accordance with the formation of a monomeric adduct $[Ce\{OSi^iPr_3\}_3(thf-d_8)_x]$.
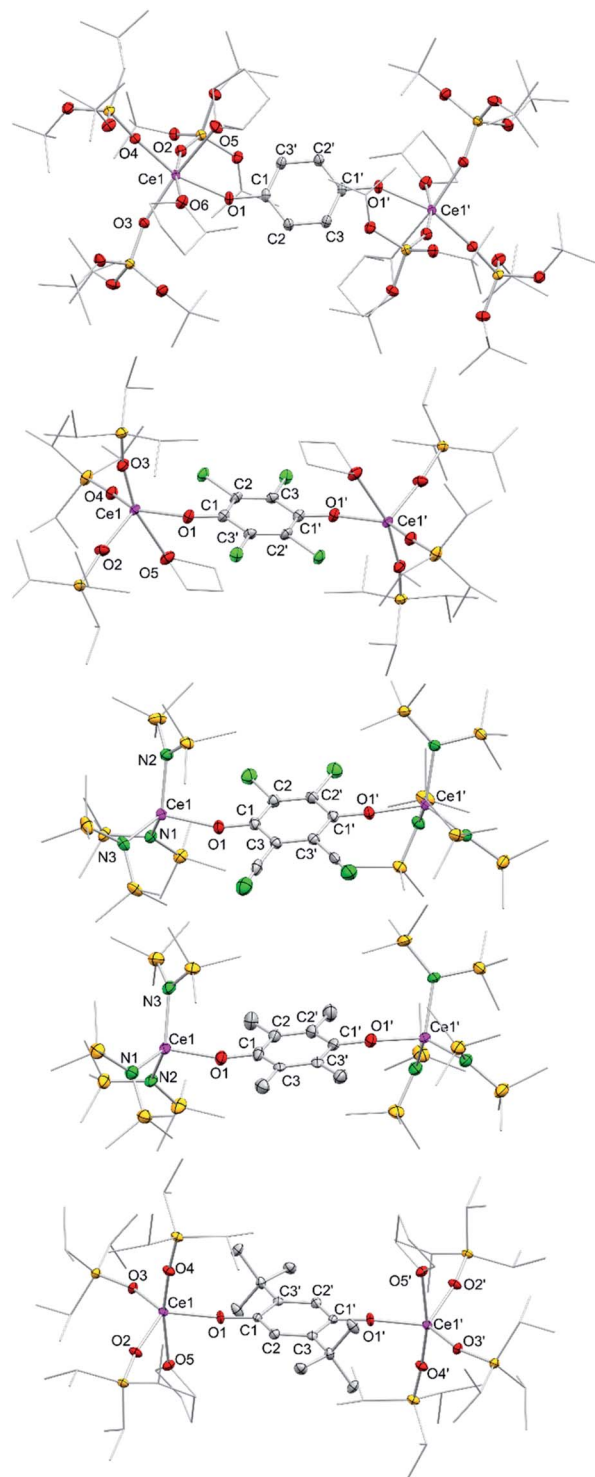
Fig. 2 Crystal structures of $[Ce\{OSi(OtBu)_3\}_3(Me\text{-thf})_2]_2(\mu_2\text{-}O_2C_6H_4)$ (**5^{hq}·2MeTHF**), $[Ce\{OSi^iPr_3\}_3(thf)]_2(\mu_2\text{-}O_2C_6Cl_4)$ (**6^{Cl4hq}**), $[Ce\{N(SiMe_3)_2\}_3]_2(\mu_2\text{-}O_2C_6Cl_2CN_2)$ (**4^{ddq}**), $[Ce\{N(SiMe_3)_2\}_3]_2(\mu_2\text{-}O_2C_6Me_4)$ (**4^{Me4hq}**), and $[Ce\{OSiiPr_3\}_3(thf)]_2(\mu_2\text{-}O_2C_6tBu_2H_2)$ (**6^{tBu2hq}**) (from top down). Ellipsoids are shown at the 50% probability level. Hydrogen atoms, disordered ligands and lattice solvents are omitted for clarity. Selected interatomic distances for **5^{hq}**, **6^{Cl4hq}**, **4^{ddq}**, and **4^{Me4hq}** are given in Tables 1 and 2. Selected bond lengths for **6^{tBu2hq}** [Å]: Ce1–O1 2.109(3), Ce1–O2 2.104(3), Ce1–O3 2.097(3), Ce1–O4 2.107(3), C1–C2 1.391(6), C2–C3 1.391(6), C1–C3′ 1.405(6), C1–O1 1.350(5).

Table 1 Selected analytical data of complexes 4^{hq}, 4^{Cl4hq}, 4^{ddhq}, 4^{Me4hq}, 4^{tBu2hq}, 4^{nhq}. Interatomic distances are given in [Å], angles in [°], chemical shifts in [ppm], μ_{eff} in [BM], UV/Vis absorption band in [nm], and E_{pc}/E_{pa} in [V vs. Fc/Fc$^+$]

Complex	4^{hq24c}	4^{Cl4hq}	4^{ddhq}	4^{Me4hq}	4^{tBu2hq}	4^{nhq}
Ce1–O1	2.0895(13)	2.149(4)	2.1731(15)	2.082(6)	2.117(2)	—
Ce1–N1	2.2388(14)	2.265(5)	2.2206(18)	2.280(7)	2.235(2)	—
Ce1–N2	2.2398(15)	2.230(5)	2.2112(18)	2.229(7)	2.246(2)	—
Ce1–N3	2.2487(14)	2.244(5)	2.2467(19)	2.238(7)	2.259(2)	—
C–C$_{arom}$	1.387(3)–1.399(2)	1.383(8)–1.392(8)	1.390(4)–1.407(3)	1.390(11)–1.408(12)	1.388(4)–1.405(4)	—
C1–O1	1.356(2)	1.324(7)	1.318(3)	1.366(10)	1.378(3)	—
Ce1–O1–C1	173.13(11)	156.1(4)	161.02(15)	162.4(6)	146.79(18)	—
^{1}H NMR^a	0.43	0.45	0.45	0.43^d	0.49	0.44
^{13}C{^{1}H} NMR^a	—	—	5.6	—	—	5.6
^{29}Si{^{1}H} NMR^a	—	−8.1	−7.3	−8.8	—	−8.1
μ_{eff}	0.67	0.68	0.59	0.89	—	1.19
UV-Vis absorption bands^b	485	319/518	384/511	362/411/681	—	339/425/474/677
$E_{pc}{}^c$	−0.699/−0.966	−0.415/−0.624	−0.546	—	—	—
$E_{pa}{}^c$	−0.558	−0.290	−0.1685	—	—	—
$E_{1/2}$	−0.76	−0.46	−0.36	—	—	—
ΔE	0.408	0.334	0.377	—	—	—

^{a} NMR spectra recorded in C$_6$D$_6$. ^{b} UV-Vis spectra recorded in toluene. ^{c} Determined in THF using c(analyte) = 2 mM and c(electrolyte) = 0.1 M and a scan rate of 50 mV s^{-1}. ^{d} Determined in toluene-d_8 at 0 °C.

Quinone oxidation of Ce[N(SiMe$_3$)$_2$]$_3$ (1)

Treatment of Ce[N(SiMe$_3$)$_2$]$_3$ (1) with each 0.5 equivalents of DDQ, Cl$_4$BQ, Me$_4$BQ, tBu$_2$BQ and NQ, in a mixture of toluene and n-hexane, immediately led to a colour change from yellow to dark brown. Upon recrystallisation from toluene/n-hexane mixtures it was possible to isolate the hydroquinolato-bridged complexes [Ce{N(SiMe$_3$)$_2$}$_3$]$_2$(μ_2-O$_2$C$_6$Cl$_4$) (4^{Cl4hq}), [Ce{N(SiMe$_3$)$_2$}$_3$]$_2$(μ_2-O$_2$C$_6$Cl$_2$(CN)$_2$) (4^{ddhq}), [Ce{N(SiMe$_3$)$_2$}$_3$]$_2$(μ_2-O$_2$C$_6$Me$_4$) (4^{Me4hq}), [Ce{N(SiMe$_3$)$_2$}$_3$]$_2$(μ_2-O$_2$C$_6$$tBu_2H_2$) (4^{tBu2hq}) and [Ce{N(SiMe$_3$)$_2$}$_3$]$_2$(μ_2-O$_2$C$_{10}$H$_6$) (4^{nhq}) in very good crystalline yields of 71 to 90% (Scheme 1). The crystal structures of the new complexes 4^{xhq} are isostructural to the previously reported derivative 4^{hq24c} and only differ in the bridging hq linker (Fig. 2). The Ce1–O1 distances of 2.084(6) to 2.173(2) Å (for a full list of interatomic distances see Table 1) are in the same range as found for other hq-bridged cerium complexes (2.086(10)–2.143(5) Å).[20g,24] Likewise, the Ce1–N bond lengths compare well to other Ce^{IV} silylamides like [Ce{N(SiMe$_3$)$_2$}$_3$]$_2$(μ_2-O$_2$C$_6$H$_4$) (2.2388(14)–2.2487(14) Å),[24c] Ce[N(SiMe$_3$)$_2$]$_3$Cl (2.217(3) Å),[20a] and Ce[N(SiHMe$_2$)$_2$]$_4$ (2.2378(11)–2.2574(11) Å).[20d] Also, the C–C distances of the hq linker converge as the expected aromatic ring is formed and the C–O distances of 1.318(3) to 1.378(3) Å corroborate the formation of C–O single bonds.

The ^{1}H NMR spectra of compounds 4^{xhq} in C$_6$D$_6$ show singlets for the trimethylsilyl (TMS) groups at 0.43 to 0.45 ppm along with signals for the bridging hydroquinolato moieties.
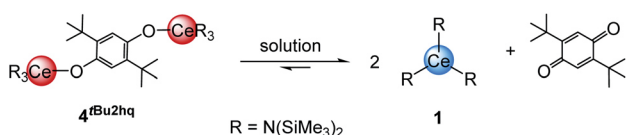
Scheme 2 Equilibrium between 4^{tBu2hq} and reformation of reactants in solution and solid state.

Further, the ^{13}C{^{1}H} NMR spectra of 4^{ddhq} and 4^{nq} display a singlet for the TMS groups at 5.6 ppm and signals in the aromatic region for the different hydroquinolates, indicative of a successful reduction of the respective benzoquinone derivatives. The characterisation of 4^{tBu2hq} in solution (C$_6$D$_6$) was not feasible, due to the prevailing equilibrium shown in Scheme 2, and ready back-formation of 1 and 2,5-di-$tert$-butyl-1,4-benzoquinone.

While the ^{1}H NMR spectrum of 4^{tBu2hq} primarily shows signals for the starting materials and only minor product signals, its DRIFT spectrum indicated the absence of any strong C=O absorption band, and therefore the stability of 4^{tBu2hq} in the solid state (see Fig. S10 and S45 in ESI†). In contrast, complexes 4^{hq}, 4^{Cl4hq} and 4^{ddhq} derived from the stronger oxidizing quinones are very stable in the solid state and in solution. This fits again well with the already pronounced instability of 4^{Me4hq} and 4^{nhq} which slowly decompose in n-hexane and toluene at ambient temperature and rapidly undergo decomposition in THF. Tracking of the progress of the decomposition by ^{1}H NMR spectroscopy revealed the formation of 1 and other paramagnetic Ce^{III} species which, however, could not be identified. The progressing decomposition can also be seen in the ligand-to-metal charge transfers observed in the UV-Vis spectra (Fig. S68, ESI†). As the spectra of 4^{hq}, 4^{Cl4hq} and 4^{ddhq} show mainly one strong absorption band at around 500 nm (ε > 5060 L mol^{-1} cm^{-1}), the spectra of 4^{Me4hq} and 4^{nhq} show several absorption bands with significantly lower intensities (ε < 4400 L mol^{-1} cm^{-1}) indicative of Ce^{III} species and therefore redox decomposition of the compounds.

All attempts to isolate putative 4^{ahq}, derived from the weakest oxidising quinone under study, namely 9,10-anthraquinone (E^0 = 89 mV; 2e$^-$/2H$^+$, vs. NHE),[5] were unsuccessful with the reaction mixtures showing no colour change immediately after addition of the anthraquinone. However, a colour change from

Table 2 Selected analytical data of complexes 5^{hq}, 5^{Cl4hq}, 5^{ddq}, 6^{hq}, 6^{Cl4hq}, 6^{ddq}. Interatomic distances are given in [Å], angles in [°], chemical shifts in [ppm], μ_{eff} in [BM], UV/Vis absorption band in [nm], and E_{pc}/E_{pa} in [V vs. Fc/Fc$^+$]

Complex	5^{hq}	5^{Cl4hq}	5^{ddq}	6^{hq}	6^{Cl4hq}	6^{ddq}
Ce1–O1	2.1244(10)	2.184(3)	—	—	2.207(2)	2.2325(16)
Ce1–O2	2.1534(10)	2.091(3)	—	—	2.095(2)	2.0841(16)
Ce1–O3	2.1334(11)	2.094(3)	—	—	2.066(2)	2.0710(17)
Ce1–O4	2.1396(11)	2.104(3)	—	—	2.080(2)	2.091(2)
C–C$_{arom}$	1.390(2)–1.395(2)	1.373(8)–1.406(5)	—	—	1.380(4)–1.407(4)	1.379(5)–1.415(3)
C1–O1	1.3540(17)	1.326(4)	—	—	1.322(3)	1.316(3)
Ce1–O1–C1	151.76(10)	140.0(2)	—	—	138.54(18)	144.85(14)
^{1}H NMR^a	1.36	1.36	1.36		1.12/1.05	1.12/1.05
^{13}C{^{1}H} NMR^a	72.5/32.6	72.8/32.4	73.0/32.5		18.0/14.0	19.1/15.1
^{29}Si{^{1}H} NMR^a	−103.2	−104.6	−105.3	7.0	9.6	10.7
μ_{eff}	0.82	0.54	0.60	0.68	0.50	0.66
UV-Vis absorption band^b	369/622	493	384/450	526^c	511	381/470
$E_{pc}^{\ d}$	−1.7855	−1.414	−1.353	−1.116/−1.816	−1.580	−1.149/−1.484
$E_{pa}^{\ d}$	−0.3625	−0.521	0.130	−1.273/−0.817	−0.729	−0.751
ΔE	1.416	0.893	1.483	0.999	0.851	0.733

^{a} NMR spectra recorded in THF-d_8. ^{b} Spectra recorded in toluene. ^{c} Spectra recorded in THF. ^{d} Determined in THF using c(analyte) = 2 mM and c(electrolyte) = 0.1 M and a scan rate of 50 mV s^{-1}.

yellow to green occurred after two days and the respective ^{1}H NMR spectrum showed multiple paramagnetic signals.

Quinone oxidation of siloxides [Ce{OSi(OtBu)$_3$}$_3$]$_2$ (2) and [Ce{OSi^{i}Pr$_3$}$_3$]$_2$ (3)

Reacting cerous siloxides **2** and **3** with the selected quinones in THF immediately gave a colour change of the reaction mixtures (from colourless to: dark purple (BQ), dark red (Cl$_4$BQ), dark yellow/orange (DDQ), pale purple (tBu$_2$BQ), pale blue (Me$_4$BQ), pale green (NQ)). The ceric compounds [CeL$_3$(thf)]$_2$(μ_2-O$_2$C$_6$H$_4$) (**5^{hq}**, **6^{hq}**), [CeL$_3$(thf)]$_2$(μ_2-O$_2$C$_6$Cl$_4$) (**5^{Cl4hq}**, **6^{Cl4hq}**), [CeL$_3$(thf)]$_2$(-μ_2-O$_2$C$_6$Cl$_2$(CN)$_2$) (**5^{ddq}**, **6^{ddq}**), with L = OSi(OtBu)$_3$ or OSi^{i}Pr$_3$ derived from quinones with a relatively strong oxidising effect were successfully isolated from these reactions (Scheme 1).

However, the weakly oxidizing quinones Me$_4$BQ and NQ did not lead to tetravalent cerium species, as indicated by the detection of only paramagnetic signals in the ^{1}H NMR spectra (for an example of such a ^{1}H NMR spectrum, see Fig. S34 in the ESI;† formation of semiquinolates, *vide infra*). The accessible complexes **5** and **6** were obtained in moderate to good crystalline yields of 42 to 71% upon recrystallisation from THF or THF/Et$_2$O mixtures. Crystals suitable for XRD analysis were obtained for complexes **5^{hq}**, **5^{Cl4hq}**, **6^{Cl4hq}**, **6^{ddhq}** and **6^{tBu2hq}**, revealing the same structural motif as complexes **4**, that is two CeL$_3$ moieties connected *via* a hydroquinolato linker (Fig. 2).

Strikingly, the ^{1}H NMR spectrum of **6^{tBu2hq}** indicated the existence of an equilibrium similar to that of ceric **4^{tBu2hq}** (*cf.* Scheme 2). However, along with the reactants **3** and tBu$_2$BQ additional signals assignable to distinct dia- and paramagnetic decomposition products were detected. Further, the crystal structures of complexes **5** and **6** show that the cerium atoms are additionally coordinated by THF donor molecules. The Ce1–O$_{siloxide}$ distances of 2.066(2) to 2.1534(10) (see Table 2 for a complete list of interatomic distances) compare well to other ceric siloxides like Ce{OSi(OtBu)$_3$}$_4$ (2.089(2)–2.157(2) Å ^{26} and

2.084–2.160 Å ^{21d}) or Ce{OSiPh$_3$}$_4$(dme) (2.098(1)–2.133(1) Å).^{29} Also, as seen for the silylamides **4**, the Ce1–O$_{hq}$ distances of 2.1244(10) to 2.2325(16), as well as the C–C and C–O distances underline the formation of an aromatic hq linker.^{20g,24} ^{1}H NMR spectroscopic measurements also validate the formation of Ce^{IV} species, showing a sharp singlet for the *tert*-butyl groups and a doublet plus a septet for the iso-propyl groups depending on the siloxy co-ligand.

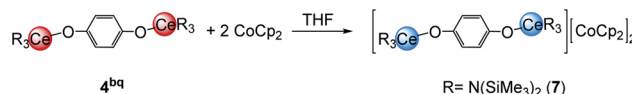## Electrochemical investigation of complexes 4^{xhq}, 5^{xhq} and 6^{xhq}

Cyclic voltammetry (CV) measurements of complexes **4^{xhq}**, **5^{xhq}** and **6^{xhq}** have been conducted at ambient temperature in 0.2 mM solutions in THF and 0.1 M [nPr$_4$N][B(C$_6$H$_3$(CF$_3$)$_2$-3,5)$_4$] as a support electrolyte, and referenced *vs.* Fc/Fc$^+$. Due to the low stability of compounds **4^{Me4hq}**, **4^{tBu2hq}** and **4^{nhq}** in polar solvents CV measurements of these complexes were not feasible. Most of the CV measurements revealed successive quasireversible (**4**) or irreversible (**5/6**) Ce^{IV} → Ce^{III} reduction steps, but badly resolved (for E_{pc} values see Tables 1 and 2). The detection of two closely adjacent redox events (E_{pc} values) in some cyclic voltammograms may correspond to a successive reduction/oxidation of the cerium centres. Similar features were also described for the hq-bridged Ce(IV)–BINOLate complex **II**.^{24b} All complexes under study display redox processes with a large separation of E_{pc} and E_{pa} ($\Delta E \approx 0.6$ V for **4**; 1.5 V for **5** and 1.0 V for **6**).

Representatively, the cyclic voltammograms of the DDQ-functionalized Ce^{III}/Ce^{IV} redox couples are depicted in Fig. 3 (top graphic). The silylamide complexes **4** gave reduction potentials similar to those reported for halogenido-functionalised ceric complexes Ce[N(SiMe$_3$)$_2$]$_3$X ($E_{1/2}$ = −0.56 (X = F), −0.30 (X = Cl), −0.31 (X = Br)) with $E_{1/2}$ values of −0.46 V for **4^{Cl4hq}** and −0.36 V for **4^{ddhq}**.^{30} Only **4^{hq}** with $E_{1/2}$ = −0.76 V gave a significantly higher stabilisation by 0.20 V. The extra-large separation of the reduction/oxidation events

observed for the siloxide complexes **5** and **6** had been noticed previously for rare-earth-metal siloxides and was assigned to oxidation-state-dependent ligand reorganisation processes.[31]

Stabilisation of the tetravalent oxidation state of cerium in complexes **4**, **5**, and **6** increases in the order of $N(SiMe_3)_2$ < $OSi(OtBu_3)_3$ < OSi^iPr_3 as co-ligand (Fig. 3/bottom) which is in accordance with previous findings.[20f,26,30,31c] Surprisingly, the stabilisation of Ce^{IV} proceeds in reverse order of the oxidation potential of the 1,4-quinones under study giving the most stable complexes for the hydroquinolato-bridged complexes and the least stable compounds for its 2,3-dichloro-5,6-dicyano-hydroquinolato congeners. A reason for this trend could be the increasingly electron-deficient nature of the aromatic hydroquinolato linkers due to the large $-I$ effect of the substituents. The Ce^{IV} oxidation state can be stabilised by increasing donor strength of the ligands.[32] Based on this, it seems surprising that isolable complexes **4^{Me4hq}** and **4^{nhq}**, derived from weakly oxidizing quinones, are not stable in solution at ambient temperature. This might be a result of another reaction pathway preferred after formation of the hydroquinolato-bridged Ce^{IV} complexes (like following up redox processes and the formation of Ce^{III} semiquinolates, *cf.* vide infra).

Fig. 3 Top: Stacked cyclic voltammograms of complexes **4^{ddq}** (red), **5^{ddq}** (blue), **6^{ddq}** (black) in THF ($v = 50$ mV s^{-1}; c(analyte) = 2 mM; $c([nPr_4N][B(C_6H_3(CF_3)_2-3,5)_4])$ = 0.1 M). Bottom: comparison of the second reduction potentials of complexes **4** (red), **5** (black), and **6** (blue) in THF *vs.* Fc/Fc$^+$. Squares: complexes with bridging 1,4-hydroquinolates; cycles: complexes with bridging tetrachloro-1,4-hydroquinolates; triangles: complexes with bridging 2,3-dichloro-5,6-dicyano-1,4-hydroquinolates.

Scheme 3 Reduction of **4^{bq}** with two equivalents of CoCp$_2$.

Reduction of silylamide 4^{hq} with cobaltocene

Having investigated the electrochemical reduction of compounds **4**, **5** and **6**, the chemical reduction with cobaltocene (CoCp$_2$) (-1.31 V *vs.* Fc/Fc$^+$ in DME)[2a] was attempted, as it has already been shown to engage in such reductions.[31a,33] Accordingly, treatment of a solution of **4^{hq}** in THF with two equivalents of CoCp$_2$ resulted in a colour change from dark brown to pale yellow (Scheme 3). The ^{1}H NMR spectrum of the reaction mixture showed complete consumption of CoCp$_2$ and only broadened signals indicating the formation of a paramagnetic Ce^{III} species. Crystallisation from a concentrated THF-d_8 solution at -40 °C gave light brown crystals of the composition [[Ce{N(SiMe$_3$)$_2$}$_3$]$_2$(μ_2-O$_2$C$_6$H$_4$)][CoCp$_2$]$_2$ (**7**) (Fig. 4).

Complex **7** shows the same structural motif as **4^{hq}** but is flanked by two cobaltocenium cations. Compared to **4^{hq}**, the Ce–N and Ce1–O1 distances are elongated by approximately 0.19 Å as expected for the larger Ce^{III} ion size.[34] On the contrary, the bonding parameters within the bridging hydroquinolato linker did not change, further corroborating a cerium-borne redox chemistry. Reacting **4^{hq}** with one equivalent of CoCp$_2$ did not lead to a mixed $Ce^{III/IV}$ complex but gave a mixture of 50% of **7** and 50% of unreacted starting material.

The reactions of CoCp$_2$ with other complexes **4** to **6** in THF-d_8 showed immediate decolourisation of the solution while the ^{1}H NMR spectra of the reaction mixtures displayed only paramagnetic signals (for an example, see Fig. S33 in the ESI†). However, the isolation of additional reduced species similar to **7** was not successful.

Fig. 4 Crystal structure of [(Ce{N(SiMe$_3$)$_2$}$_3$)$_2$(μ_2-O$_2$C$_6$H$_4$)][CoCp$_2$]$_2$ (**7**). Ellipsoids are shown at the 50% probability level. Hydrogen atoms, disordering of the cyclopentadienyl ligands and lattice THF are omitted for clarity. Selected interatomic distances [Å]: Ce1–N1 2.420(2), Ce1–N2 2.402(2), Ce1–N3 2.418(2), Ce1–O1 2.202(2), C1–O1 1.344(4), C1–C2 1.391(4), C1–C3 1.392(4), C2–C3′ 1.392(4).
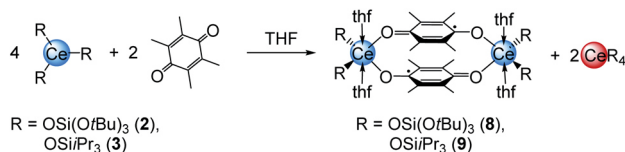
Scheme 4 Formation of cerous semiquinolates **8** and **9** from the reaction of **2** or **3** with Me$_4$BQ.

Cerium semiquinolates

A closer look at the reactions of cerous siloxides **2** and **3** with the weakly oxidising quinone Me$_4$BQ (which did not produce any tetravalent cerium species; *vide supra*) revealed another important detail of the cerium–quinone redox system. Treatment of **2** or **3** with 0.5 equivalents of Me$_4$BQ led to a colour change from colourless to light blue. Upon recrystallisation from THF dark blue crystals suitable for X-ray diffraction could be grown and were identified as cerous semiquinolates [CeL$_2$(thf)$_2$]$_2$(μ$_2$-O$_2$C$_6$Me$_4$)$_2$ (with L = OSi(OtBu)$_3$ (**8**) or OSi^{i}Pr$_3$ (**9**)) (Scheme 4).

Examining the reaction mixtures by ^{1}H NMR spectroscopy in THF-d_8 showed, besides paramagnetic signals for **8** and **9**, a sharp singlet at 1.39 ppm (for **8**) or a doublet plus a septet at 1.13 and 1.04 ppm (for **9**), indicating the formation of homoleptic Ce[OSi(OtBu)$_3$]$_4$ or [Ce(OSi^{i}Pr$_3$)$_4$], respectively, as a result of the one-electron reduction of Me$_4$bq followed by ligand redistribution. Crucially, such a reaction pathway seems unfeasible for complexes **4**, since putative homoleptic "Ce[N(SiMe$_3$)$_2$]$_4$" is unknown.[20a] Emergent kinetic constraints in the case of ceric complexes **4** were also suggested by the redox behaviour of [Ce{N(SiHMe$_2$)$_2$}$_3$]$_2$ derived from a less bulky silylamido ligand. Accordingly, the cerous bis(dimethylsilyl)amide complex was treated with one equivalent of both BQ and Me$_4$BQ in THF-d_8 and C$_6$D$_6$ (see Fig. S38–S41, ESI†). The ^{1}H NMR spectra of these reactions suggest the formation of a tetravalent species of the composition "[Ce{N(SiHMe$_2$)$_2$}$_3$]$_2$(μ$_2$-O$_2$C$_6$R$_4$)". However, the ceric products appear to be unstable in solution at ambient temperature. In C$_6$D$_6$, the formation of Ce[N(SiHMe$_2$)$_2$]$_4$ was observed in the reaction with BQ as well as other insoluble products. In THF-d_8, the resulting product seemed more stable but after 24 h in solution also traces of decomposition products were found. The Me$_4$BQ reaction in C$_6$D$_6$ also indicated successful oxidation, however, after 24 h the ^{1}H NMR spectrum revealed signals for trivalent decomposition products as well as traces of Ce[N(SiHMe$_2$)$_2$]$_4$. In THF-d_8, the putatively formed hydroquinolate complex was even less stable, showing signals for trivalent by-products directly after addition of Me$_4$BQ. In addition, the stability of **4^{bq}** was investigated in THF-d_8 showing small amounts of decomposition products like Ce[N(SiMe$_3$)$_2$]$_3$ after 24 h (Fig. S42, ESI†).

Regrettably, purification of complexes **8** and **9** was impeded by co-crystallisation with the ceric by-products CeL$_4$. The crystal structures of **8** and **9** revealed two six-coordinate cerium atoms surrounded by two siloxy ligands, two THF donor molecules and two bridging tetramethyl semiquinolato moieties (Fig. 5). The Ce1–O$_{silanolato}$ distances are elongated by about 0.1 Å compared to the respective tetravalent compounds **5** and **6** and in
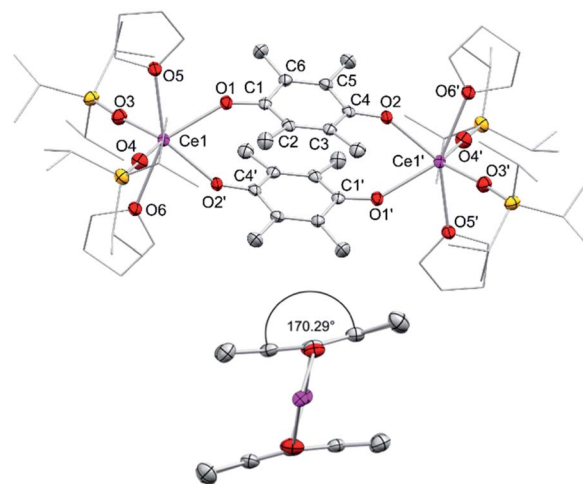
Fig. 5 Top: Crystal structure of [Ce{OSi^{i}Pr$_3$}$_2$(thf)$_2$]$_2$(μ$_2$-O$_2$C$_6$Me$_4$)$_2$ (**9**). Ellipsoids are shown at the 50% probability level. Hydrogen atoms are omitted for clarity. Selected interatomic distances [Å]: Ce1–O1 2.446(7), Ce1–O2 2.422(7), Ce1–O3 2.219(9), Ce1–O4 2.237(6), Ce1–O5 2.648(7), Ce1–O6 2.644 (7), C1–O5 1.306(5), C4–O6 1.307(5), C1–C2 1.458(6), C2–C3 1.401(6), C3–C4 1.449(8), C4–C5 1.463(6), C5–C6 1.388(6), C1–C6 1.463(8). Bottom: side view of [(Ce{OSi^{i}Pr$_3$}$_2$(thf)$_2$)$_2$(μ$_2$-O$_2$C$_6$Me$_4$)$_2$] (**9**).

accordance with other Ce^{III} siloxides like **3**, Ce{OSi(OtBu)$_3$}$_3$(thf)$_3$ (2.243(2)–2.249(2) Å), [Ce{OSi(OtBu)$_3$}$_3$]$_2$ (Ce–O$_{term}$ 2.186(3)–2.202(3) Å),[26] Ce{OSiPh$_3$}$_3$(thf)$_3$ (Ce–O$_{avg}$ 2.222(4) Å)[35] and [Ce{OSiPh$_3$}$_3$]$_2$ (Ce–O$_{term}$ 2.141(7)–2.184(6) Å).[27] As expected for semiquinolato ligands the six-membered rings display two shortened C–C and four elongated C–C bonds. Additionally, the six-membered rings are slightly bent in comparison to the flat aromatic hydroquinolato linkers in complexes **4**, **5** and **6** resulting in an angle of 170.34° for **8** and 170.29° for **9**, respectively (see Fig. 5, bottom). Notwithstanding, the bridging radicals engage in significant π-stacking as indicated by close semiquinolato–semiquinolato distances of 3.112 Å for **8** and 3.156 Å for **9**. Overall, complexes **8** and **9** display the same arrangement of the semiquinolato radical bridges as observed in complexes [LnCl$_2$(THF)$_3$(μ-Me$_4$sq)$_2$]$_2$ (Ln = Y, Gd) (Ct⋯Ct 3.097 Å; Ct = centroid of benzene rings).[13]

To investigate the electronic behaviour of the bridging semiquinolates, X-band EPR spectra of compounds **8** and **9** were recorded from a crystal powder sample at 123 K (Fig. 6). For both complexes cw-EPR spectra are composed of two distinct sets of resonances, one that results from the transition within the Kramers doublet corresponding to $m_j = \pm 1/2$ and one at half-field, $H \approx 160$ mT. The transition for the $m_j = \pm 1/2$ state associates with an axial g tensor with principal components $g_{II} = 2.094$ and g$_\perp$ = 2.032 for **8** and $g_{II} = 2.088$ and g$_\perp$ = 2.032 for **9**, respectively. The transition locating at half-field gives rise to a very broad dispersion line with $g_{II} \approx 4.359$ for **8** and $g_{II} \approx 4.351$ for **9**, respectively. Notably, an identical line pattern derives from a frozen 2-Me-THF solution at 77 K; *cf.* Fig. S67, ESI,† for pertinent details. The cw-EPR spectra corroborate the presence of Ce^{3+}, and agree with early work on mononuclear complexes of Ce^{3+}.[36] This indicates a radical–
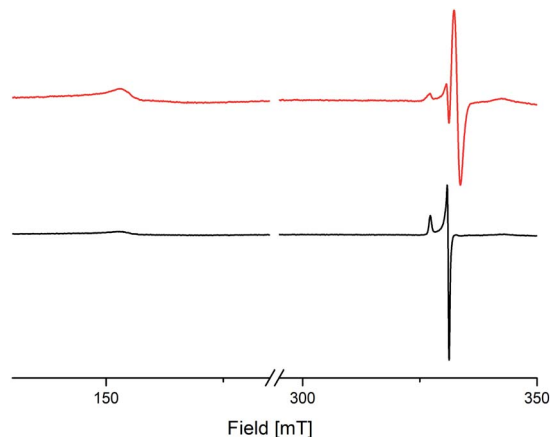
Fig. 6 X-Band cw-EPR spectra of crystalline $[Ce\{OSi(OtBu)_3\}_2(thf)_2(\mu_2\text{-}O_2C_6Me_4)]_2$ (**8**) (black trace) and $[Ce(OSi^iPr_3)_2(thf)_2)(\mu_2\text{-}O_2C_6Me_4)]_2$ (**9**) (red trace).

radical π-bonding, as it was recently shown for yttrium and gadolinium semiquinolates $[LnCl_2(thf)_2]_2(\mu_2\text{-}O_2C_6Me_4)_2$ (Ln = Y or Gd).[13] Additionally and also similar to the yttrium semiquinolate, complex **9** shows a signal with a g value of 1.999, which most likely results from a non-coupled radical impurity.

Note that the reactions of cerium siloxides **2** and **3** with 1,4-naphthoquinone resulted also in the formation of homoleptic ceric siloxides as well as paramagnetic by-products (*cf.* Fig. S36, ESI†) indicating a similar reactivity as observed for Me₄BQ. Unfortunately, any putative semiquinolate complexes could not be isolated.

Conclusions

Cerium(III) silylamides and siloxides are suitable reagents for assessing the oxidising power/reducibility of differently substituted 1,4-quinones in non-aqueous solutions. The cerium–quinone redox matching is revealed by the ease of formation of Ce^IV hydroquinolates $[CeL_3]_2(\mu_2\text{-}O_2C_6R_4)$, in the case of the parent 1,4-benzoquinone (BQ) or when R represents electron-withdrawing groups (Cl, CN). Depending on their reduction potential, alkyl-substituted BQs engage in redox equilibria, with the Ce^IV hydroquinolate species being preferentially stable in the solid state, but also afford semiquinolates *via* redox ligand redistribution. The structurally characterized siloxide semiquinolate complexes $[(CeL_2(thf)_2)(\mu_2\text{-}O_2C_6Me_4)]_2$ (L = OSi(OtBu)₃, OSi^iPr₃) exhibit a molecular arrangement, recently detected for $[LnCl_2(THF)_3(\mu\text{-}Me_4sq)_2]_2$ (Ln = Y, Gd).[13] The stabilisation of the tetravalent oxidation state in hydroquinolato-bridged complexes $[Ce^{IV}L_3]_2(\mu_2\text{-}O_2C_6R_4)$ was examined by electrochemical measurements, as well as NMR and UV/Vis spectroscopies. In accordance with previous findings,[16,18–20] the stability of the ceric complexes increases in the order of N(SiMe₃)₂ < OSi(OtBu₃)₃ < OSi^iPr₃ as supporting ligand, but surprisingly drops in reverse order of the oxidation potential of the 1,4-quinones, being the least stable for the 2,3-dichloro-5,6-dicyano-hydroquinolato congener. The preferred formation of hydroquinolato-bridged silylamides [Ce

$\{N(SiMe_3)_2\}_3]_2(\mu_2\text{-}O_2C_6R_4)$ seems kinetically favoured. Finally, the electrochemical reduction of the hydroquinolato-bridged ceric complexes $[Ce^{IV}L_3]_2(\mu_2\text{-}O_2C_6R_4)$ can be mimicked by chemical reduction with cobaltocene, as shown for the isolation and structural characterisation of cerous $[(Ce\{N(SiMe_3)_2\}_3)_2(\mu_2\text{-}O_2C_6H_4)][CoCp_2]_2$. The cerium–quinone redox matching and tuning might be used as a role-model in tetravalent praseodymium and terbium chemistry.

Conflicts of interest

There are no conflicts to declare.

Acknowledgements

Notes and references

1 N. El-Najjar, H. Gali-Muhtasib, R. A. Ketola, P. Vuorela, A. Urtti and H. Vuorela, *Phytochem. Rev.*, 2011, **10**, 353–370.

2 (*a*) N. G. Connelly and W. E. Geiger, *Chem. Rev.*, 1996, **96**, 877–910; (*b*) D. H. Evans, *Chem. Rev.*, 2008, **108**, 2113–2144.

3 (*a*) A. Osyczka, C. C. Moser, F. Daldal and P. L. Dutton, *Nature*, 2004, **427**, 607–612; (*b*) J. F. Allen and W. Martin, *Nature*, 2007, **445**, 610–612; (*c*) J. L. Nevarez, A. Turmo, J. Hu and R. P. Hausinger, *ChemCatChem*, 2020, **12**, 4242–4254.

4 J. M. Campos-Martin, G. Blanco-Brieva and J. L. G. Fierro, *Angew. Chem., Int. Ed.*, 2006, **45**, 6962–6984.

5 M. T. Huynh, C. W. Anson, A. C. Cavell, S. S. Stahl and S. Hammes-Schiffer, *J. Am. Chem. Soc.*, 2016, **138**, 15903–15910.

6 C. Frontana, Á. Vázquez-Mayagoitia, J. Garza, R. Vargas and I. González, *J. Phys. Chem. A*, 2006, **110**, 9411–9419.

7 (*a*) D. Walker and J. D. Hiebert, *Chem. Rev.*, 1967, **67**, 153–195; (*b*) S. B. Bharate, *Synlett*, 2006, **3**, 496–497.

8 (*a*) K. Ohkubo, A. Fujimoto and S. Fukuzumi, *J. Am. Chem. Soc.*, 2013, **135**, 5368–5371; (*b*) N. A. Romero and D. A. Nicewicz, *Chem. Rev.*, 2016, **116**, 10075–10166.

9 (*a*) M. Oh, G. B. Carpenter and D. A. Sweigart, *Acc. Chem. Res.*, 2004, **37**, 1–11; (*b*) S. U. Son, S. B. Kim, J. A. Reingold, G. B. Carpenter and D. A. Sweigart, *J. Am. Chem. Soc.*, 2005, **127**, 12238–12239.

10 (*a*) S. Kitagawa, *Coord. Chem. Rev.*, 2002, **224**, 11–34; (*b*) S. Masaoka, G. Akiyama, S. Horike, S. Kitagawa, T. Ida and K. Endo, *J. Am. Chem. Soc.*, 2003, **125**, 1152–1153.

11 (*a*) B. F. Abrahams, J. Coleiro, B. F. Hoskins and R. Robson, *Chem. Commun.*, 1996, 603–604; (*b*) S. Halis, A. K. Inge, N. Dehning, T. Weyrich, H. Reinsch and N. Stock, *Inorg. Chem.*, 2016, **55**, 7425–7431.

12 J. O. Moilanen, A. Mansikkamäki, M. Lahtinen, F.-S. Guo, E. Kalenius, R. A. Layfield and L. F. Chibotaru, *Dalton Trans.*, 2017, **46**, 13582–13589.

13 T. Han, J. B. Petersen, Z.-H. Li, Y.-Q. Zhai, A. Kostopoulos, F. Ortu, E. J. L. McInnes, R. E. P. Winpenny and Y.-Z. Zheng, *Inorg. Chem.*, 2020, **59**, 7371–7375.

14 (*a*) J. Yuasa, T. Suenobu and S. Fukuzumi, *J. Am. Chem. Soc.*, 2003, **125**, 12090–12091; (*b*) J. Yuasa and S. Fukuzumi, *J. Am. Chem. Soc.*, 2007, **129**, 12912–12913.

15 For examples of other structurally characterised semiquinone complexes, see: (*a*) J.-M. Lü, S. V. Rosokha, I. S. Neretin and J. K. Kochi, *J. Am. Chem. Soc.*, 2006, **128**, 16708–16719; (*b*) H. Nakamori, T. Matsumoto, T. Yatabe, K.-S. Yoon, H. Nakai and S. Ogo, *Chem. Commun.*, 2014, **50**, 13059–13061; (*c*) I.-R. Jeon, B. Negru, R. P. Van Duyne and T. D. Harris, *J. Am. Chem. Soc.*, 2015, **137**, 15699–15702.

16 Â. Domingos, I. Lopes, J. C. Waerenborgh, N. Marques, G. Y. Lin, X. W. Zhang, J. Takats, R. McDonald, A. C. Hillier, A. Sella, M. R. J. Elsegood and V. W. Day, *Inorg. Chem.*, 2007, **46**, 9415–9424.

17 (*a*) F. Sroor and F. Edelmann, in *Cerium: Molecular Structure, Technological Applications and Health Effects*, Nova Science Publishers, Hauppage, N.Y., 2012, pp. 73–106; (*b*) N. A. Piro, J. R. Robinson, P. J. Walsh and E. J. Schelter, *Coord. Chem. Rev.*, 2014, **260**, 21–36; (*c*) Y.-M. So and W.-H. Leung, *Coord. Chem. Rev.*, 2017, **340**, 172–197; (*d*) R. Anwander, M. Dolg and F. T. Edelmann, *Chem. Soc. Rev.*, 2017, **46**, 6697–6709.

18 (*a*) V. Nair, J. Mathew and J. Prabhakaran, *Chem. Soc. Rev.*, 1997, **26**, 127–132; (*b*) V. Nair and A. Deepthi, *Tetrahedron*, 2009, **65**, 10745–10755.

19 Y. Qiao and E. J. Schelter, *Acc. Chem. Res.*, 2018, **51**, 2926–2936.

20 (*a*) O. Eisenstein, P. B. Hitchcock, A. G. Hulkes, M. F. Lappert and L. Maron, *Chem. Commun.*, 2001, 1560–1561; (*b*) M. D. Walter, R. Fandos and R. A. Andersen, *New J. Chem.*, 2006, **30**, 1065; (*c*) P. Dröse, A. R. Crozier, S. Lashkari, J. Gottfriedsen, S. Blaurock, C. G. Hrib, C. Maichle-Mössmer, C. Schädle, R. Anwander and F. T. Edelmann, *J. Am. Chem. Soc.*, 2010, **132**, 14046–14047; (*d*) A. R. Crozier, A. M. Bienfait, C. Maichle-Mössmer, K. W. Törnroos and R. Anwander, *Chem. Commun.*, 2013, **49**, 87–89; (*e*) D. Schneider, T. Spallek, C. Maichle-Mössmer, K. W. Törnroos and R. Anwander, *Chem. Commun.*, 2014, **50**, 14763–14766; (*f*) U. J. Williams, J. R. Robinson, A. J. Lewis, P. J. Carroll, P. J. Walsh and E. J. Schelter, *Inorg. Chem.*, 2014, **53**, 27–29; (*g*) D. Schneider, N. Harmgarth, F. T. Edelmann and R. Anwander, *Chem.– Eur. J.*, 2017, **23**, 12243–12252; (*h*) L. A. Solola, P. J. Carroll and E. J. Schelter, *J. Organomet. Chem.*, 2018, **857**, 5–9; (*i*) N. T. Rice, J. Su, T. P. Gompa, D. R. Russo, J. Telser, L. Palatinus, J. Bacsa, P. Yang, E. R. Batista and H. S. La Pierre, *Inorg. Chem.*, 2019, **58**, 5289–5304.

21 (*a*) M. Gregson, E. Lu, J. McMaster, W. Lewis, A. J. Blake and S. T. Liddle, *Angew. Chem., Int. Ed.*, 2013, **52**, 13016–13019; (*b*) V. Lorenz, B. M. Schmiege, C. G. Hrib, J. W. Ziller, A. Edelmann, S. Blaurock, W. J. Evans and F. T. Edelmann, *J. Am. Chem. Soc.*, 2011, **133**, 1257–1259; (*c*) J. A. Bogart, C. A. Lippincott, P. J. Carroll, C. H. Booth and E. J. Schelter, *Chem.– Eur. J.*, 2015, **21**, 17850–17859; (*d*)

R. P. Kelly, L. Maron, R. Scopelliti and M. Mazzanti, *Angew. Chem., Int. Ed.*, 2017, **56**, 15663–15666.

22 (*a*) P. B. Hitchcock, M. F. Lappert and A. V. Protchenko, *Chem. Commun.*, 2006, 3546–3548; (*b*) M. P. Coles, P. B. Hitchcock, A. V. Khvostov, M. F. Lappert, Z. Li and A. V. Protchenko, *Dalton Trans.*, 2010, **39**, 6780–6788.

23 (*a*) I. J. Casely, S. T. Liddle, A. J. Blake, C. Wilson and P. L. Arnold, *Chem. Commun.*, 2007, 5037–5039; (*b*) P. L. Arnold, I. J. Casely, S. Zlatogorsky and C. Wilson, *Helv. Chim. Acta*, 2009, **92**, 2291–2303; (*c*) D. Werner, G. B. Deacon, P. C. Junk and R. Anwander, *Dalton Trans.*, 2017, **46**, 6265–6277; (*d*) U. Bayer, L. Bock, C. Maichle-Mössmer and R. Anwander, *Eur. J. Inorg. Chem.*, 2020, 101–106.

24 (*a*) A. Sen, H. A. Stecher and A. L. Rheingold, *Inorg. Chem.*, 1992, **31**, 473–479; (*b*) J. R. Robinson, C. H. Booth, P. J. Carroll, P. J. Walsh and E. J. Schelter, *Chem.– Eur. J.*, 2013, **19**, 5996–6004; (*c*) D. Werner, G. B. Deacon, P. C. Junk and R. Anwander, *Chem.– Eur. J.*, 2014, **20**, 4426–4438.

25 The reactivity of a series of methyl-substituted 1,4-benzoquinones toward π-allylnickel bromide was probed (yielding ring-allylation in 2- or 6-position), revealing enhanced reactivity of the more easily reduced BQs: L. S. Hegedus and E. L. Waterman, *J. Am. Chem. Soc.*, 1974, **96**, 6789–6791.

26 J. Friedrich, C. Maichle-Mössmer and R. Anwander, *Chem. Commun.*, 2017, **53**, 12044–12047.

27 W. J. Evans, R. E. Golden and J. W. Ziller, *Inorg. Chem.*, 1991, **30**, 4963–4968.

28 H. A. Stecher, A. Sen and A. L. Rheingold, *Inorg. Chem.*, 1989, **28**, 3280–3282.

29 P. S. Gradeff, K. Yunlu, A. Gleizes and J. Galy, *Polyhedron*, 1989, **8**, 1001–1005.

30 U. J. Williams, P. J. Carroll and E. J. Schelter, *Inorg. Chem.*, 2014, **53**, 6338–6345.

31 (*a*) J. Friedrich, Y. Qiao, C. Maichle-Mössmer, E. J. Schelter and R. Anwander, *Dalton Trans.*, 2018, **47**, 10113–10123; (*b*) C. T. Palumbo, I. Zivkovic, R. Scopelliti and M. Mazzanti, *J. Am. Chem. Soc.*, 2019, **141**, 9827–9831; (*c*) A. R. Willauer, C. T. Palumbo, R. Scopelliti, I. Zivkovic, I. Douair, L. Maron and M. Mazzanti, *Angew. Chem., Int. Ed.*, 2020, **59**, 3549–3553.

32 P. G. Eller and R. A. Penneman, *J. Less-Common Met.*, 1987, **127**, 19–33.

33 (*a*) U. Kilimann, R. Herbst-Irmer, D. Stalke and F. T. Edelmann, *Angew. Chem., Int. Ed. Engl.*, 1994, **33**, 1618–1621; (*b*) H. Fang, B. E. Cole, Y. Qiao, J. A. Bogart, T. Cheisson, B. C. Manor, P. J. Carroll and E. J. Schelter, *Angew. Chem., Int. Ed.*, 2017, **56**, 13450–13454.

34 R. D. Shannon, *Acta Crystallogr.*, 1976, **32**, 751–767.

35 P. S. Gradeff, K. Yunlu, T. J. Deming, J. M. Olofson, R. J. Doedens and W. J. Evans, *Inorg. Chem.*, 1990, **29**, 420–424.

36 K. D. Karlin and S. J. Lippard, *Progress in Inorganic Chemistry*, John Wiley and Sons, New York, 1959.

The cerium–quinone redox couples put under scrutiny

Uwe Bayer, Daniel Werner, Andreas Berkefeld, Cäcilia Maichle-Mössmer and Reiner Anwander*

Table of Contents

Experimental Section

General Procedures. All manipulations were performed under an inert atmosphere (Ar) using a glovebox (MBraun 200B; <0.1 ppm O_2, <0.1 ppm H_2O), or according to standard Schlenk techniques in oven-dried glassware. The solvents were purified with Grubbs-type columns (MBraun SPS, solvent purification system) and stored in a glovebox. Anhydrous cerium(III) chloride (99.9%) was purchased from Sigma Aldrich and activated by Soxhlet extraction with THF giving $CeCl_3(thf)_{1.04}$. Potassium bis(trimethylsilyl)amide was purchased from Sigma Aldrich and purified by high-vacuum sublimation before use. 1,4-Benzoquinone was purchased from Sigma Aldrich and purified by sublimation. Tris-*tert*-butoxy silonol, tri*iso*propyl silanol, tetramethyl-1,4-benzoquinone, 1,4-naphthoquinone and 9,10-anthraquinone were purchased from Sigma Aldrich, tetrachloro-1,4-benzoquinone and 2,5-di-*tert*-butyl-1,4-benzoquinone from TCI Deutschland GmbH and used as received. C_6D_6, toluene-d_8 and THF-d_8 were purchased from Sigma Aldrich, degassed, dried by being stirred over NaK alloy for 24 h, filtered and stored in a glovebox. Ce[N(SiMe$_3$)$_2$]$_3$ (**1**), [Ce{OSi(O*t*Bu)$_3$}$_3$]$_2$ (**2**), [Ce{N(SiMe$_3$)$_2$}$_3$]$_2$(μ_2-O$_2$C$_6$H$_4$) (**4^{hq}**), Ce$_4$(Me$_2$pz)$_{12}$·¼ *n*-hexane and [*n*Pr$_4$N][B(C$_6$H$_3$(CF$_3$)$_2$-3,5)$_4$] were synthesised according to literature procedures.[1–5] NMR spectra were recorded on a Bruker AVII+400 (^{1}H: 400.13 MHz, ^{13}C: 100.61 MHz), a Bruker AVIIIHD-300 (^{1}H: 300.13 MHz, ^{13}C: 75.47 MHz, ^{29}Si: 59.63 MHz) or a Bruker AVII+ 500 (^{1}H: 500.13 MHz, ^{13}C: 125.76 MHz, ^{29}Si: 99.36 MHz) at 26 °C. NMR shifts are referenced to a solvent resonance and reported in parts per million (ppm) relative to tetramethylsilane.[6] Analysis of the NMR spectra was performed with ACD/NMR Processor Academic Edition (Product Version: 12.01). Multiplicities of signals are given as s (singlet), bs (broad singlet), d (doublet) and dd (doublet of doublets), sept (septet). Coupling constants (J) are given in Hz. Infrared spectra were recorded on a ThermoFisher Scientific NICOLET 6700 FTIR ($\tilde{v}$ = 4000 – 400 cm^{-1}) spectrometer using a DRIFT chamber with dry KBr/sample mixtures and KBr windows. Recorded spectra were converted using Kubelka-Munk correction. Elemental analysis (C/H/N) was performed on an Elementar vario MICRO cube. UV/Vis measurements were carried out in toluene on a PG Instruments T60 UV-Vis spectrophotometer. The effective magnetic moments were determined according to Evans' Method on a Bruker AVII+400 at 25 °C (^{1}H: 400.13 MHz), using C_6D_6 as a solvent and hexamethyldisiloxane as reference.[7] Cyclic voltammetry measurements were conducted in a glovebox under argon atmosphere using a Nordic Electrochemistry ECi-200 workstation in IR-compensation mode. Data recording was done using Nordic Electrochemistry EC4 DAQ (version 4.1.90.1) and processed with Nordic Electrochemistry EC-4 VIEW (version 1.2.36.1). The experiments were performed in a 4 mL glass vial with a CHI 104 glassy carbon disc working electrode, a Ag/AgCl quasi reference electrode and a platinum wire counter electrode using c(analyte) = 2 mM and c([*n*Pr$_4$N][B(C$_6$H$_3$(CF$_3$)$_2$-3,5)$_4$]) = 0.1 M in THF. The reported potentials are given in [V] and are referenced vs. the Fc/Fc$^+$ couple which was added as an internal standard at the end of each measurement. EPR spectra were measured on a continuous wave X-Band Bruker ESP 300E using 4 mm O.D. Wilmad quartz (CFQ) EPR tubes. Spectra were referenced to the Bruker strong pitched standard g$_{iso}$= 2.0088.

Synthesis of [Ce(OSi*i*Pr₃)₃]₂ (3). *i*Pr₃SiOH (1.15 g, 6.60 mmol) was dissolved in *n*-hexane (6 mL) and added to a solution of Ce[N(SiMe₃)₂]₃ (1.37 g, 2.20 mmol) in *n*-hexane (6 mL). The solution was stirred for 16 h, then concentrated in vacuo and stored at −40 °C. After 16 h the supernatant solution was removed, and the resulting colourless crystals were dried in vacuum giving **3**. Yield: 1.01 g (70%). ^{1}H NMR (C₆D₆, 400.13 MHz, 26 °C): δ = 9.09 (bs, 12 H, terminal C*H*(CH₃)₂), 6.46 (bs, 72 H, terminal CH(C*H₃*)₂), −17.23 (bs, 36 H, μ_2-C*H*(CH₃)₂), −28.82 (bs, 6H, μ_2-CH(C*H₃*)₂) ppm; ^{1}H NMR (THF-d₈, 400.13 MHz, 26 °C): δ =2.98 (bs, 9 H, C*H*(CH₃)₂), 1.58 (bs, 54 H, CH(C*H₃*)₂) ppm; IR (DRIFT): $\tilde{v}$ = 2935 (vs), 2861 (vs), 2745 (vw), 2715 (vw), 1462 (s), 1478 (w), 1292 (vw), 1240 (w), 1157 (vw), 1051 (w), 988 (m), 911 (s), 882 (s), 841 (m), 666(s), 580 (vw), 514 (w), 464 (m), 401 (m) cm^{-1}; elemental analysis (%) calcd. for C₅₄H₁₂₆Ce₂O₆Si₆ (1320.34): C 49.12, H 9.62; found: C 48.99, H 9.56.

Synthesis of [Ce{N(SiMe₃)₂}₃]₂(μ_2-O₂C₆H₄) (4^{hq}). 1,4-Benzoquinone (0.0191 g, 0.177 mmol) was dissolved in toluene (1 mL) and added to a solution of Ce[N(SiMe₃)₂]₃ (0.220 g, 0.354 mmol) in toluene (3 mL). After being stirred for 2 h the solution was concentrated in vacuo (1-2 mL) and stored at −40 °C. After 2 days the supernatant solution was removed. The brown solid was dried in vacuum giving microcrystalline **4^{hq}**. Yield: 0.159 g (69%). ^{1}H NMR (C₆D₆, 400.13 MHz): δ = 7.28 (s, 4 H, μ_2-O₂C₆H₄), 0.42 (s, 108 H, SiMe₃) ppm; UV/Vis: 485 nm (14964 ± 3215 L mol^{-1} cm^{-1}); elemental analysis (%) calcd. for C₄₂H₁₁₂Ce₂N₆O₂Si₁₂ (1350.64): C 37.34, H 8.36, N 6.22; found: C 37.01, H 8.37, N 6.14; μ_{eff} = 0.67 BM (1.06·10^{-5} mol L^{-1}, Δ = 2.4 Hz). The ^{1}H NMR spectrum was in accordance with literature.[3]

Synthesis of [Ce{N(SiMe₃)₂}₃]₂(μ_2-O₂C₆Cl₄) (4^{Cl4hq}). Tetrachloro-1,4-benzoquinone (0.0601 g, 0.242 mmol) was dissolved in toluene (3 mL) and added to a solution of Ce[N(SiMe₃)₂]₃ (0.300 g, 0.483 mmol) in *n*-hexane (2 mL). After being stirred for 16 h the solution was stored at −40 °C and after 4 d the supernatant solution was removed. The remaining purple/brown solid was dried in vacuo producing **4^{Cl4hq}** as a dark purple solid. Yield: 0.279 g (77%). ^{1}H NMR (C₆D₆, 400.13 MHz): δ = 0.45 (s, 108 H, SiMe₃) ppm; ^{29}Si DEPT45 NMR (C₆D₆, 59.63 MHz, 26 °C): δ = −8.1 ppm; due to low solubility, a ^{13}C NMR spectrum could not be obtained; IR (DRIFT): $\tilde{v}$ = 2952 (m), 2899 (w), 1414 (vs), 1376 (w), 1251 (s), 1211 (w), 1174 (w), 934 (s), 896 (vs), 873 (s), 846 (vs), 771 (s), 731 (w), 718 (w), 675 (m), 656 (s), 607 (s), 502 (m) cm^{-1}; UV/Vis: 319 nm (ε = 11602 ± 1308 L mol^{-1} cm^{-1}), 518 nm (ε = 13180 ± 1580 L mol^{-1} cm^{-1}); elemental analysis (%) calcd for C₄₂H₁₀₈Ce₂Cl₄N₆O₂Si₁₂ (1488.42): C 33.89, H 7.31, N 5.65; found: C 34.09, H 7.17, N 5.59; μ_{eff} = 0.68 BM (1.08·10^{-5} mol L^{-1}, Δ = 2.5 Hz).

Synthesis of [Ce{N(SiMe₃)₂}₃]₂(μ_2-O₂C₆Cl₂(CN)₂) (4^{ddhq}). 2,3-Dichloro-5,6-dicyano-1,4-benzoquinone (0.0273 g, 0.121 mmol) was dissolved in toluene (3 mL) and added to a solution of Ce[N(SiMe₃)₂]₃ (0.150 g, 0.242 mmol) in *n*-hexane (2 mL). After being stirred for 16 h the solution was stored at −40 °C and after 1 d the supernatant solution was removed. The remaining purple/brown solid was dried in vacuo producing **4^{ddhq}** as a dark red solid. Yield: 0.145 g (81%). ^{1}H NMR (C₆D₆, 400.13 MHz): δ = 0.45 (s, 108 H, SiMe₃) ppm; ^{13}C{^{1}H} NMR (C₆D₆, 125.61 MHz,

26 °C): δ = 161.1 (2 C, C_{arom}–O), 132.2 (2 C, C_{arom}–Cl), 115.7 (2 C, C_{arom}–CN), 103.6 (2 C, C_{arom}–CN), 5.6 (36 C, $SiMe_3$) ppm; ^{29}Si DEPT45 NMR (C_6D_6, 59.63 MHz, 26 °C): δ = −7.3 ppm; IR (DRIFT): $\tilde{v}$ = 2953 (w), 2900 (vw), 2227 (vw), 1406 (s), 1251 (s), 1093 (vw), 1003 (m), 888 (vs), 844 (vs), 771 (m), 654 (m), 607 (s), 547 (w) cm^{-1}; UV/Vis: 384 nm (ε = 4510 ± 117 L mol^{-1} cm^{-1}), 511 nm (ε = 5060 ± 202 L mol^{-1} cm^{-1}); elemental analysis (%) calcd for $C_{44}H_{108}Ce_2Cl_2N_8O_2Si_{12}$ (1469.55): C 35.96, H 7.41, N 7.63; found: C 36.17, H 7.07, N 7.54; μ_{eff} = 0.59 BM (6.60·10^{-6} mol L^{-1}, Δ = 1.0 Hz).

Synthesis of [Ce{N(SiMe₃)₂}₃]₂(μ₂-O₂C₆Me₄) (4^Me4hq). Tetramethyl-1,4-benzoquinone (0.0264 g, 0.161 mmol) was dissolved in *n*-hexane (2 mL) and added to a solution of Ce[N(SiMe₃)₂]₃ (0.200 g, 0.322 mmol) in *n*-hexane (2 mL). After being stirred for 5 min the solution was evaporated to dryness giving **4^Me4hq** as a dark brown solid. Yield: 0.203 g (90%). ^1H NMR (toluene-d_8, 500.13 MHz, 273 K): δ =2.67 (s, 12 H, μ₂-O₂C₆Me₄), 0.43 (s, 108 H, SiMe₃) ppm; ^{29}Si INEPTND NMR (C_6D_6, 59.63 MHz, 26 °C): δ = −8.8 ppm; due to low solubility and fast decomposition, a ^{13}C NMR spectrum could not be obtained; IR (DRIFT): $\tilde{v}$ =2952 (m), 2899 (w), 1450 (w), 1399 (w), 1385 (w), 1370 (vw), 1255 (vs), 1079 (s), 984 (w), 918 (s), 903 (s), 863 (vs), 837 (s), 773 (s), 732 (w), 675 (s), 658 (vs), 609 (s), 416 (m) cm^{-1}; UV/Vis: 362 nm (ε = 1249 ± 44 L mol^{-1} cm^{-1}), 411 nm (ε = 1610 ± 49 L mol^{-1} cm^{-1}), 681 nm (ε = 556 ± 24 L mol^{-1} cm^{-1}); elemental analysis (%) calcd. for $C_{46}H_{120}Ce_2N_6O_2Si_{12}$ (1406.76): C 39.28, H 8.60, N 5.97; found: C 39.29, H 8.81, N 5.92; μ_{eff} = 0.89 BM (1.07·10^{-5} mol L^{-1}, Δ = 5.1 Hz).

Synthesis of [Ce{N(SiMe₃)₂}₃]₂(μ₂-O₂C₆tBu₂H₂) (4^tBu2hq). Ce[N(SiMe₃)₂]₃ (0.300 g, 0.483 mmol) was dissolved in *n*-hexane (3 mL) and added to a suspension of 2,5-di-*tert*-butyl-1,4-benzoquinone (0.0532 g, 0.241 mmol) in *n*-hexane (2 mL). After being stirred for 2 h the solution was stored at −40 °C and after 1 d the supernatant solution was removed. The remaining brown solid was dried in vacuo giving **4^tBu2hq** as the crude product. Yield: 0.308 g (88%). ^1H NMR (C_6D_6, 400.13 MHz): δ = 0.45 (s, 108 H, SiMe₃) ppm; due to the redox equilibrium between the species formed in the solid state and solution and the resulting low concentration of **4^tBu2hq** in solution, no other peaks corresponding to the product could be observed; IR (DRIFT): $\tilde{v}$ = 3019 (w), 2965 (m), 2952 (m), 2900 (w), 1484 (w), 1392 (w), 1355 (w), 1251 (vs), 1198 (w), 1186 (m), 1118 (w), 893 (s), 860 (vs), 837 (vs), 831 (vs), 773 (s), 673 (m), 658 (s), 634 (w), 611 (m), 463 (m), 448 (w) cm^{-1}; elemental analysis (%) calcd. for $C_{50}H_{128}Ce_2N_6O_2Si_{12}$ (1467.87): C 41.05, H 8.82, N 5.74; found: C 41.05, H 8.87, N 5.74.

Synthesis of [Ce{N(SiMe₃)₂}₃]₂(μ₂-O₂C₁₀H₆) (4^nhq). 1,4-Naphthoquinone (0.0127 g, 0.0805 mmol) was dissolved in *n*-hexane (1 mL) and added to a solution of Ce[N(SiMe₃)₂]₃ (0.100 g, 0.161 mmol) in *n*-hexane (1 mL). After being stirred for 30 min the solution was stored at −40 °C. After 10 d small reddish brown crystals were handpicked and analysed by X-ray crystallography. The supernatant solution was removed and the remaining solid was dried in vacuo giving **4^nhq** as a brown solid. Yield: 0.080 g (71%). ^1H NMR (C_6D_6, 400.13 MHz): δ = 8.57 (dd, 2 H, $^3J_{HH}$ = 6.46 Hz, $^4J_{HH}$ = 3.30 Hz, H-8, H-9), 7.52 (dd, 2 H, $^3J_{HH}$ = 6.34 Hz, $^4J_{HH}$ = 3.30 Hz, H-7, H-10),

7.24 (s, 2 H, H-2, H-3), 0.44 (s, 108 H, SiMe$_3$) ppm; ^{13}C{^{1}H} NMR (C$_6$D$_6$, 100.61 MHz, 26 °C): δ = 165.8 (2 C, C$_{arom}$–O), 125.8 (2 C, C$_{arom}$), 125.0 (2 C, C$_{arom}$), 120.7 (2 C, C$_{arom}$), 114.3 (2 C, C$_{arom}$), 5.6 (36 C, SiMe$_3$) ppm; ^{29}Si DEPT45 NMR (C$_6$D$_6$, 59.63 MHz, 26 °C): δ = −8.1 ppm; IR (DRIFT): $\tilde{\nu}$ = 3068 (w), 3041 (w), 2951 (m), 2897 (w), 1574 (w), 1449 (m), 1377 (s), 1266 (vs), 1250 (vs), 1227 (m), 1215 (m), 1151 (w), 1077 (m), 1053 (w), 1014 (w), 905 (vs), 881 (s), 841 (vs), 826 (s), 776 (vs), 758 (s), 735 (m), 674 (m), 657 (s), 611 (s), 501 (w) cm^{-1}; UV/Vis: 339 nm (ε = 8386 ± 1267 L mol^{-1} cm^{-1}), 425 nm (ε = 3956 ± 576 L mol^{-1} cm^{-1}), 474 nm (ε = 4405 ± 646 L mol^{-1} cm^{-1}), 678 nm (ε = 2391 ± 362 L mol^{-1} cm^{-1}); elemental analysis (%) calcd. for C$_{46}$H$_{114}$Ce$_2$N$_6$O$_2$Si$_{12}$ (1400.71): C 39.44, H 8.20, N 6.00; found: C 40.54, H 7.74, N 5.93; due to rapid decomposition no better microanalytical data could be obtained; μ_{eff} = 1.19 BM (1.08·10^{-5} mol L^{-1}, Δ = 9.76 Hz).

Synthesis of [Ce{OSi(O*t*Bu)$_3$}$_3$(thf)]$_2$(μ_2-O$_2$C$_6$H$_4$) (5^{hq}). 1,4-Benzoquinone (0.0116 g, 0.107 mmol) was dissolved in THF (2 mL) and added to a solution of [Ce{OSi(O*t*Bu)$_3$}$_3$]$_2$ (0.200 g, 0.215 mmol) in THF (2 mL). After being stirred for 1 h the solution was evaporated to dryness, re-dissolved in *n*-hexane (1.5 mL) and stored at −40 °C. After 8 d the supernatant solution was removed and the remaining solid was dried in vacuo giving **5^{hq}** as a dark purple solid. Yield: 0.107 g (46%). ^{1}H NMR (THF-*d$_8$*, 400.13 MHz, 26 °C): δ = 6.54 (s, 4 H, μ_2-O$_2$C$_6$H$_4$), 3.62 (m, 8 H, β-THF), 1.78 (m, 8 H, α-THF), 1.36 (s, 162 H, O*t*Bu) ppm; ^{13}C{^{1}H} NMR (THF-*d$_8$*, 100.61 MHz, 26 °C): δ = 166.9 (2 C, C$_{arom}$–O), 119.3 (4 C, C$_{arom}$–H), 72.5 (18 C, *C*(CH$_3$)$_3$), 32.6 (54 C, C(*C*H$_3$)$_3$) ppm; ^{29}Si NMR (from ^{1}H-^{29}Si HSQC, THF-*d$_8$*, 99.36 MHz, 26 °C): δ = −103.2 ppm; IR (DRIFT): $\tilde{\nu}$ = 2972 (vs), 2930 (m), 2873 (w), 1490 (s), 1473 (w), 1387 (m), 1364 (s), 1242 (vs), 1193 (vs), 1056 (vs), 1026 (vs), 986 (s), 924 (vs), 913 (vs), 836 (s), 801 (w), 698 (s), 626 (w), 539 (m), 513 (m), 499 (m), 492 (m), 455 (m), 429 (m) cm^{-1}; UV/Vis: 622 nm (ε = 4831 ± 224 L mol^{-1} cm^{-1}), 369 nm (ε = 3832 ± 286 L mol^{-1} cm^{-1}); elemental analysis (%) calcd. for C$_{86}$H$_{182}$Ce$_2$O$_{28}$Si$_6$ (2113.12): C 48.88, H 8.86; found: C 48.82, H 8.42; μ_{eff} = 0.82 BM (6.90·10^{-7} mol L^{-1}, Δ = 2.66 Hz).

Synthesis of [Ce{OSi(O*t*Bu)$_3$}$_3$(thf)]$_2$(μ_2-O$_2$C$_6$Cl$_4$) (5^{Cl4hq}). Tetrachloro-1,4-benzoquinone (0.0264 g, 0.107 mmol) was dissolved in THF (2 mL) and added to a solution of [Ce{OSi(O*t*Bu)$_3$}$_3$]$_2$ (0.200 g, 0.215 mmol) in THF (4 mL). After being stirred for 1 h the solution was stored at −40 °C. After 3 d the supernatant solution was removed and the remaining solid was dried in vacuo giving **5^{Cl4hq}** as a red solid. Yield: 0.0960 g (42%). ^{1}H NMR (THF-*d$_8$*, 400.13 MHz, 26 °C): δ = 3.62 (m, 8 H, β-THF), 1.78 (m, 8 H, α-THF), 1.36 (s, 162 H, O*t*Bu) ppm; ^{13}C{^{1}H} NMR (THF-*d$_8$*, 100.61 MHz, 26 °C): δ = 154.8 (2 C, C$_{arom}$–O), 121.3 (4 C, C$_{arom}$–Cl), 72.8 (18 C, *C*(CH$_3$)$_3$), 32.4 (54 C, C(*C*H$_3$)$_3$) ppm; ^{29}Si DEPT45 NMR (THF-*d$_8$*, 59.63 MHz, 26 °C): δ = −104.6 ppm; IR (DRIFT): $\tilde{\nu}$ = 2974 (vs), 2930 (m), 2902 (w), 2872 (w), 1471 (w), 1421 (s), 1388 (s), 1364 (s), 1242 (s), 1192 (vs), 1062 (s), 1053 (s), 1027 (s), 996 (m), 911 (s), 886 (s), 829 (m), 716 (w), 701 (m), 644 (vw), 513 (w), 495 (m), 442 (m), 431 (w) cm^{-1}; UV/Vis: 493 nm (ε = 3787 ± 433 L mol^{-1} cm^{-1}); elemental analysis (%) calcd. for C$_{86}$H$_{178}$Ce$_2$Cl$_4$O$_{28}$Si$_6$ (2250.88): C 45.89, H 7.97; found: C: 45.55, H 7.92; μ_{eff} = 0.54 BM (6.46·10^{-7} mol L^{-1}, Δ = 0.8 Hz).

Synthesis of [Ce{OSi(O*t*Bu)₃}₃(thf)]₂(*μ₂*-O₂C₆Cl₂(CN)₂) (5^{ddhq}). 2,3-Dichloro-5,6-dicyano-1,4-benzoquinone (0.0183 g, 0.0807 mmol) was dissolved in THF (2 mL) and added to a solution of [Ce{OSi(O*t*Bu)₃}₃]₂ (0.150 g, 0.161 mmol) in THF (4 mL). After being stirred for 1 h the solution was stored at −40 °C. After 3 d the supernatant solution was removed and the remaining solid was dried in vacuo giving **5^{ddhq}** as a red solid. Yield: 0.0833 g (46%). ^{1}H NMR (THF-d_8, 400.13 MHz, 26 °C): δ = 3.62 (m, 8 H, β-THF), 1.78 (m, 8 H, α-THF), 1.36 (s, 162 H, O*t*Bu) ppm; ^{13}C{^{1}H} NMR (THF-d_8, 100.61 MHz, 26 °C): δ = 160.8 (2 C, C$_{arom}$–O), 132.3 (2 C, C$_{arom}$–Cl), 115.1 (2 C, C$_{arom}$–CN), 99.3 (2 C, *C*$_{arom}$–CN), 73.0 (18 C, *C*(CH₃)₃), 32.5 (54 C, C(*C*H₃)₃) ppm; ^{29}Si DEPT45 NMR (THF-d_8, 59.63 MHz, 26 °C): δ = −105.3 ppm; IR (DRIFT): ṽ = 2974 (s), 2930 (w), 2872 (vw), 2227 (vw), 1472 (vw), 1457 (vw), 1417 (s), 1389 (m), 1364 (s), 1240 (m), 1213 (w), 1191 (s), 1058 (vs), 1026 (s), 976 (m), 887 (vs), 829 (w), 802 (vw), 701 (w), 630 (vw), 545 (w), 510 (vw), 492 (vw), 473 (vw), 444 (vw), 431 (vw) cm^{-1}; UV/Vis: 384 nm (ε = 2143 ± 375 L mol^{-1} cm^{-1}), 450 nm (ε = 2718 ± 326 L mol^{-1} cm^{-1}); elemental analysis (%) calcd. for C₈₈H₁₇₈Ce₂Cl₂N₂O₂₈Si₆ (2232.02): C 47.35, H 8.04, N 1.26; found: C: 47.40, H 7.74, N 1.40; μ_{eff} = 0.60 BM (4.59 10^{-6} mol L^{-1}, Δ = 0.72 Hz).

Synthesis of [Ce(OSi*i*Pr₃)₃(thf)]₂(*μ₂*-O₂C₆H₄) (6^{hq}). 1,4-Benzoquinone (0.0123 g, 0.114 mmol) was dissolved in THF (2 mL) and added to a solution of [Ce(OSi*i*Pr₃)₃]₂ (0.150 g, 0.114 mmol) in THF (2 mL). After being stirred for 1 h the solution was concentrated (to ~1 mL), *n*-hexane (1 mL) was added and stored at −40 °C. After 1 d the supernatant solution was removed and the remaining solid was dried in vacuo giving **6^{hq}** as a dark purple solid. The remaining crystals were dried in vacuo giving **6^{hq}** as a purple solid. Yield: 0.128 g (71%). ^{1}H NMR (THF-d_8, 400.13 MHz): δ = 6.01 (s, 4 H, *μ₂*-O₂C₆H₄), 1.14 (d, 108 H, CH(C*H₃*)₂, 1.10 (sept, 18 H, C*H*(CH₃) ppm; ^{29}Si DEPT45 NMR (THF-d_8, 59.63 MHz, 26 °C): δ = 7.0 ppm; due to low solubility, a ^{13}C NMR spectrum could not be obtained; IR (DRIFT): ṽ = 2939 (vs), 2863 (vs), 1482 (s), 1381 (vw), 1228 (s), 1070 (w), 1035 (m), 990 (m), 936 (m), 882 (s), 862 (s), 829 (s), 678 (s), 594 (vw), 519 (vw), 402 (m) cm^{-1}; UV/Vis: 526 nm (ε = 1402 ± 88 L mol^{-1} cm^{-1}); elemental analysis (%) calcd. for C₆₈H₁₄₆Ce₂O₁₀Si₆ (1572.65): C 51.93, H 9.36; found: C 52.19, H 9.03; μ_{eff} = 0.68 BM (3.29 10^{-6} mol L^{-1}, Δ = 0.76 Hz).

Synthesis of [Ce(OSi*i*Pr₃)₃(thf)]₂(*μ₂*-O₂C₆Cl₄) (6^{Cl4hq}). Tetrachloro-1,4-benzoquinone (0.0279 g, 0.114 mmol) was dissolved in THF (2 mL) and added to a solution of [Ce(OSi*i*Pr₃)₃]₂ (0.150 g, 0.114 mmol) in THF (4 mL). After being stirred for 1 h the solution was stored at −40 °C. After 3 d the supernatant solution was removed and the remaining solid was dried in vacuo giving **6^{Cl4hq}** as a red solid. Yield: 0.110 g (56%). ^{1}H NMR (THF-d_8, 400.13 MHz): δ = 1.12 (d, $^3J_{HH}$ = 6.04 Hz, 108 H, CH(C*H₃*)₂, 1.05 (sept, $^3J_{HH}$ = 5.87 Hz,18 H, C*H*(CH₃) ppm; ^{13}C{^{1}H} NMR (THF-d_8, 100.61 MHz, 26 °C): δ = 153.5 (2 C, C$_{arom}$–O), 120.3 (4 C, C$_{arom}$–Cl), 18.0 (36 C, *C*H(CH₃)₂), 14.0 (18 C, CH(*C*H₃)₂) ppm; ^{29}Si DEPT45 NMR (THF-d_8, 59.63 MHz, 26 °C): δ = 9.6 ppm; IR (DRIFT): ṽ = 2940 (vs), 2863 (vs), 1462 (m), 1421 (s), 1379 (w), 1241 (vw), 1205 (vw), 1176 (vw), 1030 (w), 992 (w), 956 (w), 905 (vs), 883 (vs), 833 (vs), 714 (m), 676 (s), 493 (m), 451

(vw), 413 (w) cm^{-1}; UV/Vis: 511 nm (ε = 3203 ± 287 L mol^{-1} cm^{-1}); elemental analysis (%) calcd. for C$_{68}$H$_{142}$Ce$_2$Cl$_4$O$_{10}$Si$_6$ (1720.42): C 47.75, H 8.37; found: C: 47.71, H 8.34; μ_{eff} = 0.50 BM (6.14 10^{-6} mol L^{-1}, Δ = 0.51 Hz).

Synthesis of [Ce(OSi*i*Pr$_3$)$_3$(thf)]$_2$(μ_2-O$_2$C$_6$Cl$_2$(CN)$_2$) (6^{ddhq}). 2,3-Dichloro-5,6-dicyano-1,4-benzoquinone (0.0258 g, 0.114 mmol) was dissolved in THF (2 mL) and added to a solution of [Ce(OSi*i*Pr$_3$)$_3$]$_2$ (0.150 g, 0.114 mmol) in THF (4 mL). After being stirred for 1 h the solution was stored at −40 °C. After 3 d the supernatant solution was removed and the remaining solid was dried in vacuo giving 6^{ddhq} as a red solid. Yield: 0.107 g (55%). ^{1}H NMR (THF-d_8, 400.13 MHz): δ = 1.12 (d, $^3J_{HH}$ = 6.94 Hz, 108 H, CH(CH_3)$_2$, 1.05 (sept, $^3J_{HH}$ = 6.62 Hz,18 H, CH(CH$_3$) ppm; ^{13}C{^{1}H} NMR (THF-d_8, 100.61 MHz, 26 °C): δ = 161.1 (2 C, C$_{arom}$−O), 131.2 (2 C, C$_{arom}$−Cl), 117.7 (2 C, C$_{arom}$−CN), 99.1 (2 C, C_{arom}−CN), 19.3 (12 C, CH(CH$_3$)$_2$), 19.1 (24 C, CH(CH$_3$)$_2$), 15.5 (6 C, CH(CH$_3$)$_2$), 15.1 (12 C, CH(CH$_3$)$_2$) ppm; ^{29}Si INEPTND NMR (THF-d_8, 59.63 MHz, 26 °C): δ = 10.7 ppm; IR (DRIFT): $\tilde{v}$ = 2941 (vs), 2863 (vs), 2222 (w), 1461 (m), 1415 (s), 1228 (w), 1085 (vw), 1025 (w), 990 (w), 939 (m), 883 (s), 828 (vs), 679 (s), 599 (vw), 540 (w), 414 (vw) cm^{-1}; UV/Vis: 470 nm (ε = 4298 ± 125 L mol^{-1} cm^{-1}), 381 nm (ε = 10725 ± 214 L mol^{-1} cm^{-1}); elemental analysis (%) calcd. for C$_{70}$H$_{142}$Ce$_2$Cl$_2$N$_2$O$_{10}$Si$_6$ (1691.55): C 49.70, H 8.46, N 1.66; found: C: 49.83, H 8.31, N 1.86; μ_{eff} = 0.66 BM (6.93 10^{-6} mol L^{-1}, Δ = 1.52 Hz)).

Synthesis of [Ce(OSi*i*Pr$_3$)$_3$(thf)]$_2$(μ_2-O$_2$C$_6$*t*Bu$_2$H$_2$)] (6^{tBu2hq}). [Ce(OSi*i*Pr$_3$)$_3$]$_2$ (0.100 g, 0.0760 mmol) was dissolved in THF (3 mL) and added to a suspension of 2,5-di-*tert*-butyl-1,4-benzoquinone (0.0167 g, 0.0760 mmol) in THF (2 mL). After being stirred for 2 h the solution was stored at −40 °C and after 2 d the supernatant solution was removed. The remaining dark purple solid was dried in vacuo giving 6^{tBu2hq} as the crude product. Yield: 0.0543 g (42%). ^{1}H NMR (THF-d_8, 500.13 MHz, 233 K): δ = 6.51 (s, 2 H, μ_2-O$_2$C$_6$*t*Bu$_2$H$_2$), 1.25 (s, 18 H, μ_2-O$_2$C$_6$*tBu$_2$H$_2$), 1.11 (d, 108 H, CH(CH_3)$_2$, 1.02 (sept, 18 H, CH(CH$_3$) ppm; IR (DRIFT): $\tilde{v}$ = 2958 (m), 2940 (m), 2887 (m), 2862 (m), 1487 (w), 1462 (w), 1392 (vw), 1366 (w), 1240 (vw), 1208 (w), 1119 (vw), 1034 (vw), 991 (w), 947 (m), 916 (w), 876 (s), 842(vs), 677 (m), 592 (vw), 570 (vw), 519 (vw), 446 (w), 412 (w) cm^{-1}; elemental analysis (%) calcd. for C$_{76}$H$_{162}$Ce$_2$O$_{10}$Si$_6$ (1684.86): C 54.18, H 9.69, found: C 53.93, H 9.42.

Reduction of [Ce{N(SiMe$_3$)$_2$}$_3$]$_2$(μ_2-O$_2$C$_6$H$_4$) (4^{hq}) with cobaltocene (CoCp$_2$)

Compound 4^{hq} (32.2 mg, 23.9 µmol) was dissolved in THF (2 mL) and CoCp$_2$ (9.0 mg, 47.8 µmol) in THF (2 mL) was added. The reaction mixture turned from dark brown to pale yellow. After being stirred for 10 min the solution was concentrated and then stored at −40 °C. After 3 d the supernatant was removed and [(Ce{N(SiMe$_3$)$_2$}$_3$)$_2$(μ_2-O$_2$C$_6$H$_4$)][CoCp$_2$]$_2$·THF (7) was obtained as light brown crystals. Yield: 0.028 g (67%). ^{1}H NMR (THF-d_8, 400.13 MHz): δ = 3.88 (s, 4 H, hq), 3.79 (s, 20 H, Cp), −1.11 (s, 108 H, SiMe$_3$) ppm; IR (DRIFT): $\tilde{v}$ = 3111 (vw), 2943 (m), 2889 (w), 1486 (s), 1416 (w), 1293 (vw), 1241 (s), 1066 (vw), 998 (vs), 867 (s), 830 (vs), 768 (m), 666 (m), 593 (w), 458 (vw) cm^{-1}; elemental analysis (%) calcd. for C$_{66}$H$_{140}$Ce$_2$Co$_2$N$_6$O$_3$Si$_{12}$ (1801.06): C 44.02, H 7.84, N 4.67; found: C: 45.08, H 7.53, N

4.32. EA calculated for one more molecule of THF in the crystal lattice: C 44.98, H 7.77, N 4.50; μ_{eff} = 3.26 B.M. (5.40 10^{-6} mol L^{-1}, Δ = 32.19 Hz).

Synthesis of [Ce{OSi(O*t*Bu)$_3$}$_2$(thf)$_2$(μ_2-O$_2$C$_6$Me$_4$)]$_2$ (8). Tetramethyl-1,4-benzoquinone (0.018 g, 0.11 mmol) was dissolved in THF (2 mL) and added to a solution of [Ce{OSi(O*t*Bu)$_3$}$_3$]$_2$ (0.200 g, 0.22 mmol) in THF (2 mL). After being stirred for 2 h the solution was stored at −40 °C. After 7 d dark turquoise crystals were handpicked and analysed by X-ray diffraction, indicating the formation of **8**. The remaining crystals were evaporated to dryness giving **8** together with [Ce{OSi(O*t*Bu)$_3$}$_4$], [Ce{OSi(O*t*Bu)$_3$}$_3$] and Me$_4$bq.

Synthesis of [Ce(OSi*i*Pr$_3$)$_2$(thf)$_2$)(μ_2-O$_2$C$_6$Me$_4$)]$_2$ (9). Tetramethyl-1,4-benzoquinone (0.018 g, 0.11 mmol) was dissolved in THF (2 mL) and added to a solution of [Ce(OSi*i*Pr$_3$)$_3$]$_2$ (0.200 g, 0.22 mmol) in THF (2 mL). After being stirred for 2 h the solution was stored at −40 °C. After 7 d dark turquoise crystals were handpicked and analysed by X-ray diffraction, indicating the formation of **9**. The remaining crystals were evaporated to dryness giving **9** together with [Ce(OSi*i*Pr$_3$)$_4$], [Ce(OSi*i*Pr$_3$)$_3$]$_2$ and Me$_4$bq.

Preliminary tests with pyrazolate complexes:

Reaction between Ce$_4$(Me$_2$pz)$_{12}$ and 9,10-anthraquinone, and isolation of [Ce$_3$(bpad)(pasq)(Me$_2$pz)$_6$(thf)] (bpad = 1,4-bis(3,5-dimethylpyrazol-1-yl)anthra-1,4-diolato; pasq = 1-(3,5-dimethylpyrazol-1-yl)anthra-1,4-semiqinolato). Ce$_4$(Me$_2$pz)$_{12}$·1/4 *n*-hexane·(0.0477 g, 0.028 mmol, trace toluene impurities not included) and 9,10-anthraquinone (0.0109 g, 0.0532 mmol) were combined in THF-*d$_8$* (NMR-scale experiment, using a J. Young-valved NMR tube). No colour change was observed and the emergence of a broad peak in the NMR occurred. ^{1}H NMR (THF-*d$_8$*, 400.13 MHz, integration for anthracene is low due to poor solubility in THF-*d$_8$*, solvent peaks not included): δ = 11.92 (br s, 3 H, Me$_2$pz-CH), 8.27 (br s, μ_2-O$_2$C$_{14}$H$_8$), 6.38 (br s, 18 H, Me$_2$pz-CH$_3$) ppm. The solution was transferred to a vial, and the solvent removed under vacuum. Toluene was added and the light-yellow solution was filtered. Upon storage at −35 °C, crystals of **[Ce$_3$(bpad)(pasq)(Me$_2$pz)$_6$(thf)]** formed. The supernatant solution was removed (see below), and the crystals were dried in vacuo, giving an off-white powder of **[Ce$_3$(bpad)(pasq)(Me$_2$pz)$_6$(thf)]** (0.0527 g, 84%); IR (Nujol) $\tilde{v}$ = 1665 (m), 1597 (w), 1583 (w), 1552 (m), 1518 (vs), 1317 (vs), 1276 (s), 1243 (s), 1196 (w), 1176 (w), 1157 (w), 1066 (s), 1035 (vs), 1007 (s), 957 (vw), 930 (s), 890 (m), 855 (vw), 770 (s), 746 (m), 721 (vs), 695 (w), 683 (vw) cm^{-1}; Elemental analysis calcd. (%) for C$_{77}$H$_{87}$Ce$_3$N$_{18}$O$_5$ (1763.43): C 52.40, H 4.97, N 14.28; Found: C 51.96, H 3.98, N 14.09. The light-yellow supernatant solution was concentrated and THF and hexane was added. The colour of the solution turned to an emerald green. Upon storage at −35 °C crystals of semiquinolate **[Ce(Me$_2$pz)$_2$(thf)$_2$(asq)]$_2$** formed amongst colourless crystals.

Isolation of [Ce(*t*Bu$_2$pz)$_3$]$_2$(μ_2-O$_2$C$_6$Me$_4$). Ce[N(SiMe$_3$)$_2$]$_3$ (0.081 g, 0.13 mmol), and *t*Bu$_2$pzH (0.074 g, 0.41 mmol, in slight excess), were stirred in THF (5 mL) for 10 minutes. The solution was evaporated to dryness leaving a pale-yellow powder. Cyclohexane (4 mL) was added and

the powder dissolved giving a pale-yellow solution. Tetramethyl-1,4-benzoquinone (0.0070 g, 0.043 mmol) was added with stirring and the solution turned immediately dark green. The solution was reduced under vacuum and toluene was added (1 mL). The mixture slowly crystallised over two days. The supernatant solution was decanted, and the crystals were submerged in *n*-paratone crystallography oil. Examination under the microscope indicated a mixture of species, colourless needle crystals, large colourless block crystals and dark red/brown crystals. The dark red/brown block crystals were analysed as **[Ce(*t*Bu$_2$pz)$_3$]$_2$(μ_2-O$_2$C$_6$Me$_4$)**.

Stability tests of putative [(Ce{N(SiHMe$_2$)$_2$}$_3$)$_2$(μ_2-O$_2$C$_6$R$_4$)] (R = H, Me) species:

Reaction between [Ce{N(SiHMe$_2$)$_2$}$_3$]$_2$ and 1,4-benzoquinone. Cerous [Ce{N(SiHMe$_2$)$_2$}$_3$]$_2$ (20 mg, 0.019 mmol) and 1,4-benzoquinone (2.0 mg, 0.019 mmol) were combined in each C$_6$D$_6$ and THF-*d$_8$* (NMR-scale experiments, using a J. Young-valved NMR tube). An immediate colour change from pale yellow to dark brown was observed in both solvents. ^{1}H NMR spectra were recorded directly after addition of 1,4-benzoquinone and after 24 h to investigate on the stability of the formed product.

Reaction between [Ce{N(SiHMe$_2$)$_2$}$_3$]$_2$ and tetramethyl-1,4-benzoquinone. Cerous [Ce{N(SiHMe$_2$)$_2$}$_3$]$_2$ (20 mg, 0.019 mmol) and tetramethyl-1,4-benzoquinone (3.1 mg, 0.019 mmol) were combined in each C$_6$D$_6$ and THF-*d$_8$* (NMR-scale experiments, using a J. Young-valved NMR tube). An immediate colour change from pale yellow to dark brownish green was observed in both solvents. ^{1}H NMR spectra were recorded directly after addition of tetramethyl-1,4-benzoquinone and after 24 h to investigate on the stability of the formed product.

NMR Spectra (solvent signals are marked with *)
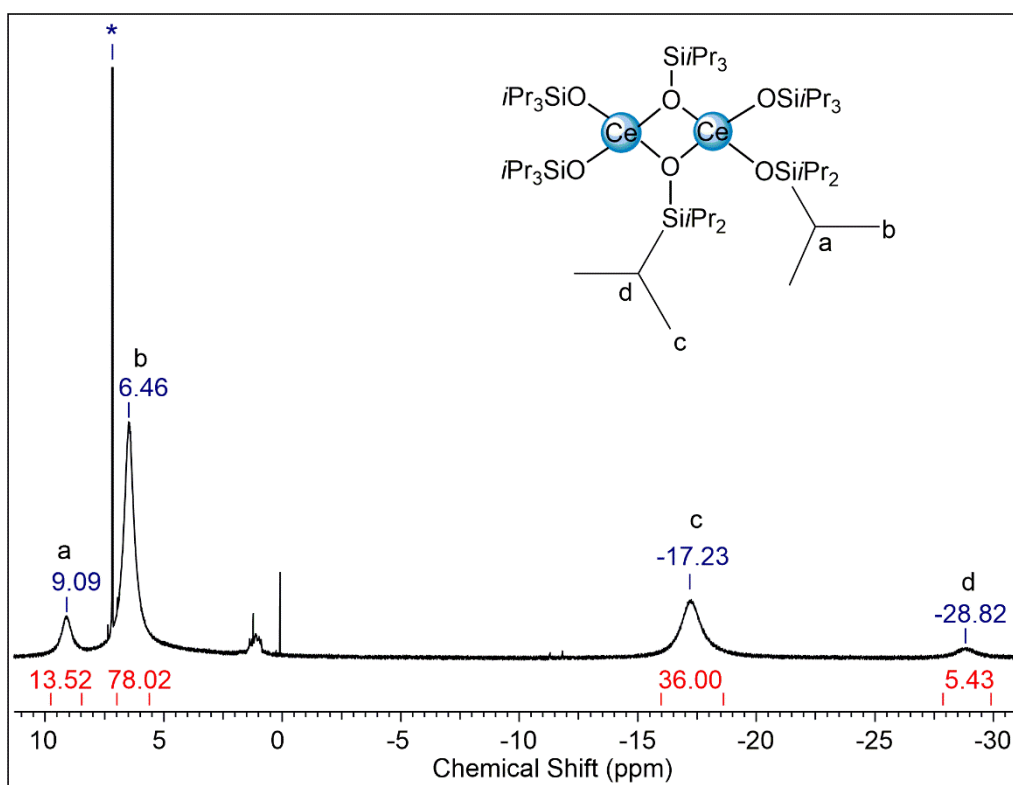
Figure S1. ^{1}H NMR spectrum (400.13 MHz, C$_6$D$_6$, 26 °C) of [Ce(OSiiPr$_3$)$_3$]$_2$ (**3**).
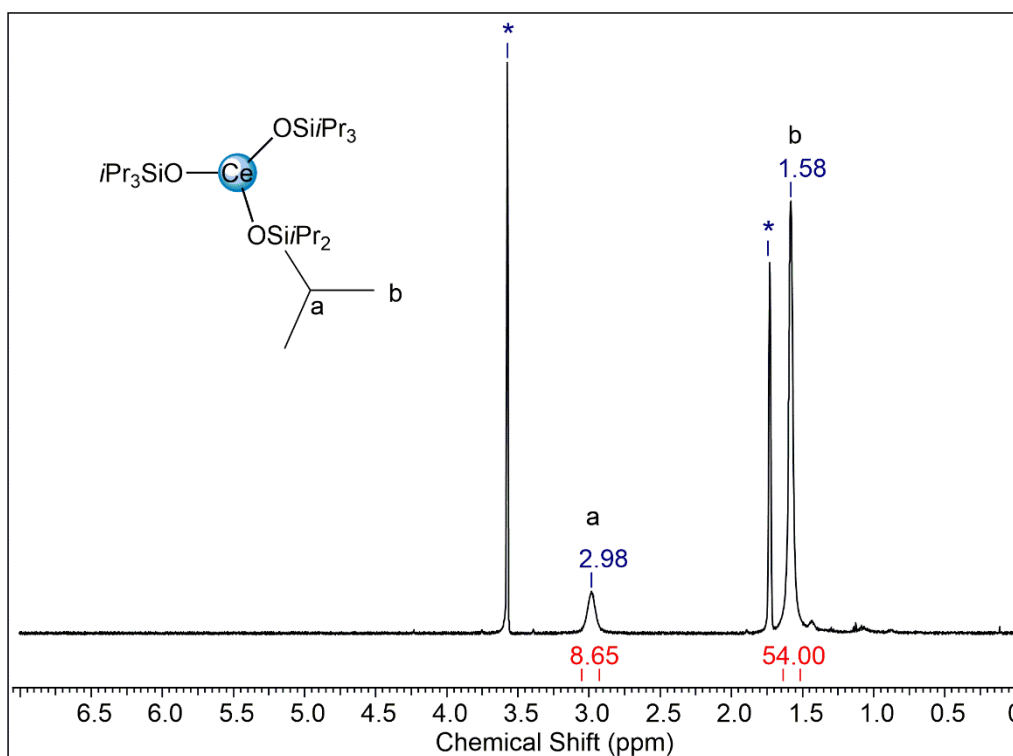
Figure S2. ^{1}H NMR spectrum (400.13 MHz, THF-d_8, 26 °C) of [Ce(OSiiPr$_3$)$_3$]$_2$ (**3**).
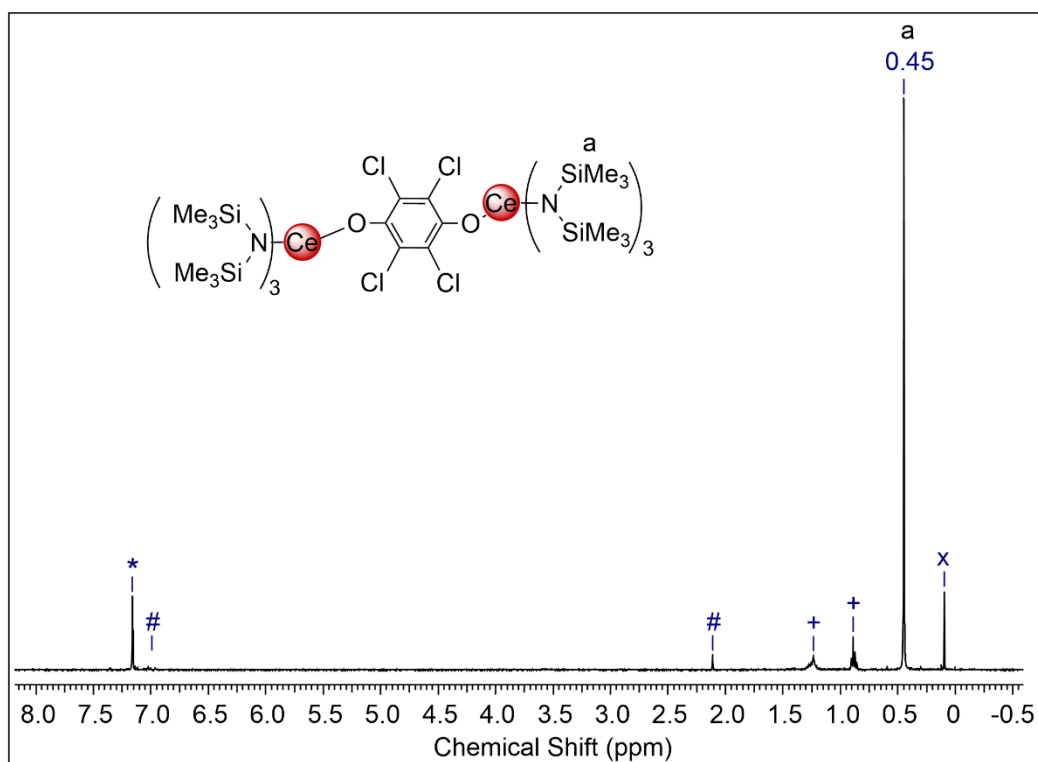
Figure S3. ^{1}H NMR spectrum (400.13 MHz, C$_6$D$_6$, 26 °C) of [Ce{N(SiMe$_3$)$_2$}$_3$]$_2$(μ_2-O$_2$C$_6$Cl$_4$) (**4^{Cl4hq}**). Trace impurities of toluene, *n*-hexane and [KN(SiMe$_3$)$_2$] are marked with #, + and x.
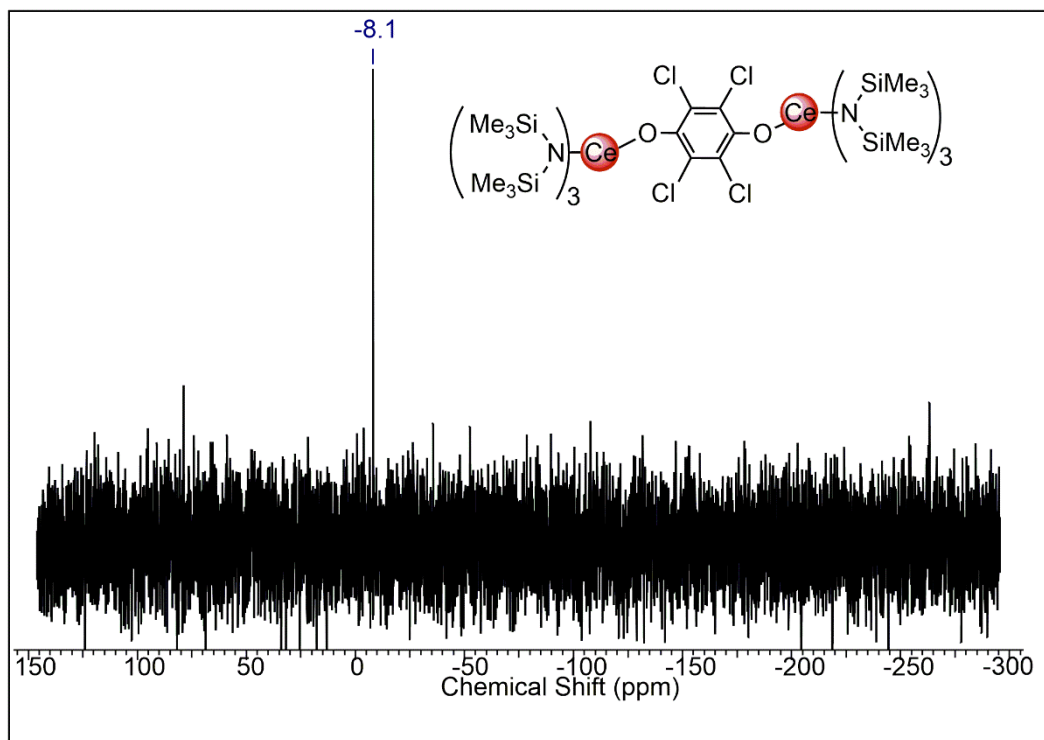
Figure S4. ^{29}Si DEPT45 NMR spectrum (69.63 MHz, C$_6$D$_6$, 26 °C) of [Ce{N(SiMe$_3$)$_2$}$_3$]$_2$(μ_2-O$_2$C$_6$Cl$_4$) (**4^{Cl4hq}**).
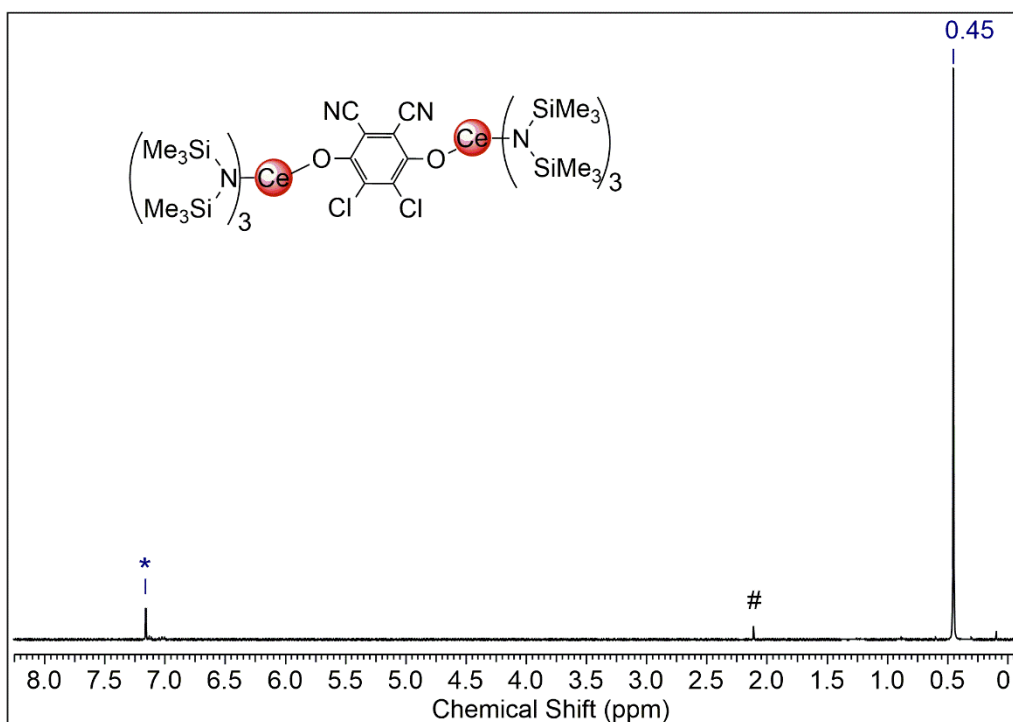
Figure S5. ^{1}H NMR spectrum (500.13 MHz, C$_6$D$_6$, 26 °C) of [Ce{N(SiMe$_3$)$_2$}$_3$]$_2$(μ_2-O$_2$C$_6$Cl$_2$(CN)$_2$) (**4^{ddhq}**). Trace impurities of toluene are marked with #.
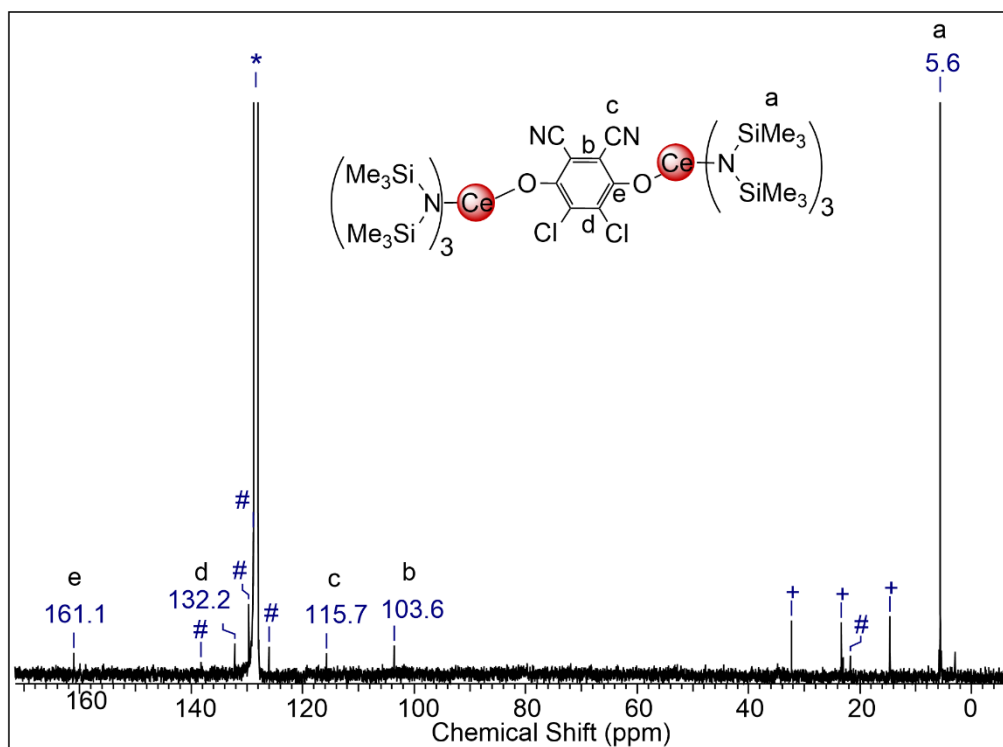
Figure S6. ^{13}C{^{1}H} NMR spectrum (125.76 MHz, C$_6$D$_6$, 26 °C) of [Ce{N(SiMe$_3$)$_2$}$_3$]$_2$(μ_2-O$_2$C$_6$Cl$_2$(CN)$_2$) (**4^{ddhq}**). Trace impurities of toluene and *n*-hexane are marked with # and +.
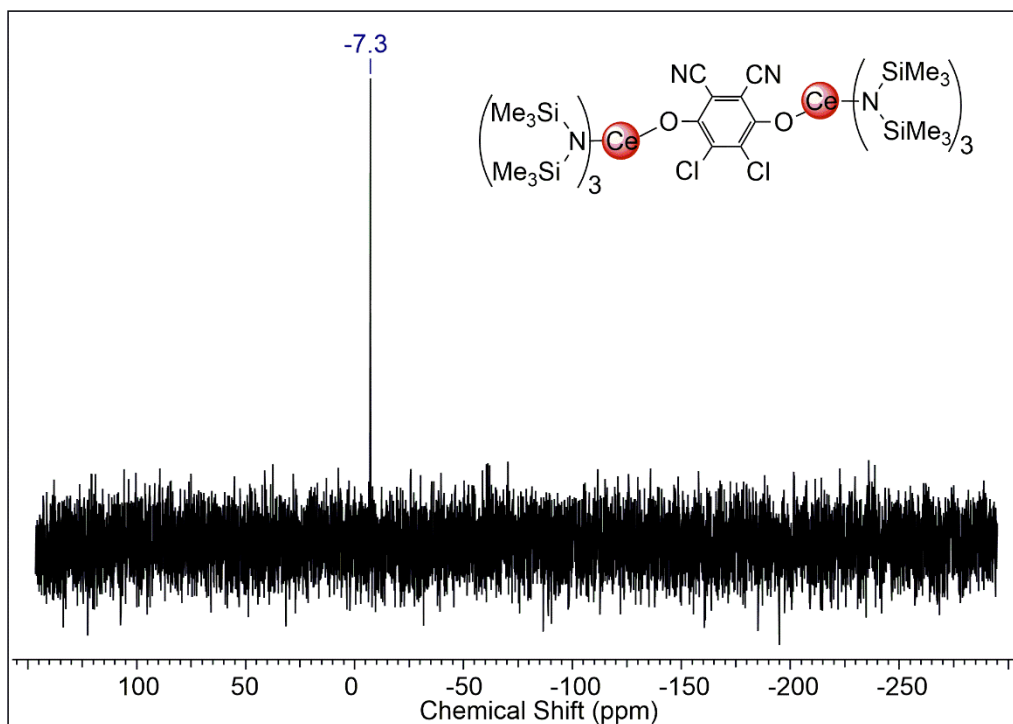
Figure S7. ^{29}Si DEPT45 NMR spectrum (69.63 MHz, C$_6$D$_6$, 26 °C) of [Ce{N(SiMe$_3$)$_2$}$_3$]$_2$(μ_2-O$_2$C$_6$Cl$_2$(CN)$_2$) (**4^{ddhq}**).
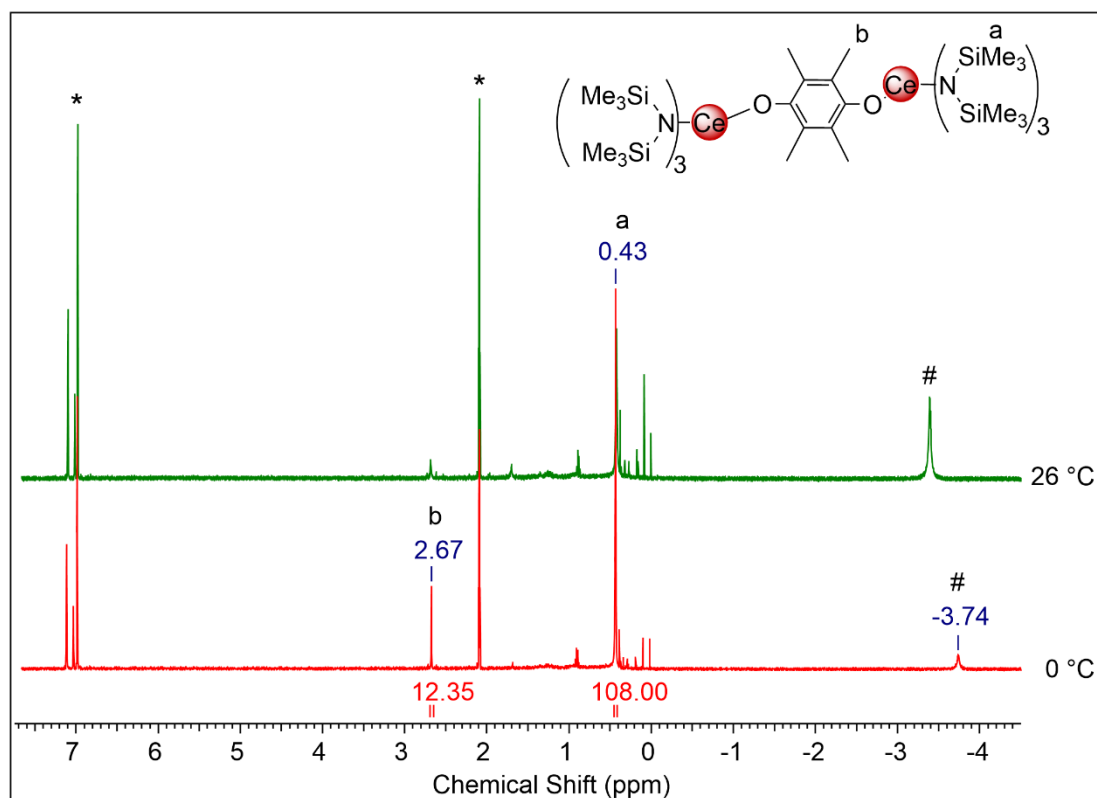
Figure S8. Stacked ^{1}H NMR spectra (500.13 MHz, toluene-d_8) of [Ce{N(SiMe$_3$)$_2$}$_3$]$_2$(μ_2-O$_2$C$_6$Me$_4$) (**4^{Me4hq}**) at 0 °C (red) and 26 °C (green), indicating decomposition in solution and formation of Ce[N(SiMe$_3$)$_2$]$_3$ (marked with #).
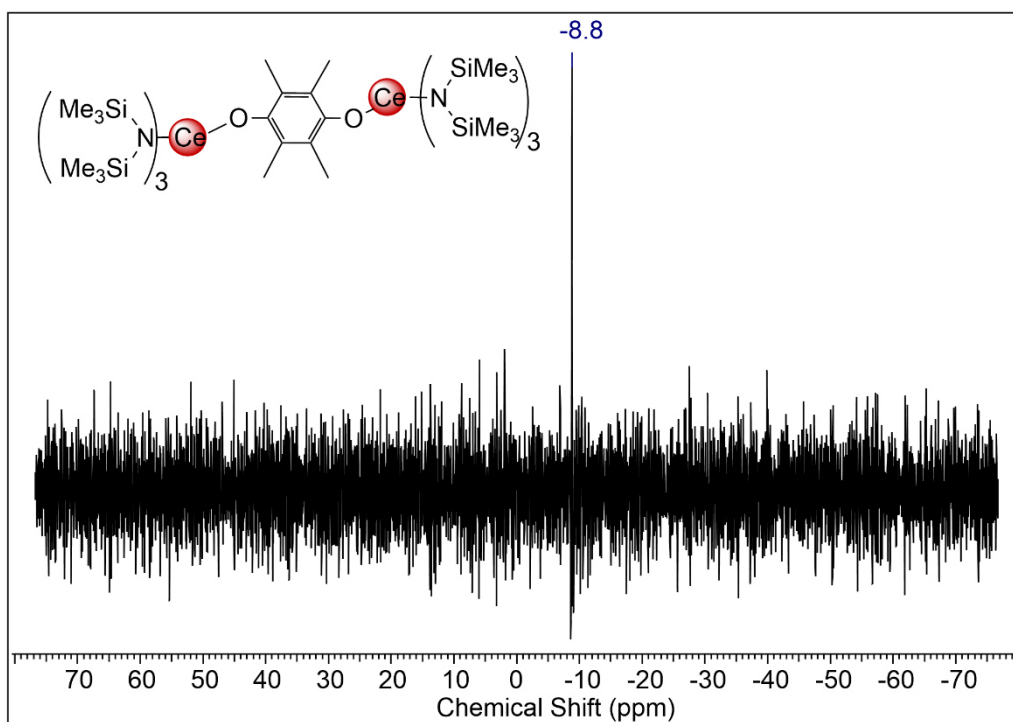
Figure S9. ^{29}Si INEPTND NMR spectrum (99.36 MHz, C$_6$D$_6$, 26 °C) of [Ce{N(SiMe$_3$)$_2$}$_3$]$_2$(μ_2-O$_2$C$_6$Me$_4$) (**4^{Me4hq}**).
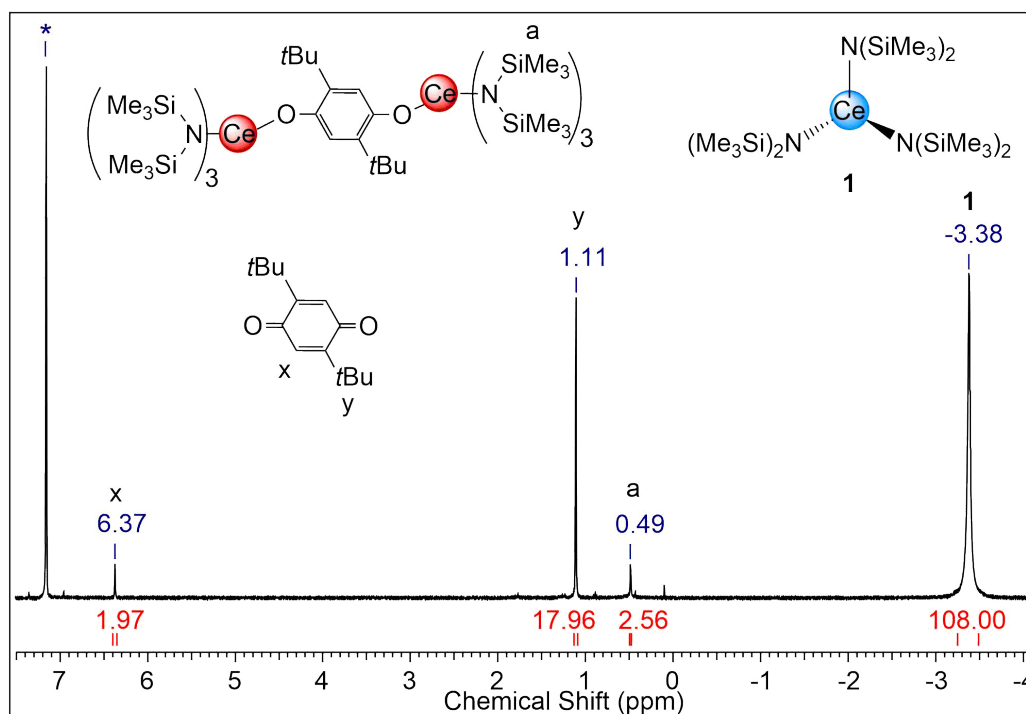
Figure S10. ^{1}H NMR spectrum (400.13 MHz, C$_6$D$_6$, 26 °C) of [Ce{N(SiMe$_3$)$_2$}$_3$]$_2$(μ_2-O$_2$C$_6$tBu$_2$H$_2$) (**4^{tBu2hq}**).
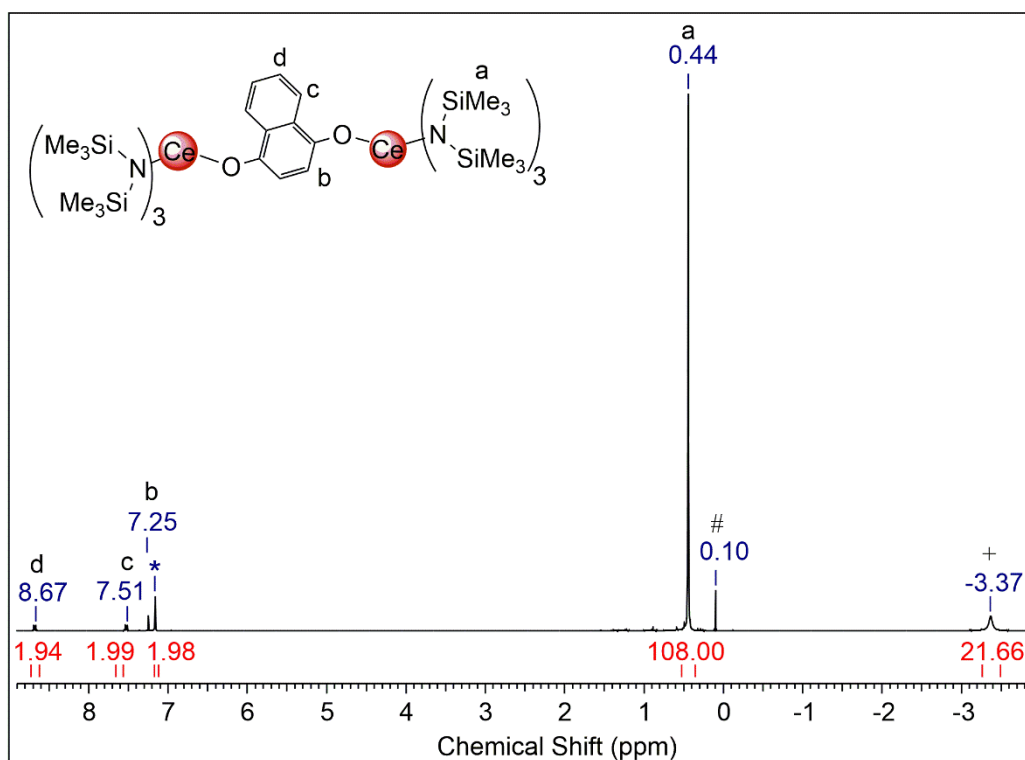
Figure S11. ^{1}H NMR spectrum (400.13 MHz, C$_6$D$_6$, 26 °C) of [Ce{N(SiMe$_3$)$_2$}$_3$]$_2$(μ_2-O$_2$C$_{10}$H$_6$) (**4^{nhq}**). Impurities of KN(SiMe$_3$)$_2$ are marked with # and Ce[N(SiMe$_3$)$_2$]$_3$ with +.
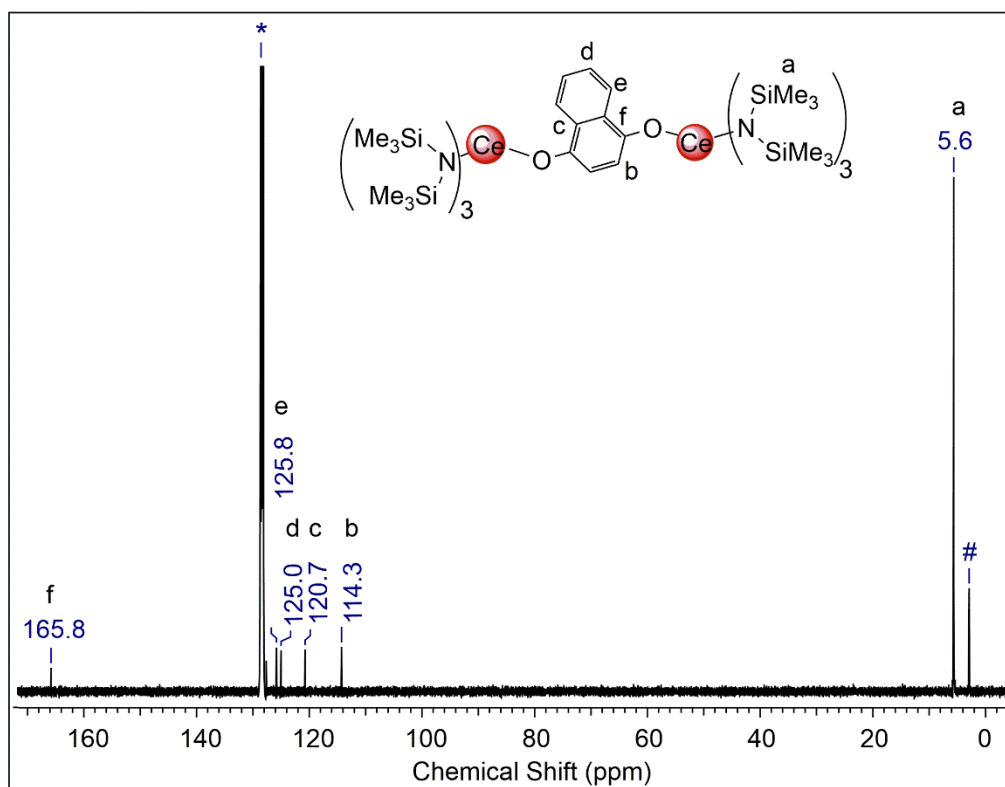
Figure S12. ^{13}C{^{1}H} NMR spectrum (100.61 MHz, C$_6$D$_6$, 26 °C) of [Ce{N(SiMe$_3$)$_2$}$_3$]$_2$(μ_2-O$_2$C$_{10}$H$_6$) (**4^{nhq}**). Impurities of KN(SiMe$_3$)$_2$ are marked with #.
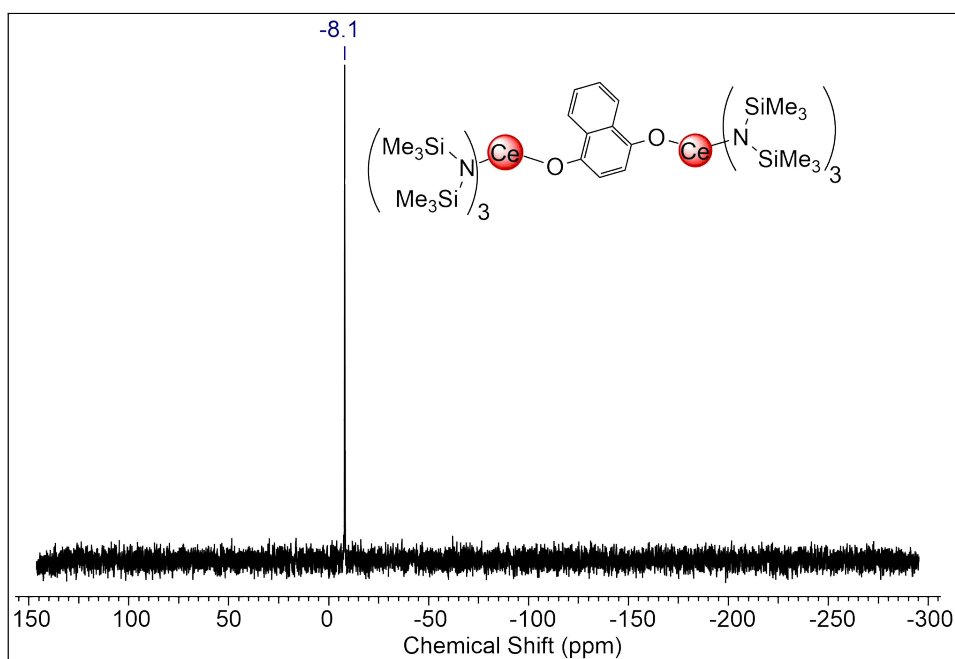
Figure S13. ^{29}Si DEPT45 NMR spectrum (69.63 MHz, C$_6$D$_6$, 26 °C) of [Ce{N(SiMe$_3$)$_2$}$_3$]$_2$(μ_2-O$_2$C$_{10}$H$_6$) (**4^{nhq}**).
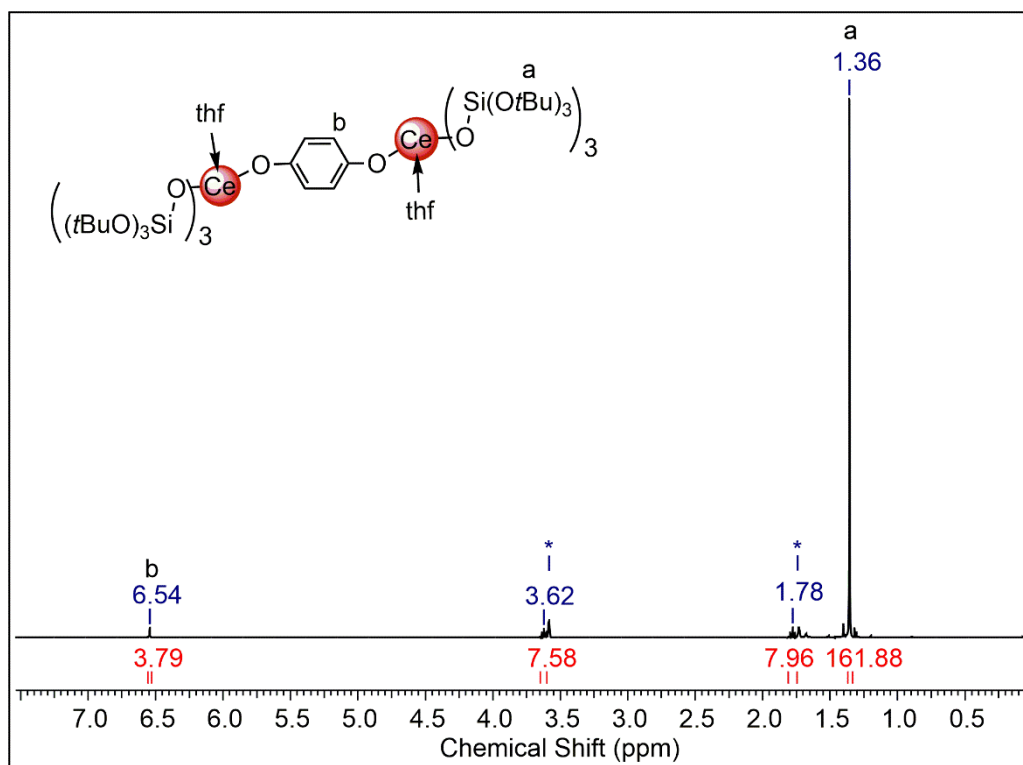
Figure S14. ^{1}H NMR spectrum (400.13 MHz, THF-d_8, 26 °C) of [Ce{OSi(OtBu)$_3$}$_3$(thf)]$_2$(μ_2-O$_2$C$_6$H$_4$) (**5^{hq}**).
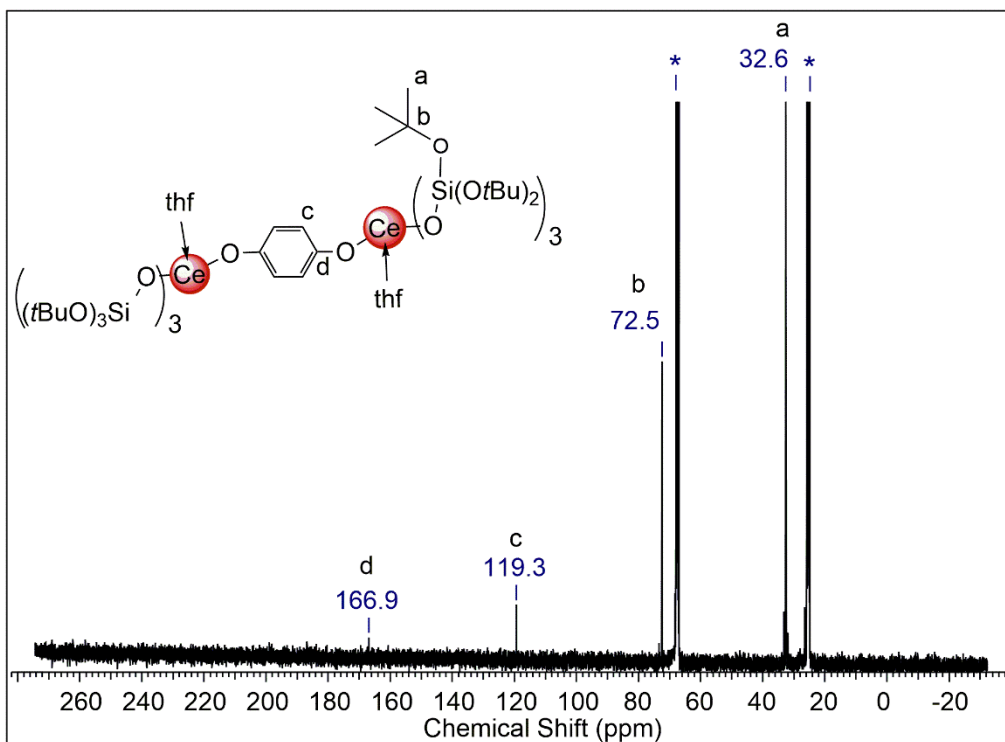
Figure S15. $^{13}C\{^{1}H\}$ NMR spectrum (100.61 MHz, THF-d_8, 26 °C) of [Ce{OSi(OtBu)$_3$}$_3$(thf)]$_2$(μ_2-O$_2$C$_6$H$_4$) (**5^{hq}**).
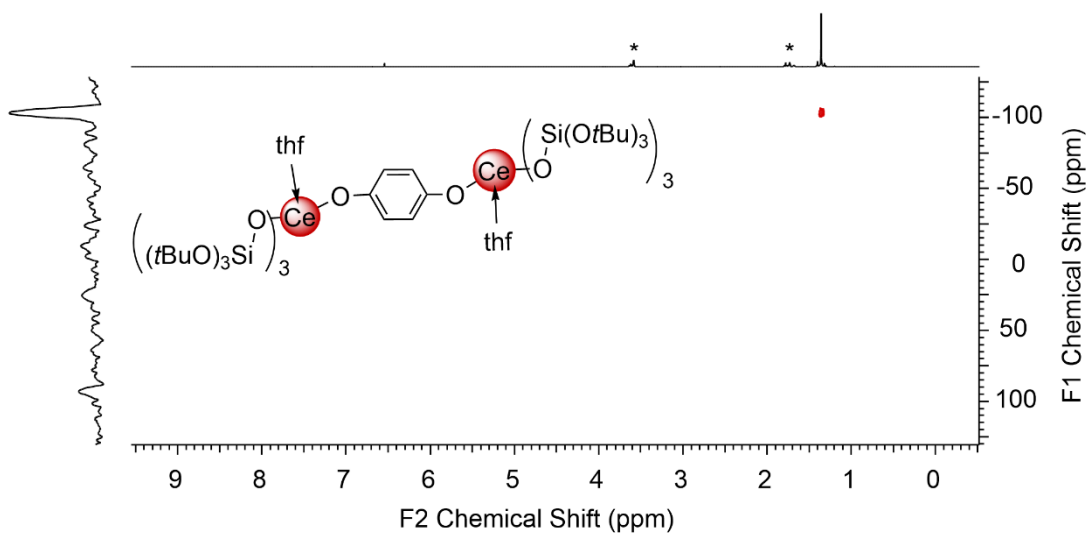
Figure S16. ^{1}H-^{29}Si HSQC NMR spectrum (99.36 MHz, THF-d_8, 26 °C) of [Ce{OSi(OtBu)$_3$}$_3$(thf)]$_2$(μ_2-O$_2$C$_6$H$_4$) (**5^{hq}**).
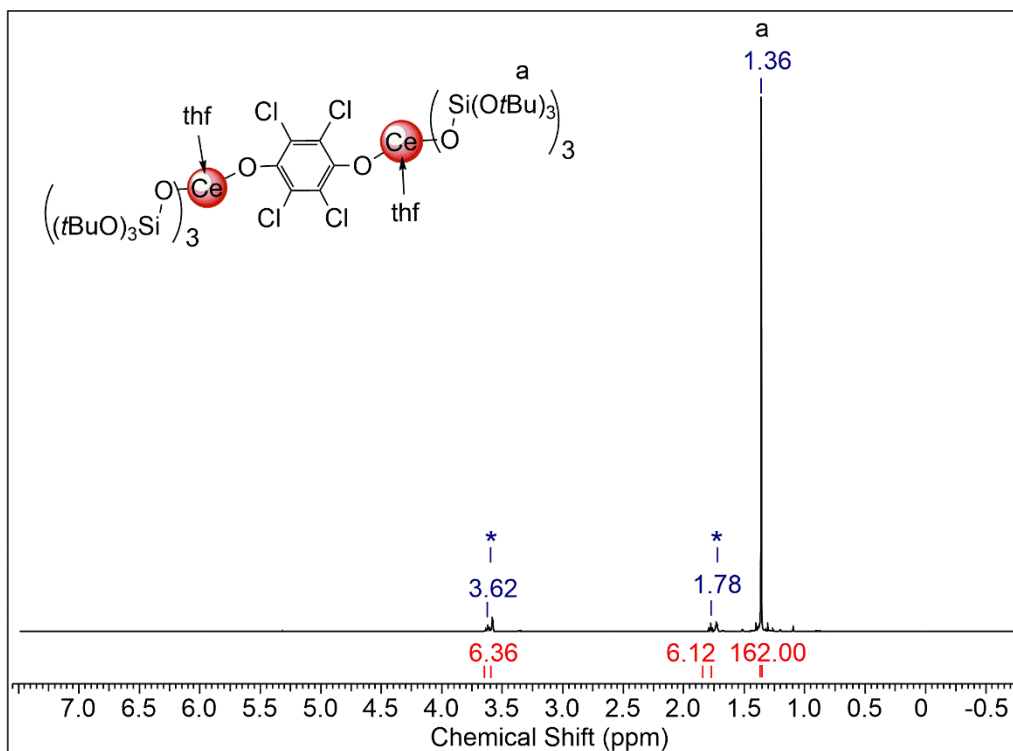
Figure S17. ^{1}H NMR spectrum (400.13 MHz, THF-d_8, 26 °C) of [Ce{OSi(OtBu)$_3$}$_3$(thf)]$_2$(μ_2-O$_2$C$_6$Cl$_4$) (**5^{Cl4hq}**).
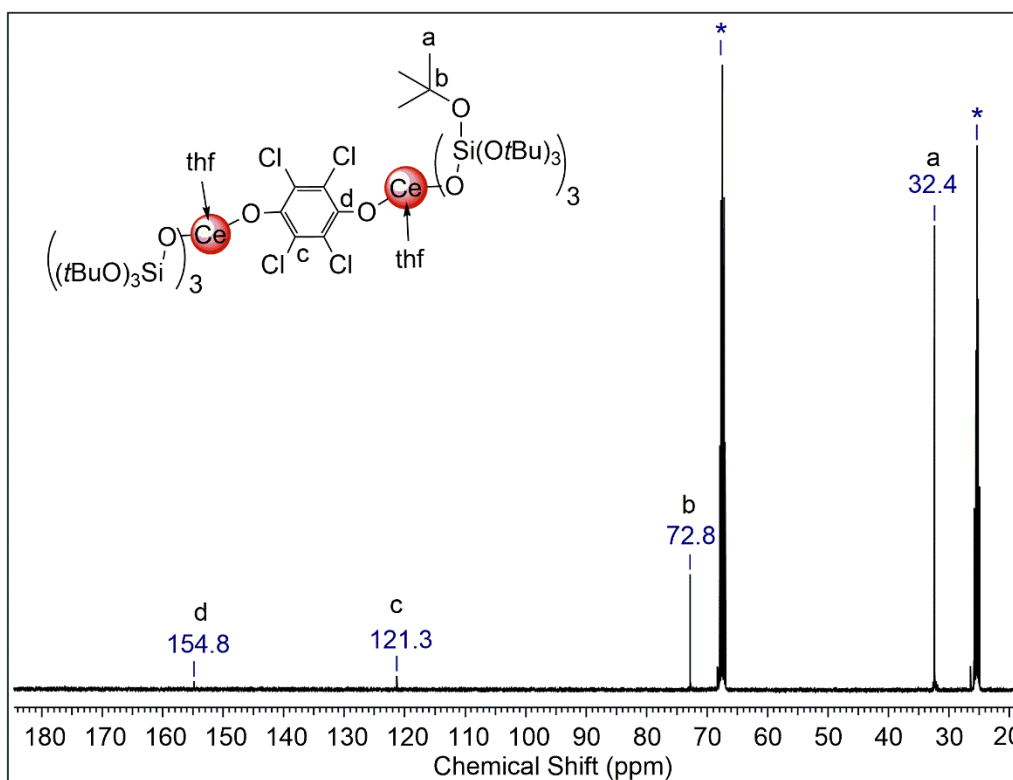
Figure S18. ^{13}C{^{1}H} NMR spectrum (100.61 MHz, THF-d_8, 26 °C) [Ce{OSi(OtBu)$_3$}$_3$(thf)]$_2$(μ_2-O$_2$C$_6$Cl$_4$) (**5^{Cl4hq}**).
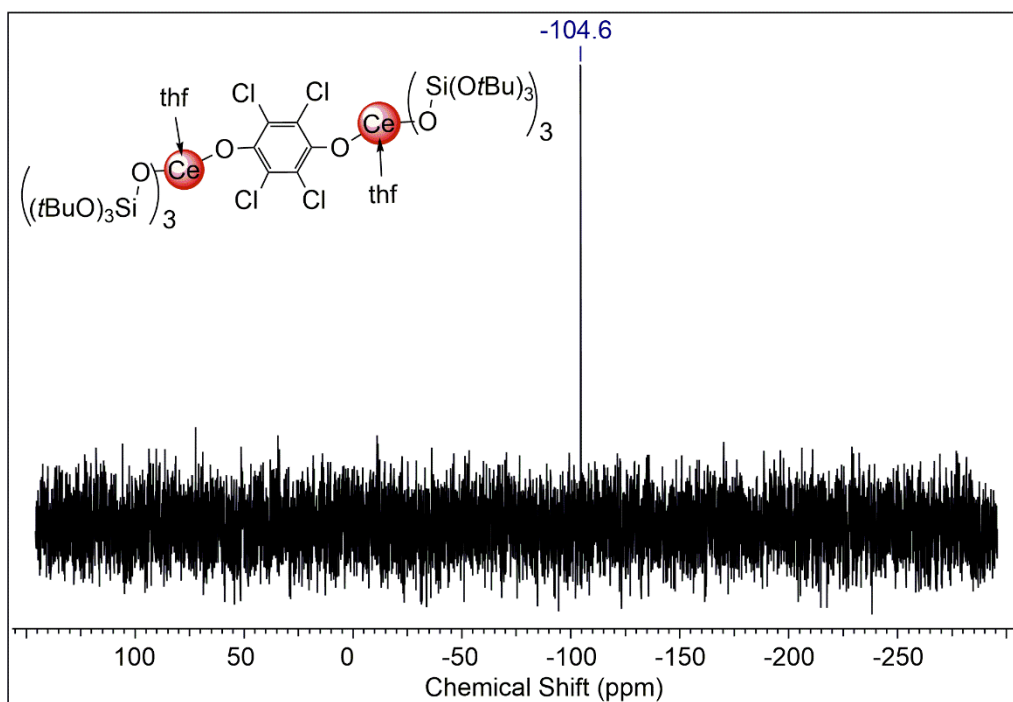
Figure S19. ^{29}Si DEPT45 NMR spectrum (69.63 MHz, THF-d_8, 26 °C) of [Ce{OSi(OtBu)$_3$}$_3$(thf)]$_2$(μ_2-O$_2$C$_6$Cl$_4$) (**5^{Cl4hq}**).
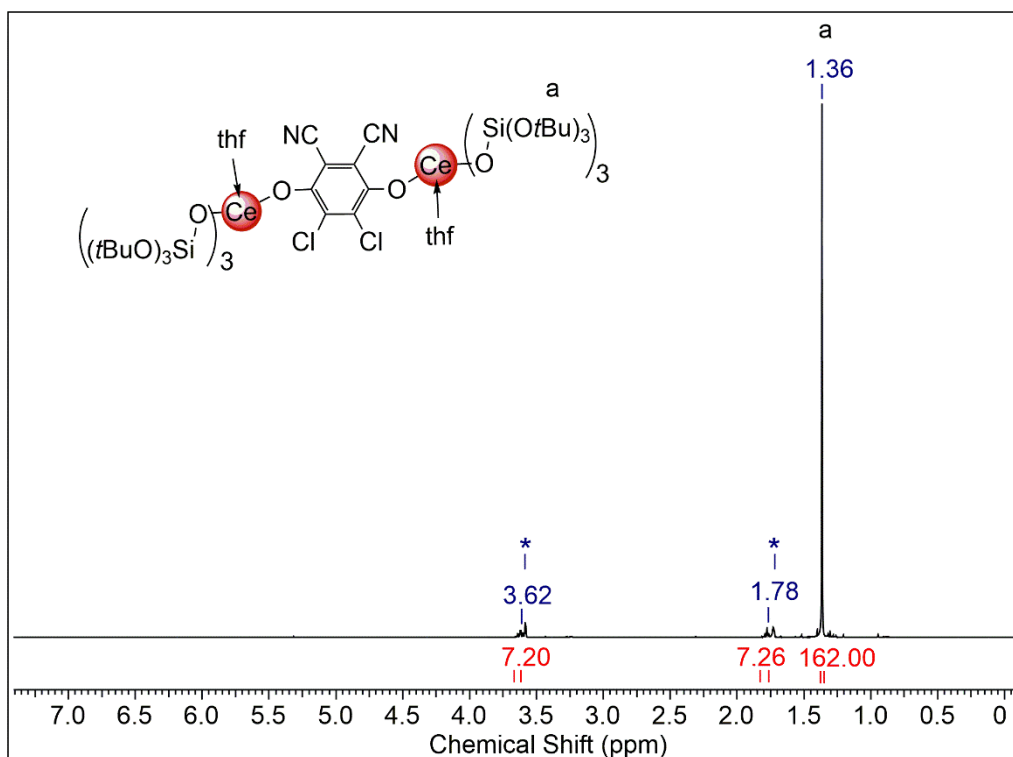
Figure S20. ^{1}H NMR spectrum (400.13 MHz, THF-d_8, 26 °C) of [Ce{OSi(OtBu)$_3$}$_3$(thf)]$_2$(μ_2-O$_2$C$_6$Cl$_2$(CN)$_2$) (**5^{ddhq}**).
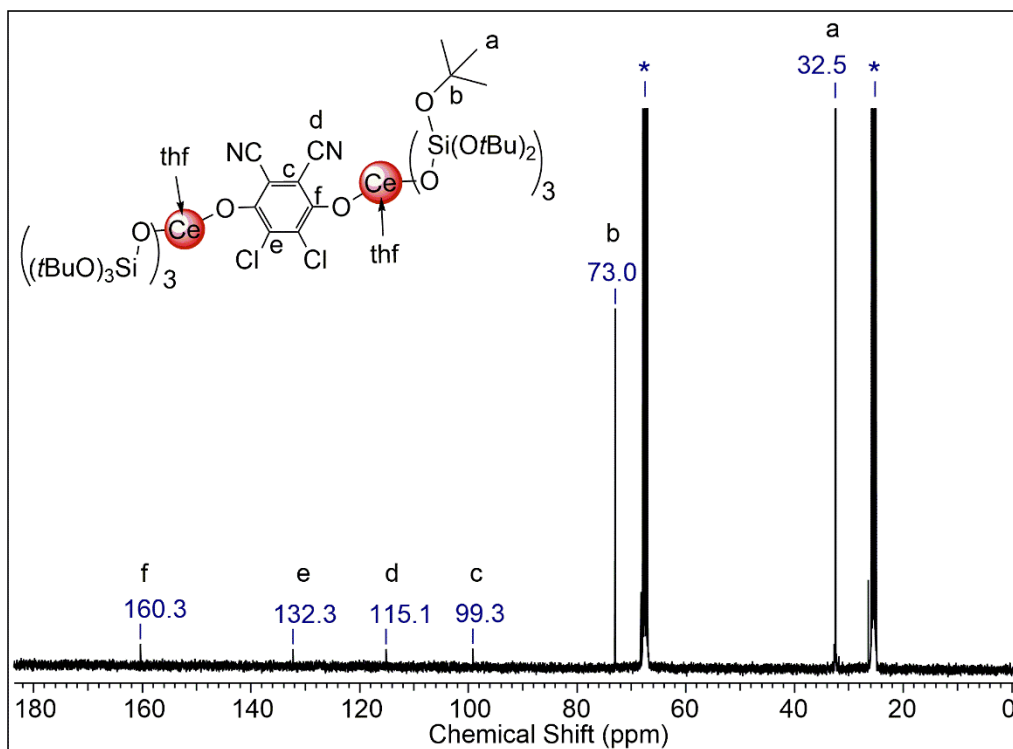
Figure S21. $^{13}C\{^1H\}$ NMR spectrum (100.61 MHz, THF-d_8, 26 °C) [Ce{OSi(OtBu)$_3$}$_3$(thf)]$_2$(μ_2-O$_2$C$_6$Cl$_2$(CN)$_2$) (**5^{ddhq}**).
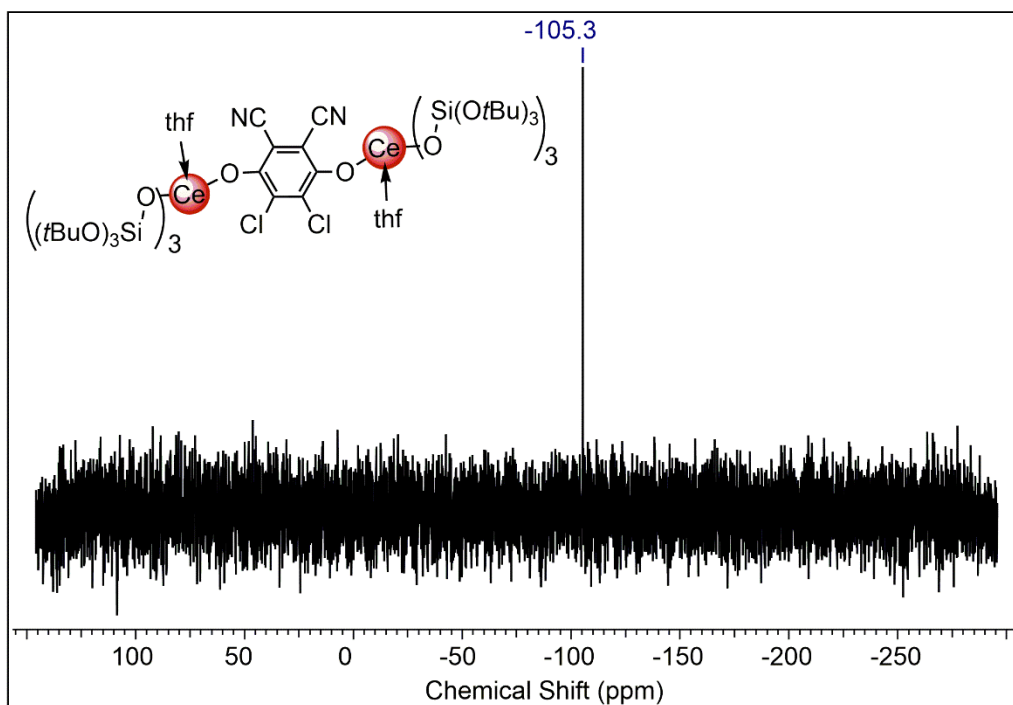
Figure S22. ^{29}Si DEPT45 NMR spectrum (69.63 MHz, THF-d_8, 26 °C) of [Ce{OSi(OtBu)$_3$}$_3$(thf)]$_2$(μ_2-O$_2$C$_6$Cl$_2$(CN)$_2$) (**5^{ddhq}**).
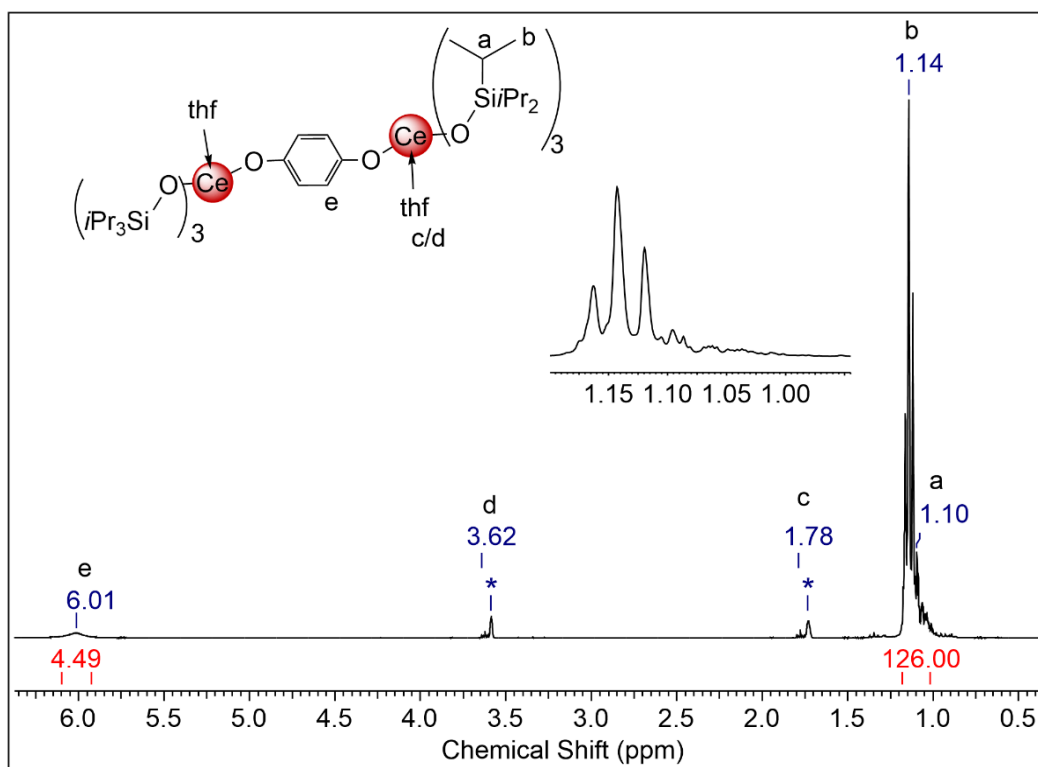
Figure S23. ^{1}H NMR spectrum (400.13 MHz, THF-d_8, 26 °C) of [Ce(OSiiPr$_3$)$_3$(thf)]$_2$(μ_2-O$_2$C$_6$H$_4$) (**6^{hq}**).
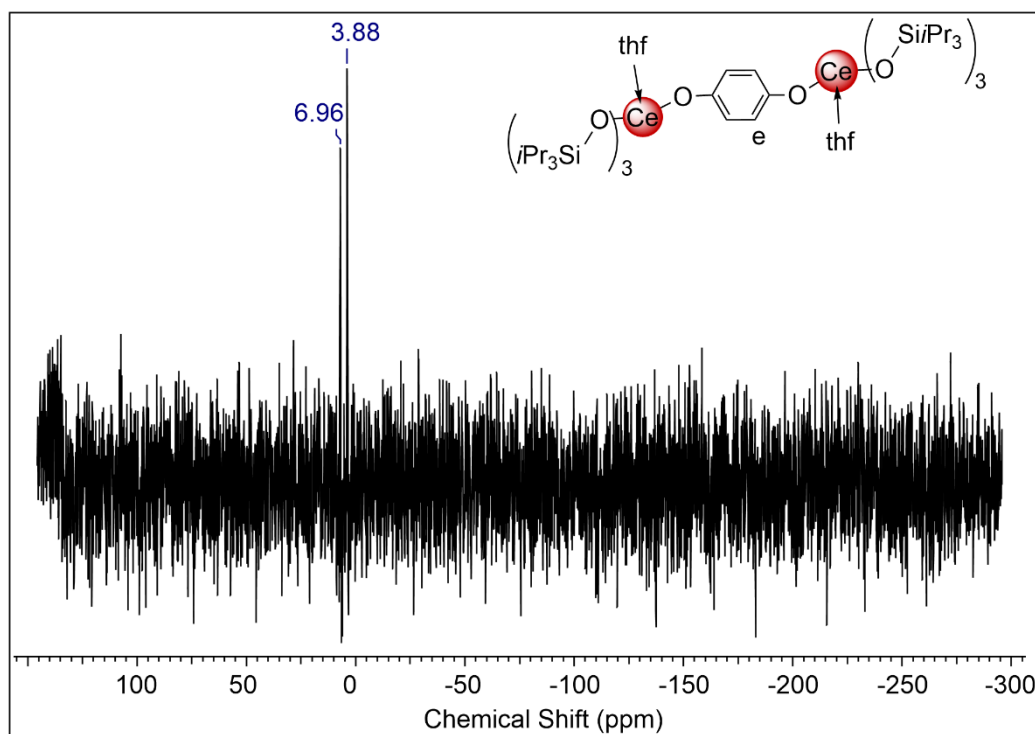
Figure S24. ^{29}Si INEPTND NMR spectrum (69.63 MHz, THF-d_8, 26 °C) of [Ce(OSiiPr$_3$)$_3$(thf)]$_2$(μ_2-O$_2$C$_6$H$_4$) (**6^{hq}**).
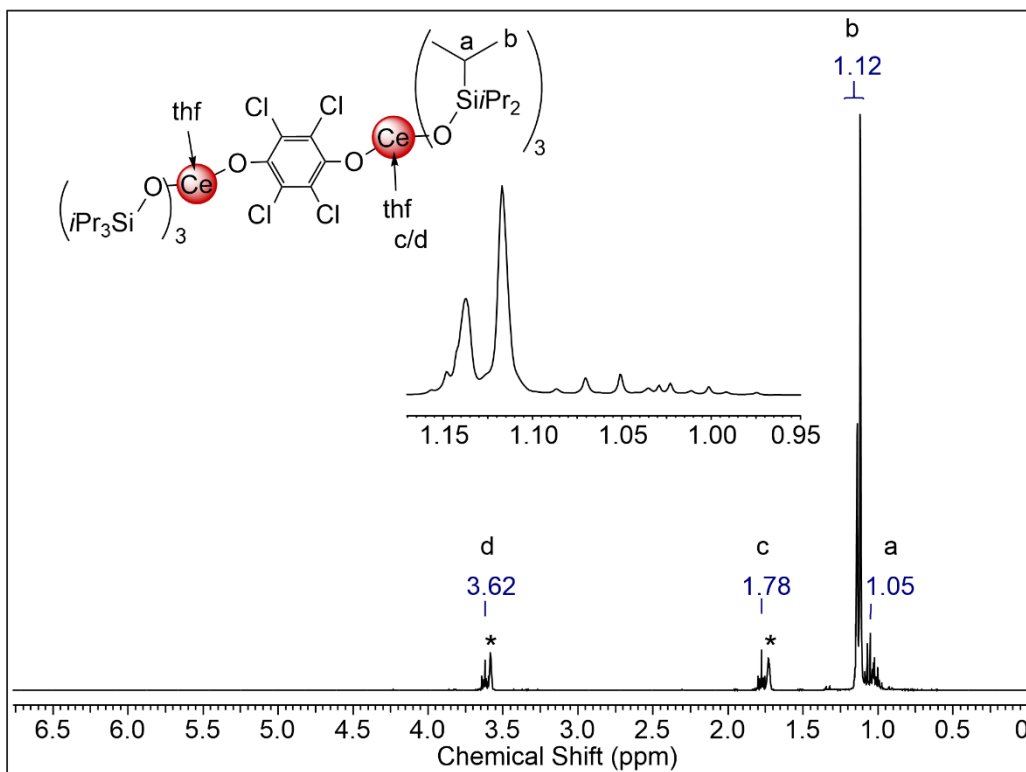
Figure S25. ^{1}H NMR spectrum (400.13 MHz, THF-d_8, 26 °C) of [Ce(OSiiPr$_3$)$_3$(thf)]$_2$(μ_2-O$_2$C$_6$Cl$_4$) (**6^{Cl4hq}**).
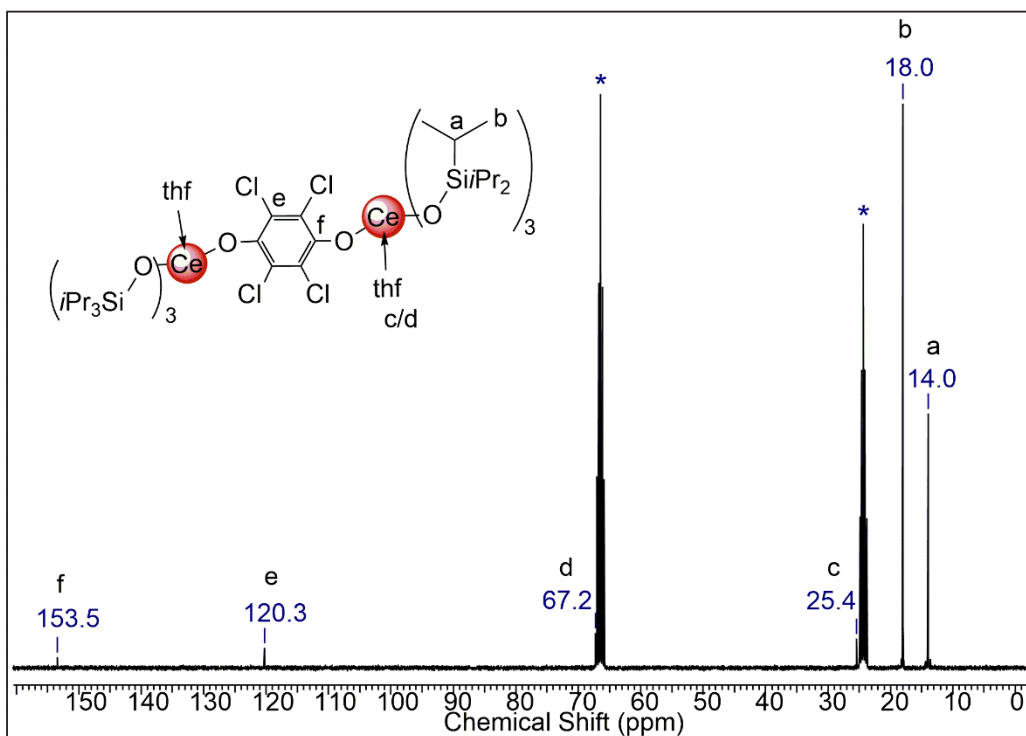
Figure S26. ^{13}C{^{1}H} NMR spectrum (100.61 MHz, THF-d_8, 26 °C) [Ce(OSiiPr$_3$)$_3$(thf)]$_2$(μ_2-O$_2$C$_6$Cl$_4$) (**6^{Cl4hq}**).
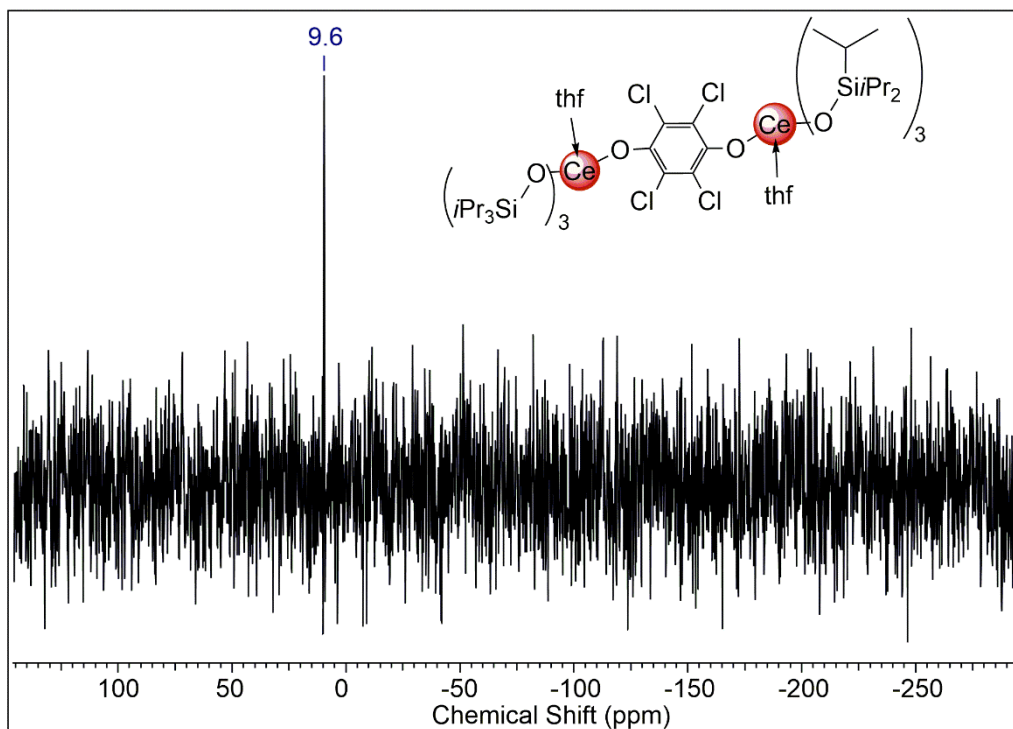
Figure S27. ^{29}Si INEPTND NMR spectrum (69.63 MHz, THF-d_8, 26 °C) of [Ce(OSiiPr$_3$)$_3$(thf)]$_2$(μ_2-O$_2$C$_6$Cl$_4$) (**6^{Cl4hq}**).
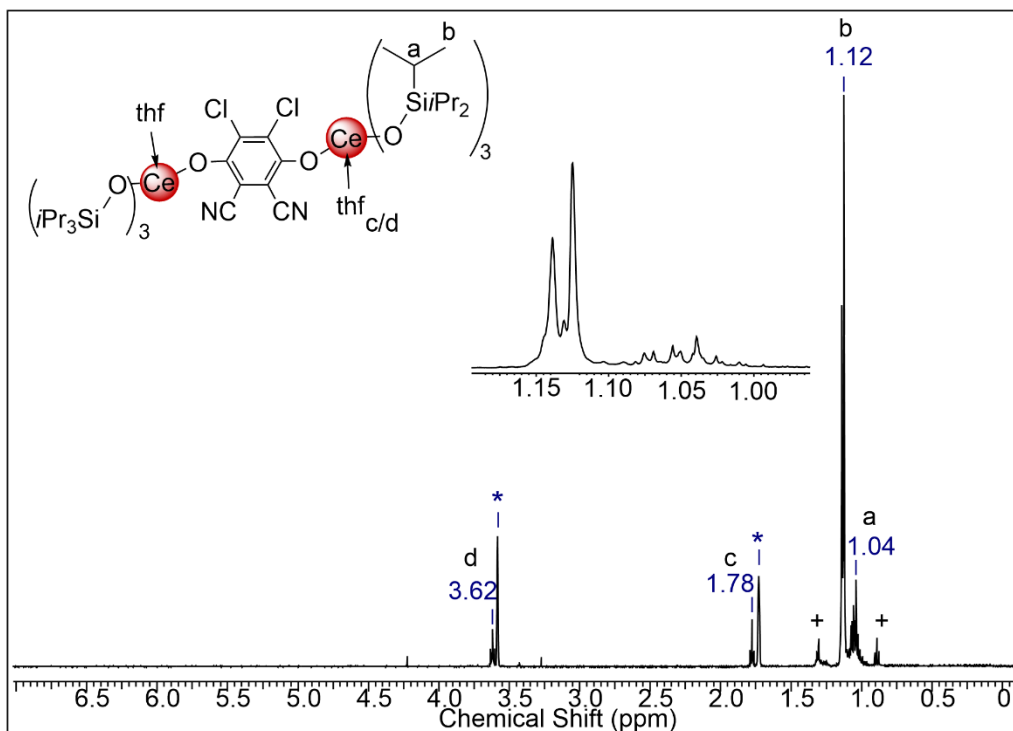
Figure S28. ^{1}H NMR spectrum (500.13 MHz, THF-d_8, 26 °C) of [Ce(OSiiPr$_3$)$_3$(thf)]$_2$(μ_2-O$_2$C$_6$Cl$_2$(CN)$_2$) (**6^{ddhq}**).
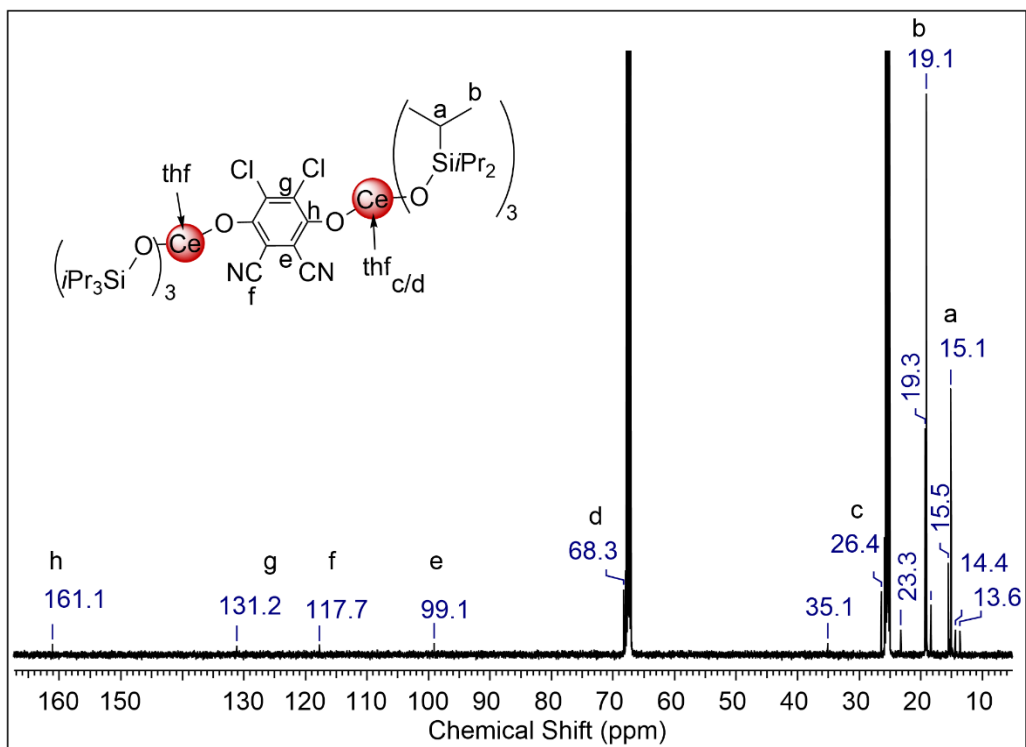
Figure S29. $^{13}C\{^1H\}$ NMR spectrum (125.76 MHz, THF-d_8, 26 °C) [Ce(OSiiPr$_3$)$_3$(thf)]$_2$(μ_2-O$_2$C$_6$Cl$_2$(CN)$_2$) (**6^{ddhq}**).
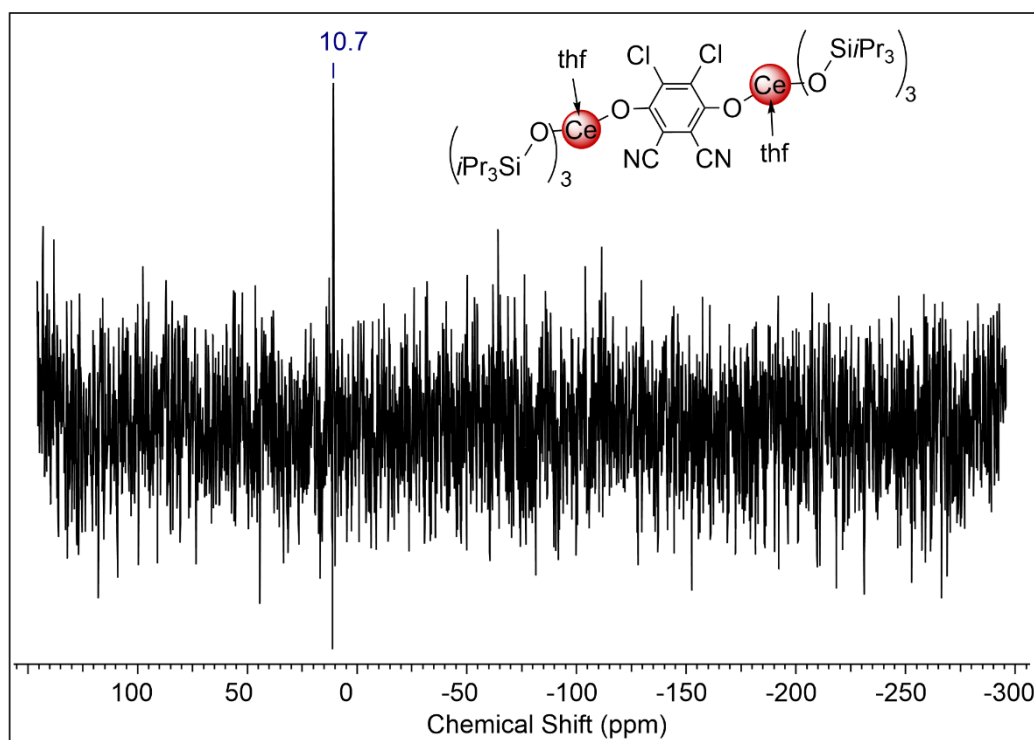
Figure S30. ^{29}Si INEPTND NMR spectrum (69.63 MHz, THF-d_8, 26 °C) of [Ce(OSiiPr$_3$)$_3$(thf)]$_2$(μ_2-O$_2$C$_6$Cl$_2$(CN)$_2$) (**6^{ddhq}**).
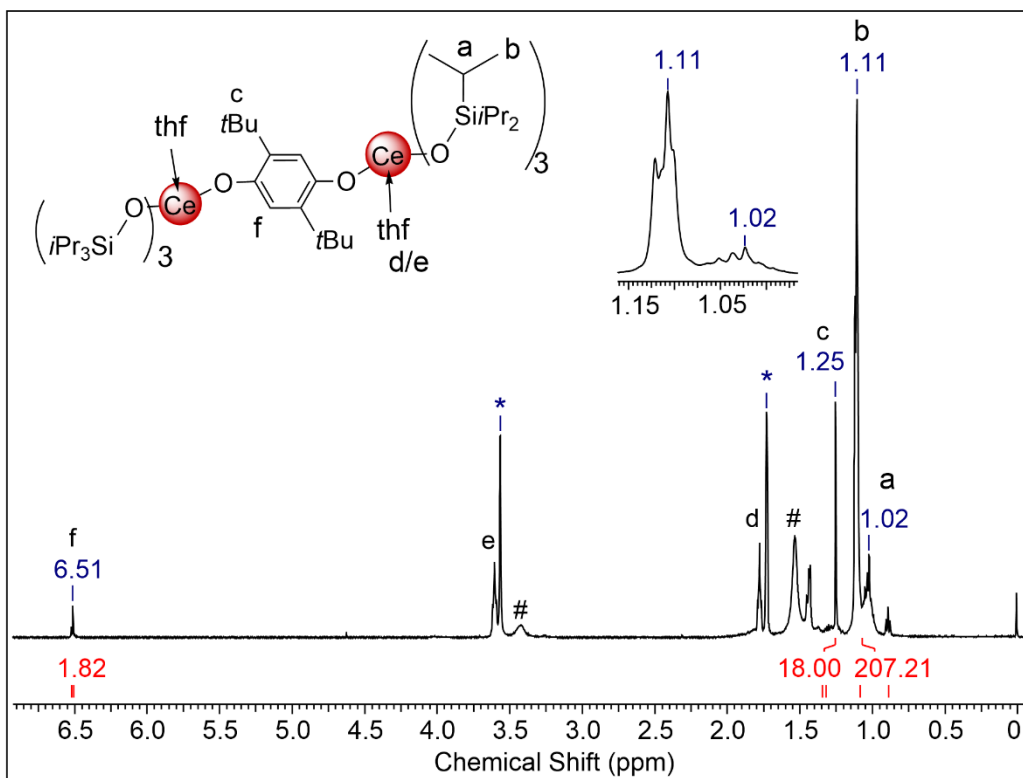
Figure S31. ^{1}H NMR spectrum (500.13 MHz, THF-d_8, 26 °C) of [Ce(OSiiPr$_3$)$_3$(thf)]$_2$(μ_2-O$_2$C$_6t$Bu$_2$H$_2$) (**6**^{tBu2hq}). The high integral for the *iso*propyl groups indicates the formation of a second tetravalent cerium tri*iso*propyl siloxide species. Impurities of [Ce(OSiiPr$_3$)$_3$]$_2$ (**3**) are marked with #.
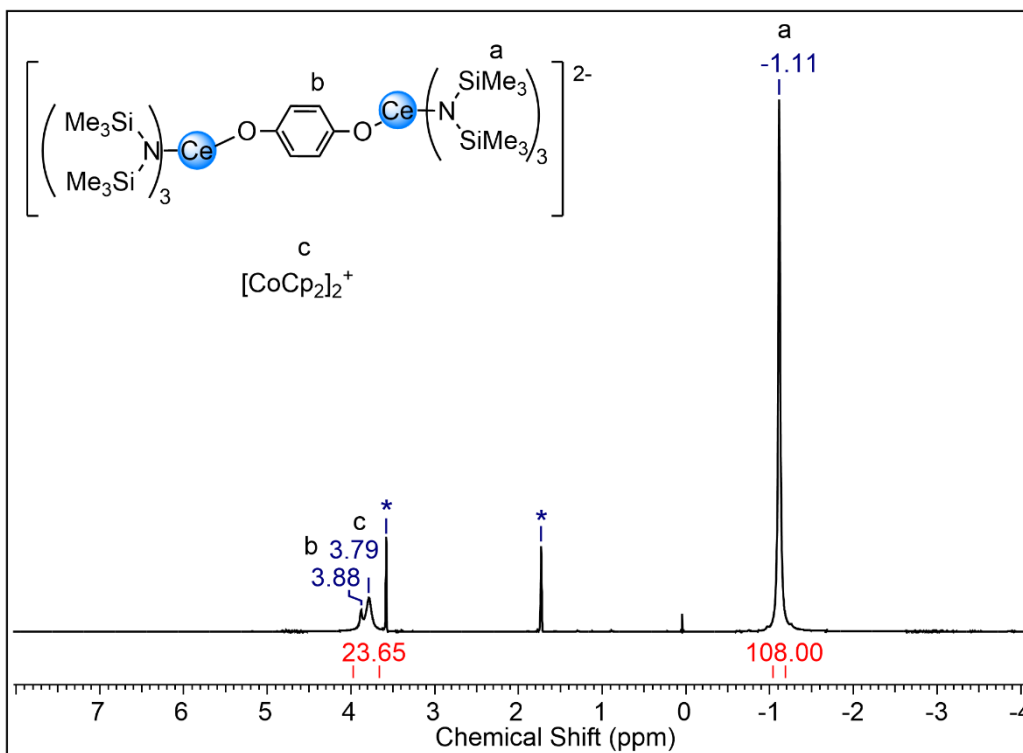
Figure S32. ^{1}H NMR spectrum (400.13 MHz, THF-d_8, 26 °C) of [(Ce{N(SiMe$_3$)$_2$}$_3$)$_2$(μ_2-O$_2$C$_6$H$_4$)][CoCp$_2$]$_2$ (**7**).
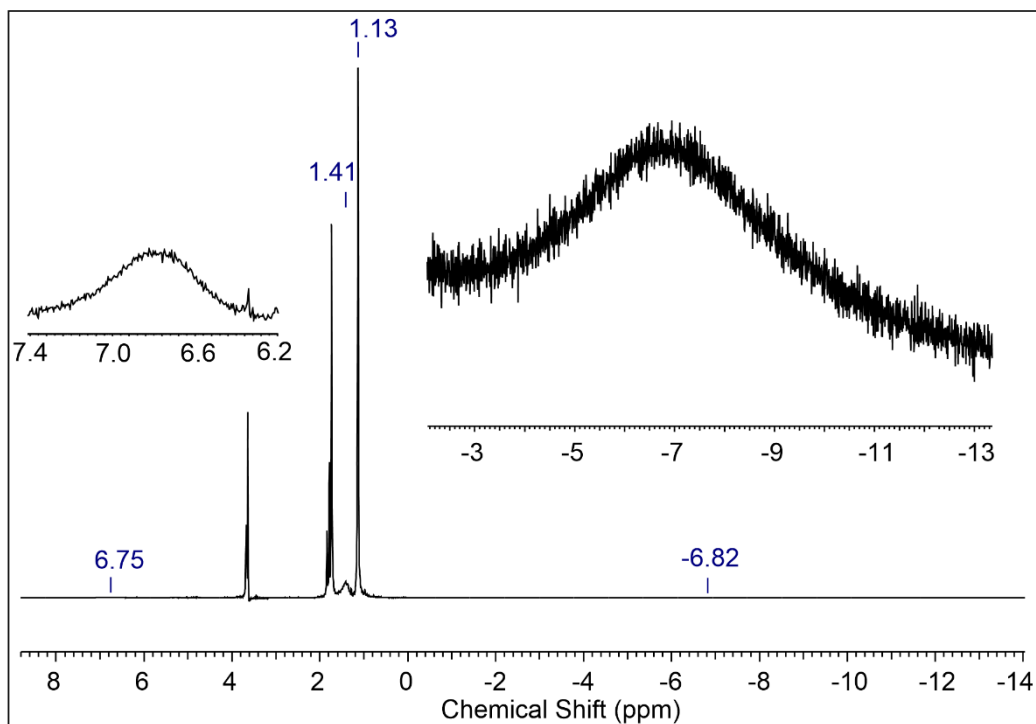
Figure S33. ^{1}H NMR spectrum (400.13 MHz, THF-d_8, 26 °C) of the reaction mixture of [Ce{OSi(OtBu)$_3$}$_3$(thf)]$_2$(μ_2-O$_2$C$_6$H$_4$) (**5^{hq}**) with two equivalents of CoCp$_2$.
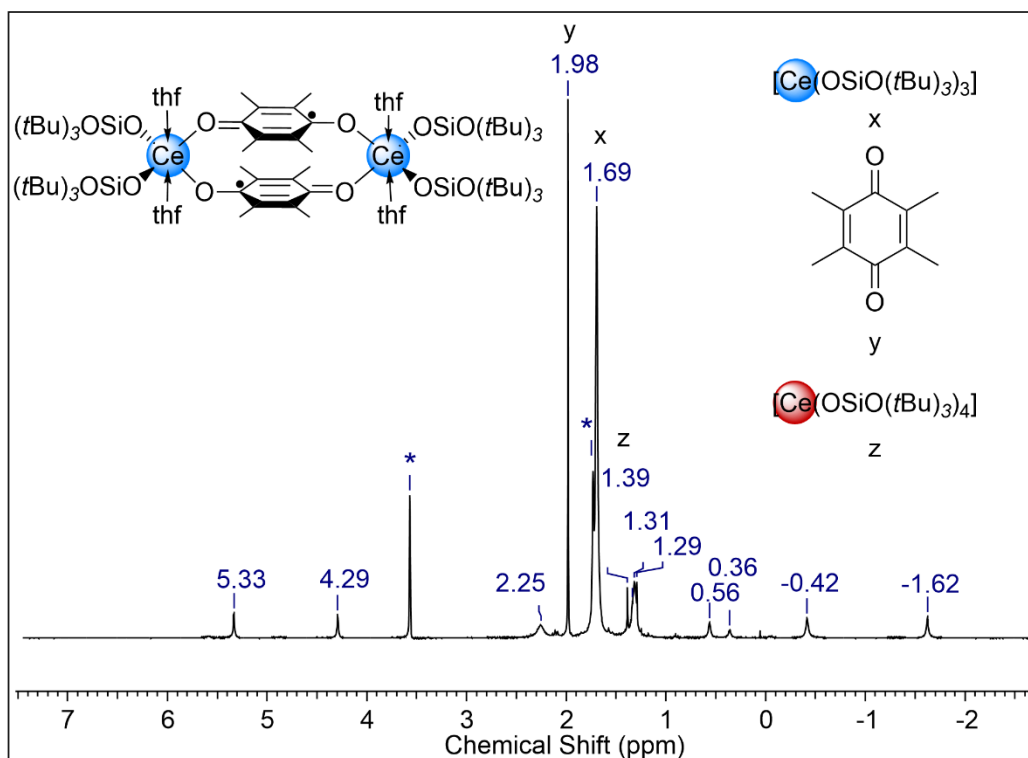
Figure S34. ^{1}H NMR spectrum (400.13 MHz, THF-d_8, 26 °C) of [Ce{OSi(OtBu)$_3$}$_2$(thf)$_2$(μ_2-O$_2$C$_6$Me$_4$)]$_2$ (**8**). Signals assigned to starting material [Ce{OSi(OtBu)$_3$}$_3$]$_2$ and Me$_4$bq, and co-product Ce[OSi(OtBu)$_3$]$_4$ are marked with x, y and z.
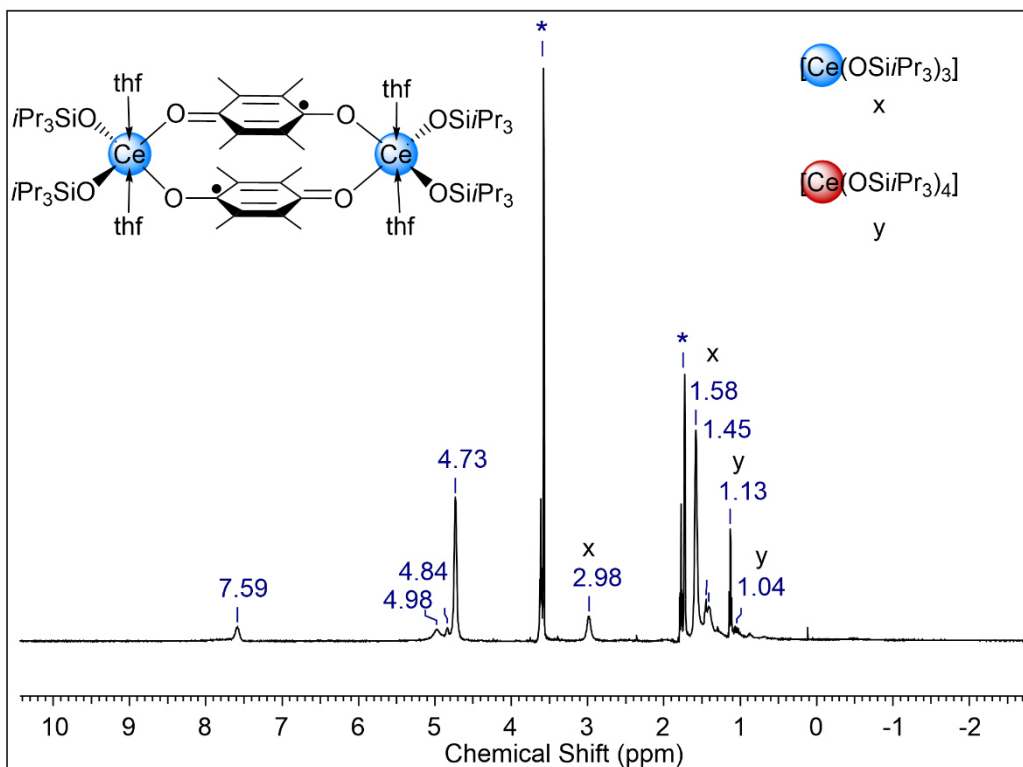
Figure S35. ^{1}H NMR spectrum (400.13 MHz, THF-d_8, 26 °C) of [Ce(OSiiPr$_3$)$_2$(thf)$_2$(μ_2-O$_2$C$_6$Me$_4$)]$_2$ (**9**). Signals assigned to starting material [Ce(OSiiPr$_3$)$_3$]$_2$ and co-product [Ce(OSiiPr$_3$)$_4$] are marked with x and y.
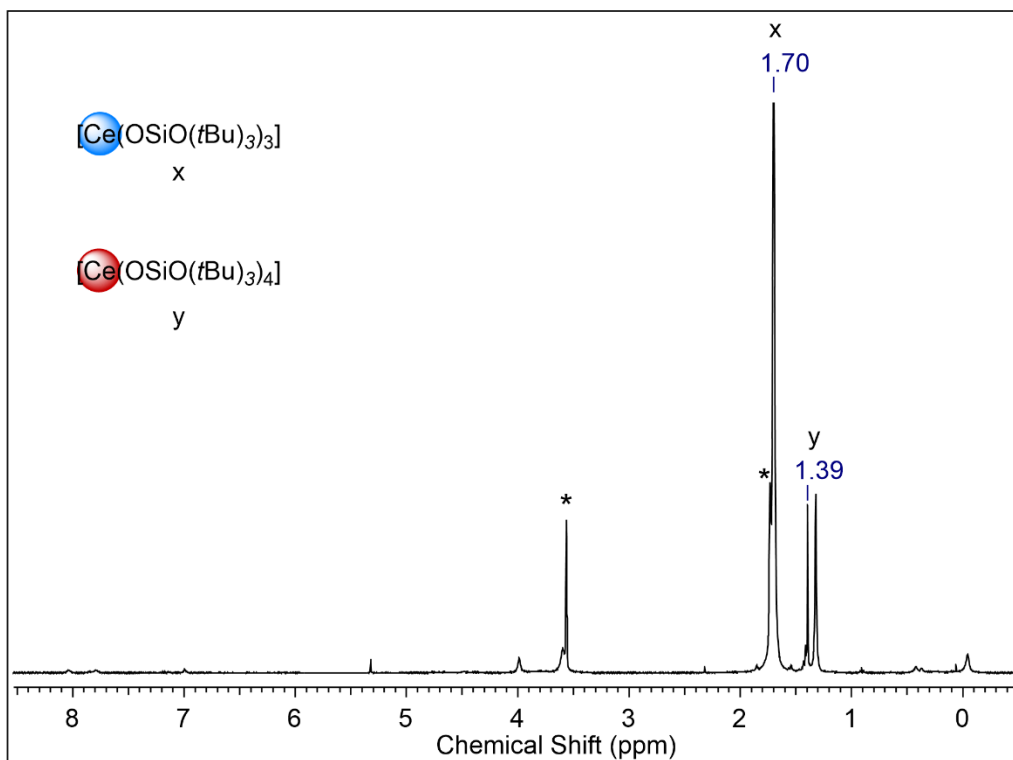
Figure S36. ^{1}H NMR spectrum (400.13 MHz, THF-d_8, 26 °C) of the reaction of [Ce(OSi(OtBu)$_3$)$_2$] (**2**) with 1,4-naphthoquinone. Signals assigned to starting material **2** and co-product Ce[OSi(OtBu)$_3$]$_4$ are marked with x and y.
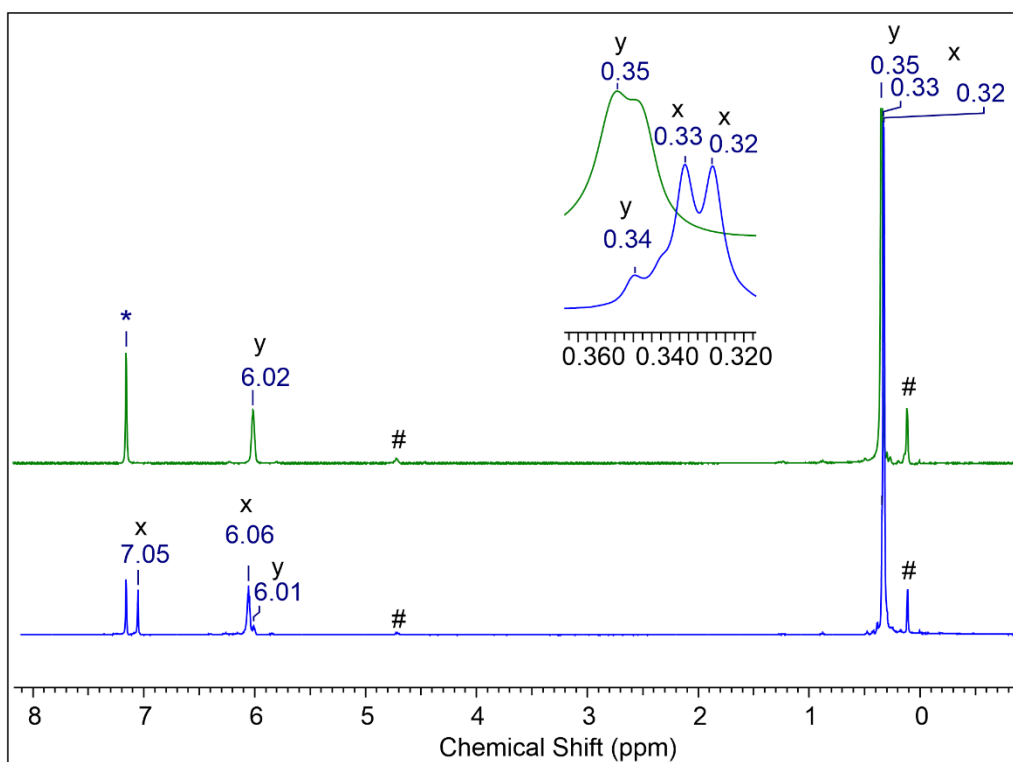
Figure S37. ^{1}H NMR spectrum (400.13 MHz, C_6D_6, 26 °C) of the reaction of [Ce{N(SiHMe$_2$)$_2$}$_3$]$_2$ with 1,4-benzoquinone recorded after 10 min (blue, bottom) and after 24 h (green, top). Signals assigned to putative [Ce{N(SiHMe$_2$)$_2$}$_3$]$_2$(μ_2-O$_2$C$_6$H$_4$) and co-product Ce[N(SiHMe$_2$)$_2$]$_4$ are marked with x and y.
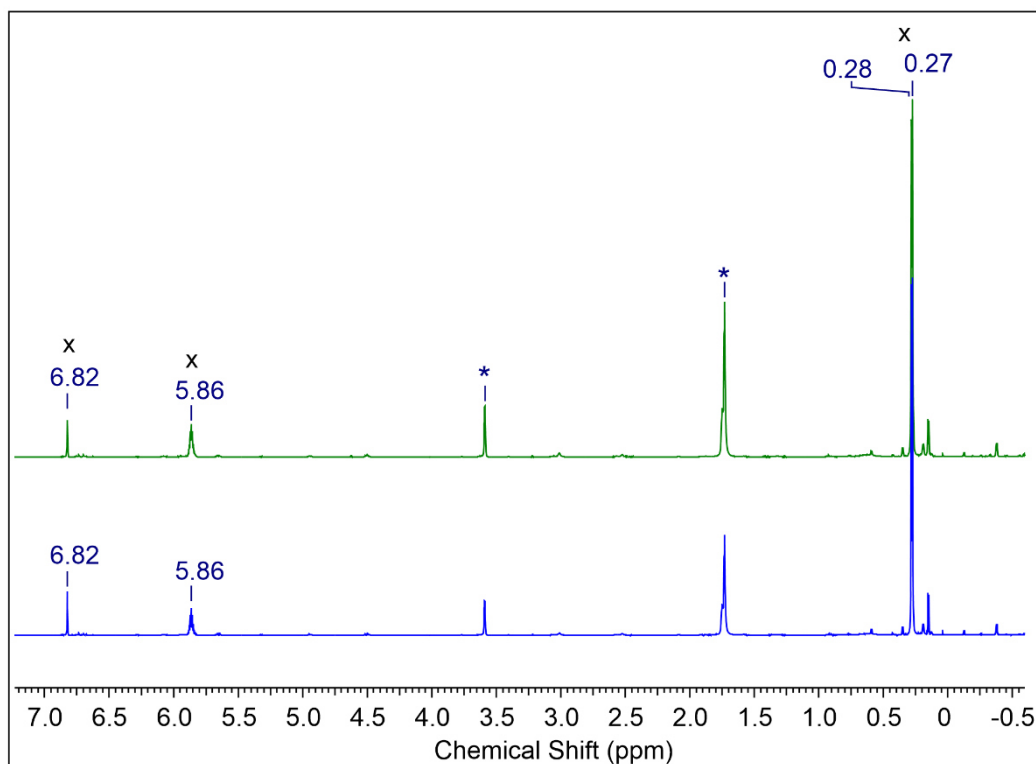
Figure S38. ^{1}H NMR spectrum (400.13 MHz, THF-d_8, 26 °C) of the reaction of [Ce{N(SiHMe$_2$)$_2$}$_3$]$_2$ with 1,4-benzoquinone recorded after 10 min (blue, bottom) and after 24 h (green, top). Signals assigned to putative [Ce{N(SiHMe$_2$)$_2$}$_3$]$_2$(μ_2-O$_2$C$_6$H$_4$) are marked with x.
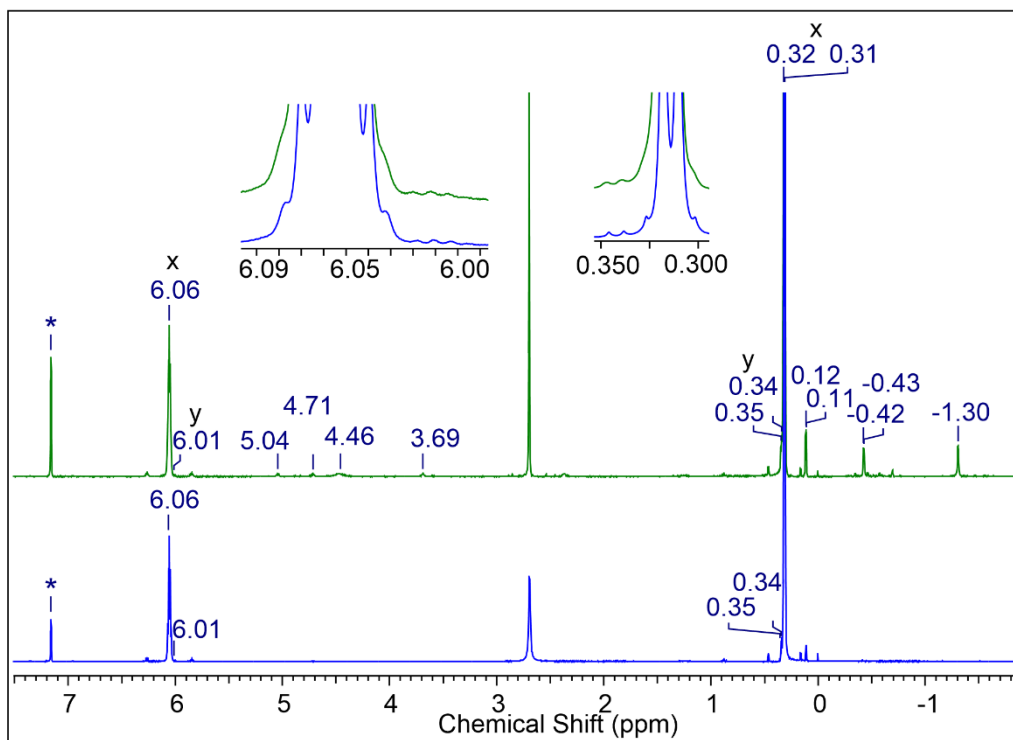
Figure S39. ^{1}H NMR spectrum (400.13 MHz, C_6D_6, 26 °C) of the reaction of [Ce{N(SiHMe$_2$)$_2$}$_3$]$_2$ with tetramethyl-1,4-benzoquinone recorded after 10 min (blue, bottom) and after 24 h (green, top). Signals assigned to putative [Ce{N(SiHMe$_2$)$_2$}$_3$]$_2$(μ_2-O$_2$C$_6$H$_4$) and co-product Ce[N(SiHMe$_2$)$_2$]$_4$ are marked with x and y.
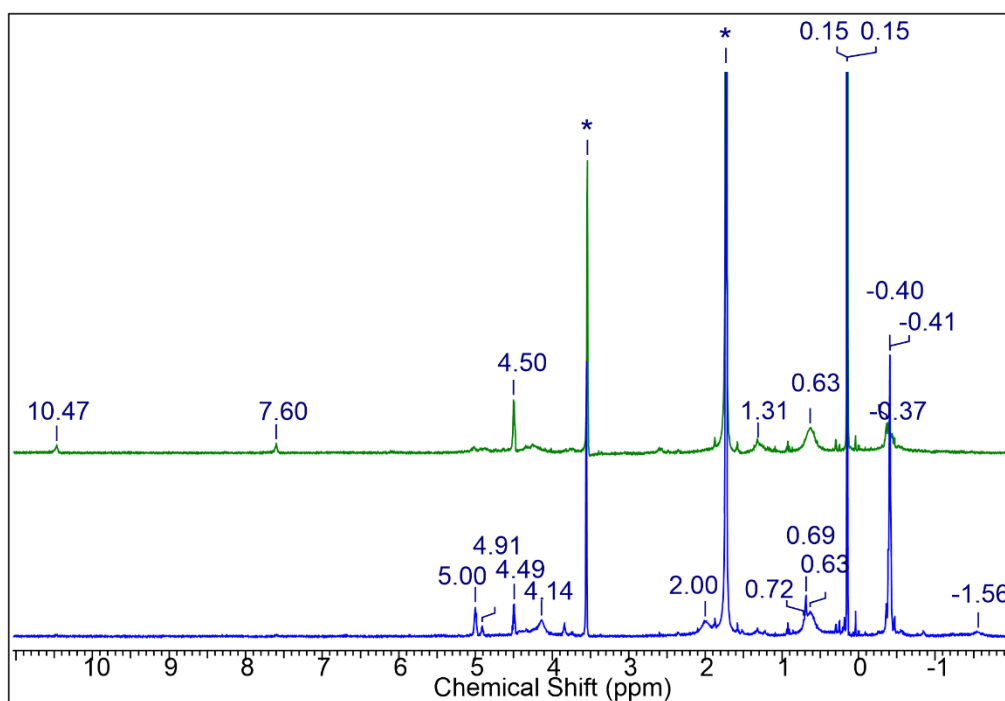
Figure S40. ^{1}H NMR spectrum (400.13 MHz, THF-d_8, 26 °C) of the reaction of [Ce{N(SiHMe$_2$)$_2$}$_3$]$_2$ with tetramethyl-1,4-benzoquinone recorded after 10 min (blue, bottom) and after 24 h (green, top).
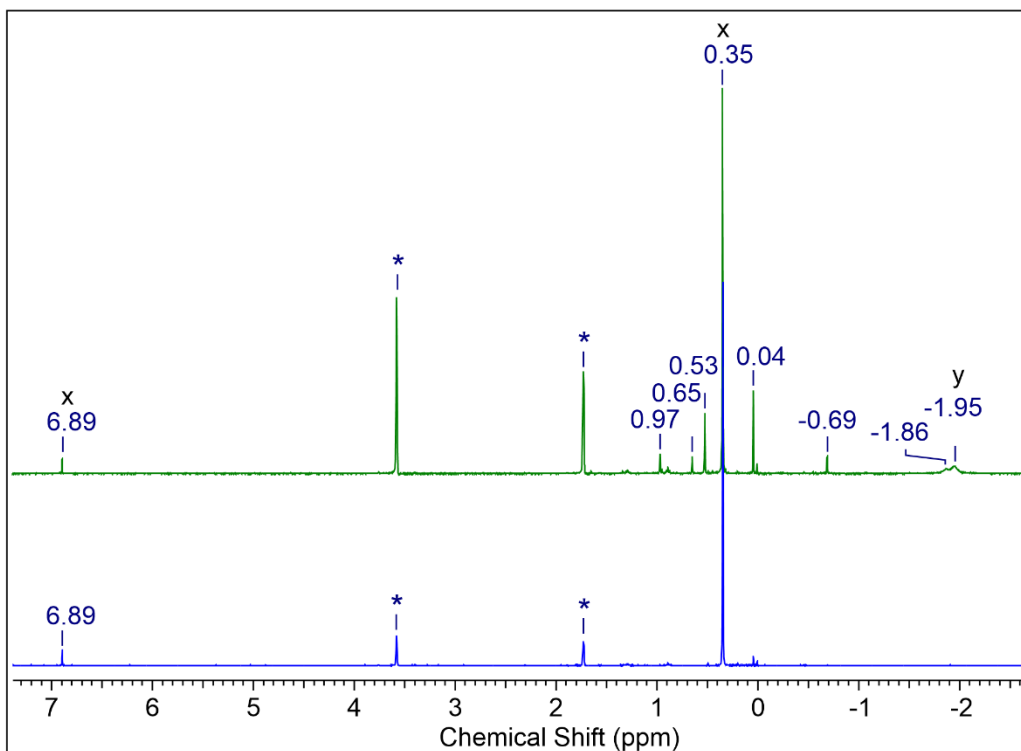
Figure S41. ^{1}H NMR spectrum (400.13 MHz, THF-d_8, 26 °C) of **4^{hq}** recorded after 10 min (blue, bottom) and after 24 h (green, top). Signals assigned to **4^{hq}** and co-product Ce[N(SiMe$_3$)$_2$]$_3$ are marked with x and y.

IR Spectra
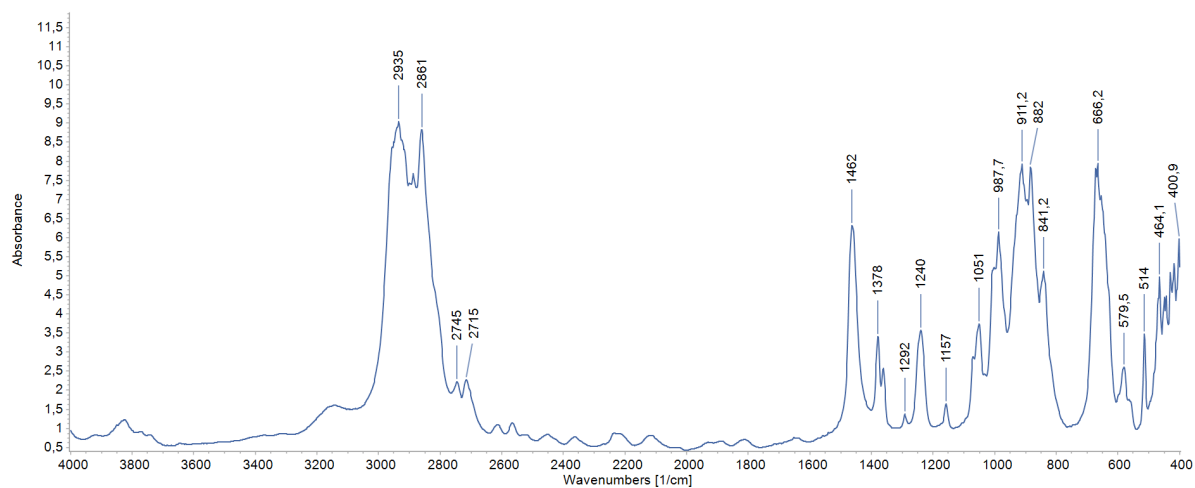
Figure S42. DRIFT spectrum of [Ce{(OSi*i*Pr$_3$)$_3$]$_2$ (**3**) at 25 °C.
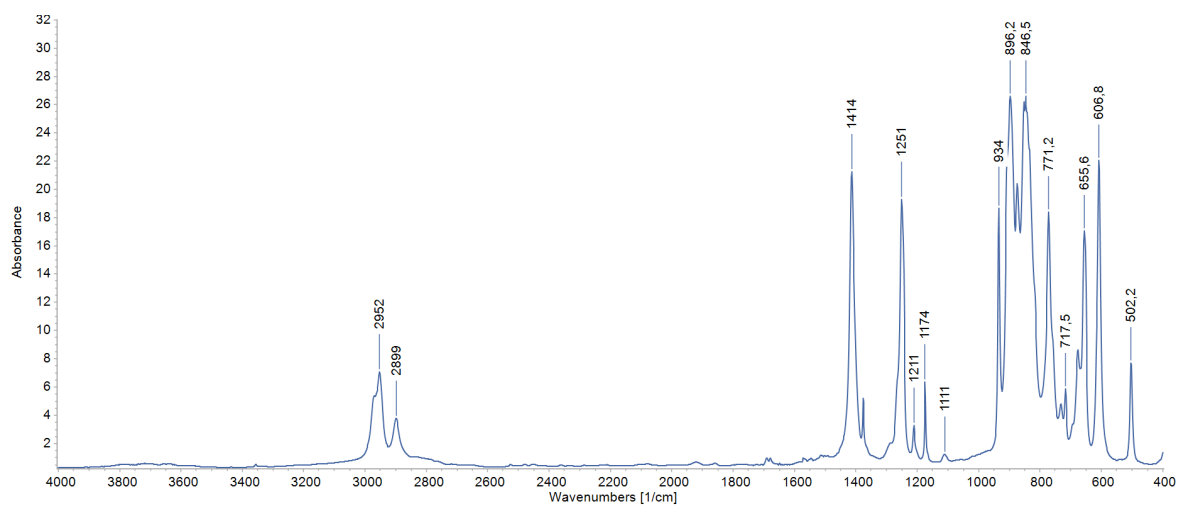
Figure S43. DRIFT spectrum of [Ce{N(SiMe$_3$)$_2$}$_3$]$_2$(μ_2-O$_2$C$_6$Cl$_4$) (**4^{Cl4hq}**) at 25 °C.
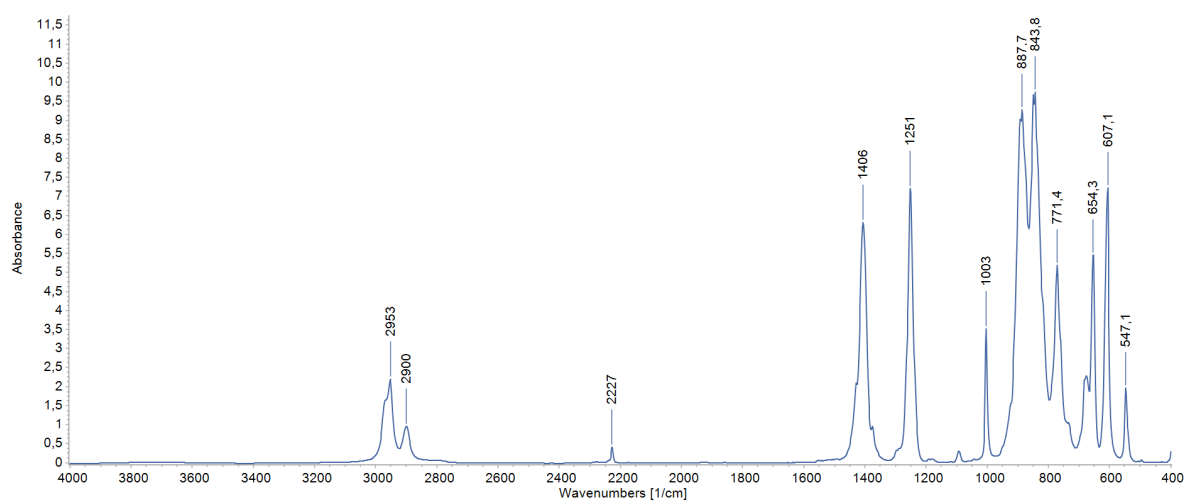
Figure S44. DRIFT spectrum of [Ce{N(SiMe$_3$)$_2$}$_3$]$_2$(μ_2-O$_2$C$_6$Cl$_2$(CN)$_2$) (**4^{ddhq}**) at 25 °C.
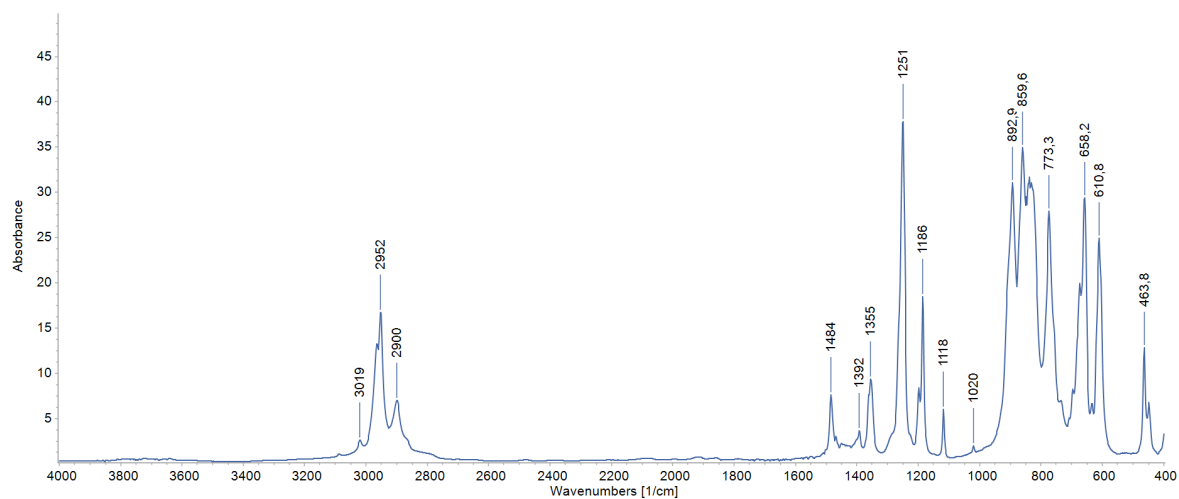
Figure S45. DRIFT spectrum of [Ce{N(SiMe$_3$)$_2$}$_3$]$_2$(μ_2-O$_2$C$_6$$tBu_2H_2$) (**4^{tBu2hq}**) at 25 °C.

Figure S46. DRIFT spectrum of [Ce{N(SiMe$_3$)$_2$}$_3$]$_2$(μ_2-O$_2$C$_6$Me$_4$) (**4^{Me4hq}**) at 25 °C.

Figure S47. DRIFT spectrum of [Ce{N(SiMe$_3$)$_2$}$_3$]$_2$(μ_2-O$_2$C$_{10}$H$_6$) (**4^{nq}**) at 25 °C.

Figure S48. DRIFT spectrum of [Ce{OSi(O*t*Bu)$_3$}$_3$(thf)]$_2$(μ_2-O$_2$C$_6$H$_4$) (**5^{hq}**) at 25 °C.

Figure S49. DRIFT spectrum of [Ce{OSi(O*t*Bu)$_3$}$_3$(thf)]$_2$(μ_2-O$_2$C$_6$Cl$_4$) (**5^{Cl4hq}**) at 25 °C.

Figure S50. DRIFT spectrum of [Ce{OSi(O*t*Bu)$_3$}$_3$(thf)]$_2$(μ_2-O$_2$C$_6$Cl$_2$(CN)$_2$) (**5^{ddhq}**) at 25 °C.

Figure S51. DRIFT spectrum of [Ce(OSi*i*Pr$_3$)$_3$(thf)]$_2$(μ_2-O$_2$C$_6$H$_4$) (**6^{hq}**) at 25 °C.

Figure S52. DRIFT spectrum of [Ce(OSi*i*Pr$_3$)$_3$(thf)]$_2$(μ_2-O$_2$C$_6$Cl$_4$) (**6^{Cl4hq}**) at 25 °C.

Figure S53. DRIFT spectrum of [Ce(OSi*i*Pr$_3$)$_3$(thf)]$_2$(μ_2-O$_2$C$_6$Cl$_2$(CN)$_2$) (**6^{ddhq}**) at 25 °C.

Figure S54. DRIFT spectrum of [Ce(OSi*i*Pr$_3$)$_3$(thf)]$_2$(μ_2-O$_2$C$_6$*t*Bu$_2$H$_2$) (**6^{tBu2hq}**) at 25 °C.

Figure S55. DRIFT spectrum of [(Ce{N(SiMe$_3$)$_2$}$_3$)$_2$(μ_2-O$_2$C$_6$H$_4$)][CoCp$_2$]$_2$ (**7**) at 25 °C.

Figure S56. DRIFT spectrum of [Ce{OSi(O*t*Bu)$_3$}$_2$(thf)$_2$(μ_2-O$_2$C$_6$Me$_4$)]$_2$ (**8**) at 25 °C.

Figure S57. DRIFT spectrum of [(Ce(OSi*i*Pr$_3$)$_2$(thf)$_2$(μ_2-O$_2$C$_6$Me$_4$)]$_2$ (**9**) at 25 °C.
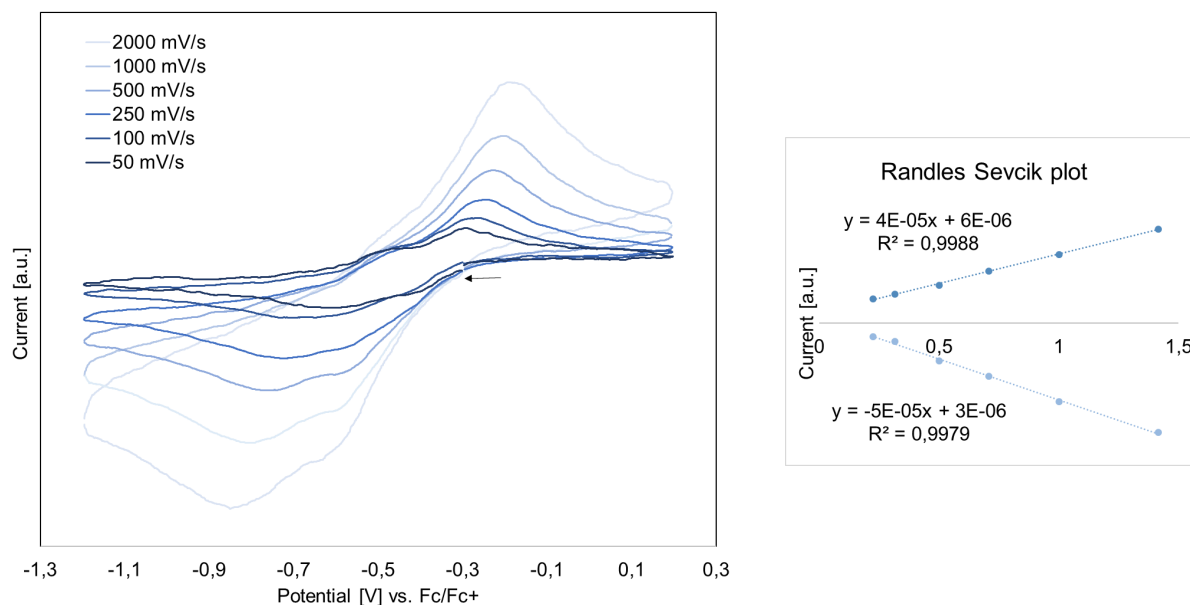
Cyclic voltammetry measurements

Figure S58. left: Cerium(III/IV) redox couple of complex **4^{hq}** in THF at ambient temperature and varying scan rates; right: corresponding Randles Sevcik plot of the anodic (top) and cathodic (bottom) redox features.

Table S1. Electrochemical data for the redox couples vs Fc/Fc$^+$ of complex **4^{hq}** in THF at ambient temperature.
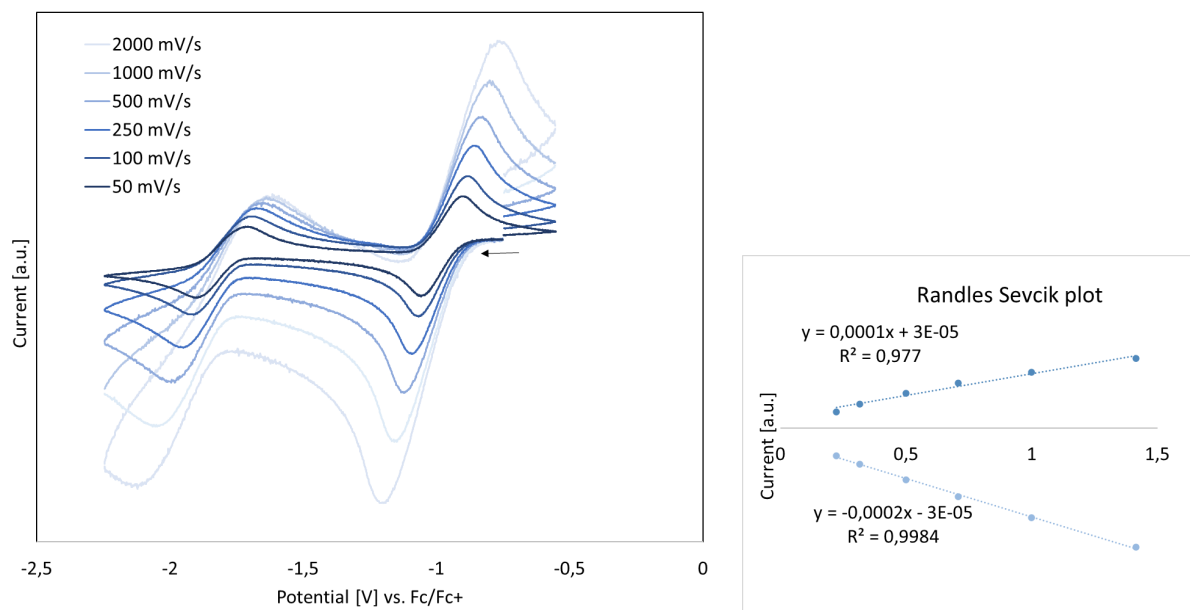
scan rate	E$_{1pa}$ [V]	E$_{2pa}$ [V]	E$_{1pc}$ [V]	E$_{2pc}$ [V]	ΔE$_{2pa/2pc}$ [V]	i$_{pa}$/i$_{pc}$
50 mV/s	-	−0.558	−0.699	−0.966	0.408	0.92
100 mV/s	-	−0.544	−0.728	−0.999	0.455	0.98
250 mV/s	-	−0.521	−0.781	−1.036	0.515	0.93
500 mV/s	-	−0.503	−0.794	−1.078	0.575	0.91
1000 mV/s	-	−0.486	−0.815	−1.182	0.696	0.84
2000 mV/s	-	−0.463	−0.835	−1.186	0.723	0.78

Figure S59a. left: Cerium(III/IV) redox couple of complex **4^{Cl4hq}** in THF at ambient temperature and varying scan rates; right: corresponding Randles Sevcik plot of the anodic (top) and cathodic (bottom) redox features.

Table S2a. Electrochemical data for the redox couples vs Fc/Fc$^+$ of complex **4^{Cl4hq}** in THF at ambient temperature.

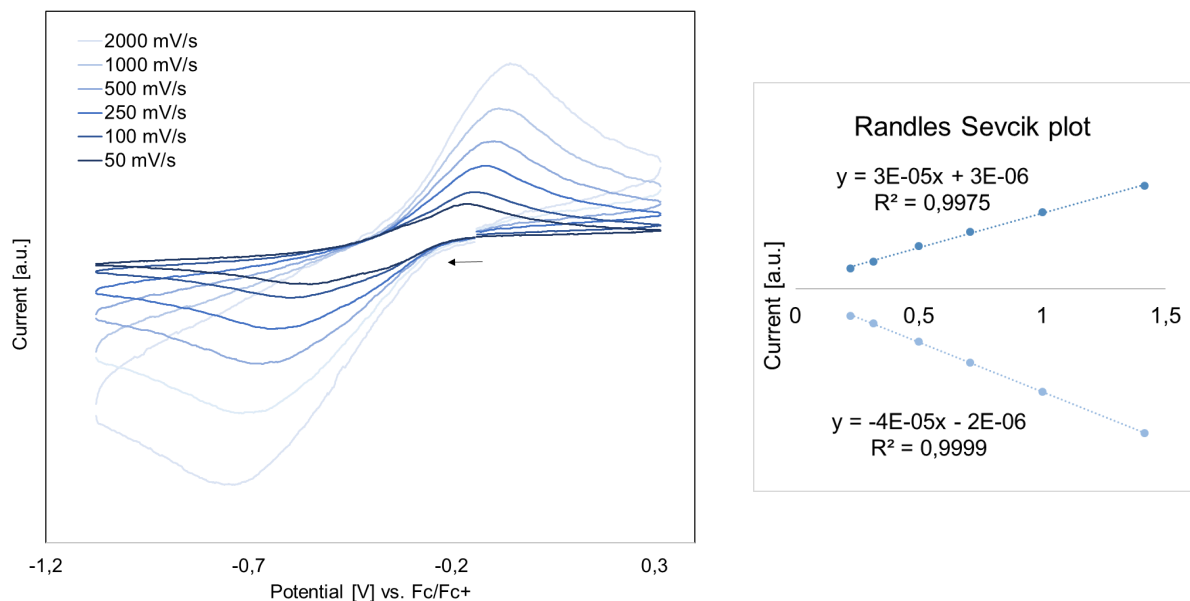| scan rate	E_{1pa} [V]	E_{2pa} [V]	E_{1pc} [V]	E_{2pc} [V]	$\Delta E_{2pa/2pc}$ [V]	i_{pa}/i_{pc}
50 mV/s	-	−0.290	−0.415	−0.624	0.334	0.90
100 mV/s	-	−0.260	−0.437	−0.728	0.468	0.91
250 mV/s	-	−0.247	−0.576	−0.726	0.479	0.70
500 mV/s	-	−0.228	−0.582	−0.771	0.543	0.76
1000 mV/s	-	−0.205	−0.597	−0.805	0.600	0.74
2000 mV/s	-	−0.194	−0.626	−0.849	0.655	0.77

Figure 59b. left: redox couple of tetrachloro-1,4-benzoquinone in THF at ambient temperature and varying scan rates; right: corresponding Randles Sevcik plot of the anodic (top) and cathodic (bottom) redox features.

Table S2b. Electrochemical data for the redox couples vs Fc/Fc$^+$ of complex tetrachloro-1,4-benzoquinone in THF at ambient temperature.

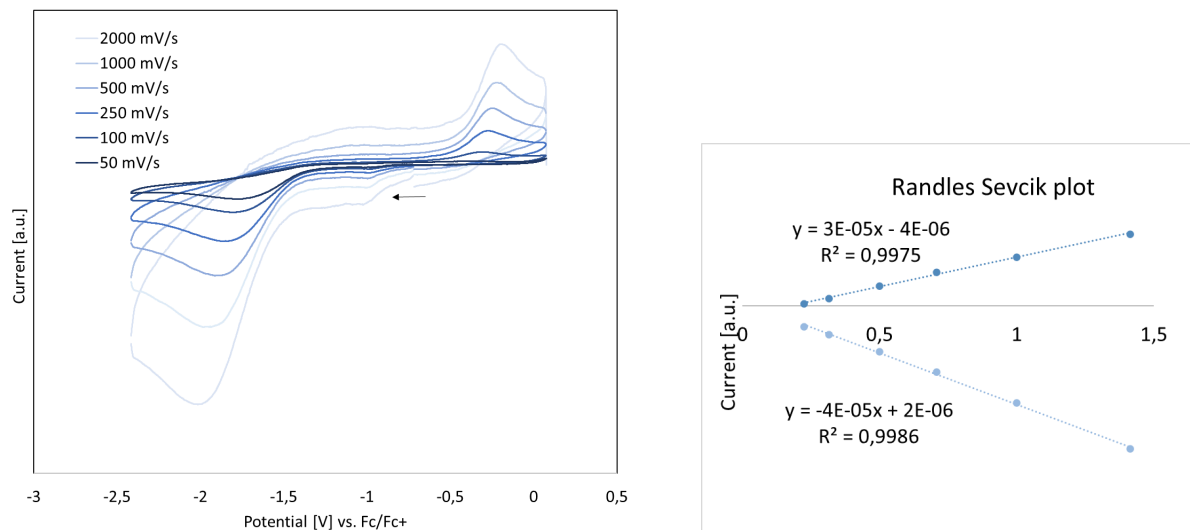| scan rate	E_{1pa} [V]	E_{2pa} [V]	E_{1pc} [V]	E_{2pc} [V]	$\Delta E_{2pa/2pc}$ [V]	i_{pa}/i_{pc}
50 mV/s	−0.4785	−1.304	−0.6735	−1.499	0.208	0.21
100 mV/s	−0.4645	−1.29	−0.6815	−1.507	0.234	0.30
250 mV/s	−0.4505	−1.276	−0.7195	−1.545	0.287	0.29
500 mV/s	−0.4185	−1.244	−0.7515	−1.577	0.332	0.26
1000 mV/s	−0.4085	−1.234	−0.8195	−1.645	0.409	0.22
2000 mV/s	−0.3855	−1.211	−0.8925	−1.718	0.526	0.18

Figure S60. left: Cerium(III/IV) redox couple of complex **4^{ddhq}** in THF at ambient temperature and varying scan rates; right: corresponding Randles Sevcik plot of the anodic (top) and cathodic (bottom) redox features.

Table S3. Electrochemical data for the redox couples vs Fc/Fc$^+$ of complex **4^{ddhq}** in THF at ambient temperature.
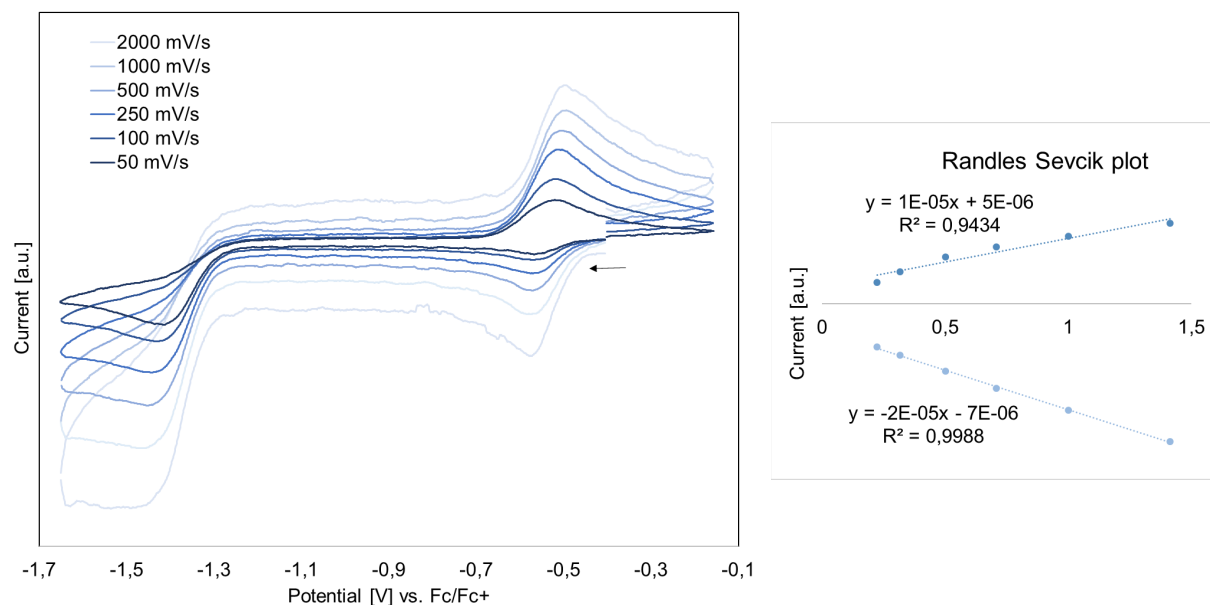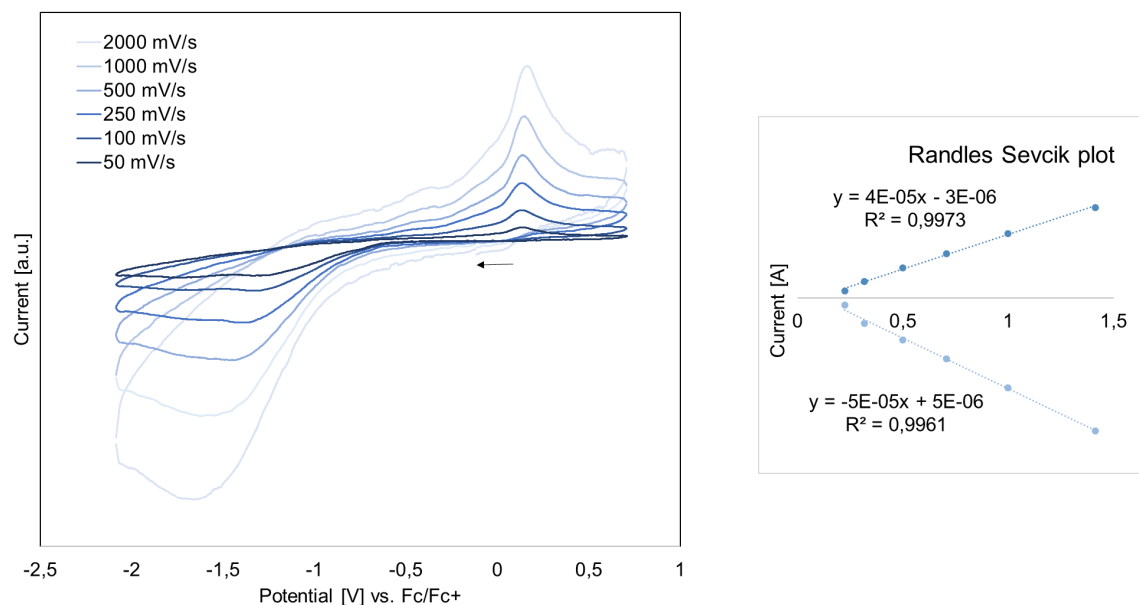
scan rate	E$_{1pa}$ [V]	E$_{2pa}$ [V]	E$_{1pc}$ [V]	E$_{2pc}$ [V]	ΔE$_{2pa/2pc}$ [V]	i$_{pa}$/i$_{pc}$
50 mV/s	-	−0.1685	-	−0.5455	0.377	0.78
100 mV/s	-	−0.1405	-	−0.5965	0.456	0.80
250 mV/s	-	−0.1165	-	−0.6495	0.533	0.82
500 mV/s	-	−0.1005	-	−0.6655	0.565	0.78
1000 mV/s	-	−0.0835	-	−0.7155	0.632	0.75
2000 mV/s	-	−0.0555	-	−0.7355	0.680	0.72

Figure S61. left: Cerium(III/IV) redox couple of complex **5^{hq}** in THF at ambient temperature and varying scan rates; right: corresponding Randles Sevcik plot of the anodic (top) and cathodic (bottom) redox features.

Table S4. Electrochemical data for the redox couples vs Fc/Fc$^+$ of complex **5^{hq}** in THF at ambient temperature.
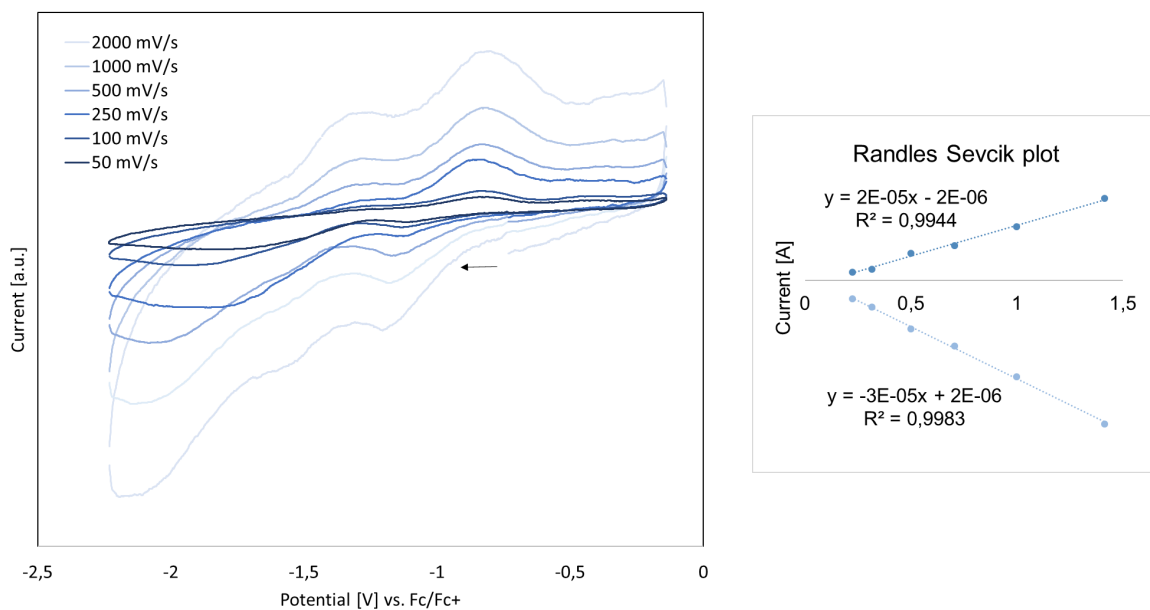
scan rate	E$_{1pa}$ [V]	E$_{2pa}$ [V]	E$_{1pc}$ [V]	E$_{2pc}$ [V]	ΔE$_{2pa/2pc}$ [V]	i$_{pa}$/i$_{pc}$
50 mV/s	-	−0.3625	-	−1.7785	1.416	0.11
100 mV/s	-	−0.3095	-	−1.8105	1.501	0.27
250 mV/s	-	−0.2725	-	−1.8425	1.57	0.44
500 mV/s	-	−0.2495	-	−1.9125	1.663	0.51
1000 mV/s	-	−0.2255	-	−1.9795	1.754	0.51
2000 mV/s	-	−0.1925	-	−2.0145	1.822	0.50

Figure S62. left: Cerium(III/IV) redox couple of complex **5^{Cl4hq}** in THF at ambient temperature and varying scan rates; right: corresponding Randles Sevcik plot of the anodic (top) and cathodic (bottom) redox features. The reductive feature at ~ −0.5 V results of a minor impurity of the sample.

Table S5. Electrochemical data for the redox couples vs Fc/Fc$^+$ of complex **5^{Cl4hq}** in THF at ambient temperature.

scan rate	E$_{1pa}$ [V]	E$_{2pa}$ [V]	E$_{1pc}$ [V]	E$_{2pc}$ [V]	ΔE$_{2pa/2pc}$ [V]	i$_{pa}$/i$_{pc}$
50 mV/s	-	−0.5205	-	−1.4135	0.893	0.49
100 mV/s	-	−0.5175	-	−1.4335	0.916	0.63
250 mV/s	-	−0.5155	-	−1.4435	0.928	0.70
500 mV/s	-	−0.5075	-	−1.4535	0.946	0.67
1000 mV/s	-	−0.4935	-	−1.4715	0.978	0.64
2000 mV/s	-	−0.4975	-	−1.5355	1.038	0.59

Figure S63. left: Cerium(III/IV) redox couple of complex **5^{ddhq}** in THF at ambient temperature and varying scan rates; right: corresponding Randles Sevcik plot of the anodic (top) and cathodic (bottom) redox features.

Table S6. Electrochemical data for the redox couples vs Fc/Fc$^+$ of complex **5^{ddhq}** in THF at ambient temperature.
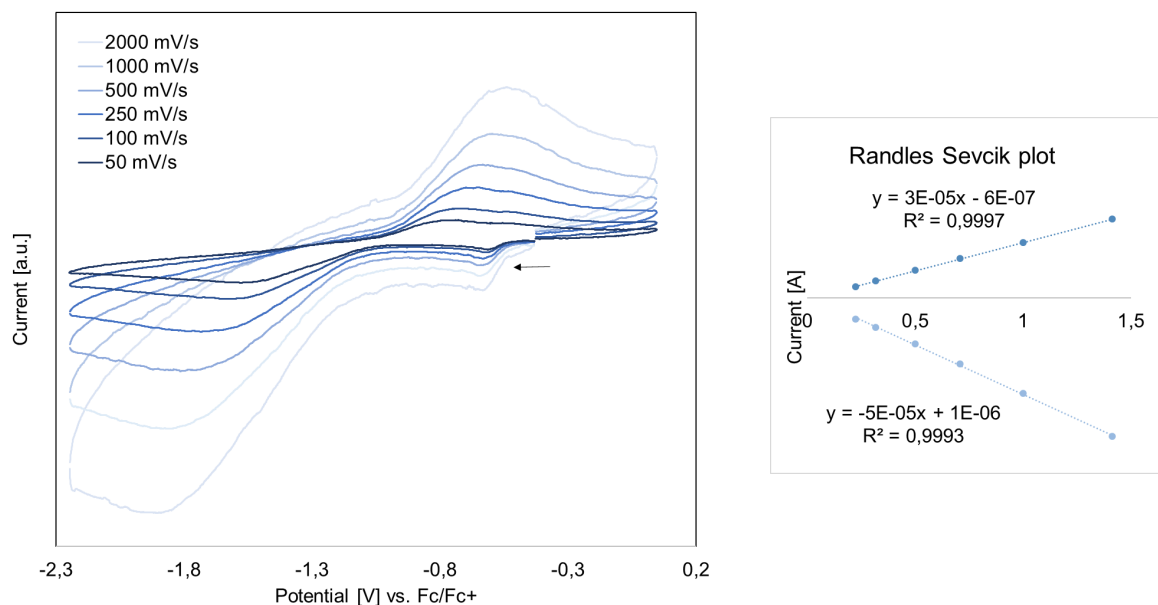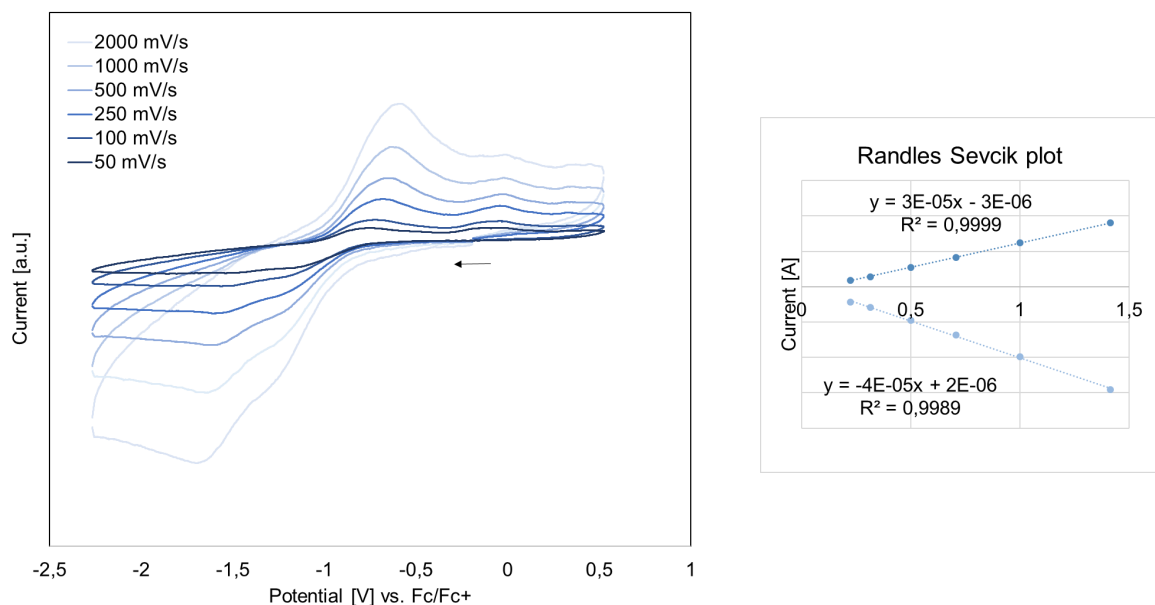
scan rate	E_{1pa} [V]	E_{2pa} [V]	E_{1pc} [V]	E_{2pc} [V]	$\Delta E_{2pa/2pc}$ [V]	i_{pa}/i_{pc}
50 mV/s	-	0.130	-	−1.353	1.483	0.95
100 mV/s	-	0.131	-	−1.312	1.443	0.63
250 mV/s	-	0.138	-	−1.394	1.532	0.72
500 mV/s	-	0.138	-	−1.434	1.572	0.73
1000 mV/s	-	0.150	-	−1.570	1.720	0.72
2000 mV/s	-	0.166	-	−1.646	1.812	0.68

Figure S64. left: Cerium(III/IV) redox couple of complex **6^{hq}** in THF at ambient temperature and varying scan rates; right: corresponding Randles Sevcik plot of the anodic (top) and cathodic (bottom) redox features.

Table S7. Electrochemical data for the redox couples vs Fc/Fc$^+$ of complex **6^{hq}** in THF at ambient temperature.
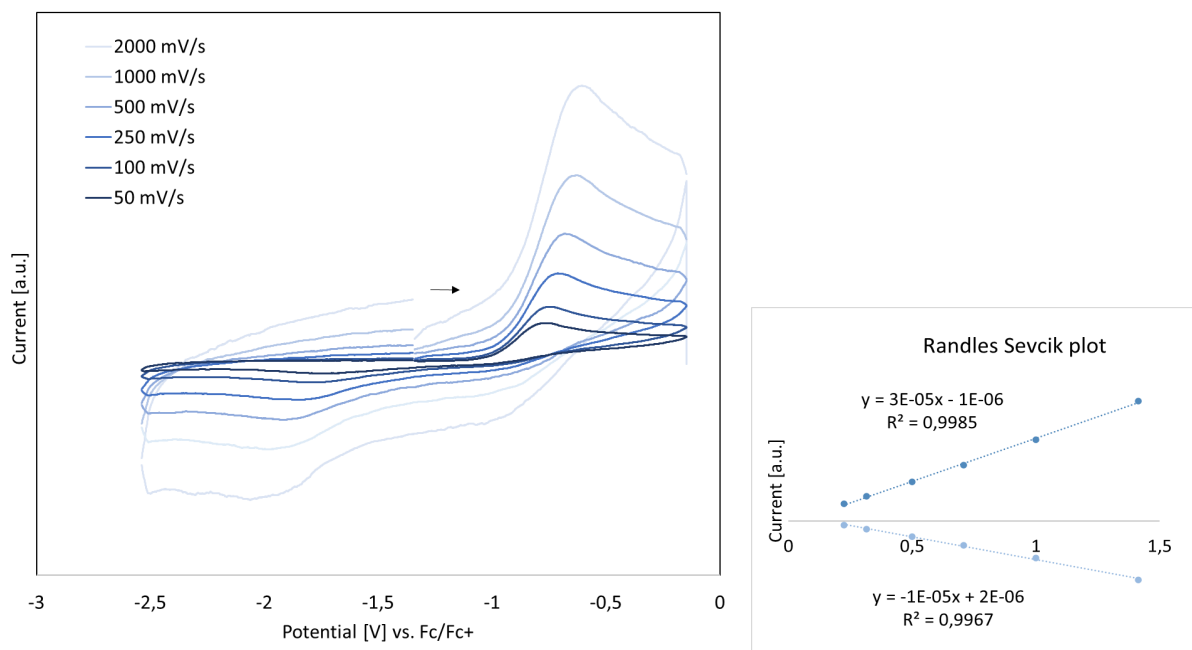
scan rate	E$_{1pa}$ [V]	E$_{2pa}$ [V]	E$_{1pc}$ [V]	E$_{2pc}$ [V]	ΔE$_{2pa/2pc}$ [V]	i$_{pa}$/i$_{pc}$
50 mV/s	−1.273	−0.817	−1.116	−1.816	0.999	0.43
100 mV/s	−1.274	−0.835	−1.131	−1.969	1.134	0.42
250 mV/s	−1.292	−0.840	−1.146	−2.075	1.021	0.55
500 mV/s	−1.300	−0.825	−1.167	−2.081	1.256	0.53
1000 mV/s	−1.306	−0.810	−1.172	−2.145	1.335	0.55
2000 mV/s	−1.312	−0.800	−1.204	−2.193	1.393	0.57

Figure S65. left: Cerium(III/IV) redox couple of complex **6^{Cl4hq}** in THF at ambient temperature and varying scan rates; right: corresponding Randles Sevcik plot of the anodic (top) and cathodic (bottom) redox features. The reductive feature at ~ −0.5 V results of a minor impurity of the sample.

Table S8. Electrochemical data for the redox couples vs Fc/Fc$^+$ of complex **6^{Cl4hq}** in THF at ambient temperature.

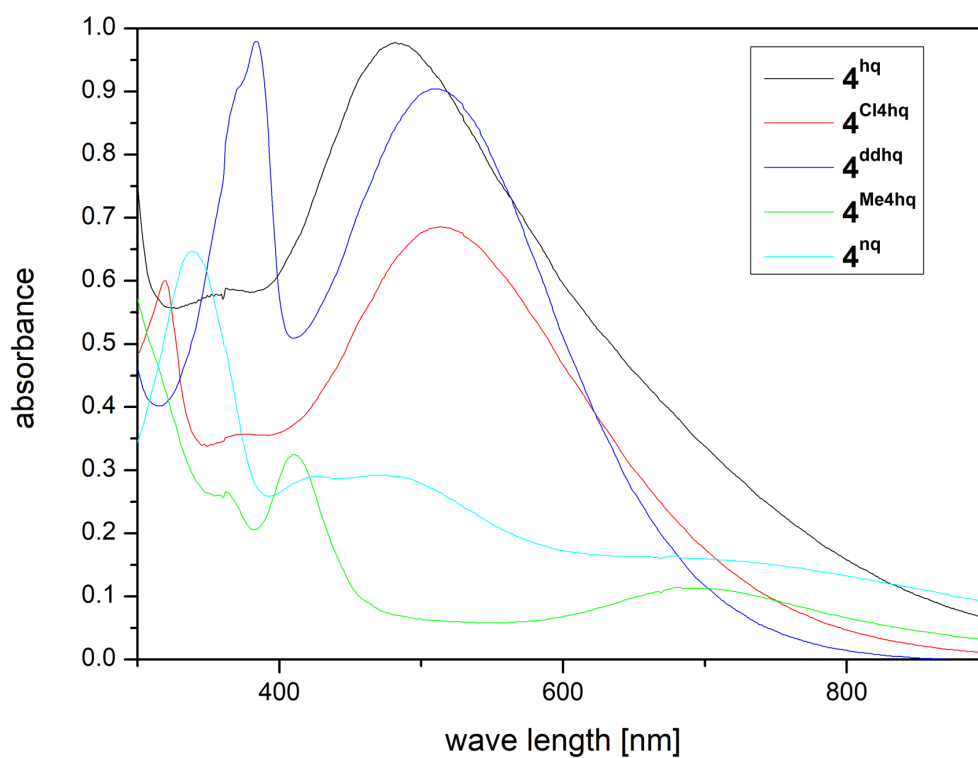| scan rate	E$_{1pa}$ [V]	E$_{2pa}$ [V]	E$_{1pc}$ [V]	E$_{2pc}$ [V]	ΔE$_{2pa/2pc}$ [V]	i$_{pa}$/i$_{pc}$
50 mV/s	-	−0.729	-	−1.580	0.851	0.52
100 mV/s	-	−0.715	-	−1.640	0.925	0.57
250 mV/s	-	−0.654	-	−1.736	1.082	0.60
500 mV/s	-	−0.633	-	−1.816	1.183	0.59
1000 mV/s	-	−0.597	-	−1.880	1.283	0.57
2000 mV/s	-	−0.542	-	−1.905	1.363	0.57

Figure S66. left: Cerium(III/IV) redox couple of complex **6ᵈᵈʰ𐞥** in THF at ambient temperature and varying scan rates; right: corresponding Randles Sevcik plot of the anodic (top) and cathodic (bottom) redox features.

Table S9. Electrochemical data for the redox couples vs Fc/Fc⁺ of complex **6ᵈᵈʰ𐞥** in THF at ambient temperature.
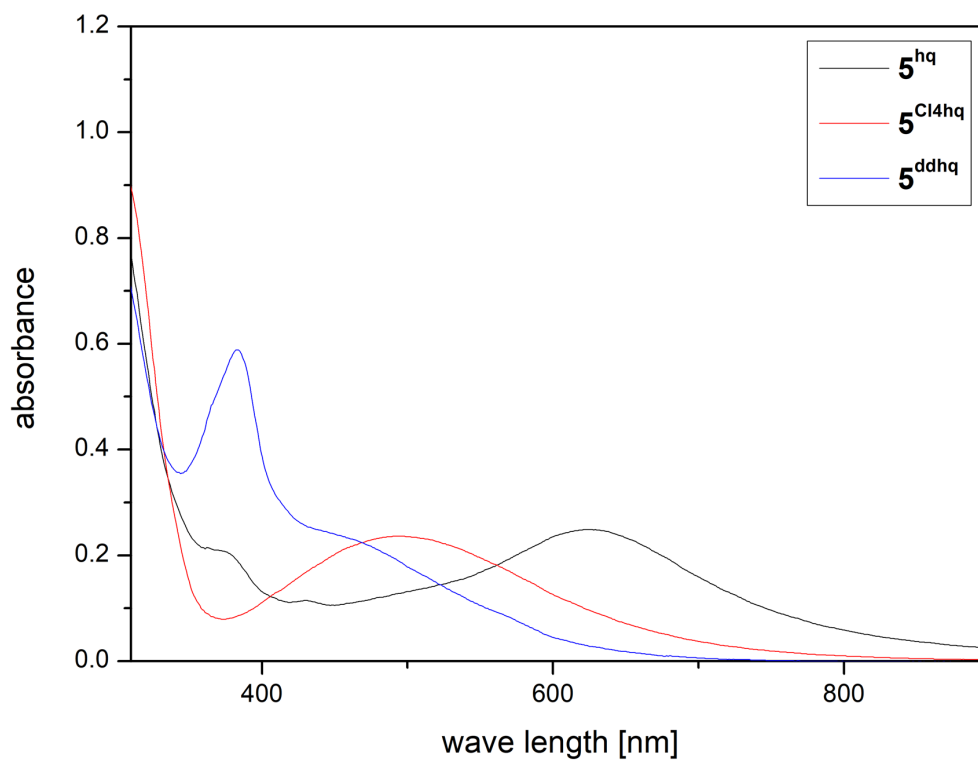
scan rate	E_{1pa} [V]	E_{2pa} [V]	E_{1pc} [V]	E_{2pc} [V]	$\Delta E_{2pa/2pc}$ [V]	i_{pa}/i_{pc}
50 mV/s	-	−0.751	−1.149	−1.484	0.733	0.40
100 mV/s	-	−0.721	−1.186	−1.565	0.844	0.48
250 mV/s	-	−0.682	−1.210	−1.609	0.927	0.58
500 mV/s	-	−0.665	−1.232	−1.619	0.954	0.60
1000 mV/s	-	−0.624	−1.252	−1.649	1.025	0.62
2000 mV/s	-	−0.592	−1.259	−1.695	1.103	0.62

Figure S67. left: Cerium(III/IV) redox couple of complex **3** in THF at ambient temperature and varying scan rates; right: corresponding Randles Sevcik plot of the anodic (top) and cathodic (bottom) redox features.

Table S10. Electrochemical data for the redox couples vs Fc/Fc$^+$ of complex **3** in THF at ambient temperature.

scan rate	E_{pa} [V]	E_{pc} [V]	$\Delta E_{pa/pc}$ [V]	i_{pa}/i_{pc}
50 mV/s	−0.605	−1.757	1.152	0.232
100 mV/s	−0.633	−1.799	1.166	0.315
250 mV/s	−0.680	−1.850	1.170	0.395
500 mV/s	−0.712	−1.919	1.207	0.428
1000 mV/s	−0.746	−1.972	1.226	0.451
2000 mV/s	−0.778	−2.061	1.283	0.487

UV/Vis spectra

Figure S68. UV/Vis spectra of **4^{hq}**, **4^{Cl4hq}**, **4^{ddhq}**, **4^{Me4hq}** and **4^{nhq}** in toluene at ambient temperature. The strong absorption band of **4^{nhq}** at 339 nm may refer to 1,4-naphthoquinone.[8]

Figure S69. UV/Vis spectra of **5^{hq}**, **5^{Cl4hq}** and **5^{ddhq}** in toluene at ambient temperature.

Figure S70. UV/Vis spectra of **6**^{hq}, **6**^{Cl4hq} and **6**^{ddhq} in toluene at ambient temperature. Due to its insolubility in toluene, **6**^{hq} was measured in THF.

EPR Spectra

Figure S71. X-Band cw-EPR spectrum of crystalline [Ce{OSi(OtBu)3}2(thf)2(μ_2-O2C6Me4)]2 (**8**) (microwave frequency = 9.315802 GHz, microwave power = 0.6325 mW, modulation amplitude = 0.2 mT, T = 123 K).

Figure S72. X-Band cw-EPR spectrum of crystalline [Ce(OSiiPr3)2(thf)2)(μ_2-O2C6Me4)]2 (**9**) (microwave frequency = 9.313522 GHz, microwave power = 0.6325 mW, modulation amplitude = 0.5 mT, T = 123 K).

Figure S73. X-Band cw-EPR spectrum of [Ce{OSi(O*t*Bu)$_3$}$_3$]$_2$ (**2**) in a frozen 2-Me-THF solution. Signal at 150 mT: microwave frequency = 9.37951 GHz, microwave power = 0.1262 mW, modulation amplitude = 0.06 mT, T = 77 K; Signal at 330 mT: microwave frequency = 9.380779 GHz, microwave power = 0.1262 mW, modulation amplitude = 0.5 mT, T = 77 K.

Crystallography

Crystals for X-ray crystallography were grown using saturated solutions of *n*-hexane (**3**), mixtures of *n*-hexane/toluene (**4**$^{\text{Cl4hq}}$, **4**$^{\text{ddhq}}$, **4**$^{\text{Me4hq}}$, **4**$^{t\text{Buhq}}$, **4**$^{\text{nhq}}$), THF (**5**$^{\text{Cl4hq}}$, **6**$^{\text{Cl4hq}}$, **6**$^{\text{ddhq}}$, **6**$^{t\text{Buhq}}$, **8**, **9**), THF-*d*$_8$ (**7**) or 2-methyltetrahydrofuran (**5**$^{\text{hq}}$), toluene (**[Ce$_3$(bpad)(pasq)(Me$_2$pz)$_6$(thf)]**), THF/*n*-hexane mixture (**[Ce(Me$_2$pz)$_2$(thf)$_2$(asq)]$_2$**), or cyclohexane/toluene mixture (**[Ce(*t*Bu$_2$pz)$_3$]$_2$(μ_2-O$_2$C$_6$Me$_4$)**). Note: crystals of **5**$^{\text{hq}}$ weren´t of sufficient quality for structural characterisation, but crystals suitable for X-ray diffraction analysis were obtained from 2-methyl-THF giving [(Ce{OSi(O*t*Bu)$_3$}$_3$(2-Methf))$_2$(μ_2-O$_2$C$_6$H$_4$)] (**5**$^{\text{hq}}$·**2MeTHF**).Suitable crystals for X-ray analysis were handpicked in a glovebox, coated with Parabar 10312 and stored on microscope slides. Data collection was done on a *Bruker* APEX II Duo diffractometer by using QUAZAR optics and Mo K$_\alpha$ ($\lambda = 0.71073$ Å). The data collection strategy was determined using COSMO[9] employing ω scans. Raw data were processed by APEX[10] and SAINT,[11] corrections for absorption effects were applied using SADABS.[12] The structures were solved by direct methods and refined against all data by full-matrix least-squares methods on F^2 using SHELXTL[12] and SHELXLE or OLEX2.[13,14] All non-hydrogen atoms were refined anisotropically. The disorders of the solvent molecules or *tert*-butyl groups were modelled using DSR,[15] a program to refinement of disordered structures with SHELXL. Plots were generated by using CCDC Mercury 3.19.1.[16] Further details regarding the refinement and crystallographic data are listed in Table S11 and in the CIF files. Highly disordered solvent within the lattice, identified as toluene (**4**$^{\text{ddhq}}$) and THF (**7**) were removed through application of the SQUEEZE program suite in PLATON.[17]

Crystallographic Data (CCDC#)

Table S11. Crystallographic data for compounds **3**, **4**[Cl4hq], **4**[ddhq] and **4**[Me4hq]

	3	**4**[Cl4hq]	**4**[ddhq]	**4**[Me4hq]
CCDC	2022461	2022465	2022472	2022473
formula	$C_{54}H_{126}Ce_2O_6Si_6$	$C_{42}H_{108}Ce_2Cl_4N_6O_2Si_{12}$	$C_{44}H_{108}Ce_2Cl_2N_8O_2Si_{12}$	$C_{46}H_{120}Ce_2N_6O_2Si_{12}$
M [g·mol⁻¹]	1320.32	1488.46	1469.60	1406.79
λ [Å]	0.71073	0.71073	0.71073	0.71073
colour	colourless	brown	black	brown
crystal dimensions [mm]	0.341 × 0.315 × 0.223	0.20 × 0.10 × 0.05	0.195 × 0.136 × 0.074	0.40 × 0.32 × 0.23
crystal system	monoclinic	monoclinic	monoclinic	monoclinic
space group	P2₁/n	P2₁/n	C2/c	C2/c
a [Å]	12.6609(5)	10.8680(16)	24.8116(11)	24.645(6)
b [Å]	23.0055(9)	16.755(2)	21.7940(10)	22.211(6)
c [Å]	12.7568(5)	20.149(3)	17.4764(8)	17.381(4)
α [°]	90	90	90	90
β [°]	109.4400(10)	90.235(4)	116.6590(10)	116.237(3)
γ [°]	90	90	90	90
V [Å³]	3503.8(2)	3668.9(9)	8445.6(7)	8534(4)
Z	2	2	4	4
F(000)	1396	1540	3048	2952
T [K]	180(2)	150(2)	100(2)	150(2)
ρcalcd [g·cm⁻³]	1.251	1.347	1.156	1.095
μ[mm⁻¹]	1.424	1.601	1.330	1.252
Data / restraints / parameters	9459 / 0 / 355	7343 / 0 / 326	10463 / 12 / 361	7314 / 0 / 327
Goodness of fit	1.039	1.034	1.037	1.090
R₁ (I > 2σ (I))[a]	0.0256	0.0488	0.0289	0.0625
ωR₂ (all data)[b]	0.0631	0.0949	0.0688	0.1511

[a] $R_1 = \Sigma(||F0|-|Fc||)/\Sigma|F0|, F0 > 4s(F0)$. [b] $\omega R_2 = \{\Sigma[w(F0^2-Fc^2)2/\Sigma[w(F0^2)^2]\}^{1/2}$.

Table S11 continued. Crystallographic data for compounds **4^{*t*Bu2hq}**, **4^{nhq}**, **5^{hq}** and **5^{Cl4hq}**

	4^{*t*Bu2hq}	**4^{nhq[c]}**	**5^{hq}**	**5^{Cl4hq}**
CCDC	2022468		2022470	2022476
formula	$C_{57}H_{136}Ce_2N_6O_2$ Si_{12}	$C_{46}H_{114}Ce_2N_6O_2$ Si_{12}	$C_{97.07}H_{204.13}$ $Ce_2O_{30}Si_6$	$C_{90}H_{186}Ce_2Cl_4$ $O_{29}Si_6$
M [g·mol⁻¹]	1555.03	1400.75	2300.34	2322.96
λ [Å]	0.71073	0.71073	0.71073	0.71073
colour	brown	brown	dark purple	purple
crystal dimensions [mm]	0.10 × 0.05 × 0.01		0.281 × 0.167 × 0.126	0.252 × 0.202 × 0.088
crystal system	triclinic	monoclinic	triclinic	orthorhombic
space group	P$\bar{1}$	P2/c	P$\bar{1}$	Pnna
a [Å]	11.4339(9)	20.343(7)	13.7919(11)	22.1584(19)
b [Å]	12.0881(10)	11.429(4)	14.0585(12)	41.418(4)
c [Å]	17.5236(14)	20.112(7)	20.0654(16)	13.4250(12)
α [°]	83.3194(13)	90	71.904(2)	90
β [°]	71.7094(12)	117.499(7)	81.904(2)	90
γ [°]	63.9637(11)	90	60.636(2)	90
V [Å³]	2065.6(3)	4148(2)	3222.7(5)	12320.8(19)
Z	1		1	4
F(000)	820		1227	4904
T [K]	150(2)		100(2)	100(2)
ρ_{calcd} [g·cm⁻³]	1.250		1.185	1.252
μ[mm⁻¹]	1.300		0.815	0.937
Data / restraints / parameters	8433 / 122 / 411		18242 / 307 / 710	13600 / 1893 / 896
Goodness of fit	1.004		1.021	1.108
R₁ (I > 2σ (I))[a]	0.0316	0.1508	0.0269	0.0527
ωR₂ (all data)[b]	0.0677	0.3537	0.0681	0.1280

[a] $R_1 = \Sigma(||F0|-|Fc||)/\Sigma|F0|, F0 > 4s(F0)$. [b] $\omega R_2 = \{\Sigma[w(F02-Fc2)2/\Sigma[w(F02)^2]\}^{1/2}$. [c] Connectivity only.

Table S11 continued. Crystallographic data for compounds **6[Cl4hq]**, **6[ddhq]**, **6[tBu2hq]** and **7**

	6[Cl4hq]	6[ddhq]	6[tBu2hq]	7
CCDC	2022471	2022467	2022466	2022474
formula	$C_{76}H_{158}Ce_2Cl_4O_{12}Si_6$	$C_{70}H_{142}Ce_2Cl_2N_2O_{10}Si_6$	$C_{76}H_{162}Ce_2O_{10}Si_6$	$C_{66}H_{132}Ce_2Co_2D_8N_6O_3Si_{12}$
M [g·mol⁻¹]	1854.59	1691.53	1684.83	1809.06
λ [Å]	0.71073	0.71073	0.71073	0.71073
colour	orange	orange	purple	brown
crystal dimensions [mm]	0.137 × 0.130 × 0.056	0.191 × 0.169 × 0.102	0.270 × 0.098 × 0.034	0.142 × 0.131 × 0.082
crystal system	monoclinic	monoclinic	triclinic	monoclinic
space group	P2₁/c	C2/c	P1̄	P2/n
a [Å]	11.2124(10)	18.228(5)	11.655(2)	11.7272(6)
b [Å]	12.5614(11)	17.588(4)	12.402(2)	20.2947(10)
c [Å]	34.289(3)	28.531(7)	17.499(3)	21.6422(11)
α [°]	90	90	92.596(3)	90
β [°]	97.212(2)	102.369(4)	93.946(3)	99.9900(10)
γ [°]	90	90	114.855(3)	90
V [Å³]	4791.2(7)	8935(4)	2281.9(7)	5072.7(4)
Z	2	4	1	2
F(000)	1956	3560	898	1880
T [K]	101(2)	100(2)	100(2)	100(2)
ρ_calcd [g·cm⁻³]	1.286	1.258	1.226	1.184
μ[mm⁻¹]	1.174	1.194	1.111	1.380
Data / restraints / parameters	12413 / 412 / 527	13667 / 138 / 495	10190 / 0 / 446	12529 / 214 / 501
Goodness of fit	1.015	1.096	1.027	1.010
R₁ (I > 2σ (I))[a]	0.0403	0.0459	0.0452	0.0395
ωR₂ (all data)[b]	0.0801	0.1268	0.0934	0.0863

[a] $R_1 = \Sigma(||F0|-|Fc||)/\Sigma|F0|, F0 > 4s(F0)$. [b] $\omega R_2 = \{\Sigma[w(F02-Fc2)2/\Sigma[w(F02)^2]\}^{1/2}$.

Table S11 continued. Crystallographic data for compounds **8**, **9**, **[Ce₃(bpad)(pasq)(Me₂pz)₆(thf)]**, **[Ce(Me₂pz)₂(thf)₂(asq)]₂** and **[Ce(*t*Bu₂pz)₃(thf)]₂(*μ₂*-O₂C₆Me₄)**

	8	9	[Ce₃(bpad) (pasq) (Me₂pz)₆(thf)]	[Ce(Me₂pz)₂ (thf)₂(asq)]₂	[Ce(*t*Bu₂pz)₃ (thf)]₂(*μ₂*- O₂C₆Me₄)
CCDC	2022469	2022475	2022464	2022462	2022463
formula	$C_{100}H_{196}Ce_2O_{28}Si_4$	$C_{72}H_{140}Ce_2O_{12}Si_4$	$C_{91}H_{103}Ce_3N_{18}O_5$	$C_{68}H_{84}Ce_2N_8O_9$	$C_{84}H_{142}Ce_2N_{12}O_4$
M [g·mol⁻¹]	2239.16	1590.43	1949.27	1437.67	1664.33
λ [Å]	0.71073	0.71073	0.71073	0.71073	0.71073
colour	clear blue	blue	clear colourless	turquoise	reddish brown
crystal dimensions [mm]	0.220 × 0.120 × 0.010	0.209 × 0.110 × 0.076	0.312 × 0.221 × 0.122	0.210 × 0.130 × 0.020	0.100 x 0.020 x 0.010
crystal system	monoclinic	monoclinic	triclinic	triclinic	monoclinic
space group	P2₁/c	P2₁/n	P1̄	P1̄	P2₁/n
a [Å]	20.8578(10)	11.29(4)	12.7863(16)	11.8590(14)	11.7195(4)
b [Å]	24.2951(10)	22.03(7)	18.594(2)	14.7713(18)	18.0849(7)
c [Å]	11.7354(5)	17.25(7)	18.631(2)	19.126(2)	21.3488(8)
α [°]	90	90	102.5253(19)	79.676(2)	4505.1(3)
β [°]	94.4068(11)	96.250(11)	90.9634(18)	76.075(2)	90
γ [°]	90	90	93.3308(18)	81.398(2)	95.3481(15)
V [Å³]	5929.2(5)	4265(27)	4314.7(9)	3179.2(7)	90
Z	2	2	2	2	2
F(000)	2384	1680	1978	1472	1756
T [K]	100(2)	100(2)	100(2)	100(2)	100(2)
ρ_calcd [g·cm⁻³]	1.254	1.238	1.500	1.502	1.227
μ[mm⁻¹]	0.864	1.160	1.619	1.477	1.049
Data / restraints / parameters	10454 / 792 / 740	9414 / 0 / 423	17755 / 273 / 1199	20302 / 0 / 792	8250 / 138 / 520
Goodness of fit	1.064	1.100	0.968	0.996	1.071
R₁ (I > 2σ (I))[a]	0.0539	0.0502	0.0410	0.0442	0.0417
ωR₂ (all data)[b]	0.1005	0.0960	0.0759	0.1024	0.0749

[a] $R_1 = \Sigma(||F0|-|Fc||)/\Sigma|F0|, F0> 4s(F0)$. [b] $\omega R_2 = \{\Sigma[w(F0^2-Fc^2)^2/\Sigma[w(F0^2)^2]\}^{1/2}$.

Figure S74. Crystal structure of [Ce{N(SiMe$_3$)$_2$}$_3$]$_2$(μ_2-O$_2$C$_6$Cl$_4$) (**4^{Cl4hq}**). Ellipsoids are shown at the 50% probability level. Hydrogen atoms and lattice toluene are omitted for clarity. Selected interatomic distances are listed in Table 1 (paper).
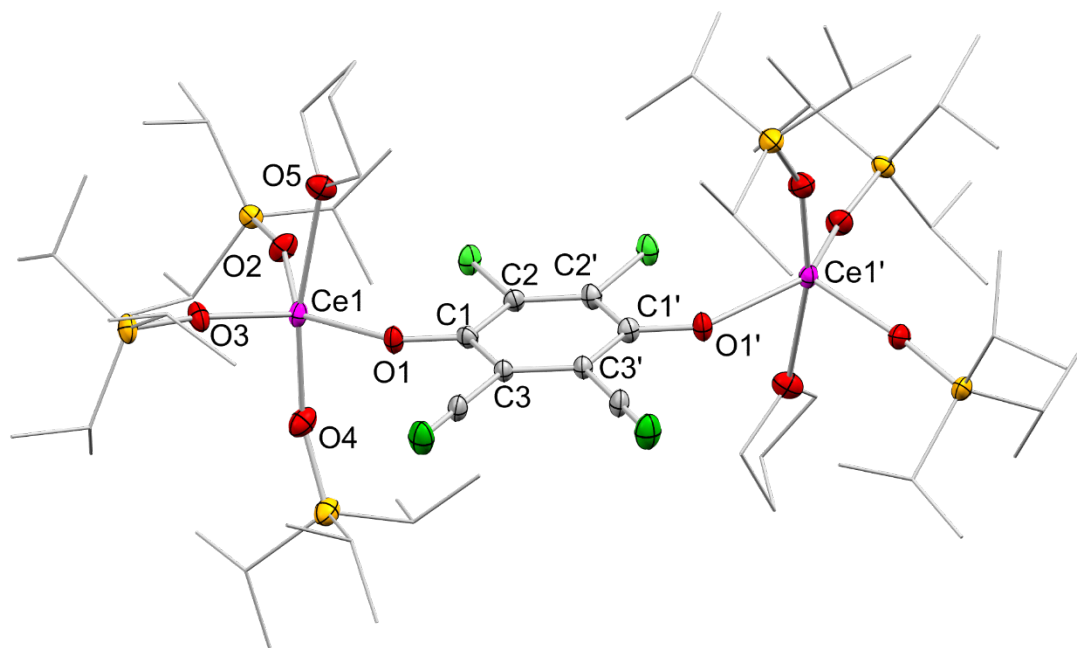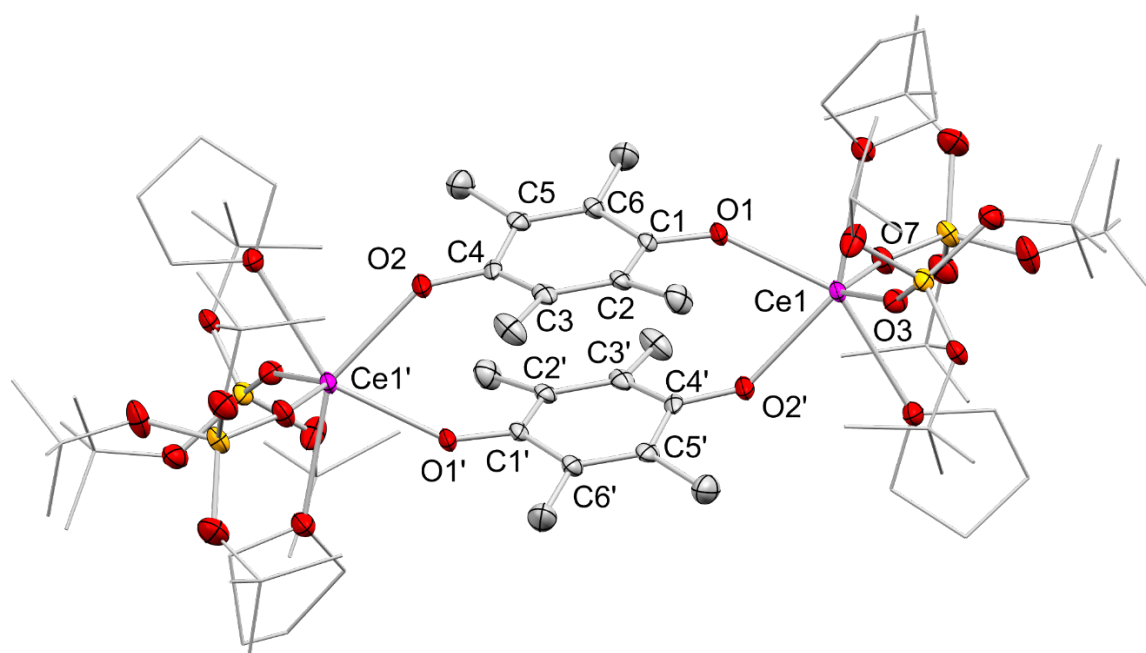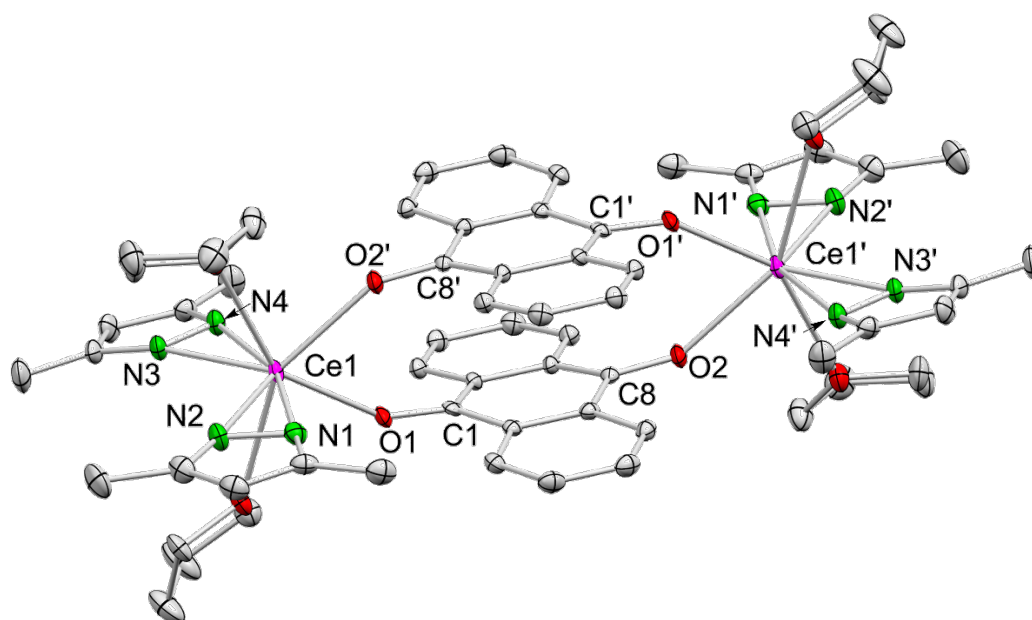

Figure S75. Crystal structure of [Ce{N(SiMe$_3$)$_2$}$_3$]$_2$(μ_2-O$_2$C$_6$tBu$_2$H$_2$) (**4^{tBu2hq}**). Ellipsoids are shown at the 50% probability level. Hydrogen atoms and lattice toluene are omitted for clarity. Selected interatomic distances are given in Table 1 (paper).

Figure S76. Connectivity of [Ce{N(SiMe$_3$)$_2$}$_3$]$_2$(μ_2-O$_2$C$_6$$tBu_2H_2$) (**4^{nhq}**). Hydrogen atoms and disordered atoms are omitted for clarity.
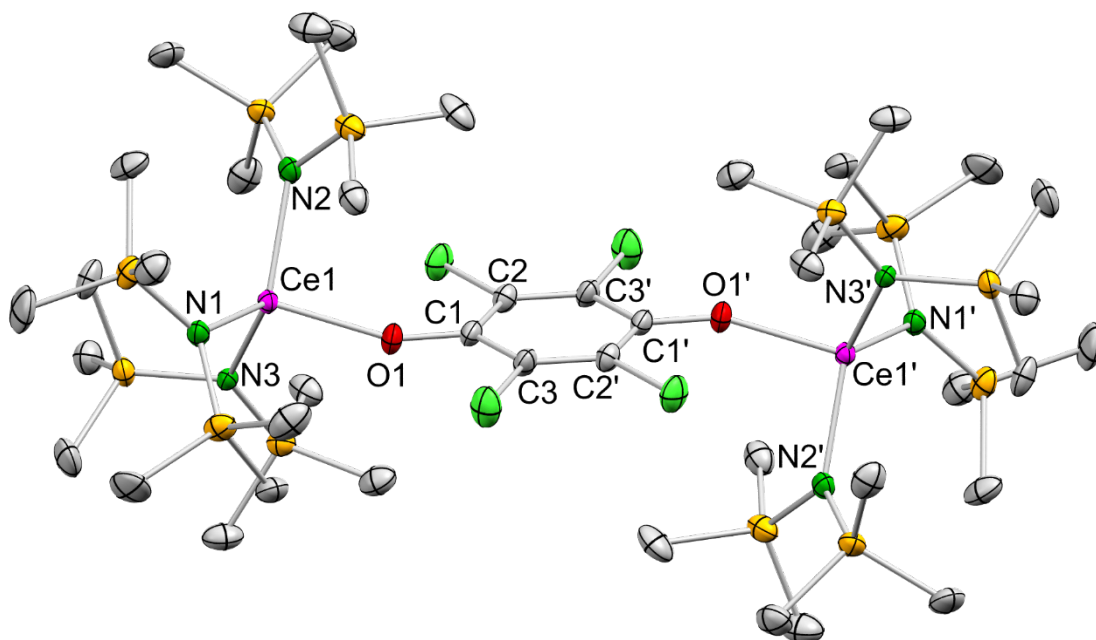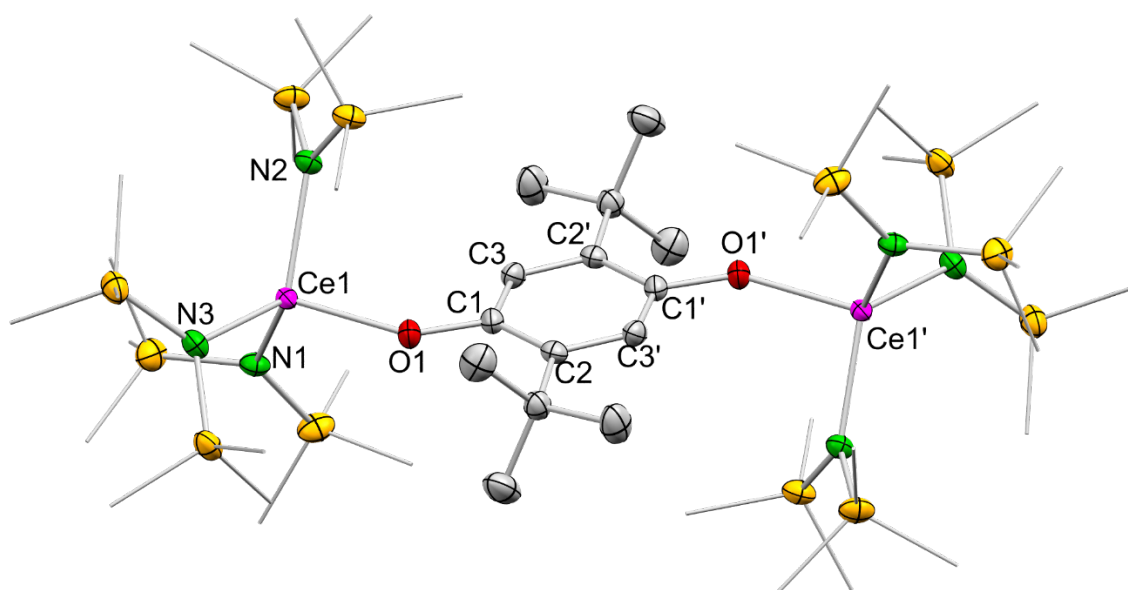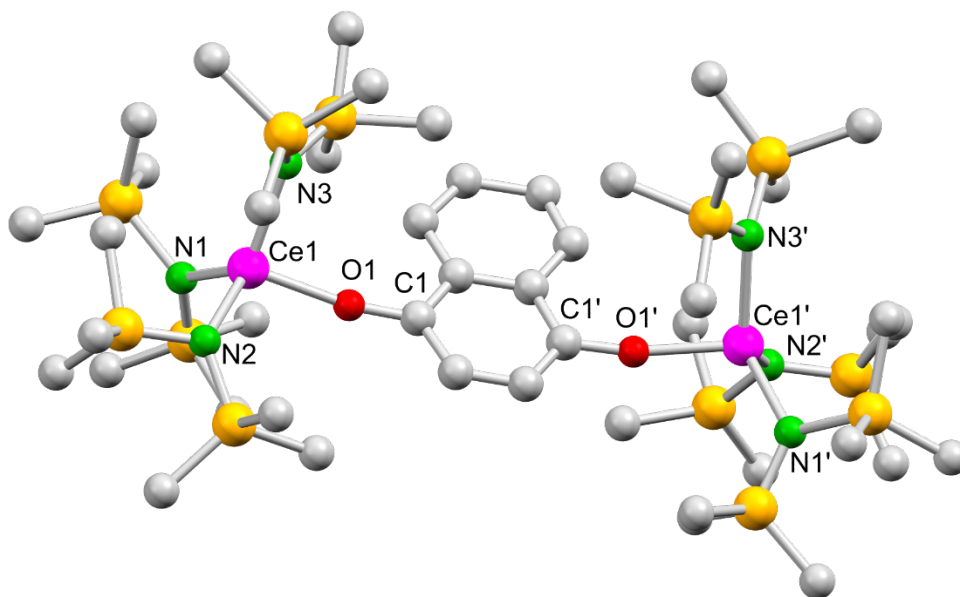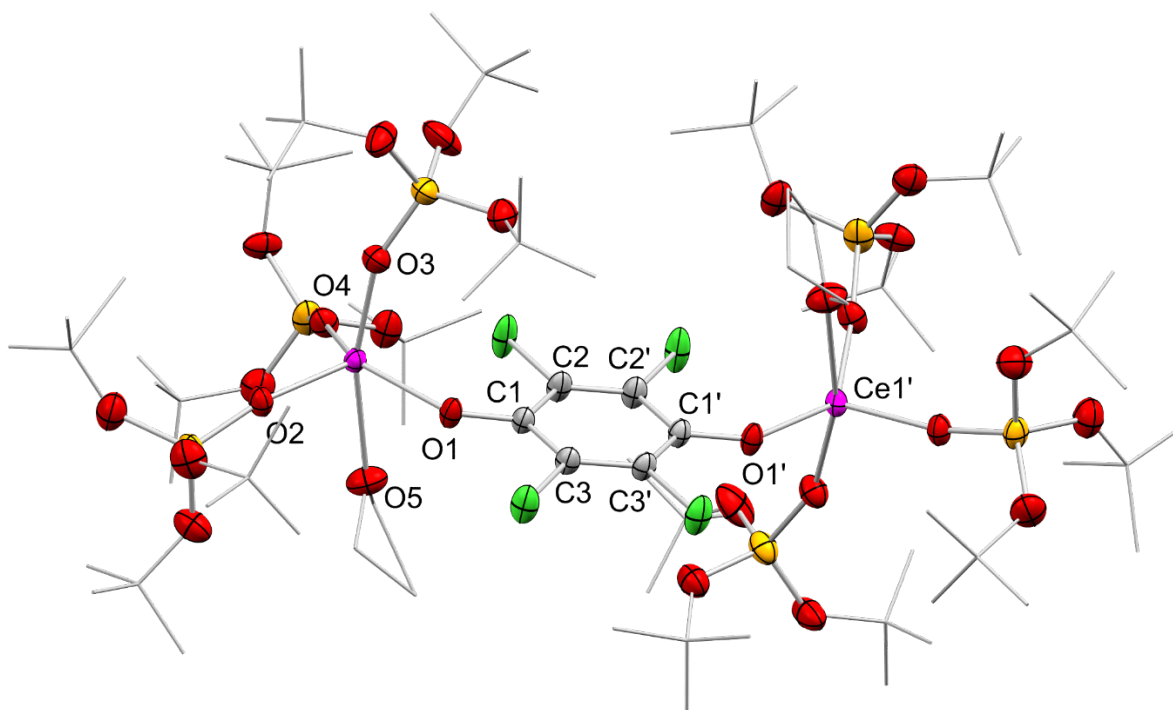
Figure S77. Crystal structure of [Ce{OSi(OtBu)$_3$}$_3$(thf)]$_2$(μ_2-O$_2$C$_6$Cl$_4$) (**5^{Cl4hq}**). Ellipsoids are shown at the 50% probability level. Hydrogen atoms and lattice THF are omitted for clarity. Selected interatomic distances are listed in Table 1 (paper).

Figure S78. Crystal structure of [Ce(OSi*i*Pr$_3$)$_3$(thf)]$_2$(μ_2-O$_2$C$_6$Cl$_2$(CN)$_2$) (**6^{ddhq}**). Ellipsoids are shown at the 50% probability level. Hydrogen atoms and lattice THF are omitted for clarity. Selected interatomic distances are given in Table 1 (paper).

Figure S79. Crystal structure of [Ce{OSi(O*t*Bu)$_3$}$_2$(thf)$_2$(μ_2-O$_2$C$_6$Me$_4$)]$_2$ (**8**). Ellipsoids are shown at the 50% probability level. Hydrogen atoms and lattice THF are omitted for clarity. Selected interatomic distances [Å]: Ce1–O1 2.370(3), Ce1–O2 2.382(3), Ce1–O3 2.235(3), Ce1–O7 2.249(3), Ce1–O12 2.571(3), Ce1–O11 2.579(3),C1–O1 1.285(6), C4–O2 1.286(6), C1–C2 1.436(7), C1–C6 1.440(7), C2–C3 1.379(7), C3–C4 1.437(7), C4–C5 1.442(7), C5–C6 1.360(7).
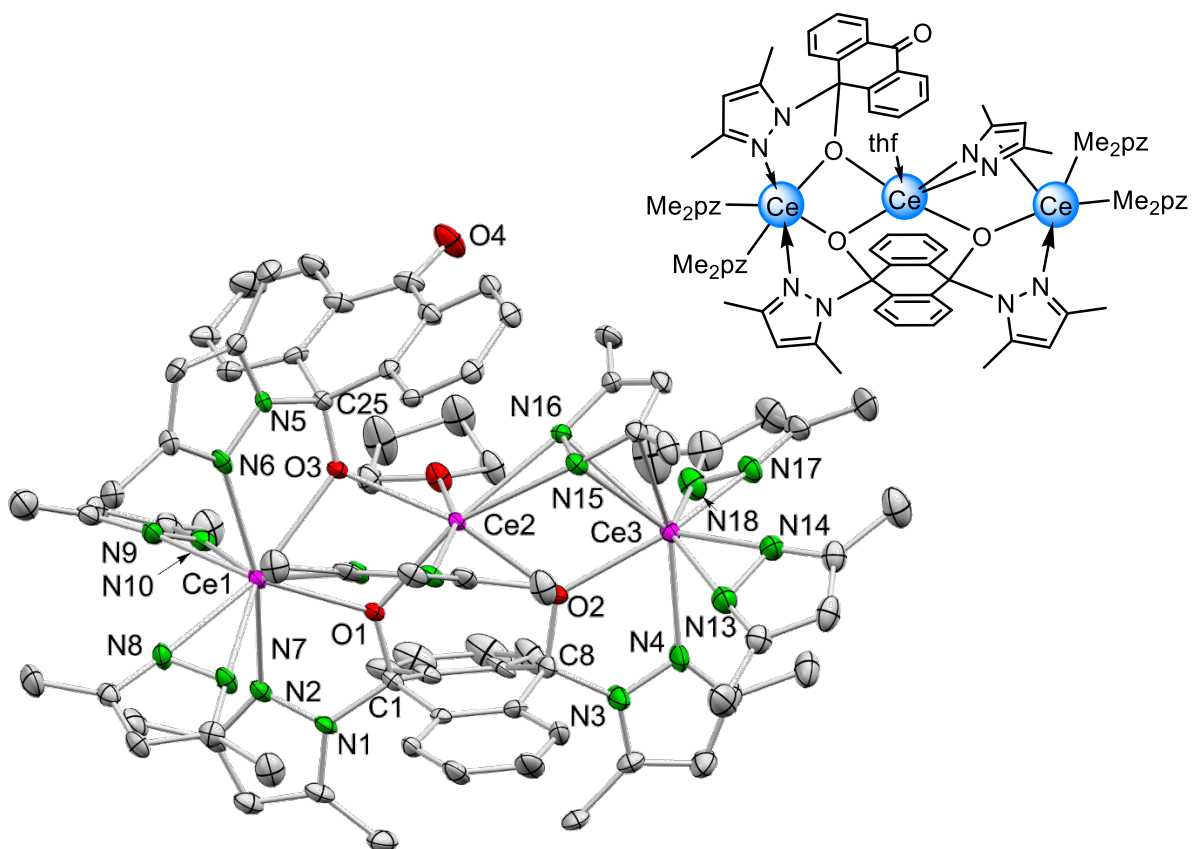
Figure S80. Crystal structure and structural representation of **[Ce₃(bpad)(pasq)(Me₂pz)₆(thf)]**. Ellipsoids are shown at the 50% probability level. Hydrogen atoms, lattice toluene and disordered atoms are omitted for clarity. Selected interatomic distances [Å]: Ce1–O1 2.488(3), Ce1–O3 2.532(2), Ce2–O1 2.379(2), Ce2–O2 2.495(3), Ce2–O3 2.421(3), Ce3–O2 2.429(3).

Figure S81. Crystal structure of **[Ce(Me₂pz)₂(thf)₂(asq)]₂**. Ellipsoids are shown at the 50% probability level. Hydrogen atoms, lattice THF and a second molecule are omitted for clarity. Selected interatomic distances [Å]: Ce1–O1 2.368(2), Ce1–O2' 2.365(2), Ce1–N1 2.510(2), Ce1–N2 2.462(3), Ce1–N3 2.468(2), Ce1–N4 2.504(2).
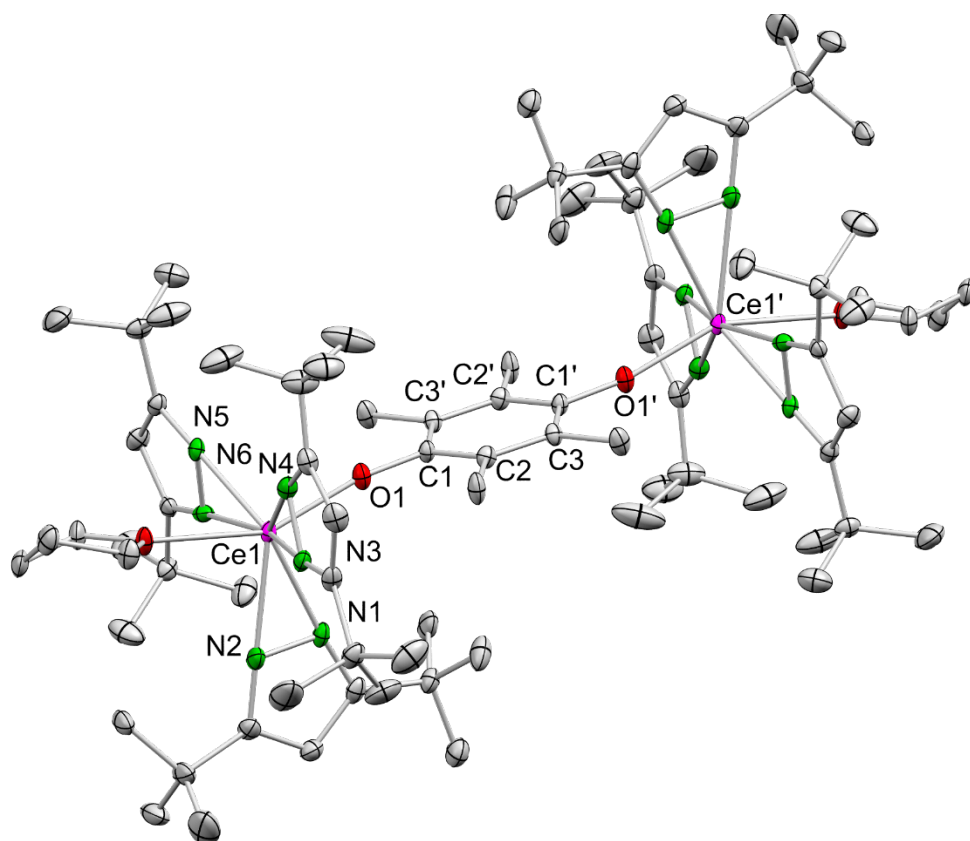
Figure S82. Crystal structure of and **[Ce(*t*Bu₂pz)₃]₂(*μ₂*-O₂C₆Me₄)**. Ellipsoids are shown at the 50% probability level. Hydrogen atoms and disordered atoms are omitted for clarity. Selected interatomic distances [Å]: Ce1–O1 2.076(2), Ce1–N1 2.339(3), Ce1–N2 2.408(3), Ce1–N3 2.377(3), Ce1–N4 2.409(3), Ce1–N5 2.412(3), Ce1–N6 2.362(3), C1–O1 1.357(4) C1–C2 1.409(5), C2–C3 1.391(5), C1–C3' 1.406(5).

References

1   P. B. Hitchcock, A. G. Hulkes, M. F. Lappert and Z. Li, *Dalton Trans.*, 2004, 129–136.
2   J. Friedrich, C. Maichle-Mössmer and R. Anwander, *Chem. Commun.*, 2017, **53**, 12044–12047.
3   D. Werner, G. B. Deacon, P. C. Junk and R. Anwander, *Chem. - Eur. J.*, 2014, **20**, 4426–4438.
4   D. Werner, U. Bayer, N. E. Rad, P. C. Junk, G. B. Deacon and R. Anwander, *Dalton Trans.*, 2018, **47**, 5952–5955.
5   R. K. Thomson, B. L. Scott, D. E. Morris and J. L. Kiplinger, *Comptes Rendus Chim.*, 2010, **13**, 790–802.
6   G. R. Fulmer, A. J. M. Miller, N. H. Sherden, H. E. Gottlieb, A. Nudelman, B. M. Stoltz, J. E. Bercaw and K. I. Goldberg, *Organometallics*, 2010, **29**, 2176–2179.
7   D. F. Evans, *J. Chem. Soc. Resumed*, 1959, 2003–2005.
8   Weast, R.C., *Handbook of Chemistry and Physics.*, CRC Press Inc, Boca Raton, Florida, 60th edn., 1979.
9   *COSMO, v. 1.61*, Bruker AXS Inc., Madiso, Wi, 2012.
10   *APEX 3, v. 2016.5-0*, Bruker AXS Inc., Madison, Wi, 2012.
11   *Saint, v. 8.34A*, Bruker AXS Inc., Madison, Wi, 2012.
12   L. Krause, R. Herbst-Irmer, G. M. Sheldrick and D. Stalke, *J. Appl. Crystallogr.*, 2015, **48**, 3–10.
13   G. M. Sheldrick, *Acta Crystallogr. Sect. Found. Adv.*, 2015, **71**, 3–8.
14   O. V. Dolomanov, L. J. Bourhis, R. J. Gildea, J. a. K. Howard and H. Puschmann, *J. Appl. Crystallogr.*, 2009, **42**, 339–341.
15   D. Kratzert, J. J. Holstein and I. Krossing, *J. Appl. Crystallogr.*, 2015, **48**, 933–938.
16   C. F. Macrae, I. J. Bruno, J. A. Chisholm, P. R. Edgington, P. McCabe, E. Pidcock, L. Rodriguez-Monge, R. Taylor, J. van de Streek and P. A. Wood, *J. Appl. Crystallogr.*, 2008, **41**, 466–470.
17   A. I. Spek, *Acta Crystallogr. Sect. C*, 2015, **71**, 9–18.

F

Appendix

Appendix

Analytical data of compounds not included in the main results or manuscripts

CeCl$_3$*
+
4 Li(NPh$_2$)
$\xrightarrow[\text{rt, 24 h}]{\text{benzene}}$
[Ce(NPh$_2$)$_4$][Li(thf)$_4$]
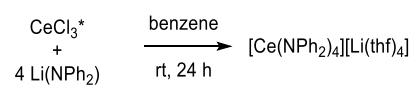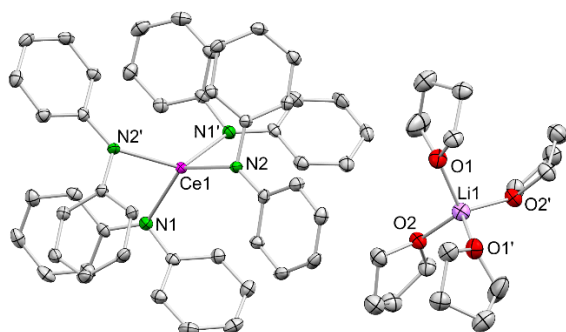
[Ce(NPh$_2$)$_4$][Li(thf)$_4$] UB179

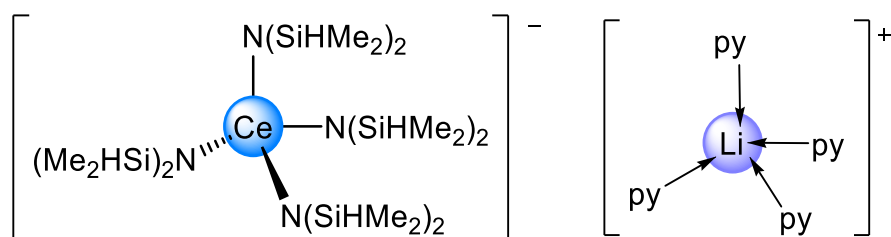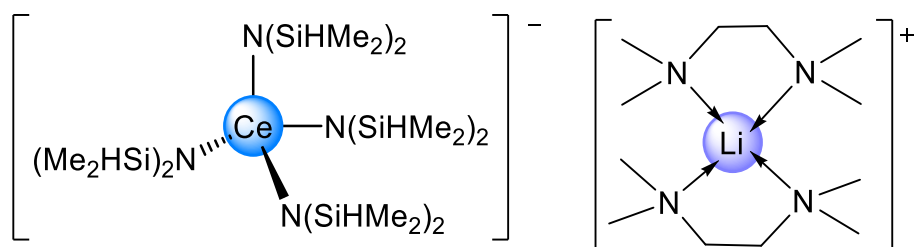R$_1$[I>sigma(I)] 2.99%, wR$_2$(all data) 7.87%
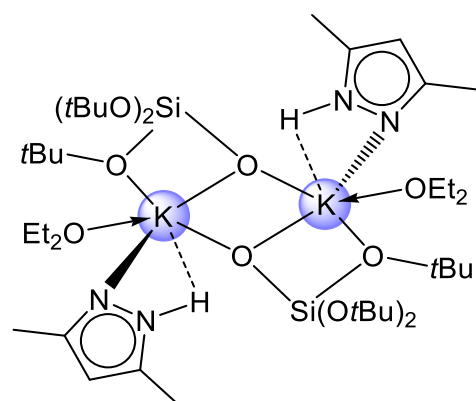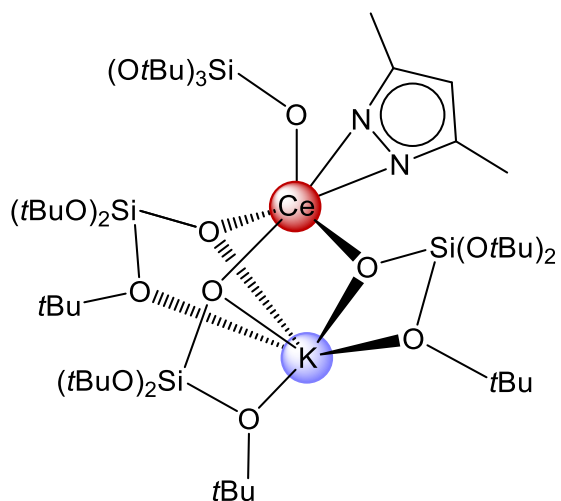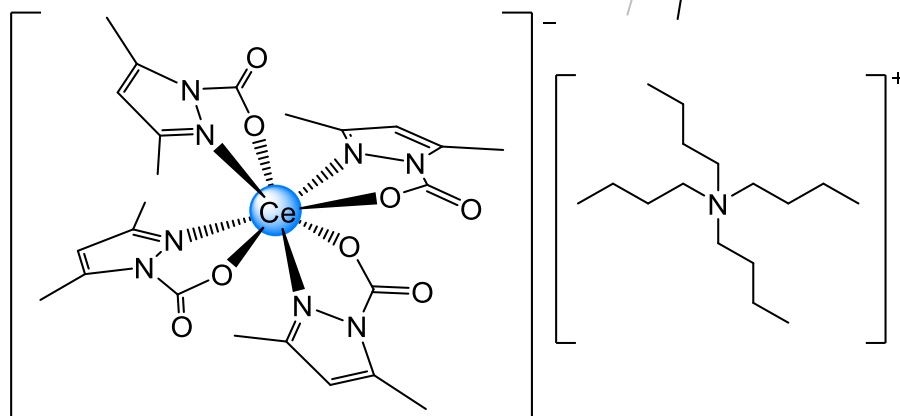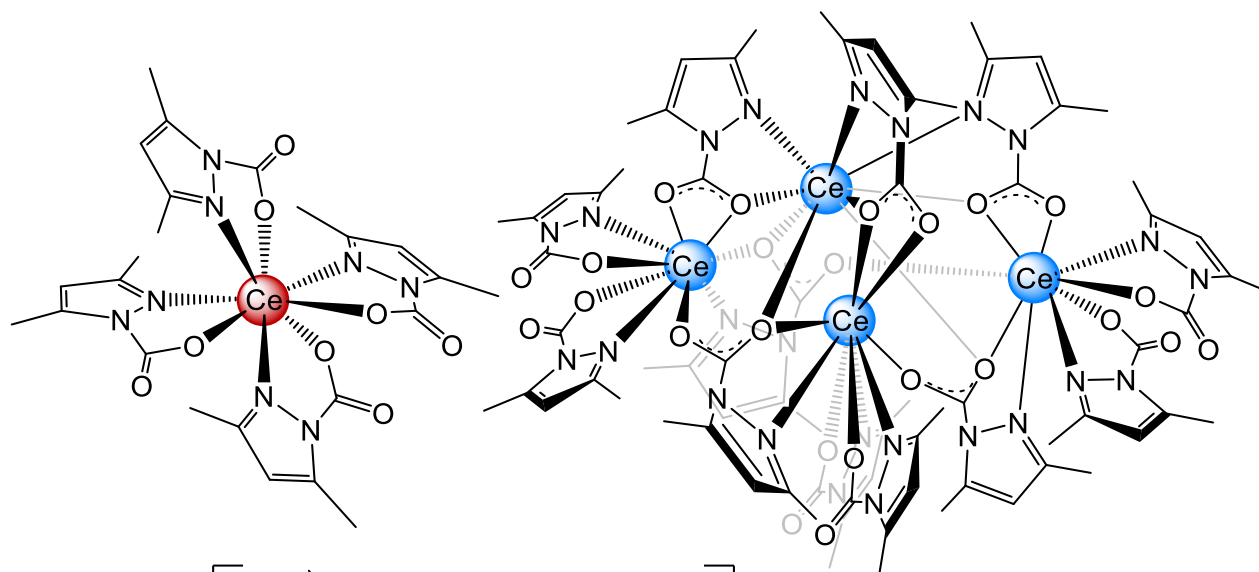
a = 17.3949(8) Å, α = 90°

b = 15.5618(7) Å, β = 90°

c = 20.1106(9) Å, γ = 90°

Structurally characterized complexes

On the following pages all X-ray structurally characterized compounds are listed as *ChemDraw* sketches.

[Ce{N(SiHMe₂)₂}][Li(do)ₓ] type -ate-complexes
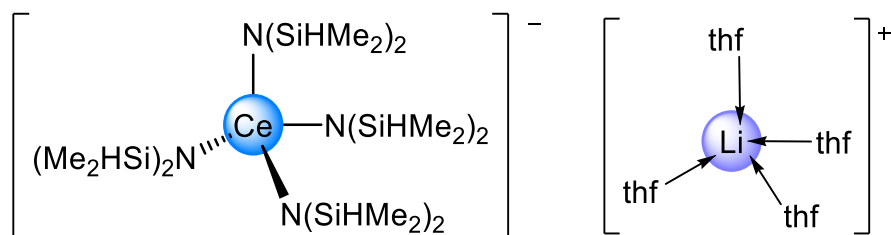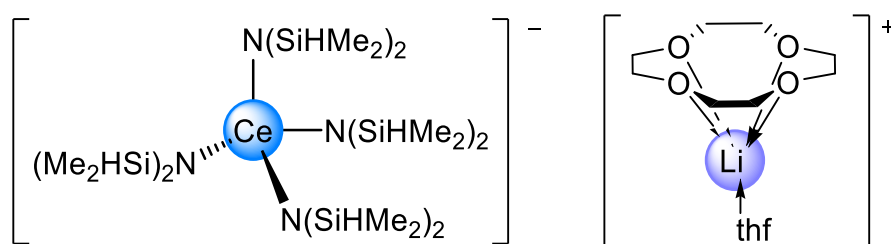
Cerium Dimethyl Pyrazolates for CO₂ Activation

Hydroquinolato bridged Ce^{IV} complexes

R = OSi(OtBu)$_3$ (x = 1)

R = N(SiMe$_3$)$_2$ (x = 0)
 OSi(OtBu)$_3$ (x = 1)
 OSiiPr$_3$ (x = 1)

R = OSiiPr$_3$ (x = 1)

R = N(SiMe$_3$)$_2$ (x = 0)
 OSiiPr$_3$ (x = 1)

R= N(SiMe$_3$)$_2$

R= OSi(OtBu)$_3$,
 OSiiPr$_3$
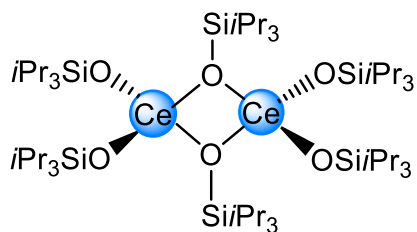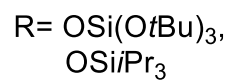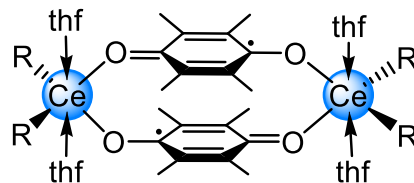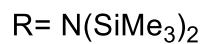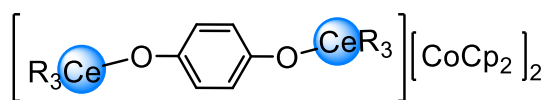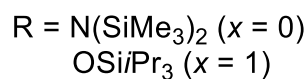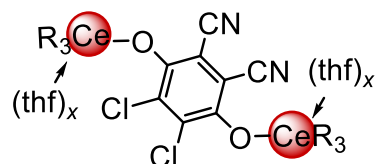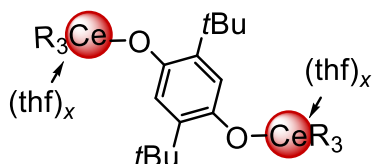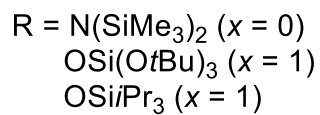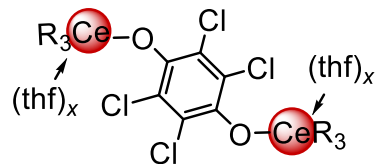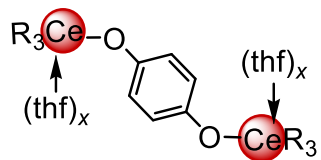
Cerium Pyrazoles and Pyrroles (unpublished)